

Pertanika Journal of

SCIENCE &

TECHNOLOGY

JST

VOL. 28 (2) APR. 2020



PERTANIKA
JOURNALS

A scientific journal published by Universiti Putra Malaysia Press

Journal of Science & Technology

About the Journal

Overview

Pertanika Journal of Science & Technology (JST) is the official journal of Universiti Putra Malaysia published by UPM Press. It is an open-access online scientific journal which is free of charge. It publishes the scientific outputs. It neither accepts nor commissions third party content.

Recognized internationally as the leading peer-reviewed interdisciplinary journal devoted to the publication of original papers, it serves as a forum for practical approaches to improving quality in issues pertaining to science and engineering and its related fields.

JST is a **quarterly** (January, April, July and October) periodical that considers for publication original articles as per its scope. The journal publishes in **English** and it is open to authors around the world regardless of the nationality.

The Journal is available world-wide.

Aims and scope

Pertanika Journal of Science and Technology aims to provide a forum for high quality research related to science and engineering research. Areas relevant to the scope of the journal include: bioinformatics, bioscience, biotechnology and bio-molecular sciences, chemistry, computer science, ecology, engineering, engineering design, environmental control and management, mathematics and statistics, medicine and health sciences, nanotechnology, physics, safety and emergency management, and related fields of study.

History

Pertanika was founded in 1978. A decision was made in 1992 to streamline Pertanika into three journals as Journal of Tropical Agricultural Science, Journal of Science & Technology, and Journal of Social Sciences & Humanities to meet the need for specialised journals in areas of study aligned with the interdisciplinary strengths of the university.

After almost 28 years, as an interdisciplinary Journal of Science & Technology, the revamped journal now focuses on research in science and engineering and its related fields.

Goal of *Pertanika*

Our goal is to bring the highest quality research to the widest possible audience.

Quality

We aim for excellence, sustained by a responsible and professional approach to journal publishing. Submissions are guaranteed to receive a decision within 14 weeks. The elapsed time from submission to publication for the articles averages 5-6 months.

Abstracting and indexing of *Pertanika*

The journal is indexed in SCOPUS (Elsevier), Clarivate-Emerging Sources Citation Index [ESCI (Web of Science)], EBSCO, DOAJ, Agricola, ASEAN CITATION INDEX [ISC], Microsoft Academic, Google Scholar, National Agricultural Science (NAL) and MyCite.

Future vision

We are continuously improving access to our journal archives, content, and research services. We have the drive to realise exciting new horizons that will benefit not only the academic community, but society itself.

Citing journal articles

The abbreviation for *Pertanika Journal of Science & Technology* is *Pertanika J. Sci. Technol.*

Publication policy

Pertanika policy prohibits an author from submitting the same manuscript for concurrent consideration by two or more publications. It prohibits as well publication of any manuscript that has already been published either in whole or substantial part elsewhere. It also does not permit publication of manuscript that has been published in full in Proceedings.

Code of Ethics

The *Pertanika* Journals and Universiti Putra Malaysia takes seriously the responsibility of all of its journal publications to reflect the highest in publication ethics. Thus all journals and journal editors are expected to abide by the Journal's codes of ethics. Refer to *Pertanika's Code of Ethics* for full details, or visit the Journal's web link at http://www.pertanika.upm.edu.my/code_of_ethics.php

International Standard Serial Number (ISSN)

An ISSN is an 8-digit code used to identify periodicals such as journals of all kinds and on all media—print and electronic. All *Pertanika* journals have ISSN as well as an e-ISSN.

Journal of Science & Technology: ISSN 0128-7680 (*Print*); ISSN 2231-8526 (*Online*).

Lag time

A decision on acceptance or rejection of a manuscript is reached in 3 to 4 months (average 14 weeks). The elapsed time from submission to publication for the articles averages 5-6 months.

Authorship

Authors are not permitted to add or remove any names from the authorship provided at the time of initial submission without the consent of the Journal's Chief Executive Editor.

Manuscript preparation

Refer to *Pertanika's INSTRUCTIONS TO AUTHORS* at the back of this journal.

Editorial process

Authors are notified with an acknowledgement containing a *Manuscript ID* on receipt of a manuscript, and upon the editorial decision regarding publication.

Pertanika follows a **double-blind peer-review** process. Manuscripts deemed suitable for publication are usually sent to reviewers. Authors are encouraged to suggest names of at least three potential reviewers at the time of submission of their manuscript to *Pertanika*, but the editors will make the final choice. The editors are not, however, bound by these suggestions.

Notification of the editorial decision is usually provided within ten to fourteen weeks from the receipt of manuscript. Publication of solicited manuscripts is not guaranteed. In most cases, manuscripts are accepted conditionally, pending an author's revision of the material.

The Journal's peer-review

In the peer-review process, three referees independently evaluate the scientific quality of the submitted manuscripts.

Peer reviewers are experts chosen by journal editors to provide written assessment of the **strengths** and **weaknesses** of written research, with the aim of improving the reporting of research and identifying the most appropriate and highest quality material for the journal.

Operating and review process

What happens to a manuscript once it is submitted to *Pertanika*? Typically, there are seven steps to the editorial review process:

1. The Journal's Chief Executive Editor (CEE) and the Editorial Board Members (EBMs) examine the paper to determine whether it is appropriate for the journal and should be reviewed. If not appropriate, the manuscript is rejected outright and the author is informed.
2. The CEE sends the article-identifying information having been removed, to three reviewers who are specialists in the subject matter represented by the article. The CEE requests them to complete the review in three weeks.

Comments to authors are about the appropriateness and adequacy of the theoretical or conceptual framework, literature review, method, results and discussion, and conclusions. Reviewers often include suggestions for strengthening of the manuscript. Comments to the editor are in the nature of the significance of the work and its potential contribution to the field.

3. The CEE, in consultation with the Editor-in-Chief (EiC), examines the reviews and decides whether to reject the manuscript, invites the author(s) to revise and resubmit the manuscript. The CEE may seek additional reviews. Final acceptance or rejection rests with the CEE and EiC, who reserve the right to refuse any material for publication. In rare instances, the manuscript is accepted with almost no revision. Almost without exception, reviewers' comments (to the author) are forwarded to the author. If a revision is indicated, the editor provides guidelines for attending to the reviewers' suggestions and perhaps additional advice about revising the manuscript.
4. The authors decide whether and how to address the reviewers' comments and criticisms and the editor's concerns. The authors return a revised version of the paper to the chief executive editor along with specific information describing how they have answered' the concerns of the reviewers and the editor, usually in a tabular form. The author(s) may also submit a rebuttal if there is a need especially when the author disagrees with certain comments provided by reviewer(s).
5. The CEE sends the revised paper out for re-review. Typically, at least one of the original reviewers will be asked to examine the article.
6. When the reviewers have completed their work, the CEE in consultation with the EiC and EBMs examine their comments and decide whether the paper is ready to be published, needs another round of revisions, or should be rejected.
7. If the decision is to accept, an acceptance letter is sent to all the author(s), the paper is sent to the Press. The article should appear online in approximately three months.

The Publisher ensures that the paper adheres to the correct style (in-text citations, the reference list, and tables are typical areas of concern, clarity, and grammar). The authors are asked to respond to any minor queries by the Publisher. Following these corrections, page proofs are mailed to the corresponding authors for their final approval. At this point, **only essential changes are accepted**. Finally, the article appears in the pages of the Journal and is posted online.

Pertanika Journal of
**SCIENCE
& TECHNOLOGY**

Vol. 28 (2) Apr. 2020



A scientific journal published by Universiti Putra Malaysia Press



EDITOR-IN-CHIEF

Luqman Chuah Abdullah

Chemical Engineering

CHIEF EXECUTIVE EDITOR

Abu Bakar Salleh

Biotechnology and Biomolecular Science

CHAIRMAN

UNIVERSITY PUBLICATIONS
COMMITTEE

Zulkifli Idrus

EDITORIAL STAFF

Journal Officers:

Kanagamalar Silvarajoo, *ScholarOne*

Siti Zuhaila Abd Wahid, *ScholarOne*

Tee Syin-Ying, *ScholarOne*

Ummi Fairuz Hanapi, *ScholarOne*

Editorial Assistants:

Siti Juridah Mat Arip

Zulinaardawati Kamarudin

PRODUCTION STAFF

Pre-press Officers:

Nur Farrah Dila Ismail

Wong Lih Jiun

WEBMASTER

IT Officer:

To be appointed

PUBLICITY & PRESS RELEASE

Magdalene Pokar (*ResearchSEA*)

EDITORIAL OFFICE

JOURNAL DIVISION

Office of the Deputy Vice Chancellor (R&I)

1st Floor, IDEA Tower II

UPM-MTDC Technology Centre

Universiti Putra Malaysia

43400 Serdang, Selangor Malaysia.

Gen Enq.: +603 9769 1622 | 1616

E-mail:

executive_editor.pertanika@upm.edu.my

URL: www.journals-ij.upm.edu.my

PUBLISHER

UPM Press

Universiti Putra Malaysia

43400 UPM, Serdang, Selangor, Malaysia.

Tel: +603 9769 8851

E-mail: penerbit@putra.upm.edu.my

URL: <http://penerbit.upm.edu.my>



EDITORIAL BOARD

2018-2020

Adem Kilicman

Mathematical Sciences
Universiti Putra Malaysia, Malaysia.

Ali A. Moosavi-Movahedi

Biophysical Chemistry
University of Tehran, Tehran, Iran.

Amu Therwath

Oncology, Molecular Biology,
Université Paris, France.

Angelina Chin

Mathematics, Group Theory and
Generalisations, Ring Theory,
University of Malaya, Malaysia.

Bassim H. Hameed

Chemical Engineering: Reaction
Engineering, Environmental Catalysis
& Adsorption,
Universiti Sains Malaysia, Malaysia.

Biswa Mohan Biswal

Medical, Clinical Oncology,
Radiotherapy
Universiti Sains Malaysia, Malaysia.

Christopher G. Jesudason

Mathematical Chemistry, Molecular
Dynamics Simulations, Thermodynamics
and General Physical Theory,
University of Malaya, Malaysia.

Hari M. Srivastava

Mathematics and Statistics,
University of Victoria, Canada.

Ivan D. Rukhlenko

Nonlinear Optics, Silicon Photonics,
Plasmonics and Nanotechnology
Monash University, Australia.

Kaniraj R. Shenbaga

Geotechnical Engineering,
India.

Kanury Rao

Senior Scientist & Head, Immunology
Group, International Center for Genetic
Engineering and Biotechnology,
Immunology, Infectious Disease Biology
and System Biology
International Centre for Genetic
Engineering & Biotechnology, New
Delhi, India.

INTERNATIONAL ADVISORY BOARD

2018-2021

Adarsh Sandhu

Editorial Consultant for Nature
Nanotechnology and Contributing
Writer for Nature Photonics, Physics,
Magneto-resistive Semiconducting
Magnetic Field Sensors, Nano-
Bio-Magnetism, Magnetic Particle
Colloids, Point of Care Diagnostics,
Medical Physics, Scanning Hall Probe
Microscopy, Synthesis and Application
of Graphene
Electronics-Inspired Interdisciplinary
Research Institute (EIIRIS), Toyohashi
University of Technology, Japan.

Graham Megson

Computer Science
The University of Westminster, U.K.

Kuan-Chong Ting

Agricultural and Biological Engineering
University of Illinois at Urbana-
Champaign, USA.

Ki-Hyung Kim

Computer and Wireless Sensor
Networks
AJOU University, Korea.

Kunnawee Kanitpong

Transportation Engineering-Road
Traffic Safety, Highway Materials and
Construction
Asian Institute of Technology, Thailand.

Megat Mohd Hamdan

Megat Ahmad
Mechanical and Manufacturing
Engineering
Universiti Pertahanan Nasional
Malaysia, Malaysia.

Mirnalini Kandiah

Public Health Nutrition, Nutritional
Epidemiology
UCSI University, Malaysia.

Mohamed Othman

Communication Technology and
Network, Scientific Computing
Universiti Putra Malaysia, Malaysia

Mohd. Ali Hassan

Bioprocess Engineering, Environmental
Biotechnology
Universiti Putra Malaysia, Malaysia.

Mohd Sapuan Salit

Concurrent Engineering and Composite
Materials
Universiti Putra Malaysia, Malaysia.

Narongrit Sombatsompop

Engineering & Technology: Materials
and Polymer Research
King Mongkut's University of
Technology Thonburi (KMUTT),
Thailand.

Prakash C. Sinha

Physical Oceanography, Mathematical
Modelling, Fluid Mechanics, Numerical
Techniques
Universiti Malaysia Terengganu,
Malaysia.

Rajinder Singh

Biotechnology, Biomolecular Sciences,
Molecular Markers/ Genetic Mapping
Malaysia Palm Oil Board, Kajang,
Malaysia.

Renuganth Varatharajoo

Engineering, Space System
Universiti Putra Malaysia, Malaysia.

Riyanto T. Bambang

Electrical Engineering, Control,
Intelligent Systems & Robotics
Bandung Institute of Technology,
Indonesia.

Roslani Abd-Shukur

Physics & Materials Physics,
Superconducting Materials
Universiti Kebangsaan Malaysia,
Malaysia.

Sabira Khatun

Engineering, Computer Systems
& Software Engineering, Applied
Mathematics
Universiti Malaysia Pahang, Malaysia.

Shiv Dutt Gupta

Director, IHMR, Health Management,
Public Health, Epidemiology, Chronic
and Non-communicable Diseases
Indian Institute of Health Management
Research, India.

Suan-Choo Cheah

Biotechnology, Plant Molecular Biology
Asiatic Centre for Genome Technology
(ACGT), Kuala Lumpur, Malaysia.

Wagar Asrar

Engineering, Computational Fluid
Dynamics, Experimental Aerodynamics
International Islamic University,
Malaysia.

Wing Keong Ng

Aquaculture, Aquatic Animal Nutrition,
Aqua Feed Technology
Universiti Sains Malaysia, Malaysia.

Yudi Samudya

Chemical Engineering, Advanced
Process Engineering
Curtin University of Technology,
Malaysia.

ABSTRACTING AND INDEXING OF PERTANIKAJOURNALS

Pertanika is over 40 years old; this accumulated knowledge has resulted in the journals being abstracted and indexed in SCOPUS (Elsevier), Clarivate-Emerging Sources Citation Index [ESCI (Web of Science)], EBSCO, DOAJ, Agricola, ASEAN CITATION INDEX [ISC], Microsoft Academic, Google Scholar, National Agricultural Science (NAL) and MyCite.

The publisher of Pertanika will not be responsible for the statements made by the authors in any articles published in the journal. Under no circumstances will the publisher of this publication be liable for any loss or damage caused by your reliance on the advice, opinion or information obtained either explicitly or implied through the contents of this publication.

All rights of reproduction are reserved in respect of all papers, articles, illustrations, related materials, published in Pertanika. Pertanika provides free access to the full text of research articles for anyone, web-wide. It does not charge either its authors or author-institution for refereeing/publishing outgoing articles or user-institution for accessing incoming articles.

No material published in Pertanika may be reproduced or stored on microfilm or in electronic, optical or magnetic form without the written authorization of the Publisher.

Copyright © 2019 Universiti Putra Malaysia Press. All Rights Reserved.



Pertanika Journal of Science & Technology
Vol. 28 (2) Apr. 2020

Contents

Foreword <i>Abu Bakar Salleh</i>	i
Engineering Sciences	
Remote Sensing of Seagrass and Seabed using Acoustic Technology in Bintan Seawater, Indonesia <i>Henry Munandar Manik and Dony Apdillah</i>	421
Time Frequency Analysis of Peking Gamelan <i>Sinin Hamdan, Iran Amri Musoddiq, Ahmad Fauzi Musib and Marini Sawawi</i>	441
Timbre Spectrum of Gamelan Instruments from Four Malay Gamelan Ensembles <i>Sinin Hamdan, Ahmad Faudzi Musib, Iran Amri Musoddiq and Marini Sawawi</i>	459
Support Vector Machine Classification Method for Predicting Jakarta Bay Bottom Sediment Type Using Multibeam Echosounder Data <i>Steven Solikin, Henry Munandar Manik, Sri Pujiyati and Susilohadi</i>	477
System Identification of Helical Strakes Suppressed Vortex-induced Vibration for Flexible Pipes <i>Ching Sheng Ooi, Meng Hee Lim, Kee Quen Lee, Hooi Siang Kang and Mohd Salman Leong</i>	493
Analysis of pH and Color of Fermented Cocoa (<i>Theobroma cacao</i> L) Beans using Response Surface Methodology <i>Sri Hartuti, Nursigit Bintoro, Joko Nugroho Wahyu Karyadi and Yudi Pranoto</i>	509
Experimental (ADV & PIV) and Numerical (CFD) Comparisons of 3D Flow Pattern around Intact and Damaged Bridge Piers <i>Ehsan Oveici, Omid Tayari and Navid Jalalkamali</i>	523
Mathematical Sciences	
Metaheuristics Approach for Maximum k Satisfiability in Restricted Neural Symbolic Integration <i>Saratha Sathasivam, Mustafa Mamat, Mohd Shareduwan Mohd Kasihmuddin and Mohd. Asyraf Mansor</i>	545

Instantaneous Speed Ratio of Traffic Flowing through a Merging Area at Kilometer 31.6 on the Highway from Shah Alam to Kuala Lumpur <i>Nur Syahirah Husin Basri, Nurul Akmal Mohamed, Muhammad Akram Adnan, Nurul Farihan Mohamed and Nurul Hila Zainuddin</i>	565
Scale-3 Haar Wavelets and Quasilinearization based Hybrid Technique for the Solution of Coupled Space-Time Fractional - Burgers' Equation <i>Geeta Arora, Ratesh Kumar and Harpreet Kaur</i>	579
Comparison of Sparse and Robust Regression Techniques in Efficient Model Selection for Moisture Ratio Removal of Seaweed using Solar Drier <i>Anam Javaid, Mohd. Tahir Ismail and Majid Khan Majahar Ali</i>	609
Effects on Parameter Estimates and Goodness of Fit Measures: Comparing Item-Level and Item-Parcel Models in Structural Equation Modeling <i>Ainur Amira Kamaruddin, Bee Wah Yap and Sayang Mohd Deni</i>	627
Medical and Health Sciences	
The Effect of Deep Breathing Exercises on Menstrual Pain Perception in Adolescents with Primary Dysmenorrhea <i>Kurniati Devi Purnamasari, Tita Rohita, Dini Nurbaeti Zen and Widya Maya Ningrum</i>	649
Effects of Prolonged Confined Isolation on Status of Inflammation, Endothelial Activation and Function: In Preparation for Possible Future Manned Space Expedition to Mars <i>Thuhairah Rahman, Radzi Ahmad, Suhaila Muid, Tengku Saifudin Tengku Ismail, Ludmila B Buravkova and Hapizah Nawawi</i>	659
Virulence Genes Detection among the Antibiotic Resistant <i>Enterococcus faecalis</i> Isolated from Bird Industry in Borneo <i>Sui Sien Leong, Samuel Lihan and Hwa Chuan Chia</i>	673
Comparison of Neurotoxic Effects of Ethanol and Endosulfan on Biochemical Changes of Brain Tissues in Javanese Medaka (<i>Oryzias javanicus</i>) and Zebrafish (<i>Danio rerio</i>) <i>Nurul Farhana Ramlan, Noraini Abu Bakar, Emmellie Laura Albert, Syaizwan Zahmir Zulkifli, Syahida Ahmad, Mohammad Noor Amal Azmai, Che Azurahaman Che Abdullah and Wan Norhamidah Wan Ibrahim</i>	689
Effect of Different Application Techniques on Marginal Adaptation of Class II Cavities Filled with Three Different Bulkfill Composite Filling Material: An <i>In Vitro</i> Study using Confocal Microscopy <i>Aulfat Ahmed Albahari, Mohammed Ahmed Dubais, Ahmed Abdullah Madfa and Waled Abdul Malek Alanesi</i>	703

Earth Sciences

- Comparison of Catches of Skipjack Tuna (*Katsuwonus pelamis* Linnaeus 1758) Purse Seines Inside and Outside of the FADs Areas 717
Achmar Mallawa

Environmental Sciences

- Comparison of Leaf Area Index from Four Plant Species on Vertical Greenery System in Pasir Gudang, Malaysia 735
Azmiah Abd Ghafar, Ismail Said, Amalina Mohd Fauzi, Mohd Shariman Shai-in and Badrulzaman Jaafar

Information, Computer and Communication Technologies

- Congestion Control in Implementing Multi Coding Schemes for Energy Optimisation in Wireless Sensor Networks 749
Samirah Nasuha Mohd Razali, Kamaruddin Mamat and Nor Shahniza Kamal Bashah



Foreword

Welcome to the Second Issue of 2020 for the Journal of Science and Technology (JST)!

JST is an open-access journal for studies in Science and Technology published by Universiti Putra Malaysia Press. It is independently owned and managed by the university for the benefit of the world-wide science community.

This issue contains 20 articles; all are regular articles. The authors of these articles come from different countries namely India, Indonesia, Iran, Iraq, Kingdom of Saudi Arabia, Malaysia, Pakistan and Russia.

Articles submitted in this issue cover various scopes of Science and Technology including environmental sciences; engineering sciences; information, computer and communication technologies; medical and health sciences; earth sciences; and mathematical sciences.

A regular article titled “The effect of deep breathing exercises on menstrual pain perception in adolescents with primary dysmenorrhea” was written by Kurniati Devi Purnamasari and colleagues from Universitas Galuh, Indonesia. Their results showed that breathing relaxation interventions have a tendency to be directly proportional to the reduction in the Visual Analogue Scale pain experienced by patients. Detailed information on this study can be found on page 649.

Thuhairah Rahman and co-researchers from Universiti Teknologi MARA had investigated the effects of prolonged confined isolation on status of inflammation, endothelial activation and function in preparation for possible future manned space expedition to Mars. Six crew members were exposed to prolonged, confined isolation for 520 days with standard exercise and diet regime throughout isolation phase. Percent change increment was observed in inflammation while percent change reduction was seen in endothelial activation. The enhanced inflammation and reduced endothelial function could possibly be attributed to the rigorous exercise instituted throughout the confinement period. Further details of the article are available on page 659.

The next article is on virulence genes detection among the antibiotic resistant *Enterococcus faecalis* isolated from bird industry in Borneo by Sui Sien Leong from Universiti Putra Malaysia (Bintulu Campus) and Universiti Malaysia Sarawak. *Enterococcus* bacteria showed a high prevalence in the faecal samples. The high incidence of virulence genes (*AS*, *ace*, *gelE*, *efaA*) indicates that these genes were widely disseminated among

the antibiotic resistance *E. faecalis* found in the birdhouses, suggesting the important issues in the pathogenesis of *E. faecalis* infection which may cause potential health risks to humans. Detailed information on this study is presented on page 673.

We anticipate that you will find the evidence presented in this issue to be intriguing, thought-provoking and useful in reaching new milestones in your own research. Please recommend the journal to your colleagues and students to make this endeavour meaningful.

All the papers published in this edition underwent Pertanika's stringent peer-review process involving a minimum of two reviewers comprising internal as well as external referees. This was to ensure that the quality of the papers justified the high ranking of the journal, which is renowned as a heavily-cited journal not only by authors and researchers in Malaysia but by those in other countries around the world as well.

We would also like to express our gratitude to all the contributors, namely the authors, reviewers, Editors-in-Chief and Editorial Board Members of JST and editors, who have made this issue possible.

JST is currently accepting manuscripts for upcoming issues based on original qualitative or quantitative research that opens new areas of inquiry and investigation.

Chief Executive Editor

Prof. Dato' Dr. Abu Bakar Salleh

executive_editor.pertanika@upm.edu.my

Remote Sensing of Seagrass and Seabed using Acoustic Technology in Bintan Seawater, Indonesia

Henry Munandar Manik^{1*} and Dony Apdillah²

¹Department of Marine Science and Technology, Faculty of Fisheries and Marine Sciences, IPB University (Bogor Agricultural University), 16680 Bogor, Indonesia

²Department of Marine Science, Faculty of Marine Science and Fisheries, Raja Ali Haji Maritime University, 29115 Tanjung Pinang, Indonesia

ABSTRACT

Seagrass were flowering plants that grow entirely under the sea. Seagrass were a significant element in coastal habitats such as Bintan waters because it acts as a protective beach. Seagrasses have the capacity to stabilize the bottom waters of sediments and were able to generate sediments that can fertilize the waters. Seagrass can be a reference in coastal area to improve the stability of the coastal environment. Seagrass beds are useful for a protected area for tiny organisms, a spawning location for aquatic biota, and a location for juvenile and larval enlargement. Distribution of seagrass abundance are essential to understand because they can define coastal regions whether they are harmed or not. Seagrass surveillance techniques were still using divers with restricted coverage of the study region. For this reason, an acoustic method was used through this research to detect seagrass and the habitats that it occupied. It can be concluded that the acoustic method can measure sound intensity or acoustic backscatter from seagrass and their habitat. The height of the seagrass can be evaluated depending on the acoustic reflection value of the seagrass. There were 3 seagrass groups based on percent closure in the research place, which were tiny to none of the seagrass groups, unusual seagrass groups, and many seagrass groups. Seagrass was mostly found in good sedimentary habitats. The increase in the quantity of manually calculated seagrass biomass was accompanied by a rise in the value of acoustic backscattering intensity. The overall accuracy of the seagrass species using the acoustic technique is 87%.

Keywords: Backscatter, biomass, hydroacoustics, seagrass

ARTICLE INFO

Article history:

Received: 25 June 2019

Accepted: 15 January 2020

Published: 15 April 2020

E-mail addresses:

henrymanik@ipb.ac.id (Henry Munandar Manik)

donyapdillah@gmail.com (Dony Apdillah)

* Corresponding author

INTRODUCTION

Seagrass is an important component in coastal habitat because it acts as a protector of beach. Seagrasses have the ability to stabilize basic water sediments and are able to produce sediments that are able to fertilize the waters. Seagrass can be a reference in strategic management of coastal areas to improve the stability of the coastal environment. Seagrass beds are a protected area for small organisms, a place for spawning aquatic biota, and a place for juvenile and larval enlargement. Distribution maps and abundance of seagrasses are important to know because they can indicate if coastal areas are damaged or not (Anderson et al., 2008).

Seagrass is an important component of nearshore ecosystems that supports many estuarine species, including a number of commercial fisheries (Ardizzone et al., 2006). The distribution of seagrasses is controlled by light availability, and also by several physical, geological and geochemical factors in the environment near the coast (Belzunce et al., 2005). Many habitat requirements for seagrass beds can be disrupted by human activities, and loss of seagrass habitats is often associated with anthropogenic causes (Bozzano et al., 1998). Damage to seagrass beds throughout the world has caused many government agencies and environmental groups to develop monitoring programs for this important coastal resource (Brouwer, 2008; Buia et al., 1992).

One innovation that is generally utilized as a device in evaluation and mapping of seagrasses is acoustic technology. The application of acoustic technology begins with its ability to detect fish, zooplankton, benthos and depth of water. With the development of information technology and material science, acoustic instruments can be used to detect oil and gas (Sidiq et al., 2019). Underwater acoustic methods for seabed mapping have been extensively developed over the past few decades. In particular, the development of bathymetry has enabled the creation of detailed maps of seabed topography and acoustic backscatter data; this data has been used to predict the type of sediment and habitat (Carbo & Molero, 1997). Several studies have compared backscatter responses to watershed types (examples of sampling, video images from the seabed) to assess the ability of different acoustic technologies to classify sea floor types (Di Maida et al., 2011; Duarte, 1987; Komatsu, 2007). Backscatter intensity is carried out through sound measurement to detect sediment and energy from sediments back to the transmitter with acoustic reflection and scattering. This has been shown to be related to the nature of sediments (Komatsu, 2007; Komatsu et al., 2003). The backscatter intensity of the muddy seabed has been shown to be inversely proportional to sediment porosity, percent sludge content and clay content percent.

Seagrass beds in Bintan for commercial species of penaeid shrimp and fish are significant nursery habitat. Seagrass is a major food for dugongs, dugongs (Miller) and green turtles, *Chelonia mydas* (Linnaeus) (Lefebvre et al., 2009) and acts as an absorber

of nutrients and sediments. Seagrasses play a significant role in preserving sediment stability and water clarity in coastal regions, linked to marine ecology, environmental, and also climate factors in the study area. Seagrass meadow is a significant economically and environmentally sound source. Management uses information on seagrass structure, abundance and distribution for seagrass protection areas.

It is therefore important to know accurate information about seagrass habitats (distribution, abundance and species composition), to determine the sampling design applied in surveys of seagrass habitats. Surveys that rely on diving-based operations are usually difficult to do in murky waters and over large areas. Dive based surveys also increase the safety risk of divers where there are attacks from dangerous marine animals. So that it needs a reliable remote sensing technique to observe seagrasses that will help reduce this risk and increase the intensity and resolution of the data collected.

Current remote sensing techniques (satellite imagery and aerial photography) are useful for mapping seagrass beds of dense habitat in clear waters in temperate climates, but in the tropics, they are inadequate to detect seagrasses with low biomass or turbid water. Recent advances in acoustic techniques for surveying benthic habitats indicate new possibilities for application in surveys of seagrass beds in the tropics. In this research an initial evaluation of acoustic techniques for surveying Bintan's tropical seagrass habitat and comparing this technique with diving-based survey methods will be used.

The acoustic or sonar method is an important tool in fisheries studies, mapping the types of seabed, underwater vegetation, sediments and sub-lower sediment types. Acoustic instruments are also used under water to look for sinking ships, airplanes and falling pipelines. The advantage of using acoustic waves is being able to propagate through visual media or other media to extract information in the marine environment. Acoustic signals are less absorbing than optic to turbidity or depth. Data collected at higher spatial resolutions and large areas can be surveyed quickly compared to diving-based surveys.

Management based on Marine Ecosystems

The acoustic scattering of seagrasses is poorly understood compared to rocks and sediments. Several studies have analyzed the acoustic response of different seagrass species to understand the mechanism of underlying physical scattering. Laboratory experiments have shown the speed of sound in resonators filled with plants to depend on plant biomass and tissue characteristics, which vary for different seagrass species (Maceina & Shireman, 1980; McCarthy & Sabol, 2000). The acoustic response of seagrass is also influenced by photosynthetic activity, which produces free gas bubbles in plant sand in the water column (Minami et al., 2010; Miner, 1993; Orłowski, 2009).

Aim

The aims of this research were:

1. to determine the feasibility of mapping tropical seagrass beds using an acoustic method.
2. to assess the efficacy of seagrass biomass acoustic methods.
3. to find out how acoustic survey techniques are effective in describing the kinds of seabed sediments.
4. to assess the efficiency of the mapping of tropical seagrass habitats using acoustic methods.

The expected results from the study were identification and classification of seagrass genera based on acoustic backscattering values. Another result is looking at the correlation of the seabed type based on the reflection coefficient value with seagrass habitat.

MATERIALS AND METHODS

In April-June 2018, surveys were performed at sea (Figure 1). Acoustic methods were surveyed in each region, followed by diving. The Garmin GPS was used for recording the position of each acoustic data point and for seagrasses and sediments sampling place. Positioning is a key element for the identification and mapping of seagrass. Acoustic data were used to analyze biomass and sediment information.

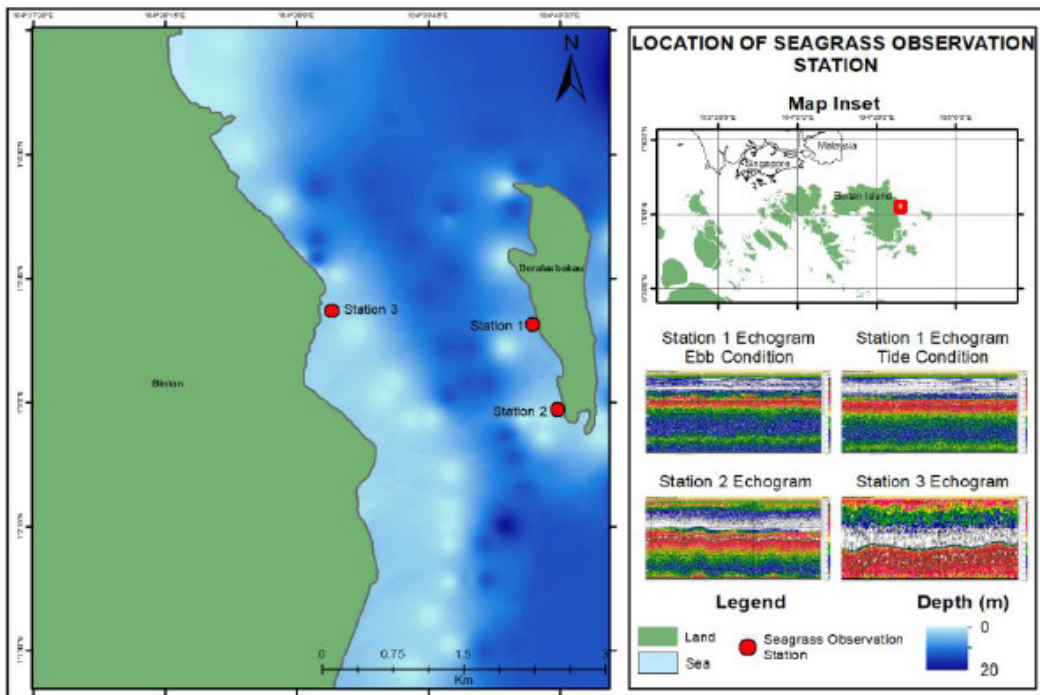


Figure 1. Research Location for Detection and Quantification of Seagrasses

This study gave an assessment of the acoustic methods used in the Bintan Island waters to map tropical seagrass habitats. Underwater acoustic method and visual estimation were used to detect seagrasses using diver. Underwater acoustic technology used in this research was Simrad EK15 single-beam echosounders. The acoustic transducer transmits one single vertical beam towards the seagrass and seafloor for determining the water depth. Acoustic data stored as a raw files integrated with GPS data with NMEA format. A part of the incident wave is backscattered in all directions and another part penetrates to the seabed. This backscattered energy is received by the transducer echosounder and used for depth and echo strength measurements. For this study the transducer was installed in a fixed position below the ship (Figure 2).

Dive-based surveys were conducted to check the parameters of seagrass beds on a good or wide spatial scale. Although this method is labor intensive, it provides qualitative and quantitative data. Qualitative information can be in the presence / absence, percent cover and / or composition of species. Quantitative data can include measurements of density or biomass, composition of species, growth characteristics of seagrass beds and depth distribution in certain locations. This survey method requires extensive field resources (labor and time) and involves increasing the risk of safety of divers where dangerous marine animals occur. Coupled with intensive dive seagrass data, acoustic remote sensing data can be used to map the distribution of seagrass communities with high densities over large areas.

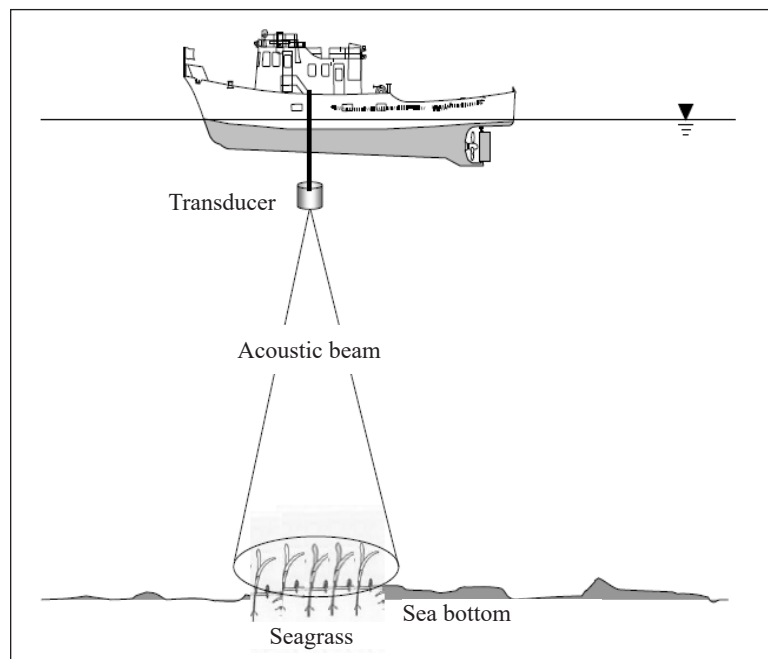


Figure 2. Equipment used in acoustic survey of seagrass

Calculation of Seagrass Biomass

Acoustic signal and images were produced by Matlab software. Quantification of acoustic signals were used to survey the biomass of seagrasses in each of the three locations. Acoustic echo received by the transducer is influenced by the density of seagrass.

Measurement of seagrass biomass, composition of seagrass species and sediment characteristics were calculated at each site surveyed. Divers recorded estimates of the amount of biomass of seagrasses. Seagrass species were identified according to previous research (Pasqualini et al., 2000). For seagrass data collection, seawater depth (bathymetry) and acoustic backscatter were the common data used. The positioning of seagrass is a vital component for vegetation mapping.

Measurement of Sediment Properties

The type of sediment is measured along the transect using a backscatter technique. Acoustic data and sediment sampling were collected simultaneously. Sediment samples were obtained from the survey area using a standard van veen grab. The grain size analysis was measured by sieving each sample through a series of standard nets. Percentage composition of dry weight was determined for each grain size category: gravel ($> 2000 \mu\text{m}$), coarse sand ($> 500 \mu\text{m}$), sand ($> 250 \mu\text{m}$), fine sand ($> 63 \mu\text{m}$) and mud ($< 63 \mu\text{m}$). The average size of the sediment grain for each sediment sample was calculated from the sediment composition data and each grain size class.

Calibration of Underwater Acoustic Instrumentation

The calibration of the acoustic instrument was conducted to measure the standard Target Strength value using a ball sphere with a frequency of 200 kHz. The target strength calibration results would be verified by theoretical acoustic sphere ball measurements. Calibration value would determine the level of accuracy of the instruments used such as the factor transmitting and receiving transducer, the speed of sound propagating in the water column and the noise factor. The configuration system for underwater acoustic instruments used was given in Figure 3.

Acoustic Data Collection and Processing in Bintan Waters

Research tools used include underwater acoustic instruments, sphere balls for calibration, underwater cameras, diving equipment, sediment samplers, global positioning systems (GPS), computer devices (Figure 4) and research vessels. Sea wave conditions when collecting data as shown were calm.

The installation and setup of the acoustic sensor (transducer) was placed on the left side of the ship and is lowered 1 meter below sea level (Figure 5) with a water depth of about 20 m.

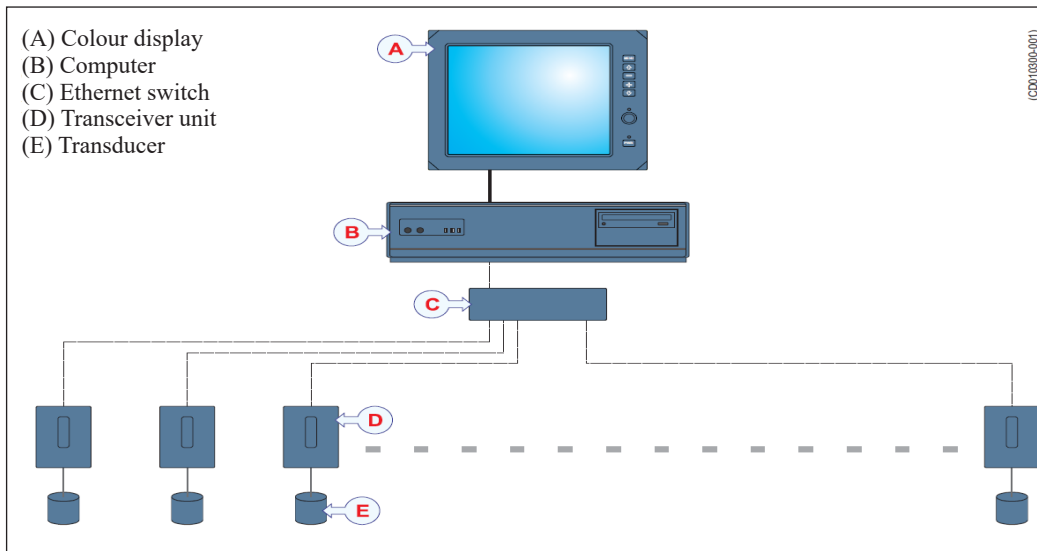


Figure 3. Configuration system of underwater acoustics instrument (Simrad manual)



Figure 4. Research vessel used during acoustic survey



Figure 5. Installation and set-up of underwater transducer

RESULTS

Seagrass Acoustic Instrument

The detection results of the seagrass acoustic instrument are shown in Figures 6, 7, 8 and 9. The value of the acoustic backscattering volume (SV) of seagrass at station 1 at low tide was -47.45 to -39.45 dB and the bottom SV was -25.26 to -12.74 dB (Figure 6). The average height of seagrass acoustically was 57 cm. At station 1 when the tide was obtained, the seagrass SV value was -47.45 to -39.45 dB while the watershed SV was -25.26 to -12.74 dB with an acoustic average seagrass height of 57 cm (Figure 7). At station 2 the seagrass SV values were -52.45 to -42.83 dB and the watershed SV values were -30.50 to -16.59 dB with an acoustic average seagrass height of 40.3 cm (Figure 8). At station 3 the seagrass

SV value was -49.27 to -35.73 dB and the SV of the water base was -31.62 to -23.47 dB with the average height of seagrass acoustically was 27.7 cm (Figure 9).

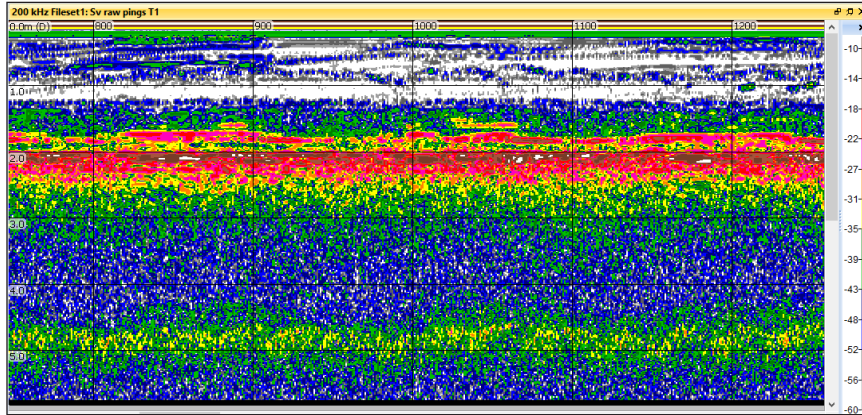


Figure 6. Seagrass detection during low tide using acoustics

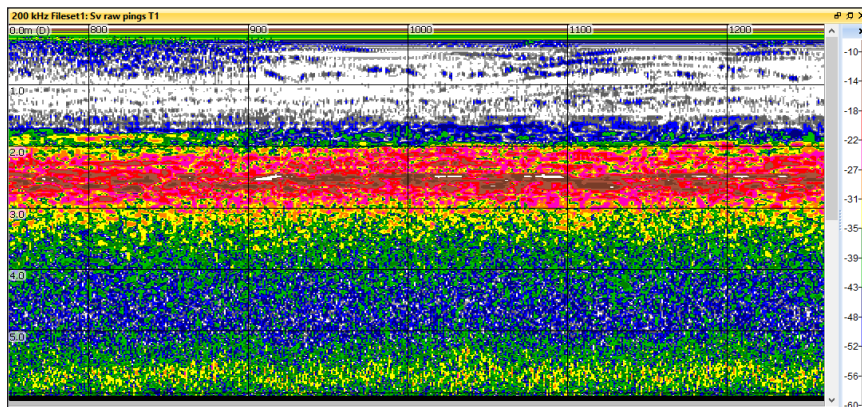


Figure 7. Detection of seagrass during high tide

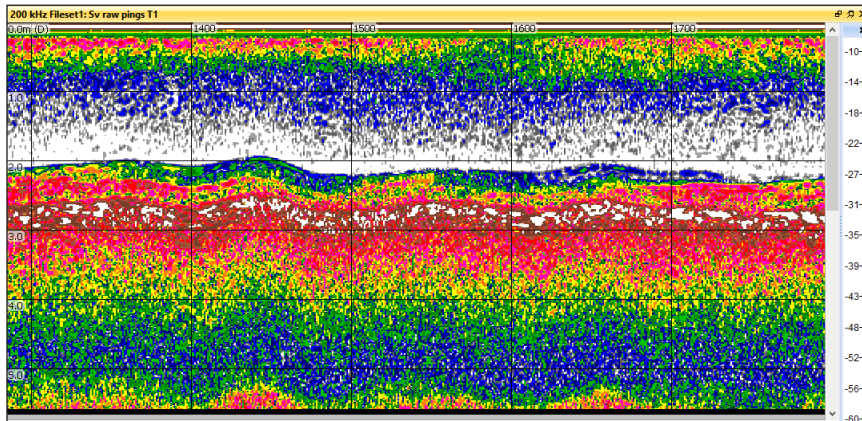


Figure 8. Seagrass detection in calm sea condition at station 2

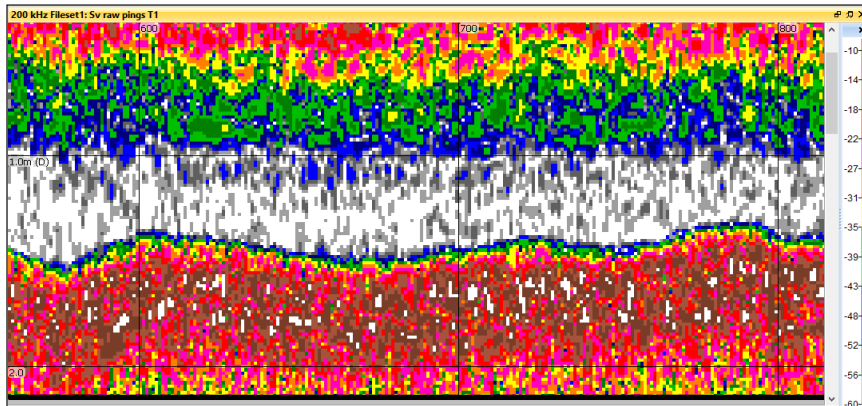


Figure 9. Seagrass detection in calm sea condition at station 3

Acquisition of Sediment samples in Bintan seawaters is shown in Figure 10.



Figure 10. Sediments at Bintan seawaters

Seagrass Data Collection

Ground truth survey is vital for object identification and classification. Measurement of seagrass biomass using the transect method is shown in Figure 11. Seagrass classification was used for extracting information from acoustic images (echogram). Seagrass belongs to four families known as Posidoniaceae, Zosteraceae, Cymodoceaceae, and Hydrocharitaceae.

Classification of stations based on the presence of seagrass can be divided into 3 categories including locations with dense seagrass numbers, scattered seagrasses, and little seagrasses until there are no seagrasses (Figure 12).

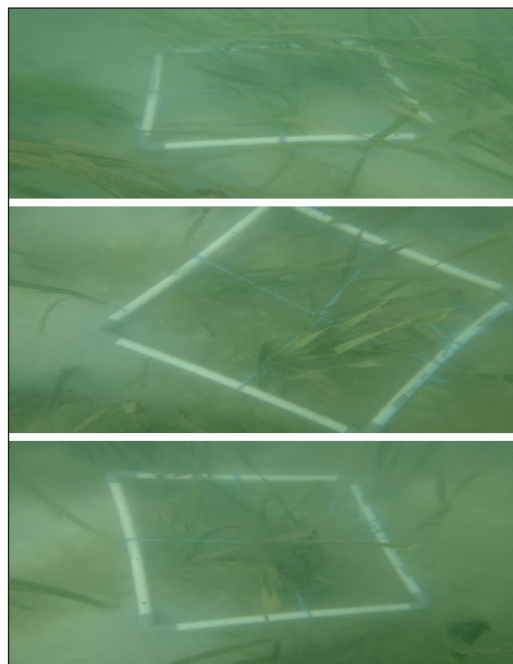


Figure 11. Measurement of seagrass biomass using the transect method.

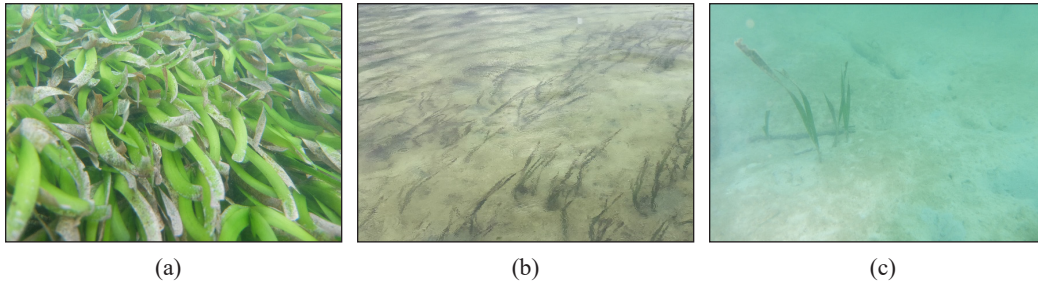


Figure 12. Examples of underwater images of video camera belonging to three categories of relative abundance of seagrass: (a) dense seagrass; (b) sparse seagrass; and (c) little to no seagrass.

Table 1 represents 3 categories of relative abundance of seagrasses based on underwater and underwater acoustic videos. Table 2 is a sea floor map matrix error based on the criteria of 95% confidence level and depth range. Table 3 is a comparison of data obtained from biological samples and acoustic data.

Table 1
Three categories of relative abundance of seagrass

Categories	Underwater Photo		Acoustic Data (Beam Depth)		
	95 % Confidence Level		Depth Range (m)		Mean Bottom Depth (m)
	Mean	S.D	Mean	S.D	
Dense seagrass	1.62	0.31	3.15	0.41	3.2
Sparse seagrass	0.57	0.16	2.28	0.18	2.9
Little to no seagrass	0.14	0.12	0.15	0.14	3.11

Table 2 shows error matrix of seagrass map of 95% CL and depth range. Overall accuracy of depth range (0.83) was slightly higher than of 95% CL (0.80).

Table 2
Error matrix for seagrass map

	Reference Data			User Accuracy	
	Dense	Sparse	No		
(A) 95 % Confidence Level					
Classified	Dense	8	1	0	0.89
	Sparse	5	1	0	0.6
	Little to No	4	0	15	0.8
Producer accuracy		0.65	0.7	0.9	Overall accuracy 0.87
(B) Depth Range					
Classified	Dense	6	1	1	0.89
	Sparse	2	1	0	0.6
	Little to No	4	0	16	0.8
Producer accuracy		0.75	0.6	0.93	Overall accuracy 0.85

Table 3
Comparison of data derived from biological samples and acoustic

	Station 1	Station 2	Station 3
Sampling area (m ²)	0.25	0.25	0.25
Biomass (kg/0.25 m ²)	2.25	1.18	2.4
Mean SV (dB)	-28.9	-35.8	-33.3
Mean TS (dB)	-52.1	-54.2	-53.1
Mean Height, biological sample (m)	0.3	0.4-0.5	0.3-0.5

From Table 3, the relationship between data from biological sampling and the results of detection of acoustic instruments was obtained. These results indicate that the SV value was related to seagrass biomass. The higher the value of seagrass biomass was followed by an increase in the value of acoustic volume backscattering strength (SV). The average height of seagrass conducted manually by divers showed that acoustic measurements were not much different from manual measurements.

Comparison of the classification of underwater videos and acoustic classifications for seagrass densities was given by criterion 1 a bit until there were no seagrasses, rare seagrasses, and abundant seagrasses (Figure 13).

Results of acoustic detection to determine the percentage of seagrass closure are provided to all stations shown in Figure 14. These findings show distinct percentage closures for all stations. Figure 15 shows the quantification of the outcomes of recording seagrass identification to calculate seagrass acoustic backscattering strength using scientific or quantitative fish finder. The findings of sediment assessment based on grain size of the Bintan waters are shown in Figure 16.

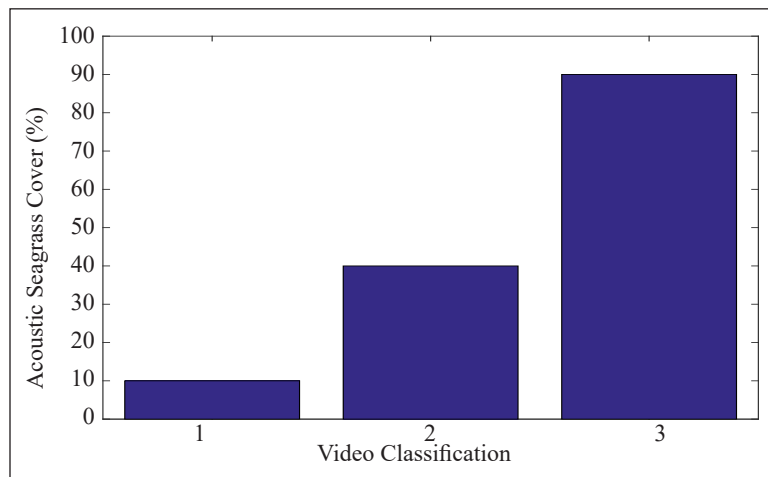


Figure 13. Comparison of acoustic and video classification for different densities of seagrass (1, little to no seagrass; 2 sparse; 3 dense)

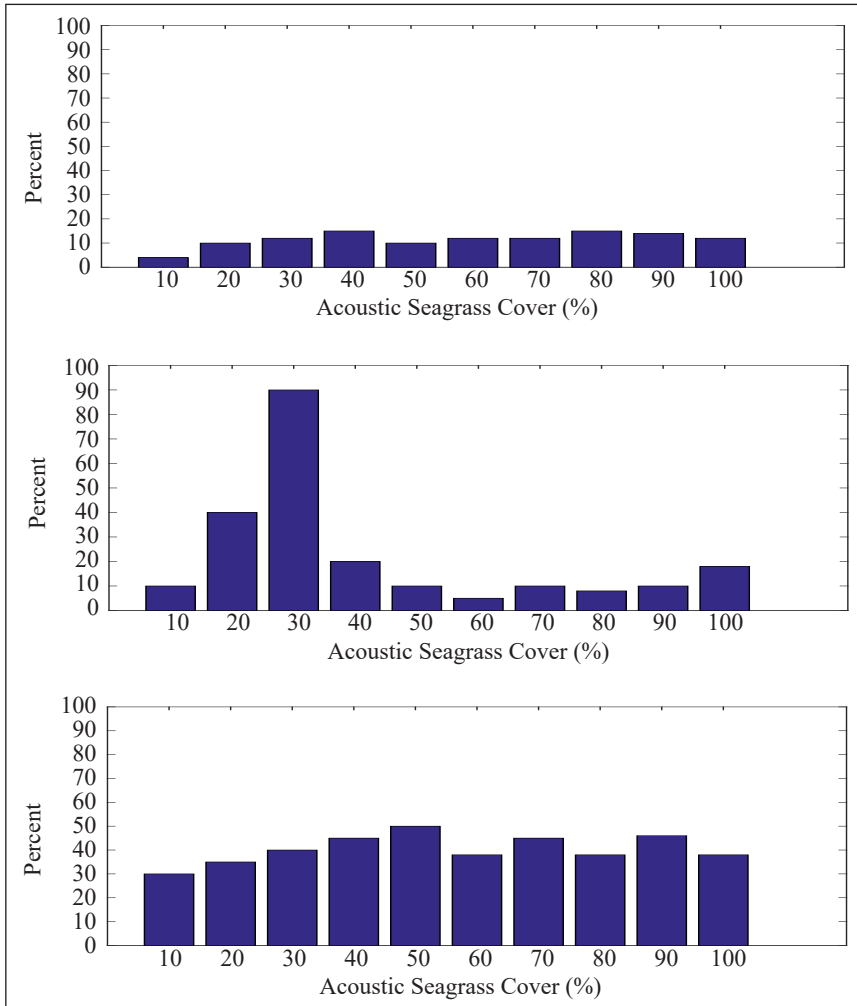


Figure 14. Seagrass percent cover using acoustic method

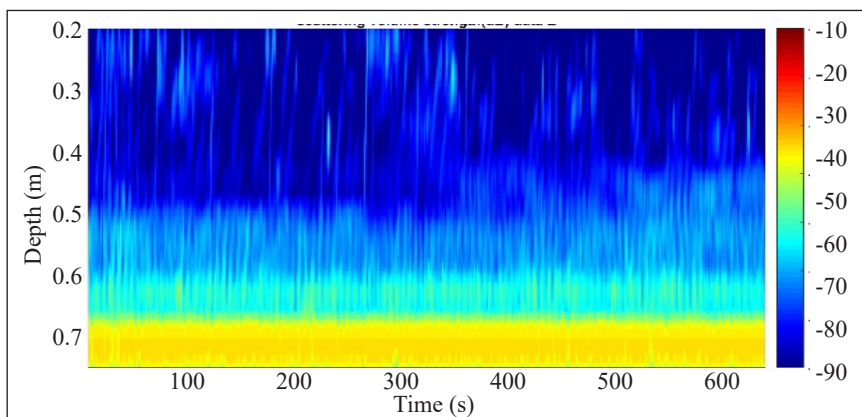


Figure 15. Acoustic backscattering (SV) of seagrass

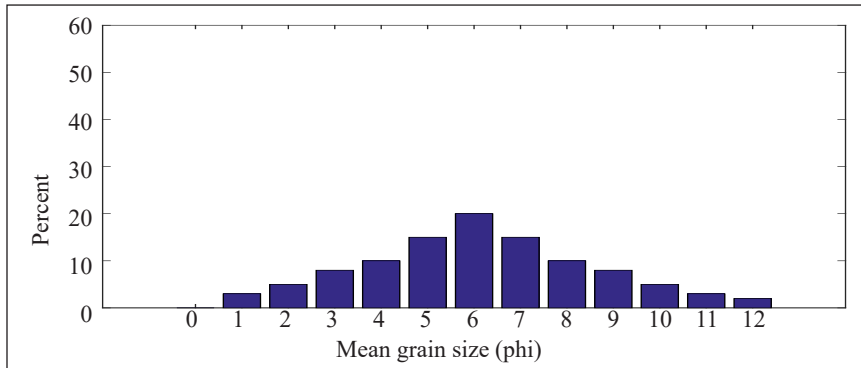


Figure 16. Sediment grain size distribution

Table 4 shows the location and size of the grain size of sediments in Bintan waters and Figure 17 shows the relationship of seagrass biomass with fine-sized sediments.

Table 4
Location and grain size parameters for samples collected at Bintan seawaters

Station	Gravel	Sand	Silt	Clay	Mean (phi)	Mean (mm)	Variance	Skewness	Kurtosis
1	0	95.8	2.8	1.4	2.7	0.15	1.37	3.25	18.75
2	0	92.5	5.2	1.3	2.65	0.16	1.28	3.35	16.6
3	0	96.5	2.3	1.2	2.33	0.2	1.07	3.53	23.5
4	0	99	1	0	2.04	0.24	0.58	0.24	3.93
5	0	100	0	0	0.86	0.55	1.95	-0.15	2.99
6	17.5	82.5	0	0	0.88	0.54	1.95	-1.25	3.34
7	13.3	86.7	0	0	1.12	0.46	1.64	-1.57	4.77
8	40	60	0	0	-0.34	1.27	2.35	-0.23	1.45
9	62.4	37.6	0	0	-1.35	2.58	2.18	0.44	1.53
10	62.3	37.3	0.7	0	-0.91	1.88	2.05	0.11	1.54

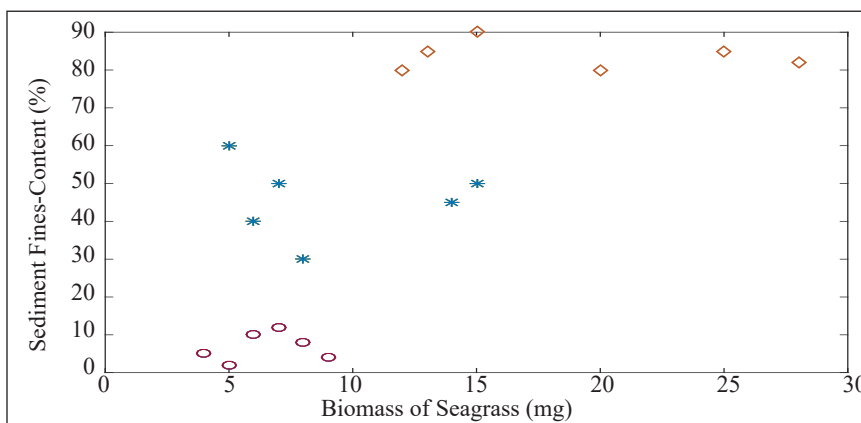


Figure 17. The relationship between sediment-fines content and seagrass biomass

Figure 18 was the acoustic backscattering from the seabed where clay had a small backscatter compared to sand or rough rock. This was caused by the acoustic impedance of coarse sand is higher than very fine sand. The other reason is the grain size of very find sand was lower than coarse sand. Reverberation level from mud (silt and clay) had smaller value compared to other sediments (Figure 19).

Figure 20 is the intensity value of the acoustic reflection of the water column and seagrass bottom. Basic seagrass waters range from -35.0 dB to -20.0 dB.

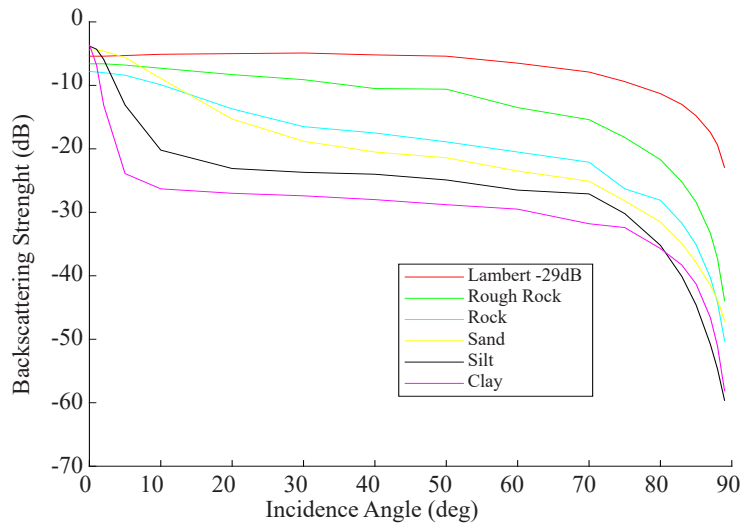


Figure 18. Acoustic backscattering strength of sea bottom

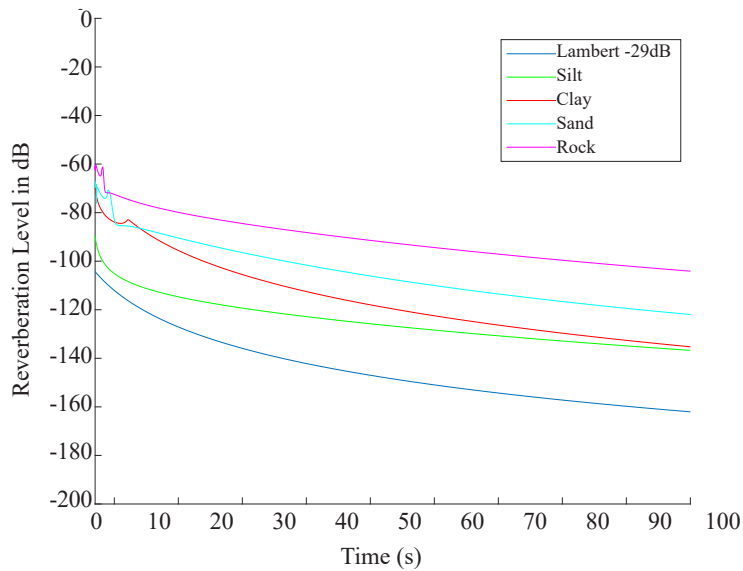


Figure 19. Reverberation level of sea bottom

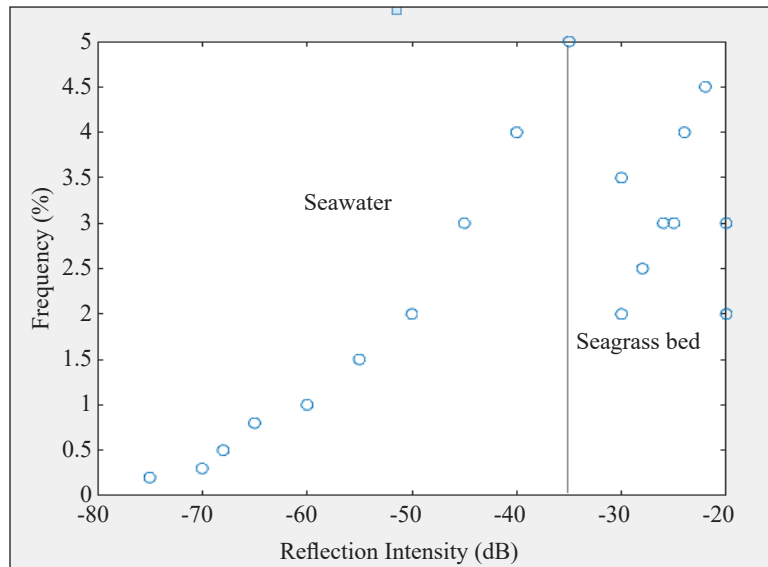


Figure 20. Acoustic reflection intensity of Seagrass bed

DISCUSSION

The coastal area of Bintan waters has high potential natural resource. Seagrass meadow is one of a chain of coastal ecosystems that greatly determines the sustainability of the marine ecosystem. Some functions of seagrass beds include protecting mangrove ecosystems and land from the influence of ocean waves. Another thing is that seagrass beds have a function of protecting coral reefs on the seabed and can inhibit pollution from the land so as to maintain the quality of sea water.

Seagrass beds on the east coast of Bintan Island have an area of more than 2500 ha with high species diversity, where 10 species of seagrass are found in 12 species in Indonesian waters. Seagrass beds in Bintan waters need to be protected because of the presence of rare animals such as dugong and turtles which can be a special income in the tourism sector.

From the results of the study, we found 6 types of seagrass such as *Cymodocea rotundata* (CR), *C. serrulata* (CS), *Enhalus acoroides* (EA), *Thalassia hemprichii* (TH), *Thalassodendron ciliatum* (TC), and *Syringodium isoetifolium* (SI).

This study shows that acoustic remote sensing was able to detect seagrass height and to measure backscatter of seagrass. The value of acoustic backscatter indicated the species of seagrass. This area of study also corresponds with dense seagrass, sparse seagrass, and little to no seagrass. These characteristics were classified with depth range and 95 % Confidence Level (CL). We found depth range measurement was influenced by the length of seagrass. Therefore, for seagrass mapping the method of depth range and 95 % CL were practical need.

This study also shows acoustic backscatter (SV) correlated with seagrass biomass. The higher of SV indicated the higher concentration of seagrass biomass. Each individual species of seagrass had a specific value of Target Strength (TS). By this TS value the discrimination of seagrass species was possible. It was supported using underwater image produced by acoustic instrument.

This work found a novel approach to distinguish bottom sediment characterized by grain size using acoustic remote sensing. The sediment type in this area consisted of clay, silt, sand, and gravel. Our method had shown the ability of acoustic frequency used of 200 kHz to distinguish seagrass species and sediment type in shallow water. Biomass of seagrass was distributed in sediment fine. The backscattering of seabed was influenced by sea bottom type, frequency of acoustic instrument, orientation of transducer, and reverberation level.

We found seagrass percent covered by acoustic method was nearly equal with conventional method. The proportion of substrate by seagrass was used for accurate assessment of biomass density. Therefore, this acoustic method was indispensable method for rapid assessment of seagrass distribution.

High plant density results in higher echo amplitude and other seafloor factors. Using scuba divers, the acoustic detection accuracy was computed as 87 %. Backscatter of seagrass depends on the leaf canopy, echosounder frequency and sea bottom substrate. The frequency of transducer affects the received echo level in decibel. These results are in agreement with the other researchers (De Falco et al., 2000; Parnum, 2007; Parnum et al., 2004; Kenny et al., 2003).

Acoustic technology is capable of detecting seagrass and basic aquatic habitats that inhabit it. It was proven that hydroacoustic method could survey large areas within short time (Short et al., 2010). The acoustic signal from vegetations and sediment differentiate underwater meadows (Bostrom et al., 2006). Seawater turbidity and light are the major environmental factors that control seagrass distribution (Phinn et al., 2008). In this area, we found a very large plant with long leaves and poor resistance to perturbation (Green et al., 2003). The seagrass beds play key role in ecological ecosystem and fish habitat (Moyer et al., 2005). The important role of seagrass in the marine environment and as bioindicator, to assess the distribution, biomass, and species (Descamp et al., 2005). The ability of acoustic method was obtained by measuring the value of acoustic backscattering from detected objects. This was caused by the difference value of acoustic impedance between seawater and seagrass (Wilson and Dunton, 2009). Single beam acoustic system has been used for discriminating bottom type (Manik et al., 2006; Serpetti et al., 2011, Manik, 2012). Seagrass produces a strong backscatter just above the seabed (Sabol et al., 2002). In this study, seagrass have a complex structure including small patches that change from higher density areas to lower density ones over short distances (Tseng, 2009).

Overall, we found the acoustic remote sensing was potentially a valuable technology for detection, quantification, and characterization of seagrass.

CONCLUSION

From the results of the study it can be concluded that the acoustic method can measure sound intensity or acoustic backscatter from seagrass and its surrounding habitat. Seagrass height can be measured based on the acoustic reflection value of seagrass. In the study location there were 3 seagrass groups based on percent closure, which were small to none of seagrass groups, rare seagrass groups, and many seagrass groups. Seagrass is mostly in fine sedimentary habitats. The increase in the amount of seagrass biomass calculated manually is followed by an increase in the value of acoustic backscattering strength. Identification of seagrass species using the acoustic method has an overall accuracy of 87%.

ACKNOWLEDGEMENTS

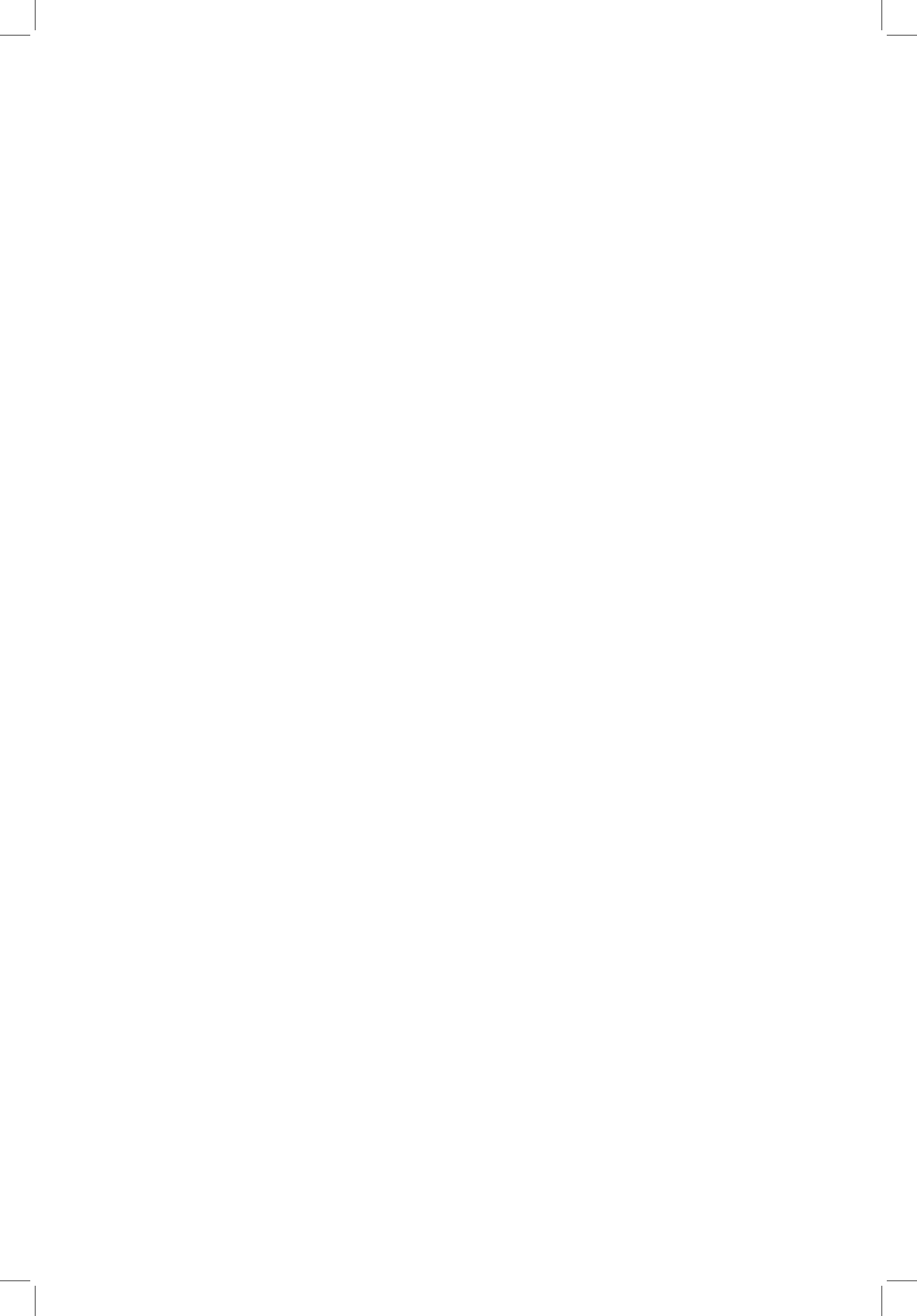
The authors acknowledge the funding from Ministry of Research, Technology, and Higher Education of Indonesia. The authors would like to thank the rest of the graduate research team for their collaborative effort during data collection. The authors are also indebted to the anonymous referees whose suggestions have far improved the exposition of the paper.

REFERENCES

- Anderson, J. T., Van Holliday, D., Kloser, R., Reid, D. G., & Simard, Y. (2008). Acoustic seabed classification: current practice and future directions. *ICES Journal of Marine Science*, 65(6), 1004-1011.
- Ardizzone, G., Belluscio, A., & Maiorano, L. (2006). Long-term change in the structure of a *Posidonia oceanica* landscape and its reference for a monitoring plan. *Marine Ecology*, 27(4), 299-309.
- Belzunce, M., Navarro, R. M., & Rapoport, H. F. (2005). Seed and early plantlet structure of the Mediterranean seagrass *Posidonia oceanica*. *Aquatic Botany*, 82(4), 269-283.
- Bostrom, C., Jackson, E.L., & Simenstad, C. A. (2006). Seagrass landscapes and their effects on associated fauna: A review. *Estuarine, Coastal and Shelf Sciences*, 68(3-4), 383-403.
- Bozzano, R., Castellano, L., & Siccardi, A. (1998, September 21-25). Characterization of submerged aquatic vegetation by a sector-scanning sonar. In *Proceedings of the 4th European Conference on Underwater Acoustics* (pp. 159-164). Italian National Research Council, Rome, Italy.
- Brouwer, P. (2008). *Seafloor classification using a single beam echosounder* (Master's thesis). University of Delft, The Netherlands.
- Buia, M. C., Zupo, V., & Mazzella, L. (1992). Primary production and growth dynamics in *Posidonia oceanica*. *Marine Ecology*, 13(1), 2-16.
- Carbó, R., & Molero, A. C. (1997). Scattering strength of a *Gelidium* biomass bottom. *Applied Acoustics*, 51(4), 343-351.
- De Falco, G., Ferrari, S., Cancemi, G., & Baroli, M. (2000). Relationship between sediment distribution and *Posidonia oceanica* seagrass. *Geo-Marine Letters*, 20(1), 50-57.

- Descamp, P., Pergent, G., Ballesta, L., & Foulquié, M. (2005). Underwater acoustic positioning systems as tool for *Posidonia oceanica* beds survey. *Comptes Rendus Biologies*, 328(1), 75-80.
- Di Maida, G., Tomasello, A., Luzzu, F., Scannavino, A., Pirrotta, M., Orestano, C., & Calvo, S. (2011). Discriminating between *Posidonia oceanica* meadows and sand substratum using multibeam sonar. *ICES Journal of Marine Science*, 68(1), 12-19.
- Duarte, C. M. (1987). Use of echosounder tracings to estimate the aboveground biomass of submerged plants in lakes. *Canadian Journal of Fisheries and Aquatic Sciences*, 44(4), 732-735.
- Green, E. P., Short, F. T., & Frederick, T. (2003). *World atlas of seagrasses*. Berkeley, USA: University of California Press.
- Kenny, A. J., Cato, I., Desprez, M., Fader, G., Schüttenhelm, R. T. E., & Side, J. (2003). An overview of seabed-mapping technologies in the context of marine habitat classification. *ICES Journal of Marine Science*, 60(2), 411-418.
- Komatsu, T. (2007). Mapping and quantifying a Sargassum forest off Osaka (Toyama Bay, the Sea of Japan) by using narrow multibeam sonar and GIS. *GIS/Spatial Analyses in Fisheries and Aquatic Sciences*, 3, 97-114.
- Komatsu, T., Mikami, A., Sultana, S., Ishida, K., Hiraishi, T., & Tatsukawa, K. I. (2003). Hydro-acoustic methods as a practical tool for cartography of seagrass beds. *Otsuchi Marine Science*, 28, 72-79.
- Lefebvre, A., Thompson, C. E., Collins, K. J., & Amos, C. L. (2009). Use of a high-resolution profiling sonar and a towed video camera to map a *Zostera marina* bed, Solent, UK. *Estuarine, Coastal and Shelf Science*, 82(2), 323-334.
- Maccina, M. J., & Shireman, J. V. (1980). The use of a recording fathometer for determination of distribution and biomass of hydrilla. *Journal of Aquatic Plant Management*, 18, 34-39.
- Manik, H. M. (2012). Seabed identification and characterization using sonar. *Advances in Acoustics and Vibration*, 2012, 1-12.
- Manik, H. M., Furusawa, M., & Amakasu, K. (2006). Measurement of sea bottom surface backscattering strength by quantitative echo sounder. *Fisheries Science*, 72(3), 503-512.
- McCarthy, E. M., & Sabol, B. (2000, September 11-14). Acoustic characterization of submerged aquatic vegetation: military and environmental monitoring applications. In *OCEANS 2000 MTS/IEEE Conference and Exhibition. Conference Proceedings* (Cat. No. 00CH37158) (Vol. 3, pp. 1957-1961). Providence, RI, USA.
- Minami, K., Yasuma, H., Tojo, N., Fukui, S. I., Ito, Y., Nobetsu, T., & Miyashita, K. (2010). Estimation of kelp forest, *Laminaria* spp., distributions in coastal waters of the Shiretoko Peninsula, Hokkaido, Japan, using echosounder and geostatistical analysis. *Fisheries Science*, 76(5), 729-736.
- Miner, S. P. (1993, July 19-23). Application of acoustic hydrosurvey technology to the mapping of eelgrass (*Zostera marina*) distribution in Humboldt Bay, California. In *Proceedings of the 8th Symposium on Coastal and Ocean Management* (pp. 2429-2442). New Orleans, Louisiana, USA.
- Moyer, R. P., Riegl, B., Banks, K., & Dodge, R. E. (2005). Assessing the accuracy of acoustic seabed classification for mapping coral reef environments in South Florida (Broward County, USA). *Revista de Biologia Tropical*, 53, 175-184.

- Orlowski, A. (2009). Acoustic transects as units for classifying the benthic habitat. *Acta Acustica United with Acustica*, 95(4), 620-627.
- Parnum, I. M. (2007). *Benthic habitat mapping using multibeam sonar systems* (Doctoral dissertation). Curtin University, Australia.
- Parnum, I. M., Siwabessy, P. J. W., & Gavrilov, A. N. (2004, November 3-5). Identification of seafloor habitats in coastal shelf waters using a multibeam echosounder. In *Proceedings of the Annual Conference of the Australian Acoustical Society* (pp. 1-6). Gold Coast, Australia.
- Pasqualini, V., Clabaut, P., Pergent, G., Benyoussef, L., & Pergent-Martini, C. (2000). Contribution of side scan sonar to the management of Mediterranean littoral ecosystems. *International Journal of Remote Sensing*, 21(2), 367-378.
- Phinn, S., Roelfsema, C., Dekker, A., Brando, V., & Anstee, J. (2008). Mapping seagrass species, cover and biomass in shallow waters: An assessment of satellite multi-spectral and airborne hyper-spectral imaging systems in Moreton Bay (Australia). *Remote sensing of Environment*, 112(8), 3413-3425.
- Sabol, B. M., Melton, R. E., Chamberlain, R., Doering, P., & Haunert, K. (2002). Evaluation of a digital echo sounder system for detection of submersed aquatic vegetation. *Estuaries*, 25(1), 133-141.
- Serpetti, N., Heath, M., Armstrong, E., & Witte, U. (2011). Blending single beam RoxAnn and multi-beam swathe QTC hydro-acoustic discrimination techniques for the Stonehaven area, Scotland, UK. *Journal of Sea Research*, 65(4), 442-455.
- Short, F. T., Carruthers, T. J. R., Waycott, M., Kendrick, G. A., Fourqurean, J. W., Callabine, A., ... & Dennison, W. C. (2010). *Thalassia hemprichii*. *The IUCN Red List of Threatened Species*. Retrieved February 3, 2020, from <https://dx.doi.org/10.2305/IUCN.UK.2010-3.RLTS.T169015A6561794.en>.
- Sidiq, A. P., Manik, H. M., & Nainggolan, T. B. (2019). Comparative Study of Seismic Migration Method in Characterizing Oil and Gas Reservoirs in Kangean Block, Bali Sea Using Model Based Acoustic Impedance Inversion. *Journal of Tropical Marine Science and Technology*, 11(1), 205-219.
- Tseng, Y. T. (2009). *Recognition and assessment of seafloor vegetation using a single beam echosounder* (Doctoral dissertation). Curtin University, Australia.
- Wilson, P. S., & Dunton, K. H. (2009). Laboratory investigation of the acoustic response of seagrass tissue in the frequency band 0.5–2.5 kHz. *The Journal of the Acoustical Society of America*, 125(4), 1951-1959.



Time Frequency Analysis of Peking Gamelan

Sinin Hamdan^{1*}, Iran Amri Musoddiq², Ahmad Fauzi Musib³ and Marini Sawawi¹

¹Faculty of Engineering, Universiti Malaysia Sarawak, 94300, Kota Samarahan, Sarawak, Malaysia

²Faculty Applied and Creative Art, Universiti Malaysia Sarawak, 94300, Kota Samarahan, Sarawak, Malaysia

³Faculty of Human Ecology, Universiti Putra Malaysia, 43400, Serdang, Selangor, Malaysia

ABSTRACT

The tone of peking 1, 2, 3, 5, 6, 1' was investigated using time-frequency analysis (TFA). The frequencies were measured using PicoScope oscilloscope, Melda analyzer in Cubase version 9 and Adobe version 3. Three different approaches for time-frequency analysis were used: Fourier spectra (using PicoScope), spectromorphology (using Melda analyzer) and spectrograms (using Adobe). Fourier spectra only identify intensity-frequency within entire signals, while spectromorphology identify the changes of intensity-frequency spectrum at fixed time and Adobe spectrograms identify the frequency with time. PicoScope reading produces the spectra of the fundamental and overtone frequencies in the entire sound. These overtones are non-harmonic since they are non-integral multiples of the fundamental. The fundamental frequencies of peking 1, 2, 3, 5, 6 were 1066Hz (C6), 1178Hz (D6), 1342Hz (E6), 1599Hz (G6) and 1793Hz (A6) respectively while peking 1' was 2123Hz (C7) i.e. one octave higher than peking 1. Melda analyzer reading proved that all peking sustained the initial fundamental frequency and overtone at t=0 until 2s. TFA from Adobe reading provides a description of the sound in the time-frequency plane. From TFA, peking 1, 2 and 6 exhibited a much gentler attack and more rapid decay than peking 3, 5 and 1'.

Keywords: FFT, fundamental, gamelan, overtones frequencies, peking

ARTICLE INFO

Article history:

Received: 09 August 2019

Accepted: 28 January 2020

Published: 15 April 2020

E-mail addresses:

hsinin@unimas.my (Sinin Hamdan)

amiran@unimas.my (Iran Amri Musoddiq)

faudzimusib@upm.my (Ahmad Fauzi Musib)

smarini@unimas.my (Marini Sawawi)

* Corresponding author

INTRODUCTION

Mantle Hood was one of the earliest pioneers of gamelan in the West that initiated gamelan performance study and understood the widest applications of gamelan (Sorrell, 1990). The measurements of scales and tunings were carried out in metallophones and xylophones found in Southeast Asia and on African xylophone with fixed tunings

and related to equal temperaments (Schneider, 2001). When digital signal processing was introduced in the 1980s sound analysis and re-synthesis became available for investigating tone systems and tunings of non-Western music cultures (Schneider & Beurmann, 1990, Schneider & Beurmann, 1993). Ellis and Hipkins (1884), Stumpf (1901) and Kunst (1934) studied the metallophones of the Indonesian gamelan because the tunings in gamelan were different from the Western systems and was difficult to explain in terms of their origins with regard to relevant perceptual and cognitive issues. The data from some of the measurements helps in understanding the structure of *slendro* and *pelog* (Lentz, 1965; Hood, 1966; Morton 1976). New interpretations and hypotheses regarding the gamelan tone systems and their possible relationships to those of other regions were presented (Rahn, 1979; van Zanten, 1986; Widdess, 1993; Voisin, 1994). This topic has gained attraction for several generations of earlier researchers.

Gamelan music is in *pelog* or *slendro*, and cannot be reproduced by the piano tunings. This avoids confusion of Western music with specifically Javanese gamelan instrument. Composers such as Henry Cowell, John Cage and Lou Harrison were pioneers that were interested in Eastern cultures (Sorrell, 1990). Javanese, Balinese and Sundanese gamelans exist largely in America. In California, Dennis Murphy, William Colvig, Daniel Schmidt and Paul Drescher built their own gamelan from aluminium, scrapped cars and other materials (Sorrell, 1990). The American pieces for gamelan were composed along with the production of these instruments, where the Westerners rather than Indonesians who objected to such works. Historically the Javanese incorporated instruments from the Dutch military bands into their ensembles during the colonial period.

The most comprehensive set of data on gamelan tunings was published by Indonesian scientists (Surjodiningrat et al., 1972). Nevertheless, these measurements and numerical data lack of explanation of tuning as an art because it is regarded as a process guided by musical sensibilities and experience (Vetter, 1989). To understand tuning, the concepts and terminology of a tuner and his actions while tuning need to be considered and understood. The behavior and verbal comments of tuners must be taken into account where these data need to be checked with regard to reliability and cultural validity. Even a complete tuning event recorded with all of the verbal commentaries of a tuner might not necessarily reveal his cognitive framework regarding concepts such as step, scale, or octave equivalence in every detail (Schneider, 2001). The uniqueness of our research is visualizing the sound sonically through PicoScope oscilloscopes and Melda analyzer in Cubase version 9. The sound spectra of all peking are obtained from PicoScope measurements. After the data sound was captured and recorded the FFT was also analyze using Melda analyzer in Cubase version 9 to obtain dominant frequency for each tone at specific time.

The tuning of the seventeen keys (wooden bars) of Buganda *arnadinda* xylophone by Evaristo Muyinda when visiting the Ethnological Museum of Berlin in 1983 was recorded

in complete detail in order to find out whether or not *Muyinda* tune the instrument according to the equiptatonic scale (Kubik, 1991). This experiment yielded some interesting results which indicated that the tuning was additive in nature (i.e. carried out by adding up an interval about the size of a major second) rather than being based on the division of an octave into equal parts. However, it is not totally clear whether his intention with respect to the tuning was finally achieved. The tuning was measured objectively by calculating the frequencies of the spectral components which represent the base mode of vibration of each bar which is *not* equiptatonic. It shows considerable deviations (standard deviation=30.6, range=97.5 cents) from the unit step of 240 cents that has been proposed with respect to both certain African scales and the Javanese and Balinese *slendro* (Schneider & Beurmann, 1990). The spectral components for the description of the tuning are decisive with respect to pitch. Precise measurement in this case permits examination of the work of the tuner and compared the interpretations that a number of ethnomusicologists have given as to intended tuning and scale structure with factual data.

Idiophones are instruments which, as the term implies, sound by themselves. Sound generation in instruments typically consist of three dimensional solid bodies such as bars, slabs, lamellae, plates, or shells is effected by an impulse which accelerates a given bar and plate. This causes a pattern of vibrations which consist of the eigen modes (natural frequencies) of the given body. In certain idiophones, bars or shells are set in motion by means of one or several mallets (e.g., gamelan instruments such as the Balinese *gangsa* (Kartomi, 1985). With the case of gongs such as the *bonang* or *trompong* the compound shape of each of the bossed result in complex patterns regarding both temporal and spectral behavior. Without going into details of vibrational theory (Cremer & Heckl, 1967; Fletcher & Rossing, 1998; Schneider, 1999), it can be said that bending stiffness and other factors (material and dimensions) of the vibrating solid cause in-harmonicity within the pattern of vibration as well as in the pattern of spectral components that can be extracted from the sound radiated. Since solids typically vibrate in two or even three dimensions, and produce a great many eigen modes, patterns of vibration can be quite irregular or even chaotic (in terms of nonlinear dynamics) in certain idiophones, notably in flat gongs such as the Asian *tam-tam* (Schneider, 1999). Further, because there are different types of vibration as well as frequency dispersion, in metallophones such as the Javanese *saron* (also called *peking*), modes need not be immediately and fully developed at the onset. Rather, actual distribution of spectral energy and temporal development of patterns of vibration depends considerably on the place at which the mallet hits the bar or plate as well as on the magnitude of the force transmitted through the impulse. As can be imagined, the number of eigen modes elicited in general increases in proportion with the force that is applied (Perrin et al., 2013). Thus, in styles of soft playing, the pattern of vibration is simpler and the spectral energy contained in a sound is lower than is the case in styles such as the *gong kebayar* in Balinese music

(McPhee, 1966) known for loudness as well as a metallic sound. There are, however, some instruments which respond in a very sensitive way to even small impulses because damping and other loss factors are small. This is particularly in the gender family which comprise of very thin bronze plates as keys suspended over tube resonators. In these instruments, a rich spectrum (including components at rather high frequencies (Schneider, 1999)), for each single plate is produced with the use of relatively small force.

In gamelan performances the mallet makes the contact and on some instruments the hands are used for damping. The tuning of gamelan is easy to grasp and distinguish one gamelan from the other. There are two types of tone set in gamelan instrument. There are pelog and slendro tuning. Slendro is a pentatonic scale with five notes and no semitones (exactly like the scale on the black notes of the piano). The five notes of slendro are more or less equally spaced but the black notes have clear difference between the whole tone and minor third. Pelog is easily distinguished from slendro because it has seven notes (not all seven are used) and the size of interval varies far more than slendro and includes semitones.

The terms simple and complex tone invariably stand for sinusoidal and non-sinusoidal sound respectively. Any periodic sound wave should be heard as a sum of sinusoidal components or partial with their corresponding frequencies. A complex tone is the sum of sinusoidal components or partial which are harmonics (Plomp, 1976). In general, a typical musical tone consists of a large number of harmonics with frequency ratios 1: 2: 3: 4: 5 etcetera. The sound of music instrument results in the sensation of single note with a single definite pitch which is equal to the pitch of the fundamental and a specific timbre depending upon the relative amplitude of the harmonics. Gamelan has their own characteristic in term of their tone and pitch. The intensity and frequency of the instruments are different between gamelan. The instruments also have different shapes and material. The peking has the shape of a bar with rounded shapes on the top side (Sethares, 2005). The frequency of gamelan Swastigitha and Kyai Kaduk Manis has been measured by Surjodiningrat et al. (1972) using oscilloscope (Sudarjana et al., 1993) while the gong frequency was measured by Kuswanto using sonogram (Pramudya et al., 2018).

In Pramudya et al. (2018) paper the bonang barung and peking frequencies were measured using Audacity. It is low cost software to record and analyse the sound. It can process the sounds to generate the FFT of them. The sounds were measured in the non-acoustical room (Hall of Universitas Ahmad Dahlan- a regular meeting room) where the gamelan is located. The frequency of Bonang Barung and Peking was measured at night to reduce the noise. Audacity software is used along with a computer, microphone, and speakers, to generate and observe the frequency spectra of various audio waveforms, from simple waveforms such as sine waves to more complex waveforms. Audacity as an education tool in high school level physics classrooms, including several in which students play simple musical instruments and study the resulting spectra in the time and frequency

domain. The gamelan frequency especially the Laras Pelog of Bonang Barung is measured using Audacity and the frequency measurement between the Bonang Barung and Peking using Audacity is compared. Our experiments were conducted in the University Malaysia Sarawak (UNIMAS) Faculty of Applied and Creative Art (FACA) Music department studio with full acoustic room facility. The signal produced from both PicoScope and Melda analyzer both displayed sharp and distinct fundamental and overtone frequencies peak compared to the low signal level from the background noise. The PicoScope detects the whole voltage versus time signal and generate the whole intensity (dB) versus frequency signal. Using PicoScope the signals displayed voltage versus fundamental and overtone peaks at a particular time or intensity (dB) versus fundamental and overtone peaks at a particular frequency. When using Melda analyzer the spectrogram displays the intensity (dB) versus frequency at a specific time. Using Melda analyzer the changes of the intensity versus frequency can be detected every 0.5 second interval and thus displaying the changes of the intensity of the fundamental and overtones frequencies over time.

The intuitive tuning by the gamelan tuner in each village is normally based on what one feels to be true even without conscious reasoning. Using their instinct knowledge or understanding the tuning are based on their feelings rather than facts or proofs. Having said that, each has its references and therefore this study could be one out of many tuning schemes waiting to be extracted and scheme out. In this paper, we investigate the comparison of frequency measurements of peking using PicoScope oscilloscope, Melda analyzer in Cubase version 9 and Adobe version 3. The physical parameters of the tone that were analyzed are the sound pressure level and frequency. The non-harmonicity of the overtones was measured by the PicoScope while the time evolution of the dominant pitches was detected by the Melda analyzer. Fourier analysis yields the frequency content and associated TFA to understand the sound. The purpose of this work is to study the TFA in a peking sound. FFT performs a TFA of an input signal by hitting the peking. The time-frequency content of the signal is visualized by creating a spectrogram which is done by PicoScope, Melda analyzer and Adobe. The output is a time-frequency with intensity varying according to the frequency content of the signal. Understanding the spectra gives the pitch based on the equal tempered scale. Spectrograms display frequencies on a uniform scale, whereas musical scales such as the well-tempered scale are based on a logarithmic scale for frequencies (Johnston, 2009). Since the human ear is not capable of distinguishing the individual harmonics of a complex tone, the identification of the partials may be nearly impossible in listening to tones in a musical context (Plomp, 1976). Thus, experimental evidence using Adobe analyzing the frequency leads to TFA. We interviewed the behavior and verbal comments of tuners, but these data need to be checked with regards to reliability and cultural validity. Even a complete tuning event, recorded with all of the verbal commentaries of a tuner might not necessarily reveal his cognitive

framework regarding concepts such as step, scale, or octave equivalence in every detail. Each assessed peking includes considerably distinct harmonic structures that have not been discussed in the research of Mantle Hood (Sorrell, 1990). Therefore, the objective of this work is studying peking harmonics which is a necessity since the peking is a major instrument of melody in any gamelan ensemble. Preliminary results of peking tuning from University Putra Malaysia (UPM), University Kebangsaan Malaysia (UKM), Universiti Teknologi Mara (UiTM) and Universiti Malaysia Sarawak (Unimas) indicate that there is a distinction in tuning for each peking evaluated despite the fact that the scale is usually Pelog or Salendro. This uniqueness can only be sonically visualized through PicoScope oscilloscopes and Melda analyzer in Cubase version 9. The sound spectra of all peking are obtained from PicoScope measurements. After the data sound was captured and recorded the FFT was also analyzed using Melda analyzer in Cubase version 9 to obtain dominant frequency for each tone at specific time.

MATERIAL AND METHODS

The cast bronze peking 1, 2, 3, 5, 6 and 1' was chosen from a range of Malay gamelan ensemble. Figure 1 showed a set of 6 peking. The acoustic spectra of the measured sets of just-tuned cast bronze peking which were made in Indonesia was captured using PicoScope oscilloscopes and Melda analyzer in Cubase version 9 to investigate the fundamental and overtone frequencies. Excitation was done by beating the peking with a mallet by an expert peking player. The microphone was held above the top surface along the axis of symmetry of the peking at a distance of about 20 cm. The frequency of peking was measured using PicoScope oscilloscope. The Picoscope software display the real signal which is voltage versus time and dBU versus frequency as shown in Figure 2. The frequency reading was verified by recording a sound of 1KHz from a signal generator. The microphone is a flat response microphone capable of capturing only 20Hz-20kHz. The setup to capture the sound is based on Owsinski (2009).

The arrangement of microphone and apparatus for the measurement are shown in Figure 3. The microphone was placed right above the bar. The PicoScope computer software (Pico Technology, 3000 series, Eaton Socon, UK) was used to view and analyze the time signals from PicoScope oscilloscopes (Pico Technology, 3000 series, Eaton Socon, UK) and data loggers for real time signal acquisition. PicoScope software enables analysis using FFT, a spectrum analyzer, voltage-based triggers, and the ability to save/load waveforms to a disk. Figure 2 shows the schematic diagram of the experimental setup. The peking was placed to where the sound could be captured with minimum interference. In our work the recording was done in the University Malaysia Sarawak (UNIMAS) Faculty of Applied and Creative Art (FACA) Music department studio with full acoustic room facility. The signal produced

from both PicoScope and Melda analyzer both displayed sharp and distinct fundamental and overtone frequencies peak compared to the low signal level from the background noise.

The amplifier (Behringer Powerplay Pro XL, Behringer, China) ensured the sound capture was loud enough to be detected by the signal converter. The peking spectra were also digitally recorded using the Melda analyzer in Cubase version 9. In conducting this study, the audio signal derived from the striking of the peking played by an expert peking player was recorded. The audio signal was recorded in mono, at 24-bit resolution, 48 kHz sampling rate. The audio signal was recorded with the aid of a digital audio interface in a .wav format. To ensure the recorded audio signal of the peking was at the optimum level, audio signal calibration of the recording system was carried out. A test tone of 1 kHz sine wave was used in calibrating the recording system. Here the 'unity' calibration level was at +4dBu or -10dBV and was read by the recording device at '0 VU'. In this regard the EBU recommended the digital equivalent of 0VU is that the test tone generated to the recording device of the experimentation is recorded at -18 dBFS (Digital) or +4dBu (Analog) which is equivalent to 0VU. In this thorough procedure of calibration, no devices are unknowingly boosting or attenuating its amplitude in the signal chain at the time of the recording is carried out. The recording apparatus was the Steinberg UR22 mkII audio interface, Audio-Technica AT4050 microphone, XLR cable (balance), with microphone position on axis (<20 cm), microphone setting with low cut (flat) 0dB.



Figure 1. A typical Malay Gamelan Peking

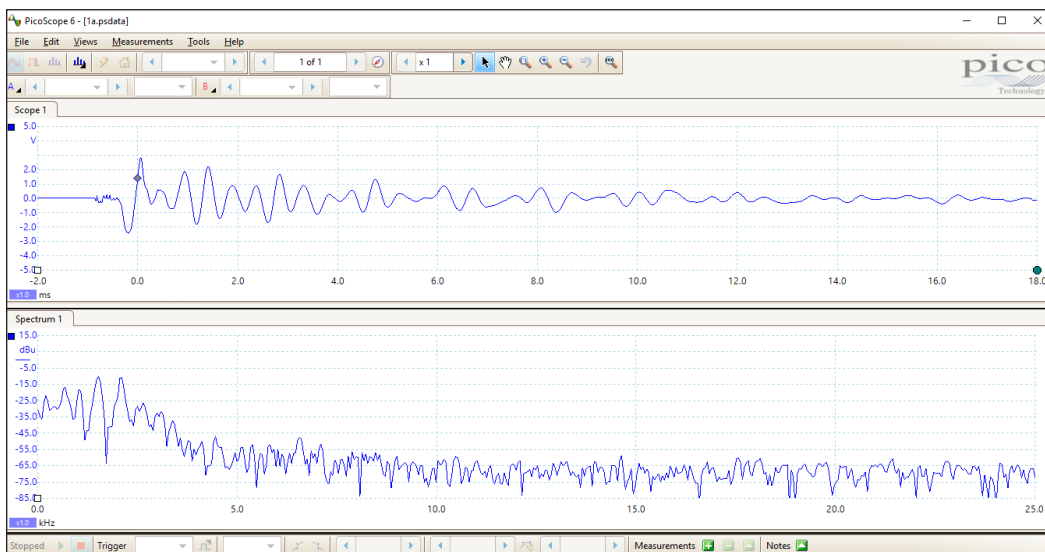


Figure 2. A typical signal which is voltage versus time and dBu versus frequency using the Picoscope software

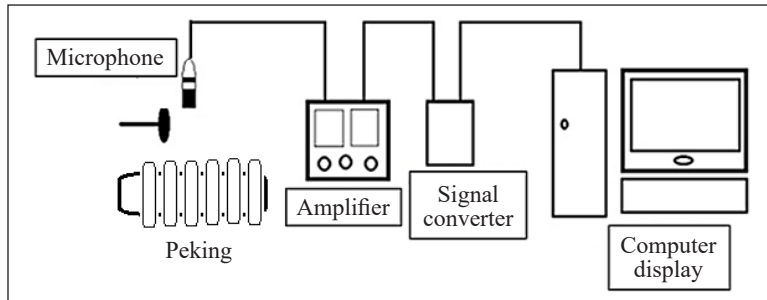


Figure 3. Schematic diagram of the experimental setups

RESULTS AND DISCUSSION

The sound spectrum of all peking from PicoScope measurements is shown in Figure 4 until Figure 9. Table 1 shows the calculated ratio for first, second, third, fourth and fifth overtone with respect to the fundamental frequency for each peking.

Table 1 shows that the overtones are non-harmonic of the fundamental except the first, second, third, fourth and fifth overtone for peking 6, 1, (2 & 1'), 3 and 2 respectively (highlight in bold). These non-harmonics yield difficulties in discriminating sound wave by human ear since individual harmonics are not easily distinguish because human ear is not capable of distinguishing the individual harmonics of a complex tone and the identification of the partials may be nearly impossible in listening to tones in a musical context (Plomp, 1976). Therefore, identification of the partial may be nearly impossible when listening to peking. From Figure 4 to Figure 9, the frequencies that are present in the signal are easily identified, but no information about time localization is available. After the data sound was captured and recorded the FFT was also analyzed using Melda analyzer in Cubase version 9 to obtain dominant frequency for each tone at specific time. The spectrogram from the Melda was used to identify time localized frequency content. Figure 10 to Figure 14 show typical pulse signal from peking 1 spectrogram at $t=0, 0.5, 1, 1.5$ and $t=2s$.

From the FFT analysis the dominant frequency of peking instruments using Melda analyzer is obtained in Table 2.

Table 1

The calculated ratio for first, second, third, fourth and fifth overtone with respect to the fundamental frequency for each peking

	f_0 (kHz)	1 st / f_0	2 nd / f_0	3 rd / f_0	4 th / f_0	5 th / f_0
Peking 1	1.05	2.76	3.11	4.80	4.81	6.7
Peking 2	1.18	2.18	2.67	5.05	6.22	7.03
Peking 3	1.32	2.55	2.74	4.66	5.03	-
Peking 5	1.57	2.20	2.34	4.45	4.75	5.38
Peking 6	1.77	1.93	2.62	4.32	4.88	-
Peking 1'	2.10	1.76	2.55	4.02	-	-

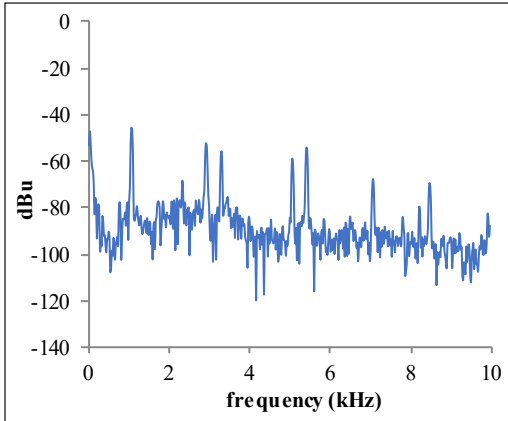


Figure 4. The sound spectrum of Peking 1 from PicoScope measurement

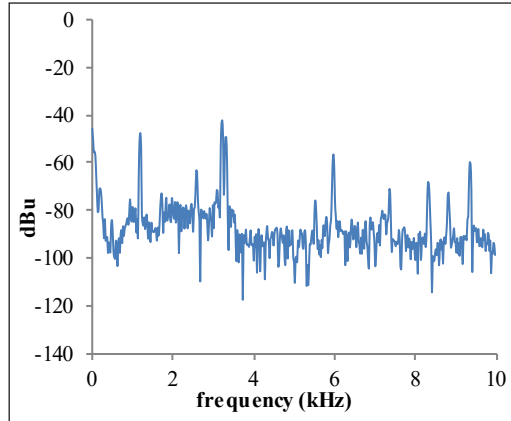


Figure 5. The sound spectrum of Peking 2 from PicoScope measurement

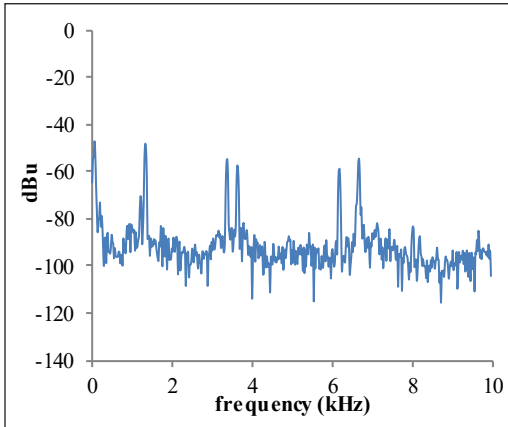


Figure 6. The sound spectrum of Peking 3 from PicoScope measurement

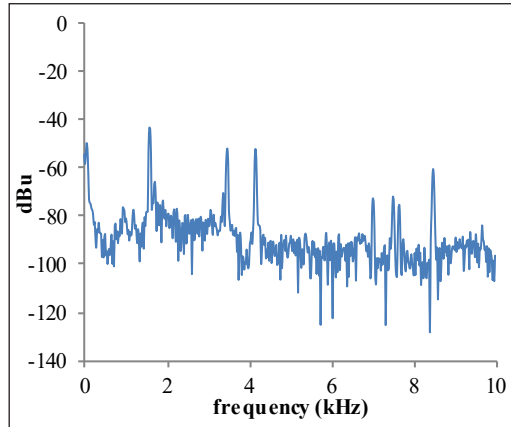


Figure 7. The sound spectrum of Peking 5 from PicoScope measurement

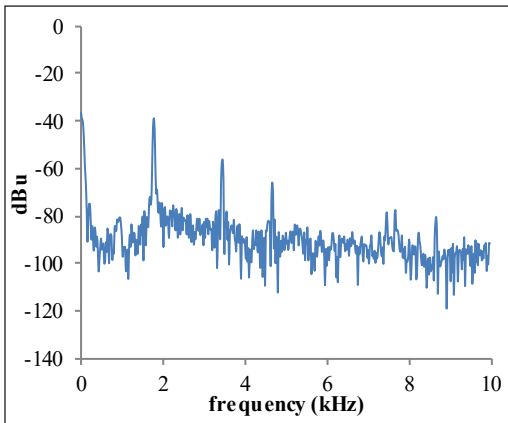


Figure 8. The sound spectrum of Peking 6 from PicoScope measurement

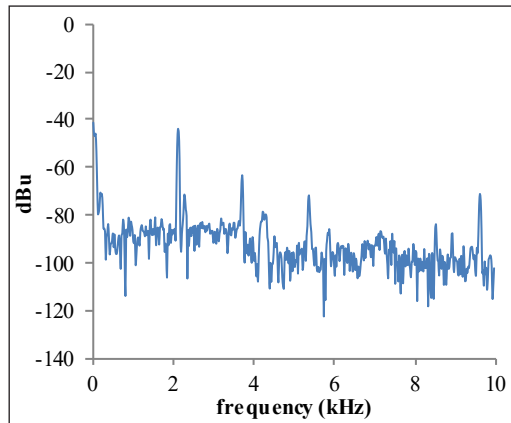


Figure 9. The sound spectrum of Peking 1' from PicoScope measurement

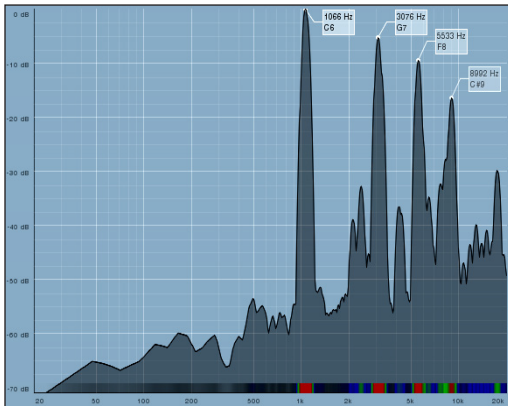


Figure 10. Typical FFT analysis of peking 1 at t=0 sec from Melda analyzer in Cubase version 9 measurement

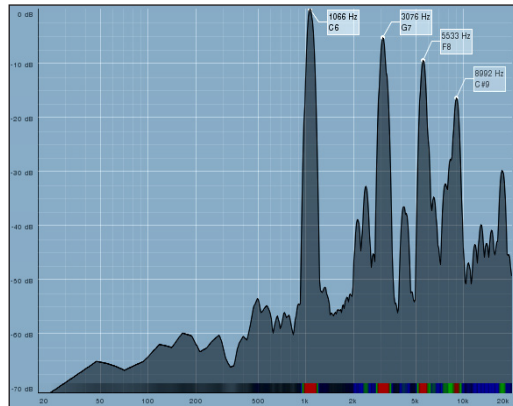


Figure 11. Typical FFT analysis of peking 1 at t=0.5sec from Melda analyzer in Cubase version 9 measurement

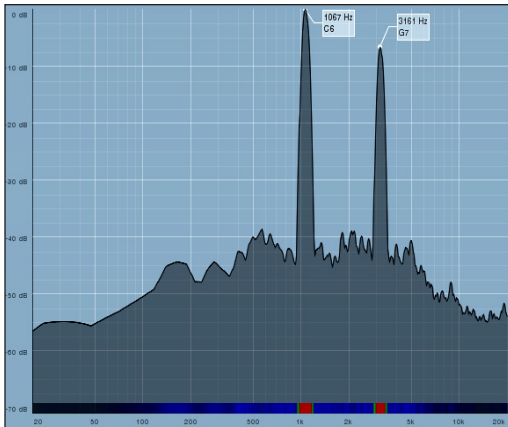


Figure 12. Typical FFT analysis of peking 1 at t=1 sec from Melda analyzer in Cubase version 9 measurement

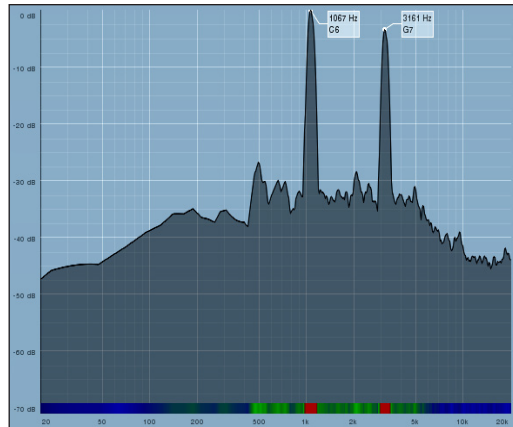


Figure 13. Typical FFT analysis of peking 1 at t=1.5sec from Melda analyzer in Cubase version 9 measurement

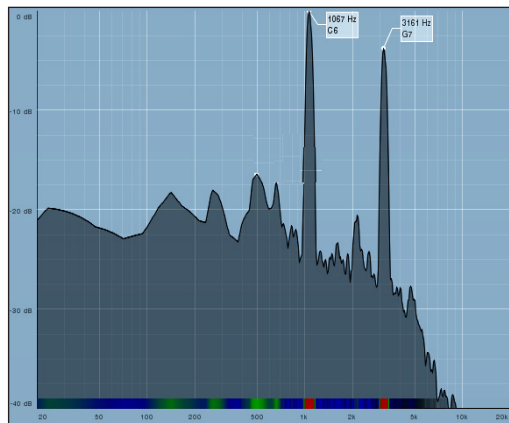


Figure 14. Typical FFT analysis of peking 1 at t=2 sec from Melda analyzer in Cubase version 9 measurement

Table 2

The dominant frequency (Hz) of peking 1, 2, 3, 5, 6 and 1' with their pitch using Melda analyzer

	frequency at t=0s (Hz)	frequency at t=0.5s (Hz)	frequency at t=1s (Hz)	frequency at t=1.5s (Hz)	frequency at t=2s (Hz)
Peking 1	1066(C6)	1067(C6)	1067(C6)	1067(C6)	1067(C6)
	3076(G7)	3161(G7)	3161(G7)	3161(G7)	3161(G7)
	5533(F8)	5494(F8)			
	8992(C#9)				
Peking 2	1178(D6)	1180(D6)	1180(D6)	1180(D6)	1180(D6)
	3247(G#7)	3139(G7)	3139(G7)	3139(G7)	3139(G7)
	6040(F#8)				
	13000(G#9)				
Peking 3	1342(E6)	1342(E6)	1342(E6)	1342(E6)	1342(E6)
	3404(G#7)	3379(G#7)			
	6774(G#8)				
Peking 5	1599(G6)	1599(G6)	1599(G6)	1599(G6)	1599(G6)
	3521(A7)	3467(A7)	3467(A7)		
	7101(A8)				
Peking 6	1793(A6)	1793(A6)	1793(A6)	1793(A6)	1793(A6)
	3423(A7)	3423(A7)	3423(A7)	3423(A7)	3423(A7)
	5356(E8)	5356(E8)			
Peking 1'	2123(C7)	2123(C7)	2123(C7)	2123(C7)	2123(C7)
	3545(A7)	3511(A7)	3511(A7)	3545(A7)	3545(A7)

The measurements of frequency from peking using Melda analyzer are compared to the other measurements using different gamelan ensembles and methods (Table 3). Table 3 shows the frequency of pelog and slendro peking from other work using different ensembles and methods as references (Pramudya et al., 2018). Table 3 also shows the comparison to other frequency measurement on different gamelan ensembles i.e. from gamelan ITB (Institute Technology Bandung, Indonesia) using different methods (Pramudya et al., 2018).

From the results, the frequency measurements have small different compared to the references. These differences are due to different gamelan ensembles and methods. The frequency measurement of slendro peking 1, 2, 3, 5, 6 and 1' are having similar values as shown by the differences in Table 3. The peking in our works 1, 2, 3, 5, 6, 1' has the frequency 1066, 1178, 1342, 1599, 1793 and 2123 as compared to 1046 (C6), 1174 (D6), 1318 (E6), 1568 (G6), 1760 (A6), and 2093 (C7) respectively from the piano scale Table 3. This fact is interesting since the frequency different between our peking and the piano scale is quite small. Figure 15 to Figure 20 show the TFA from peking 1, 2, 3, 5, 6 and 1' over time with the black and grey part that explains its intensity at the frequency range on the vertical axis. The vertical scale on this figure is a frequency scale (in Hz), and the horizontal scale is a time scale (in second). This figure provides a description of the sound in the time frequency plane.

Table 3
The frequencies of pelog and slendro peking and their comparison to the other measurements (Pramudya et al., 2018)

Pelog tone	Hertz (Pramudya et al., 2018)	Gamelan ITB (Pramudya et al., 2018)	Slendro tone	Hertz (**) (Pramudya et al., 2018)	Gamelan ITB (Pramudya et al., 2018)	Our work (*)	**.*	Piano scale (***)	*-***
Peking 1	1176	1208	Peking 6'	928	928	-	-		
Peking 2	1272	1300	Peking 1	1075	1073	1066	9	1046	20
Peking 3	1409	1391	Peking 2	1234	1246	1178	56	1174	4
Peking 4	1643	1639	Peking 3	1423	1418	1342	81	1318	24
Peking 5	1765	1757	Peking 5	1636	1639	1599	37	1568	31
Peking 6	1862	1854	Peking 6	1870	1854	1793	77	1760	33
Peking 7	2101	2050	Peking 1'	2118	2167	2123	-5	2093	30



Figure 15. Time-frequency analysis from peking 1



Figure 16. Time-frequency analysis from peking 2

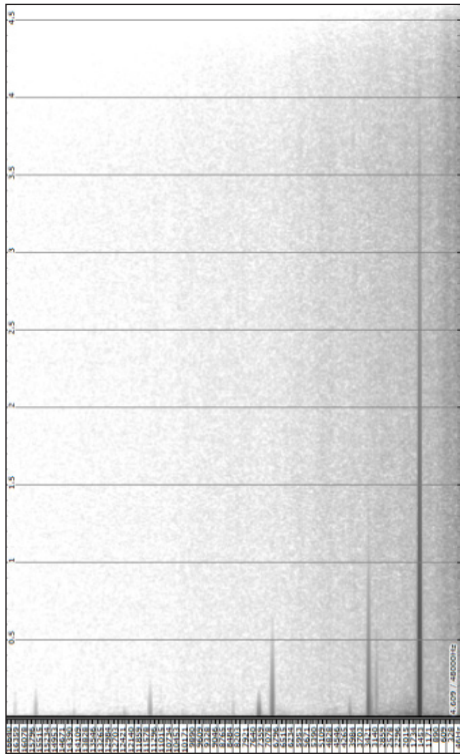


Figure 18. Time-frequency analysis from peking 5

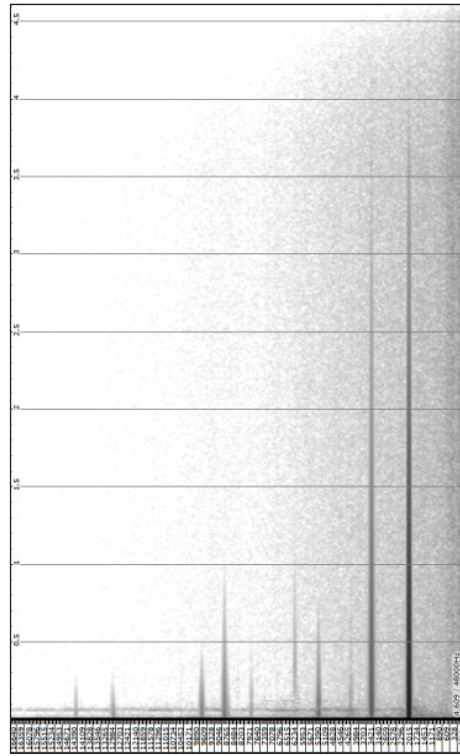


Figure 20. Time-frequency analysis from peking 1'

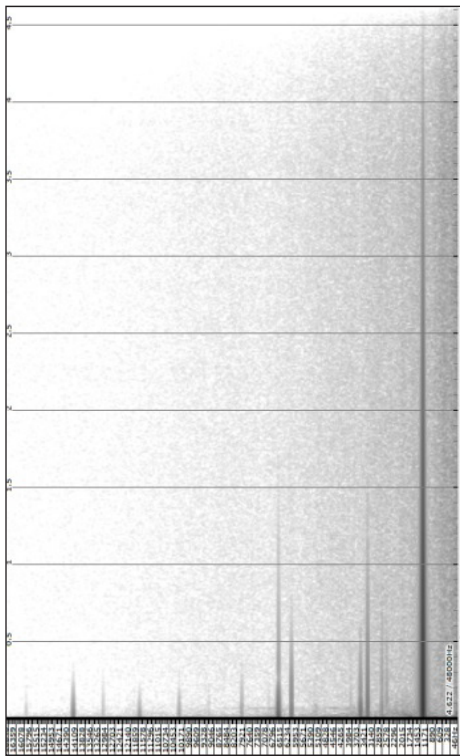


Figure 17. Time-frequency analysis from peking 3

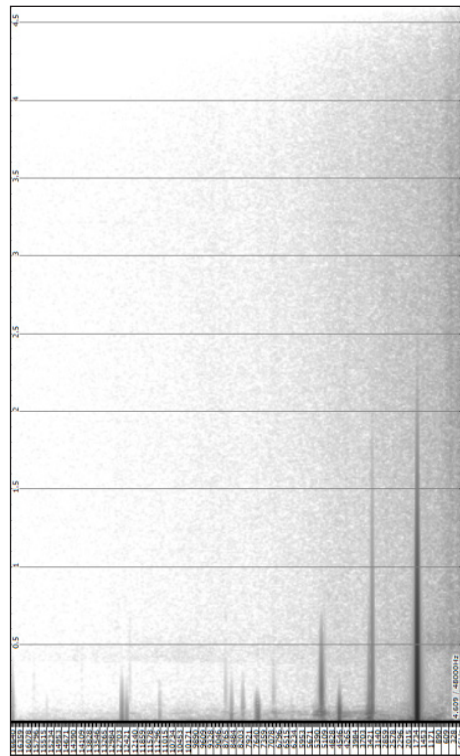


Figure 19. Time-frequency analysis from peking 6

From the TFA, peking 1, 2, 6 and 1' obviously show 2 distinct peaks at the fundamental and overtone frequencies while peking 3 and 5 show a small intensity of overtones. The larger values of these spectra are displayed darker. The gray regions represent values that are near zero in magnitude. The spectra for the individual frequency are clearly separated in the y-axis and clearly divided into line segments, lying above each frequency and corresponding to the fundamentals and overtones in each note. There are clear differences between the attack and decay of the spectral line segments for the frequency obtained from peking. These differences are visible where a very prominent attack due to the striking by the mallet which is showed in the black regions in its spectrogram near the beginning of the fundamental and first overtone line segments for each frequency. These regions can be termed non-harmonic spectra, since they are non-integral multiples of the fundamental. These regions arise from transient, non-linear effects during the attack of each note. There is also a longer decay for peking 3, 5 and 1' due to the slow damping down of the peking vibrations which is evident in the overlapping of the black and gray part for each note line segment. Peking 1, 2 and 6 exhibits a much gentler attack and rapid decay than Peking 3, 5 and 1'. It is well known that, in addition to the harmonic structure of fundamentals and overtones, the precise features of attack and decay in notes are important factors in human perception of musical quality. This comparison of 5 peking illustrates how all of these features of musical notes can be quantitatively captured in the TFA provided by spectrograms.

Figure 21 illustrates a uniform scale of frequencies in the Adobe spectrogram of peking 1'. In this spectrogram there is a number of spectral line segments crowded together at the lower end of the frequency scale. Figure 21 identifies the pitch of the sound by the high pixel intensity. The fundamental and overtones frequencies correspond to the pitch of the sound. These line segments correspond to the fundamental and higher frequency peaks in the Fourier spectrum for the sound in Figure 22. Figure 22 spectrum shows a fundamental at 2.1 kHz which is close to the standard frequency of 2093Hz (for C7) and overtones at 3.7 kHz (which is close to the standard frequency of 3729 Hz for A#7), 5.36 kHz and 9.6 kHz. It is these frequencies that are crowded together in the spectral lines at the lower end of the spectrogram in Figure 21. These overtones frequencies ratio are approximately 1.8, 2.6, and 4.6 since $3.7/2.1=1.76\approx 1.8$, $5.36/2.1=2.55\approx 2.6$ and $9.6/2.1=4.57\approx 4.6$ respectively. These overtones ratio are non-harmonic since they are non-integral multiples of the fundamental. It may be that they are overtones resulting from body cavity resonances in the peking. The sound can also be associated to the intensity frequency profile at particular time given by the spectrogram as shown in figure 14. It is straight forward to interpret the rest of the spectrogram with respect to time. The numbers on the vertical axis is directly interpreted as physical frequency values. These attributes are determined by Adobe for computing the frequency in Hertz and the pitch corresponding to the equal tempered scale.

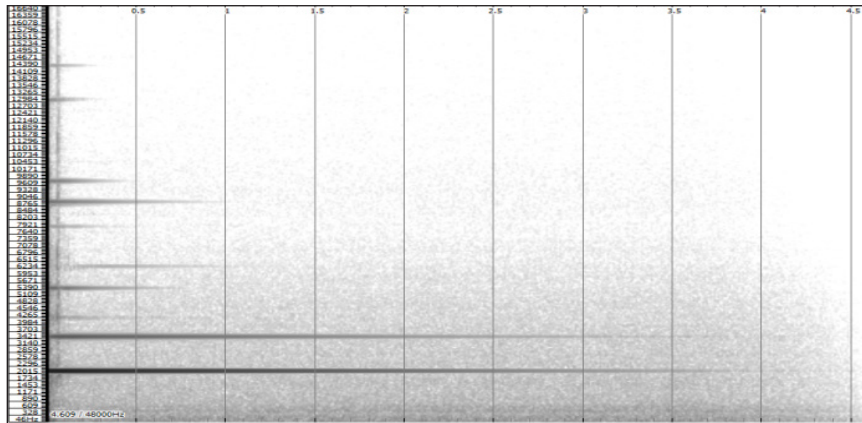


Figure 21. Time-frequency analysis (TFA) from Adobe for peking 1'

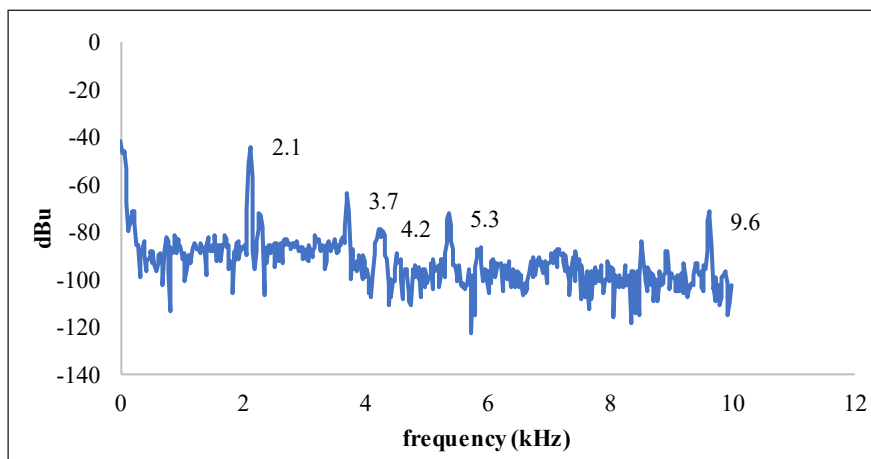


Figure 22. Frequency spectrum from PicoScope reading for peking 1'

CONCLUSION

The intuitive tuning by the gamelan tuner is normally based on their instinct knowledge or understanding the tuning is based on their feelings rather than facts or proofs. Each tuner has its references. Therefore, this study attempted to extract the intuitive tuning by the gamelan tuner and examined it using three different time-frequency analysis approaches: Fourier spectra (using PicoScope), spectromorphology (Using Melda analyzer) and spectrograms (using Adobe). PicoScope reading provides the fundamental and several overtones frequencies in the entire signals, while spectromorphology identify the changes of frequency spectrum at fixed time and Adobe spectrograms identify the frequency with time. The spectromorphology are associated with the intensity frequency profile captured at one particular time from the intensity frequency content of the signal. Adobe provides TFA with the black and grey part that explains its intensity at the frequency range stated

on the vertical axis. The peaks from PicoScope are non-harmonic since they are non-integral multiples of the fundamental. Melda reading proved that all peking sustained the initial fundamental frequency and overtone at $t=0$ until 2s. TFA provides a description of the sound in the time frequency plane. From TFA, peking 1, 2 and 6 exhibit a much gentler attack and more rapid decay than peking 3, 5 and 1'. These non-harmonics yield difficulties in discriminating sound wave by human ear since individual harmonics are not easily distinguished because human ear is not capable of distinguishing the individual harmonics of a complex tone and the identification of the partials may be nearly impossible in listening to tones in a musical context. The identification of the partial may be nearly impossible when listening to peking but the frequencies that are present in the signal are easily identified, with information about time localization giving dominant frequency for each tone at specific time.

ACKNOWLEDGEMENT

This research is funded under Fundamental Research Grant Scheme (FRGS), with reference no. FRGS/1/2013/SG02/ UNIMAS/02/1) Investigating the Vibration of Damped and Free Vibrating Plates Material of Gamelan Instruments, awarded by the Ministry of Education. The authors wish to express their great sadness on the passing of one of the authors Mr. Iran Amri Musoddiq on 31 March 2020 due to COVID-19.

REFERENCES

- Cremer, L., & Heckl, M. (1967). *Korperschall*. Heidelberg, Germany: Springer.
- Ellis, A. J., & Hipkins, A. J. (1884). II. Tonometrical observations on some existing non-harmonic musical scales. *Proceedings of the Royal Society of London*, 37(232-234), 368-385.
- Fletcher, N. H., & Rossing, T. D. (1998). *The physics of musical instruments*. New York, NY: Springer.
- Hood, M. (1966). Sléndro and pélog redefined. *Selected Reports*, 1(1), 28-48.
- Johnston, I. (2009). *Measured tones: The interplay of physics and music*. Boca Raton, Florida: CRC Press.
- Kartomi, M. J. (1985). *Musical instruments of Indonesia*. Melbourne, Australia: Indonesian Arts Society.
- Kubik, G. (1991). Theorie, aufführungspraxis und kompositionstechniken der hofmusik von Buganda [Theory, performance practice and several compositional techniques court music of Buganda]. *Hamburger Jahrbuch für Musikwissenschaft*, 2, 23-162.
- Kunst, J. (1934). *De Toonkunst van Java* [From toon art from Jawa]. The Hague, Netherlands: Martinus Nijhoff Publishers.
- Lentz, D. A. (1965). *The gamelan music of Java and Bali*. Michigan, USA: University of Nebraska Press.
- McPhee, C. (1966). *Music in Bali*. New Haven, Connecticut: Yale University Press.
- Morton, D. (1976). *The traditional music of Thailand*. Berkeley, USA: University of California Press.

- Owsinski, B. (2009). *The recording engineer's handbook*. Boston, MA: Course Technology PTR.
- Perrin, R., Hamden, S., Halkon, B. J., & Swallowe, G. M. (2013). Studies with a small gamelan gong. *Proceeding of the Institute of Acoustics*, 35(1), 337-344.
- Plomp, R. (1976). *Aspects of tone sensation*. London, England: Academic Press Inc.
- Pramudya, Y., Widayanti, L., & Melliagrina, F. (2018). Frequency measurement of bonang barung and peking in Javanese gamelan using audacity. *Journal of Physics: Conference Series*, 1075(1), 1-7.
- Rahn, J. (1978). Javanese pélog tunings reconsidered. *Yearbook of the International Folk Music Council*, 10, 69-82.
- Sethares, W. A. (2005). *Tuning, timbre, spectrum, scale*. Heidelberg, Germany: Springer Science & Business Media.
- Schneider, A. (2001). Sound, pitch, and scale: From "Tone measurements" to sonological analysis in ethnomusicology. *Ethnomusicology*, 45(3), 489-519.
- Schneider, A., & Beurmann, A. E. (1990). Okutuusa Amadinda: Zur Frage aquidistanter Tonsysteme und Stimmungen in Afrika [What inspires us Amadinda: To question aquidistanter sound system and moods in Afrika]. In P. Petersen (Ed.), *Musikkulturgeschichte Festschrift für Constantin Floros* [Music culture given to festival for constantin floros] (pp.493-526). Wiesbaden, Germany: Breitkopf & Haertel Publishing.
- Schneider, A., & Beurmann, A. E. (1993). Notes on the acoustics and tuning of gamelan instruments. In B. Arps (Ed.), *Performance in Java and Bali* (pp. 197-218). London, England: School of Oriental and African Studies.
- Schneider, A. (1999). Autoregressive spectral analysis and wavelet gammatone filtering of idiophone sounds: Implications for pitch perception. In I. Zannos (Ed.), *Music and signs* (pp. 99-116). Bratislava, Slovakia: ASCO.
- Sorrell, N. (1990). *A guide to gamelan*. London, England: Faber and Faber Limited.
- Stumpf, C. (1901). Tonsystem und Musik der Siamesen [Sound system and music the Siamesen]. *Beiträge zur Akustik und Musikwissenschaft*, 3, 69-146.
- Sudarjana, P. J., Surjodiningrat, W., & Susanto, A. (1993). *Tone measurements of outstanding Javanese gamelans in Yogyakarta and Surakarta*. Yogyakarta, Indonesia: Gadjah Mada University Press.
- Surjodiningrat, W., Sudarjana, P. J., & Susanto, A. (1972). *Tone measurements of outstanding Javanese gamelans in Jogjakarta and Surakarta* (2nd Ed.) Jogjakarta, Indonesia: Gadjah Mada University Press.
- Van Zanten, W. (1986). The tone material of the kacapi in Tembang Sunda in West Java. *Ethnomusicology*, 30, 84-112.
- Vetter, R. (1989). A retrospect on a century of gamelan tone measurements. *Ethnomusicology*, 33, 217-227.
- Voisin, F. (1994). Musical scales in Central Africa and Java: Modeling by synthesis. *Leonardo Music Journal*, 4, 85-90.
- Widdess, R. (1993). Slendro and Pelog in India? In B. Arps Ed.), *Performance in Java and Bali* (pp. 186-196). London, England: School of Oriental and African Studies.



Timbre Spectrum of Gamelan Instruments from Four Malay Gamelan Ensembles

Sinin Hamdan^{1*}, Ahmad Faudzi Musib², Iran Amri Musoddiq³ and Marini Sawawi¹

¹Faculty of Engineering, Universiti Malaysia Sarawak, 94300 UNIMAS, Kota Samarahan, Sarawak, Malaysia

²Faculty of Human Ecology, Universiti Putra Malaysia, 43400 UPM, Serdang, Selangor, Malaysia

³Faculty Applied and Creative Art, Universiti Malaysia Sarawak, 94300 UNIMAS, Kota Samarahan, Sarawak, Malaysia

ABSTRACT

Gamelan in general is categorized as a group of gongs. This traditional Malay gamelan ensemble is in a slendro scale i.e. five notes per octave. The rhythms, pitch, duration and loudness classify the various groups of gongs such as bonang, kenong, gender, peking and gambang. The cast bronze peking, kenong and bonang were chosen from a range of Malay gamelan ensemble from Universiti Malaysia Sarawak (UNIMAS), Universiti Putra Malaysia (UPM), Universiti Kebangsaan Malaysia (UKM) and Universiti Teknologi Mara (UiTM). The sounds were recorded by PicoScope Oscilloscope. The PicoScope software displays waveform and spectrum in time and frequency domain respectively. The peking lowest and highest frequencies from UiTM were 293 Hz and 1867 Hz, from UPM were 644 Hz and 1369 Hz, from UKM were 1064 Hz and 2131 Hz and from UNIMAS were 1072 Hz and 2105 Hz respectively. The kenong lowest and highest frequencies from UiTM were 259 Hz and 463 Hz, from UPM were 294 Hz and 543 Hz, from UKM were 300 Hz and 540 Hz and from UNIMAS were 293 Hz and 519 Hz respectively. The fundamental frequencies of

bonang from UPM were higher than that of UKM, UiTM and UNIMAS. The harmonics were not successive but interrupted by another frequency. The harmonics of each bonang was similar except for gamelan from UKM.

Keywords: Bonang, fundamental frequencies, kenong, overtone, peking

ARTICLE INFO

Article history:

Received: 20 August 2019

Accepted: 02 January 2020

Published: 15 April 2020

E-mail addresses:

hsinin@unimas.my (Sinin Hamdan)

faudzi@upm.edu.my (Ahmad Faudzi Musib)

amiran@unimas.my (Iran Amri Musoddiq)

smarini@unimas.my (Marini Sawawi)

* Corresponding author

INTRODUCTION

The Malay gamelan normally consists of seven main instruments i.e. gambang, bonang, saron demung, kenong, small gong and big gong and 2 instruments from saron group namely saron barung and saron panerus (Sumarsam, 2003). The gamelan is a collection of bronze gongs, gong-chimes, metallophones, drums, flute, bowed and plucked string instruments. Each gamelan is different from the other where iron sometimes is replaced with bronze. Gambang is also one of the main instruments in a gamelan ensemble which consists of pieces of hard wood placed on wooden box which function as a sound resonator. This piece of wood is hit with a set of covered wood mallet and produces certain pitch. Gendang is another traditional instrument that is very significant in the traditional Malay music ensemble like gamelan. The surface is made from goat or cow leather and its tension is made by rattan. The resonator is made from hard wood such as *merbau*. Recently, gamelan music is also played in the West (Suprpto et al., 1993, Sumarsam, 2002, Sumarsam, 2003, Spiller, 2004). The melody of a single instrument is not separable from the whole ensemble. The instruments are tuned to either five-tone slendro or seven-tone pelog. The Malay gamelan instruments have their own pitch characteristics compared to the Javanese gamelan. Hence, the intensity and frequency of the instruments are different between each other. The peking (also known as Saron Panerus) bar shape has rounded top side while the kenong has the shape of an inverted bowl (Sethares, 2005). Figure 1 and 2 show a typical set of peking bar and a typical kenong kettle respectively. The frequency of Gamelan Swastigitha and Gamelan Kyai Kaduk Manis has been measured using oscilloscope (Sudarjana et al., 1993) whereas the frequency of gong has been measured using sonogram by Kuswanto, 2012 as stated by Pramudya et al. (2018).

The lowest and the highest frequencies of Pelog Peking are 1176.1 ± 1.1 Hz and 2101.0 ± 0.0 Hz, respectively, whereas the lowest and the highest frequencies of Slendro Peking are 928.1 ± 2.2 Hz and 2118.1 ± 1.1 Hz, respectively (Pramudya et al., 2018). Table 1 shows the frequencies of each peking and their comparison to the other measurements.

Table 1

The frequencies of each Peking and their comparison to the other measurements (Pramudya et al., 2018)

Tone of pelog	Frequency	Gamelan ITB	Tone of slendro	frequency	Gamelan ITB
1	1176	1208	6	928.1	928
2	1272	1300	1	1075	1073
3	1409	1391	2	1234	1246
4	1643	1639	3	1423	1418
5	1765	1757	5	1636	1639
6	1862	1854	6	1870	1854
7	2101	2050	1	2118	2167



Figure 1. A typical peking



Figure 2. A typical kenong

Saron is a metallophone consisting of six or seven bronze bars that form one octave (either slendro or pelog tuning). The saron families consist of saron demung, saron barung, and saron panerus. Saron barung provides the medium octave while saron panerus gives the highest octave as it has thicker and narrower bars than saron demung. Saron panerus forms the core melody. Saron demung has the largest bars and produces the lowest pitch. Saron barung is one octave higher than the saron demung where the higher pitch is produced by the smaller bar. The bars are 35.5cm long and 9 cm wide. The mallet is struck at an angle to produce a full sound. The note is dampened half a beat before it is struck again for repeated notes (Tenzer, 2006). Every saron is distinguished from the size and the different sound. These saron groups consist of 6 arranged blades of bronze and they are hit using mallet. Saron demung's size is bigger compared to saron barung and saron panerus. Saron panerus has the smallest size. The 6 bronze blades in saron are arranged according to the scale tones 1, 2, 3, 5, 6 and 1'.

Kenong is also made of bronze and it functions as a colotomic instrument in gamelan music. Colotomy describes the rhythmic and metric patterns of gamelan music. It acts to mark off nested time intervals or dividing rhythmic time into such nested cycles. Kenong has fixed pitch based on the western tempered scale. It consists of 5 medium-size gongs which are arranged according to the scale tones of 1, 2, 3, 5, 6 (the sound 1' replaced by 1). Gong is the main complement in gamelan music composition. There are 2 types of gong that are different in sizes and they are called the big gong and the small gong. Bonang is a musical instrument from idiophone category which has the shape of a kettle (small gong) and having sound characteristic based on low humming principle. Bonang starts the opening of the music which later followed by another gamelan instrument. Bonang is also made from bronze and it is the main melodic instrument in a gamelan ensemble. The lowest and highest frequencies of the first row of Pelog Bonang Barung are 609.6 ± 0.1265 Hz and 1050 ± 0.09487 Hz, respectively. For the second row, the lowest and highest frequencies are 300.1 Hz and 512.8 Hz, respectively (Pramudya et al., 2018). Table 2 shows the frequencies of each kettle on the second row (lower pitch) of Pelog Bonang Barung and their comparison to the other measurements.

Table 2

The frequencies of each kettle on the second row (lower pitch) of Pelog Bonang Barung and their comparison to the other measurements (Pramudya et al., 2018)

Tone	Frequency	Swastigitha	Kyai kaduk Manis
1	300.1	300	310
2	322.3	324	336
3	345.8	353	362
4	411.0	415	424
5	459.5	444	445
6	476.1	472	482
7	512.8	525	538

Figure 3 shows a set of 10 bonang ensembles (the upper row is called bonang penerus, the lower row is called bonang barung).



Figure 3. A set of 10 bonang ensemble (the upper row is the bonang penerus, the lower row is the bonang barung)

Studies on Javanese gamelan were done by experts from the West and East. The tones measurement has been pioneered by Ellis and Hipkins (1884) scientifically. Sudarjana et al. (1993) investigated the vibration frequency of gamelan instrument tone system. Sudarjana et al. (1993) measured the tone of Javanese gamelan and Schneider (2001) studied the sound, pitch and scale of idiophones such as gamelan instrument. In this work, we measure the fundamental and overtone frequency which is also called the timbre. Fourier transformation determines fundamentals, harmonics and sub harmonics. Different intensity and harmonics or sub harmonics (overtones) distinguish each instrument characteristics.

The relationship between time and frequency has been well-established which include the study of the sound that coincides with the Fourier analysis. Fourier analysis yields the frequency content to understand the sound. In the Fourier analysis, the signal in real voltage-time axis is converted to dB-frequency axis. In PicoScope only dB-frequency is displayed for the whole spectra. In Melda analyser, the dB is displayed with a frequency at one specific time. While PicoScope displays only changes of frequency in the whole

spectra, Melda analyser displays several frequencies at one particular time. Melda analyser displays changes of several frequencies at different time. It also shows how the fundamental frequency changes with time and overtone frequency become dominant after certain period of time.

The purpose of this work is to study the tone in a peking/kenong/bonang. These spectra are used to identify the pitch of the sound produced by the signal. These spectra display several peaks which are obviously dominant and can be classified as the fundamental and overtones peaks. These peaks coincide with the notes intended for the sound produced from the instruments signal. The individual peak represents the pitch/notes of the instruments. The first highest dominant fundamental frequency determined the pitch of the instrument. The addition of the frequency with the overtones creates the sound and the quality of this sound is determined from the harmonic/non-harmonic frequencies.

The musical scales such as the well-tempered scale are based on a logarithmic scale for frequencies, but spectrograms display frequencies on a uniform scale (Johnston, 1989). Since the human ear is not capable of distinguishing the individual harmonics of a complex tone, the identification of the partials may be nearly impossible in listening to tones in a musical context (Plomp, 1976). Thus, experimental evidence using the spectra is utmost important for analysing the frequency. The pitch is sometimes guessed by Mother Nature using the tuner’s ear. In a field trip to Jogjakarta, the tuner used a pianica to listen the pitch and tune the instrument using his hearing solely. Experimental evidence using the spectra produces a series of frequencies which can be analysed consisting of the dominant fundamental frequency and all the possible overtones frequencies. The scheme of peking slendro and kenong slendro note arrangement is shown in Figure 4.-

PEKING SLENDRO	C6 (1046.5)	D6 (1174.7)	E6 (1318.5)	G6 (1568.9)	A6 (1760.0)	C7 (2093.0)
KENONG SLENDRO	D4 (293.67)	E4 (329.63)	G4 (392.00)	A4 (440.0)	C5 (523.25)	- -

Figure 4. The tuning schemes of peking slendro and kenong slendro with the note arrangement

In this work we study the colour of sound of Malay gamelan peking/kenong/bonang from Universiti Malaysia Sarawak (UNIMAS), Universiti Putra Malaysia (UPM), Universiti Kebangsaan Malaysia (UKM) and Universiti Teknologi Mara (UiTM). The colour of sound indicates a collection of frequency starting from the fundamental and all the possible overtone- sometimes defined as the timbre. Sound from a generated pure sinusoidal wave produces only one frequency and does not produce any colour of sound. We investigate the sound frequency using PicoScope.

MATERIAL AND METHODS

The peking, kenong and bonang are part of the gamelan ensemble from UKM, UPM, UiTM and UNIMAS. The frequency was measured at the studio hall of UKM, UPM, UiTM and UNIMAS. The acoustic spectra of the measured sets of just-tuned cast bronze peking, kenong and bonang which were made in Indonesia were captured using PicoScope oscilloscopes to investigate the fundamental and the overtone frequencies. Excitation was done by beating by an expert player. The microphone was held above the top surface along the axis of symmetry at a distance of about 20 cm (Figure 5). The PicoScope computer software (Pico Technology, 3000 series, Eaton Socon, UK) was used to view and analyse the time signals from PicoScope oscilloscopes (Pico Technology, 3000 series, Eaton Socon, UK) and data loggers for real time signal acquisition. PicoScope software enables analysis using Fast Fourier transform (FFT), a spectrum analyser, voltage-based triggers, and the ability to save/load waveforms to a disk. Figure 5 shows the schematic diagram of the experimental setup. The peking/kenong/bonang was placed to where the sound could be captured with minimum interference. The amplifier (Behringer Powerplay Pro XL, Behringer, China) ensured the sound capture was loud enough to be detected by the signal converter.

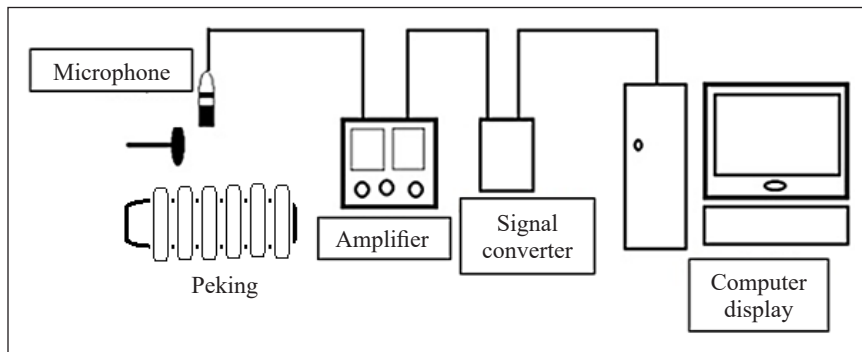


Figure 5. Schematic diagram of the experimental setups

In this study, the audio signal derived from the striking by an expert player was recorded. The audio signal was recorded in mono, at 24-bit resolution and 48 kHz sampling rate. The audio signal was recorded with the aid of a digital audio interface in a wave format. To ensure the recorded audio signal was at the optimum level, audio signal calibration of the recording system was carried out. A test tone of 1 kHz sine wave was used in calibrating the recording system. Here the 'unity' calibration level was at +4dBu or -10dBV and was read by the recording device at '0 VU'. In this regard, the EBU recommended the digital equivalent of 0VU is that the test tone generated to the recording device of the experimentation was recorded at -18 dBFS (Digital) or +4dBu (Analog) which is equivalent to 0VU. In this thorough procedure of calibration, no devices were unknowingly boosting

or attenuating its amplitude in the signal chain at the time of the recording was carried out. The recording apparatus was the Steinberg UR22 mkII audio interface, Audio-Technica AT4050 microphone, XLR cable (balance), with microphone position on axis (<20 cm) and microphone setting with low cut (flat) 0dB.

RESULTS AND DISCUSSION

The PicoScope measured the intensity and time of the signal. The Fast Fourier Transform (FFT) analysed the fundamental and overtone frequency for each tone. The typical FFT spectra of peking and kenong from UNIMAS are shown in Figure 6 and 7 respectively.

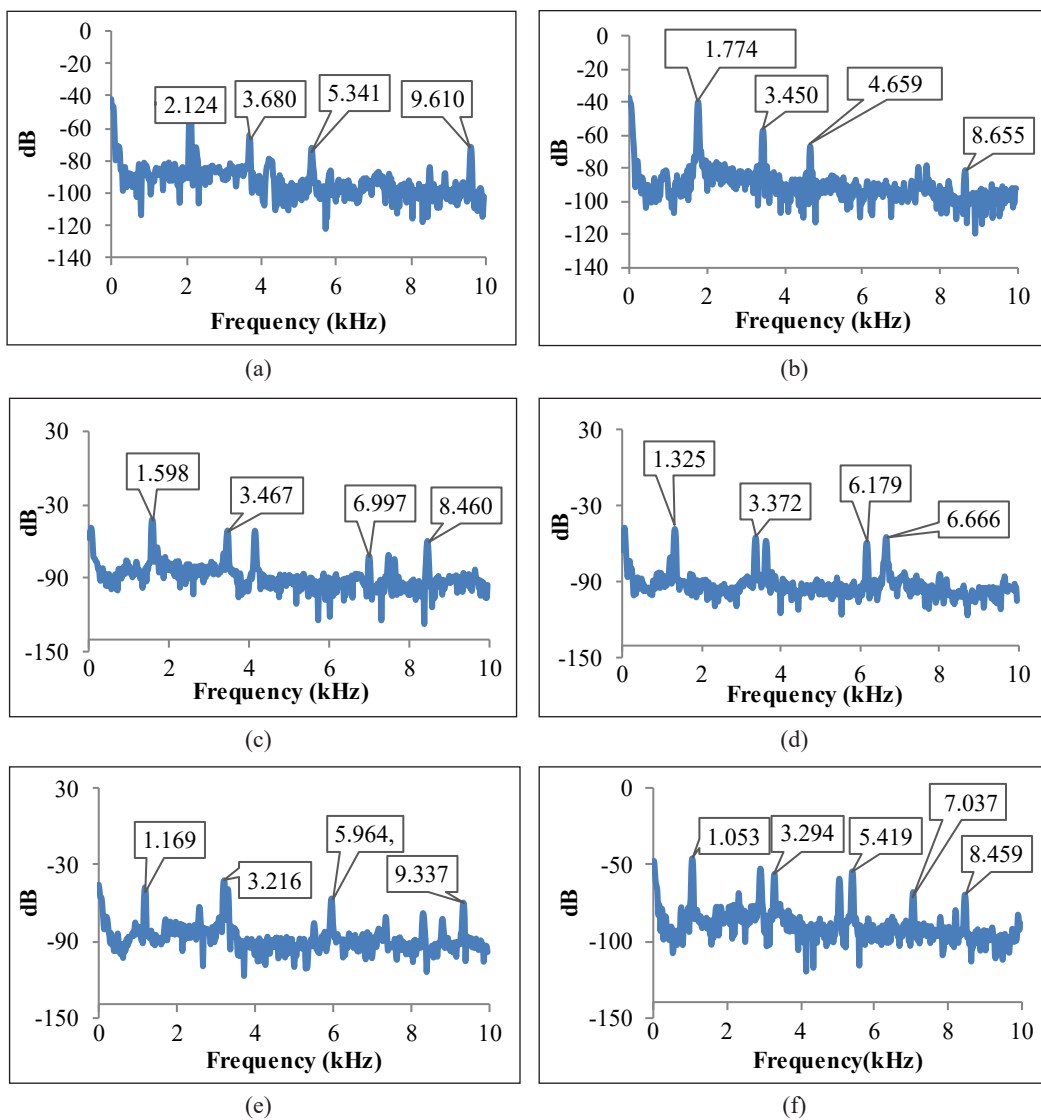


Figure 6. Spectra of peking (a) 1 (C6), (b) 2 (D6), (c) 3 (E6), (d) 5 (G6), (e) 6 (A6) and (f) 1' (C7) from UNIMAS

Table 3 shows the ratio of overtone to fundamental (f_0) frequency for each peking from UNIMAS, UKM, UiTM and UPM. Table 4 shows the ratio of overtone to fundamental (f_0) frequency for each kenong from UNIMAS, UKM, UiTM and UPM. $1^{st}/f_0$, $2^{nd}/f_0$ and $3^{rd}/f_0$ indicate the ratio of the first, second and third overtone frequency to the fundamental frequency. The bold numbers in the table indicate the exact harmonic of the overtone frequencies.

The results of kenong from this work are compared to gamelan Swastigitha and Kyai Kaduk Manis (Sudarjana et al., 1993). Table 5 shows the fundamental frequency of kenong from UNIMAS, UKM, UPM, UiTM and gamelan Swastigitha and Kyai Kaduk Manis.

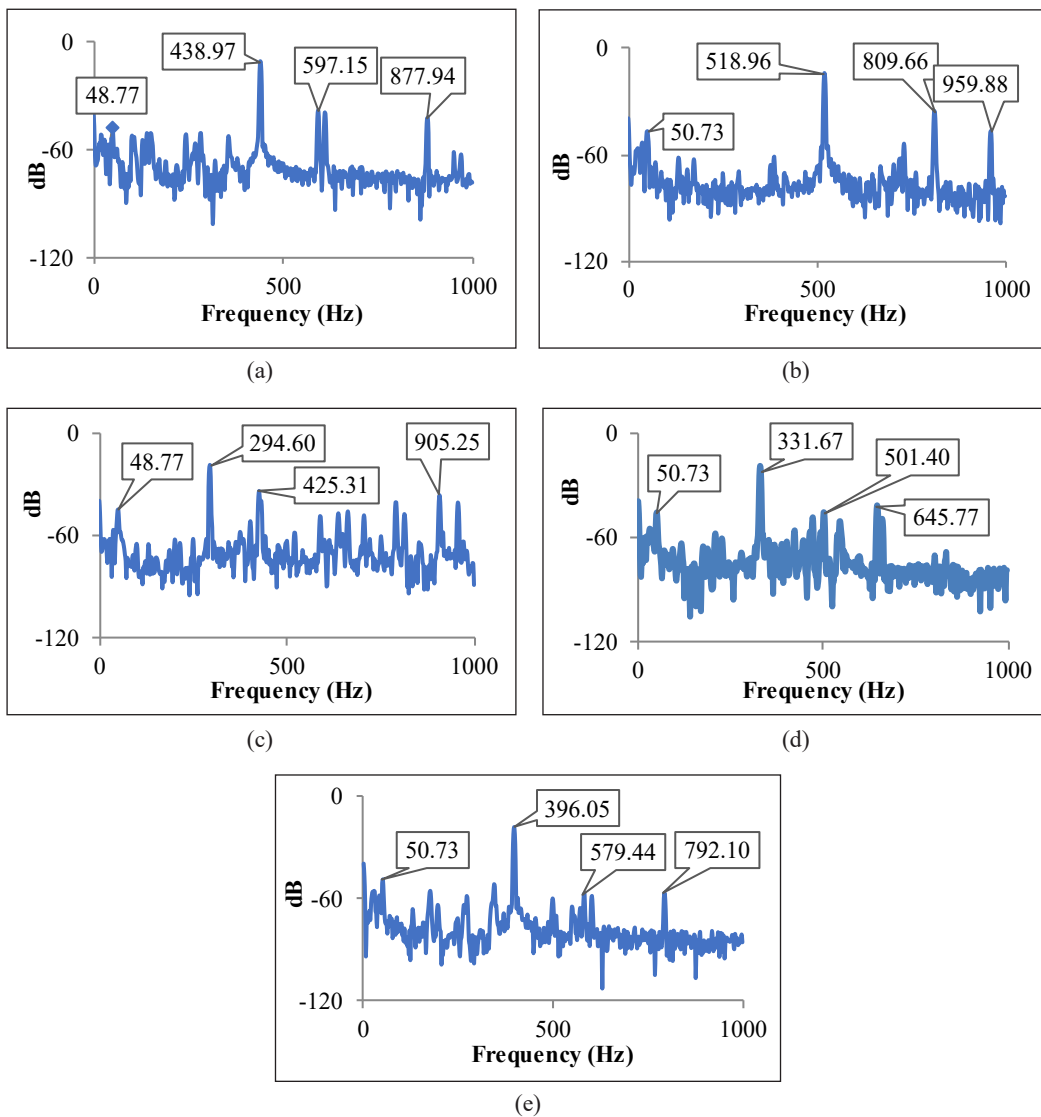


Figure 7. Spectra of Kenong (a) A, (b) C, (c) D, (d) E and (e) G from UNIMAS

Table 3
Ratio of overtone to fundamental (f_n) for each peking from UNIMAS, UKM, UiTM and UPM

Overtone/ f_0	UNIMAS			UKM			UiTM			UPM		
	1 st / f_0	2 nd / f_0	3 rd / f_0	1 st / f_0	2 nd / f_0	3 rd / f_0	1 st / f_0	2 nd / f_0	3 rd / f_0	1 st / f_0	2 nd / f_0	3 rd / f_0
Peking 1'	1.76	2.54	4.57	1.69	-	3.84	1.73	2.45	4.17	1.50	-	-
Peking 6	1.93	2.64	4.87	1.81	-	3.89	2.00	2.48	4.49	1.61	-	-
Peking 5	2.19	2.63	5.36	2.05	2.49	-	2.46	4.36	6.87	1.77	2.38	-
Peking 3	2.54	4.65	-	2.54	4.41	-	1.44	1.55	-	1.86	-	-
Peking 2	2.70	5.02	7.00	2.54	-	-	1.27	2.48	3.26	2.02	2.81	3.06
Peking 1	2.72	5.05	7.91	2.91	4.39	7.09	1.59	4.01	10	1.88	2.45	2.77

Table 4
Ratio of overtone to fundamental (f_n) for each bonang from UNIMAS, UKM, UiTM and UPM

	UNIMAS			UKM			UiTM			UPM		
	1 st / f_0	2 nd / f_0	3 rd / f_0	1 st / f_0	2 nd / f_0	3 rd / f_0	1 st / f_0	2 nd / f_0	3 rd / f_0	1 st / f_0	2 nd / f_0	3 rd / f_0
Kenong C	1.56	1.85	1.37	1.37	1.99	1.39	1.39	2.00	2.00	1.30	2.00	2.00
Kenong A	1.33	1.99	1.41	1.41	2.00	1.61	1.61	3.00	3.00	1.48	2.00	2.00
Kenong G	1.46	1.99	1.56	1.56	3.06	1.72	1.72	3.00	3.00	1.51	2.00	2.00
Kenong E	1.51	1.95	1.64	1.64	3.13	1.76	1.76	3.54	3.54	1.50	2.00	2.00
Kenong D	1.44	2.00	1.71	1.71	3.76	1.72	1.72	4.38	4.38	1.50	4.65	4.65

The results show that the frequencies from Malay gamelan were different compared to Javanese gamelan. Table 5 shows that the slendro kenong from UNIMAS is very close to the frequency obtained from the equal temperament scale.

Table 5

The fundamental frequency of kenong from UNIMAS, UKM, UPM, UiTM and gamelan Swastigitha and Kyai Kaduk Manis (Sudarjana et al., 1993)

Equal temperament (Hz)	UNIMAS	UKM	UPM	UiTM	Swastigitha	KyaiKaduk manis
B3(246)	-	-	-	-	-	242
C4(261.6)	-	-	-	259	-	-
D4(293.67)	293	300	294	292	-	-
E4(320.63)	332	344	330	-	-	320
F4(349)	-	-	-	349	357	-
F#4(369)	-	-	368	-	-	369
G4(392)	396	403	-	391	-	-
G#4(415)	-	-	-	-	412	421
A4(440)	441	453	436	-	-	-
A#4(466)	-	-	-	463	472	478
C5(523.25)	519	540	543	-	-	-
C#5(554)	-	-	-	-	-	557
D#5(622)	-	-	-	-	623	-

Figure 8 and 9 display typical frequency spectrum for bonang barung and bonang penerus sets from UNIMAS respectively. Table 6 presents the fundamental and overtone frequency (in hertz) for each bonang from UKM, UPM, UiTM and UNIMAS respectively.

The harmonics were not successive but interrupted by another frequency. In the spectra, there existed a series of frequencies starting from the highest dominant pitch followed by the overtone pitch. In an ideal case all the overtones are harmonic or in-harmonic which decay accordingly. But in some cases, there exist an interrupted pitch which is not in the harmonic or in-harmonic series. This interrupted frequency is due to the uncertain vibration of the uneven structure of the musical material. The harmonics of each bonang was similar except for gamelan UKM. This phenomenon is different from the assumption which states that percussion instruments have harmonic overtones. Percussion instruments consist of pitch and non-pitch instruments. The pitch instruments normally have harmonic overtones. Although gongs are pitch percussion, this phenomenon is different with the assumption which states that percussion instruments have harmonic overtones instruments because gongs are percussion instruments which do not have harmonic overtones. This is due to the nature of manufacturing using beating and hammering process. The different overtone

frequency indicates their timbre is different for each bonang. The number of harmonics of all bonang for all Malay gamelan set were very inconsistent as shown in bold in Table 6. From Table 6, gamelan UKM has 3 harmonics i.e. penerus 1, penerus 2, penerus 3 and barung 2 showed 2nd harmonic while penerus 3 showed 3rd harmonics. From Gamelan UPM has 2 harmonics i.e. barung 5 showed 3rd harmonic while penerus 6 showed 2nd harmonic. Gamelan UiTM has 1 harmonic i.e. penerus 5 and penerus 6 showed 2nd harmonic. Gamelan UNIMAS has 2 harmonics i.e. barung 1, penerus 5 and penerus 6 showed 2nd harmonic while penerus 1 showed 3rd harmonic. The timbre differences between the bonang may be due to differences in both material and manufacture. Nevertheless, the fundamental

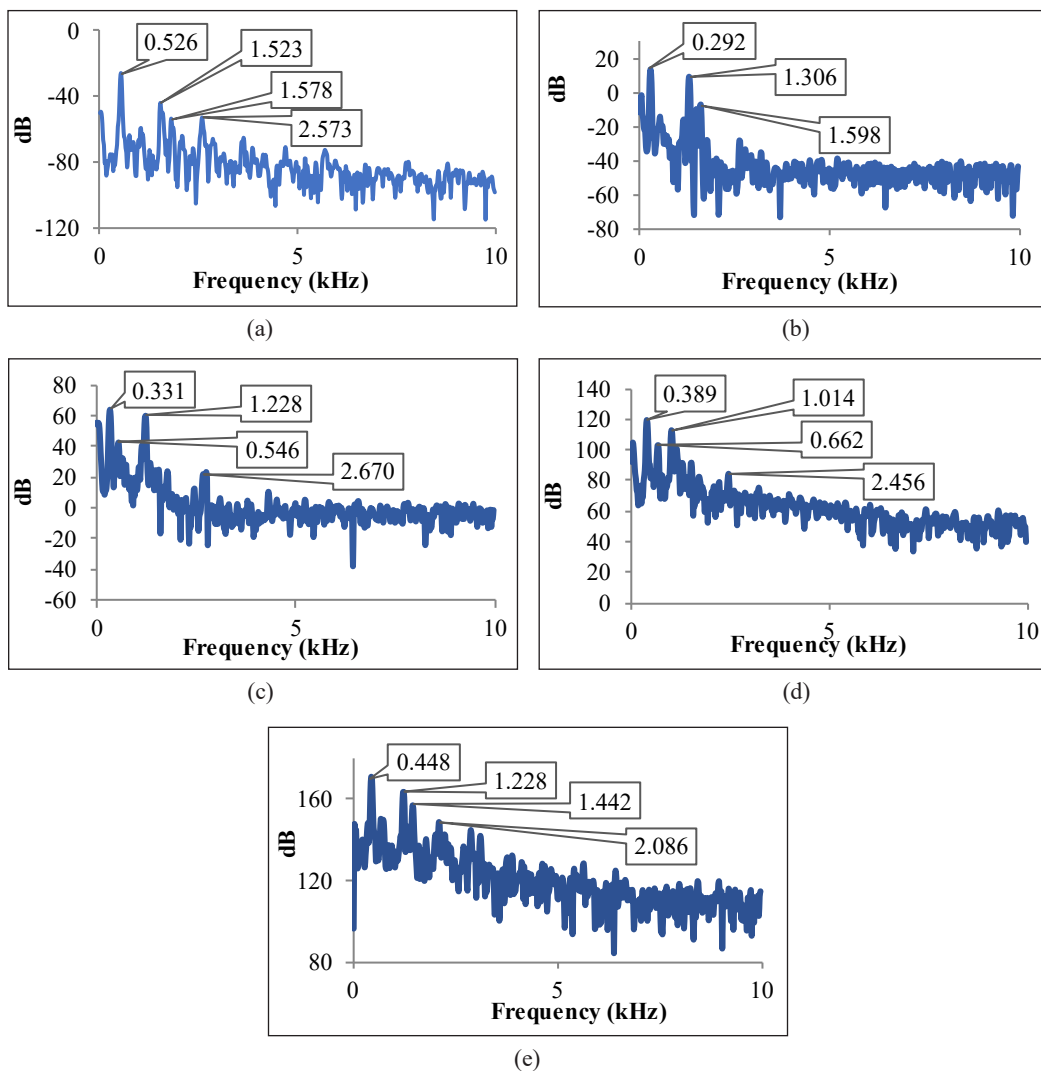


Figure 8. Frequency spectrum for bonang barung set (a) 1, (b) 2, (c) 3, (d) 5, (e) 6 from UNIMAS showing the fundamental, first, second and third overtone frequency

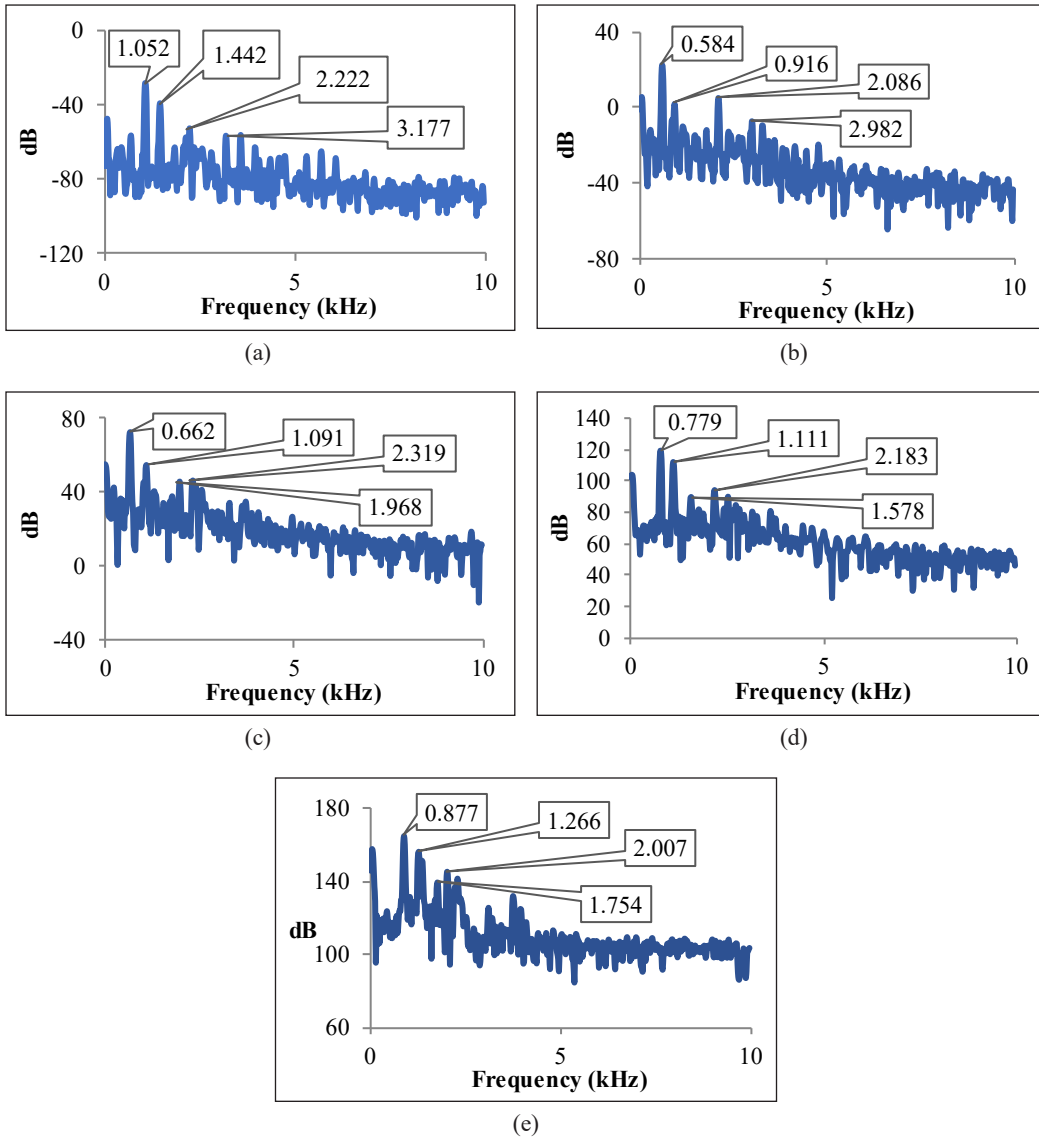


Figure 9. Frequency spectrum for bonang penerus set (a) 1, (b) 2, (c) 3 (d) 5, (e) 6 from UNIMAS showing the fundamental, first, second and third overtone frequency

pitch tends to be similar except for gamelan UPM. This result will be more meaningful if comparisons are made with more Malay gamelan sets.

Comparison between the results in Table 6 showed a variation in the fundamental and the overtones frequencies of the bonang set from UKM, UPM, UiTM and UNIMAS respectively. These differences are plotted in Figure 10 and 11 for the individual bonang penerus and bonang barung 1, 2, 3, 5 and 6 respectively from different universities. Bonang penerus 1 showed consistency in their fundamental and 1st overtone frequencies (Figure

Table 6
Fundamental and overtone frequency (in kHz) for each bonang

	UKM			UPM			UiTM			UNIMAS		
	f_1/f_0	f_2/f_0	f_3/f_0	f_1/f_0	f_2/f_0	f_3/f_0	f_1/f_0	f_2/f_0	f_3/f_0	f_1/f_0	f_2/f_0	f_3/f_0
Penerus 1	1.32	2.03	-	1.30			1.45	2.13	-	1.37	2.11	3.01
Barung 1	1.52	2.28	2.78	1.25	1.68		1.58	2.45	2.79	2.88	3.00	4.89
Penerus 2	1.49	2.00	3.31	1.43			1.64	3.79	-	1.56	3.57	5.10
Barung 2	3.77	3.98	-	1.26			4.29	9.21	-	4.47	5.13	
Penerus 3	1.43	2.00	3.04	1.41			1.61	3.59	-	1.66	3.06	3.57
Barung 3	1.65	3.61	7.49	1.43			3.48	4.41	5.35	1.19	3.88	8.58
Penerus 5	1.47	-	-	1.46			1.62	2.98	3.54	1.43	2.00	2.77
Barung 5	1.66	2.86	-	1.26	1.35	2.03	1.73	3.10	3.39	1.70	2.60	6.26
Penerus 6	1.41	2.00	2.21	1.45	3.15		1.56	2.00	2.74	1.42	2.00	2.29
Barung 6	2.77	-	-	1.27	1.36	1.79	1.65	3.24	3.59	2.81	3.36	4.86

Notes. The bold numbers in the table indicate the exact harmonic of the overtone frequencies.

10a). Bonang penerus 1 from UPM did not display 2nd overtone frequency and only bonang penerus 1 from UNIMAS displayed 3rd overtone frequency. Bonang barung 1 also showed consistency in their fundamental and 1st overtone frequencies, except from UNIMAS (Figure 11a). Bonang barung 1 from UNIMAS displayed all higher overtone frequency. All bonang barung 1 (except from UPM) displayed 3rd overtone frequency.

Bonang penerus 2 also showed consistency in their fundamental and 1st overtone frequencies except from UPM (Figure 10b). Although bonang penerus 2 from UPM displayed higher frequencies in both fundamental and 1st overtone, both 2nd and 3rd overtone disappear. Bonang penerus 2 from UiTM also did not display 3rd overtone frequency. Bonang penerus 2 from UNIMAS displayed highest 3rd overtone frequency. Although bonang barung 2 from UPM displayed the highest fundamental frequency, the 1st overtone for bonang barung 2 from UPM displayed the lowest frequency (Figure 11b). Like bonang penerus 2, bonang barung 2 from UPM also did not display the 2nd overtone. All bonang barung 2 did not display the 3rd overtone.

Bonang penerus 3 from UPM were displaying both highest frequencies in the fundamental and 1st overtone but both frequencies are missing in the 2nd and 3rd overtone (Figure 10c). Only bonang penerus 3 from UKM and UNIMAS displayed 3rd overtone. Bonang barung 3 from UPM still showed the highest fundamental frequency with the 1st overtone almost similar to UiTM (Figure 11c). Once again like bonang penerus 3, the 2nd and 3rd overtone for bonang barung 3 from UPM were missing.

Bonang penerus 5 displayed consistent fundamental and 1st overtone frequency from all universities (Figure 10d). It was found that only bonang penerus 5 from UiTM and UNIMAS displayed 2nd and 3rd overtone frequencies. Bonang barung 5 like bonang penerus 3 from UPM were displaying both highest frequencies in the fundamental and 1st overtone

(Figure 11d). Unlike bonang penerus 3 from UPM, (where both frequencies are missing in the 2nd and 3rd overtone) bonang barung 5 from UPM displayed both 2nd and 3rd overtone. Bonang barung 5 from UKM did not display 3rd overtone.

Although in the above discussion bonang barung 5, like bonang penerus 3 from UPM were displaying both highest frequencies in the fundamental and 1st overtone, bonang penerus 6 from UPM displayed the lowest frequencies in the fundamental, 1st overtone, 2nd

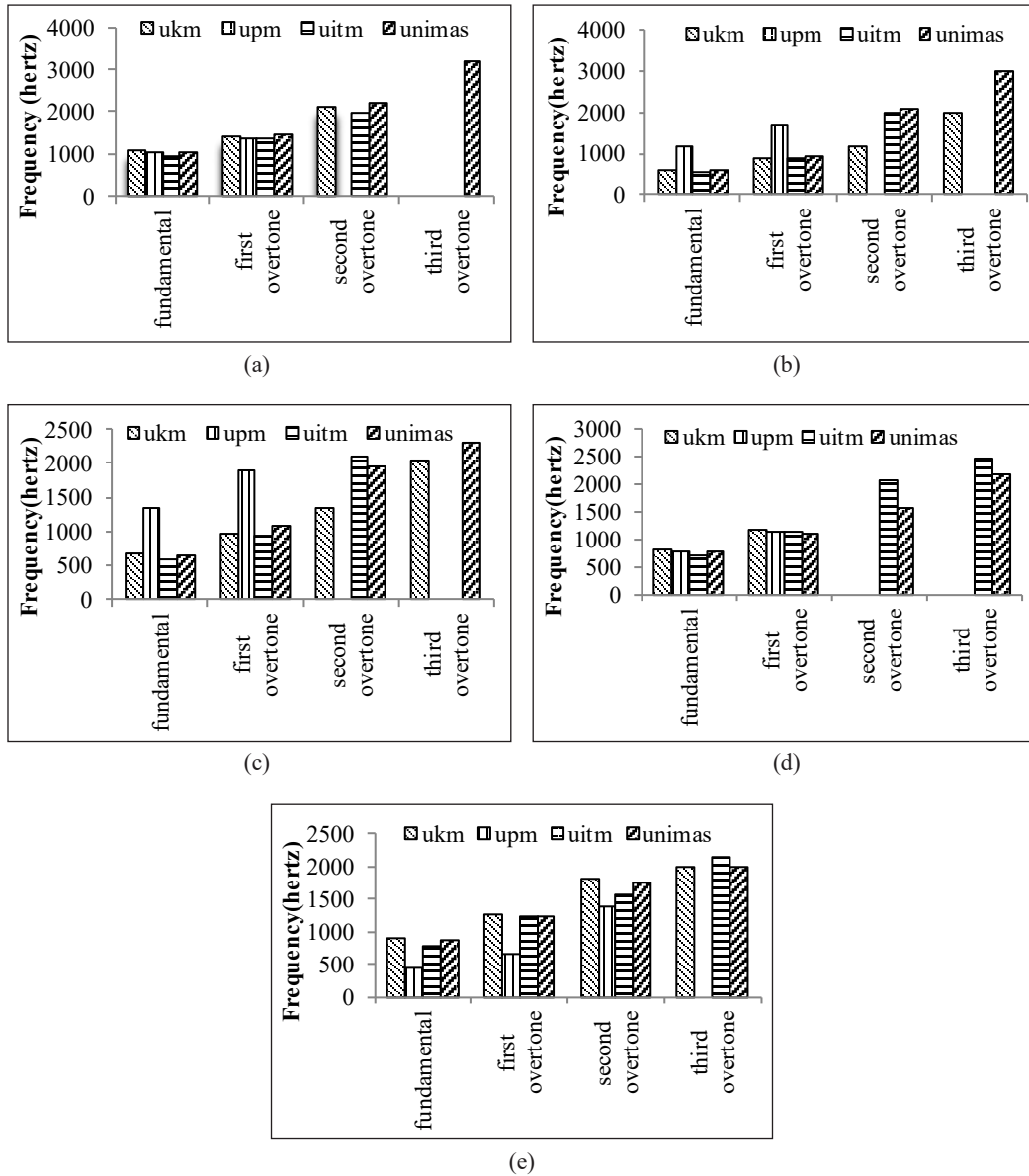


Figure 10. Fundamental and overtones frequencies of bonang penerus (a) 1, (b) 2, (c) 3, (d) 5, (e) 6 from UKM, UPM, UiTM and UNIMAS

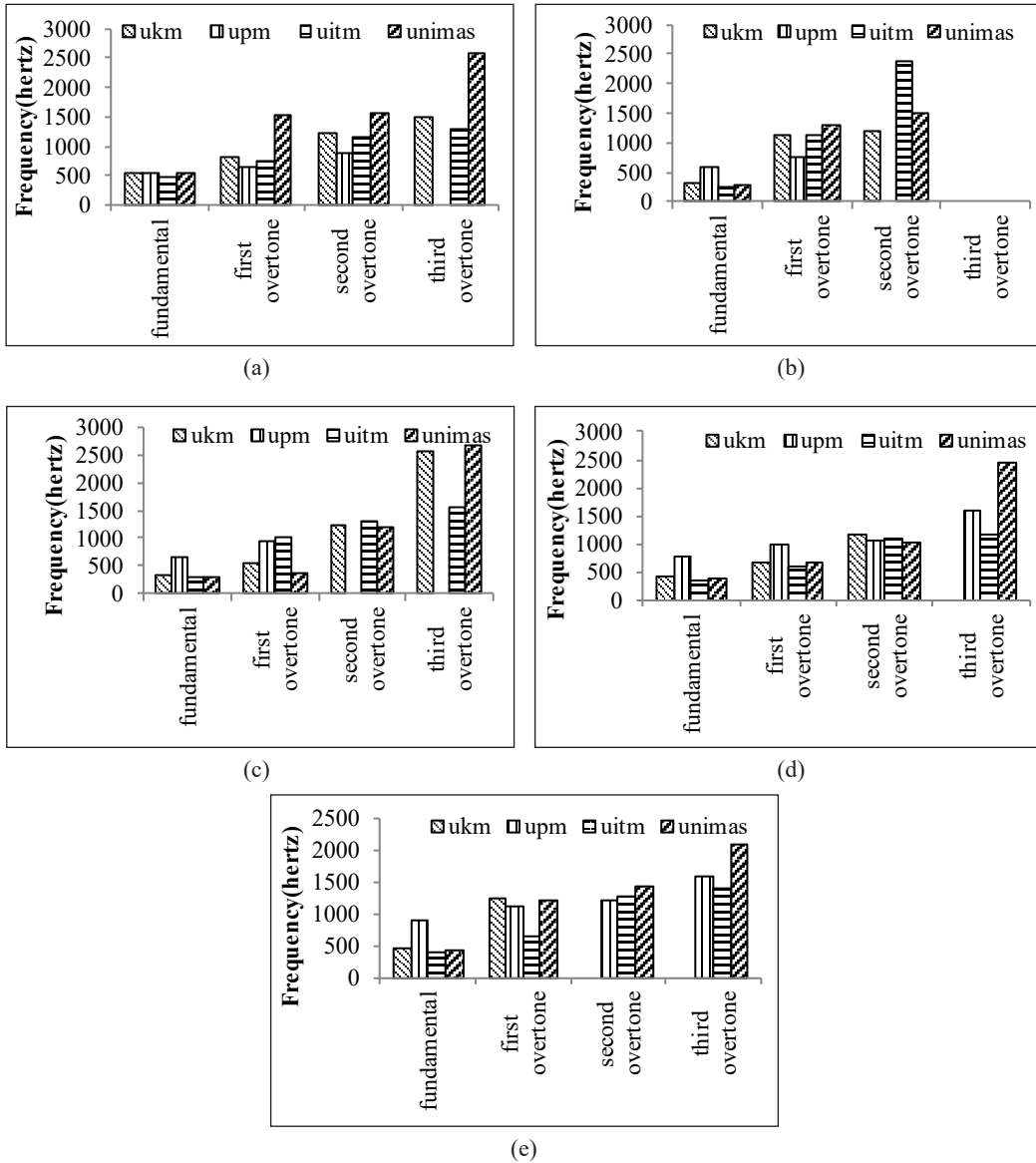


Figure 11. Fundamental and overtones frequencies of bonang barung (a) 1, (b) 2, (c) 3, (d) 5 and (e) 6 from UKM, UPM, UiTM and UNIMAS

overtone and totally missing in the 3rd overtone (Figure 10e). Although bonang penerus 6 from UPM showed the lowest fundamental frequency, surprisingly bonang barung 6 from UPM showed the highest fundamental frequency (Figure 11e). Only bonang barung 6 from UiTM showed inconsistent 1st overtone frequency and bonang barung 6 from UKM showed missing 3rd overtone frequency.

The fundamental pitch of bonang from UPM was higher compared to other bonang from UKM, UiTM and UNIMAS as indicated in Figure 12 and 13 below. The trend in

the fundamental frequency of bonang from Malay gamelan UKM, UiTM and UNIMAS was almost similar. It can be concluded that UPM Malay gamelan sets are from different materials. Both bonang penerus and bonang barung from UPM had higher fundamental frequencies than other Malay gamelan sets except for bonang penerus 5 and bonang penerus 6 which showed lower frequencies.

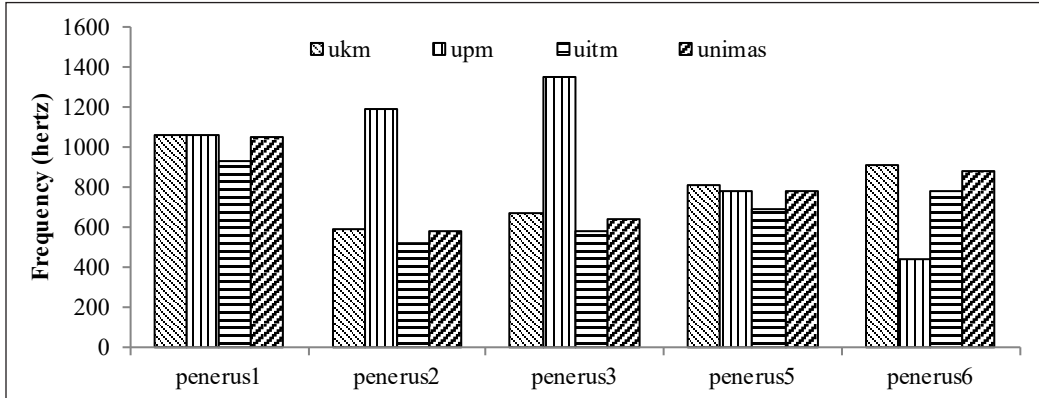


Figure 12. Fundamental frequency of bonang penerus UKM, UPM, UiTM and UNIMAS

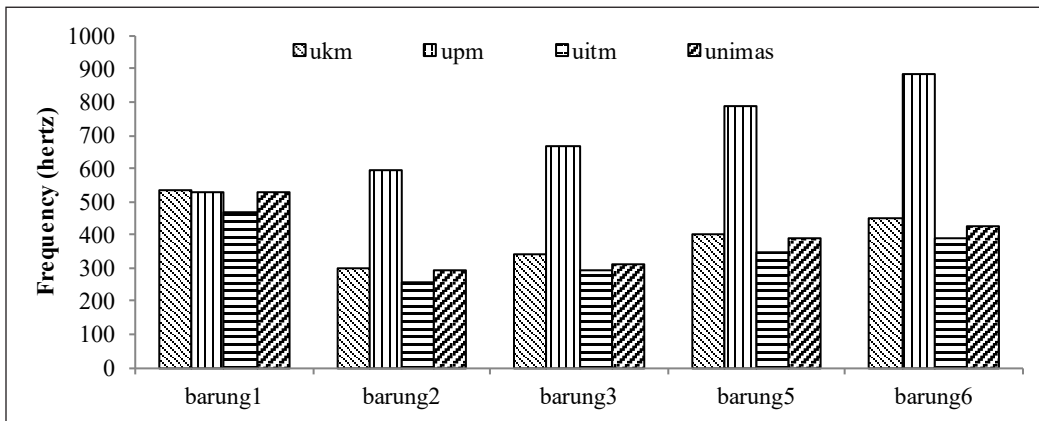


Figure 13. Fundamental frequency of bonang barung UKM, UPM, UiTM and UNIMAS

CONCLUSION

In this paper we have examined slendro peking and slendro kenong from four Malay gamelan ensemble. PicoScope reading produces spectral peaks within entire signals and provides the fundamental and several overtones frequencies in the entire signal. The peaks from peking are non-harmonic spectra since they are non-integral multiples of the fundamental except for peking 5 from UKM, peking 2 from UPM and peking 6 from UiTM

(shown in bold). The two tone quality of the kenong sets namely the kenong of gamelan Swastigitha and Kyai Kaduk Manis are compared with kenong D, E, G, A and C from this study which are well tuned to D4, E4, G4, A4 and C5 based on the C major scale. The kenong of gamelan Swastigitha used their tuning set to F4, G#4, A#4 and D#5 with 3 sharp. Whereas the kenong of gamelan Kyai Kaduk Manis are tuned to B3, E4, F#4, G#4, A#4 and C#5 in the A major scale (with 3 sharps i.e. F#, C# and G#). This study confirms that one gamelan is inevitably different in intonation, tone, and feels from another gamelan. In this research, this tuning was read with PicoScope analysis and it proved that the transmission of the tuner onto the tuning of the gamelan set can be shown on the aspect of intonation, tone, and feels. From this work, the fundamental frequencies of bonang penerus and bonang barung of gamelan UPM are higher than that of UKM, UiTM and UNIMAS, the harmonics are not successive, but interrupted by another frequency. The number of harmonics of each bonang of UKM, UPM, UiTM and UNIMAS are different where only gamelan UKM has three harmonics frequencies and the fundamental frequencies tend to be similar except for gamelan UPM.

ACKNOWLEDGEMENT

This research is funded under Fundamental Research Grant Scheme (FRGS), with reference no. FRGS/1/2013/SG02/ UNIMAS/02/1) Investigating the Vibration of Damped and Free Vibrating Plates Material of Gamelan Instruments, awarded by the Ministry of Education. The authors would like to thank Badan Kebudayaan UKM, Faculty of Music UiTM and Department of Music UPM for their assistant in using their Malay gamelan instruments. The authors wish to express their great sadness on the passing of one of the authors Mr. Iran Amri Musoddiq on 31 March 2020 due to COVID-19.

REFERENCES

- Ellis, C. J. (1984). The nature of Australian Aboriginal music. *International Journal of Music Education*, 1, 47-50.
- Johnston, I. (1989). *Measured tones: The interplay of physics and music*. Philadelphia, USA: IOP publishing Ltd.
- Plomp, R. (1976). *Aspects of tone sensation*. London, UK: Academic Press.
- Pramudya, Y., Widayanti, L., & Melliagrina, F. (2018). Frequency measurement of bonang barung and peking in Javanese gamelan using audacity. *Journal of Physics: Conference Series*, 1075(1), 1-6.
- Schneider, A. (2001). Sound, pitch, and scale: From “tone measurements” to sonological analysis in ethnomusicology. *Ethnomusicology*, 45(3), 489-519.
- Sethares, W. A. (2005). *Tuning, timbre, spectrum, scale*. Berlin, Germany: Springer-Verlag.
- Spiller, H. (2004). *Gamelan: The traditional sounds of Indonesia*. Santa Barbara, California: ABC-CLIO, Inc.

- Sumarsam. (2002). *Hayatan gamelan, kedalaman lagu, teori dan perspektif* [Gamelan Appreciation, Song Depth, Theory and Perspective]. Surakarta, Indonesia: STSI Press.
- Sumarsam. (2003). *Gamelan: Cultural interaction and musical development in Central Java*. Chicago, USA: University of Chicago Press.
- Suprpto, Sukisno, & Suwanto, T. (1993). *Gamelan pakurmatan kraton Yogyakarta* [Gamelan Appreciation Kraton Yogyakarta]. Yogyakarta, Indonesia: Taman Budaya Propinsi Daerah Istimewa.
- Sudarjana, P. J., Surjodiningrat, W., & Susanto, A. (1993). *Tone measurements of outstanding Javanese gamelans in Yogyakarta and Surakarta*. Yogyakarta, Indonesia: Gadjah Mada University Press.
- Tenzer, M. (2006). *Analytical studies in world music*. Oxford, England: Oxford University Press.

Support Vector Machine Classification Method for Predicting Jakarta Bay Bottom Sediment Type using Multibeam Echosounder Data

Steven Solikin¹, Henry Munandar Manik^{2*}, Sri Pujiyati² and Susilohadi³

¹Graduate School of Marine Technology, PMDSU Batch II, IPB University, IPB Dramaga Campus, Bogor 16680, Indonesia

²Department of Marine Science and Technology, Faculty of Fisheries and Marine Science, IPB University, IPB Dramaga Campus, Bogor 16680, Indonesia

³Centre for Research and Development of Marine Geology, Ministry of Energy and Mineral Resources, Jl. Dr. Djujungan No. 236 Pasteur, Bandung, Indonesia

ABSTRACT

The need for accurate seafloor maps is increasing along with the increase in marine activities, such as dredging, construction of buildings on the coast and offshore, and navigation of ships to prevent shipwrecks while sailing. The hydroacoustic technology used in this study is the multibeam echosounder system (MBES), which is the most advance acoustic instrument today. MBES can sweep very large areas in a short time, so that the survey costs can be reduced. The aim of this research was firstly to classify the seabed sediment in G-Island, Jakarta Bay using supervised classification technique. Secondly, to analyze the acoustic characteristic of the seabed sediment and compare it with the physical characteristic of the sediment. This research was conducted on October 31st to November 5th 2016 in the waters of G-Island, Jakarta Bay. In this study, supervised classification techniques were applied. The supervised classification techniques used in this research

was Support Vector Machine (SVM). SVM produces classifications with 5 main classes, namely clay, fine silt, medium silt, coarse silt and fine sand. The overall accuracy value of the SVM method was 80.25% with the Kappa coefficient value of 0.2031 which is categorized into the fair class in its classification.

Keywords: Jakarta Bay, multibeam echosounder, supervised classification, support vector machine

ARTICLE INFO

Article history:

Received: 16 September 2019

Accepted: 04 December 2019

Published: 15 April 2020

E-mail addresses:

steven_solikin@apps.ipb.ac.id (Steven Solikin)

henrymanik@ipb.ac.id (Henry Munandar Manik)

sripujiyati@yahoo.com (Sri Pujiyati)

s.susilohadi@mgj.esdm.go.id (Susilohadi)

* Corresponding author

INTRODUCTION

The seabed is a habitat for various types of marine life, either fish or other benthic miofauna (Parnum et al., 2004). On the seafloor there are also various chemical, physical and biological processes, such as sediment transport and biological pump mechanics. Behind the benefits of the seabed, research on the seabed is more complex than the application of other hydroacoustic technologies (Lurton, 2002). Various problems such as rough surface of the seabed, absorption in sediments is greater than in the water column, and the presence of scatterers of other acoustic signals on the surface and in the sediments makes the study of the seabed becomes more difficult, but also more interesting to do.

One of the hydroacoustic technologies instrument that always used for seabed research is multibeam echosounder. Multibeam echosounder (MBES) is an acoustic equipment that is intensively used in water-based mapping, mainly because this technology has more capabilities, especially its broad coverage and high resolution for bathymetry data acquisition (Anderson et al., 2008) when compared with equipment such as singlebeam echosounder, side scan sonar or Light Detection And Ranging (LiDAR). Seabed mapping becomes very important because it provides detailed and accurate information about the topography of the seafloor. This information is very much needed in various aquatic applications such as making navigation maps to ensure the safety of ship traffic and searching for sinking vessels.

The MBES technology is an extension of the singlebeam echosounder (SBES) technology which only transmits one beam vertically to the bottom of the water, while the multibeam is able to transmit hundreds of beams to the bottom and its beam pattern widens and transversely to the hull (Lurton, 2010). Each beam that is emitted will get a point of depth so that if the depth points are connected it will form a topographic profile. There are two types of datasets produced by multibeam echosounder, bathymetry and backscatter data.

Information about the seabed can be used extensively, both by oceanographers to study habitat for benthic animals (Friedlaner & Perrish, 1998), as well as by industry players, even the military (Sternlicht & Moustier, 2003). Along with the increasing exploitation of marine resources, effective management of the marine environment is very important to note. Therefore, information about accurate seabed is needed to answer this challenge. Information about the bottom of the water can be obtained using MBES.

Various methods of seabed classification using MBES data to obtain benthic habitat information have been developed in the last two decades (Fonseca & Mayer, 2007). Generally there are three types of MBES data sets that are used as input in the classification process: backscatter mosaics, backscatter angular responses, and bathymetry (Manik, 2011). Backscatter is the key on determining sea surface conditions (Huang et al., 2013). The backscatter intensity obtained from the receiver provides preliminary information on the type of sediment at a spatially observed location (Huang et al., 2014; Fonseca et al., 2009).

The aim of this research was firstly to classify the seabed sediment in G-Island, Jakarta Bay using supervised classification technique. The supervised classification technique used in this research was Support Vector Machine (SVM) that is based on machine learning. Secondly, to analyze the acoustic characteristic of the seabed sediment and compare it with the physical characteristic of the sediment.

METHODS

Acoustic Data Acquisition

This research began with the data acquisition stage using the MBES acoustic instrument in the waters of Jakarta Bay. Data that can be obtained from the MBES instrument are bathymetry data and backscatter data (Marsh & Brown, 2009). Data acquisition was conducted on October 31st to November 5th 2016. Bathymetry data became the base map in the making of the Jakarta Bay seabed sediment classification map, while backscatter data were analyzed for further comparison with the sediment sample data and the output results are classification of Jakarta Bay sediments.

The survey was done using a public vessel with dimensions of 12 x 2.5 metres. Technical specifications of the survey was explained as the distance between the lanes ranges from ± 100 metres with the number of main survey lines used for this research is

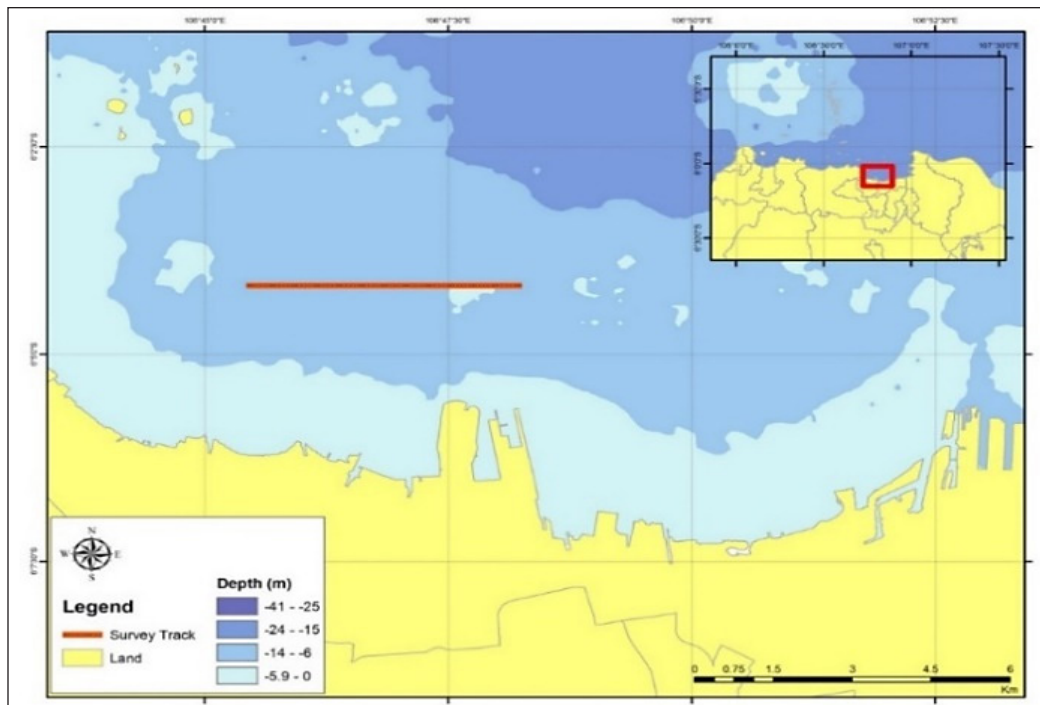


Figure 1. Location of survey area in the waters of G-Island, Jakarta Bay
The red line shows the data acquisition lane using the MBES instrument.

30 lanes of main and 3 lanes of cross. Figure 1 shows the map of the survey location in Jakarta Bay.

The MBES instrument used to obtain bathymetry and backscatter data was SIMRAD Kongsberg EM 2040 with the output frequency of 300 kHz. The frequency of 300 kHz can be used in shallow waters and waters with medium depth (<450 m). The MBES data obtained were data that had been corrected for vessel movement, bow aberration, and GPS delay correction using the Teledyne TSS DMS-05 motion sensor which has an accuracy of slant and bobbing of 0.05°. Determination of the positioning position used Veripos DGPS which had a horizontal accuracy of 0.13 metres and a vertical accuracy of 0.32 metres at a 95% confidence level. The assistance software used as a navigation guide was Automatic Data Logging (ADL) Hydro-Pro, and software for data acquisition using the Seafloor Information System (SIS).

Seabed Sediment Sample Data Acquisition

In addition to the MBES data, sediment samples were taken as validation material for the classification of sediments based on the geoaoustic properties of the sediments. Sediment samples were taken as many as 7 samples that were randomly distributed in the survey area. Sediment samples were taken using a grab sampler. Sediment samples taken are sediment samples on the bottom surface of the water only because of the limitations of the grab sampler to penetrate the sediment layer. Sediment samples obtained, placed in plastic samples and then analyzed the grain size in the laboratory.

In addition to sediment sample data, secondary data to determine sediment types in Jakarta Bay waters were also obtained from the Hydrography and Oceanography Center, Indonesia Navy based on 2016 data. This secondary data was juxtaposed with primary sediment sample data to add validation to the MBES data obtained. The type of ground truth sediments obtained through the 2016 Hydrography and Oceanography Center, Indonesia Navy data show that the Jakarta Bay waters are dominated by clay (Table 1).

Table 1
Number of points and sediment types in Jakarta Bay

No.	Sediment type	Number of points
1	Clay	3276
2	Clayey sand	14
3	Coarse silt	62
4	Fine silt	25
5	Medium silt	16
6	Sandy clay	15
7	Sandy mud	10
8	Sandy silt	89
9	Silty clay	13
10	Very fine sand	1

Data processing analysis of sediment samples was carried out using the wet sieve method using a multilevel sieve to separate the size of the sediment grains based on the grain size fraction. The fractions are determined based on Shephard's triangle (Shepard, 1954) where each fraction was divided into:

1. Gravel (gravel) fraction: a combination of rock and gravel material
2. Sand fraction (sand): a combination of fine sand to coarse sand material
3. Mud fraction: a combination of clay and silt material

Bathymetry Data Quality

The bathymetry data obtained by MBES must be in accordance with standards set by the International Hydrographic Organization (IHO). Therefore, quality control (QC) is needed in the form of bathymetry data correction. The accuracy requirements for bathymetry measurements were set into 4 levels (order) based on the S-44 IHO (2008).

Table 2
List of minimum standards for bathymetry surveys

Order	Special	1a	1b	2
Area	Areas where under-keel clearance is critical	Areas shallower than 100 metres where under-keel clearance is less critical but features of concern to surface shipping may exist	Areas shallower than 100 metres where under-keel clearance is not considered to be an issue for the type of surface shipping expected to transit the area	Areas generally deeper than 100 metres where a general description of the seafloor is considered adequate
Horizontal accuracy	2 m	5 m + 5% depth	20 m + 5% depth	150 m + 5% depth
Depth accuracy	a = 0.25 m b = 0.0075	a = 0.5 m b = 0.013	a = 1.0 m b = 0.023	same with order 2

This correction is related to the level of accuracy of the data in providing information about the actual depth value in the observed area, and to determine the quality of the data to be classified into the hydrographic order. This correction was done by comparing the value of depth at the point of intersection (cross check) between the transverse lane and the longitudinal lane, so that the deviation of depth will be obtained. The error limit at each point of correction of water depth must not exceed the fault tolerance limit set by IHO (2008). All uncertainties in calculating the vertical uncertainty should be combined statistically to obtain a total vertical uncertainty (TVU). The maximum allowable TVU for specific depth is presented in Equation [1].

$$\sigma = \pm \sqrt{a^2 - (b \times d)^2} \quad [1]$$

where:

- σ : maximum allowable TVU for a specific depth (m)
- a : represent the depth error constant (m)
- b : a coefficient which represents a replacement factor for depth error
- d : depth (m)
- $b \times d$: represents that portion of uncertainty that varies with depth

Support Vector Machine Classification

Classification technique that was used in this study was supervised classification which was the machine learning (computer based) technique. The machine learning which was now being developed and applied was Support Vector Machine (SVM). This method is rooted in statistical learning theory and works very well on high dimensional data sets. In SVM, a selected amount of data will contribute to form the model used in the classification to be studied. In addition, SVM only stores a small portion of the training data to be used at the time of prediction. The data that contribute is called the support vector, therefore the method is called SVM (Prasetyo, 2014).

The basic idea of SVM is to maximize hyperplane (decision boundary). Hyperplane which is the best separator between two classes can be found by measuring the hyperplane's margin and finding its maximum point. Margin is the distance between the hyperplane and the closest data from each class. The closest data is referred to as a support vector. Hyperplane with maximum margins provides better generalization to the classification method.

Model and Data Correlation

Accuracy level analysis between classification models and field data was performed using Kappa coefficient statistical analysis. The Kappa coefficient was developed by Cohen (1960). The Kappa coefficient was introduced for remote sensing research in the early 1980s (Congalton & Mead, 1983; Congalton, 1991) and had been an excellent test to be used to analyze the accuracy of object classification results.

In general, the Kappa coefficient can be used to measure the degree of agreement of two assessors in classifying objects into groups, as well as to measure alternative agreements of new methods with existing methods. The equation to get the Kappa coefficient is expressed in Equation [2]:

$$\kappa = \frac{N \sum_{i=1}^r X_{ii} - \sum_{i=1}^r X_{i+} X_{+i}}{N^2 - \sum_{i=1}^r X_{i+} X_{+i}} \quad [2]$$

where

κ : Kappa coefficient;

N : number of observations;

X_{ii} : observation in i^{th} row i^{th} column;

X_{i+} : marginal total in i^{th} row;

X_{+i} : marginal total in i^{th} column.

A simpler equation is shown in Equation [3]:

$$\kappa = \frac{p_0 - p_e}{1 - p_e} \quad [3]$$

where

$$p_0 = \frac{\sum X_{ii}}{N} = \text{accuracy of the agreement observed,}$$

$$p_e = \frac{\sum X_{i+} X_{+i}}{N^2} = \text{estimation of chance of agreement.}$$

Class results from the Kappa coefficient value classification are divided into 5 classes; poor, fair, moderate, good, and very good (Altman, 1991). Kappa coefficient value distribution classes can be interpreted as in Table 3.

Table 3
Classification of the level of agreement between the Kappa coefficient values

κ VALUE	(STRENGTH OF AGREEMENT)
< 0.20	POOR
0.21 – 0.40	FAIR
0.41 – 0.60	MODERATE
0.61 – 0.80	GOOD
0.81 – 1.00	VERY GOOD

RESULTS AND DISCUSSION

Seabed Topography

Acquisition of sound velocity data at the study site using the AMD Oceanography CTD instrument which was carried out every day before the rating survey was conducted. The value of sound velocity (sound velocity profile, SVP) varied every day. Figure 2 shows the daily sound speed profile for 5 days from November 1st to 5th.

The results of SVP measurements at the study site ranged from 1542.5 ms^{-1} to 1544.5 ms^{-1} with a maximum depth of 12 m. This sound speed value would be a correction factor for the acoustic waves that were transmitted and received by the MBES instrument. Tidal data acquisition was carried out using the Thalimedes instrument at Pantai Mutiara dock. Figure 3 shows the tidal graph at the study site from October 31st to November 5th, 2016.

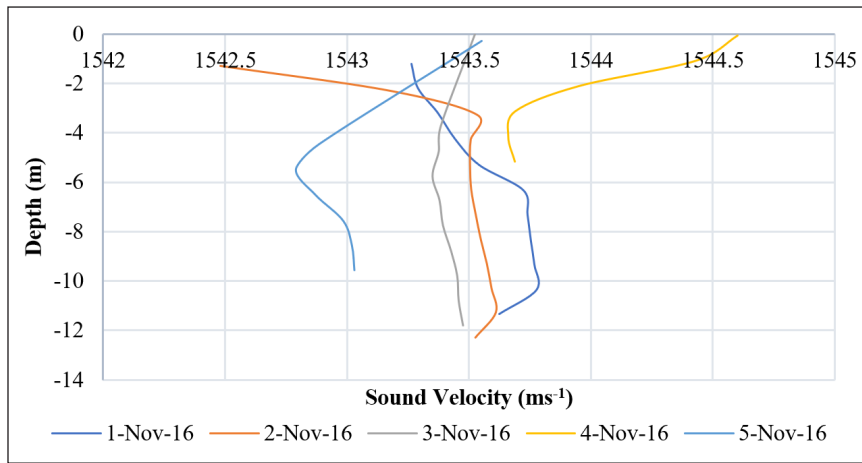


Figure 2. Sound velocity profile at the study site on November 1st to 5th, 2016

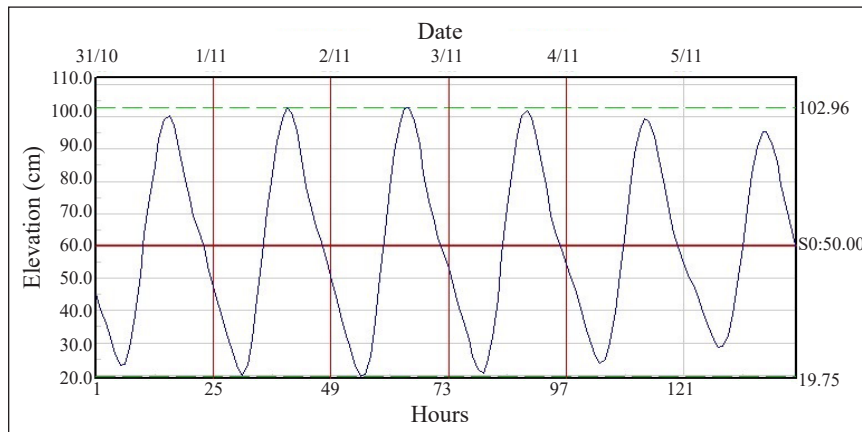


Figure 3. Tidal charts at the study site on October 31st to November 5th, 2016

The tidal graph at the study site shows the lowest tidal value is 19.75 cm and the highest tide is 102.96 cm on November 2nd, 2016. Tidal type at the study site is included in the type of daily tidal (diurnal). These results are in accordance with research conducted by Indriani et al. (2010) which showed that the type of tides in the waters of Jakarta Bay was a single daily tide. Tidal correction is needed in the processing of bathymetry data generated by MBES to get the true depth value. Tidal corrections carried out in this study used the mean sea level (MSL) value as a benchmark. The MSL value is the middle value of the tidal graph, so that all bathymetry data obtained later be reduced or added to the MSL value obtained in this study. The MSL value was computed from tidal analysis by calculating the trend of the tidal graph. MSL value obtained in this study was 60 cm.

After the data was corrected by tidal values, bathymetry profiles could be generated. Bathymetry profiles or topographic forms of the seabed surface were obtained from MBES

data which had been corrected by vessel motion, position, tides, and sound velocity profiles. The bathymetry profile at the study site is shown in Figure 4.

The bathymetry profile in the study site based on the corrected MBES data showed a depth value between 9.75 m to 17.10 m. The bathymetry profile obtained showed the water in Jakarta Bay were shallow. The shallower area is in area A, while the deepest area in the study area is in area B. In area B a basin is suspected to be a pipe planting area.

The level of precision and accuracy of bathymetry data in this study was maintained in accordance with 2008 IHO standards. According to the IHO (2008) statute, the bathymetry data quality control results from MBES are validated with reference surfaces as locations for checking data quality. The reference surface in this case was the cross depth obtained from cross lane data. The method used was to compare bathymetry data from MBES results

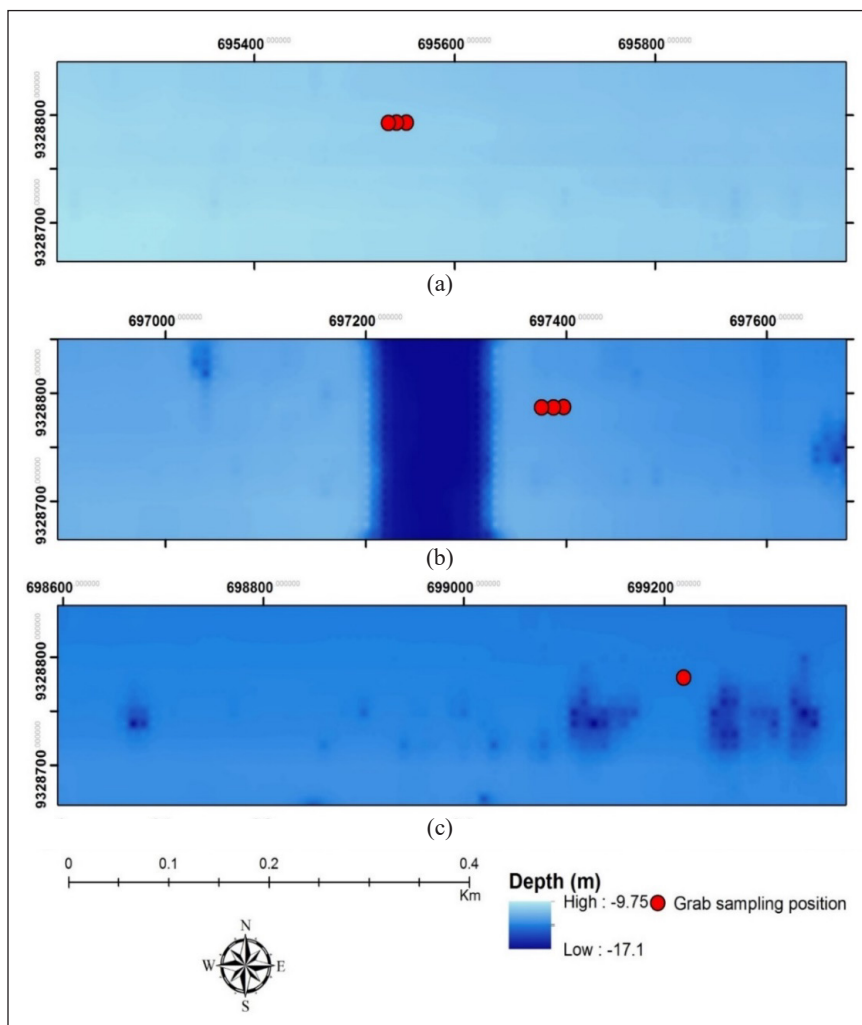


Figure 4. Bathymetry profile in study site

in the main lane with the cross lane (cross). This method aims to find fault tolerance limits. Calculation of bathymetry data quality aims to determine the value of the deviation in the same position at different times. Table 4 shows the position of the correction point, the error value and the calculation of the maximum allowable TVU.

Table 4
Bathymetry data quality on cross lanes

Longitude	Latitude	MB depth	Cross depth	Average depth	Difference	Maximum allowable TVU
-6.106	106.777	6.171	6.056	6.114	0.115	0.2500
-6.097	106.798	3.729	3.840	3.785	0.111	0.2500
-6.074	106.756	9.515	9.470	9.493	0.045	0.2500
-6.076	106.777	9.784	9.654	9.719	0.130	0.2500
-6.073	106.786	8.856	8.827	8.8415	0.029	0.2500
-6.072	106.787	11.641	11.375	11.508	0.266	0.2500
-6.070	106.761	10.434	10.360	10.397	0.074	0.2500
-6.069	106.781	13.822	12.262	13.042	1.560	0.2503
-6.071	106.794	19.045	18.323	18.684	0.722	0.2501
-6.075	106.786	11.343	10.499	10.921	0.844	0.2501
-6.073	106.765	8.941	8.479	8.71	0.462	0.2500
-6.071	106.757	14.269	13.268	13.7685	1.001	0.2501

The intersection point between the main lane and the cross lane at this study site consists of 12 points. The maximum measured error value is 1.56 meters and the minimum measured error value is 0.03 meters. By using Equation [1] an error tolerance limit value (σ) of 0.25 meters is obtained. Based on the results of manual calculations, the depth error tolerance limit between the main lane with the cross lane, it can be said that all the bathymetry data error values at the correction point are within the error tolerance limits for the measurement of water depths in the special order hydrographic survey classification.

Support Vector Machine Classification

The bottom sediments of G-Island waters, Jakarta Bay, had been classified using supervised classification techniques. The Support Vector Machine method was applied in this supervised classification technique. As many as 3.8 million points were extracted from the MBES raw data. Each point contained information about the location (latitude and longitude) and the value of backscatter intensity obtained from the MBES data.

Due to some software limitations in the classification process, 3.8 million points were reduced to approximately 40 thousand points. Reduction of the data was done by eliminating data with the same coordinates, so it would not affect the accuracy results of the classification. Of the 40 thousand data points, 20% of the data was used as training data

sets, or around 8 thousand points. From these 8 thousand points, another 20% of data was taken for class accuracy testing and obtained 5 main classes in the classification using this SVM method, namely clay, coarse silt, medium silt, fine silt, and very fine sand.

The backscatter value obtained from this MBES data using the SVM method ranged from -56 dB to -14 dB. The distribution of the backscatter intensity distribution from the MBES data is shown in Figure 5.

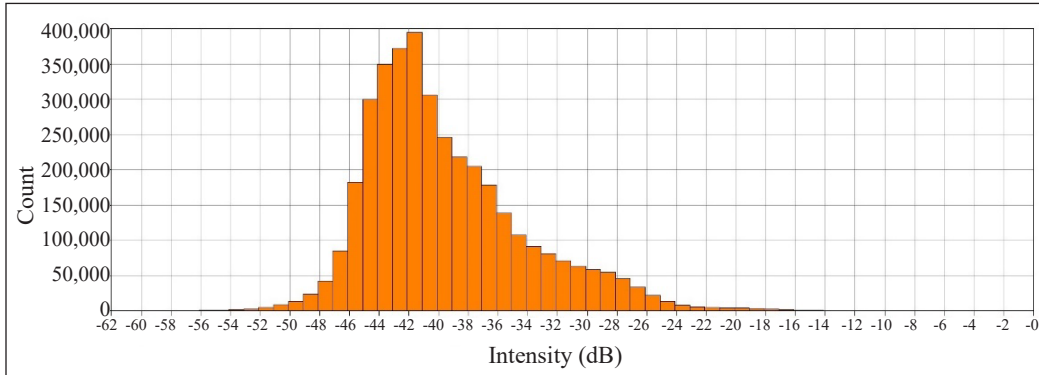


Figure 5. Frequency distribution versus backscatter intensity of MBES data using SVM method

The distribution of the most intensity values is in the range of -43 dB to -42 dB with a frequency of nearly 400 thousand points. With the highest frequency distribution in the range of -40 dB, it can be said that sediments in G-Island waters are dominated by fine sediments (De Falco et al, 2010). The results of the G-Island waters sediment type classification are shown in Figure 6.

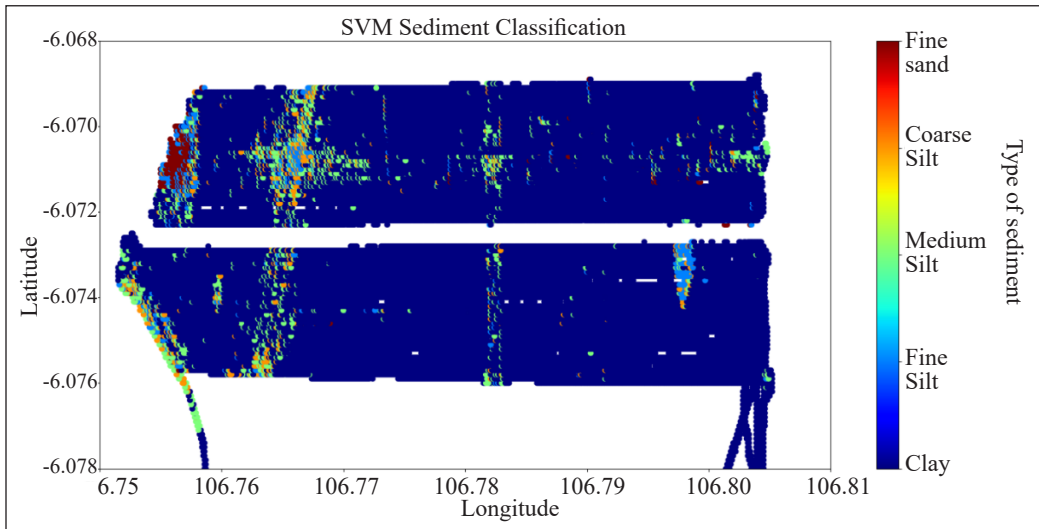


Figure 6. Classification of G-Island sediments using the SVM method

From Figure 6 we can see the spatial distribution of sediment types in the G-Island waters. From the results obtained, it appears that the type of sediment in the G-Island waters is dominated by the type of clay sediment from the classification processing results using the SVM method. Clay sediments are marked in dark blue, fine silt sediments are marked in bright blue, medium silt sediments are marked in green, coarse silt sediments are marked in orange, and fine sand is marked in red. Figure 7 shows the overlapping results between the results of the classification using the SVM method with Google Earth imagery.

From the overlapping results (Figure 7), it can be seen that the type of sediment close to the reclamation island, G-Island, the type of sediment tends to be larger and coarser. This can be caused by material or sediment originating from the reclaimed island. However, the type of sediment that dominated in the G-Island waters was still clay. The distribution of clay sediment reached 90% in these waters when referring to ground truth data.

Although the SVM method has succeeded in classifying sediment types with results similar to ground truth data, there are still some shortcomings in this method, including the inability of this method to produce classes according to ground truth. There are four classes that have not been successfully classified by this method; sandy silt, sandy clay, sandy mud, silty clay, and clayey sand. Another drawback is that there are still misclassifications of this method, such as errors in determining class. Sediments which should be categorized as silt are classified as clay by this method.

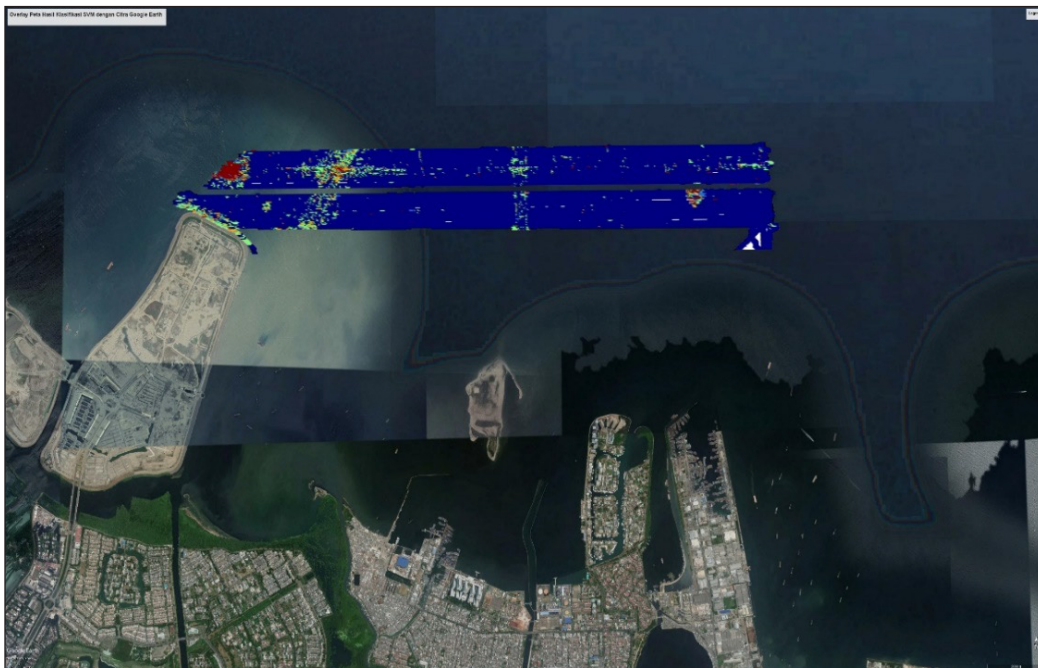


Figure 7. Overlapping between Google Earth imagery and the results of the SVM classification in the G-Island waters

SVM Accuracy Test

Supervised classification techniques also need to do an accuracy test to find out how accurate the classification model is made and how it fits with ground truth data. The accuracy test used in this method is the Kappa coefficient test.

The overall accuracy value for the SVM method generated from the Kappa test is 0.8025 with an agreement of chance value of 0.7522 at a 95% confidence interval. The accuracy value of 0.8025 is quite large for classification, which means 80.25% of the data has been successfully classified correctly by this method.

The Kappa coefficient value obtained in this study is 0.2031. This value is classified into fair class of the strength of agreement variable. These results are similar to studies conducted by Stephens and Diesing (2014) which show that the accuracy and Kappa coefficient values of the SVM method are worth 0.78 and 0.39. Testing the accuracy of this method also calculates the values of producers's accuracy and user's accuracy.

Producer's accuracy is classification accuracy which is seen from the point of view of the producer. This shows how often class results are displayed spatially correctly or the probability of a benthic habitat in an area is classified correctly, while user's accuracy is the classification accuracy seen from the point of view of the map user, not the maker. User accuracy indicates how often the class on the map can represent the real situation. Table 5 shows the classes obtained from the results of the SVM classification and the values of the producer's and user's accuracy of those classes.

Table 5
The value of producer's accuracy and user's accuracy of the classes classified by the SVM method

Class	Number of points that correctly classified	References points	Classification points	User's accuracy (%)	Producer's accuracy (%)
Clay	2796	3276	2839	98.49	85.35
Fine Silt	2	25	295	0.68	8.00
Medium Silt	3	15	238	1.26	20.00
Coarse Silt	23	62	143	16.08	37.10
Very Fine Sand	1	1	5	20.00	100.00

From Table 5 it can be explained that the value of producer's accuracy and user's accuracy will not be the same. In the case of the SVM method in this study, for example, the value of producer's accuracy for the clay class is 85.35%, while the value of user's accuracy is 98.49%. This shows that 85.35% of the clay class has been correctly identified as "clay", and as many as 98.49% of the points identified as "clay" are the actual classifications for clay. As many as 1.51% of the points are misclassified into the other four classes. These results are of course categorized as having a large enough accuracy value. This is due to the dominant class in the study area is the clay class.

In the coarse silt class, the value of the producer's accuracy for the coarse silt class is 37.10%, while the value of the user's accuracy is 16.08%. This shows that 37.10% of the coarse silt class was correctly identified as "coarse silt", and only 16.08% of the points identified as "coarse silt" were the actual classifications for coarse silt. 83.92% of the points are categorized incorrectly in other classes (clay, fine silt, medium silt, and fine sand).

CONCLUSIONS

The aims of this study was to test the supervised classification technique for their ability to predict substrate type using MBES and ground truth data. We have shown that satisfactory results can be obtained from using legacy data. The value of backscatter intensity obtained from the supervised classification techniques, is ranged from -54 dB to -14 dB using SVM classification. The basic sediment types of Jakarta Bay waters can be mapped into 5 main classes (clay, fine silt, medium silt, coarse silt, and very fine sand). The SVM method produces an accuracy level of 80.25% with a Kappa coefficient of 0.2031.

ACKNOWLEDGMENTS

The authors would like to thank Ministry of Research, Technology, and Higher Education of Republic of Indonesia for funding this research through PMDSU Batch II scheme and we also would like to thank Hydrography and Oceanography Center, Indonesia Navy for collaboration in survey activity and providing the secondary data in Jakarta Bay.

REFERENCES

- Altman, D. G. (1991). *Practical statistics for medical research*. London, UK: Chapman and Hall.
- Anderson, J. T., Holliday, D. V., Kloser, R., Reid, D. G., & Simrad, Y. (2008). Acoustic seabed classification: Current practice and future directions. *ICES Journal of Marine Science*, 65(6), 1004-1011.
- Cohen, J. (1960). A coefficient of agreement for nominal scales. *Educational and Psychological Measurement*, 20(1), 37-46.
- Congalton, R. G. (1991). A review of assessing the accuracy of classifications of remotely sensed data. *Remote Sensing Environment*, 37(1), 35-46.
- Congalton, R. G., & Mead, R. (1983). A quantitative method to test for consistency and correctness of photointerpretation. *Photogrammetric Engineering and Remote Sensing*, 49(1), 69-74.
- De Falco, G., Tonielli, R., Di Martino, G., Innangi, S., Simeone, S., & Parnum, I. M. (2010). Relationships between multibeam backscatter, sediment grain size and *Posidonia oceanica* seagrass distribution. *Continental Shelf Research*, 30(18), 1941-1950.
- Fonseca, L. E., & Mayer, L. A. (2007). Remote estimation of surficial seafloor properties through the application angular range analysis to multibeam sonar data. *Marine Geophysics Research*, 28(2), 119-126.

- Fonseca, L. E., Brown, C., Calder, B., Mayer, L. A., & Rzhonov, Y. (2009). Angular range analysis of acoustic themes from Stanton Banks Ireland: a link between visual interpretation and multibeam echosounder angular signatures. *Applied Acoustics*, 70(10), 1298-1304.
- Friedlander, A. M., & Parrish, F. (1998). Habitat characteristics affecting fish assemblages on a Hawaiian coral reef. *Journal of Experimental Marine Biology and Ecology*, 224(1), 1-30.
- Huang, Z., Siwabessy, P. J. W., Nichol, S. L., & Brooke, B. P. (2014). Predictive mapping of seabed substrata using high-resolution multibeam sonar data: A case study from a shelf with complex geomorphology. *Marine Geology*, 357, 37-52.
- Huang, Z., Siwabessy, P. J. W., Nichol, S. L., Anderson, T., & Brooke, B. P. (2013). Predictive mapping of seabed cover types using angular response curves of multibeam backscatter data. *Continental Shelf Research*, 61, 12-22.
- IHO. (2008). *Standards for hydrographic surveys*. Monaco: International Hydrographic Bureau.
- Indriani, I., Kurniawati, N., & Hendri, M. (2010). Tide current simulation model outside Tanjung Priok port using SMS 8.1 software. *Maspri Journal*, 2010, 79-83.
- Lurton, X. (2002). *An introduction to underwater acoustics, principles and application*. Chichester, UK: Springer Praxis.
- Lurton, X. (2010). *An introduction to underwater acoustics principles and application*. Berlin, Heidelberg: Springer.
- Manik, H. M. (2011). Underwater acoustic detection and signal processing near the seabed. In N. Z. Kolev (Ed), *Sonar systems* (pp. 255-274). Rijeka, Croatia: InTech.
- Marsh, I., & Brown, C. (2009). Neural network classification of multibeam backscatter and bathymetry data from Stanton Bank (Area IV). *Applied Acoustic*, 70(10), 1269-1276.
- Parnum, I. M., Siwabessy, P. J. W., & Gavrilov, A. N. (2004, November 3-5). Identification of seafloor habitats in coastal shelf waters using a multibeam echosounder. In *Proceeding of ACOUSTICS 2004* (pp. 1-6). Gold Coast, Australia.
- Prasetyo, E. (2014). *Data mining mengolah data menjadi informasi menggunakan matlab [DATA MINING, Processing Data To Information Using Matlab]*. Yogyakarta, Indonesia: Andi Offset.
- Shepard, F. P. (1954). Nomenclature based on sand-silt-clay ratios. *Journal of Sediment Petrol*, 24(3), 151-158.
- Stephens, D., & Diesing, M. (2014). A comparison of supervised classification methods for the prediction of substrate type using multibeam acoustic and legacy grain-size data. *PLoS ONE*, 9(4), 1-14.
- Sternlicht, D. D., & de Moustier, C. P. (2003). Time-dependent seafloor acoustic backscatter (10–100 kHz). *Journal of Acoustical Society America*, 114(5), 2709-2725.



System Identification of Helical Strakes Suppressed Vortex-induced Vibration for Flexible Pipes

Ching Sheng Ooi^{1*}, Meng Hee Lim¹, Kee Quen Lee², Hooi Siang Kang^{3,4} and Mohd Salman Leong¹

¹Institute of Noise and Vibration, Universiti Teknologi Malaysia, 54100 Kuala Lumpur, Malaysia

²Intelligent Dynamic and System I-kohza, Malaysian-Japan International of Technology, Universiti Teknologi Malaysia, 54100 Kuala Lumpur, Malaysia

³School of Mechanical Engineering, Faculty of Engineering, Universiti Teknologi Malaysia, 81310 Johor Bahru, Malaysia

⁴Marine Technology Center, Universiti Teknologi Malaysia, 81310 Johor Bahru, Johor, Malaysia

ABSTRACT

Previous studies have indicated that the pipe-surface-mounted helical strakes effectively reduce vortex-induced vibration (VIV) under a uniform flow application, particularly during the lock-in region. Since VIV experiments are time-consuming, observation is generated with an interval helical strakes parameter in pitch and height to lessen tedious procedures and repetitive post-processing analyses. The aforementioned result subset is insufficient for helical strakes design optimisation because the trade-off between the helical strakes dimension, lock-in region and flow velocity are non-trivial. Thus, a parametric model based on an improved recursive least squares (RLS) parameter estimation technique is proposed to define the statistical relationship between input, or strakes and pipe dimension, and output, or VIV amplitude ratio. As results suggested, revised RLS estimated VIV model demonstrated an optimal prediction with the highest coefficient of determination and lowest Integral Absolute Error. The feasibility of VIV parametric model was validated by embed into Genetic Algorithm (GA) as the fitness function to acquire a desirable helical

strakes dimension with minimum VIV amplitude. The rapid generation of optimal helical strakes dimension which returned the highest VIV suppression implied a superior simulation method compared to the experimental outcome.

ARTICLE INFO

Article history:

Received: 04 October 2019

Accepted: 07 February 2020

Published: 15 April 2020

E-mail addresses:

chingshengooi@gmail.com (Ching Sheng Ooi)

limmenghee@gmail.com (Meng Hee Lim)

lkquen@utm.my (Kee Quen Lee)

kanghs@utm.my (Hooi Siang Kang)

salman.leong@gmail.com (Mohd Salman Leong)

* Corresponding author

Keywords: Genetic algorithm, helical strakes, recursive least squares, vortex-induced vibration

INTRODUCTION

Vortex-induced vibration (VIV) is defined as the oscillation of a structure when subjected to the influence of fluids in motion. When synchronization between shedding vortex and structural natural frequency takes place, a unique occurrence, the lock-in region, results from VIV magnitude amplification (Chizfahm et al., 2018). This undesirable event generates excessive hydrodynamic, lift and drag force which leads to material property degradation. Consequently, equipment and accessories with a relatively high aspect ratio and low mass ratio, such as risers, airplane wings, and turbine blades, are prone to fatigue after exposure to VIV over a certain period. However, the aforementioned parts are critical components in the system as a whole; thus, undermining VIV development would limit basic component functionality, system efficiency, and contribute to disastrous incident.

In recent years, numerous research efforts have dedicated themselves to understanding the causes of VIV so as to minimize the effects on structural integrity. For example, a two degree higher-order nonlinear oscillator model was developed, aiming to perform VIV forecast for cylinders with respect to mass ratio and damping ratio (Kang et al., 2018). The model and parameter sensitivity were built on the fundamental Van der Pol equation, which had been validated with experimental outcomes. A virtual damping–spring (VCK) based variable added mass system yield mean damped natural frequency approximately matched oscillating frequency while the phase between force and displacement levelled with VIV lock-in range resonance in perpendicular direction (Garcia & Bernitsas, 2018). The VCK-based method is practical to find suitable mass increments for VIV suppression purposes.

On the other hand, a reduced order model deduced from a high-fidelity analysis of sectional pipe is employed for in-line and cross-flow oscillation measures (Stabile et al., 2018). Performance of the reduced order model is subjected to system-parameter identification to obtain full scale indication. Based on the Scale-Adaptive Simulation ($k - \omega$ SST – SAS) model, twisted design has been found capable of diverting hydrodynamic force with respect to cylinder length direction when compared to conventional square shapes (Wu et al., 2018). A novel image processing EFD/SVM has been proposed to detect and identify segments of VIV wake-patterns in a non-destructive manner for effective classification outcomes (Lin, 2018). By combining time domain and filtered VIV frequency responses, an improved semi-empirical predictor is established to track wave profiles regardless of steady uniform or turbulent flow (Ulveseter et al., 2018).

A new VIV wake oscillator provides appropriate prediction by considering the Reynolds number, lock-in regions and peak-amplitude formulae as estimation functions (Gao et al., 2018). Parameter identification techniques have been applied to gain VIV amplitude, frequency, and phase lag from time domain vortex induced hydrodynamic force using computational fluid dynamics (CFD) simulation (Pigazzini et al., 2018). In order

to eliminate premature convergence in VIV modal space prediction, a non-iterative root search is selected to solve hydrodynamic force and dynamic response equations together without power-balance (Lu et al., 2018). GA has been adopted in Facchinetti variable optimization to allow greater efficiency in flow induced vibration energy harvesting (Ashok et al., 2018). For aeroelastic force modelling, positive curvature in circular structures has proven effective in cross-wind oscillation damping (Lupi et al., 2018). A hybrid Euler-Van der Pol equation is coupled with the Newmark-beta method to explain VIV response of marine risers in three-dimensional space, including in-line, cross-flow, and structural dynamics (Komachi et al., 2018). The simulation is able to develop conclusions regarding stress-fatigue proportionality.

A VIV-related literature review demonstrates that extensive knowledge has been acquired over years of thoughtful investigation, ranging from experimental studies to numerical simulation modelling. The adopted countermeasure approaches involving product design modification in conjunction with suppression tools and excessive VIV value monitoring have proven to be useful. Nonetheless, modelling techniques require an understanding of sophisticated mathematical equations and posteriori-based assumptions. In addition, it is laborious to conduct exhaustive experiments in a repetitive manner. Due to VIV turbulent characteristics and various manipulating variables, obtaining a practical, universal solution is a tedious process.

As a result, the objective of this case study was to demonstrate a straightforward system identification methodology to identify VIV mathematical relationship. The simulation deployed VIV amplitude data collection when helical strakes acted as suppression tool for flexible risers (Quen et al., 2014). A feasible system identification technique was implemented to estimate unknown parameters with a target of fitting VIV curves given the strakes dimension input and flow velocity range. The particular method of improved RLS was selected due to its accuracy and iterative estimation update nature. The performance of the VIV model was validated using GA by means of a fitness function searching for optimal strakes dimension, which generated minimal VIV response. Section 2 describes the methodology of RLS in detail, following by experiment setup. Section 3 tabulates hindsight on simulation findings.

MATERIALS AND METHODS

The case study focused on VIV generated under uniform flow application, as experimented in (Quen et al., 2014). The controlled data measurement procedure is explained, followed by the presentation of novel parameter estimation technique and Matlab software simulation design.

Experimental Setup

A poly vinyl chloride (PVC) cylinder was operated as the riser model with settings as detailed in Table 1. The highly flexible cylinder was designed to move freely in an axial direction at one end and in restricted torsion effect with universal joints at both ends. Detailed riser configurations can be found in Sanaati and Kato (2013).

Table 1
Helical strakes and risers' parameters

Outer diameter (D)	18 mm
Inner diameter (d)	13 mm
Length (L)	2.92 m
Pre-tension (T)	147 N
Bending stiffness (EI)	9.0 Nm ²
Spring stiffness (k_s)	6.5 N/m
Cylinder axial stiffness (EA/L)	100 N/mm
Cylinder air weight	1.64 N/m
Total weight including internal water (m)	2.97 N/m
Mass ratio	1.17
Damping ratio (ζ)	0.028
Applied strakes' height (h)	0.05D, 0.1D, 0.15D
Applied strakes' pitch (p)	5D, 10D, 15D
Number of helix	3-start helical
Flow speed (U)	0.1-1.0 m/s
Subcritical Reynolds number range (Re)	1380-13,800
Natural frequency (f_n)	2.92, 2.82, 2.82, 2.86, 2.85, 2.78



Figure 1. Schematic diagram of cylinder pipe with three-start helical strakes

The cylinder specimens were soaked at a 0.35 m depth from the water surface level in a basin of 100 m × 7.8 m × 4.35 m and were towed to create a uniform flow speed, U . To initiate a subcritical Reynolds number, U was regulated between 0.1 and 1.0 m/s, with a step increment of 0.03 m/s. As displayed in Figure 1, The strakes' dimension was increased gradually from 0.05 to 0.15 times the cylinder diameter in height and 5 to 15 times the cylinder diameter for pitch length, respectively. Hence, 25-cylinder towing speed

steps were repeated for six unique strakes combinations ($N = 6$). The strakes' dimension range is defined based on laminar boundary layer thickness, as measured by Pohlhausen's approximation. For every strakes setup, the vibration response was recorded using a charge-coupled device (CCD) camera installed at the centre of the cylinder before being analysed by a motion-tracking software. Additionally, thorough experiment information can be obtained in Sanaati's description (Sanaati, 2012).

Vibration amplitude for strakes application was examined in contrast to the bare cylinder baseline amplitude ratio. The comparison is expressed using amplitude ratio (AR), and reduced velocity (V_r). The AR is defined as the normalisation of the standard deviation of time series vibration amplitude reading with respect to the outer diameter of the cylinder ($AR = A_\sigma/D$). The reduced velocity, $V_r = U/f_n D$, indicates the scaling of uniform cylinder towing speed, U , as a function of its natural frequency and outer diameter. Based on 25 regular step intervals of U , the V_r values are pre-set within a range of 1.909 and 17.755. Dimensionless AR and V_r indications are chosen as the variables for y-axis and x-axis respectively. Therefore, the AR value represents induced vibration weightage to the corresponding reduced velocity. The presented amplitude ratio versus reduced velocity measurement is an appropriate VIV reduction instrument when cylinder diameter variation is of concern.

System Identification Technique: Recursive Least Square Parameter Estimation

The least squares (LS) technique was developed by C. F. Gauss initially to estimate planet orbital motion (Young, 2011). In present, LS has evolved to estimate a fitting curve through measurement points. The fitting curve is described as a line which contains a minimal sum squared error when compared to available measurement points. For example, given the n th order difference equation, as below:

$$y_{0k} = a_1 x_{k1} + a_2 x_{k2} + \dots + a_n x_{kn} \quad (1)$$

where output y_{0k} is the summation of n number of parameter α multiply input data x for k th data observation. Reorganizing Equation 1 into a stacked equation for linearity purpose provides:

$$y_{0k} = [x_{k1} \ x_{k2} \ \dots \ x_{kn}] [\alpha_1 \ \alpha_2 \ \dots \ \alpha_n] = \varphi_k^T \theta \quad (2)$$

For k th observation, $\varphi_k \in R^n$ is denoted as the regressor vector with n input data while θ is regarded as parameter vector. Both regressor vector and parameter vector comprises of n real number elements. If the data observation is repeated for N iteration time, the Equation 2 can be summarised in Equation 3 for $k = 1, 2, \dots, N - 1, N$:

$$\begin{aligned}
 \begin{bmatrix} y_{0_1} \\ y_{0_2} \\ \vdots \\ y_{0_N} \end{bmatrix} &= \begin{bmatrix} x_{11} & x_{12} & \cdots & x_{1n} \\ x_{21} & x_{22} & \cdots & x_{2n} \\ \vdots & \vdots & \ddots & \vdots \\ x_{N1} & x_{N2} & \cdots & x_{Nn} \end{bmatrix} \begin{bmatrix} \alpha_1 \\ \alpha_2 \\ \vdots \\ \alpha_n \end{bmatrix} \\
 Y_0 &\approx \Phi\theta \tag{3}
 \end{aligned}$$

where $Y_0 \in R^N$ represents a vector consists of N stacked real number output signals, y_{0k} while input data matrix, $\Phi \in R^{N \times n}$ is the combination of N row of regressor vector, φ_k . However, due to uncertainties such as measurement errors and inconsistency, output generally possesses noise sequence, e_k . Equation 3 becomes $Y = \Phi\theta + e$, where Y is the summation of Y_0 and stacked error vector, e . A cost function, V with argument θ is then introduced to minimise curve fitting error (Equation 4):

$$V(\theta) = \frac{1}{2} \sum_{k=1}^N \varepsilon_k^2 = \frac{1}{2} \varepsilon^T \varepsilon = \frac{1}{2} \|\varepsilon\|^2 \tag{4}$$

where ε is the residual of model output. Thus, LS optimization was achieved via sum squared error minimisation, as presented in Söderström and Stoica (2002).

$$\begin{aligned}
 \arg \min_{\theta} V(\theta) &= \frac{1}{2} (Y - \Phi\theta)^T (Y - \Phi\theta) \\
 &= \frac{1}{2} (Y^T Y - Y^T \Phi\theta - \theta^T \Phi^T Y + \theta^T \Phi^T \Phi\theta) \tag{5}
 \end{aligned}$$

Minimum error value is obtained by setting a partial derivative of Equation 5 to zero:

$$\frac{\partial V(\theta)}{\partial \theta} = -\Phi^T Y + \Phi^T \Phi\theta \tag{6}$$

Then, rearranging input and output in Equation 6 provides the LS estimated parameter solution, $\hat{\theta}$:

$$\hat{\theta} = (\Phi^T \Phi)^{-1} \Phi^T Y \tag{7}$$

Noting that $(\Phi^T \Phi)^{-1}$ is known as covariance matrix P . Equation 7 can be modified recursively over N observations, if elements for $k = 1, 2, \dots, N - 1, N$ observation are known.

$$P_k^{-1} = P_{k-1}^{-1} + \varphi_k \varphi_k^T \tag{8}$$

$$\hat{\theta}_{k-1} = P_{k-1} \sum_{i=1}^{k-1} \varphi_i y_i$$

$$\sum_{i=1}^{k-1} \varphi_i y_i = P_{k-1}^{-1} \hat{\theta}_{k-1}$$

$$\hat{\theta}_k = P_k (P_{k-1}^{-1} \hat{\theta}_{k-1} + \varphi_k y_k) \quad (9)$$

By updating Equation 8 into Equation 9, the one-step ahead prediction using RLS is obtained:

$$\begin{aligned} \hat{\theta}_k &= P_k [(P_k^{-1} + \varphi_k \varphi_k^T) \hat{\theta}_{k-1} + \varphi_k y_k] \\ &= \hat{\theta}_{k-1} + P_k \varphi_k (y_k - \varphi_k^T \hat{\theta}_{k-1}) \end{aligned} \quad (10)$$

where $(y_k - \varphi_k^T \hat{\theta}_{k-1})$ is denoted as one-step ahead prediction error and $P_k \varphi_k$ is the correction gain updated from gain vector L_k denoted by expansion of Equation 8 with matrix inversion lemma (Hostetter, 1987):

$$L_k = P_{k-1} \varphi_k (1 + \varphi_k^T P_{k-1} \varphi_k)^{-1} \quad (11)$$

$$P_k = P_{k-1} - L_k \varphi_k^T P_{k-1} \quad (12)$$

The notable difference between LS and RLS is that LS consider stacked regressor vector and targeted output simultaneously, as explained in Equation 7, whilst RLS perform parameter estimation fine-tuning over N iterations. The recursive update algorithm offers an advantage over standard LS by using less bulky dataset and better convergence, particularly with complex dataset problems accompanied by limited data sampling N . By means of a less bulky dataset, RLS only require an estimated parameter vector from the previous iteration and input and output data from the current observation to perform a parameter estimation and correction gain update (refer to Equation 10, 11 and 12). However, the iterative update algorithm requires additional computational effort as compared to the LS estimation in Equation 7 (Wang & Ding, 2013).

Recent RLS development comprises measuring the dynamic behaviour of excavators with rotational inertia (Oh & Seo, 2018), motion synchronisation controller fine-tuning for gimbal systems (Lee & Jung, 2018), battery pack insulation fault detection for electric vehicles (EVs) (Tian et al., 2018), time-dependent Surface Processes and Acoustic Communication Experiment (SPACE08) underwater communication channel tracking

with a graphical model (Yellepeddi & Preisig, 2018), and estimation of disturbance signal embedded in active vibration control (AVC) feedback mechanisms for a closed-loop damping system model (Oveisi et al., 2018).

Recursive Least Square Parameter Estimation Simulation Integrated Development Environment

The VIV experiment dataset is subject to LS and RLS simulations using *Matlab* software R2019a. For every step of V_r , parameter estimation techniques generate $\hat{\theta}$ by observing *AR* experiment results of six unique strake dimensions ($N = 6$) as output and n matching strakes dimension input. In other words, LS and RLS estimate n weighting coefficients corresponding to every V_r with the target of simulate actual *AR* value with minimal squared error. The estimated parameter vector is designed to contain two elements in accordance with strakes' height and pitch dimensions. When the $\hat{\theta}$ desired is identified, only the strake dimension is needed to simulate *AR* as predicted output, \hat{y} .

It is worth mentioning that estimated parameter elements are assigned as zero during standard LS and RLS initialisation to avoid bias. Alternatively, for improved RLS, the LS estimated parameter vector is set up as the initial estimated parameter instead of zero vector, $\hat{\theta}_{RLS,N=1} = \hat{\theta}_{LS}$. The argument is that the additional parameter re-evaluation stage could provide faster convergence, especially for current VIV dataset with limited amount of observation data N . Standard estimation performance indicators such as coefficient of determination R_f^2 and integral absolute error (*IAE*) are measured to quantify the output variation between estimation model simulation and VIV experiment dataset.

Lastly, the most probable *AR* estimation model is substituted as the GA fitness function in *Matlab* software. The GA platform performs a heuristic search for the minimum of a given function. For VIV case studies specifically, GA is responsible for discovering optimal strakes input dimensions, which yield minimal fitness function output *AR*. The minimal fitness function output criterion includes both the minimum global maxima *AR* value over V_r range, and minimum average *AR* value.

The desirable estimated parameter is updated into Equation 3 prior the simulation as a fitness function for *Matlab* syntax *ga*. The input variables for *ga* fitness function are the strakes' pitch and height. All unique strakes' input combinations within the search boundary are considered as potential solutions. A heuristically defined strakes dimension which simulate unprecedented minimum global maxima and average *AR* is selected as the optimal strakes candidate and benchmark for the next GA iteration. The GA iterative process is terminated when the following condition is met: either there has been no improvement over a predetermined period cycle or the target value has been achieved. The iterative simulation process overview is exhibited in Figure 2. The simulation results and discussion are presented in the next section.

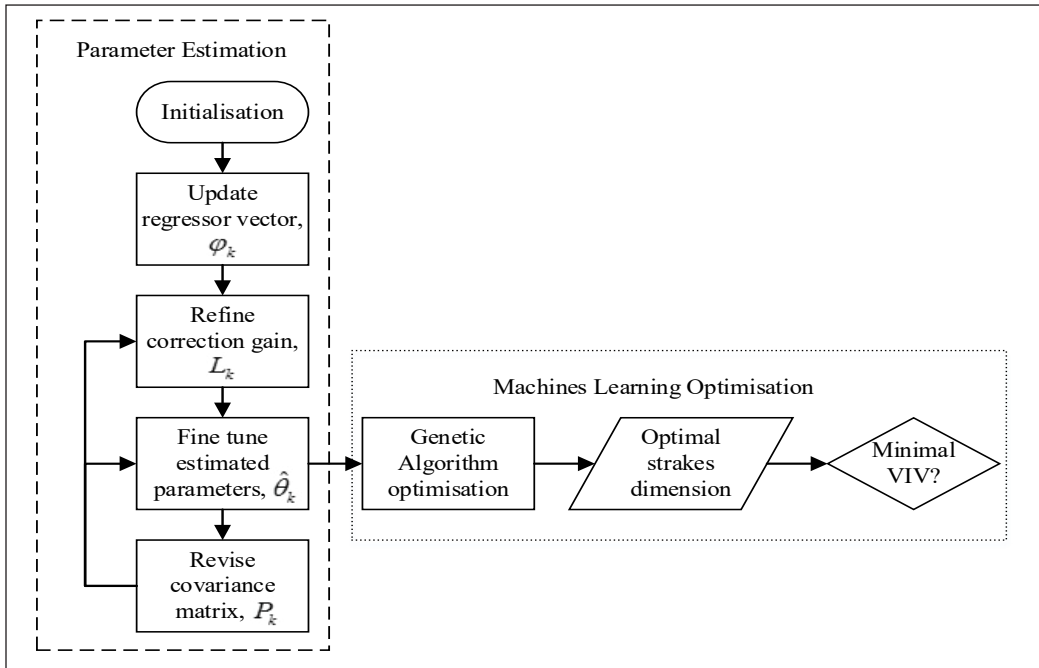


Figure 2. RLS parameter estimation iterative process for Machine Learning Optimisation

RESULTS AND DISCUSSION

First, improved RLS, standard RLS, and LS simulated outputs are compared to actual experiment results with identical strakes' dimensions by employing standard estimation measures: R_T^2 and IAE . \hat{y} is the simulated output and y is the actual output. The next step includes embedding the estimation model with the highest accuracy as GA fitness function to identify optimal strakes' dimensions with minimal AR response.

Table 2
Model efficacy for parameter estimation techniques

Strakes dimension			$R_T^2 = \frac{\sum(\hat{y} - y)^2}{\sum(y - \bar{y})^2}$	$IAE = \frac{\sum(\hat{y} - y)}{N}$		
Setting	Pitch	Height	LS and RLS	Improved RLS	LS and RLS	Improved RLS
1	0	0	80.8%	40.3%	0.063	0.111
2	5*D	0.1*D	86.4%	88.1%	0.031	0.026
3	10*D	0.05*D	85.9%	97.4%	0.034	0.014
4	10*D	0.1*D	19.1%	73.1%	0.038	0.021
5	15*D	0.1*D	-380.7%	-139.0%	0.033	0.027
6	10*D	0.15*D	82.3%	95.0%	0.021	0.013

Table 2 depicts the efficacy results using three parameter estimation techniques: LS, RLS and improved RLS. The closer the model performance is to 100 percent R_T^2 and zero IAE , the more representative the estimated parameter is in reflecting actual output. Overall, for six strakes' dimension settings, apart from bare cylinder, the improved RLS method provides better R_T^2 and IAE indication. This observation is likely caused by the RLS algorithm trade-off of bare cylinder AR tracking accuracy for cylinder with additional strakes. Although LS and RLS sufficiently simulated AR with a majority R_T^2 over 80% and IAE lower than 0.04, an improved RLS is still capable of enhancing the efficacy by minor fine-tuning of the estimated parameter.

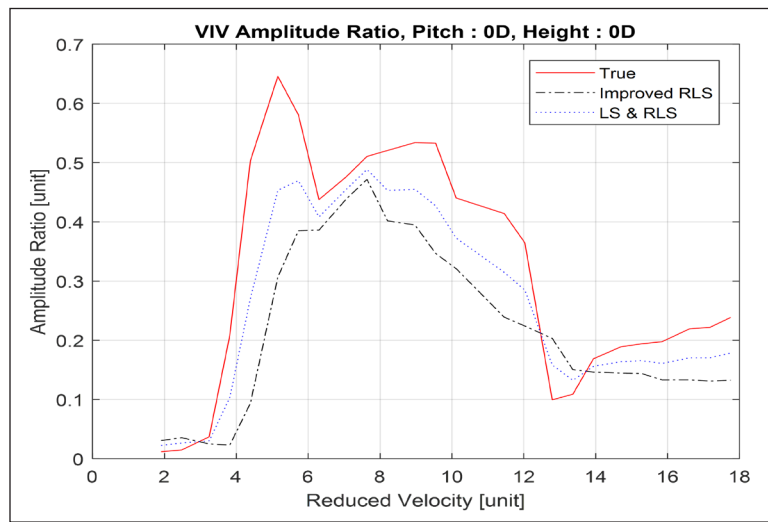


Figure 3. AR versus V_r for setting: 1

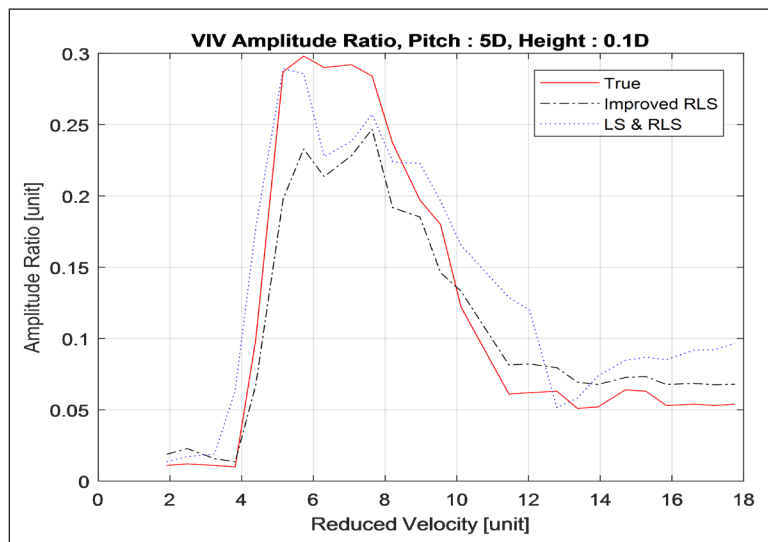


Figure 4. AR versus V_r for setting: 2

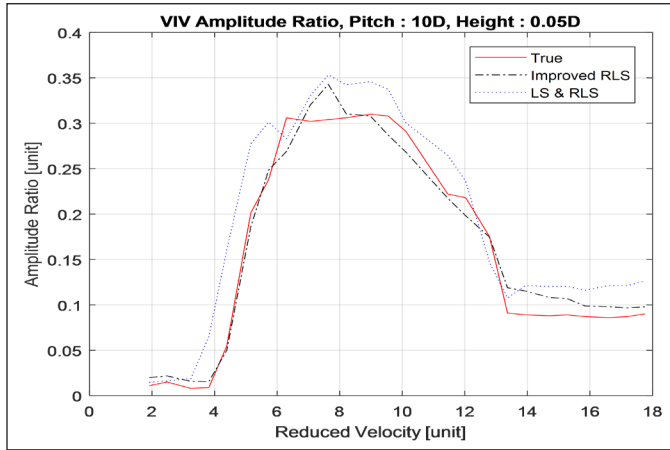


Figure 5. AR versus V_r for setting: 3

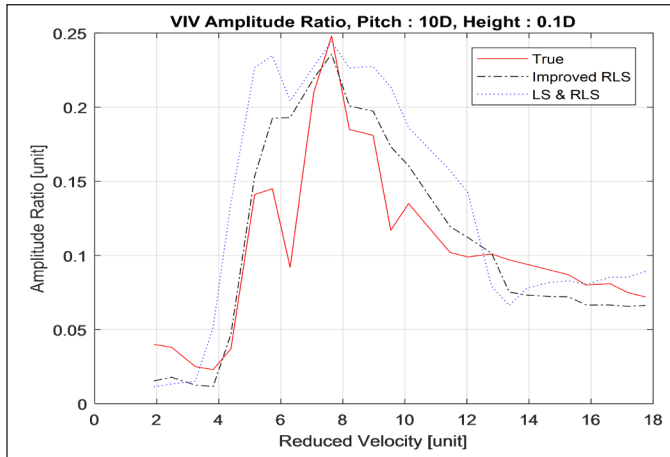


Figure 6. AR versus V_r for setting: 4

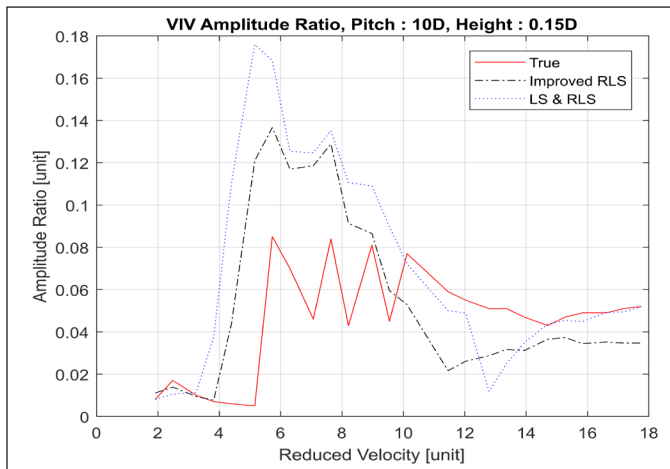


Figure 7. AR versus V_r for setting: 5

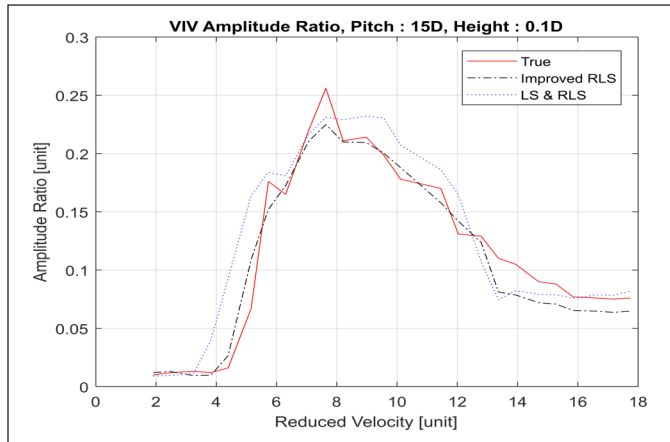


Figure 8. AR versus V_r for setting: 6

Figure 3 to 8 exhibit the VIV parameter model simulation outcomes against actual experimental result for 6 different strakes dimension setting. Preliminary inspection revealed that the majority of the tracking errors occurred near lock-in regions since AR changes were more rapid, with steep slopes and spikes. The prediction error is likely due to influence from external factors and insufficient data sampling. As a result, all related models suffer the most errors whilst tracking strakes dimension with 10 times diameter in pitch and 0.15 times diameter in height, the fifth strakes' setting. However, compared to classic LS and RLS, improved RLS is still capable of simulating AR with resemble lock-in patterns when strakes material is present. The visible similarity between improved RLS simulated output and actual AR around the lock-in regions is of concern in VIV suppression. Hence, it can be concluded that the improved RLS algorithm produced the most probable estimated parameters for the given dataset.

The advantage of improved RLS in numerical analysis and visualisation is further supported in Figure 9 with the trace of covariance matrix, P over six observations in a semilog scale. It can be noticed that P for the improved RLS method gradually converged from 2^{10} to 8.381 at the end of the simulation, which is equivalent to the value acquired by standard the LS and RLS. Even though the LS method experienced convergence at the end of the simulation, the improved RLS identified room for improvement through adaptive correction gains and by using $\hat{\theta}_{LS}$ as an initial estimated parameter.

To perform strakes' dimension optimisation, the search space is set to cover solely the given dataset range since AR behaviour is uncertain beyond range boundary. Additionally, after conducting AR observations, it is believed that the minimal AR value is likely to vary between the fifth and sixth settings. With the improved RLS estimation model as fitness function, the GA simulation discover the optimal strakes' dimension as 14.02 times D and 0.16 times D for pitch and height, respectively. This has been validated by comparing the

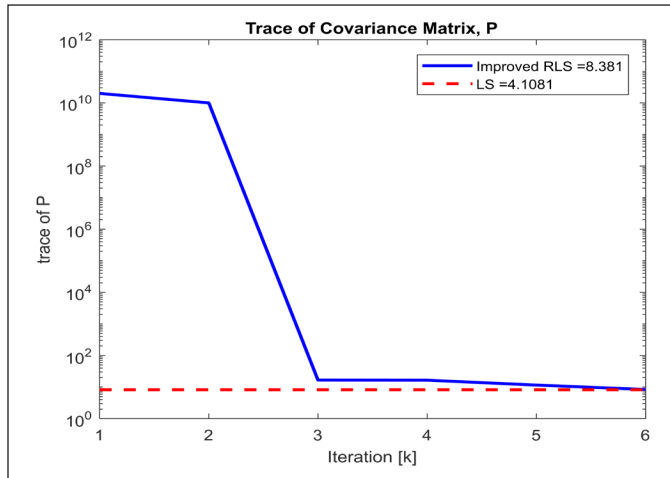


Figure 9. Trace of Covariance Matrix, P

AR simulated by GA-generated optimal strakes input and the fifth strakes setting using the improved RLS model. GA data evaluation in Table 3 shows that global maxima and average AR revealed with GA-simulated optimal strakes are considerably lower than the fifth setting. Figure 10 further illustrates that GA-simulated optimal strakes provide better VIV suppression over fifth strakes setting, particularly around the lock-in region (V_r , ranging from 4 to 10). GA-simulated optimal strakes were deemed to be more superior since less strakes material is required to perform optimum suppression effects. This outcome evidenced the feasibility of performing system identification of VIV responses to obtain an optimal dimension of suppression tools, with a representable dataset and estimated parameter.

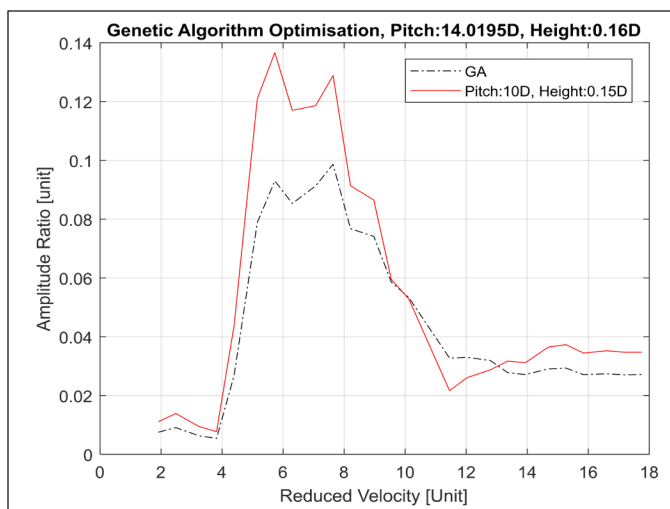


Figure 10. AR for GA-simulated optimal strakes dimension and setting: 5

Table 3
GA optimisation evaluation

Setting	Pitch	Height	Global Maxima AR	Average AR
GA	14.02*D	0.16*D	0.10	0.043
5	15*D	0.1*D	0.14	0.054

CONCLUSIONS

The present investigation involves the system identification of helical strakes suppressed VIV for PVC pipes. With respect to the provided dataset, the VIV response simulated by a proposed improved RLS technique stipulates a satisfactory outcome compare to the actual values. Standard parameter estimation methods benchmarking suggested that the improved RLS model is a fast and accurate option to assist an experimental approach in VIV monitoring. Not only can minimal VIV response be obtained by indicating optimal strakes dimensions, an improved RLS model embedded GA also helped to eliminate trial-and-error processes when conducting VIV experiments. Nonetheless, it is inevitable that the model accuracy plunges as the VIV is suppressed due to turbulent lock-in region behaviour and unpredictable changes. Improvement can be achieved with an optimal strakes range extension which requires further experimental initiative.

ACKNOWLEDGMENTS

This work was supported in part by the Institute of Noise and Vibration UTM through the Higher Institution Centre of Excellence (HiCoE) under Grant R.K130000.7809.4J226, Grant R.K130000.7809.4J227, and Grant R.K130000.7809.4J228, and in part by the UTM Research University under Grant Q.K130000.2543.11H36.

REFERENCES

- Ashok, P., Chandra, C. J., Neeraj, P., & Santhosh, B. (2018). Parametric study and optimization of a Piezoelectric energy harvester from flow induced vibration. *IOP Conference Series: Materials Science and Engineering*, 310, 1-10.
- Chizfahm, A., Yazdi, E. A., & Eghtesad, M. (2018). Dynamic modeling of vortex induced vibration wind turbines. *Renewable Energy*, 121, 632-643.
- Gao, X. F., Xie, W. D., Xu, W. H., Bai, Y. C., & Zhu, H. T. (2018). A novel wake oscillator model for vortex-induced vibrations prediction of a cylinder considering the influence of Reynolds number. *China Ocean Engineering*, 32(2), 132-143.
- Garcia, E. M. H., & Bernitsas, M. M. (2018). Effect of damping on variable added mass and lift of circular cylinders in vortex-induced vibrations. *Journal of Fluids and Structures*, 80, 451-472.
- Hostetter, G. H. (1987). Chapter 13 – Recursive estimation. In D. F. Elliott (Ed.), *Handbook of digital signal processing* (pp. 899-940). New York, NY: Academic Press.

- Kang, Z., Zhang, C., & Chang, R. (2018). A higher-order nonlinear oscillator model for coupled cross-flow and in-line VIV of a circular cylinder. *Ships and Offshore Structures*, 13(5), 488-503.
- Komachi, Y., Mazaheri, S., & Tabesgpour, M. R. (2018). Wake and structure model for simulation of cross-flow/in-line vortex induced vibration of marine risers. *Journal of Vibroengineering*, 20(1), 152-164.
- Lee, S. D., & Jung, S. (2018). An adaptive control technique for motion synchronization by on-line estimation of a recursive least square method. *International Journal of Control, Automation and Systems*, 16(3), 1103-1111.
- Lin, T. K. (2018). An edge-feature-description-based scheme combined with support vector machine for the detection of vortex-induced vibration. *International Journal of Innovative Computing, Information and Control*, 14(3), 833-845.
- Lu, Z., Fu, S., Zhang, M., Ren, H., & Song, L. (2018). A modal space based direct method for vortex-induced vibration prediction of flexible risers. *Ocean Engineering*, 152, 191-202.
- Lupi, F., Niemann, H. J., & Höffer, R. (2018). Aerodynamic damping model in vortex-induced vibrations for wind engineering applications. *Journal of Wind Engineering and Industrial Aerodynamics*, 174, 281-295.
- Oh, K. S., & Seo, J. H. (2018). Inertia parameter estimation of an excavator with adaptive update rule using performance analysis of kalman filter. *International Journal of Control, Automation and Systems*, 16(3), 1226-1238.
- Oveisi, A., Hosseini-Pishrobat, M., Nestorović, T., & Keighobadi, J. (2018). Observer-based repetitive model predictive control in active vibration suppression. *Structural Control and Health Monitoring*, 25(5), 1-23.
- Pigazzini, R., Contento, G., Martini, S., Puzzer, T., Morgut, M., & Mola, A. (2018). VIV analysis of a single elastically-mounted 2D cylinder: Parameter Identification of a single-degree-of-freedom multi-frequency model. *Journal of Fluids and Structures*, 78, 299-313.
- Quen, L. K., Abu, A., Kato, N., Muhamad, P., Sahekhaini, A., & Abdullah, H. (2014). Investigation on the effectiveness of helical strakes in suppressing VIV of flexible riser. *Applied Ocean Research*, 44, 82-91.
- Sanaati, B. (2012). *An experimental study on the VIV hydrodynamics of pre-tensioned flexible cylinders with single and multiple configurations* (PhD thesis). Osaka University, Japan.
- Sanaati, B., & Kato, N. J. (2013). Vortex-induced vibration (VIV) dynamics of a tensioned flexible cylinder subjected to uniform cross-flow. *Journal of Marine Science and Technology*, 18(2), 247-261.
- Söderström, T., & Stoica, P. (2002). Instrumental variable methods for system identification. *Circuits Systems and Signal Process*, 21, 1-9.
- Stabile, G., Matthies, H. G., & Borri, C. (2018). A novel reduced order model for vortex induced vibrations of long flexible cylinders. *Ocean Engineering*, 156, 191-207.
- Tian, J., Wang, Y., Yang, D., Zhang, X., & Chen, Z. (2018). A real-time insulation detection method for battery packs used in electric vehicles. *Journal of Power Sources*, 385, 1-9.
- Ulveseter, J. V., Thorsen, M. J., Sævik, S., & Larsen, C. M. (2018). Time domain simulation of riser VIV in current and irregular waves. *Marine Structures*, 60, 241-260.

- Wang, S., & Ding, R. (2013). Three-stage recursive least squares parameter estimation for controlled autoregressive autoregressive systems. *Applied Mathematical Modelling*, 37(12-13), 7489-7497.
- Wu, C. H., Ma, S., Kang, C. W., Lim, T. B. A., Jaiman, R. K., Weymouth, G., & Tutty, O. (2018). Suppression of vortex-induced vibration of a square cylinder via continuous twisting at moderate Reynolds numbers. *Journal of Wind Engineering and Industrial Aerodynamics*, 177, 136-154.
- Yellepeddi, A., & Preisig, J. C. (2018). Efficient system tracking with decomposition graphic-structured inputs and application to adaptive equalization with cyclostationary inputs. *IEEE Transaction on Signal Processing*, 66(10), 2645-2658.
- Young, P. C. (2011) Recursive least squares estimation. In C. P. Young (Ed.), *Recursive estimation and time-series analysis* (pp. 29-46). Heidelberg, Germany: Springer.

Analysis of pH and Color of Fermented Cocoa (*Theobroma cacao* L) Beans using Response Surface Methodology

Sri Hartuti¹, Nursigit Bintoro^{2*}, Joko Nugroho Wahyu Karyadi² and Yudi Pranoto³

¹Department of Agricultural Engineering, Universitas Syiah Kuala. Jl. Tgk. Hasan Krueng Kalee, No. 3, Kopelma Darussalam-Banda Aceh 23111, Indonesia

²Department of Agricultural and Biosystems Engineering, Universitas Gadjah Mada. Jl. Flora No. 1, Bulaksumur, Yogyakarta 55281, Indonesia

³Department of Food and Agricultural Product Technology, Universitas Gadjah Mada. Jl. Flora No. 1, Bulaksumur, Yogyakarta 55281, Indonesia

ABSTRACT

Cocoa (*Theobroma cacao* L) is a tropical plant that is widely used as a basic ingredient in chocolate production. The quality and taste of chocolate are greatly influenced by the stages and processes of post-harvest handling. Some post-harvest processes that are recognized for improving cocoa quality are pod storage, fermentation, and drying. The quality of cocoa beans can be known based on several physical and chemical parameters, including the color and pH of cocoa beans. This study aimed to analyze the effect of pod storage before fermentation (X_1), aeration rate (X_2) and aeration mode (X_3) during the fermentation process on pH (Y_1), chroma (Y_2), and hue (Y_3) of cocoa beans after fermentation and drying. Response surface methodology (RSM) was used to observe the relationships among the X_1 , X_2 , X_3 variables and the Y_1 , Y_2 , and Y_3 of dried cocoa beans, with the following treatments: $X_1 = 1; 5; 9$ days, $X_2 = 0.2; 0.3; 0.4$ liters/minute, $X_3 =$ intermittent 1; intermittent 2; and continue. The pH, chroma and hue of dried cocoa beans were: 4.873-6.517, 9.99-32.20, and 28.85-71.53, respectively. Furthermore, analysis of variance showed that pod storage before fermentation process significantly affected the hue but did not significantly affect

the pH and chroma. The aeration rate had a significant effect on the pH and hue but did not have a significant effect on the chroma, while the aeration mode had no significant effect on the pH, chroma, and hue of dried cocoa beans.

Keywords: Aeration, cocoa bean fermentation, color $L^* a^* b^*$, pH, pod storage

ARTICLE INFO

Article history:

Received: 07 November 2019

Accepted: 28 January 2020

Published: 15 April 2020

E-mail addresses:

sri.hartuti@unsyiah.ac.id (Sri Hartuti)

nursigit@ugm.ac.id (Nursigit Bintoro)

jkugroho@ugm.ac.id (Joko Nugroho Wahyu Karyadi)

pranoto@ugm.ac.id (Yudi Pranoto)

* Corresponding author

INTRODUCTION

The post-harvest handling processes of cocoa beans which have large impacts on the quality of dried cocoa beans are pod storage before fermentation (cacao pod ripening), fermentation, and drying of cocoa beans (Kongor et al., 2016; Krähmer et al., 2015). The quality of cocoa beans is also greatly influenced by complex chemical and biochemical changes in cocoa beans during fermentation and drying processes (Afoakwa et al., 2012). Even the fermentation and drying process is noticeably able to increase the flavor precursors of cocoa beans (Misnawi, 2008), and to determine the characteristics of quality cocoa in chocolate industry (Barrientos et al., 2019).

In addition to changes in air temperature, changes in pH, color, aroma, taste, and other physical appearances of cocoa pulp and nib also indicate that a fermentation process has occurred. A change in the color of fresh cocoa beans from purple to brown after fermentation and drying processes is an indicator that should be considered in determining the quality of cocoa beans (Hartuti et al., 2018). In general, color assessment used is color model $L^* a^* b^*$ (Mendoza, et al., 2007; Afoakwa et al., 2012; Akhiriani et al., 2012). Hartuti et al. (2019) stated that pod storage time before fermentation, aeration rate, and fermentation temperature affected the color values of L^* , a^* , b^* , chroma, hue, and RGB of dried cocoa beans. Fermented cocoa beans have higher reddish and yellowish colors than unfermented cocoa beans. Afoakwa et al. (2012) also stated that an increase in pod storage could make the colors of cocoa beans darker, more yellowish and less reddish.

In addition to the color, the quality of fermented cocoa beans can also be determined by the acidity (pH) of cocoa beans (Apriyanto et al., 2016). Kongor et al. (2016) mentioned that the color and acidity of cocoa beans were indicators that could be used to observe the quality of cocoa beans. The characteristics of fermented cocoa beans are also determined by measuring any changes in the pH, acidity and fermentation index of cocoa beans during fermentation process (Apriyanto et al. 2016). Increased pod storage increases the pH of the cocoa beans at the end of fermentation. The pH of cocoa beans increased from 4.80 for non-stored pods to 7.01 for 10-days-stored pods, after 6 days of fermentation (Afoakwa et al., 2013). Meanwhile, Muzaiifa et al. (2017) stated that cocoa beans fermented for 6 days with 2 different aeration intervals (stirring every 24 and 48 hours) had pH of 5.88 and 6.51 at the end of fermentation, respectively.

Response surface methodology (RSM) is a method that can be used to determine the relationship and interaction between independent variables and response variables. RSM analysis for food processing, such as pH, color and others, has been used by other researchers, e.g. to observe: the effect of flour replacement and particle size on the color of wheat bread (Marcin et al., 2016), the effect of a change in the time and temperature of frying pan on the change of the color of papaya chips (Wexler et al., 2016), the optimization

of an ultrasound-assisted extraction condition for flavonoid compounds from cocoa pods using RSM (Yusof et al., 2019), the effect of pod storage, aeration rate and temperature on the color of dried cocoa beans using RSM (Hartuti et al, 2019), the effect of polyphenol and pH on cocoa flavor (Noor-Sofalina et al., 2009), the changes in nib acidification and biochemical composition during fermentation of cocoa (Afoakwa et al., 2013).

The purpose of this study was to analyze and evaluate the combined effects of pod storage before fermentation, as well as the effects of aeration control and aeration mode during fermentation, on the pH and color of dried cocoa beans using the RSM.

MATERIALS AND METHODS

Sample Preparation

The samples of cocoa pods used in this study were obtained from a farmer's plantation in Hargobinangun Village, Pakem Subdistrict, Sleman Regency, Yogyakarta, Indonesia. The cacao pods (a variety of Trinitario, which is a hybrid of Criollo and Forastero) were chosen based on uniform maturity. They were marked by -green, full yellow, and slightly orange-yellow of the pods skins with average harvest ages of 5-6 months since flowering. Harvested cocoa pods were stored in a room with ambient temperatures of 28 - 31 °C and relative humidity of 80 - 90% for 1, 5, and 9 days before fermentation. After the pod storage time was over, the cocoa pods were opened and separated from their skins and placentas, without any treatment before fermentation, except the pod storage process. One (1) kg of cocoa beans was prepared and put into a tightly closed reactor and fermented for 5 days for each treatment.

Fermentation Process

The cocoa fermentation process was carried out using a packed-bed fermenter. The fermentation equipment used in this study referred to the fermentation equipment used by Saludes et al. (2007), but with some modifications. The modifications were made to the type and amount of material used as fermenter heat sources. A heater in the equipment used by Saludes et al. (2007) was replaced with 4 incandescent lamps and 4 fans as shown in Figure 1. The reactor (cocoa bean container) was placed in a fermentation chamber equipped with an air temperature control system, aeration rate, and aeration mode. Fermentation temperature was measured and controlled using temperature sensors inside and outside the reactor, which were connected to a data logger. The temperature of the fermenter was controlled to minimize heat loss from the inside of the reactor into the surrounding environment. The aeration rate was measured using an airflow meter and flowed into the reactor inlet.

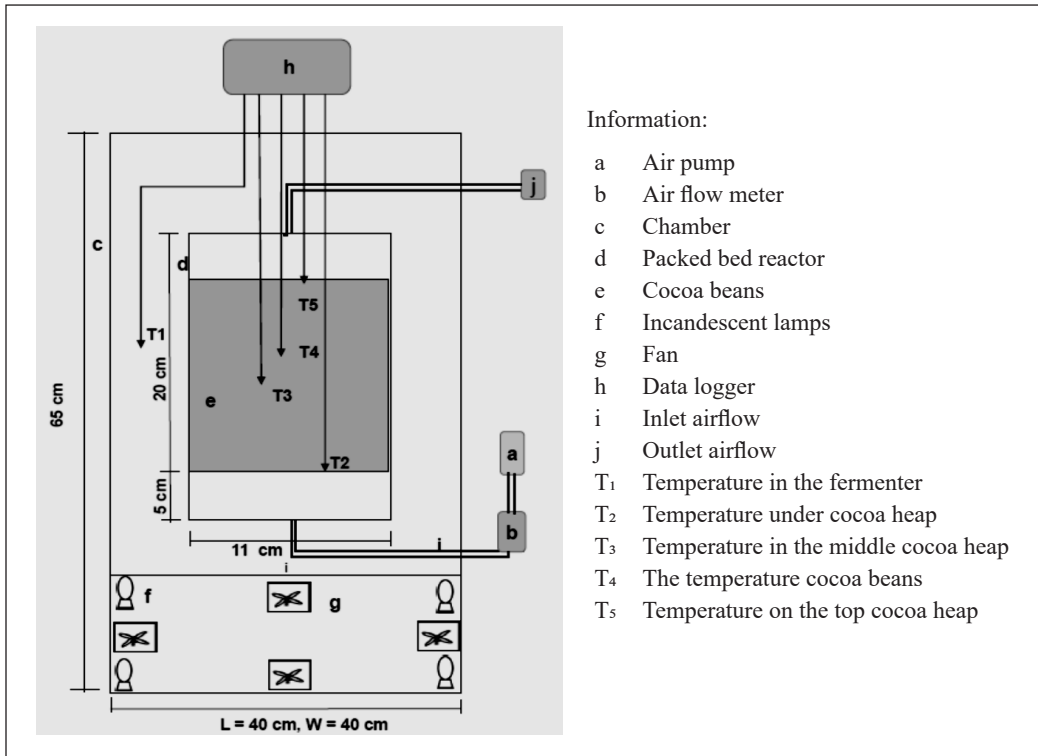


Figure 1. Schematic diagram of experimental cocoa fermentation system

The fermentation process was carried out for 5 days. Initially, 1 kg of cocoa beans were put into the reactor tube, then closed and left for 1 day. Air aeration started to be performed on the second day of the fermentation or after 24 hours fermentation process. Aeration was given with 3 variations of aeration rate (0.2; 0.3; 0.4 liters/minute) and aeration mode (intermittent 1; intermittent 2; and continuous). Intermittent aeration mode was given during the fermentation of cocoa beans at certain time intervals. Intermittent 1, air aeration was given at intervals of 1-hour aeration (1-hour aeration on) and 2 hours without aeration (2 hours aeration off). Intermittent 2, air aeration was given at intervals of 2 hours aeration (2 hours aeration on) and 1 hour without aeration (1-hour aeration off). Furthermore, for the continuous aeration mode, air aeration was given continuously until the end of the fermentation process. After the cocoa bean fermentation process was finished, cocoa beans were dried using a drying cabinet (Shumis, model PSN-150 with a 12 kW heater and a maximum temperature of 200 °C) with a temperature of 50 °C for 22-25 hours (until the moisture content of dried cocoa beans reached 7 – 7.5%), and then the color and pH analysis of the dried cocoa beans was carried out.

pH Determination

The measurement of the pH of the dried fermented cocoa beans was done in several steps. Firstly, a pH meter and a standard buffer solution of pH 4.0 and pH 7.0 were prepared. Then the samples consisting of about 12-20 seeds were taken and tested. Then, the outer skin and ground cocoa beans were separated using a blender and weighed about 10 g to be put into a beaker. 90 ml of hot (between 70°C to 80°C) distilled water was added and stirred slowly until a “no lump” suspension was formed. Then, the filtrate was filtered and cooled to a temperature of $27 \pm 2^\circ\text{C}$, then the pH was determined as quickly as possible at the temperature (BSN, 2008).

Color Determination

The color of each sample was measured with a color meter TES 135A. The measurement was based on the $L^*a^*b^*$ color system. The L^* , a^* and b^* colour space parameters of the samples were calculated as: L^* ($L_s - L_0$) for lightness; a^* ($a_s - a_0$) for extent of green color; b^* ($b_s - b_0$) for blue color (Mendoza et al., 2007; Afoakwa et al., 2012; Marcin et al., 2016; Saunshia et al., 2018). Moreover, based on the obtained color values of L^* , a^* , and b^* , the chroma and hue were calculated according to Equations 1 and 2 (Wexler et al., 2016; Afoakwa, 2016; Hartuti et al., 2019).

$$C^* = \sqrt{a^{*2} + b^{*2}} \tag{1}$$

$$h = \arctan\left(\frac{b^*}{a^*}\right) \text{ or } h = \tan^{-1}\left(\frac{b^*}{a^*}\right) \tag{2}$$

Where, C^* is the chroma coordinates to indicate brightness; and h is the hue angle value.

Data Analysis

The experimental design in this study used a central composite design (CCD) of three factors (pod storage, aeration rate, and aeration mode) on the pH and color of dried cocoa beans. The experimental design, limit, and level of the variables in this study are as shown in Table 1.

Table 1
Limits and levels of independent variables on the fermentation of cocoa beans

Variable (X)	Limits and Levels		
	-1	0	+1
Pods storage, X_1 (days),	1	5	9
Aeration rate, X_2 (L/min)	0.2	0.3	0.4
Aeration mode, X_3 (hours/hours)	Intermittent 1	Intermittent 2	Continue

The data were analyzed using the RSM computed with Minitab 14 software package to determine the effects of pod storage before fermentation (X_1), aeration rate (X_2), and aeration mode (X_3) variables on the pH, chroma and hue of dried cocoa beans, which consisted of 20 treatments. The data analysis using the RSM will deliver a mathematical Equation 3 (Bezerra et al., 2008; Hartuti et al., 2019) as follows:

$$Y = \beta_0 + \beta_1 X_1 + \beta_2 X_2 + \beta_3 X_3 + \beta_{11} X_1^2 + \beta_{22} X_2^2 + \beta_{33} X_3^2 + \beta_{12} X_1 X_2 + \beta_{13} X_1 X_3 + \beta_{23} X_2 X_3 \quad [3]$$

Where, Y is response to pH, chroma, and hue of dried cocoa beans; β_0 is intercepting/constant; $\beta_1, \beta_2, \beta_3$ are linear coefficients; $\beta_{11}, \beta_{22}, \beta_{33}$ are quadratic coefficients; $\beta_{12}, \beta_{13}, \beta_{23}$ are interaction coefficients.

RESULTS AND DISCUSSIONS

The results showed that the storage of cocoa before fermentation, aeration rate, and aeration mode affected the pH and color of the dried cocoa beans. The results of the calculations of the average pH of the cocoa beans after fermentation and drying are as shown in Figure 2, while those of the average color of L^*, a^*, b^* , chroma, and hue are as shown in Table 2. The pH of the dried cocoa beans in the study was 4.873-6.517. Some samples of the cocoa beans had pH values outside the range of 5.0-5.5 as the expected pH values in order to obtain good flavor (Biehl et al., 1989). Meanwhile, fermented cocoa beans with pH values of 4.0-4.5 have a lower flavor potential (Biehl & Voigt, 1994 in Araujo et al., 2018). In general, the pH values resulted in the study were quite good because cocoa beans that have a higher pH can produce less sour chocolate products, which is one of the characteristics of a good chocolate product (Araujo et al., 2018).

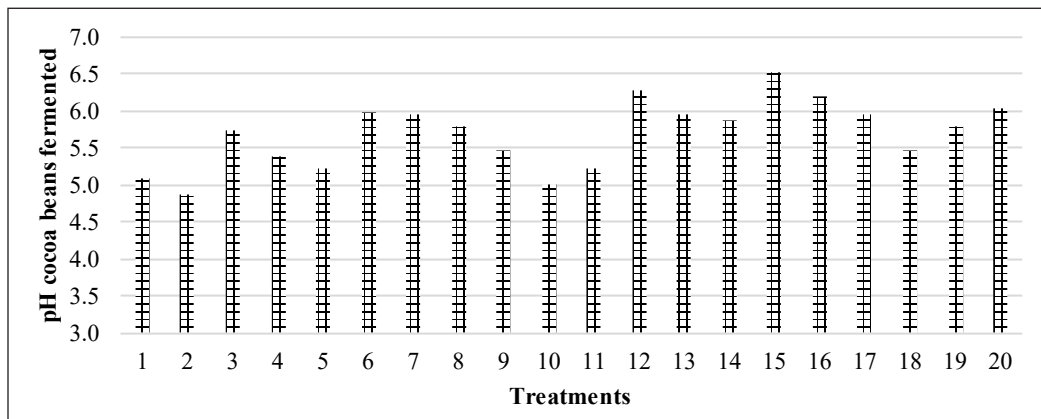


Figure 2. pH cocoa beans

Table 2
*L**, *a**, *b** color, chroma, and hue of dried fermented cocoa beans

No.	Treatments			Average color measurement			Color of dried fermented cocoa beans	
	X ₁	X ₂	X ₃	L*	a*	b*	Chroma ©	Hue (H)
1	-1	-1	-1	25.70	5.93	8.03	9.99	53.55
2	+1	-1	-1	19.57	8.37	23.43	24.88	70.35
3	-1	+1	-1	19.13	6.57	9.70	11.71	55.90
4	+1	+1	-1	17.07	6.03	8.67	10.56	55.16
5	-1	-1	+1	26.47	12.00	15.12	19.30	51.58
6	+1	-1	+1	24.23	7.98	13.50	15.68	59.40
7	-1	+1	+1	35.69	15.38	8.47	17.56	28.85
8	+1	+1	+1	26.00	14.53	10.59	17.98	36.09
9	-1	0	0	27.20	11.42	6.45	13.12	29.46
10	+1	0	0	33.02	12.64	9.97	16.10	38.26
11	0	-1	0	12.20	4.93	14.77	15.57	71.53
12	0	+1	0	14.97	8.00	7.87	11.22	44.52
13	0	0	-1	20.30	14.42	15.33	21.05	46.75
14	0	0	+1	25.27	18.53	26.33	32.20	54.87
15	0	0	0	20.70	11.53	13.80	17.98	50.11
16	0	0	0	17.79	10.63	12.70	16.56	50.07
17	0	0	0	23.60	9.23	10.40	13.91	48.40
18	0	0	0	17.87	6.50	9.67	11.65	56.08
19	0	0	0	26.17	15.83	25.67	30.15	58.34
20	0	0	0	14.90	4.77	9.77	10.87	63.99

The chroma and hue analysis was used to measure the color levels. The findings showed that the color indicators, both the chroma and the hue scores were different in each treatment. The highest chroma from the dried cocoa beans was obtained in treatment 14 (32.20), while the lowest chroma was obtained in treatment 1 (9.99). Meanwhile, the highest hue from the dried cocoa beans was obtained in treatment 11 (71.53), while the lowest hue was obtained in treatment 7 (28.85) (Table 2).

Analysis of pH of Fermented Cocoa Beans using RSM

The analysis results of the response surface methodology showed that pod storage, aeration rate, and aeration mode had significant effects on the pH of cocoa beans, as presented in Table 3. The pH values of the dried cacao beans are presented in Figure 3-5. Figure 3 shows that the treatment variations of pods storage (X₁) and aeration rate (X₂); at aeration mode of (X₃) = intermittent 2, resulted in pH values of 5.0 - 6.0, where a higher aeration rate will cause a higher pH and vice versa. Figure 2 also shows that aeration rates of < 0.3 liters/minute with 1-9 days pod storage resulted in lower pH values than the aeration rates of (X₂) > 0.3 liters/minute with 1-9 days pod storage.

Table 3
Regression coefficients and R² values of the RSM for each response variable

Variables	pH (Y ₁)	Chroma (Y ₂)	Hue (Y ₃)
Constant	5.8479*	17.576*	51.9294*
X ₁	-0.0462	1.352	3.9920*
X ₂	0.2729*	-1.639	-8.5890*
X ₃	0.1739	2.453	-5.0920
X ₁ *X ₁	-0.5125*	-4.049	-14.2159*
X ₂ *X ₂	-0.0210	-5.264	9.9491
X ₃ *X ₃	0.1610	7.966*	2.7341
X ₁ *X ₂	-0.1328	-1.500	-2.2650
X ₁ *X ₃	0.1497	-2.118	-0.1250
X ₂ *X ₃	-0.0760	1.645	-4.1500
R-Sq	74.3%	54.4%	75.8%

Notes: * significant at p < 0.05; X₁ = pods storage; X₂ = aeration rate; X₃ = aeration mode

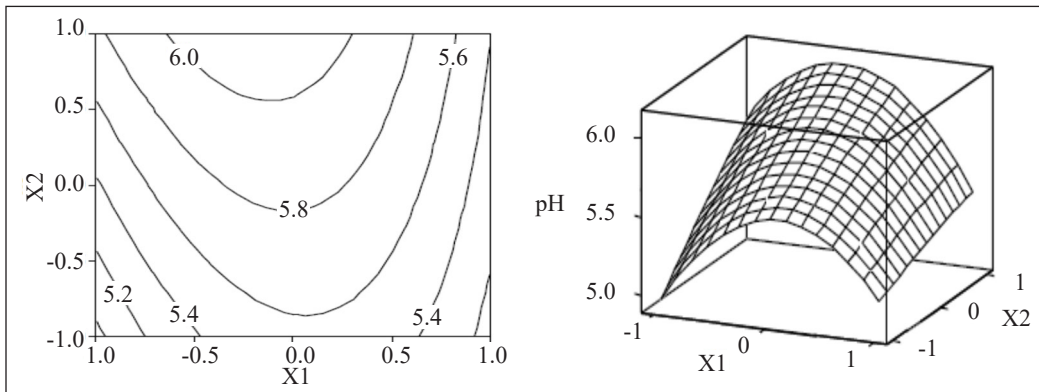


Figure 3. The plot contour and surface of pH of dried fermented cocoa beans (Y₁) in relationships with X₁ and X₂ at X₃ = Intermittent 2

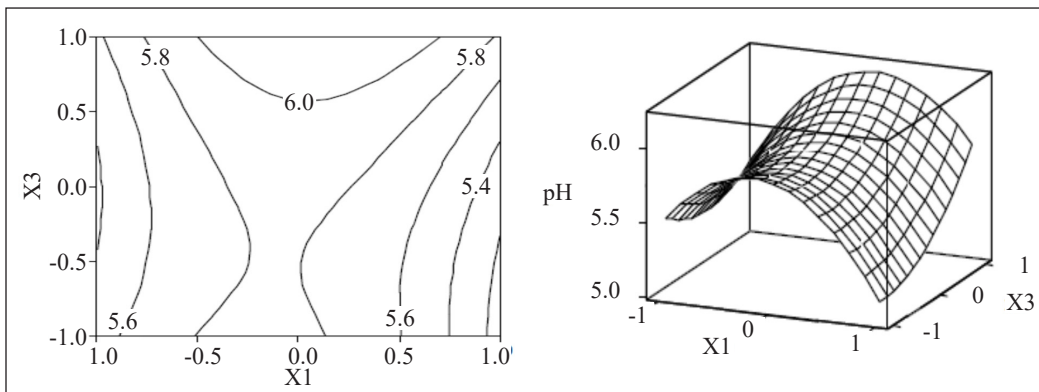


Figure 4. Plot contour and surface of pH cocoa beans fermented (Y₁) relationships with X₁ and X₃ at X₂ = 0.3 liters/minute

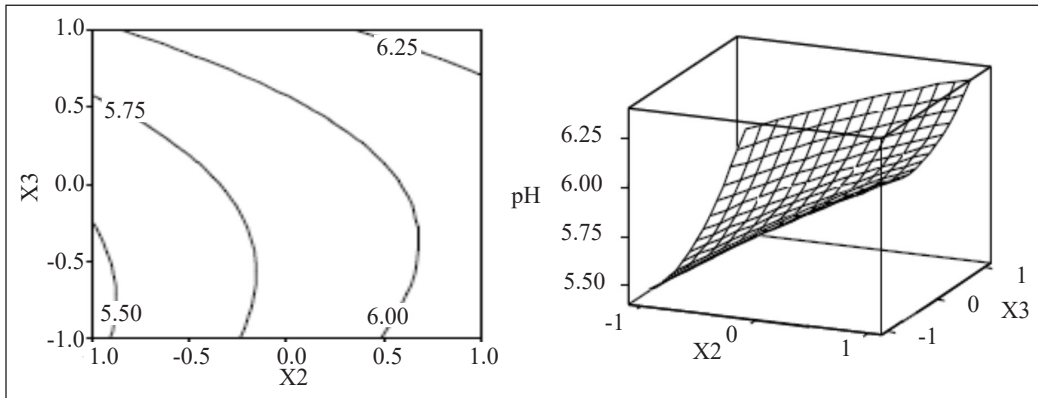


Figure 5. Plot contour and *surface* of pH cocoa beans fermented (Y_1) relationships with X_2 and X_3 at $X_1 = 5$ days

The changes in the pH values of the dried fermented cocoa beans as shown in Fig. 4 were 5.1-6.1, with the variations of pod storage (X_1) and aeration mode (X_3), at aeration rate (X_2) of 0.3 liters/ minute. The highest pH of the dried cocoa beans was 6.1, which was obtained in treatments $X_1 = 5$ days, $X_3 =$ continuous mode, and $X_2 = 0.3$ liters/minute. Meanwhile the lowest pH of the dried cocoa beans (5.1) was obtained in treatments $X_1 = 9$ days, $X_3 =$ intermittent 1, and $X_2 = 0.3$ liters/minute. Meanwhile, at all variation levels of X_2 and X_3 , and when $X_1 = 5$ days, the pH values of the dried fermented cocoa beans were 5.4-6.3, as shown in Fig. 5. The highest pH was obtained at continuous aeration mode and aeration rate of 0.4 liters/minute, while the lowest pH was obtained at an aeration rate of 0.2 liters/ minute and aeration mode of intermittent 1.

RSM analysis (based on ANOVA analysis, surface and contour plot) showed that aeration rate (X_2) significantly affected the pH of the dried cocoa beans. It is known that an increase in aeration rates will also increase the pH values of cocoa beans because an increase in aeration rate causes more water vapor containing acidic properties in cocoa beans to be pushed out of the reactor, thus increasing pH value. Nevertheless, X_1 and X_3 variables had smaller effects on the pH values. Table 3 shows that X_1 and X_3 variables had no significant effect on the pH values of the dried fermented cocoa beans.

Analysis of Color of Fermented Cocoa Beans using RSM

Based on the analysis of the variants of the chroma and hue of the dried cocoa beans as listed in Table 3, R^2 values were 54.4% and 75.8%, respectively. It means that pod storage, aeration rate, and aeration mode had effects of 54.4% on the chroma and 75.8% on the hue of the cocoa beans. Therefore, it is assumed that other factors may affect the changes of the chroma and hue of the dried cocoa beans.

Table 3 shows that pod storage, aeration rate, and aeration mode had no significant effects on the chroma. Nonetheless, pod storage and aeration rate had significant effects on the hue, while aeration mode did not. The changes of the chroma and hue of dried cocoa beans can also be known based on the contour and surface plots produced by RSM analysis. Figure 6 shows that the highest chroma was 17.8, which was obtained at $X_1 = 5-6$ days, $X_2 = 0.3$ liters/minute, and $X_3 =$ intermittent 2, while the lowest chroma was 7.20, which was obtained at $X_1 = 1$ day, $X_2 = 0.4$ liters/minute, and $X_3 =$ intermittent 2. The surface and contour plots as shown in Figure 7 show that the highest chroma was 28.01, which was obtained at $X_1 = 5$ days, $X_3 =$ continuous, and $X_2 = 0.3$ liters/minute, while the lowest chroma was 11.58, which was obtained at $X_1 = 1$ day, $X_3 =$ intermittent 2 and $X_2 = 0.3$ liters/minute. Furthermore Figure 8 shows that the highest chroma was 27.99, which was obtained at $X_1 = 5$ days, $X_2 = 0.3$ liters/minute and $X_3 =$ continuous, and the lowest chroma of the cocoa beans was 10.17, which was obtained at $X_1 = 5$ days, $X_2 = 0.4$ liters/minute and $X_3 =$ intermittent 2.

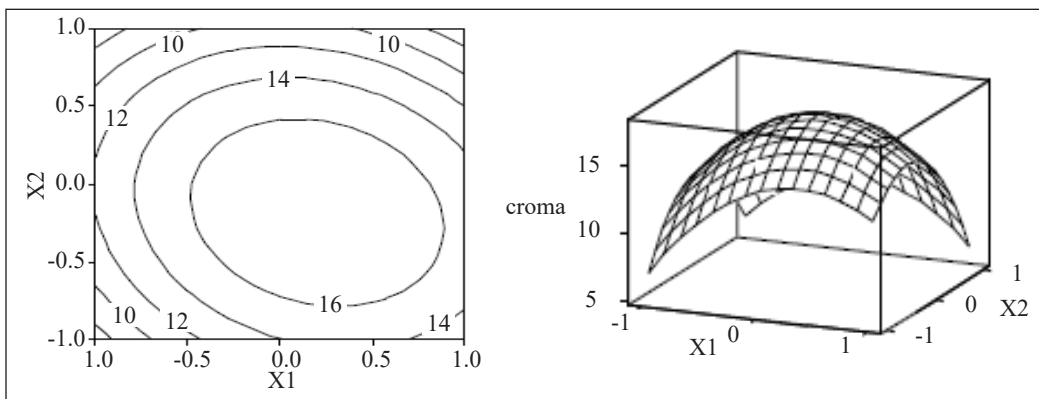


Figure 6. Plot contour and *surface* of chroma cocoa beans fermented (Y_2) relationships with X_1 and X_2 , at $X_3 =$ intermittent 2

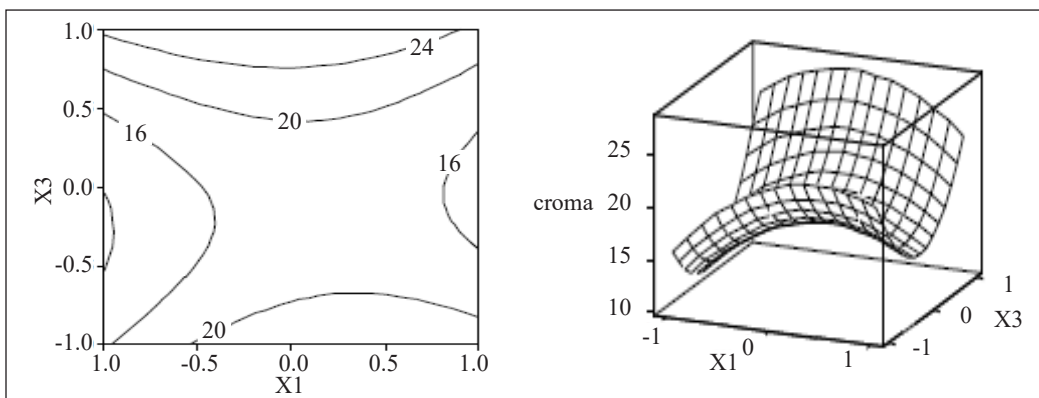


Figure 7. Plot contour and *surface* of chroma cocoa beans fermented (Y_2) relationships with X_1 and X_3 , at $X_2 = 0.3$ liter/minute

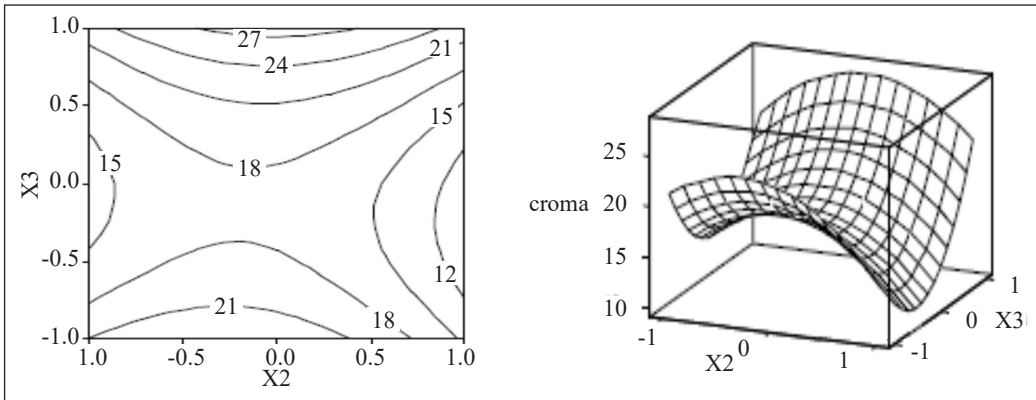


Figure 8. Plot contour and surface of chroma cocoa beans fermented (Y_2) relationships with X_2 and X_3 at $X_1 = 5$ days

Figure 9 shows that the highest hue of the cocoa beans was 70.86, which was obtained at $X_1 = 5$ days, $X_2 = 0.2$ liters/minute, and $X_3 =$ intermittent 2, while the lowest hue was 33.21, which was obtained at $X_1 = 1$ day, $X_2 = 0.35$ liter/minute, and $X_3 =$ intermittent 2. Moreover, the surface and contour plots as shown in Figure 10, where at $X_2 = 0.3$ liters/minute, the highest hue of the cocoa beans was 60.03, which was obtained at $X_1 = 5$ days and $X_3 =$ intermittent 1. Meanwhile, the lowest hue was 31.71, which was obtained at $X_1 = 1$ day, $X_3 =$ continuous. Furthermore, Figure 11 shows that the highest hue of the cocoa beans was 73.82, which was obtained at $X_2 = 0.2$ liters/minute and $X_3 =$ intermittent 1, and the lowest hue was 45.51, which was obtained at $X_2 = 0.36$ liters/minute and $X_3 =$ continuous, and X_1 set at 5 days.

The findings showed that hue is significantly affected by pod storage and aeration rate. Sulaiman et al. (2017) also stated that the color of cocoa beans was significantly affected by the duration of fermentation and pod storage. However, aeration mode does not significantly

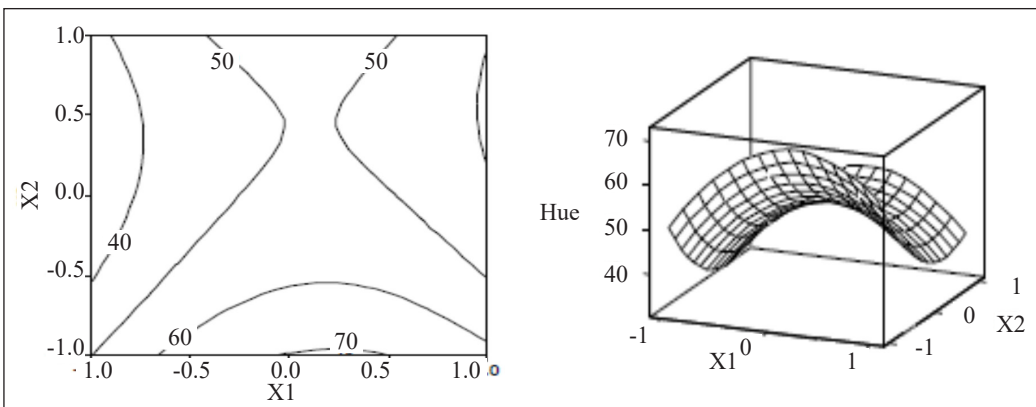


Figure 9. Plot contour and surface of hue cocoa beans fermented (Y_3) relationships with X_1 and X_2 , at $X_3 =$ Intermittent 2

affect the hue because the aeration given was very small, so the air contained in the reactor tube could not penetrate the pulps and cocoa beans properly. As a result, aeration mode did not affect the changes in the colors of the cocoa beans. In fact, the color characteristics of cocoa beans are not the only indicators used to measure the quality of cocoa beans.

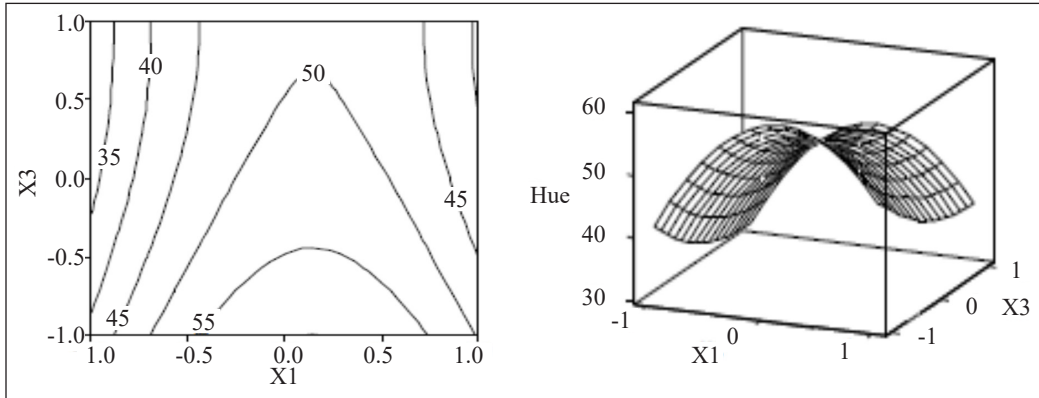


Figure 10. Plot contour and surface of hue cocoa beans fermented (Y_3) relationships with X_1 and X_3 at $X_2 = 0.3$ liter/minute

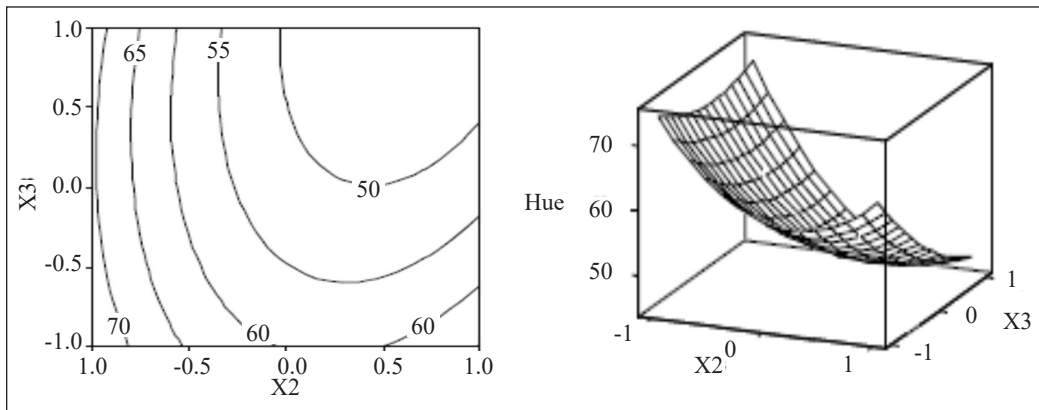


Figure 11. Plot contour and surface of hue cocoa beans fermented (Y_3) relationships with X_2 and X_3 at $X_1 = 5$ days

CONCLUSIONS

Pod storage before fermentation, aeration rate, and aeration mode have different effects on pH, color L^* , a^* , b^* , chroma, and hue of dried cocoa beans. The pH, chroma, and hue values of the dried cocoa beans are 4.873-6.517, 9.99-32.20, and 28.85-71.53, respectively. The results of the ANOVA analysis showed that pod storage affects hue significantly, but it does not affect the pH and chroma significantly. The aeration rate has a significant effect on pH and hue color, but it does not have a significant effect on chroma. Additionally, aeration mode does not have a significant effect on pH, chroma, and hue of dried cocoa beans.

ACKNOWLEDGEMENT

The authors are grateful for the support received from the Ministry of Education and Culture, and to Mr. Dualim who helped us a lot in laboratory activities.

REFERENCES

- Afoakwa, E. O., Jennifer, Q., Agnes, S. B., Jemmy, S. T., & Firibu, K. S. (2012). Influence of pulp-preconditioning and fermentation on fermentative quality and appearance of Ghanaian cocoa (*Theobroma cacao*) Beans. *International Food Research Journal*, 19(1), 127-133.
- Afoakwa, E. O., Kongor, J. E., Takrama, J., & Budu, A. S. (2013). Changes in nib acidification and biochemical composition during fermentation of pulp pre-conditioned cocoa (*Theobroma cacao*) Beans. *International Food Research Journal*, 20(4), 1843-1853.
- Afoakwa, E. O. (2016). *Chocolate science and technology* (2nd Ed.). Chichester, United Kingdom: Wiley Blackwell.
- Akhiriani, S., Susijahadi, S., Djumarti, D., & Wahyudi, T. (2012, June 25-26). The effect of the addition of yeast isolates on the colour differentiation in cocoa beans during the fermentation. In *Proceedings International Conference on Agribusiness Marketing (ICAM)* (pp. 181-190). Jember, Indonesia.
- Apriyanto, M., Sutardi, S., Supriyanto, S., & Harmayani, E. (2016). Study on effect of fermentation to the quality parameter of cocoa bean in Indonesia. *Asian Journal of Dairy and Food Research*, 35(2), 160-163.
- Araujo, Q. R., Loureiro, G. A. H. A., Rohsius, C., & Baligar, V. C. (2018). Impact of soils and cropping systems on biochemical attributes of dry cacao beans. *Agrotrópica*, 30(3), 175-194.
- Barrientos, L. D. P., Oquendo, J. D. T., Garzón, M. A. G., & Álvarez, O. L. M. (2019). Effect of the solar drying process on the sensory and chemical quality of cocoa (*Theobroma cacao* L.) cultivated in Antioquia, Colombia. *Food Research International*, 115(52), 259-267.
- Bezerra, M. A., Santelli, R. E., Oliveira, E. V., Villar, L. S., & Escaleira, L. A. (2008). Response surface methodology (RSM) as a tool for optimization in analytical chemistry. *Talanta*, 76(5), 965-977.
- Biehl, B., Meyer, B., Crone, G., & Pollmann, L. (1989). Chemical and physical changes in the pulp during ripening and post-harvest storage of cocoa pods. *Journal of the Science of Food and Agriculture*, 48(2), 189-208.
- BSN. (2008). *Biji Kakao. SNI 2323:2: 1-37* [Cocoa beans. SNI 2323:2: 1-37.]. Badan Standarisasi Nasional. Retrived July 3, 2017, from http://akses-sispk.bsn.go.id/Upload/Dokumen/SK_SNI/17441_SK%20SNI%20No86-9-2008.PDF
- Hartuti, S., Karyadi, J. N. W., Bintoro, N., & Pranoto, Y. (2018). Fermentasi isothermal biji kakao (*Theobroma cacao* L.) dengan sistem aerasi terkendali [Isothermal fermentation of cocoa beans (*Theobroma cacao* L.) with controlled aeration system]. *Agritech*, 38(4), 364-374.
- Hartuti, S., Karyadi, J. N. W., Bintoro, N., & Pranoto Y. (2019). Characteristics of dried cocoa beans (*Theobroma cacao* L.) color using response surface methodology. *Planta Tropika: Jurnal Agrosains (Journal of Agro Science)*, 7(1), 82-92.

- Kongor, J. E., Hinneh, M., Walle, D. V. D., Afoakwa, E. M., Boeckx, P., & Dewettinck, K. (2016). Factors Influencing quality variation in cocoa (*Theobroma cacao* L.) bean flavour profile - A review. *Food Research International*, *82*, 44-52.
- Krähmer, A., Engel, A., Kadow, D., Ali, N., Umaharan, P., Kroh, L. W., & Schulz, H. (2015). Fast and neat - Determination of biochemical quality parameters in cocoa using near infrared spectroscopy. *Food Chemistry*, *181*, 152-159.
- Marcin, K., Jarosław, W., Monika, P., & Agnieszka, W. (2016). Application of the response surface methodology in optimizing oat fiber particle size and flour replacement in wheat bread rolls. *CYTA - Journal of Food*, *14*(1), 18-26.
- Mendoza, F., Dejmek, P., & Aguilera, J. M. (2007). Colour and image texture analysis in classification of commercial potato chips. *Food Research International*, *40*(9), 1146-1154.
- Misnawi, S. (2008). Physico-chemical changes during cocoa fermentation and key enzymes involved. *Review Penelitian Kopi dan Kakao*, *24*(1), 47-64.
- Muzaifa, M., Abubakar, A., & Haris, F. (2017). Profile of the growth of microorganisms in the fermentation of Aceh cocoa beans. *Jurnal Teknologi Industri dan Pertanian Indonesia*, *9*(2), 50-54.
- Noor-Sofalina, S. S., Jinap, S., Nazamid, S., & Nazimah, S. A. H. (2009). Effect of polyphenol and pH on cocoa maillard-related flavour precursors in a lipidic model system. *International Journal of Food Science and Technology*, *44*, 168-180.
- Saludes, R. B., Iwabuchi, K., Kayanuma, A., & Shiga, T. (2007). Composting of dairy cattle manure using a thermophilic-mesophilic sequence. *Biosystems Engineering*, *98*(2), 198-205.
- Saunshia, Y., Sandhya, M. V. S., Lingamallu, J. M. R., Padela, J., & Murthy P. (2018). Improved fermentation of cocoa beans with enhanced aroma profiles. *Food Biotechnology*, *32*(4), 257-72.
- Sulaiman, K. B., Yang, T. A., & Fazilah, A. (2017). colour and antioxidant properties of cocoa beans from pods colour and antioxidant properties of cocoa beans from pods storage and fermentation using. *International Journal of Science and Technology*, *3*(2), 295-307.
- Wexler, L., Perez, A. M., Cubero-Castillo, E., & Vaillant, F. (2016). Use of response surface methodology to compare vacuum and atmospheric deep-fat frying of papaya chips impregnated with blackberry juice. *CyTA - Journal of Food*, *14*(4), 578-586.
- Yusof, A. H. M., Gani, S. S. A., Zaidan, U. H., Halmi, M. I. E., & Zainuddin, B. H. (2019). Optimization of an ultrasound-assisted extraction condition for flavonoid compounds from cocoa. *Molecules*, *24*(4), 1-16.

Experimental (ADV & PIV) and Numerical (CFD) Comparisons of 3D Flow Pattern around Intact and Damaged Bridge Piers

Ehsan Oveici¹, Omid Tayari^{1*} and Navid Jalalkamali²

¹Department of Civil Engineering, Kerman Branch, Islamic Azad University, 7635131167 Imam Ali Blvd., Kerman, Iran

²Department of Water Engineering, Kerman Branch, Islamic Azad University, 7635131167 Imam Ali Blvd., Kerman, Iran

ABSTRACT

Numerous bridges fail all over the world every year because of ignoring the role of hydraulic factors, including flow and scour patterns in bridge designs. Hence, investigation of the flow pattern around intact and damaged bridge piers gains significant importance. This study provided experimental and numerical investigations of the flow pattern around damaged and intact bridge piers (short cylindrical and pillar elements). This topic is applicable to flooding conditions of rivers when and where the remainders of bridges and other structures on the river path could affect the flow pattern, making further flow pattern investigations under such conditions necessary. The experiments had been conducted in a straight channel with a length of 12 meters in Kerman, Iran. To collect the three dimensional flow velocity components, Acoustic Doppler Velocimetry (ADV) was employed. Further, Particle Image Velocimetry (PIV) was utilized to compare the results of ADV. SSIIM software helped model the flow in this study, and Navier–Stokes equations and $k-\epsilon$ turbulent

model was used for solving the flow field. Generally, the results obtained through the comparisons are indicative of an appropriate correspondence between the numerical and the experimental data. The results indicated that installing the piers along the channel resulted in displacement of the maximum bed shear stress from the last one-third zone of the channel to mid-channel. Also, the maximum bed shear stress increased by 72% in comparison to the case with no piers

ARTICLE INFO

Article history:

Received: 02 December 2019

Accepted: 29 January 2020

Published: 15 April 2020

E-mail addresses:

ehsanoveici@iauk.ac.ir (Ehsan Oveici)

tayari@iauk.ac.ir (Omid Tayari)

njalalkamali@iauk.ac.ir (Navid Jalalkamali)

* Corresponding author

installed. Moreover, the maximum water level variations occurred in the case with both intact and damaged piers installed, where there was water level reduction downstream and water level increase upstream of the pier.

Keywords: 3D flow velocity, acoustic Doppler velocimetry, bed shear stress, bridge piers, experimental model, particle image velocimetry, SSIIM

INTRODUCTION

Statistics have shown a significant increase in the number of damaged bridges as time passes. This difference may to some extent be attributed to statistical flaws in past years or the increase in the number of bridge constructions; however, Melville and Coleman (2000) believed that not only were new scientific rules ignored in construction of bridges in recent years, but inaccessibility of the practical results of research on scour to those active in this field and eventually the current status of our knowledge on scour and bridge hydraulics also counted as the main reasons for the increase in the number of instances of such damage. The extremely important issue of bridge failure has had numerous scientists seeking to know as much as possible about scouring phenomena and complex flow patterns. They have tried to predict behavior under varied circumstances by resorting to different methods, including incorporation of physical, numerical and field research models. A number of these will be cited in the following:

Chiew and Melville (1987) studied the effect of flow velocity, flow depth, and sediment particle size on the scour depth around cylindrical piers. They found that where the flow velocity was higher than the incipient motion value, increasing the flow velocity by up to twice the incipient motion value reduced the scour depth to a minimum value. Breusers and Raudkivi (1991) examined the scour around piers by altering cross-sections. They concluded that the pier with increased cross-section upward (towards the water surface) increased the scour, and the pier with decreased cross-section upward reduced the scour. Bozkus and Yildiz (2001) studied the effect of a single pier inclination, and Bozkus and Cesme (2010) addressed the effect of dual bridge piers on scour depth in a straight channel. They reported a reduction of scour depth by increasing the pier's angle in the downstream direction. Vaghefi et al. (2016b) studied and compared flow patterns and local scour around inclined and vertical cylindrical piers under clear water conditions. They investigated the effect of pier inclination in three directions: upstream, downstream, and perpendicular to the flow. They demonstrated that for every degree of increase in pier inclination, the scour depth was reduced by about 1% in comparison to a vertical pier position. Khajeh et al. (2017) undertook an experimental study and comparison of scour depth and position around an inclined cylindrical pier and a vertical pier at a 180-degree sharp bend apex. They concluded that installation of the pier towards the outer bank had created alternating sedimentary dunes at the downstream side of the pier in the vicinity of the inner bank. Jaman et al. (2017) carried out an experimental study of scour around three identical

circular-type piers arranged inline and eccentrically in a staggered manner. Two inline piers were positioned towards the flow, and the eccentric one was placed in the middle region of the two inline piers. They found that vortices' strengths for the eccentric-middle and inline-rear piers were the greatest and the lowest, respectively, compared with strength of the inline-front pier. Karimi et al. (2017) studied the effect of bridge pier inclination angle on the scouring process under clear water conditions in a straight channel. Results of their study indicated that the minimum and the maximum scour depths occurred from 0 to 15-degree angles. Vaghefi et al. (2018b) examined scour around a triad series of piers, perpendicular to or in the direction of the flow, under clear water conditions in a laboratory flume with a width of 100 cm and a 180-degree sharp bend. As the results of their study indicated, with installation of the piers in perpendicular and streamwise directions, the maximum scour hole occurred at the 60-degree angle, around the piers, with sedimentary dunes observed at the downstream side of the piers. Bozkus et al. (2018) examined the effects of inclination of upstream and downstream piers in triad and quad pier groups on scouring. To this aim, they conducted tests for two different cases involving three and four piers either in a perpendicular position or with inclination angles of 10 and 15 degrees, with two diameters of 50 and 70 mm under clear water and steady-state sediment conditions. Totally, they ran 72 tests and concluded that increasing the pier diameter and the flow rate increased the scour. Omara et al. (2018) incorporated Flow-3D model in order to obtain the water surface, flow velocity, bed shear stress, and scour depth around vertical and inclined piers. They also compared these with experimental data and demonstrated that the Flow-3D model could efficiently model the depth of the free surface water and the velocity of the flow with a high accuracy. Asadollahi et al. (2019) carried out numerical and experimental comparison of the flow and scour patterns around single and triad piers which were installed in a 180-degree sharp bend. Results of their comparisons suggested the appropriate calculations of the numerical data and the great competency of SSIIM in modeling the flow and scour patterns with a maximum error of only 4% reported for the scour and sedimentation.

As noted, most research efforts attempted to date to investigate bridge piers in rivers concern the scour phenomenon and study of its mechanism and the maximum values around conventional piers (Breusers & Raudkivi, 1991; Bozkus & Yildiz, 2001; Bozkus & Cesme, 2010; Khajeh et al., 2017; Jaman et al., 2017; Karimi et al., 2017; Vaghefi et al., 2018b; Bozkus et al., 2018). Few researchers have ever addressed the complex flow pattern around intact and damaged bridge piers. Firstly, 3D analysis of the complex flow pattern around intact and damaged bridge piers requires great hydrodynamic knowledge and sufficient proficiency on this topic. Secondly, the laboratory equipment required for this research (ADV and PIV velocimeters) are barely accessible to researchers due to their great cost. Therefore, this study investigated the flow pattern in a straight channel under the influence of a single intact pier, a single damaged pier, and the effect of both piers

with an experimental method (by using two different velocimeters: ADV and PIV) and a numerical method (by using CFD model). Application and significance of this point were further experienced under flooding conditions of rivers, for the wreckage of the bridges and other structures were present on river paths and could influence the flow pattern. The need to investigate the flow pattern is more evident under such conditions. In addition, although the bed of this channel is rigid, calculation of bed shear stress in this study allows estimation of the scour phenomenon under mobile bed conditions as well.

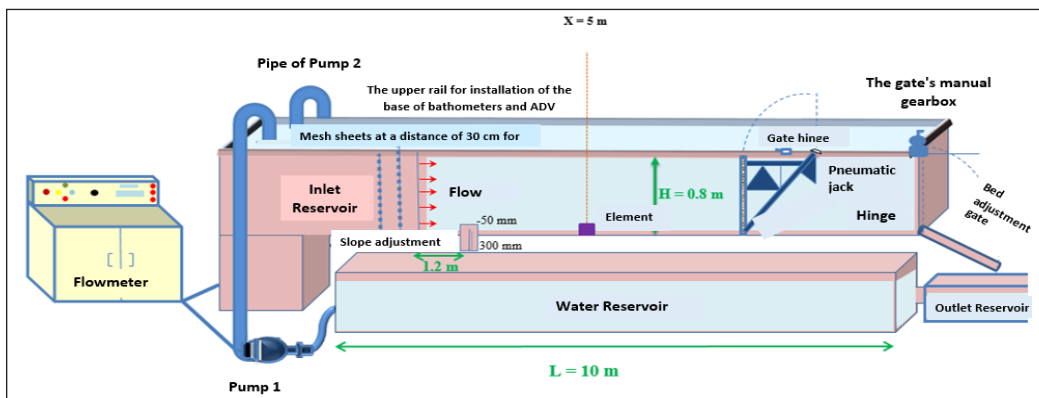
MATERIALS AND METHODS

Introduction of the Experimental Model

Laboratory Channel. To conduct the intended study, a 1-meter-wide, 0.8-meter-high laboratory channel with glass walls and steel frames was designed and constructed in the laboratory of hydraulic structures at Islamic view of the channel in the laboratory. As seen in Figure 1, the channel's effective length is 12 meters. The laboratory channel bed is rigid



(a)



(b)

Figure 1. (a) A view of the channel in the laboratory; and (b) a schematic view with the components of the channel in the laboratory of the hydraulic structures at Islamic Azad University, Kerman Branch

and is made of steel. Side reservoirs with an approximate capacity of 10 m³ have been used as sources of water in this channel. Two H25-200 centrifugal pumps, with a snail-shaped scroll made by Pumpiran Co. pump water from the reservoirs were embedded at the side of the channel into the channel's inlet reservoir. The discharge capacity of 60 liters per second was kept constant throughout every experiment by using an AKTEK ultrasonic flow meter with ± 1 mm/s accuracy. Water had been pumped into the inlet reservoir with this discharge capacity by the pumps. These pumps are linear, and each is capable of generating a maximum 190 m³/s discharge. Further, the water level at the upstream is 20 cm, the depth which was set by using the butterfly gate at the end of the downstream path for conducting the experiments, because the ratio of width to depth of the flow must be equal to or greater than 5 or 6 in order to reduce the effect of the channel sidewalls according to Nezu and Nakagawa (1993). To calm the inlet flow and to reduce the initial turbulence during the experiments, two mesh sheets were also embedded at the inlet reservoir connection 25 cm apart from each other.

Bridge Piers. Elements used in conducting the experiments include a short cylindrical element (with a diameter of 10 cm and a height of 5 cm), and a column element (with a diameter of 4 cm and a height of 40 cm), where the short cylindrical element represents the damaged bridge piers or flood debris present on the flow path, and the column element represents a bridge pier in river. The cylindrical element is made of solid steel, and the column is hollow PVC pipe with 3-mm-thick walls with a powerful magnet installed at the end to make it adhere to the channel bed. The height of these elements had been determined according to recommendations of Yeow et al. (2016). Furthermore, these two values had been specified for determination of the element's diameters according to research results:

1. According to observations by Chiew and Melville (1996), the bed element's diameter must be smaller than or equal to 10% of the channel width to remove the effect of channel sidewalls on the flow pattern.
2. According to Raudkivi and Ettema (1983) standard, the channel width must be at least 6.25 times the pier diameter.

These elements were located at mid-channel at a distance of 5 meters from upstream.

ADV and Relevant Software Programs. Vectrino 3D velocimeter, which is one of the most advanced ADV's (Acoustic Doppler Velocimetry), had been utilized to measure velocity components and determine the 3D flow pattern. The device function involves sending a sound wave with a specific frequency and receiving its reflection from the flow to identify the flow velocity from the extent of variations in the initial frequency. This device has two side-looking and down-looking probes based on the position of its sensor to be used to measure different sections of the field (Nortek, 2009). To carry out the experiment, a frequency of

25 Hz and a time of 1 minute were assumed (Vaghefi & Akbari, 2019). Hence, the device is capable of collecting the flow velocity in three directions up to 1500 data per minute. During the experiments, it has always been considered to keep the values of “Coloration” and “Signal to Noise Ratio” above their standard values (respectively 80 and 20%) in order to increase the accuracy of the velocimeter’s measurements. The information on the data measured at different times was recorded by Vectrino and saved as ADV format. Then these data were converted into vno format in order to be used in Explorer V for filtration. They were then converted into a format usable in Excel after analysis and velocity averaging (Akbari & Vaghefi, 2017). Figure 2 illustrates a view of data collection by ADV around intact and damaged bridge piers.



Figure 2. Position of ADV for data collection around the two elements present in the channel

Particle Image Velocimetry (PIV). PIV had been utilized along with a down-looking probe of ADV to measure the flow velocity throughout these experiments. The main advantage of this velocimeter to ADV was the fact that it did not cause local turbulence and streamline variations caused by the presence of probes on the flow path in measurements, and hence increasing the accuracy of data measurement (Rusello et al., 2006; Hurther & Lemmin, 2001; Voulgaris & Trowbridge, 1998). Furthermore, since velocity data were collected at points and at very close intervals, PIV was the best choice for monitoring velocity variations around the hydraulic structures, the vicinity of the water surface, and the walls, especially in turbulent flows. Figure 3 depicts the flow velocity measurement by using PIV. According to this figure, when collecting the flow velocity by using PIV, the laser source is installed on top of the flume by using a mobile platform in such a way as to create a rectangular plane. This plane, as wide as the flow depth, has a streamwise alignment (the length of which depends on the distance of the laser), and is two dimensional. Then the camera was installed on a tripod with an adjustable height at a distance of 91 cm from the outer wall of the flume. After the connections between the laser, the camera, and the data collection and the recording system (a computer equipped with a special card) were constructed with a switch, eventually, the data collection and recording operation was undertaken by running the velocity data recording software (rtcontrol) (Thielicke & Stamhuis, 2014). Also, PIVLab software has been utilized for processing and analyzing the output images (Raffel et al., 2018).



Figure 3. A view of the flow velocity measurement by using PIV and the relevant equipment

The Number of Data Collection and Experiments. A finer mesh was generally used throughout the experiment in the area of the elements and their downstream side. For instance, Figure 4 illustrates the grid network for the experiment with no piers present. In this figure, Z denotes the water depth at the channel's entrance, Y represents the channel width, L is the channel length, and H is the channel height. However, considering the higher sensitivity of the experiments involving piers and the need for more accuracy, finer meshes had been used so that the 3D velocity profile occurred in 13 cross-sections along

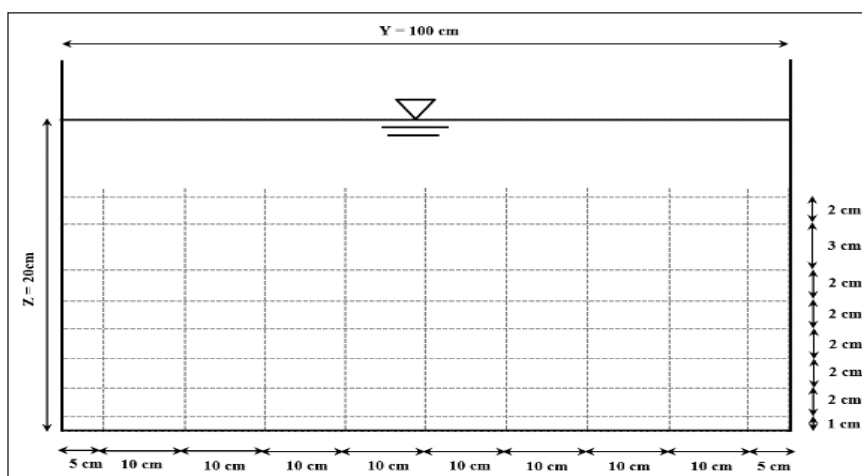


Figure 4. Channel transverse grid for determining the position of the collected points in the experiment with no piers present (the figure has no scales)

the channel and 7 levels of depth, and 20 points were collected in every transverse axis. Considering the aims of this study, the number and order of the specified experiments are presented in Table 1.

Table 1
The number and order of flow pattern experiments

Experiment No.	Experiment Name	Structure Type (Channel Bed Conditions)
1	Test 1	Bed without piers
2	Test 2	Bed with a damaged pier
3	Test 3	Bed with an intact pier
4	Test 4	Bed with both piers

Numerical Model

SSIIM Software. SSIIM (Sediment Simulation in Intakes with Multiblock option) is considered as one of the best CFD software programs. It is used for numerical analysis of scour and flow patterns in channels and rivers and generally the issues about river engineering and hydraulics. This software solves Navier-Stokes equations with the standard K- ϵ turbulence model on a 3D network. The Finite Volume Method had also been used with the power algorithm and the second-order directional algorithm for discretization. Further, the SIMPLE method was used for the relationship between the pressure and the velocity terms. By using an implicit solution, the velocity field was calculated in the geometry, and by using the calculated velocity field and solving the continuity equation of the sediment, the bed variations were calculated.

Governing Equations of Flow. The Navier-Stokes equations are the equations governing the flow in this software, and the turbulence model is used for solving them. SSIIM numerical model is capable of employing different turbulence models. After considering the previous studies conducted by other researchers (Vaghefi et al., 2016c; Vaghefi et al., 2017) and different turbulence models, the K- ϵ model was selected as the turbulence model. Navier-Stokes equations for incompressible fluids with a constant density in a vector are as follows (Equation 1):

$$\frac{\partial U_i}{\partial t} + U_j \frac{\partial U_i}{\partial x_j} = \frac{1}{\rho} \frac{\partial}{\partial x_i} \left(-P \delta_{ij} - \overline{\rho u_i u_j} \right) \quad (1)$$

where

x_1 , x_2 , and x_3 are distances in three directions; U_1 , U_2 , and U_3 denote velocity in three directions; P is the total pressure; and δ_{ij} is Kronecker delta, which is unity if $i=j$, and null otherwise.

The first term on the left in the above equation is the transient term (temporal variations), and the next term is the displacement term. The first term on the right is the pressure term, and the next term pertains to the Reynolds stress. Evaluation of the latter requires a turbulence model. Boussinesq proposed Equation 2 to state the Reynolds stress term for k-ε turbulence stress:

$$-\overline{u_i u_j} = \nu_T \left(\frac{\partial U_j}{\partial x_i} + \frac{\partial U_i}{\partial x_j} \right) + \frac{2}{3} k \delta_{ij} \quad (2)$$

$$\nu_T = c_\mu \frac{k}{\epsilon} \quad (3)$$

k (the flow kinetic energy), P_k, and ε (the kinetic energy loss) are modeled as Equations 4 - 6:

$$\frac{\partial k}{\partial t} + U_j \frac{\partial k}{\partial x_j} = \frac{\partial}{\partial x_j} \left(\frac{\nu_T}{\sigma_k} \frac{\partial k}{\partial x_j} \right) + P_k - \epsilon \quad (4)$$

$$P_k = \nu_T \frac{\partial U_j}{\partial x_i} \left(\frac{\partial U_j}{\partial x_i} + \frac{\partial U_i}{\partial x_j} \right) \quad (5)$$

$$\frac{\partial \epsilon}{\partial t} + U_j \frac{\partial \epsilon}{\partial x_j} = \frac{\partial}{\partial x_j} \left(\frac{\nu_T}{\sigma_\epsilon} \frac{\partial \epsilon}{\partial x_j} \right) + C_{\delta 1} \frac{\epsilon}{k} P_k + C_{\delta 2} \frac{\epsilon^2}{k} \quad (6)$$

In the k-ε turbulence model in the above equations, the constant values are as follows:

$$c_\mu = 0.09 \quad C_{\epsilon 1} = 1.44 \quad C_{\epsilon 2} = 1.92 \quad \sigma_k = 1.0 \quad \sigma_\epsilon = 1.3$$

Water Surface Profile. The free surface was computed using a fixed-lid approach with zero gradients for all variables. The location of the fixed lid and its movement as a function of time and the water flow field were computed by pressure and the Bernoulli algorithm: It uses the Bernoulli equation along the water surface to compute the water surface location based on one fixed point that does not move. Considering two consecutive cross-sections “j” and “j+1”, we can use the extended Bernoulli equation to write Equation 7:

$$W_{j+1} + a_{j+1} \cdot V_{j+1}^2 / 2g = W_j + a_j \cdot V_j^2 / 2g + h_r \quad (7)$$

where W_j denotes the water surface elevation above water level (or a reference surface), V_j is the average velocity in a cross-section, the coefficient a_j is equal to unity, and h_r is the friction loss due to the influence of roughness (Equation 8):

$$h_r = J_e \cdot \Delta x \quad (8)$$

where J_e denotes the energy gradient and Δx is the horizontal distance between cross sections “j” and “j+1”. The energy gradient J_e can be quantified by making use of the Gauckler-Manning-Strickler equation to yield Equation 9:

$$J_e = 1 / (k_{st}^2 \cdot R_{h.m}^{4/3} \cdot V_m^2) \quad (9)$$

where k_{st} is the Strickler coefficient, and V_m and $R_{h.m}$ are the mean average velocity and the mean hydraulic radius of the two consecutive cross-sections (Vaghefi et al., 2016c).

Grid System. The sizes of mesh near the bridge piers were smaller than those upstream and downstream of the piers so that better results might be achieved. A structured grid was used in SSIIM-1 (Olsen, 2003). Figure 5 illustrates the mesh grid considered for longitudinal and cross sections, and in fact the computational domain intended for this study. With the aim of sensitivity analysis for the mesh grid of the model, three different grids (fine, medium, and coarse) were used with respective dimensions of 3067894, 1073226, and 500769. Based on these mesh grids, the best model had been analyzed on the number of cells and efficiency. Table 2 provides the values of the comparison of the numerical model with the experimental results for the case without piers. Comparisons presented in this table are given for the longitudinal velocity at a distance of 4 meters from the channel upstreamside. In this table, R^2 is the coefficient of determination and RMSE stands for Root Mean Square Error. According to this table, it may be observed that the appropriate mesh grid of the numerical model with the most similar results to the experimental model has 1073226 cells. Moreover, the appropriate time required for the software to carry out computations for the finer mesh has been several times greater than that required for the average mesh. Therefore, the average mesh has the most efficiency and the best evaluation

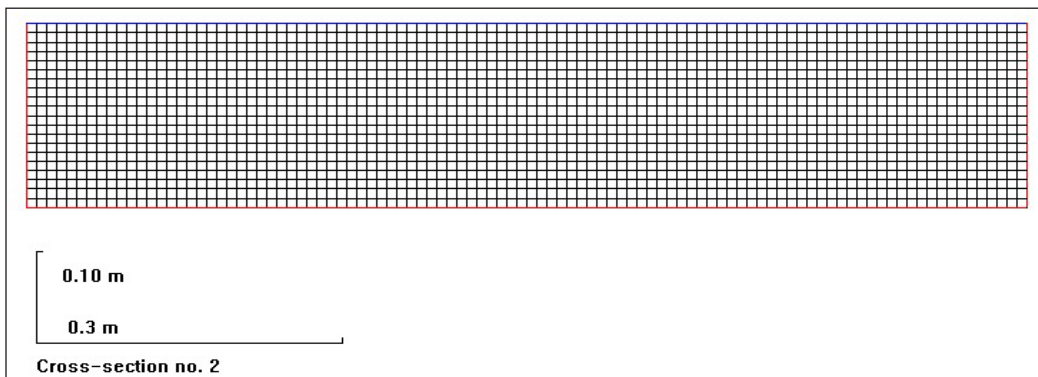


Figure 5. An illustration of the mesh grid and the computational domain considered for longitudinal and cross sections

and has been selected as the optimum mesh for numerical modeling. The grid systems in the vertical, lateral and longitudinal directions (stream wise) respectively have 21, 101, and 506 lines, and in total they have 1073226 cells.

Table 2

The results of evaluating the efficiency of the cells' size and sensitivity analysis of the mesh for the longitudinal velocity at a distance of 4 meters upstream

Mesh Size	R ²	RMSE
Coarse mesh	0.9383	0.0195
Medium mesh	0.9823	0.0107
Fine mesh	0.9771	0.0478

Boundary Conditions. The discharge value must be defined as the input boundary condition. The gradient of all the parameters at the output boundary equals zero. Besides, the discharge at the downstream side must also be defined as the output boundary condition. The ε gradient (the kinetic energy loss) and also the value of k (the kinetic energy) are assumed to be zero at the water surface. The flux passing through the bed and wall is null, and the law of the wall proposed by Schlichting (1979) is used as in Equation (10), where U is velocity, U^* denotes shear velocity, K represents a constant coefficient equal to 0.4, y is the distance of the wall from the center of the cell, and K_s is roughness equal to d_{90} in the soil gradation curve (Olsen, 1999; Olsen, 2001; Olsen, 2003):

$$\frac{U}{U^*} = \frac{1}{K} \ln(30y/K_s) \quad (10)$$

The analysis was made under clear water conditions, for the maximum scour depth occurs under such conditions (assuming a non-rigid bed). The input discharge at the upstream side of the channel equaled 60 liters per second. The water depth and the Froude number at the channel's entrance were 20 cm and 0.34, respectively. Also, the channel walls and the bed had been assumed rigid.

Initial Conditions. The input discharge at the upstream side of the channel equaled 60 liters per second. The water depth and the Froude number at the channel's entrance were 20 cm and 0.34, respectively. Also, the channel walls and the bed had been assumed rigid.

RESULTS AND DISCUSSION

The open-channel flow has a thoroughly three-dimensional structure and is turbulent due to the dominant boundary conditions (the input flow intensity as well as bed and wall conditions). It is naturally vital to gain sufficient knowledge of hydrodynamic phenomena in open-channel flows with no obstacles before investigation of complex flow patterns and

the structure of turbulent flows resulting from construction of intact and damaged bridge piers. Hence, in every section related to the results of this study, every parameter calculated and analyzed in four cases, without the piers, with a damaged pier, with an intact pier, and with both intact and damaged piers, has been provided following these results.

Verification

First, to validate the results obtained from the numerical model made by SSIIM software, they were compared and validated with the experimental results collected by using ADV under the same conditions. Figure 6 depicts experimental and numerical results of longitudinal velocity components at a cross-section at a distance of 5 m from the upstream side of the channel and at mid-channel in four cases (without piers, with a damaged pier, with an intact pier, and with both intact and damaged piers). As is observed in these figures, in every case, the flow velocity is the minimum near the bed but increases towards the water surface where the boundary layer fades. It may be observed in Figure 6 that the highest difference between numerical and experimental data is at the layers near the bed. This has also been reported in studies of other researchers who have compared ADV collected data with those of CFD software programs (Vaghefi et al., 2016c; Vaghefi et al., 2019c; Asadollahi et al., 2019).

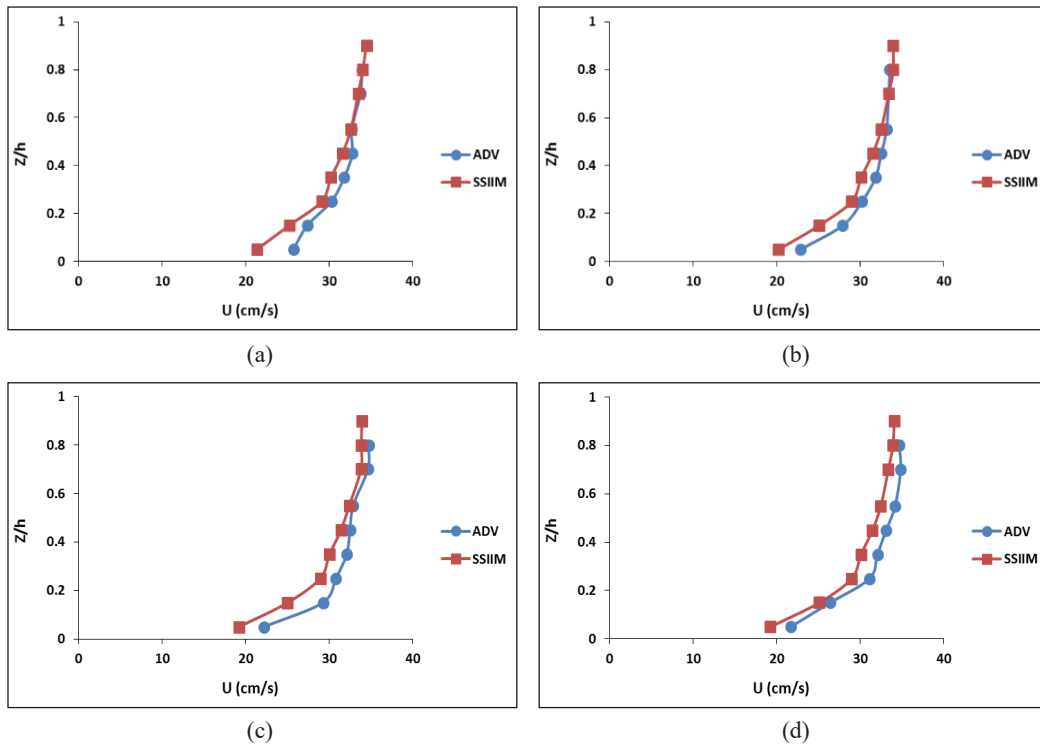


Figure 6. Comparison of numerical and experimental data for a) Test 1, b) Test 2, c) Test 3, and d) Test 4

In every case presented in Figure 6, ADV has provided higher values than SSIIM output data. Moreover, in Test 1, there is less flow turbulence due to the absence of structures on the flow path, and there is a higher correspondence observed between numerical and experimental data. Lack of a total correspondence between numerical and experimental results in other cases is due to the difference in the nature of the numerical and experimental studies. On the other hand, the high sensitivity present in the experimental research due to the difficulty of data collection in sensitive areas such as the vicinity of the pier and also the contacts between the velocimeter probes and the pier could reduce the accuracy of the collected data and lead to differences between numerical and experimental results. Also, simplifications made in solving the equations through numerical calculations contribute another factor reducing the complete validity of the numerical results. Nevertheless, the average error present in every case is less than 5% and it indicates similarity of the results obtained through SSIIM software and the experimental results, which is, in fact, indicative of data analysis validity.

Comparison between ADV and PIV Data

Figure 7 presents longitudinal velocity components at a cross-section at a distance of 5 m from the upstream sections and at mid-channel for all four cases to compare PIV and ADV data. As is clear in the figure, PIV data enjoy a higher unity and number because they are collected in-depth and at a specific level. This entails a clearer observation of flow variations and higher accuracy in measurements; it is not possible to collect data up to the vicinity of the water surface by ADV because the data are collected at a distance of 5 cm from the probe. As is observed in Figure 7, the values collected by ADV are higher than PIV velocity values. Furthermore, again, the difference in these data is evident in the values collected near the bed, the issue previously reported by other researchers comparing ADV and PIV data (Kara et al., 2012; Tominaga & Nezu, 1991; Nabipour et al., 2018).

As previously stated, the main advantage of PIV over ADV is the fact that no local turbulence and streamline variations occur due to the absence of probes on the flow path when measuring velocity, and the accuracy of data measurement is enhanced. Recent years have seen numerous studies conducted on 3D velocity components collected using ADV by researchers including Goring and Nikora (2002), Shinnee et al. (2004), Westerweel and Scarano (2005), Mori et al. (2007), Duncan et al. (2011), Razaz and Kawanisi (2011), Razaz et al. (2013), Islam and Zhu (2013), Yafei (2015), Vaghefi et al. (2017), Vaghefi et al. (2019a), and Vaghefi et al. (2019b). There have been studies addressing spike data, and proposing an algorithm for removing such data, and they have also proved the presence of data inconsistent with the pattern of other data. Nevertheless, the difference between the average flow longitudinal velocity data for the conducted experiments has been approximately 4% (3.9%), which is negligible, for the same 4% error has also been

reported in previous studies (Lemmin & Rolland, 1997); whereas, the error is much bigger in transverse and vertical velocity components as well as in turbulence components (Kara et al., 2012; Tominaga & Nezu, 1991).

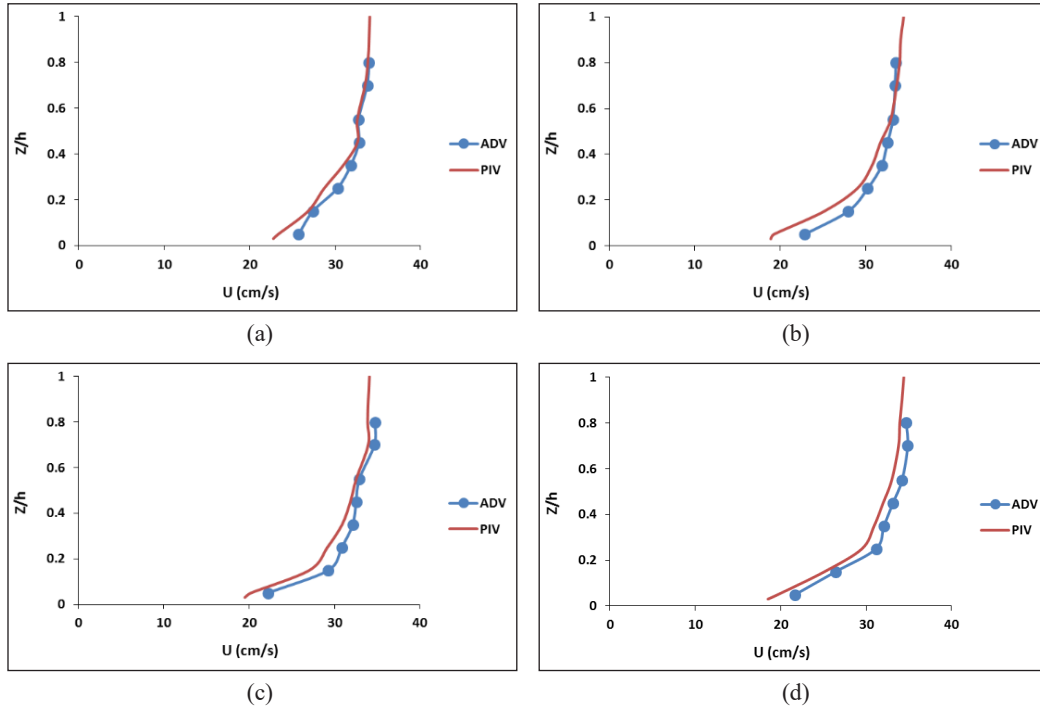


Figure 7. Comparison of ADV and PIV experimental data in a) Test 1, b) Test 2, c) Test 3, and d) Test 4

Streamlines

This section investigates streamlines at the cross section and longitudinal section, and plans to study the flow pattern under the influence of intact and damaged piers in a channel with or without piers.

Streamlines at Cross Sections. Figure 8 depicts an instance of streamlines at a cross-section at a distance of 5 m from the upstream side of the channel in four different cases. As is seen in this figure, the effect of present damaged and intact piers on flow pattern variations in the river path is evident, for the streamlines create return flows after colliding with the intact pier; whereas, in the case of the damaged pier, the flow passes over the pier due to its submergence. The combined effect of damaged and intact piers creates downflow streams in the area of the piers, the fact which has resulted in bed shear stress increase; therefore, assuming mobile bed conditions, it causes scour in the vicinity of the bridge piers. Presence of these downflow streams has also been reported in the studies of other researchers including Vaghefi et al. (2018a), where they employed protective structures

along with spur dikes, as well as the research where they additionally used submerged, short spur dikes (Vaghefi et al., 2016a). Further, a tranquil and semi-stagnant area has been formed between the two piers due to the creation of low-velocity streams. This phenomenon occurs under the influence of the intact pier located near the inner wall of the channel as an obstacle to high-velocity streams.

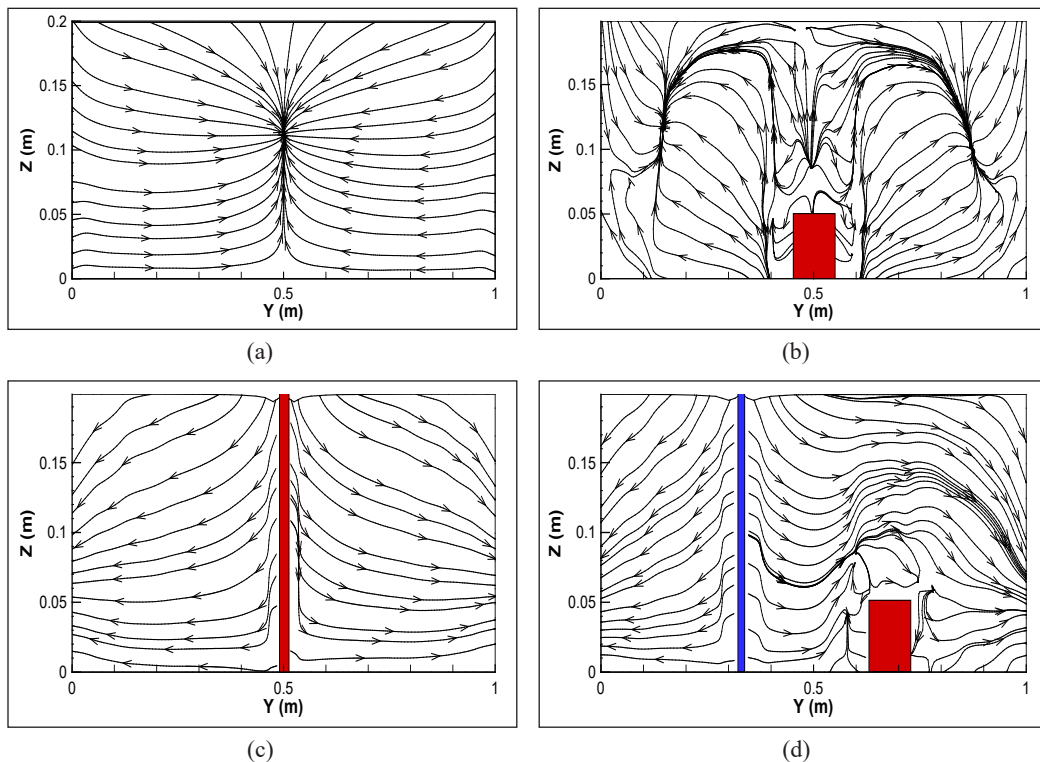


Figure 8. An instance of streamlines at cross-section at a distance of 5 m upstream in a) Test 1, b) Test 2, c) Test 3, and d) Test 4

Streamlines at Longitudinal Sections. To study the streamlines at longitudinal sections, Figure 9 illustrates the results of analysis of these streamlines at mid-channel in four different cases. As is observed, when there are no structures on the flow path, the streamlines have stretched along the path; whereas, with the installation of the 5 cm-high damaged pier, the streamlines at this area shift path into upflow after collision with the pier, and then appear downflow after passing over the pier. Downflow streamlines indicate the destructive streamlines and suggest the possibility of scour at the downstream side of the pier (Vaghefi et al., 2016c); therefore, the flow velocity is expected to decrease in this area. However, it is different for the intact pier because it is not submerged, and the downflow streamlines have appeared at the upstream side of this intact pier. The effects entailing creation of upflow and downflow streams in the vicinity of the pier may be observed on water level variations.

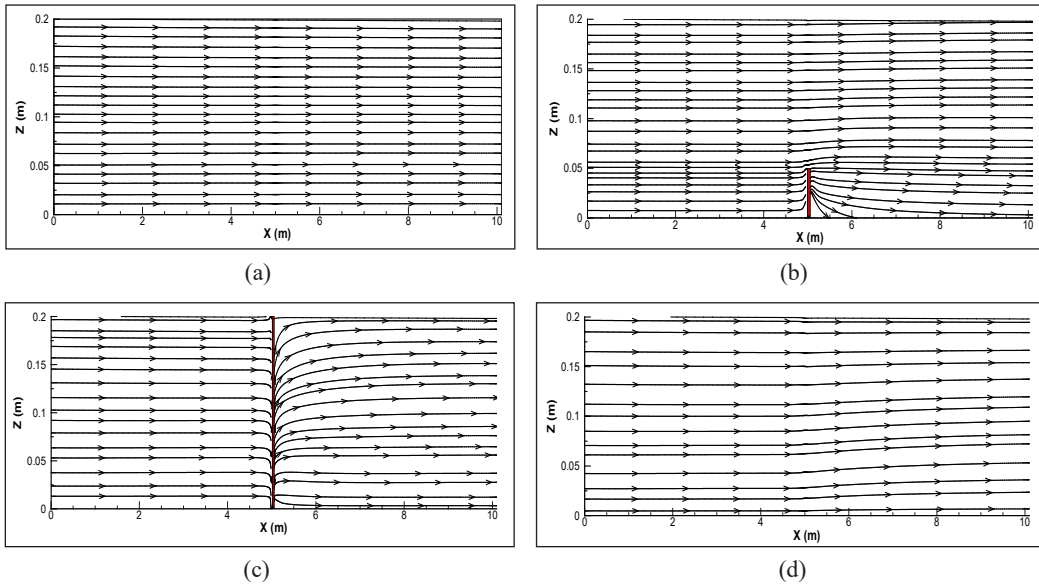


Figure 9. An instance of streamlines at longitudinal section at mid-channel in a) Test 1, b) Test 2, c) Test 3, and d) Test 4

Streamlines in Plan Views. To observe the influence of the piers in the channel, the study of the streamlines in plan is highly critical. As the magnifications of streamlines near the water surface in Figure 10 demonstrate, due to submergence of the damaged pier, no

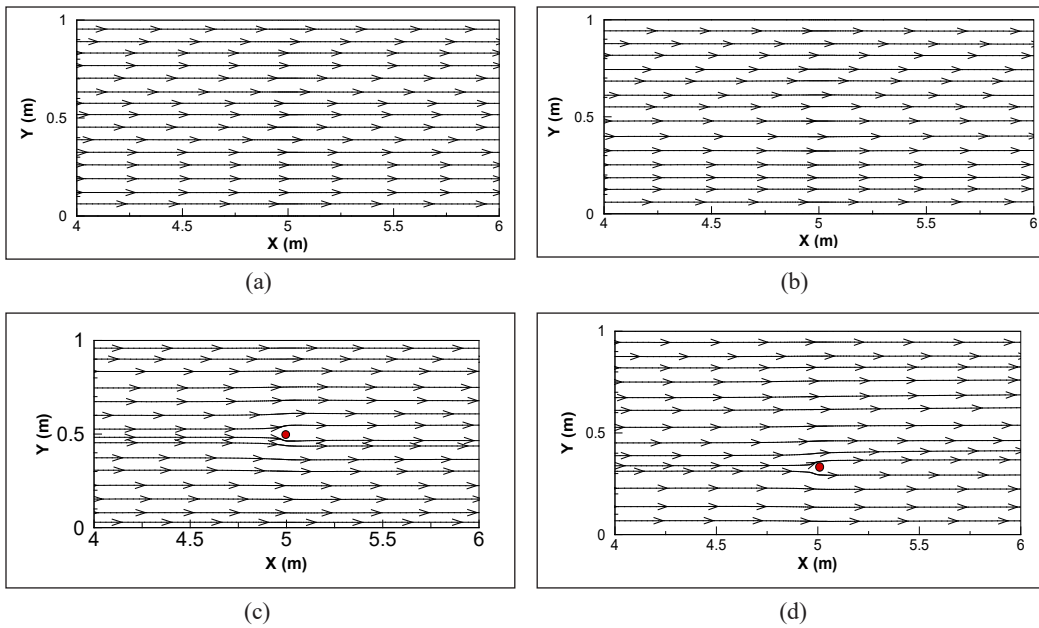


Figure 10. An instance of streamlines near the water surface in a) Test 1, b) Test 2, c) Test 3, and d) Test 4

significant effects have been observed in streamline variations at the water surface compared to the case with no piers installed. Although the streamline density due to presence of the pier is observable, the streamline variations are more significant where the intact pier is installed. Alteration and collision of the flow with the pier and increase in its density where both piers are installed are the combined effects resulting in velocity increase in this case.

Water Level Variations

Water level variations along the channel have been depicted in Figure 11 in different cases in the presence or absence of piers. As is observed in this figure, the water level is significantly influenced by presence of the intact pier, and its variations compared to the

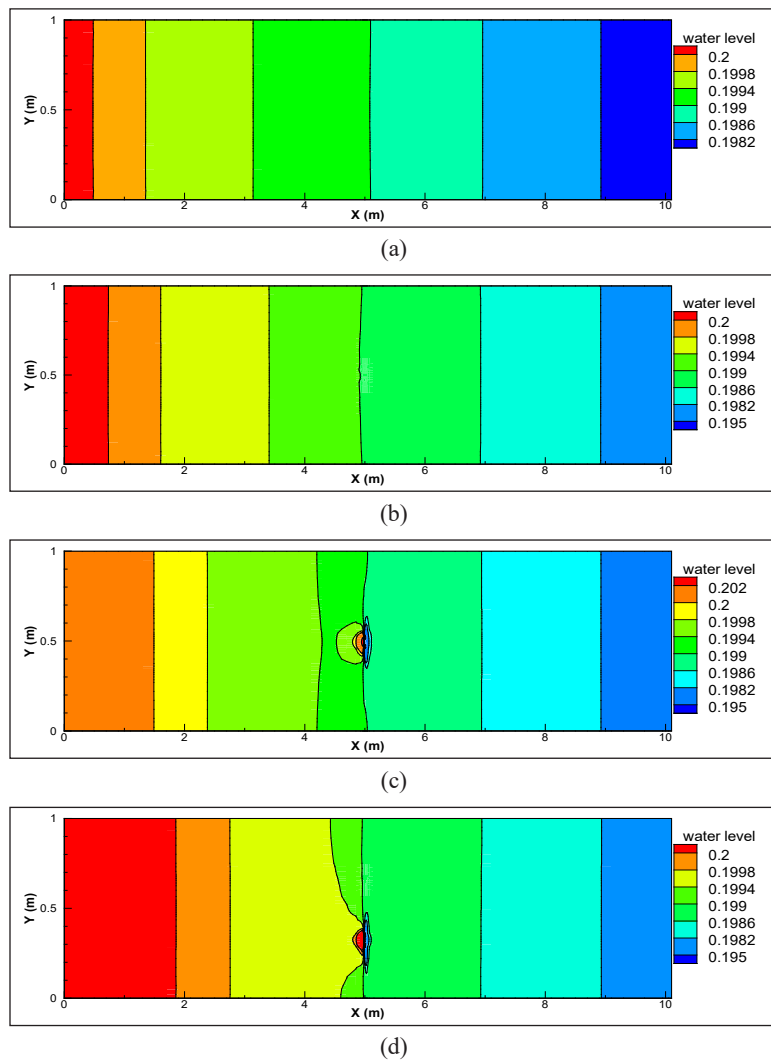


Figure 11. Water level variations in a) Test 1, b) Test 2, c) Test 3, and d) Test 4

installation of the damaged pier are evident. According to this figure, the water level is lowered at the downstream side of the intact pier due to the presence of downflow streams, and it is raised at the upstream side due to presence of upflow streams. However, this is intensified with installation of both piers so that it influences a wider range at mid-channel.

Bed Shear Stress Variations

Shear stress is a parameter of high significance. Through knowledge of this parameter, assessment of scouring or sedimentation at different points of bed is made viable (Abdi Chooplou & Vaghefi, 2019). Therefore, Figure 12 illustrates bed shear stress variations in

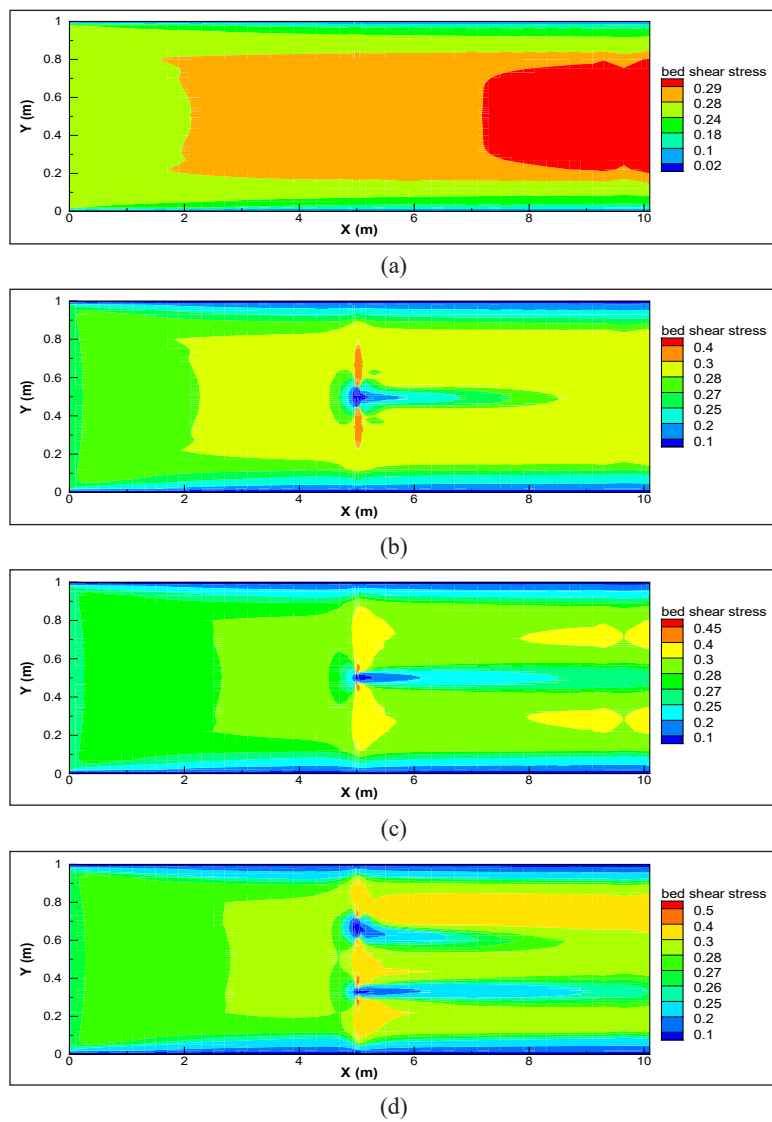


Figure 12. Bed shear stress variations in a) Test 1, b) Test 2, c) Test 3, and d) Test 4

different cases. Variations in position and the maximum value of bed shear stress affected by installation of the pier may be observed in this figure. As seen in Figure 12, installation of the piers has moved the maximum bed shear stress from the last one-third of the channel to mid-channel, in the vicinity of the piers. It is also observed that in the vicinity of the piers, the areas demonstrate less stress as a result of the present tranquil flow; however, at the upstream and downstream sides of the piers, the maximum stress occurs. Therefore, a 72% increase in the maximum bed shear stress occurs in the case of both piers installed as compared to the case with no piers.

CONCLUSIONS

This study has examined the flow pattern around intact and damaged bridge piers using experimental and numerical methods. To this aim, ADV and PIV had been utilized to conduct flow pattern experiments. Also, SSIIM was the numerical model used in this study. A summary of the most important conclusions obtained from this work is indicated below:

- A comparison between ADV and SSIIM data indicates the validity of the numerical model data and capability of this software to simulate the flow pattern around intact and damaged bridge piers.
- The maximum difference between numerical and experimental data is at layers near the bed; however, the total average of the errors in all four cases is 5% and acceptable.
- The difference between the average flow longitudinal velocities collected using ADV and PIV has been approximately 4%, which is negligible.
- The combined effect of damaged and intact piers creates downflow streams in the area of the piers.
- A tranquil and semi-stagnant area has been formed between the two piers due to the creation of low-velocity streams.
- The maximum water level variations occur in the case with both intact and damaged piers installed due to presence of upflow and downflow streams at the downstream and upstream sides of the piers.
- Installation of damaged and intact piers has moved the position of the maximum bed shear stress from the last one-third of the channel to mid-channel.
- The maximum bed shear stress has increased by 72% in comparison to the case with no piers installed.

ACKNOWLEDGEMENT

The authors of the paper would like to extend their most sincere appreciation to Islamic Azad University of Kerman branch for their cooperation in construction and installation of the flume.

REFERENCES

- Abdi Chooplou, C., & Vaghefi, M. (2019). Experimental study of the effect of displacement of vanes submerged at channel width on distribution of velocity and shear stress in a 180 degree bend. *Journal of Applied Fluid Mechanics*, 12(5), 1417-1428.
- Akbari, M., & Vaghefi, M. (2017). Experimental investigation on streamlines in a 180° sharp bend. *Acta Scientiarum Technology*, 39(4), 425-432.
- Asadollahi, M., Vaghefi, M., & Tabib Nazhad Motlagh, M. J. (2019). Experimental and numerical comparison of flow and scour patterns around a single and triple bridge piers located at a sharp 180 degrees bend. *Scientia Iranica*, 2019, 1-46.
- Khajeh, S. B. M., Vaghefi, M., & Mahmoudi, A. (2017). The scour pattern around an inclined cylindrical pier in a sharp 180-degree bend: an experimental study. *International Journal of River Basin Management*, 15(2), 207-218.
- Bozkus, Z., & Cesme, M. (2010). Reduction of scouring depth by using inclined piers. *Canadian Journal of Civil Engineering*, 37(12), 1621-1630.
- Bozkus, Z., & Yildiz, O. (2001, August 27-31). Experimental investigation of scouring around inclined bridge piers. In *Proceedings of Wetlands Engineering and River Restoration* (pp. 1-12). Reno, Nevada.
- Bozkuş, Z., Özalp, M. C., & Dinçer, A. E. (2018). Effect of pier inclination angle on local scour depth around bridge pier groups. *Arabian Journal for Science and Engineering*, 43(10), 5413-5421.
- Breusers, H. N. C., & Raudkivi, A. J. (1991). *Scouring hydraulic structures design manual*. Rotterdam, Netherlands: IAHR, AA Balkema.
- Chiew, Y. M., & Melville, B. W. (1987). Local scour around bridge piers. *Journal of Hydraulic Research*, 25(1), 15-26.
- Chiew, Y. M., & Melville, B. W. (1996, June 22-28). Temporal development of local scour depth at bridge piers. In *Proceedings of North American Water and Environment Congress* (pp. 59-65). Anaheim, California, USA.
- Duncan, J., Dabiri, D., Hove, J., & Gharib, M. (2011). Universal outlier detection for particle image velocimetry (PIV) and particle tracking velocimetry (PTV) data. *Measurement Science and Technology*, 21(5), 1-5.
- Goring, D. G., & Nikora, V. I. (2002). Despiking acoustic doppler velocimeter data. *Journal of Hydraulic Engineering*, 128(1), 117-126.
- Hurther, D., & Lemmin, U. (2001). A correction method for turbulence measurements with a 3D acoustic Doppler velocity profiler. *Journal of Atmospheric and Oceanic Technology*, 18(3), 446-458.
- Islam, M. R., & Zhu, D. Z. (2013). Kernel density-based algorithm for despiking ADV data. *Journal of Hydraulic Engineering*, 139(7), 785-793.
- Jaman, H., Das, S., Kuila, A., & Mazumdar, A. (2017). Hydrodynamic flow patterns around three inline eccentrically arranged circular piers. *Arabian Journal for Science and Engineering*, 42(9), 3973-3990.
- Kara, S., Stoesser, T., & Sturm, T. W. (2012). Turbulence statistics in compound channels with deep and shallow overbank flows. *Journal of Hydraulic Research*, 50(5), 482-493.

- Karimi, N., Heidarnejad, M., & Masjedi, A. (2017). Scour depth at inclined bridge piers along a straight path: A laboratory study. *Engineering Science and Technology, an International Journal*, 20(4), 1302-1307.
- Lemmin, U., & Rolland, T. (1997). Acoustic velocity profiler for laboratory and field studies. *Journal of Hydraulic Engineering*, 123(12), 1089-1098.
- Melville, B. W., & Coleman, S. E. (2000). *Bridge scour*. Colorado, USA: Water Resources Publication.
- Mori, N., Suzuki, T., & Kakuno, S. (2007). Noise of acoustic Doppler velocimeter data in bubbly flows. *Journal of Engineering Mechanics*, 133(1), 122-125.
- Nabipour, M., Neyshabouri, A. A. S., Dodaran, R. S., Zarrati, A. R., Mohajeri, H., & Zabetian, M. (2018). Experimental study of side looking ADV probe accuracy in a turbulent flow field. *Journal of Mechanical Engineering*, 18, 406-412.
- Nezu, I., & Nakagawa, H. (1993). *Turbulence in open channel flows*. Rotterdam, Netherlands: IAHR, AA Balkema.
- Nortek, A. S. (2009). *Vectrino velocimeter user guide*. Vangkroken, Norway: Nortek AS.
- Olsen, N. R. B. (1999). *Computational fluid dynamics in hydraulic and sedimentation engineering*. Trondheim, Norway: The Norwegian University of Science and Technology.
- Olsen, N. R. B. (2001). *CFD modeling for hydraulic structures*. Trondheim, Norway: The Norwegian University of Science and Technology.
- Olsen, N. R. B. (2003). Three-dimensional CFD modeling of self-forming meandering channel. *Journal of Hydraulic Engineering*, 129(5), 366-372.
- Omara, H., Elsayed, S. M., Abdeelaal, G. M., Abd-Elhamid, A. F., & Tawfik, A. (2018). Hydromorphological numerical model of the local scour process around bridge piers. *Arabian Journal for Science and Engineering*, 44(5), 4183-4199.
- Raffel, M., Willert, C. E., Scarano, F., Kähler, C. J., Wereley, S. T., & Kompenhans, J. (2018). *Particle image velocimetry: a practical guide*. Berlin, Germany: Springer.
- Raudkivi, A. J., & Ettema, R. (1983). Clear-water scour at cylindrical piers. *Journal of Hydraulic Engineering*, 109(3), 338-350.
- Razaz, M., & Kawanisi, K. (2011). Signal post-processing for acoustic velocimeters: Detecting and replacing spikes. *Measurement Science and Technology*, 22(12), 1-11.
- Razaz, M., Kawanisi, K., Nistor, I., & Sharifi, S. (2013). An acoustic travel time method for continuous velocity monitoring in shallow tidal streams. *Water Resources Research*, 49(8), 4885-4899.
- Rusello, P., Lohrmann, A., Siegel, E., & Maddux, T. (2006, September 10-13). Improvements in acoustic Doppler velocimetry. In *Proceedings of 7th International Conference on Hydrosience and Engineering* (pp. 1-16). Philadelphia, USA.
- Schlichting, H. (1979). *Boundary layer theory*. New York, USA: McGraw-Hill.
- Shinneeb, A. M., Bugg, J. D., & Balachandar, R. (2004). Variable threshold outlier identification in PIV data. *Measurement Science and Technology*, 15(9), 1722-1732.

- Thielicke, W., & Stamhuis, E. J. (2014). PIVlab-towards user-friendly, affordable and accurate digital particle image velocimetry in MATLAB. *Journal of Open Research Software*, 2(1), 1-30.
- Tominaga, A., & Nezu, I. (1991). Turbulent structure in compound open-channel flows. *Journal of Hydraulic Engineering*, 117(1), 21-41.
- Vaghefi, M., & Akbari, M. (2019). A procedure for setting up 180-degree sharp bend flume including construction and examinations with hydraulic structures. *Scientia Iranica*, 26(6), 103-121.
- Vaghefi, M., Alavinezhad, M., & Akbari, M. (2016a). The effect of submergence ratio on flow pattern around short T-head spur dike in a mild bend with rigid bed using numerical model. *Journal of the Chinese Institute of Engineers*, 39 (6), 666-674.
- Vaghefi, M., Ghodsian, M., & Salimi, S. (2016b). The effect of circular bridge piers with different inclination angles toward downstream on scour. *Sadhana*, 41(1), 75-86.
- Vaghefi, M., Safarpoor, Y., & Akbari, M. (2016c). Numerical investigation of flow pattern and components of three-dimensional velocity around a submerged T-shaped spur dike in a 90° bend. *Journal of Central South University*, 23(11), 2984-2998.
- Vaghefi, M., Safarpoor, Y., & Akbari, M. (2017). Numerical comparison of the parameters influencing the turbulent flow using a T-shaped spur dike in a 90° bend. *Journal of Applied Fluid Mechanics*, 10(1), 231-241.
- Vaghefi, M., Faraji, B., Akbari, M., & Eghbalzadeh, A. (2018a). Numerical investigation of flow pattern around a T-shaped spur dike in the vicinity of attractive and repelling protective structures. *Journal of the Brazilian Society of Mechanical Sciences and Engineering*, 40(2), 93-108.
- Vaghefi, M., Tabibnezhad, M. J., Hashemi, S. S., & Moradi, S. (2018b). Experimental study of bed topography variations due to placement of a triad series of vertical piers at different positions in a 180° bend. *Arabian Journal of Geosciences*, 11(5), 102-115.
- Vaghefi, M., Mahmoodi, K., & Akbari, M. (2019a). Detection of outlier in 3D flow velocity collection in an open-channel bend using various data mining techniques. *Iranian Journal of Science and Technology, Transactions of Civil Engineering*, 43(2), 197-214.
- Vaghefi, M., Mahmoodi, K., & Akbari, M. (2019b). Application of artificial neural networks to predict flow velocity in a 180 degree sharp bend with and without a spur dike. *Soft Computing*, 2019, 1-17.
- Vaghefi, M., Radan, P., & Akbari, M. (2019c). Flow pattern around attractive, vertical, and repelling T-shaped spur dikes in a mild bend using CFD Modeling. *International Journal of Civil Engineering*, 17(5), 607-617.
- Voulgaris, G., & Trowbridge, J. H. (1998). Evaluation of the acoustic Doppler velocimeter (ADV) for turbulence measurements. *Journal of Atmospheric and Oceanic Technology*, 15(1), 272-289.
- Westerweel, J., & Scarano, F. (2005). Universal outlier detection for PIV data. *Experiments in Fluids*, 39(6), 1096-1100.
- Yafei, H. (2015). Discussion on the development of algorithm for despiking ADV data. *International Journal of Science and Research*, 4(8), 1018-1020.
- Yeow, S. C., Chanson, H., & Wang, H. (2016). Impact of a large cylindrical roughness on tidal bore propagation. *Canadian Journal of Civil Engineering*, 43(8), 724-734.

Metaheuristics Approach for Maximum k Satisfiability in Restricted Neural Symbolic Integration

Saratha Sathasivam¹, Mustafa Mamat², Mohd Shareduwan Mohd Kasihmuddin^{1*} and Mohd. Asyraf Mansor³

¹*School of Mathematical Sciences, Universiti Sains Malaysia, 11800 USM, Penang, Malaysia*

²*Faculty of Informatics and Computing, Universiti Sultan Zainal Abidin, 21300 UniSZA, Kuala Terengganu, Terengganu, Malaysia*

³*School of Distance Education, Universiti Sains Malaysia, 11800 USM, Penang, Malaysia*

ABSTRACT

Maximum k Satisfiability logical rule (MAX- k SAT) is a language that bridges real life application to neural network optimization. MAX- k SAT is an interesting paradigm because the outcome of this logical rule is always negative/false. Hopfield Neural Network (HNN) is a type of neural network that finds the solution based on energy minimization. Interesting intelligent behavior has been observed when the logical rule is embedded in HNN. Increasing the storage capacity during the learning phase of HNN has been a challenging problem for most neural network researchers. Development of Metaheuristics algorithms has been crucial in optimizing the learning phase of Neural Network. The most celebrated metaheuristics model is Genetic Algorithm (GA). GA consists of several important operators that emphasize on solution improvement. Although GA has been reported to optimize logic programming in HNN, the learning complexity increases as the number of clauses increases. GA is more likely to be trapped in suboptimal fitness as the number of clauses increases. In this paper, metaheuristic algorithm namely Artificial Bee Colony (ABC) were proposed in learning MAX- k SAT programming. ABC is swarm-based metaheuristics that capitalized the capability of Employed Bee, Onlooker Bee, and Scout Bee. To this end, all the learning models were tested in a new restricted learning environment. Experimental results obtained from the computer simulation demonstrate the effectiveness of ABC in modelling MAX- k SAT.

ARTICLE INFO

Article history:

Received: 16 April 2019

Accepted: 19 July 2019

Published: 15 April 2020

E-mail addresses:

saratha@usm.my (Saratha Sathasivam)

must@unisza.edu.my (Mustafa Mamat)

shareduwan@usm.my (Mohd Shareduwan Mohd Kasihmuddin)

asyrafman@usm.my (Mohd. Asyraf Mansor)

* Corresponding author

INTRODUCTION

In the past decades, Boolean Satisfiability (SAT) has become a popular subject in artificial intelligence (AI) that attracted researchers from various field of studies. There are basically two reasons. First, the SAT is a direct transformation from real life application to mathematical formulation. In that sense, SAT serves as a foundation for more real-life applications such as Very Large Scale Integrated (VLSI) system (Mansor et al., 2016a), neural network (Kasihmuddin et al., 2018a), pattern recognition, logic mining and knowledge based paradigm. Second, SAT is a foundation to the various algorithm because interestingly, there are no efficient algorithms to comply with NP problem compared to P problem (Rojas, 2013). Hence, researchers in this field always find the approximation algorithm to comprehend SAT problem without the need of mathematical complexity. The mentioned reasons motivate the researcher (Kasihmuddin et al., 2017) to incorporate SAT with other AI applications. Applications pertaining to the hybrid SAT structure can be used to solve various on-demand applications such as scheduling and optimization problem. Such realization leads to the creation of a more effective algorithm to satisfy more variant of SAT program (Asirelli et al., 1985). Inspired by the extended version of Boolean SAT, Maximum k satisfiability (MAX- k SAT) starts to gain popularity in the heart of researcher because MAX- k SAT utilized false/negative output compared to other SAT representation (Poloczek et al., 2017). MAX- k SAT is commonly known as a logical rule that allocates symbolic binary/bipolar value to a Boolean variable with k literals for each neuron that satisfies the maximum number of clauses (Lynce et al., 2018).

Execution of the Artificial neural network (ANN) in AI is to acquire knowledge and use that information to model the intelligent system that can solve important problems. Hopfield Neural Network (HNN) is a dynamical neural system which possesses a memory that is associative and consists of interconnected neurons (Layeb, 2012). All neurons in HNN work in a dynamical manner with pre-defined threshold to mimic the actual human brain mechanism (Hopfield, 1982). The vital characteristics of HNN are the energy minimization via Lyapunov energy. Several NP problems such as travelling salesman problem (Mérida-Casermeiro et al., 2001), scheduling problem (Liang & Hsu, 1996), N Queen (Ohta, 2002) represent the state of a neuron as a possible optimal solution. In this case, the neuron state will be “excited” via pre-determined local field and synaptic weight will be updated via Hebbian learning. Interestingly, the neurons will iterate until HNN converges to minimum energy (possible desired solution). Abdullah (1992) and Sathasivam (2006) introduced the merger between two different disciplines by implementing HornSAT in HNN. In these studies, HornSAT was converted to Boolean Algebra and the synaptic weight of the network was obtained by comparing cost function and Lyapunov energy function. The most interesting insight from these mergers was, there was a fixed energy value for every satisfied clause. This is due to the property of HornSAT that is always

satisfiable. More specifically, the sum of all Lyapunov energy value becomes the absolute minimum energy for logic programming in HNN. Based on this paradigm, several researchers extend the usage of logic programming in the neural network. Hamadneh et al. (2012) proposed logic programming in Radial Basis Function Neural Network (RBFNN). The proposed network utilized HornSAT and satisfiable clauses in RBFNN. The usage of different SAT representation had been extended to k SAT (Mansor et al., 2016b). The primary motivation of this extension is the number of variables inside any clause is always $k \leq 3$ (Kullmann, 1999). After the introduction of k SAT, this representation has been a prominent logical rule in HNN. Several recent studies indicate that k SAT is compatible in doing pattern Satisfiability (Mansor et al., 2016a), and very large-scale integration circuit modelling (Mansor et al, 2018). The usage of k SAT in HNN also has been extended to another hybrid HNN model such as kernel HNN (Alzaeemi & Sathasivam, 2018). All the mentioned HNN- k SAT model only focus on satisfiable logic programming. Recently, the first attempt in representing non-satisfiable logic programming in HNN has been studied by Kasihmuddin et al. (2018b). The proposed model utilized Maximum k Satisfiability in doing HNN. The proposed merger created a new horizon in finding the global minimum solution although the final logical outcome was negative.

In another development, a variant of logic programming in HNN has been explored by several paradigms such as pattern reconstruction and circuit verifications. This suggests an obvious question: could learning phase of HNN be a learning environment with predetermined constraints, so that, under suitable condition, the learning model of HNN must fulfill the certain learning constraints? This question has been positively discussed when Sathasivam and Ng (2013) proposed agent-based modelling (ABM) to simulate the environment of logic programming in HNN. Each factor that affects the interaction among “agents” is examined by using ABM. Mansor et al. (2016b) proposed VLSI circuit configuration by using k SAT in HNN. The proposed method created SAT environment based on the circuit configuration which consisted of millions of transistors. Mansor et al. (2016a) proposed pattern SAT by embedding k SAT inside some square matrices. This finding led to a solid foundation for pattern recognition via k SAT. By introducing environmental constraints, the various model could be constructed or tested during the learning phase of HNN.

Artificial bee colony (ABC) has been increasingly viewed as an optimization technique for continuous problem (Karaboga, 2005). Karaboga and Basturk (2007) conducted a comprehensive study to compare the effectiveness of ABC with other existing metaheuristics algorithm such as Genetic Algorithm (GA), Particle Swarm optimization (PSO) and Differential Evolution (DE). The simulation results illustrated that ABC had the best performance compared to other metaheuristic algorithms. Several advancements were implemented to improve the accuracy of ABC (Karaboga, 2009; Banitalebi et al., 2015). In

another perspective, the usage of binary ABC has been prominent in solving the constraint optimization problem. Ozturk et al. (2015) proposed binary ABC for solving 0-1 knapsack problem by intelligently adopting genetic operators. Kashan et al. (2012) proposed a binary ABC by replacing vector subtraction operator from original ABC algorithm with differential expression (Pampará & Engelbrecht, 2011). The proposed expression employed a measure of dissimilarity between binary vectors. Another important study in binary ABC was done by Jia et al. (2014). This study capitalized bitwise operation to portray the movement of employed bee and onlooker bee. The proposed ABC algorithm has been extended to HNN-*k*SAT (Kasihmuddin et al., 2016) where the hybrid network was able to achieve more than 95% of global minima ratio with reasonable computation time. Unfortunately, global minimum ratio and computational time show very little, the effectiveness of ABC in HNN-*k*SAT. In this study, ABC was a learning model for clausal checking in HNN-MAX*k*SAT in a new simulated learning environment. The results showed that ABC displayed the best performance for all performance metric in the restricted learning environment.

MATERIALS AND METHOD

Maximum *k* Satisfiability

Karp (1972) had elaborated the concept of MAX-*k*SAT as the generalized variant of Boolean satisfiability logical rule structure as compared to the satisfiable logic, namely *k* Satisfiability (*k*SAT). According to Chu et al. (2019), MAX-*k*SAT is a complex and well-known variant of NP-hard problem, commonly being leveraged in various applications such as in digital circuit fault detection and encoding various engineering problems. Thus, MAX-*k*SAT has diversified the propositional Boolean Satisfiability logic variant in term of finding the optimal interpretation that contributes into negative outcome (Mansor et al., 2017). Therefore, the general definition of MAX-*k*SAT is given as follows:

Definition 1.1 (Maximum *k* Satisfiability)

Given a Boolean conjunctive normal form (CNF), the Maximum *k* Satisfiability problem can be demarcated as searching the interpretation that maximizes the number of satisfied unit of clauses for a particular Boolean MAX-*k*SAT formula.

Similarly, the MAX-*k*SAT is constructed as a logical rule in CNF with *n* clauses and *k* variable each. Zhang et al. (2003) had defined the structure of MAX-*k*SAT as a pair of (η, α) given α is the combination of the possible bipolar interpretation, $\{1, -1\}^n$. In addition, α is a mapping $\eta \rightarrow Z$ which refers to the score of the interpretations where *Z* is scored depending on a particular satisfied clauses. Hence, MAX-*k*SAT representation comprises identifying the best bipolar string assignments in $P_{MAX-kSAT}$ that at the same time satisfied at least *h* clauses out of *m* clauses. In the case of MAX-*k*SAT, the condition

will be strictly $h < m$. The modified MAX- k SAT formula for $k = 2$ has been coined by Kasihmuddin et al. (2018a):

$$P_{MAX-kSAT} = (A \vee B) \wedge (A \vee \neg B) \wedge (\neg A \vee B) \wedge (\neg A \vee \neg B) \wedge (C \vee D) \quad (1)$$

where $k = 2$ denotes the number of literals strictly in a particular clause.

According to Zhang et al. (2003), there are 2^n possible bipolar interpretations for a particular MAX- k SAT problem, whereby n denotes the number of literals. Specifically, Equation (1) has no complete interpretation that make $P_{MAX-kSAT}$ to become true or fully satisfiable. The computation of the fitness for $P_{MAX-kSAT}$ can be done by using Equation (2).

$$f_{P_{MAX-kSAT}} = \sum_{i=1}^{NC} C_i \quad (2)$$

where NC denotes the number of the clause and C_i is the number of satisfied MAX- k SAT clause. A point to ponder for $P_{MAX-kSAT}$ is the fitness value that will never attain the maximum number of the clause due to existence of the falsified clauses. Henceforth, MAX- k SAT will consider the minimum number of falsified clauses in a complete interpretation. In this paper, the MAX- k SAT logic programming is carried out in restricted learning in HNN. Since, the MAX- k SAT works exceptionally well with the conventional learning in HNN (Kasihmuddin et al., 2018b), the impact of restricted learning will be investigated extensively in this work. In fact, the MAX- k SAT logic programming is chosen due to the negative outcome produced as compared with the k SAT programming. Therefore, the real-life problem involving the negative outcomes can be encoded in the form of MAX- k SAT to be further extracted by the data mining algorithm.

Hopfield Neural Network

HNN is broadly employed to store and process the patterns due to the capability of its content addressable memory (CAM). In particular, HNN is a class of dynamic recurrent network with symmetrical connected weight corresponds to the interconnected units emulated the biological human brain. The HNN is considered due to a few edges over the other variant of recurrent or feedforward neural network. It comprises good characteristics namely parallel computation, fast convergence and acceptable capacity of the CAM (Hopfield, 1982). Based on the architecture of HNN standpoint, HNN comprises interconnected units called neurons. Hence, the neuron state in HNN is denoted as $S_i(t)$ where $i = 1, 2, \dots, N$. Consequently, the bipolar neuron combinations in HNN is well represented as $S_i \in \{-1, 1\}$. In this work, the state will updated asynchronously per execution.

The excitation of the neuron in HNN can be represented mathematically as in S_i .

$$S_i = \begin{cases} 1 & \text{if } \sum_j W_{ij} S_j \geq \xi \\ -1 & \text{Otherwise} \end{cases} \quad (3)$$

where W_{ij} is the weight for unit j to i and ξ refers to the threshold of the HNN. The implementation of MAX- k SAT in HNN is denoted as HNN-MAX k SAT. In this case, HNN-MAX k SAT will consider the k neurons per clause. The local field is prominent to properly squash the retrieved output before generating the final state. Moreover, the local field formulation for $k = 3$ is shown in Equation (4), whereas for $k = 2$ is given in Equation (5) (Sathasivam et al., 2011).

$$h_i = \sum_{k=1, l \neq j \neq k}^N W_{ijk}^{(3)} S_j S_k + \sum_{j=1, l \neq j \neq k}^N W_{ij}^{(2)} S_j + W_i^{(1)}, \quad k = 3 \quad (4)$$

$$h_i = \sum_{j=1, l \neq j \neq k}^N W_{ij}^{(2)} S_j + W_i^{(1)}, \quad k = 2 \quad (5)$$

where i and j are corresponded to neurons N . These local fields determine the effectiveness and variability of the final states obtained by HNN. Thus, the generated final interpretation classifies whether the solution is overfit or not. Precisely, the updating rule is given as

$$S_i(t + 1) = \text{sgn}[h_i(t)] \quad (6)$$

The relation is limited to be symmetric and zero diagonal $W_{ij}^{(2)} = W_{ji}^{(2)}$, $W_{ii}^{(2)} = W_{jj}^{(2)} = W_{kk}^{(2)} = W_{iii}^{(3)} = W_{jjj}^{(3)} = W_{kkk}^{(3)} = 0$ which further derive and formulate the final energy of respective variant of HNN-MAX k SAT as given:

$$H_{P_{MAX2SAT}} = -\frac{1}{2} \sum_{i=1, l \neq j}^N \sum_{j=1, l \neq j}^N W_{ij}^{(2)} S_i S_j - \sum_{i=1}^N W_i^{(1)} S_j, \quad k = 2 \quad (7)$$

$$H_{P_{MAX3SAT}} = -\frac{1}{3} \sum_{i=1, l \neq j \neq k}^N \sum_{j=1, l \neq j \neq k}^N \sum_{k=1, l \neq j \neq k}^N W_{ijk}^{(3)} S_i S_j S_k - \frac{1}{2} \sum_{i=1, l \neq j}^N \sum_{j=1, l \neq j}^N W_{ij}^{(2)} S_i S_j - \sum_{i=1}^N W_{(i=1)}^{(1)} S_j, \quad k = 3 \quad (8)$$

Therefore, for the cumulative cases, all permutations that involves i , j , and k for MAX k SAT clauses are considered. Ultimately, the final energy recorded by HNN-MAX k SAT is always stable (Zhang et al., 2016) and reduces with the dynamics (Sathasivam, 2008).

Restricted Learning in HNN-MAX k SAT

The ability of HNN-MAX k SAT to adapt to change in its environment provide vital insight into the effectiveness of the learning model. In this section, restricted learning paradigm was implemented to HNN-MAX k SAT for the first time. During learning phase, the initial neuron state of S_i that represents the variable in MAX k SAT is given by

$$S_i = \{S_1, S_2, S_3, S_4, \dots, S_N\} \tag{9}$$

By examining the inconsistencies of the MAX- k SAT logical rule, the learned neuron assignment must minimize the cost function $E_{P_{MAXkSAT}}$.

$$\min[E_{P_{MAXkSAT}}] \tag{10}$$

where $E_{P_{MAXkSAT}} \neq 0$ for all MAX- k SAT clauses. The neuron state will be updated based on the following condition

$$S_i = \begin{cases} S_i : S_i \in \{-1, 1\}, i \in I, & NH \leq \Omega \\ S_i^{new}, & NH > \Omega \end{cases} \tag{11}$$

where I is an index set and $NH, \Omega \in I$. NH and Ω are defined as learning iteration and maximum iteration respectively (Xu et al., 2019). In other words, the proposed HNN-MAX k SAT models will search the correct interpretation until $NH > \Omega$. The new state of S_i^{new} emerges and proceeds to retrieval phase of HNN. This simulated learning environment is completely different than HNN proposed in Sathasivam (2010) and Mansor et al. (2017). The learning iteration of HNN in the mentioned work is increased indefinitely $\Omega \rightarrow \infty$ until $E_{P_{MAXkSAT}}$ reached the desired minimum value. The restricted learning paradigm of HNN-MAX k SAT is defined as RHNN-MAX k SAT models. Figure 1 shows the implementation of k SAT programming in HNN in restricted learning environment.

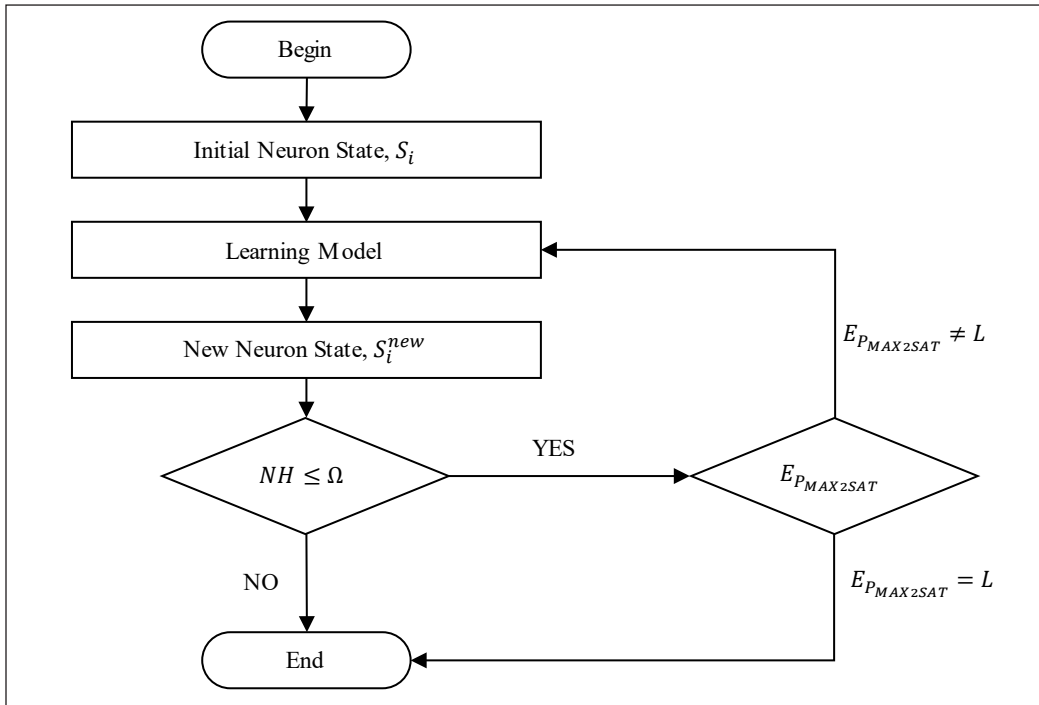


Figure 1. Restricted Learning Environment

Genetic Algorithm

Genetic algorithm (GA) is popular state of the art metaheuristic algorithm that reduce the burden of the computation in optimization problem without usage of complex Mathematical equation. It started with Golberg and Holland (1988) that had meticulously proven the idea of solution improvement in every iteration. Kasihmuddin et al. (2016) proposed an HNN embedded with *k*SAT system integrated with GA during the learning phase. The implementation of GA during learning phase of HNN-MAX*k*SAT is defined as RHNN-MAX*k*SATGA. Bipolar strings in this particular case is representing the possible satisfied assignments of RHNN-MAX*k*SATGA. The stages involved in RHNN-MAX*k*SATGA are as follows:

Stage 1: Initialization. 100 bipolar string will be generated where each element of $\{1, -1\}$ is denoted by True and False.

Stage 2: Fitness Evaluation. Bipolar string from stage 1 will be evaluated based on the following equation:

$$f_{MAX-kSAT} = \max[C_1(x) + C_2(x) + C_3(x) \dots + C_N(x)] \quad (12)$$

where $C_1, C_2, C_3, \dots, C_N$ are the clause verified using by GA and N represents the

clause number depicted in the formula. The choice of fitness function in Equation (12) is crucial to avoid the possible local maxima due the floating number produced during iteration.

Stage 3: Selection. Ten (10) bipolar strings that acquire the highest number of satisfied clauses will be selected. The selection process will dismiss potential non-fit MAX- k SAT solution.

Stage 4: Bipolar Crossover. The exchange of information between two sub-structure of bipolar string occurred randomly. The position of the crossover will be selected randomly. The main purpose of crossover is to diversify the potential fitness of the offspring.

Prior to crossover

Bipolar string $X = -1 \ 1 \ -1 \ -1 \ -1 \ -1 \ -1 \ -1$

Bipolar string $Y = 1 \ -1 \ -1 \ -1 \ 1 \ 1 \ 1 \ -1$

Post crossover

Bipolar string $X = 1 \ 1 \ -1 \ -1 \ -1 \ -1 \ -1 \ -1$

Bipolar string $Y = 1 \ -1 \ -1 \ -1 \ 1 \ -1 \ 1 \ -1$

Stage 5: Mutation. Mutation includes state exchange from 1 to -1 or -1 to 1. As a general point, mutation will potentially increase the average fitness of the whole solution and reduce the fitness of the low fit bipolar string. Stage 1 to 5 is repeated for until it reaches predetermined number of generations.

Artificial Bee Colony

ABC is a well-known swarm optimization method in finding near optimal solution. Since inconsistencies of bipolar string can be easily described as a cost function of MAX- k SAT logic, the perspective of ABC shifted toward bipolar optimization (Ning et al., 2018). In this case, the integration of ABC during the learning phase of HNN is abbreviated as RHNN-MAX k SATABC. The bipolar string is represented as a food source and bees were entrusted to locate the optimal food source (Karaboga & Basturk, 2008). The three optimization layers in ABC namely employed bees, onlooker bees and scout bee will explore the global solution of the search space (Zhang & Zhang, 2017). During the learning phase, the fittest bee is the one with the highest fitness value. The main stages of ABC in RHNN-MAX k SATABC is as follows:

Stage 1: Initialization. 50 employed bees, 50 onlooker bees and 1 scout bee are initialized. Each bee carries bipolar string of MAX- k SAT which is denoted by True and False.

Stage 2: Verification of Fitness. The fitness of each bee in Stage 1 (except for scout bee) will be evaluated based on the Equation (2).

Stage 3: Employed Bee Stage. In this stage, employed bee will identify new food position for $v_{ij}^{Employed}$ (bipolar string) in a given neighbourhood. The location of the food is given as follows

$$v_{ij}^{Employed} = y_{ij} \vee (\phi_{ij} \otimes (y_{ij} \wedge y_{kj})) \tag{13}$$

where

y_{ij} food source at initial stage

y_{kj} food source that is observed

ϕ_{ij} variables where,

$$\phi_{ij} = \begin{cases} 1, rand(0,1) < 0.5 \\ -1, rand(0,1) \geq 0.5 \end{cases}$$

\otimes is a ‘XOR’ operator

\wedge is an ‘AND’ operator

\vee is an ‘OR’ operator

Stage 4: Onlooker Bee Stage. Onlooker bees were selected food source based on the fitness of the employed bees in stage 3. The new position of the food source is based on roulette wheel selection (RWS) (Goldberg & Deb, 1991). The probability model for information exchange is given as

$$p_i^{Onlooker} = \frac{f_{v_{ij}^{Employed}}}{\sum_{i=1}^{SN} f_{v_{ij}^{Employed}}} \tag{14}$$

where $\sum_{i=1}^{SN} f_{v_{ij}^{Employed}}$ portrays targeted RHNN-MAXkSAT fitness and SN shows the bee’s group count. Similar to Equation (13), onlooker bees are seeked for the closest food origin by using the following equation

$$v_{ij}^{Onlooker} = y_{ij} \vee (\phi_{ij} \otimes (y_{ij} \wedge y_{kj})) \tag{15}$$

where all the variable in Equation (15) are similar with the information given in Equation (13). Stage 1 until Stage 4 is repeated until the pre-determined trials.

Stage 5: Scout Bee Stage. If the position of the food for employed bees cannot be improved through the number of trials, scout bee abandons the current food source. Bipolar state in scout bee will be randomly generated. If the food source obtained $f_{v_{ij}^{Onlooker}} = f_{NC}$ or $f_{v_{ij}^{Employed}} = f_{NC}$, the best bipolar assignment is outputted.

Implementation RHNN-MAX k SAT Model

The robustness of the learning method is a very critical criterion of any given network. Worth mentioning that, the earliest celebrated optimization learning model in HNN was proposed by Sathasivam (2006) and Sathasivam (2010). The mentioned paper proposed Exhaustive Search (ES) in finding the correct HornSAT interpretation during the learning phase of HNN. In this case, ES is a conventional method during the learning phase of RHNN-MAX k SAT. The learning phase of all RHNN-MAX k SAT models is used to derive the optimal cost function by maximizing the number of satisfied clauses in MAX k SAT. Hence, the main task of the proposed network is to create a “model” that behave according to MAX k SAT logical rule. The following algorithm shows the implementation of RHNN-MAX k SAT models:

1. Transform MAX- k SAT clauses to Boolean algebra (if applicable).
2. Neurons is assigned to respective variable in MAX- k SAT clauses.
3. By defining the inconsistencies of MAX- k SAT, derive the cost function by assigning $X = \frac{1}{2}(1 + S_X)$ and $\bar{X} = \frac{1}{2}(1 - S_X)$. The neuron's state shows true if $S_X = 1$ and false if $S_X = -1$. In this case, variable inside each clause is connected with addition \vee and the overall clause is connected by multiplication (\wedge).
4. Bipolar assignment that minimizes the cost function will be obtained via ES, GA and ABC. The proposed learning model will exit the learning loop if $NH \geq \Omega$.
5. Obtain the synaptic weight matrix of the HNN model corresponds -MAX k SAT logical rule.
6. Compute the lowest minimum energy of -MAX k SAT by using Equation (7) and Equation (8).
7. Compute the final neuron state via Equation (4) and (5).
8. By using Equation (6) and Equation (7), calculate the final energy of the neuron state in step 7.

In order to obtain a fair comparison among all RHNN-MAX k SAT models, all source code is implemented via Microsoft Visual Basic C++ 2013 for Windows 10. Similar device

is used in every simulation to avoid the possible bad sector. Table 1 to Table 3 show all the parameters involved in each RHNN-MAX k SAT models.

Table 1
List of Parameters in RHNN-MAX k SATES

Parameter	Parameter value
Neuron Combination	100
Tolerance Value (<i>Tol</i>)	0.001
Ω	10^3 and 10^5
No_String	100
Selection_Rate	0.1

Table 2
List of Parameters in RHNN-MAX k SATGA

Parameter	Parameter value
Neuron Combination	100
Tolerance Value (<i>Tol</i>)	0.001
Ω	10^3 and 10^5
No_Chromosomes	100
Selection_Rate	0.1
Mutation_rate	0.01
Generation	1000

Table 3
List of Parameters in RHNN-MAX k SATABC

Parameter	Parameter value
Neuron Combination	100
Tolerance Value (<i>Tol</i>)	0.001
Ω	10^3 and 10^5
No_Employed	50
No_Onlooker	50
No_Scout	1
Trial	10
Limit	100

RESULT AND DISCUSSION

Compared to previous HNN model such as Kasihmuddin et al. (2017), this experiment has been proposed in a restricted learning environment. In relation with several studies done by Cai et al (2016), all the proposed RHNN-MAX k SAT model were tested up to 400 variables. The learning iteration for all proposed models had been restricted to iterate up to $\Omega = 10^3$ and $\Omega = 10^5$.

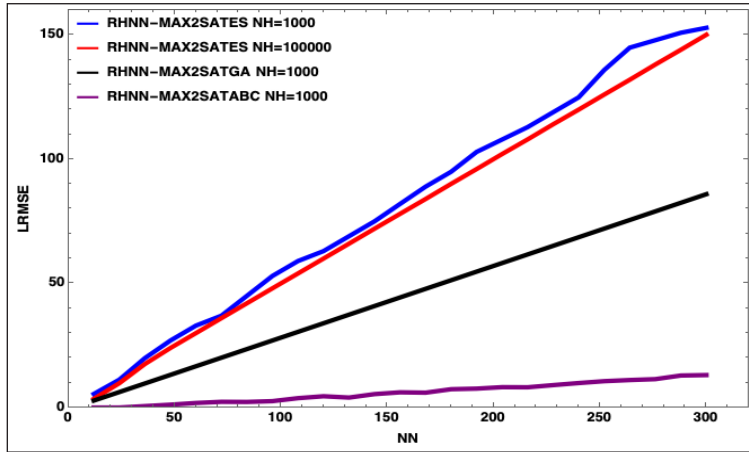


Figure 2. Root Mean Square Error (RMSE) of RHNN-MAX2SAT models

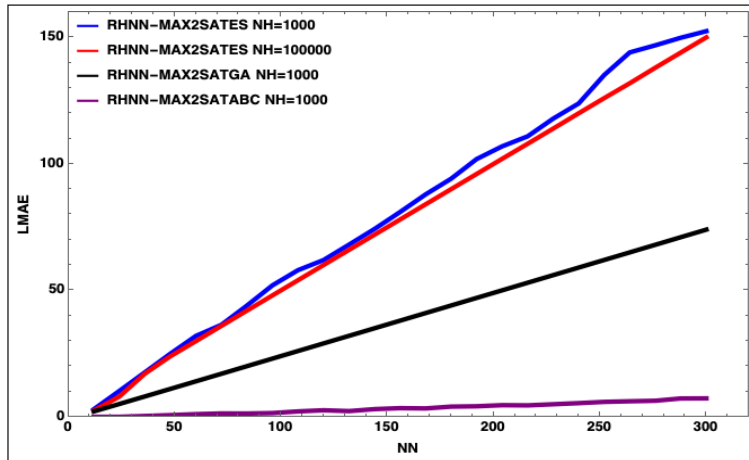


Figure 4. Mean Absolute Error (MAE) of RHNN-MAX2SAT models

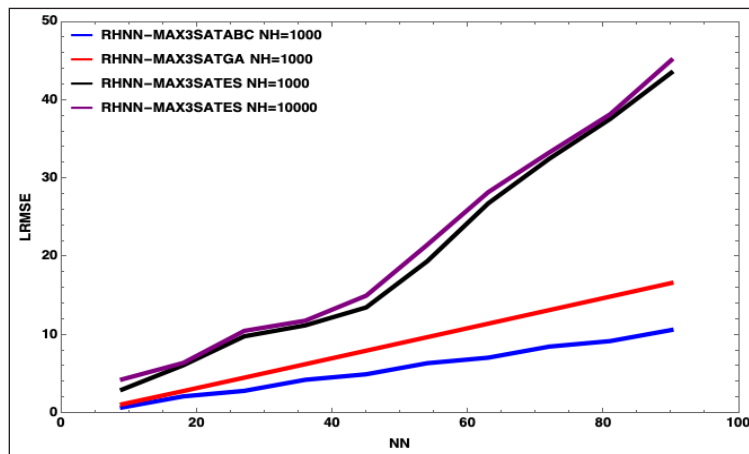


Figure 3. Root Mean Square Error (RMSE) of RHNN-MAX3SAT models

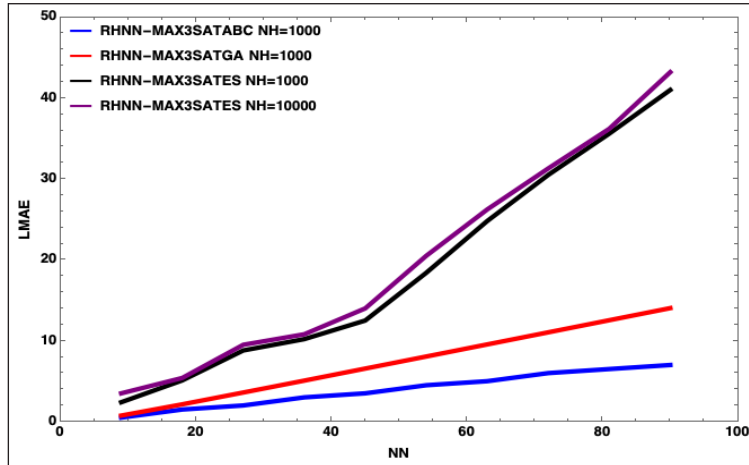


Figure 5. Mean Absolute Error (MAE) of RHNN-MAX3SAT models

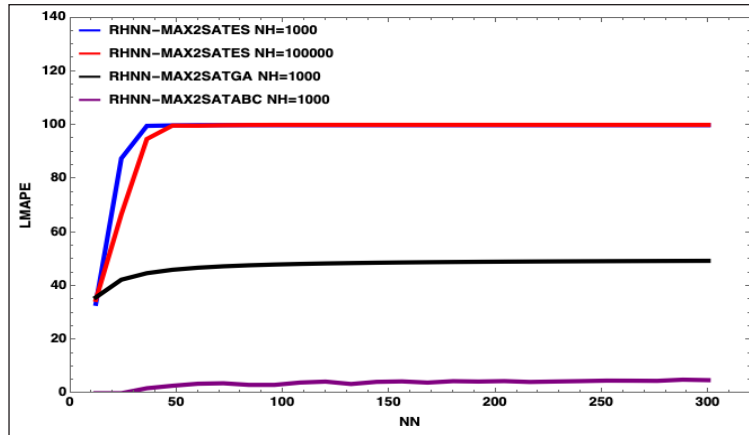


Figure 6. Mean Absolute Percentage Error (MAPE) of RHNN-MAX2SAT models

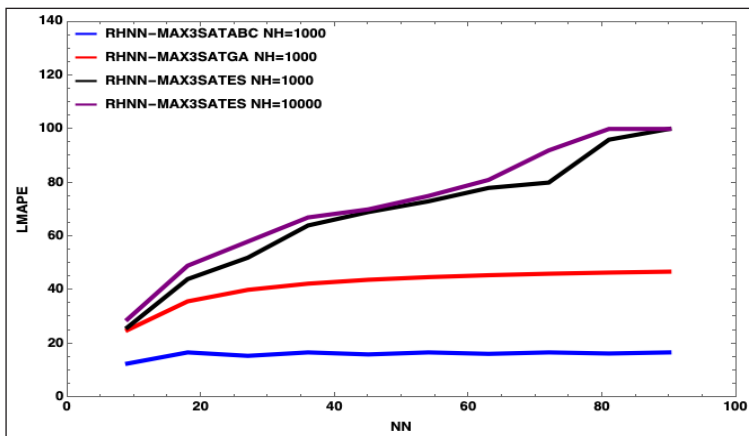


Figure 7. Mean Absolute Percentage Error (MAPE) of RHNN-MAX3SAT models

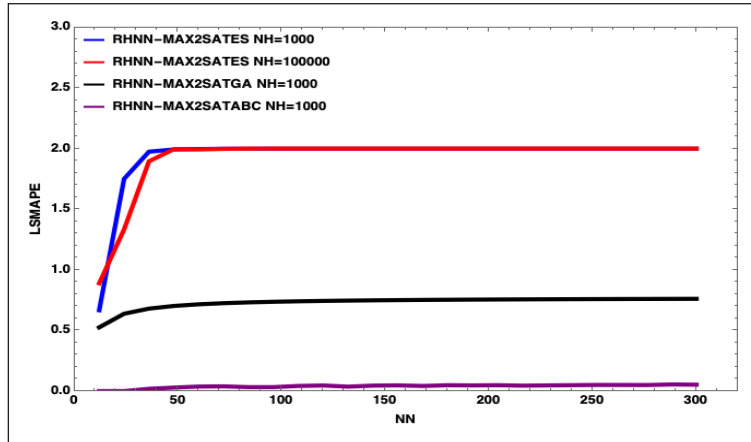


Figure 8. Symmetric Mean Absolute Percentage Error (SMAPE) of RHNN-MAX2SAT models

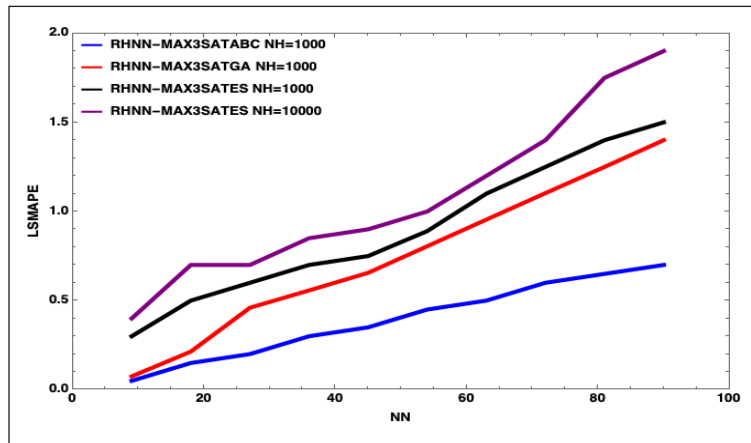


Figure 9. Symmetric Mean Absolute Percentage Error (SMAPE) of RHNN-MAX2SAT models

Table 4
Zm of RHNN-MAX2SAT models

NN	RHNN-MAX2SATES	RHNN-MAX2SATGA	RHNN-MAX2SATABC
12	1	1	1
24	0.99	1	1
36	0.9925	1	1
48	0.812	1	1
60	0.657	1	1
72	0.3158	1	1
84	0.007	1	1
96	0	1	1
108	0	1	1
120	0	1	1

Table 5
Z_m of RHNN-MAX3SAT models

<i>NN</i>	RHNN-MAX3SATES	RHNN-MAX3SATGA	RHNN-MAX3SATABC
9	0.9984	1	1
18	0.7551	1	1
27	0.6458	1	1
36	0.5626	1	1
45	0.3503	1	1
54	0.1867	1	1
63	0.1414	1	1
72	0.0322	1	1
81	0.0065	0.9999	1
90	0	0.9985	1

Figure 2, Figure 3, Figure 4, Figure 5 and Table 4 demonstrate the value of RMSE, MAE, MAPE, SMAPE and Z_m respectively for all RHNN-MAX k SAT models. Learning errors (RMSE, MAE, SMAPE and Z_m) are the benchmark for accuracy and Z_m is a benchmark for the feasibility of the RHNN-MAX k SAT model. The result is very significant because the successful implementation of RHNN-MAX k SAT model shows the HNN system is adaptable to \neg -MAX k SAT logical rule. Worth mentioning that, the final outcome of the network is negative and the induced final state were expected to achieve the maximum number of satisfied clauses. The result in Figure 2 to Figure 9 and Table 4 and Table 5 allow the following observations:

1. RHNN-MAX k SATABC provides the best result in terms of RMSE, MAE, MAPE, and SMAPE. RHNN-MAX k SATES is only capable of managing a smaller number of clauses.
2. RHNN-MAX k SATGA requires more iteration to develop the fitness of bipolar string before effective crossover could take place. This is due to a large number of the non-fit bipolar string during an early stage of RHNN-MAX k SATGA.
3. RHNN-MAX k SATABC is reported to obtain the most consistent bipolar string during the learning phase. Interaction and exchange of information between employed bee and onlooker bee by using Equation (13) to Equation (15) reduce the possibility of the network to reach the scout bee phase.
4. After $NN = 20$, the final neuron state in RHNN-MAX k SATES is approaching maximum metric error. In this case, the learning phase was trapped in trial and error state.

RHNN-MAX k SATABC has the best value of Z_m (approaching 1) compared to the other learning model. It was observed (refer Table 4 and 5) that more than 95% of the final state of the neuron in RHNN-MAX k SATABC and RHNN-MAX k SATGA achieved the global

minimum solution. It is likely due to the learning rate acquired by both models increase the storage capacity of RHNN-MAX k SAT. The observation can be further explained in Sathasivam (2010) where higher relaxation time during the learning phase will increase the value of Z_m . In another perspective, the value for the ratio of satisfied clauses (RSC) for RHNN-MAX k SATGA and RHNN-MAX k SATABC are consistently 0.857143 for $k = 2$ and 0.9091 for $k = 3$ restricted learning environment. All RSC values have good agreement with the analytical study done by Paul et al. (2016).

CONCLUSION

In this paper, three hybrid learning models in doing –MAX k SAT were proposed. All the proposed hybrid networks were tested in a restricted environment where $NH \leq \Omega$. On the basis of results obtained by simulation, RHNN-MAX k SATABC is the best network compared to other RHNN-MAX k SAT models. On the other hand, the integrated approaches proposed here provide a few options that can help the neural network deal with a false or negative outcome. It suggests that there are countless real-life applications that give significance to the negative result. The proposed method is a solid foundation to other SAT representation such as Majority Satisfiability, Minimum Satisfiability, and Weighted Satisfiability.

ACKNOWLEDGEMENT

This research was supported by Short Term Grant (304/PMATHS/6315226) by Universiti Sains Malaysia.

REFERENCES

- Abdullah, W. A. T. W. (1992). Logic programming on a neural network. *International Journal of Intelligent Systems*, 7(6), 513-519.
- Alzaeemi, S. A., & Sathasivam, S. (2018). Linear kernel Hopfield neural network approach in horn clause programming. In D. Mohamad, A. B. Akbarally, H. Maidinsah, M. M. Jaffar, M. Mohamed, S. R. Sharif & W. E. Z. W. A. Rahman (Eds.), *AIP Conference Proceedings* (Vol. 1974, No. 1, p. 020107). Melville, NY: AIP Publishing.
- Asirelli, P., De Santis, M., & Martelli, M. (1985). Integrity constraints in logic databases. *The Journal of Logic Programming*, 2(3), 221-232.
- Banitalebi, A., Aziz, M. I. A., Bahar, A., & Aziz, Z. A. (2015). Enhanced compact artificial bee colony. *Information Sciences*, 298, 491-511.
- Cai, S., Luo, C., Lin, J., & Su, K. (2016). New local search methods for partial MaxSAT. *Artificial Intelligence*, 240, 1-18.

- Chu, Y., Luo, C., Cai, S., & You, H. (2019). Empirical investigation of stochastic local search for maximum satisfiability. *Frontiers of Computer Science*, 13(1), 86-98.
- Goldberg, D. E., & Deb, K. (1991). A comparative analysis of selection schemes used in genetic algorithms. In G. J. E. Rawlins (Ed.), *Foundations of genetic algorithms* (Vol. 1, pp. 69-93). San Mateo, CA: Morgan Kaufmann Publishers, Inc.
- Goldberg, D. E., & Holland, J. H. (1988). Genetic algorithms and machine learning. *Machine learning*, 3(2), 95-99.
- Hamadneh, N., Sathasivam, S., Tilahun, S. L., & Choon, O. H. (2012). Learning logic programming in radial basis function network via genetic algorithm. *Journal of Applied Sciences (Faisalabad)*, 12(9), 840-847.
- Hopfield, J. J. (1982). Neural networks and physical systems with emergent collective computational abilities. *Proceedings of the national academy of sciences*, 79(8), 2554-2558.
- Jia, D., Duan, X., & Khan, M. K. (2014). Binary artificial bee colony optimization using bitwise operation. *Computers and Industrial Engineering*, 76, 360-365.
- Karaboga, D. (2005). *An Idea Based on Honey Bee Swarm for Numerical Optimization* (Vol. 200) (Technical report-tr06). Erciyes University, Turkey.
- Karaboga, D., & Basturk, B. (2007). A powerful and efficient algorithm for numerical function optimization: artificial bee colony (ABC) algorithm. *Journal of Global Optimization*, 39(3), 459-471.
- Karaboga, D., & Basturk, B. (2008). On the performance of artificial bee colony (ABC) algorithm. *Applied Soft Computing*, 8(1), 687-697.
- Karaboga, N. (2009). A new design method based on artificial bee colony algorithm for digital IIR filters. *Journal of the Franklin Institute*, 346(4), 328-348.
- Karp, R. M. (1972). Reducibility among combinatorial problems. In R. E. Miller, J. W. Thatcher & J. D. Bohlinger (Eds.), *Complexity of Computer Computations* (pp. 85-103). Boston, MA: Springer.
- Kashan, M. H., Nahavandi, N., & Kashan, A. H. (2012). DisABC: A new artificial bee colony algorithm for binary optimization. *Applied Soft Computing*, 12(1), 342-352.
- Kasihmuddin, M. S. M., Mansor, M. A., & Sathasivam, S. (2016). Artificial bee colony in the Hopfield network for maximum k-satisfiability problem. *Journal of Informatics and Mathematical Sciences*, 8(5), 317-334.
- Kasihmuddin, M. S. M., Mansor, M. A., & Sathasivam, S. (2017). Hybrid genetic algorithm in the Hopfield network for logic satisfiability problem. *Pertanika Journal of Science and Technology*, 25(1), 139-152.
- Kasihmuddin, M. S. M., Mansor, M. A., & Sathasivam, S. (2018a). Discrete Hopfield neural network in restricted maximum k-satisfiability logic programming. *Sains Malaysiana*, 47(6), 1327-1335.
- Kasihmuddin, M. S. M., Mansor, M. A., & Sathasivam, S. (2018b). Satisfiability based reverse analysis method in diabetes detection. In D. Mohamad, A. B. Akbarally, H. Maidinsah, M. M. Jaffar, M. Mohamed, S. R. Sharif & W. E. Z. W. A. Rahman (Eds.), *AIP Conference Proceedings* (Vol. 1974, No. 1, p. 020020). Melville, NY: AIP Publishing.
- Kullmann, O. (1999). New methods for 3-SAT decision and worst-case analysis. *Theoretical Computer Science*, 223(1-2), 1-72.

- Layeb, A. (2012). A clonal selection algorithm based tabu search for satisfiability problems. *Journal of Advances in Information Technology*, 3(2), 138-146.
- Liang, R. H., & Hsu, Y. Y. (1996). Short-term hydro-scheduling using Hopfield neural network. IEE Proceedings-Generation, Transmission and Distribution, 143(3), 269-275.
- Lynce, I., Manquinho, V., & Martins, R. (2018). Parallel maximum satisfiability. In Y. Hamadi & L. Sais (Eds.), *Handbook of Parallel Constraint Reasoning* (pp. 61-99). Cham, Switzerland: Springer.
- Mansor, M. A. B., Kasihmuddin, M. S. B. M., & Sathasivam, S. (2017). Robust Artificial immune system in the Hopfield network for maximum k-satisfiability. *International Journal of Interactive Multimedia and Artificial Intelligence*, 4(4), 63-71.
- Mansor, M. A., Kasihmuddin, M. S. M., & Sathasivam, S. (2016a). Enhanced Hopfield network for pattern satisfiability optimization. *International Journal of Intelligent Systems and Applications*, 8(11), 27-33.
- Mansor, M. A., Kasihmuddin, M. S. M., & Sathasivam, S. (2016b). VLSI circuit configuration using satisfiability logic in Hopfield network. *International Journal of Intelligent Systems and Applications (IJISA)*, 8(9), 22-29.
- Mansor, M. A., Sathasivam, S., & Kasihmuddin, M. S. (2018). 3-satisfiability logic programming approach for cardiovascular diseases diagnosis. In D. Mohamad, A. B. Akbarally, H. Maidinsah, M. M. Jaffar, M. Mohamed, S. R. Sharif & W. E. Z. W. A. Rahman (Eds.), *AIP Conference Proceedings* (Vol. 1974, No. 1, p. 020022). Melville, NY: AIP Publishing.
- Mérida-Casermeyro, E., Galán-Marín, G., & Munoz-Perez, J. (2001). An efficient multivalued Hopfield network for the traveling salesman problem. *Neural Processing Letters*, 14(3), 203-216.
- Ning, J., Liu, T., Zhang, C., & Zhang, B. (2018). A food source-updating information-guided artificial bee colony algorithm. *Neural Computing and Applications*, 30(3), 775-787.
- Ohta, M. (2002). Chaotic neural networks with reinforced self-feedbacks and its application to N-Queen problem. *Mathematics and computers in simulation*, 59(4), 305-317.
- Ozturk, C., Hancer, E., & Karaboga, D. (2015). A novel binary artificial bee colony algorithm based on genetic operators. *Information Sciences*, 297, 154-170.
- Pampará, G., & Engelbrecht, A. P. (2011, April 11-15). Binary artificial bee colony optimization. In 2011 IEEE Symposium on Swarm Intelligence (pp. 1-8). Paris, France.
- Poloczek, M., Schnitger, G., Williamson, D. P., & Van Zuylen, A. (2017). Greedy algorithms for the maximum satisfiability problem: Simple algorithms and inapproximability bounds. *SIAM Journal on Computing*, 46(3), 1029-1061.
- Rojas, R. (2013). *Neural networks: A systematic introduction*. Heidelberg, Germany: Springer-Verlag.
- Sathasivam, S. (2006). *Logic Mining in Neural Networks* (Doctoral thesis). University of Malaya, Kuala Lumpur, Malaysia.
- Sathasivam, S. (2008, April 2-4). Energy landscapes for Hopfield network programmed with program clauses. In 4th IASTED International Conference in Advances Computer Science and Technology (pp. 179-182). Langkawi, Malaysia.

- Sathasivam, S. (2010). Upgrading logic programming in Hopfield network. *Sains Malaysiana*, 39(1), 115-118.
- Sathasivam, S., & Ng, P. F. (2013). Developing agent based modeling for doing logic programming in Hopfield network. *Applied Mathematical Sciences*, 7(1), 23-35.
- Sathasivam, S., Hamadneh, N., & Choon, O. H. (2011). Comparing neural networks: Hopfield network and RBF network. *Applied Mathematical Sciences*, 5(69), 3439-3452.
- Xu, Z., He, K., & Li, C. M. (2019). An iterative Path-Breaking approach with mutation and restart strategies for the MAX-SAT problem. *Computers and Operations Research*, 104, 49-58.
- Zhang, H., Shen, H., & Manya, F. (2003). Exact algorithms for MAX-SAT. *Electronic Notes in Theoretical Computer Science*, 86(1), 190-203.
- Zhang, S., Yu, Y., & Wang, Q. (2016). Stability analysis of fractional-order Hopfield neural networks with discontinuous activation functions. *Neurocomputing*, 171, 1075-1084.
- Zhang, X., & Zhang, X. (2017). A binary artificial bee colony algorithm for constructing spanning trees in vehicular ad hoc networks. *Ad Hoc Networks*, 58, 198-204.

Instantaneous Speed Ratio of Traffic Flowing through a Merging Area at Kilometer 31.6 on the Highway from Shah Alam to Kuala Lumpur

Nur Syahirah Husin Basri¹, Nurul Akmal Mohamed^{1*}, Muhammad Akram Adnan², Nurul Farihan Mohamed³ and Nurul Hila Zainuddin¹

¹Mathematics Department, Faculty of Science & Mathematics, Universiti Pendidikan Sultan Idris, 35900 Tanjong Malim, Perak, Malaysia

²Faculty of Civil Engineering, Universiti Teknologi Mara, 40450 Shah Alam, Selangor, Malaysia

³Kolej GENIUS Insan, Universiti Sains Islam Malaysia, Bandar Baru Nilai, 71800, Nilai, Negeri Sembilan, Malaysia

ABSTRACT

This study aims to evaluate a continuous flow model that involves a ramp area at kilometer 31.6 on the highway from Shah Alam to Kuala Lumpur, to analyze the findings of numerical results of instantaneous speed ratios and to observe the convergence patterns for each section. The continuous flow model assumes traffic flow to be similar to the heat equation in regard to the concept of the one-dimensional viscous flow of a compressible fluid. For the methodology, for solving an initial value-boundary value problem, an initial condition together with a set of boundary conditions are required to solve the partial differential equation. The boundary conditions are chosen to assess the suitability of the design of the entrance ramp in Malaysia, which is for right hand drive traffic. Highway traffic data

were collected on the tapered acceleration lane and obtained by the videotaping method. The Maple programming language was used to write a numerical code in order to evaluate the instantaneous speed ratio in terms of a Fourier series. Our results show that the realistic results of instantaneous speed ratios on the ramp at kilometer 31.6 from Shah Alam to Kuala Lumpur are acceptable when compared to the theoretical results. Therefore, a very minimal collision rate is expected due to the well-designed

ARTICLE INFO

Article history:

Received: 15 September 2019

Accepted: 04 December 2019

Published: 15 April 2020

E-mail addresses:

earesya@yahoo.com (Nur Syahirah Husin Basri)

akmal.mohamed@fsmpt.upsi.edu.my (Nurul Akmal Mohamed)

akram@uitm.edu.my (Muhammad Akram Adnan)

farihan@usim.edu.my (Nurul Farihan Mohamed)

nurulhila@fsmpt.upsi.edu.my (Nurul Hila Zainuddin)

* Corresponding author

ramp at kilometer 31.6 from Shah Alam to Kuala Lumpur. It is beneficial to study the mathematical model and theories of traffic flows on the merging area to enhance the efficiency of the traffic flowing on highways.

Keywords: Continuous flow model, heat equation, highway operation, macroscopic model, partial differential equation

INTRODUCTION

Presently, highways are the main road system in the movement of traffic and goods. Highways have provided the motorist with a high level of service. In the 1950s, the highway concept appeared from the roadway concept (Adnan, 2007). Many researchers and highway planners in the field of highway design and traffic engineering have shown their interest in cars following theories and models.

Macroscopic models of traffic flow consider the flow of traffic to be similar to the physical flow of fluid (Lazar et al., 2016). Traffic dynamics are described as a function of space and time corresponding to the partial differential equation of aggregate macroscopic quantities such as traffic density, traffic average flow or velocity (Lazar et al., 2017). As mentioned by Drew (1964), continuous flow models are realistic when applied to freeway traffic flow.

The available research on highways mostly focuses on physical studies rather than evaluating mathematical models. In addition, the research develops car theories and models macroscopically for traffic that is left hand drive, for example Lighthill and Witham (1955), Harr and Leornads (1962) and Drew (1964). Research by Reddy (1966) based the theory of traffic flow on the one-dimensional movement of fluid or gas. In the past 20 years, most of the research undertaken focused on developing a new car theory and models, for instance models by Daganzo (2002), Wong and Wong (2002), Mathew (2014) and Van Wageningen-Kessels et al. (2015).

This paper focuses on a continuous flow model for traffic flowing onto the merging area of a ramp at kilometer 31.6 on the highway from Shah Alam to Kuala Lumpur. One of the macroscopic models in use is the continuous flow model which originated from the hydrodynamic analogy of vehicle flow. This is based on the assumption that the traffic flow on highways operates in the same way as a one-dimensional viscous flow of compressible fluid. The parameters that are used in this paper are instantaneous speed ratio and easiness to flow F_0 . Both parameters are important in evaluating the continuous flow model.

Reddy (1966) took the Fourier series solution to the first iterations only. We tried to set the equation restricted to a number of iterations, n . We used the number of iterations n instead of tolerance as a stopping criteria because we wanted to see the pattern of the convergence for every selected easiness to flow value, F_0 . Reddy (1966) used the parameter

easiness to flow F_0 as a dependent variable, which is similar to our study. This means it is appropriate to compare our results with the theoretical results stated by Reddy (1966).

The motivating pressure potential P corresponds to the fluid dynamic relationship between flow velocity and potential velocity. Hence, the velocity of vehicles between two points depends on the difference in potential at these points (Harr & Leonards, 1962). Thus, we assume that the motivating pressure potential P is similar to the theory of one-dimensional viscous flow of compressible fluid.

The findings of this study will give a better understanding of the continuous flow model as well as methods for improving the design of the entrance ramp at kilometer 31.6 on the highway from Shah Alam to Kuala Lumpur. The results obtained are important for evaluation and decision-making relating to traffic flow ramp design.

The objectives of this paper are (a) to evaluate the continuous flow model by determining the instantaneous speed ratio for every selected value of the parameter easiness to flow F_0 on a ramp area at kilometer 31.6 from Shah Alam to Kuala Lumpur, (b) to analyze the findings of the numerical results of the instantaneous speed ratios for every selected easiness to flow F_0 value, and (c) to observe the pattern of the convergence for every selected easiness to flow F_0 value.

METHODS

These notations are used throughout the paper.

P = Motivating pressure potential,

X = A specific position along the highway,

L = A particular length of highway upstream of the merging point,

V = Vehicle speed,

t = Time,

Q = Highway volume per time t ,

R_w = Number of ramp vehicles merging per time t ,

R_v = Number of ramp vehicles merging per length L ,

$\frac{V(X, t)}{\bar{V}}$ = Ration of instantaneous speed at a point X , to the average of length L ,

F_0 = Parameter easiness to flow,

n = Number of iterations.

The general heat Equation (1) is given as:

$$\frac{\partial^2 P}{\partial X^2} - a^2 \frac{\partial P}{\partial t} = C \quad (1)$$

where a^2 and C are constant.

A set of boundary conditions is required to solve the Partial Differential Equation (PDE) in (1). Some of the boundary conditions are explained as in Equation (2), (3) and (4).

The driver is ignorant of the changes in the motivating pressure potential ahead on the highway at time $t = 0$.

$$P(X, 0) = P_0 \tag{2}$$

Pressure potential changes at the entrance ramp due to the merging of vehicles, which is at distance $X = L$ from initial potential to P_0 to P_1 ,

$$P(L, t) = P_1 \tag{3}$$

The pressure potential is P_0 and the vehicles are unaffected by the entrance ramp ahead at $X = 0$.

$$P(0, t) = P_0 \tag{4}$$

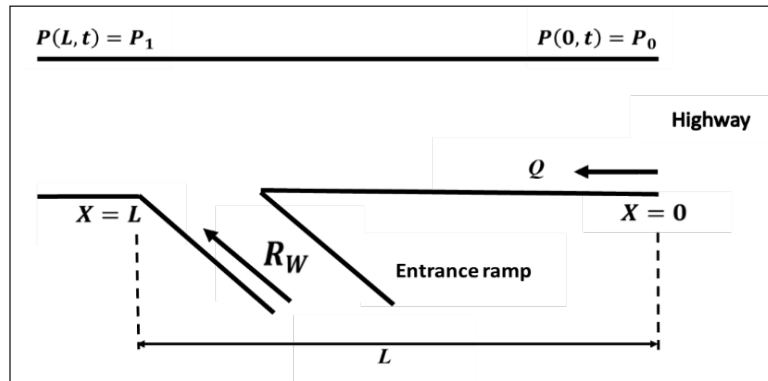


Figure 1. Illustration of the highway and entrance ramp with boundary conditions (BCs).

The mathematical model is represented in the following initial boundary value problem as in Equation (5), (6), (7) and (8).

$$P_{XX} = a^2 P_t + C, \quad 0 \leq X \leq L, t > 0 \tag{5}$$

$$P(0, t) = P_0, \quad t > 0 \tag{6}$$

$$P(L, t) = P_1 \quad t > 0 \tag{7}$$

$$P(X, 0) = P_0 \quad 0 < X < L \tag{8}$$

The solution of the initial boundary value problem (IBVP), as in Equations (1), (2), (3) and (4), is carried out using the separation of variables (SOV) method as follows:

$$P_{\infty} = \frac{V(X, t)}{\bar{V}} = 1 + \frac{R_w}{2QL} (L - 2X) + \sum_{n=1}^{\infty} \left(\frac{0.2R_w L (-1)^n}{Q} \left(-\cos\left(\frac{n\pi - 1}{n^2}\right) \right) + 2(-1)^{2n-2} \right) \cdot e^{-n^2 F_0} \cdot \cos\left(\frac{n\pi X}{L}\right) \tag{9}$$

The Fourier series of the solution as shown in Equation (9) needs to be set with the number of iterations n such that the infinite iteration in Equation (9) is restricted to a number of iterations. This is a necessity to handle the time-consuming and memory-consuming process of the numerical computations.

In this step, we want to investigate the number of the iterations needed in order to get the convergence values of instantaneous speed ratio with an acceptable error. We can take the first iteration P_1 , the second iteration P_2 , third iteration P_3 and so on. The equations after we place the number of iterations n in (9) are shown respectively as in Equation (10), (11), (12), (13) and (14):

$$P_1 = \frac{V(X, t)}{\bar{V}} = 1 + \frac{R_w}{2QL} (L - 2X) + \left(2 - \frac{0.4R_w}{Q} \right) \left(e^{-F_0} \cos\left(\frac{\pi X}{L}\right) \right) \tag{10}$$

$$P_2 = \frac{V(X, t)}{\bar{V}} = 1 + \frac{R_w}{2QL} (L - 2X) + \left(2 - \frac{0.4R_w}{Q} \right) \left(e^{-F_0} \cos\left(\frac{\pi X}{L}\right) \right) + \left(2e^{-4F_0} \cos\left(\frac{2\pi X}{L}\right) \right) \tag{11}$$

$$P_3 = \frac{V(X, t)}{\bar{V}} = 1 + \frac{R_w}{2QL} (L - 2X) + \left(2 - \frac{0.4R_w}{Q} \right) \left(e^{-F_0} \cos\left(\frac{\pi X}{L}\right) \right) + \left(2e^{-4F_0} \cos\left(\frac{2\pi X}{L}\right) \right) + \left(2 - \frac{0.4R_w}{9Q} \right) \left(e^{-9F_0} \cos\left(\frac{3\pi X}{L}\right) \right) \tag{12}$$

$$P_4 = \frac{V(X, t)}{\bar{V}} = 1 + \frac{R_w}{2QL} (L - 2X) + \left(2 - \frac{0.4R_w}{Q} \right) \left(e^{-F_0} \cos\left(\frac{\pi X}{L}\right) \right) + \left(2e^{-4F_0} \cos\left(\frac{2\pi X}{L}\right) \right) + \left(2 - \frac{0.4R_w}{9Q} \right) \left(e^{-9F_0} \cos\left(\frac{3\pi X}{L}\right) \right) + \left(2e^{-16F_0} \cos\left(\frac{4\pi X}{L}\right) \right) \tag{13}$$

$$\begin{aligned}
 P_5 = \frac{V(X, t)}{\bar{V}} = & 1 + \frac{R_w}{2QL} (L - 2X) + \left(2 - \frac{0.4R_w}{Q}\right) \left(e^{-F_0} \cos\left(\frac{\pi X}{L}\right)\right) + \left(2e^{-4F_0} \cos\left(\frac{2\pi X}{L}\right)\right) \\
 & + \left(2 - \frac{0.4R_w}{9Q}\right) \left(e^{-9F_0} \cos\left(\frac{3\pi X}{L}\right)\right) + \left(2e^{-16F_0} \cos\left(\frac{4\pi X}{L}\right)\right) \\
 & + \left(2 - \frac{0.4R_w}{25Q}\right) \left(e^{-25F_0} \cos\left(\frac{5\pi X}{L}\right)\right)
 \end{aligned} \tag{14}$$

Highway traffic data were provided by the Faculty of Civil Engineering, Universiti Teknologi Mara (UiTM) under file code 600/IRDC/ST/5/3/1102. The data were collected from a tapered acceleration lane using a videotaping method. This research involves a ramp area at kilometer 31.6 on the highway from Shah Alam to Kuala Lumpur where L (the length of the highway upstream of the merging area point) and X (a specific position along the highway) are varied in 20 m increments.

The Maple programming language (Maple 2017) was used to write a code to evaluate the Fourier series with a finite number of iterations, P_1, P_2, P_3, P_4 and P_5 as Equations (10), (11), (12), (13) and (14). All the values of P_1, P_2, P_3, P_4 and P_5 are instantaneous speed ratios. According to Reddy (1966) the instantaneous speed ratio can be predicted if the accuracy of easiness to flow F_0 is 1 or above. However, the theory of easiness to flow F_0 has never been observed. Reddy (1966) suggested the easiness to flow F_0 computation was restricted to R_w/Q being less than 5.0.

Hence, the values of the easiness to flow parameter F_0 range from 0.1 to 5.0. The location along the highway X/L is plotted on the x -axis and instantaneous speed ratio is plotted on the y -axis.

RESULTS AND DISCUSSION

Instantaneous Speed Ratio and Error $|P_n - P_{n-1}|$

This section discusses the results of the numerical errors $|P_n - P_{n-1}|$ of Equation (9) that describe the instantaneous speed ratio on the ramp at kilometer 31.6 from Shah Alam to Kuala Lumpur. On this specific ramp, we have the values of the volume of traffic on the highway per time Q the ramp vehicles merging per time R_w and the length of section L which are given by 6482 vehicles per hour (vph), 774.656 vph and 170 meters, respectively. Table 1-5 show the numerical results of P_n and the numerical errors $|P_n - P_{n-1}|$ of Equation (9) where $1 \leq n \leq 5, n \in \mathbb{N}$ for easiness to flow $F_0 = 0.50, 0.70, 1.00, 3.00$ and 5.00 .

The numerical results of P_n are important for us to see the pattern of instantaneous speed ratio along the merging area. These realistic results are necessary to compare with the theoretical results as mentioned in Reddy (1966) (Figure 1). The similarity of the

patterns for realistic and theoretical results gives the impression that the design of the ramp on at kilometer 31.6 from Shah Alam to Kuala Lumpur is acceptable and satisfactory. The calculations of errors $|P_n - P_{n-1}|$ are important to analyze how accurate and fast the convergence of solution P_n is for each of the easiness to flow F_0 values. This is essential to observe whether or not the series solution in Equation (9) is a fast converging series.

From our observations, when the easiness to flow F_0 is approaching 5.00, the reading values of instantaneous speed ratio converge faster as shown in Tables 1-5. Note that some of the numerical values of the error for instantaneous speed ratio in Tables 3-5 appear as zero due to the limitation of up to only double precision in computing the numbers.

Instantaneous Speed Ratio–Distance Graphs

In this study, the series solution in Equation (9) is taken up to the fifth iteration P_5 . A programming code was written in the Maple programming language (Maple 2017) for the evaluation of the Equations (10), (11), (12), (13) and (14). The results for the instantaneous speed ratio on the ramp at kilometer 31.6 from Shah Alam to Kuala Lumpur will be elaborated upon below.

This section discusses plotted data for the first iteration P_1 , second iteration P_2 , third iteration P_3 , fourth iteration P_4 and fifth iteration P_5 which are presented in Figure 2-4. The instantaneous speed ratio for all of easiness to flow F_0 values continuously decreased from the starting point 0 to the length L . Note that the instantaneous speed ratio is almost static at value 1 whenever the parameter easiness to flow F_0 is approaching 5.00. Note also that the curves are declining with steeper slopes for lower F_0 .

As we can see in Figure 2, when the number of iterations n is equal to 1 ($n = 1$), the graph intersects at the middle of L i.e. $X = L/2$. The negative values for the instantaneous speed ratio at specific position X at $X = 140$ meters until $X = 170$ meters for easiness to flow $F_0 = 0.50$ and $F_0 = 0.70$ do not mean the vehicles were traveling in the opposite direction or returning back, since the first iteration P_1 still does not reach the desired solution. We note that as the number of iterations increases (Figure 3-6), all the negative values of the instantaneous speed ratio trend toward values that are ≥ 0 . Figure 6 shows the graph of the instantaneous speed ratio versus position X when we increase the number of iterations n to be equal to five $n = 5$. The values of instantaneous speed ratio do not differ much after $n = 5$ since the errors $|P_5 - P_4|$ trend toward 0 as displayed in Table 1. Therefore, Figure 6 already gives us the converged values of the instantaneous speed ratio.

When comparing Figure 3 through Figure 6, we can notice some profound differences. As already mentioned while discussing Table 1, we see that the curves of lower F_0 values, e.g. $F_0 = 0.50$ and $F_0 = 0.70$, converge slower than those of bigger F_0 values, e.g. $F_0 = 1.00$, 3.00 and $F_0 = 5.00$. Other than that, we also note that the curves for low values of easiness flow i.e. ($F_0 = 0.50$ and $F_0 = 0.70$) do not reach 1 in the middle of section length L , unlike

Instantaneous Speed Ratio and Error at Kilometer 31.6 from Shah Alam to Kuala Lumpur

Table 1
 Number of iterations for instantaneous speed ratio when easiness to flow $F_0=0.50$ and error $|P_n - P_{n-1}|$

X/L	P_1	P_2	P_3	P_4	P_5	$P_{6 \rightarrow 10000}$	$ P_2 - P_1 $	$ P_3 - P_2 $	$ P_4 - P_3 $	$ P_5 - P_4 $
0.0	2.26E+00	2.54E+00	2.56E+00	2.56E+00	2.56E+00	2.56E+00	2.70E-01	2.22E-02	6.71E-04	7.45E-06
0.1	2.17E+00	2.37E+00	2.38E+00	2.38E+00	2.38E+00	2.38E+00	2.00E-01	9.90E-03	6.19E-05	2.04E-06
0.2	1.92E+00	1.95E+00	1.93E+00	1.93E+00	1.93E+00	1.93E+00	2.49E-02	1.34E-02	6.59E-04	6.34E-06
0.4	1.55E+00	1.39E+00	1.37E+00	1.37E+00	1.37E+00	1.37E+00	1.63E-01	2.18E-02	1.84E-04	5.51E-06
0.5	1.11E+00	8.49E-01	8.43E-01	8.44E-01	8.44E-01	8.44E-01	2.66E-01	6.08E-03	6.25E-04	3.32E-06
0.6	6.60E-01	4.30E-01	4.46E-01	4.47E-01	4.47E-01	4.47E-01	2.30E-01	1.64E-02	2.99E-04	7.32E-06
0.7	2.49E-01	1.75E-01	1.96E-01	1.95E-01	1.95E-01	1.95E-01	7.40E-02	2.07E-02	5.70E-04	6.87E-07
0.8	-6.34E-02	5.71E-02	5.91E-02	5.87E-02	5.87E-02	5.87E-02	1.20E-01	2.05E-03	4.04E-04	6.95E-06
0.9	-2.37E-01	-3.83E-03	-4.32E-03	-3.83E-03	-3.83E-03	-3.83E-03	2.34E-01	4.96E-04	4.96E-04	4.49E-06
1.0	-2.65E-01	5.25E-03	-1.70E-02	-1.63E-02	-1.63E-02	-1.63E-02	2.70E-01	2.22E-02	6.71E-04	7.45E-06

Table 2
 Number of iterations for instantaneous speed ratio when easiness to flow $F_0=0.70$ and error $|P_n - P_{n-1}|$

X/L	P_1	P_2	P_3	P_4	P_5	$P_{6 \rightarrow 10000}$	$ P_2 - P_1 $	$ P_3 - P_2 $	$ P_4 - P_3 $	$ P_5 - P_4 $
0.0	2.05E+00	2.17E+00	2.17E+00	2.17E+00	2.17E+00	2.17E+00	1.21E-01	3.67E-03	2.73E-05	5.00E-08
0.1	1.97E+00	2.06E+00	2.06E+00	2.06E+00	2.06E+00	2.06E+00	8.97E-02	1.64E-03	2.52E-06	1.40E-08
0.2	1.76E+00	1.77E+00	1.77E+00	1.77E+00	1.77E+00	1.77E+00	1.12E-02	2.21E-03	2.69E-05	4.30E-08
0.4	1.46E+00	1.38E+00	1.38E+00	1.38E+00	1.38E+00	1.38E+00	7.32E-02	3.61E-03	7.48E-06	3.70E-08
0.5	1.09E+00	9.75E-01	9.74E-01	9.74E-01	9.74E-01	9.74E-01	1.19E-01	1.00E-03	2.55E-05	2.23E-08
0.6	7.19E-01	6.16E-01	6.19E-01	6.19E-01	6.19E-01	6.19E-01	1.03E-01	2.71E-03	1.22E-05	4.94E-08
0.7	3.81E-01	3.48E-01	3.51E-01	3.51E-01	3.51E-01	3.51E-01	3.32E-02	3.42E-03	2.32E-05	4.60E-09
0.8	1.22E-01	1.77E-01	1.77E-01	1.77E-01	1.77E-01	1.77E-01	5.41E-02	3.39E-04	1.65E-05	4.68E-08
0.9	-2.27E-02	9.05E-02	8.74E-02	8.74E-02	8.74E-02	8.74E-02	1.13E-01	3.12E-03	2.02E-05	3.03E-08
1.0	-4.65E-02	7.49E-02	7.12E-02	7.13E-02	7.13E-02	7.13E-02	1.21E-01	3.67E-03	2.73E-05	5.02E-08

Table 3
 Number of iterations for instantaneous speed ratio when easiness to flow $F_0=1.00$ and error $|P_n - P_{n-1}|$

X/L	P_1	P_2	P_3	P_4	P_5	$P_{6 \rightarrow 10000}$	$ P_2 - P_1 $	$ P_3 - P_2 $	$ P_4 - P_3 $	$ P_5 - P_4 $
0.0	1.79E+00	1.83E+00	1.83E+00	1.83E+00	1.83E+00	1.83E+00	3.66E-02	2.47E-04	2.25E-07	0.00E+00
0.1	1.73E+00	1.75E+00	1.75E+00	1.75E+00	1.75E+00	1.75E+00	2.70E-02	1.10E-04	2.10E-08	0.00E+00
0.2	1.57E+00	1.58E+00	1.58E+00	1.58E+00	1.58E+00	1.58E+00	3.37E-03	1.49E-04	2.21E-07	0.00E+00
0.4	1.34E+00	1.32E+00	1.32E+00	1.32E+00	1.32E+00	1.32E+00	2.20E-02	2.42E-04	6.20E-08	0.00E+00
0.5	1.07E+00	1.04E+00	1.03E+00	1.03E+00	1.03E+00	1.03E+00	3.59E-02	6.75E-05	2.10E-07	0.00E+00
0.6	7.89E-01	7.58E-01	7.58E-01	7.58E-01	7.58E-01	7.58E-01	3.11E-02	1.82E-04	1.00E-07	0.00E+00
0.7	5.35E-01	5.25E-01	5.25E-01	5.25E-01	5.25E-01	5.25E-01	1.00E-02	2.30E-04	1.91E-07	0.00E+00
0.8	3.40E-01	3.56E-01	3.56E-01	3.56E-01	3.56E-01	3.56E-01	1.63E-02	2.28E-05	1.36E-07	0.00E+00
0.9	2.29E-01	2.63E-01	2.63E-01	2.63E-01	2.63E-01	2.63E-01	3.41E-02	2.10E-04	1.66E-07	0.00E+00
1.0	2.09E-01	2.46E-01	2.46E-01	2.46E-01	2.46E-01	2.46E-01	3.66E-02	2.47E-04	2.25E-07	0.00E+00

Table 4
 Number of iterations for instantaneous speed ratio when easiness to flow $F_0=3.00$ and error $|P_n - P_{n-1}|$

X/L	P_1	P_2	P_3	P_4	P_5	$P_{6 \rightarrow 10000}$	$ P_2 - P_1 $	$ P_3 - P_2 $	$ P_4 - P_3 $	$ P_5 - P_4 $
0.0	1.16E+00	1.16E+00	1.16E+00	1.16E+00	1.16E+00	1.16E+00	1.23E-05	0.00E+00	0.00E+00	0.00E+00
0.1	1.14E+00	1.14E+00	1.14E+00	1.14E+00	1.14E+00	1.14E+00	9.07E-06	0.00E+00	0.00E+00	0.00E+00
0.2	1.10E+00	1.10E+00	1.10E+00	1.10E+00	1.10E+00	1.10E+00	1.13E-06	0.00E+00	0.00E+00	0.00E+00
0.4	1.06E+00	1.06E+00	1.06E+00	1.06E+00	1.06E+00	1.06E+00	7.39E-06	0.00E+00	0.00E+00	0.00E+00
0.5	1.01E+00	1.01E+00	1.01E+00	1.01E+00	1.01E+00	1.01E+00	1.21E-05	0.00E+00	0.00E+00	0.00E+00
0.6	9.62E-01	9.62E-01	9.62E-01	9.62E-01	9.62E-01	9.62E-01	1.04E-05	0.00E+00	0.00E+00	0.00E+00
0.7	9.16E-01	9.16E-01	9.16E-01	9.16E-01	9.16E-01	9.16E-01	3.36E-06	0.00E+00	0.00E+00	0.00E+00
0.8	8.77E-01	8.77E-01	8.77E-01	8.77E-01	8.77E-01	8.77E-01	5.47E-06	0.00E+00	0.00E+00	0.00E+00
0.9	8.50E-01	8.50E-01	8.50E-01	8.50E-01	8.50E-01	8.50E-01	1.14E-05	0.00E+00	0.00E+00	0.00E+00
1.0	8.41E-01	8.41E-01	8.41E-01	8.41E-01	8.41E-01	8.41E-01	1.23E-05	0.00E+00	0.00E+00	0.00E+00

Table 5
 Number of iterations for instantaneous speed ratio when easiness to flow $F_0=5.00$ and error $|P_n - P_{n-1}|$

X/L	P_1	P_2	P_3	P_4	P_5	$P_{6 \rightarrow 10000}$	$ P_2 - P_1 $	$ P_3 - P_2 $	$ P_4 - P_3 $	$ P_5 - P_4 $
0.0	1.07E+00	1.07E+00	1.07E+00	1.07E+00	1.07E+00	1.07E+00	4.00E-09	0.00E+00	0.00E+00	0.00E+00
0.1	1.06E+00	1.06E+00	1.06E+00	1.06E+00	1.06E+00	1.06E+00	3.00E-09	0.00E+00	0.00E+00	0.00E+00
0.2	1.04E+00	1.04E+00	1.04E+00	1.04E+00	1.04E+00	1.04E+00	0.00E+00	0.00E+00	0.00E+00	0.00E+00
0.4	1.02E+00	1.02E+00	1.02E+00	1.02E+00	1.02E+00	1.02E+00	3.00E-09	0.00E+00	0.00E+00	0.00E+00
0.5	1.00E+00	1.00E+00	1.00E+00	1.00E+00	1.00E+00	1.00E+00	4.00E-09	0.00E+00	0.00E+00	0.00E+00
0.6	9.86E-01	9.86E-01	9.86E-01	9.86E-01	9.86E-01	9.86E-01	3.50E-09	0.00E+00	0.00E+00	0.00E+00
0.7	9.67E-01	9.67E-01	9.67E-01	9.67E-01	9.67E-01	9.67E-01	1.10E-09	0.00E+00	0.00E+00	0.00E+00
0.8	9.50E-01	9.50E-01	9.50E-01	9.50E-01	9.50E-01	9.50E-01	1.80E-09	0.00E+00	0.00E+00	0.00E+00
0.9	9.34E-01	9.34E-01	9.34E-01	9.34E-01	9.34E-01	9.34E-01	3.90E-09	0.00E+00	0.00E+00	0.00E+00
1.0	9.27E-01	9.27E-01	9.27E-01	9.27E-01	9.27E-01	9.27E-01	4.20E-09	0.00E+00	0.00E+00	0.00E+00

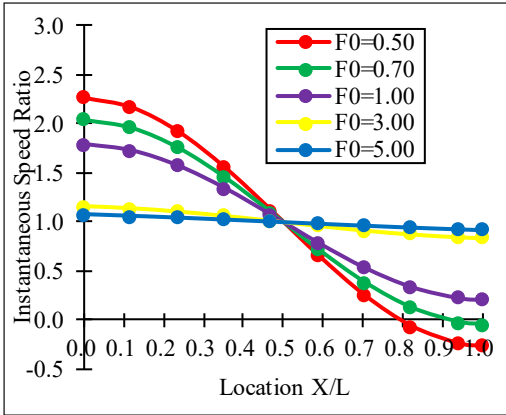


Figure 2. The instantaneous speed ratio versus location X/L which is plotted for the first iteration P_1 at every value of the easiness to flow parameter, $F_0 = 0.50, 0.70, 1.00, 3.00$ and 5.00 .

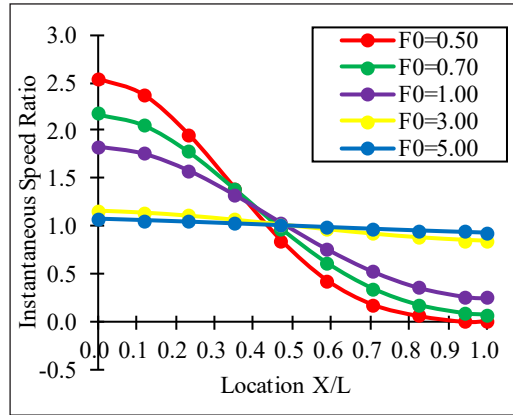


Figure 3. The instantaneous speed ratio versus location X/L which is plotted for the second iteration P_2 at every value of the easiness to flow parameter, $F_0 = 0.50, 0.70, 1.00, 3.00$ and 5.00 .

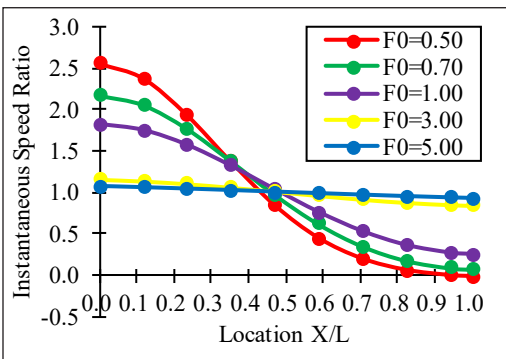


Figure 4. The instantaneous speed ratio versus location X/L which is plotted for the third iteration P_3 at every value of the easiness to flow parameter, $F_0 = 0.50, 0.70, 1.00, 3.00$ and 5.00 .

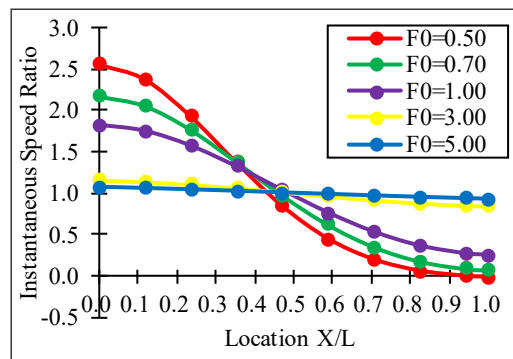


Figure 5. The instantaneous speed ratio versus location X/L which is plotted for the fourth iteration P_4 at every value of the easiness to flow parameter, $F_0 = 0.50, 0.70, 1.00, 3.00$ and 5.00 .

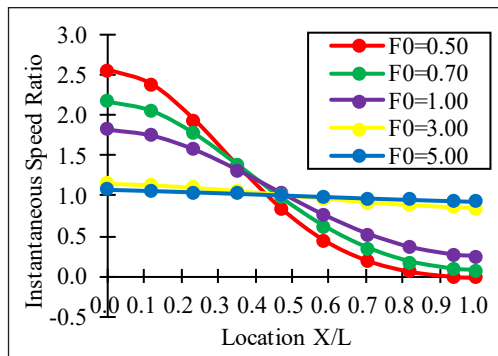


Figure 6. The instantaneous speed ratio versus versus location X/L which is plotted for the fifth iteration P_5 at every value of the easiness to flow parameter, $F_0 = 0.50, 0.70, 1.00, 3.00$ and 5.00 .

the curves of bigger values of F_0 . Instead, the curves reach 1 for instantaneous speed ratios earlier when the values of F_0 are small, e.g. $F_0 = 0.50$ and $F_0 = 0.70$. This is due to the necessity for drivers to slow down their vehicles for at least $1/5$ of $L/2$ to avoid collision.

In our numerical experiments, $1/5$ of $L/2$ takes the value $X/L = 0.4$ from the starting point. From Figure 6, we observe that the realistic data taken on the ramp at kilometer 31.6 from Shah Alam to Kuala Lumpur fulfills this minimum necessity to avoid collision. We can see that at $X = 0.4$, the instantaneous speed ratio is already almost 1 for all the values of easiness to flow F_0 .

We attempted to calculate the instantaneous speed ratio to infinite iterations such that $n = \infty$ but this failed due to the limitations of our computer memory. The greatest number of iterations n that we could achieve in generating the results for P_n was $n = 10000$. However, the results of the instantaneous speed ratio when $n = 10000$ are not much different graphically (Figure 6) compared to when $n = 5$.

The x -axis of Figure 7 is the dependent variable of the ratio X/L which takes the values $0 \leq X/L \leq 1$. In our numerical experiments, $L = 170$ meters. If we compare the graph of our converged numerical results in Figure 6 with the theoretical results in Figure 7, we notice several similarities. We observe that for higher F_0 values such as $F_0 \rightarrow 5.00$, the instantaneous speed ratio is more stable at 1. This is due to the fact that the vehicles slow down due to heavy traffic.

For the lower traffic flow that is when we have lower values of easiness to flow, the theory suggests that the vehicles to slow down to about $1/5$ from the merging point at $L/2$. Therefore, the vehicles need to slow down and the instantaneous speed ratio is expected to reach toward 1 at $X/L = 0.4$. If we look at the theoretical graph in Figure 7, the instantaneous speed ratio is ≤ 1.4 when $X/L = 0.4$. From our realistic graph in Figure 6, we observe that the instantaneous speed ratio is ≤ 1.34 when $X/L = 0.4$ which is acceptable for avoiding collision.

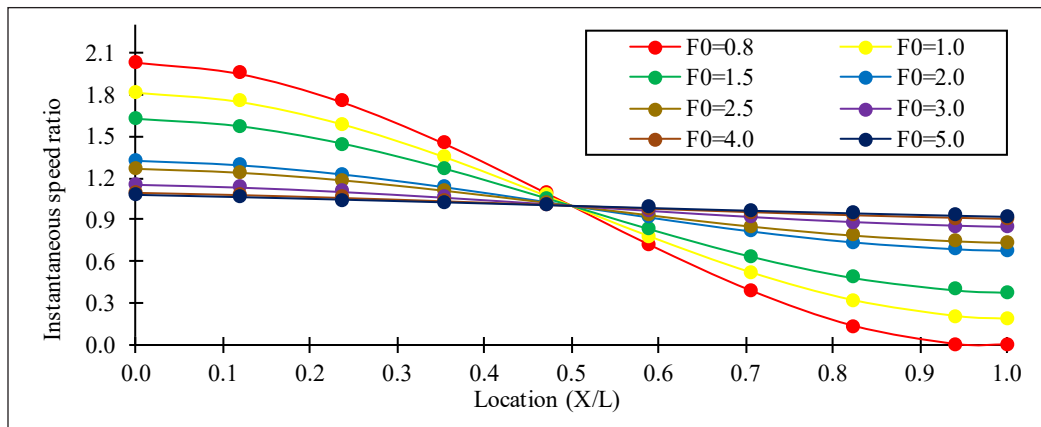


Figure 7. Theoretical speed ratio–distance graph by Reddy (1966)

CONCLUSION

In this paper, the model that we took into consideration was the continuous flow model which was established on the idea that traffic flow was analogous to the flow of a one-dimensional fluid or gas. The model is analogous to the model by Reddy (1966). Unlike Reddy (1966), whose model represented left hand drive traffic, the model that we solved here was for right hand drive traffic. We solved the model, an IBVP, and the solution was formed in terms of a Fourier series which was also denoted as the instantaneous speed ratio.

We evaluated the continuous flow model by measuring the instantaneous speed ratio on the ramp at kilometer 31.6 from Shah Alam to Kuala Lumpur. On the whole, the instantaneous speed ratio at lower values of the easiness to flow parameter, $F_0 = 0.50$ and $F_0 = 0.70$, shows slower convergence compared to when we have higher values of F_0 , i.e. $F_0 = 1.00, 3.00$ and $F_0 = 5.00$.

In a nutshell, the one-dimensional viscous flow of compressible fluid theory provides a good theoretical model to explain the variations of instantaneous speed ratio on the merging area of a highway due to the traffic conditions. Other than that, this study can help us to find improvements to the design of the entrance ramp.

One of the suggestions is to provide a sufficient length for acceleration at the entrance ramp. It is useful to evaluate the reasonableness of the parameters and analyze their numerical values in order to enhance the efficiency of the traffic flowing at the merging area on highways.

In our studies, we deduce that the instantaneous speed ratio on the ramp at kilometer 31.6 from Shah Alam to Kuala Lumpur is acceptable since as $X/L \rightarrow 0.4$, the instantaneous speed ratio ≤ 1.34 which is less than 1.4 as suggested by Reddy (1966) as in the theoretical graph in Figure 7. Therefore, minimal collisions are expected due to the well-designed ramp at kilometer 31.6 from Shah Alam to Kuala Lumpur.

ACKNOWLEDGMENT

The authors would like to thank Universiti Pendidikan Sultan Idris and Ministry of Higher Education in Malaysia for their financial contribution in respect for this study under Geran Penyelidikan Universiti (GPU)(code no : 2018-0153-103-01) and Fundamental Research Grant Scheme (FRGS) (code no:2019001010702)(FRGS/1/2018/STG06/UPSI/02/4).

REFERENCES

- Adnan, M. A. (2007). *Development of entrance ramp merging density model based on an urban expressway traffic condition* (PhD Thesis). Universiti Sains Malaysia, Malaysia.
- Daganzo, C. F. (2002). A behavioral theory of multi-lane traffic flow. Part I: Long homogeneous freeway sections. *Transportation Research Part B: Methodological*, 36(2), 131-158.

- Drew, D. R. (1964). *Theoretical approaches to the study and control of freeway congestion*. Texas, US: Texas Transportation Institute.
- Harr, M. E., & Leonards, G. A. (1962). *A Theory of traffic flow for evaluation of the geometric aspects of highways*. Washington D. C.: Highway Research Board.
- Lazar, H., Rhoulami, K., & Rahmani, M. D. (2016). A review analysis of optimal velocity models. *Periodica Polytechnica Transportation Engineering*, 44(2), 123-131.
- Lazar, H., Rhoulami, K., & Rahmani, M. D. (2017). Microscopic evaluation of extended car-following model in multi-lane roads. *Informatica*, 42(1), 117-125.
- Lighthill, M. J., & Whitham, G. B. (1955). On kinematic waves II. A theory of traffic flow on long crowded roads. *Proceedings of the Royal Society of London. Series A. Mathematical and Physical Sciences*, 229(1178), 317-345.
- Mathew, T. V. (2014). Transportation systems engineering. *Cell Transmission Models, IIT Bombay*. Retrieved February 19, 2019 from https://nptel.ac.in/content/storage2/courses/105101008/downloads/cete_48.pdf
- Reddy, M. S. (1966). *Quantitative evaluation of the effect of merging vehicles on freeway operation* (Doctoral dissertation). Texas A & M University, US.
- Van Wageningen-Kessels, F., Van Lint, H., Vuik, K., & Hoogendoorn, S. (2015). Genealogy of traffic flow models. *EURO Journal on Transportation and Logistics*, 4(4), 445-473.
- Wong, G. C. K., & Wong, S. C. (2002). A multi-class traffic flow model—An extension of LWR model with heterogeneous drivers. *Transportation Research Part A: Policy and Practice*, 36(9), 827-841.

Scale-3 Haar Wavelets and Quasilinearization based Hybrid Technique for the Solution of Coupled Space-Time Fractional - Burgers' Equation

Geeta Arora¹, Ratesh Kumar^{1*} and Harpreet Kaur²

¹Department of Mathematics, Lovely Professional University, Punjab, India

²Department of Mathematics, I.K. Gujral Punjab Technical University, Punjab, India

ABSTRACT

The aim of this study is to develop a hybrid method using scale 3 Haar wavelets for obtaining the solution of coupled space-time fractional Burgers' equation. Scale 3 Haar wavelets were used to estimate the solution by series approximation. Caputo and Riemann-Liouville definitions were used to handle the fractional derivatives and integrals in the problem. A quasi-linearization technique was implemented to handle the nonlinearity in the problems. Two examples of coupled space-time fractional Burgers' equations were studied to analyze the performance of the proposed technique.

Keywords: Caputo derivatives, fractional coupled Burgers' Equation, Quasi-linearization, Riemann-Liouville integration, scale 3 Haar wavelets

INTRODUCTION

Fractional calculus emerges as a great tool in explaining the physical and chemical phenomenon with alienate kinetics having microscopic complex behavior. There are fractional differential models which have a non-differentiable but continuous solution such as Weierstrass type functions (Zahle & Ziezold, 1996). These kinds of characteristics are not possible to explain with the help of ordinary or partial differential models. Earlier the field of fractional calculus was purely mathematical without any visible application but

in these days, fractional calculus has gained a huge importance in the field of science and technology because of its application in the various field like theory of thermoelasticity (Povstenko, 2009), viscoelastic fluids (Tripathi et al., 2010), dynamics of earthquakes (Lopes et al., 2013) and fluid dynamics (Momani & Odibat, 2006a). It

ARTICLE INFO

Article history:

Received: 15 September 2019

Accepted: 02 January 2020

Published: 15 April 2020

E-mail addresses:

geetadma@gmail.com (Geeta Arora)

rateshqadian@gmail.com (Ratesh Kumar)

maanh52@gmail.com (Harpreet Kaur)

* Corresponding author

has also been observed experimentally and from the real-time observation that there are many complex systems in the real world like relaxation in viscoelastic material, pollution diffusion in the surrounding, charge transport in amorphous semiconductors and many more which show anomalous dynamics. This capability of fractional differential equations of explaining the abnormal dynamic of the system with more efficiency and accuracy has gained huge attention from the scientific community. Many of the important classical differential equations with integer-order has got extensions to the generalized fraction differential equation with an arbitrary order for in-depth study of the corresponding physical model. But general analytic solution for many fractional differential equations which are non-homogeneous in nature are very difficult and cumbersome to achieve. Moreover, finding the solution of such equations becomes more challenging when there are nonlinearities in the equations.

Therefore, many researchers are involved in developing the various numerical and semi-analytic schemes for finding solutions to the different problems governed by these differential equations. Some of the fractional differential equations which had been recently studied because of their capability of explaining the real time phenomena's were fractional Black-Scholes equation (Duan et al., 2017), time-fractional Klein–Gordon equations (Hosseini et al., 2018; Inc et al., 2018), time-fractional Fisher's equation (Atangana, 2016; Zhang et al., 2014), fractional Bagley Torvik equation (Ray, 2012), time-fractional Burgers' equation (Inc, 2008; Khan et al., 2012), Fitzhugh–Nagumo fractional differential equation (Kumar et al., 2018), fractional Ginzburg–Landau equation (Mohebbi, 2018; Shen et al., 2018), fractional Korteweg–de Vries–Burgers' equation (Odibat & Momani, 2009; Wang, 2006), nonlinear fractional order oscillatory Van der Pol system (Ray & Patra, 2013), fractional Poisson equation (Heydari et al., 2013), fractional Riccati differential equations (Momani & Shawagfeh, 2006), fractional Schrodinger equation (Bezerra et al., 2018), fractional Sine-Gordon equations (Karayer et al., 2018), fractional Bioheat equations (Singh et al., 2011), time fractional Caudrey–Dodd–Gibbon–Sawada–Kotera equation (Baleanu et al., 2018), Sharma–Tasso–Olver equation (Roy et al., 2018), Fokker–Planck fractional equation (Mahdy & Marai, 2018; Zhang et al., 2018), fractional Telegraph equation (Momani, 2005; Tawfik et al., 2018), time-fractional generalized Boussinesq equation (Lu et al., 2018), Navier–Stokes time-fractional differential equation (Momani & Odibat, 2006b), time-fractional wave equation (Odibat & Momani, 2006) and two-dimensional fractional Helmholtz equations (Abuasad et al., 2019).

Fractional coupled Burgers' equation is also a very important equation in the field of fluid mechanics to study the motion of fluids concentrations under the effect of gravity. It is a mathematical model of time-dependent sedimentation or creaming of different concentrations of two kinds of particles in fluid colloids or suspensions, under the effect of gravity (Esipov, 1995). Burgers' equations are the special case of Navier Stokes'

equations and are very much important in the field of science and technology. Researchers are in continuous progress to study the different characteristics of the phenomenon governed by the fractional models by developing the different algorithms to solve time-fractional coupled Burgers' equation such as Fractional Variational iteration method (FVIM) (Prakash et al., 2015), Differential Transformation Method (DTM) (Liu & Hou, 2011), Homotopy Perturbation Method (HPM) (Yildirim & Kelleci, 2010), Coupled Fractional Reduced Differential Transform Method (CFRDTM) (Ray, 2013) and Adomian Decomposition Method (ADM) (Chen & An, 2008). But the study of characteristics of different concentrations of two kinds of particles governed by fractional coupled Burgers' equation has not been investigated yet by any of the scale 3 Haar wavelet-based technique simultaneously with space and time fraction.

Wavelets are one of the modernistic orthonormal functions which have the capability of dilation and translation. Because of these properties, numerical techniques that involve wavelet bases are showing the qualitative improvement in contrast with other methods. In literature, dyadic wavelets are in preponderance. In 1995, Chui and Lian had developed the scale 3 Haar wavelets by using the process of multiresolution analysis. In 2018, Mittal and Pandit (2018a, 2018b & 2019) had used the scale 3 Haar wavelets for solving the various types of differential equations and found that these wavelet bases were equally competent in solving the various types of mathematical models governed by differential equations. Also, it was shown by them that the scale 3 Haar wavelet had a faster rate of convergence as compared to the dyadic wavelets. Moreover, investigation of characteristics of the solution to the fractional coupled Burgers' equation has not been done yet by the Scale 3 Haar wavelet methods as far as our knowledge is concerned. This encourages us to develop a new technique using scale 3 Haar wavelet for analyzing the behavior of systems governed by the fractional coupled Burgers' equation.

The prime objective of the proposed work is to provide a new numerical technique for obtaining the solution of space-time fractional-coupled Burgers' equation (Equation 1) emerging in the field of fluid dynamics using scale 3 Haar wavelet bases

$$\begin{cases} \frac{\partial^\alpha u}{\partial t^\alpha} = \frac{\partial^2 u}{\partial x^2} - \eta u \frac{\partial^\beta u}{\partial x^\beta} - \mu \frac{\partial(uv)}{\partial x} \\ \frac{\partial^\gamma v}{\partial t^\gamma} = \frac{\partial^2 v}{\partial x^2} - \xi v \frac{\partial^\delta v}{\partial x^\delta} - \lambda \frac{\partial(uv)}{\partial x} \end{cases}, \quad x \in [a, b], \quad t \in [0, T] \quad (1)$$

subjected to the boundary constraints (Equation 2)

$$u(a, t) = f_1(t), \quad u(b, t) = f_2(t), \quad v(a, t) = \varphi_1(t), \quad v(b, t) = \varphi_2(t) \quad \forall t \in [0, T] \quad (2)$$

and with the constraints at the initial value (Equation 3)

$$u(x, 0) = h(x) \quad , \quad v(x, 0) = p(x) \quad \forall x \in [a, b] \quad (3)$$

where $\alpha, \beta, \gamma, \delta$ represents the order of fractional derivatives such that $0 < \alpha, \beta, \gamma, \delta \leq 1$. Different variations can be observed in the solution space by giving different values to these four parameters $\alpha, \beta, \gamma, \delta$. However, on taking $\alpha = \beta = \gamma = \delta = 1$ the fractional-coupled Burgers' equation will respond like a classical coupled Burgers' equation with integer order. $\eta, \zeta, \mu, \lambda$ are arbitrary constants depending upon the system parameter like Peclet number and Reynold number.

The manuscript follows the sequence of sections as described: In section 2, explicit forms of scale 3 Haar wavelets with their families and procedure to find their integrals have been explained briefly. Representation of the solution using scale 3 Haar wavelets is explained in section 3. Section 4 explains the method of solution using scale 3 Haar wavelets. In section 5, the convergence of the method is discussed. In section 6, solutions of two different coupled Burgers' fractional equations are produced using the present method to analyze the efficiency and performance of the present method. In section 7, the conclusion drawn from the results and future research ideas are given.

Scale 3 Haar Wavelets and its Integrals

The mathematical expressions for father wavelet (Scale 3 Haar function) and mother wavelets for scale 3 Haar wavelet family with dilation factor three (Chui & Lian, 1995; Mittal & Pandit, 2018a) are given in Equation 4, 5 and 6

$$\text{Haar scaling function } h_1(t) = \begin{cases} 1 & 0 \leq t < 1 \\ 0 & \text{elsewhere} \end{cases} \quad (4)$$

$$h_i(t) = \psi^1(3^j t - k) = \frac{1}{\sqrt{2}} \begin{cases} -1 & \alpha_1(i) \leq t < \alpha_2(i) \\ 2 & \alpha_2(i) \leq t < \alpha_3(i) \\ -1 & \alpha_3(i) \leq t < \alpha_4(i) \\ 0 & \text{elsewhere} \end{cases}, \text{ for } i = 2, 4, \dots, 3p - 1 \quad (5)$$

$$h_i(t) = \psi^2(3^j t - k) = \sqrt{\frac{3}{2}} \begin{cases} 1 & \alpha_1(i) \leq t < \alpha_2(i) \\ 0 & \alpha_2(i) \leq t < \alpha_3(i) \\ -1 & \alpha_3(i) \leq t < \alpha_4(i) \\ 0 & \text{elsewhere} \end{cases}, \text{ for } i = 3, 6, \dots, 3p \quad (6)$$

where $\alpha_1(i) = \frac{k}{p}, \alpha_2(i) = \frac{3k+1}{3p}, \alpha_3(i) = \frac{(3k+2)}{3p}, \alpha_4(i) = \frac{k+1}{p}, p = 3^j, j = 0, 1, 2, \dots, k = 0, 1, 2, \dots, p - 1$.

Here i, j, k respectively represent the wavelet number, level of resolution (dilation) and translation parameters of wavelet family. The values of i (for $i > 1$) can be calculated with the help of j, k by using the following relations $i - 1 = 3^j + 2k$ for even values of i and $i - 2 = 3^j + 2k$ for odd values of i . By using this relation for different dilation and translations of $h_2(t), h_3(t)$ we will get the wavelet family as $h_1(t), h_2(t), h_3(t), h_4(t), h_5(t), h_6(t)...$ where $h_2(t)$ and $h_3(t)$ are also called mother wavelets and rest all the wavelets which we have obtained from mother wavelets are called daughter wavelets.

The main difference which makes the scale 3 Haar wavelets better than the dyadic wavelets is that only one mother wavelet is responsible for the construction of whole wavelet family but in case of scale 3 Haar wavelets, two mother wavelets with different shapes are responsible for the construction of the whole family. Because of this fact, scale 3 Haar wavelets increase the convergence rate of the solution. The construction of scale 3 Haar wavelet family is done by using the properties of Multi-resolution analysis which are described below

Now one can easily integrate the equations (Equation 4, 5 and 6) with the desired number of times over the interval $[A, B]$ by using Riemann Liouville Integral formula (Das, 2011) as given in Equation 7

$$q_{\beta,i}(t) = \frac{1}{\Gamma(\beta)} \int_A^t h_i(x)(t-x)^{\beta-1} dx$$

$$\forall 0 \leq \beta \leq m, \quad m = 1,2,3 \dots \dots, \quad i = 1,2,3, \dots \dots 3p \tag{7}$$

After evaluating the above integrals for Equation 4, we get Equation 8

$$q_{\beta,i}(t) = \frac{t^\beta}{\Gamma(\beta+1)} \text{ for } i = 1 \tag{8}$$

Using Equation 7 on Equation 5, we get the values of $q_{\beta,i}(t)$'s for $i = 2, 4, 6, 8 \dots, 3p - 1$ are given by Equation 9

$$q_{\beta,i}(t) = \frac{1}{\sqrt{2}} \left\{ \begin{array}{ll} 0 & \text{for } 0 \leq t \leq \alpha_1(i) \\ \frac{-1}{\Gamma(\beta+1)}(t-\alpha_1(i))^\beta & \text{for } \alpha_1(i) \leq t \leq \alpha_2(i) \\ \frac{1}{\Gamma(\beta+1)}[-(t-\alpha_1(i))^\beta + 3(t-\alpha_2(i))^\beta] & \text{for } \alpha_2(i) \leq t \leq \alpha_3(i) \\ \frac{1}{\Gamma(\beta+1)}[-(t-\alpha_1(i))^\beta + 3(t-\alpha_2(i))^\beta - 3(t-\alpha_3(i))^\beta] & \text{for } \alpha_3(i) \leq t \leq \alpha_4(i) \\ \frac{1}{\Gamma(\beta+1)}[-(t-\alpha_1(i))^\beta + 3(t-\alpha_2(i))^\beta - 3(t-\alpha_3(i))^\beta + (t-\alpha_4(i))^\beta] & \text{for } \alpha_4(i) \leq t \leq 1 \end{array} \right\} \tag{9}$$

Using Equation 7 on Equation 6, we get the values of $q_{\beta,i}(t)$'s for $i = 3, 5, 7, 9 \dots, 3p$ which are given by Equation 10

$$q_{\beta,i}(t) = \sqrt{\frac{3}{2}} \left\{ \begin{array}{ll} 0 & \text{for } 0 \leq t \leq \alpha_1(i) \\ \frac{1}{\Gamma(\beta+1)}(t - \alpha_1(i))^\beta & \text{for } \alpha_1(i) \leq t \leq \alpha_2(i) \\ \frac{1}{\Gamma(\beta+1)}[(t - \alpha_1(i))^\beta - (t - \alpha_2(i))^\beta] & \text{for } \alpha_2(i) \leq t \leq \alpha_3(i) \\ \frac{1}{\Gamma(\beta+1)}[(t - \alpha_1(i))^\beta - (t - \alpha_2(i))^\beta - (t - \alpha_3(i))^\beta] & \text{for } \alpha_3(i) \leq t \leq \alpha_4(i) \\ \frac{1}{\Gamma(\beta+1)}[(t - \alpha_1(i))^\beta - (t - \alpha_2(i))^\beta - (t - \alpha_3(i))^\beta + (t - \alpha_4(i))^\beta] & \text{for } \alpha_4(i) \leq t \leq 1 \end{array} \right\} \quad (10)$$

Approximation of Solution

Using the properties of scale 3 Haar wavelets, any function $x(t) \in L_2(R)$ can be expressed as given in Equation 11

$$u(t) = \sum_{i=0}^{\infty} a_i h_i(t) = a_1 h_1(t) + \sum_{\text{even } i} a_i \psi^1(3^j t - k) + \sum_{\text{odd } i} a_i \psi^2(3^j t - k) \quad (11)$$

Here a_i 's are the wavelet coefficients whose values are to be determined by the proposed method. But for computational purpose, one can consider a finite number of terms. By considering the first $3p$ terms to approximate the function $u(t)$ we get Equation 12

$$u(t) \approx u_{3p} = \sum_{i=0}^{3p} a_i h_i(t) \quad (12)$$

where $p = 3^j, j = 0, 1, 2 \dots$

METHOD OF SOLUTION

By applying the quasi-linearization technique to linearize the non-linear terms of Equation 1, 2 and 3, we get the equivalent expression given by Equation 13, 14, 15 and 16

$$(uv_x)_{r+1} = u_{r+1}(v_x)_r + u_r(v_x)_{r+1} - u_r(v_x)_r \quad (13)$$

$$(vu_x)_{r+1} = v_{r+1}(u_x)_r + v_r(u_x)_{r+1} - v_r(u_x)_r \quad (14)$$

$$(uu_\beta)_{r+1} = u_{r+1}(u_\beta)_r + u_r(u_\beta)_{r+1} - u_r(u_\beta)_r \quad (15)$$

$$(vv_\delta)_{r+1} = v_{r+1}(v_\delta)_r + v_r(v_\delta)_{r+1} - v_r(v_\delta)_r \quad (16)$$

Using Equation 13, 14, 15 and 16, non-linear coupled fractional differential Equation 1, 2 and 3 transformed into a sequence of linear differential Equations 17 and 18

$$\begin{aligned} \left(\frac{\partial^\alpha u}{\partial t^\alpha}\right)_{r+1} &= (u_{xx})_{r+1} - \eta(u_{r+1}(u_\beta)_r + u_r(u_\beta)_{r+1} - u_r(u_\beta)_r) \\ &\quad - \mu[(u_{r+1}(v_x)_r + u_r(v_x)_{r+1} - u_r(v_x)_r) + (v_{r+1}(u_x)_r + v_r(u_x)_{r+1} - v_r(u_x)_r)] \end{aligned} \quad (17)$$

$$\begin{aligned} \left(\frac{\partial^\gamma v}{\partial t^\gamma}\right)_{r+1} &= (u_{xx})_{r+1} - \xi(v_{r+1}(v_\delta)_r + v_r(v_\delta)_{r+1} - v_r(v_\delta)_r) \\ &\quad - \lambda[(u_{r+1}(v_x)_r + u_r(v_x)_{r+1} - u_r(v_x)_r) + (v_{r+1}(u_x)_r + v_r(u_x)_{r+1} - v_r(u_x)_r)] \end{aligned} \quad (18)$$

subjected to the boundary constraints given by Equation 19

$$\begin{aligned} u(a, t_{r+1}) &= f_1(t_{r+1}) \quad , u(b, t_{r+1}) = f_2(t_{r+1}) \quad , v(a, t_{r+1}) = \varphi_1(t_{r+1}) \\ v(b, t_{r+1}) &= \varphi_2(t_{r+1}) \end{aligned} \quad (19)$$

and with the constraints on initial values given by Equation 20

$$u(x, 0) = h(x), v(x, 0) = p(x), \forall x \in [a, b] \quad , t_{r+1} \in [0, T] \text{ and } r = 0, 1, 2 \dots m - 1 \quad (20)$$

here t_{r+1} represents $(r + 1)^{\text{th}}$ approximation for t in the process of quasilinearization.

$$u_{xx}(x, t) = \sum_{i=1}^{3m} a_i h_i(x) \quad (21)$$

$$v_{xx}(x, t) = \sum_{i=1}^{3m} b_i h_i(x) \quad (22)$$

Integrating the Equation 21 and 22 with respect to t from t_r to t_{r+1} to we get

$$u_{xx}(x, t_{r+1}) = (t_{r+1} - t_r) \sum_{i=1}^{3m} a_i h_i(x) + u_{xx}(x, t_r) \quad (23)$$

$$v_{xx}(x, t_{r+1}) = (t_{r+1} - t_r) \sum_{i=1}^{3m} b_i h_i(x) + v_{xx}(x, t_r) \quad (24)$$

Now integrating Equation 23 and 24 with respect to x within the limits 0 to x we get

$$u_x(x, t_{r+1}) = (t_{r+1} - t_r) \sum_{i=1}^{3m} a_i q_{i,1}(x) + u_x(x, t_r) + (u_x(0, t_{r+1}) - u_x(0, t_r)) \quad (25)$$

$$v_x(x, t_{r+1}) = (t_{r+1} - t_r) \sum_{i=1}^{3m} b_i q_{i,1}(x) + v_x(x, t_r) + (v_x(0, t_{r+1}) - v_x(0, t_r)) \quad (26)$$

Again, integrating the Equation 25 and 26 with respect to x within the limits 0 to x we get

$$u(x, t_{r+1}) = (t_{r+1} - t_r) \sum_{i=1}^{3m} a_i q_{i,2}(x) + (u(x, t_r) - u(0, t_r)) + x(u_x(0, t_{r+1}) - u_x(0, t_r)) + u(0, t_{r+1}) \quad (27)$$

$$v(x, t_{r+1}) = (t_{r+1} - t_r) \sum_{i=1}^{3m} b_i q_{i,2}(x) + (v(x, t_r) - v(0, t_r)) + x(v_x(0, t_{r+1}) - v_x(0, t_r)) + v(0, t_{r+1}) \quad (28)$$

on substitute the values of unknown quantities $u_x(0, t_{r+1}) - u_x(0, t_r)$, $v_x(0, t_{r+1}) - v_x(0, t_r)$ by evaluating it from the above equations using $x = 1$ in the Equation 27 and 28, we get

$$u(x, t_{r+1}) = (t_{r+1} - t_r) \sum_{i=1}^{3m} a_i (q_{i,2}(x) - x q_{i,2}(1)) + (u(x, t_r) - u(0, t_r)) + x(u(1, t_{r+1}) - u(0, t_{r+1})) - x(u(1, t_r) - u(0, t_r)) + u(0, t_{r+1}) \quad (29)$$

$$v(x, t_{r+1}) = (t_{r+1} - t_r) \sum_{i=1}^{3m} b_i (q_{i,2}(x) - x q_{i,2}(1)) + (v(x, t_r) - v(0, t_r)) + x(v(1, t_{r+1}) - v(0, t_{r+1})) - x(v(1, t_r) - v(0, t_r)) + v(0, t_{r+1}) \quad (30)$$

$$u_x(x, t_{r+1}) = (t_{r+1} - t_r) \sum_{i=1}^{3m} a_i (q_{i,1}(x) - q_{i,2}(1)) + u_x(x, t_r) + (u(1, t_{r+1}) - u(0, t_{r+1})) - (u(1, t_r) - u(0, t_r)) \quad (31)$$

$$v_x(x, t_{r+1}) = (t_{r+1} - t_r) \sum_{i=1}^{3m} b_i (q_{i,1}(x) - q_{i,2}(1)) + v_x(x, t_r) + (v(1, t_{r+1}) - v(0, t_{r+1})) - (v(1, t_r) - v(0, t_r)) \quad (32)$$

$$\frac{\partial^\alpha u}{\partial t^\alpha}(x, t_{r+1}) = \frac{(t_{r+1} - t_r)^{1-\alpha}}{\Gamma(2-\alpha)} \sum_{i=1}^{3m} a_i (q_{i,2}(x) - x q_{i,2}(1)) + x \frac{\partial^\alpha}{\partial t^\alpha} (u(1, t_{r+1}) - u(0, t_{r+1})) + \frac{\partial^\alpha u}{\partial t^\alpha}(0, t_{r+1}) \quad (33)$$

$$\begin{aligned} \frac{\partial^\beta u}{\partial x^\beta}(x, t_{r+1}) &= (t_{r+1} - t_r) \sum_{i=1}^{3m} a_i (q_{i,2-\beta}(x) - \frac{x^\beta}{\Gamma(2-\beta)} q_{i,2}(1)) + \frac{\partial^\beta u}{\partial x^\beta}(x, t_r) \\ &+ \frac{x^\beta}{\Gamma(2-\beta)} [(u(1, t_{r+1}) - u(0, t_{r+1})) - (u(1, t_r) - u(0, t_r))] \end{aligned} \quad (34)$$

$$\begin{aligned} \frac{\partial^\gamma v}{\partial t^\gamma}(x, t_{r+1}) &= \frac{(t_{r+1} - t_r)^{1-\gamma}}{\Gamma(2-\gamma)} \sum_{i=1}^{3m} b_i (q_{i,2}(x) - x q_{i,2}(1)) \\ &+ x \frac{\partial^\alpha}{\partial t^\alpha} (v(1, t_{r+1}) - v(0, t_{r+1})) + \frac{\partial^\alpha v}{\partial t^\alpha}(0, t_{r+1}) \end{aligned} \quad (35)$$

$$\begin{aligned} \frac{\partial^\delta v}{\partial x^\delta}(x, t_{r+1}) &= (t_{r+1} - t_r) \sum_{i=1}^{3m} a_i (q_{i,2-\delta}(x) - \frac{x^\delta}{\Gamma(2-\delta)} q_{i,2}(1)) + \frac{\partial^\delta v}{\partial x^\delta}(x, t_r) \\ &+ \frac{x^\delta}{\Gamma(2-\delta)} [(v(1, t_{r+1}) - v(0, t_{r+1})) - (v(1, t_r) - v(0, t_r))] \end{aligned} \quad (36)$$

Now using the boundary constraints and discretizing the space variable as $x \rightarrow x_l$ where $x_l = \frac{2l-1}{6p}$, $l = 0, 1, 2, \dots, 2p$ in the Equation 29, 30, 31, 32, 33, 34, 35 and 36 and substituting the values obtained in Equation 17 and 18 the following system of equations (Equation 37) are obtained for different values of r

$$\left. \begin{aligned} a_{1 \times 3p} A_{3p \times 3p} + b_{1 \times 3p} B_{3p \times 3p} &= C_{1 \times 3p} \\ b_{1 \times 3p} D_{3p \times 3p} + a_{1 \times 3p} E_{3p \times 3p} &= F_{1 \times 3p} \end{aligned} \right\} \quad (37)$$

Where the Equation 38, 39, 40, 41, 42 and 43 respectively represents the values of A , B , C , D , E and F as

$$A = \left[\begin{array}{c} \frac{(t_{r+1} - t_r)^{1-\alpha}}{\Gamma(2-\alpha)} (q_{i,2}(x_l) - x_l q_{i,2}(1)) \\ - (t_{r+1} - t_r) \left\{ \begin{array}{c} h_i(x_l) - \eta \left(\begin{array}{c} (u_\beta)_r (q_{i,2}(x_l) - x_l q_{i,2}(1)) \\ + u_r \left(q_{i,2-\beta}(x_l) - \frac{x_l^\beta}{\Gamma(2-\beta)} (q_{i,2}(1)) \right) \end{array} \right) \\ - \mu \left((v_x)_r (q_{i,2}(x_l) - x_l q_{i,2}(1)) + v_r (q_{i,1}(x_l) - q_{i,2}(1)) \right) \end{array} \right\} \end{array} \right] \quad (38)$$

$$B = \left[\mu (t_{r+1} - t_r) \left((u_x)_r (q_{i,2}(x_l) - x_l q_{i,2}(1)) + u_r (q_{i,1}(x_l) - q_{i,2}(1)) \right) \right] \quad (39)$$

$$\begin{aligned}
 C = & u_{xx}(x_l, t_r) \\
 & - \eta \left[(u_\beta)_r \left((u(x_l, t_r) - f_1(t_r)) + x_l(f_2(t_{r+1}) - f_1(t_{r+1})) - x_l(f_2(t_r) - f_1(t_r)) + f_1(t_{r+1})) \right) \right. \\
 & + u_r \left(\frac{\partial^\beta u}{\partial x^\beta}(x_l, t_r) + \frac{x_l^\beta}{\Gamma(2-\beta)} \left((f_2(t_{r+1}) - f_1(t_{r+1})) - (f_2(t_r) - f_1(t_r)) \right) \right) - u_r(u_\beta)_r \left. \right] \\
 & - \mu \left[\left\{ (v_x)_r \left((u(x_l, t_r) - f_1(t_r)) + x_l(f_2(t_{r+1}) - f_1(t_{r+1})) - x_l(f_2(t_r) - f_1(t_r)) + f_1(t_{r+1})) \right) \right\} \right. \\
 & + u_r \left(v_x(x_l, t_r) + \left((\varphi_2(t_{r+1}) - \varphi_1(t_{r+1})) - (\varphi_2(t_r) - \varphi_1(t_r)) \right) \right) - u_r(v_x)_r \left. \right\} \\
 & + (u_x)_r \left((v(x_l, t_r) - \varphi_1(t_r)) + x_l \left((\varphi_2(t_{r+1}) - \varphi_1(t_{r+1})) - x_l \left((\varphi_2(t_r) - \varphi_1(t_r)) \right) + \varphi_1(t_{r+1}) \right) \right) \\
 & + v_r \left(u_x(x_l, t_r) + (f_2(t_{r+1}) - f_1(t_{r+1})) - (\varphi_2(t_r) - \varphi_1(t_r)) \right) - v_r(u_x)_r \left. \right] \\
 & - x_l \left(\frac{\partial^\alpha}{\partial t^\alpha} (f_2(t) - f_1(t)) \right)_{t=t_{r+1}} - \left(\frac{\partial^\alpha f_1(t)}{\partial t^\alpha} \right)_{t=t_{r+1}} \tag{40}
 \end{aligned}$$

$$\begin{aligned}
 D = & \left[\frac{(t_{r+1} - t_r)^{1-\gamma}}{\Gamma(2-\gamma)} (q_{i,2}(x_l) - x_l q_{i,2}(1)) \right. \\
 & - (t_{r+1} - t_r) \left\{ h_i(x_l) - \xi \left((v_\delta)_r (q_{i,2}(x_l) - x_l q_{i,2}(1)) + v_r \left(q_{i,2-\delta}(x_l) - \frac{x_l^\delta}{\Gamma(2-\delta)} (q_{i,2}(1)) \right) \right) \right. \\
 & \left. \left. - \lambda \left((u_x)_r (q_{i,2}(x_l) - x_l q_{i,2}(1)) + u_r (q_{i,1}(x_l) - q_{i,2}(1)) \right) \right\} \right] \tag{41}
 \end{aligned}$$

$$E = \left[\lambda (t_{r+1} - t_r) \left((v_x)_r (q_{i,2}(x_l) - x_l q_{i,2}(1)) + v_r (q_{i,1}(x_l) - q_{i,2}(1)) \right) \right] \tag{42}$$

$$\begin{aligned}
 F = & v_{xx}(x_l, t_r) \\
 & - \xi \left[(v_\delta)_r \left((v(x_l, t_r) - \varphi_1(t_r)) + x_l(\varphi_2(t_{r+1}) - \varphi_1(t_{r+1})) - x_l(\varphi_2(t_r) - \varphi_1(t_r)) + \varphi_1(t_{r+1}) \right) \right. \\
 & + v_r \left(\frac{\partial^\delta v}{\partial x^\delta}(x_l, t_r) + \frac{x_l^\delta}{\Gamma(2-\delta)} \left((\varphi_2(t_{r+1}) - \varphi_1(t_{r+1})) - (\varphi_2(t_r) - \varphi_1(t_r)) \right) \right) - v_r(v_\delta)_r \left. \right] \\
 & - \lambda \left[\left\{ (v_x)_r \left((u(x_l, t_r) - f_1(t_r)) + x_l(f_2(t_{r+1}) - f_1(t_{r+1})) - x_l(f_2(t_r) - f_1(t_r)) + f_1(t_{r+1})) \right) \right\} \right. \\
 & + u_r \left(v_x(x_l, t_r) + (\varphi_2(t_{r+1}) - \varphi_1(t_{r+1})) - (\varphi_2(t_r) - \varphi_1(t_r)) \right) - u_r(v_x)_r \left. \right\} \\
 & + (u_x)_r \left((v(x_l, t_r) - \varphi_1(t_r)) + x_l(\varphi_2(t_{r+1}) - \varphi_1(t_{r+1})) - x_l(\varphi_2(t_r) - \varphi_1(t_r)) + \varphi_1(t_{r+1}) \right) \\
 & + v_r \left(u_x(x_l, t_r) + (f_2(t_{r+1}) - f_1(t_{r+1})) - (f_2(t_r) - f_1(t_r)) \right) - v_r(u_x)_r \left. \right] \\
 & - x_l \left(\frac{\partial^\alpha}{\partial t^\alpha} (\varphi_2(t) - \varphi_1(t)) \right)_{t=t_{r+1}} - \left(\frac{\partial^\alpha \varphi_1(t)}{\partial t^\alpha} \right)_{t=t_{r+1}} \tag{43}
 \end{aligned}$$

The process of the solution starts by taking $r = 0, t_0 = 0$ and the boundary conditions given in Equation 44 as

$$\begin{aligned}
u(x_l, t_r) &= u(x_l, 0) = h(x_l), u_x(x_l, t_r) = u_x(x_l, 0) = h_x(x_l), \\
u_{xx}(x_l, t_r) &= u_{xx}(x_l, 0) = h_{xx}(x_l) \\
v(x_l, t_r) &= v(x_l, 0) = p(x_l), v_x(x_l, t_r) = v_x(x_l, 0) = p_x(x_l), \\
v_{xx}(x_l, t_r) &= v_{xx}(x_l, 0) = p_{xx}(x_l)
\end{aligned} \tag{44}$$

The values of wavelet coefficients can be calculated successively for different values of $r = 0, 1, 2, \dots$ by using the Equation 45 and 46

$$a_{1 \times 3p} = (C - FD^{-1}B) * (A - ED^{-1}B) \tag{45}$$

$$b_{1 \times 3p} = (C - FE^{-1}A) * (B - DE^{-1}A) \tag{46}$$

Then by putting the values of the wavelet coefficient a_i 's and b_i 's in the Equation 49 and 50 one can obtain numerically approximated solution successively for $u(x, t)$ and $v(x, t)$ for $r = 0, 1, 2, 3, \dots$ using Equation 47 and 48

$$\begin{aligned}
u(x_l, t_{r+1}) &= (t_{r+1} - t_r) \sum_{i=1}^{3m} a_i(q_{i,2}(x_l) - x_l q_{i,2}(1)) + (u(x_l, t_r) - f_1(t_r)) \\
&\quad + x_l(f_2(t_{r+1}) - f_1(t_{r+1})) - x_l(f_2(t_r) - f_1(t_r)) + f_1(t_{r+1})
\end{aligned} \tag{47}$$

$$\begin{aligned}
v(x_l, t_{r+1}) &= (t_{r+1} - t_r) \sum_{i=1}^{3m} b_i(q_{i,2}(x_l) - x_l q_{i,2}(1)) + (v(x_l, t_r) - \varphi_1(t_r)) \\
&\quad + x_l(\varphi_2(t_{r+1}) - \varphi_1(t_{r+1})) - x_l(\varphi_2(t_r) - \varphi_1(t_r)) + \varphi_1(t_{r+1})
\end{aligned} \tag{48}$$

at various times by using successive iteration for $r = 0, 1, 2, 3, \dots$

Convergence Analysis

To establish the convergence of the proposed method, we considered the asymptotic extension of Equation 47 and 48 for a fixed value of $t = t_{r+1}$ and $x = x_1$ as given below (Equation 49 and 50)

$$u(x, t) = \Delta t * \sum_{i=1}^{\infty} a_i(q_{i,2}(x) - x q_{i,2}(1)) + A + Bx ,$$

$$\text{Where } A = u(x_l, t_r) + f_1(t_{r+1}) - f_1(t_r),$$

$$B = (f_2(t_{r+1}) - f_1(t_{r+1})) - (f_2(t_r) - f_1(t_r)) \tag{49}$$

$$v(x, t) = \Delta t * \sum_{i=1}^{\infty} b_i(q_{i,2}(x_i) - x q_{i,2}(1)) + C + Dx ,$$

Where $C = (v(x_l, t_r) - \varphi_1(t_r)) + \varphi_1(t_{r+1}) ,$

$$D = (\varphi_2(t_{r+1}) - \varphi_1(t_{r+1})) - (\varphi_2(t_r) - \varphi_1(t_r)) \tag{50}$$

Now the convergence of the theorem will be proven with the help of the following lemma

Lemma 1: let $u(x) \in L^2(R)$ be any square-integrable function such that

$$|u^m(x)| \leq M, \forall x \in (0,1) \text{ and } D_*^\alpha u(x) = \sum_{i=1}^{\infty} a_i h_i(x). \text{ Then } |a_i| \leq \frac{2\sqrt{2}M}{3\Gamma(m-\alpha+1)} \times \frac{1}{3^{j(m-\alpha+\frac{1}{2})}}$$

Proof: Let $D_*^\alpha u(x) = \sum_{i=1}^{\infty} a_i h_i(x)$ be the exact solution and $D_*^\alpha u_{3p}(x) = \sum_{i=1}^{3p} a_i h_i(x)$

be the approximated solution

Now the error at the J^{th} level of resolution can be represented by Equation 51 and the value of a_i is given by Equation 52

$$\begin{aligned} \|E_j\|^2 &= \|D_*^\alpha u(x) - D_*^\alpha u_{3p}(x)\|^2 = \|\sum_{i=3p+1}^{\infty} a_i h_i(x)\|^2 = \\ &\langle \sum_{i=3p+1}^{\infty} a_i h_i(x) , \sum_{i=3p+1}^{\infty} a_i h_i(x) \rangle \\ &= \int_{-\infty}^{\infty} \sum_{i=3p+1}^{\infty} \sum_{k=3p+1}^{\infty} a_i a_k h_i(x) h_k(x) dx = \sum_{i=3p+1}^{\infty} \sum_{k=3p+1}^{\infty} a_i a_k \int_0^1 h_i(x) h_k(x) dx \\ &= \sum_{i=3p+1}^{\infty} a_i a_i = \sum_{i=3p+1}^{\infty} |a_i|^2 \tag{51} \end{aligned}$$

$$\begin{aligned} a_i &= 3^{\frac{j}{2}} \int_0^1 h_i(x) D_*^\alpha u(x) dx = 3^{\frac{j}{2}} \left(\int_0^1 \psi_i^1(x) D_*^\alpha u(x) dx + \int_0^1 \psi_i^2(x) D_*^\alpha u(x) dx \right) \\ &= 3^{\frac{j}{2}} \left[\left(\int_{\alpha_1(i)}^{\alpha_2(i)} \frac{-1}{\sqrt{2}} D_*^\alpha u(x) dx + \int_{\alpha_2(i)}^{\alpha_3(i)} \sqrt{2} D_*^\alpha u(x) dx + \int_{\alpha_3(i)}^{\alpha_4(i)} \frac{-1}{\sqrt{2}} D_*^\alpha u(x) dx \right) + \right. \\ &\quad \left. \left(\int_{\alpha_1(i)}^{\alpha_2(i)} \frac{\sqrt{3}}{2} D_*^\alpha u(x) dx + \int_{\alpha_3(i)}^{\alpha_4(i)} \frac{-\sqrt{3}}{2} D_*^\alpha u(x) dx \right) \right] \tag{52} \end{aligned}$$

By applying the mean value theorem (Sahoo & Riedel, 1998) of integral on Equation 52, we get $\varepsilon_1 \in (\alpha_1(i), \alpha_2(i))$, $\varepsilon_2 \in (\alpha_2(i), \alpha_3(i))$, $\varepsilon_3 \in (\alpha_3(i), \alpha_4(i))$ (Equation 53) such that

$$\begin{aligned}\int_{\alpha_1(i)}^{\alpha_2(i)} D_*^\alpha u(x) dx &= (\alpha_2(i) - \alpha_1(i)) D_*^\alpha u(\varepsilon_1) = \frac{1}{3^p} D_*^\alpha u(\varepsilon_1) \\ \int_{\alpha_2(i)}^{\alpha_3(i)} D_*^\alpha u(x) dx &= (\alpha_3(i) - \alpha_2(i)) D_*^\alpha u(\varepsilon_2) = \frac{1}{3^p} D_*^\alpha u(\varepsilon_2) \\ \int_{\alpha_3(i)}^{\alpha_4(i)} D_*^\alpha u(x) dx &= (\alpha_4(i) - \alpha_3(i)) D_*^\alpha u(\varepsilon_3) = \frac{1}{3^p} D_*^\alpha u(\varepsilon_3)\end{aligned}\quad (53)$$

Now using Equation 53, Equation 52 becomes Equation 54

$$\begin{aligned}a_i &= \frac{3^{\frac{j}{2}}}{3^p} \left(\left(\frac{\sqrt{3}-1}{\sqrt{2}} \right) D_*^\alpha u(\varepsilon_1) + \sqrt{2} D_*^\alpha u(\varepsilon_2) - \left(\frac{\sqrt{3}-1}{\sqrt{2}} \right) D_*^\alpha u(\varepsilon_3) \right) \\ &= \frac{3^{\frac{j}{2}}}{3^p} \left(\left(\frac{\sqrt{3}-1}{\sqrt{2}} \right) D_*^\alpha u(\varepsilon_1) + \sqrt{2} D_*^\alpha u(\varepsilon_2) - \left(\frac{\sqrt{3}-1}{\sqrt{2}} \right) D_*^\alpha u(\varepsilon_3) \right) \\ &= 3^{\frac{-j-2}{2}} \left(\left(\frac{\sqrt{3}-1}{\sqrt{2}} \right) D_*^\alpha u(\varepsilon_1) + \sqrt{2} D_*^\alpha u(\varepsilon_2) - \left(\frac{\sqrt{3}-1}{\sqrt{2}} \right) D_*^\alpha u(\varepsilon_3) \right)\end{aligned}\quad (54)$$

Now by using the Caputo definition of fractional derivatives (Das, 2011) on Equation 54, we get Equation 55,

$$\begin{aligned}a_i &= 3^{\frac{-j-2}{2}} \left(\left(\frac{\sqrt{3}-1}{\sqrt{2}} \right) \left(\frac{1}{\Gamma(m-\alpha)} \int_0^{\varepsilon_1} \frac{u^m(z)}{(\varepsilon_1-z)^{\alpha-m+1}} dz \right) + \sqrt{2} \left(\frac{1}{\Gamma(m-\alpha)} \int_0^{\varepsilon_2} \frac{u^m(z)}{(\varepsilon_2-z)^{\alpha-m+1}} dz \right) \right. \\ &\quad \left. - \left(\frac{\sqrt{3}-1}{\sqrt{2}} \right) \left(\frac{1}{\Gamma(m-\alpha)} \int_0^{\varepsilon_3} \frac{u^m(z)}{(\varepsilon_3-z)^{\alpha-m+1}} dz \right) \right) \\ &= \frac{3^{\frac{-j-2}{2}}}{\sqrt{2} \Gamma(m-\alpha)} \left((\sqrt{3}-1) \int_0^{\varepsilon_1} \frac{u^m(z)}{(\varepsilon_1-z)^{\alpha-m+1}} dz - 2 \int_{\varepsilon_2}^0 \frac{u^m(z)}{(\varepsilon_2-z)^{\alpha-m+1}} dz \right. \\ &\quad \left. - (\sqrt{3}-1) \left(\int_0^{\varepsilon_1} \frac{u^m(z)}{(\varepsilon_3-z)^{\alpha-m+1}} dz + \int_{\varepsilon_1}^{\varepsilon_3} \frac{u^m(z)}{(\varepsilon_3-z)^{\alpha-m+1}} dz \right) \right) \\ &= \frac{3^{\frac{-j-2}{2}}}{\sqrt{2} \Gamma(m-\alpha)} \left((\sqrt{3}-1) \left(\int_0^{\varepsilon_1} \frac{u^m(z)}{(\varepsilon_1-z)^{\alpha-m+1}} dz - \int_0^{\varepsilon_1} \frac{u^m(z)}{(\varepsilon_3-z)^{\alpha-m+1}} dz \right) \right. \\ &\quad \left. - (\sqrt{3}-1) \left(\int_{\varepsilon_1}^{\varepsilon_3} \frac{u^m(z)}{(\varepsilon_3-z)^{\alpha-m+1}} dz \right) - 2 \int_{\varepsilon_2}^0 \frac{u^m(z)}{(\varepsilon_2-z)^{\alpha-m+1}} dz \right)\end{aligned}\quad (55)$$

Taking modulus on both side of Equation 55 and applying the properties of modulus, we get Equation 56, 57, 58, 59, 60, 61 and 62

$$a_i = \left| \frac{3^{-\frac{j-2}{2}}}{\sqrt{2} \Gamma(m-\alpha)} \left((\sqrt{3}-1) \left(\int_0^{\varepsilon_1} \frac{u^m(z)}{(\varepsilon_1-z)^{\alpha-m+1}} dz - \int_0^{\varepsilon_1} \frac{u^m(z)}{(\varepsilon_3-z)^{\alpha-m+1}} dz \right) - (\sqrt{3}-1) \left(\int_{\varepsilon_1}^{\varepsilon_3} \frac{u^m(z)}{(\varepsilon_3-z)^{\alpha-m+1}} dz \right) - 2 \int_{\varepsilon_2}^0 \frac{u^m(z)}{(\varepsilon_2-z)^{\alpha-m+1}} dz \right) \right| \tag{56}$$

$$|a_i| \leq \frac{3^{-\frac{j-2}{2}}}{\sqrt{2} \Gamma(m-\alpha)} \left[(\sqrt{3}-1) \left| \int_0^{\varepsilon_1} \frac{u^m(z)}{(\varepsilon_1-z)^{\alpha-m+1}} dz - \int_0^{\varepsilon_1} \frac{u^m(z)}{(\varepsilon_3-z)^{\alpha-m+1}} dz \right| + (\sqrt{3}-1) \left| \int_{\varepsilon_1}^{\varepsilon_3} \frac{u^m(z)}{(\varepsilon_3-z)^{\alpha-m+1}} dz \right| + 2 \left| \int_{\varepsilon_2}^0 \frac{u^m(z)}{(\varepsilon_2-z)^{\alpha-m+1}} dz \right| \right] \tag{57}$$

$$|a_i| \leq \frac{3^{-\frac{j-2}{2}}}{\sqrt{2} \Gamma(m-\alpha)} \left[(\sqrt{3}-1) \int_0^{\varepsilon_1} |u^m(z)| \left| \frac{1}{(\varepsilon_1-z)^{\alpha-m+1}} - \frac{1}{(\varepsilon_3-z)^{\alpha-m+1}} \right| dz + (\sqrt{3}-1) \int_{\varepsilon_1}^{\varepsilon_3} |u^m(z)| \frac{1}{(\varepsilon_3-z)^{\alpha-m+1}} dz + 2 \int_{\varepsilon_2}^0 |u^m(z)| \frac{1}{(\varepsilon_2-z)^{\alpha-m+1}} dz \right] \tag{58}$$

$$|a_i| \leq \frac{3^{-\frac{j-2}{2}} M}{\sqrt{2} \Gamma(m-\alpha)} \left[(\sqrt{3}-1) \int_0^{\varepsilon_1} \left[\frac{1}{(\varepsilon_1-z)^{\alpha-m+1}} - \frac{1}{(\varepsilon_3-z)^{\alpha-m+1}} \right] dz + (\sqrt{3}-1) \int_{\varepsilon_1}^{\varepsilon_3} \frac{1}{(\varepsilon_3-z)^{\alpha-m+1}} dz + 2 \int_{\varepsilon_2}^0 \frac{1}{(\varepsilon_2-z)^{\alpha-m+1}} dz \right] \tag{59}$$

$$|a_i| \leq \frac{3^{-\frac{j-2}{2}} M}{\sqrt{2} \Gamma(m-\alpha)} \left[\frac{(\sqrt{3}-1)}{(m-\alpha)} \left[(\varepsilon_3 - \varepsilon_1)^{m-\alpha} - \varepsilon_3^{m-\alpha} \right] + \varepsilon_1^{m-\alpha} + (\varepsilon_3 - \varepsilon_1)^{m-\alpha} \right] - 2\varepsilon_2^{m-\alpha} \tag{60}$$

$$m-\alpha > 0, \varepsilon_1 < \varepsilon_3 \Rightarrow \varepsilon_1^{m-\alpha} < \varepsilon_3^{m-\alpha} \Rightarrow \varepsilon_1^{m-\alpha} - \varepsilon_3^{m-\alpha} < 0, \varepsilon_2 > 0 \Rightarrow -2\varepsilon_2^{m-\alpha} < 0 \Rightarrow \varepsilon_1^{m-\alpha} - \varepsilon_3^{m-\alpha} - 2\varepsilon_2^{m-\alpha} < 0$$

$$|a_i| \leq \frac{3^{-\frac{j-2}{2}} M}{\sqrt{2} \Gamma(m-\alpha)} \left[\frac{(\sqrt{3}-1)}{(m-\alpha)} [2(\varepsilon_3 - \varepsilon_1)^{m-\alpha}] \right] < \frac{4 \cdot 3^{-\frac{j-2}{2}} M}{\sqrt{2} \Gamma(m-\alpha+1)} = \frac{2\sqrt{2} \cdot 3^{-\frac{j-2}{2}} M}{\Gamma(m-\alpha+1)} \times \frac{1}{3^{j(m-\alpha)}} \tag{61}$$

$$|a_i| \leq \frac{2\sqrt{2} M}{3\Gamma(m - \alpha + 1)} \times \frac{1}{3^{j(m-\alpha+\frac{1}{2})}} \quad (62)$$

Theorem 1: - If $u(x, t)$ represent the exact solution and $u_{3m}(x, t)$ represents the Scale 3 Haar wavelet-based approximated solution, then for a fixed value of $t = t_l$

$$\|E_j\| = \|u(x, t) - u_{3m}(x, t)\| \leq \frac{4\sqrt{2}M K |\Delta t|}{\Gamma(m - \alpha + 1)} \left(\frac{3^{-j(m-\alpha+\frac{1}{2})}}{1 - 3^{-(m-\alpha-\frac{1}{2})}} \right)$$

Proof. At j^{th} level of resolution, error estimation for the solution is given by

$$\begin{aligned} \|E_j\| &= \|u(x, t) - u_{3m}(x, t)\| = |\Delta t * \sum_{i=3m+1}^{\infty} a_i (q_{i,2}(x) - x q_{i,2}(1))| \\ \|E_j\|^2 &= |\Delta t|^2 * \left| \sum_{i=3m+1}^{\infty} a_i (q_{i,2}(x) - x q_{i,2}(1)) \right|^2 = \\ & \left| \int_{-\infty}^{\infty} \left(\sum_{i=3m+1}^{\infty} a_i (q_{i,2}(x) - x q_{i,2}(1)) \cdot \sum_{k=3m+1}^{\infty} a_k (q_{k,2}(x) - x q_{k,2}(1)) \right) dx \right| \\ &\leq |\Delta t|^2 * \left| \sum_{i=3m+1}^{\infty} \sum_{k=3m+1}^{\infty} \int_0^1 a_i a_k (q_{i,2}(x) - x q_{i,2}(1)) (q_{k,2}(x) - x q_{k,2}(1)) dx \right| \\ &\leq |\Delta t|^2 * |a_i a_k M_{i,k}| \end{aligned}$$

$$\text{Where } M_{i,k} = \text{Sup}_{i,k} \int_0^1 (q_{i,2}(x) - x q_{i,2}(1)) (q_{k,2}(x) - x q_{k,2}(1)) dx$$

$$\begin{aligned} \|E_j\|^2 &\leq |\Delta t|^2 * \sum_{i=3m+1}^{\infty} \left| a_i (a_{3m} M_{i,3m} + a_{3m+1} M_{i,3m+1} + a_{3m+2} M_{i,3m+2} \right. \\ & \quad \left. + a_{3m+3} M_{i,3m+3} + \dots) \right| \\ &\leq |\Delta t|^2 * \sum_{i=3m+1}^{\infty} |a_i M_i (a_{3m} + a_{3m+1} + a_{3m+2} + a_{3m+3} + \dots)| \end{aligned}$$

$$\text{Where } M_i = \text{Sup}_{i,k} M_{i,k}$$

Using Lemma 1 in the equation we get

$$\|E_j\|^2 \leq \frac{4\sqrt{2} K}{\Gamma(m-\alpha+1)} \frac{|\Delta t|^2 3^{-j(m-\alpha+\frac{1}{2})}}{1-3^{-(m-\alpha-\frac{1}{2})}} \sum_{i=3m+1}^{\infty} |a_i M_i|$$

$$\text{Take } M = \text{Sup}_i M_i$$

$$\|E_j\|^2 \leq \frac{4\sqrt{2} K |\Delta t|^2 M 3^{-j(m-\alpha+\frac{1}{2})}}{\Gamma(m-\alpha+1) 1-3^{-(m-\alpha-\frac{1}{2})}} \sum_{i=3m+1}^{\infty} |a_i| = \frac{4\sqrt{2} K |\Delta t|^2 M 3^{-j(m-\alpha+\frac{1}{2})}}{\Gamma(m-\alpha+1) 1-3^{-(m-\alpha-\frac{1}{2})}} * \frac{4\sqrt{2} K}{\Gamma(m-\alpha+1)} \frac{3^{-j(m-\alpha+\frac{1}{2})}}{1-3^{-(m-\alpha-\frac{1}{2})}}$$

$$\|E_j\| = \frac{4\sqrt{2M} K |\Delta t|}{\Gamma(m - \alpha + 1)} \left(\frac{3^{-j(m-\alpha+\frac{1}{2})}}{1 - 3^{-(m-\alpha-\frac{1}{2})}} \right) \tag{63}$$

It is clear from the Equation 63 that error bound is inversely proportional to the level of resolution which means that with the increase in the level of resolution, error bound decreases i.e. $j \rightarrow \infty \Rightarrow \|E_j\| \rightarrow 0$. This proves the convergence of solution $u(x, t)$. In a similar way, the convergence of $v(x, t)$ solution can be proved. It ensures the stability of the solutions.

RESULTS AND DISCUSSIONS FROM NUMERICAL EXPERIMENT

To describe the appropriateness of the present scheme for fractional coupled Burgers’ equation, solutions of two problems obtained by the present scheme had been analyzed and absolute errors were calculated to check the efficiency of the present scheme with the help of following formulas

$$\text{Absolute error} = |u_{exact}(t_i) - u_{num}(t_i)|$$

where t_i represents the collocation points of the domain.

Numerical Experiment No. 1: - Consider the following space-time fractional coupled Burgers’ Equation 64

$$\begin{cases} \frac{\partial^\alpha u}{\partial t^\alpha} = \frac{\partial^2 u}{\partial x^2} + 2u \frac{\partial^\beta u}{\partial x^\beta} - \frac{\partial(uv)}{\partial x} \\ \frac{\partial^\gamma v}{\partial t^\gamma} = \frac{\partial^2 v}{\partial x^2} + 2v \frac{\partial^\delta v}{\partial x^\delta} - \frac{\partial(uv)}{\partial x} \end{cases}, \quad x \in [0, 1], \quad t \in [0, T] \tag{64}$$

Subjected to the boundary conditions given in Equation 65

$$u(0, t) = 0, u(1, t) = e^{-t} \sin 1, \quad v(0, t) = 0, v(1, t) = e^{-t} \sin 1 \quad \forall t \in [0, T] \tag{65}$$

and with the initial condition given in Equation 66

$$u(x, 0) = \sin x, \quad v(x, 0) = \sin x \quad \forall x \in [0, 1] \tag{66}$$

The exact solution of the Equation 64 subjected to the conditions given in Equation 65 and 66 for $\alpha = \beta = \gamma = \delta = 1$ is

$$u(x, t) = e^{-t} \sin x \quad , \quad v(x, t) = e^{-t} \sin x$$

The numerical solution obtained by applying the given methodology for Equation 64 subjected to the conditions given in Equation 65 and 66 is

$$u(x_l, t_{r+1}) = (t_{r+1} - t_r) \sum_{i=1}^{3m} a_i (q_{i,2}(x_l) - x_l q_{i,2}(1)) + (u(x_l, t_r) - f_1(t_r)) \\ + x_l (f_2(t_{r+1}) - f_1(t_{r+1})) - x_l (f_2(t_r) - f_1(t_r)) + f_1(t_{r+1})$$

$$v(x_l, t_{r+1}) = (t_{r+1} - t_r) \sum_{i=1}^{3m} b_i (q_{i,2}(x_l) - x_l q_{i,2}(1)) + (v(x_l, t_r) - \varphi_1(t_r)) \\ + x_l (\varphi_2(t_{r+1}) - \varphi_1(t_{r+1})) - x_l (\varphi_2(t_r) - \varphi_1(t_r)) + \varphi_1(t_{r+1})$$

at the various times by using successive iteration for $r = 0, 1, 2, 3, \dots$. The process of finding the solution in the discrete form starts by taking $r = 0, t_0 = 0$ and $f_1(t_r) = 0, f_2(t_r) = e^{-t_r} \sin 1, \varphi_1(t_r) = 0, \varphi_2(t_{r+1}) = e^{-t_r} \sin 1$ for $r = 0, t_0 = 0$ and rest all the values will be obtained using the iterative process.

Results obtained for example 1 are also reported by the way of figures and tables. It can be seen from Figure 1 and Figure 2 that the solution obtained by the proposed method for the case (when $\alpha = \beta = \gamma = \delta = 1$) is in good agreement with the analytical solution available in the literature. Table 1 and Figure 3 show the absolute errors in the results obtained at the different collocation points for the case $\alpha = \beta = \gamma = \delta = 1$ and it is of order 10^{-5} which assures the efficiency and reliability of the proposed method. In Table 2, results obtained by the present method are compared with another method (Ray, 2013) available in the literature and it is found that the present method outperforms over another method available in the literature. Table 3 explains the absolute error in the solution for different values of Δt which illustrate the direct dependence of absolute error on meshsize for time variable. For better visibility contour plots and 2D-solution plots are also given in Figure 4 and Figure 5. Most important fact has been explained by the Figure 6 and Figure 7 that when we shift from one classical order derivative (integer-order 0) to another classical order derivative (integer-order 1) in the coupled Burgers' equation the behavior of the solution does not remain the same, in fact many variations have been observed in the solution space with the variation in the order of time derivative or space derivative which gives the better insight of microscopic behavior of poly-dispersive sedimentation phenomena of two different types of particle concentration in the fluid.

Table 1
Absolute error in numerical results $u(x,t)$ at collocation points for integer order $\alpha = \beta = \gamma = \delta = 1$ with $\eta = \zeta = -2, \mu = \lambda = 1$ and $\Delta t = 0.1$

Time (t)	x	0.0556	0.1667	0.2778	0.3889	0.5	0.6111	0.7222	0.8333	0.9444
0.1		2.30×10^{-5}	5.82×10^{-5}	9.26×10^{-5}	1.24×10^{-4}	1.52×10^{-4}	1.76×10^{-4}	1.97×10^{-4}	2.15×10^{-4}	2.30×10^{-4}
0.2		6.66×10^{-5}	1.69×10^{-4}	2.68×10^{-4}	3.59×10^{-4}	4.39×10^{-4}	5.09×10^{-4}	5.70×10^{-4}	6.22×10^{-4}	6.67×10^{-4}
0.3		1.04×10^{-4}	2.62×10^{-4}	4.16×10^{-4}	5.56×10^{-4}	6.80×10^{-4}	7.88×10^{-4}	8.82×10^{-4}	9.63×10^{-4}	1.03×10^{-3}
0.4		1.30×10^{-4}	3.27×10^{-4}	5.19×10^{-4}	6.93×10^{-4}	8.47×10^{-4}	9.82×10^{-4}	1.10×10^{-3}	1.20×10^{-3}	1.29×10^{-3}
0.5		1.42×10^{-4}	3.57×10^{-4}	5.64×10^{-4}	7.53×10^{-4}	9.20×10^{-4}	1.07×10^{-3}	1.19×10^{-3}	1.30×10^{-3}	1.39×10^{-3}
0.6		1.38×10^{-4}	3.44×10^{-4}	5.44×10^{-4}	7.25×10^{-4}	8.85×10^{-4}	1.03×10^{-3}	1.15×10^{-3}	1.25×10^{-3}	1.34×10^{-3}
0.7		1.17×10^{-4}	2.89×10^{-4}	4.55×10^{-4}	6.06×10^{-4}	7.40×10^{-4}	8.57×10^{-4}	9.58×10^{-4}	1.04×10^{-3}	1.12×10^{-3}
0.8		7.87×10^{-5}	1.94×10^{-4}	3.05×10^{-4}	4.05×10^{-4}	4.94×10^{-4}	5.72×10^{-4}	6.39×10^{-4}	6.97×10^{-4}	7.46×10^{-4}
0.9		2.80×10^{-5}	6.86×10^{-5}	1.08×10^{-4}	1.43×10^{-4}	1.74×10^{-4}	2.02×10^{-4}	2.25×10^{-4}	2.46×10^{-4}	2.63×10^{-4}

Table 2
Comparison of Numerical results at Random collocation Points available in Literature for Experiment. No.1 at integer-order $\alpha = \beta = \gamma = \delta = 1$ with $\eta = \zeta = -2, \mu = \lambda = 1$ and $\Delta t = 0.1$

Collocation Points (x, t)	Exact Solution $u(x, t) = v(x, t) = e^{-t} \sin x$	Numerical Solution $u(x, t)$	Numerical Solution $v(x, t)$	Scale 3 Haar wavelet method (Absolute Error)	Reduced differential Transform method (Absolute Error) (Ray, 2013)
(0.1,0.1)	0.090333	0.090329	0.090329	4.09×10^{-6}	1.62×10^{-5}
(0.2,0.2)	0.162657	0.162730	0.162730	7.38×10^{-5}	2.52×10^{-4}
(0.3,0.3)	0.218927	0.219199	0.219199	2.73×10^{-4}	1.24×10^{-3}
(0.4,0.4)	0.261035	0.261596	0.261596	5.61×10^{-4}	3.77×10^{-3}
(0.5,0.5)	0.290786	0.291659	0.291659	8.73×10^{-4}	8.86×10^{-3}
(0.6,0.6)	0.309882	0.311006	0.311006	1.12×10^{-3}	1.76×10^{-2}
(0.7,0.7)	0.319909	0.321135	0.321135	1.23×10^{-3}	3.11×10^{-2}
(0.8,0.8)	0.322329	0.323434	0.323434	1.11×10^{-3}	5.07×10^{-2}
(0.9,0.9)	0.318477	0.319182	0.319182	7.05×10^{-4}	7.71×10^{-2}

Table 3

Maximum absolute error in numerical results $u(x,t)$ and $v(x,t)$ at the integer order $\alpha = \beta = \gamma = \delta = 1$ with $\eta = \xi = -2, \mu = \lambda = 1$ for different values of Δt

Δt	$\ E(u)\ _{\infty}$	$\ E(v)\ _{\infty}$
0.0100	1.22142096728672410^{-4}	1.22142096728672410^{-4}
0.0010	$2.218389533070741 \times 10^{-6}$	$2.218389533070741 \times 10^{-6}$
0.0001	2.41311621795858910^{-8}	2.41311621795858910^{-8}

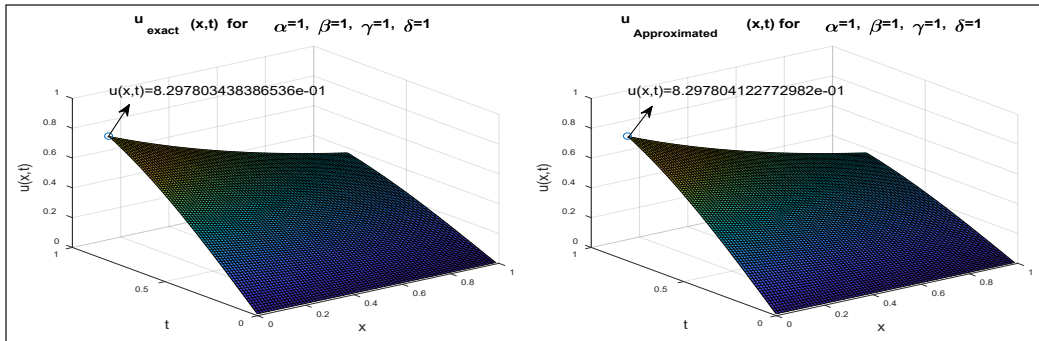


Figure 1. 3D Graphical representation of exact and approximated solution $u(x,t)$ of Experiment No. 1 for integer order $\alpha = \beta = \gamma = \delta = 1$ with $\eta = \xi = -2, \mu = \lambda = 1$ and $\Delta t = 0.01$

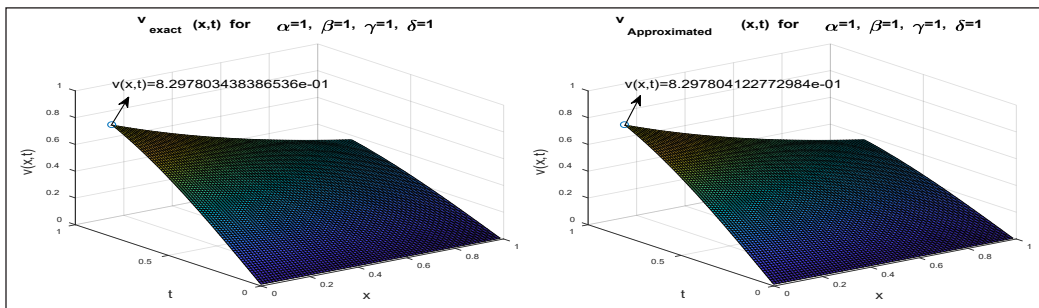


Figure 2. 3D Graphical representation of exact and approximated solution $v(x,t)$ of Experiment No. 1 at integer order $\alpha = \beta = \gamma = \delta = 1$ with $\eta = \xi = -2, \mu = \lambda = 1$ and $\Delta t = 0.01$

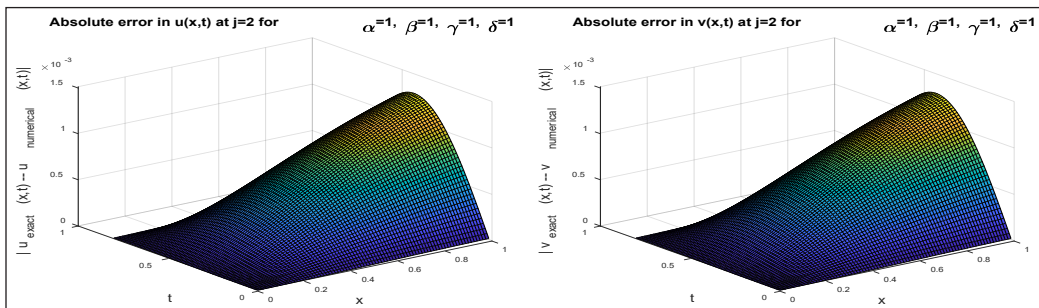


Figure 3. Surface plot of absolute error in the solutions $u(x,t)$ and $v(x,t)$ of Experiment No. 1 for $j=3$ at the integer order $\alpha = \beta = \gamma = \delta = 1$ with $\eta = \xi = -2, \mu = \lambda = 1$ and $\Delta t = 0.01$

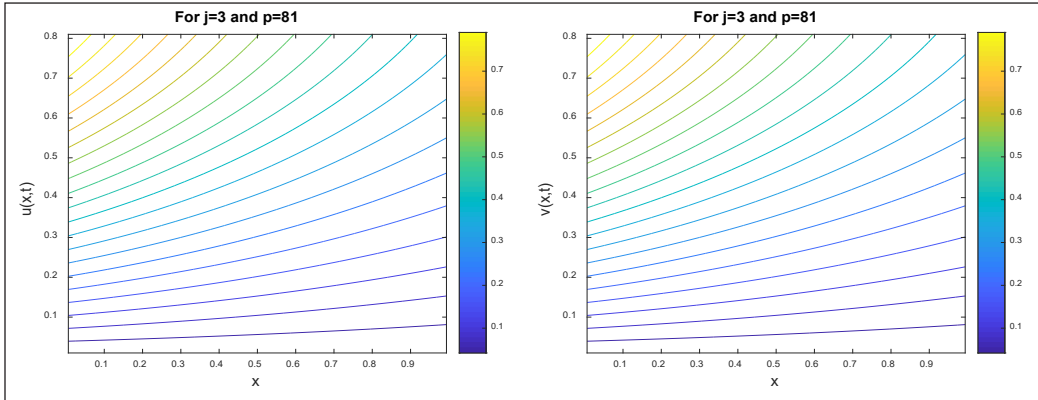


Figure 4. Contour representation of solutions $u(x,t)$ and $v(x,t)$ of Experiment No. 1 at the integer order $\alpha = \beta = \gamma = \delta = 1$ with $\eta = \xi = -2$, $\mu = \lambda = 1$ and $\Delta t = 0.01$

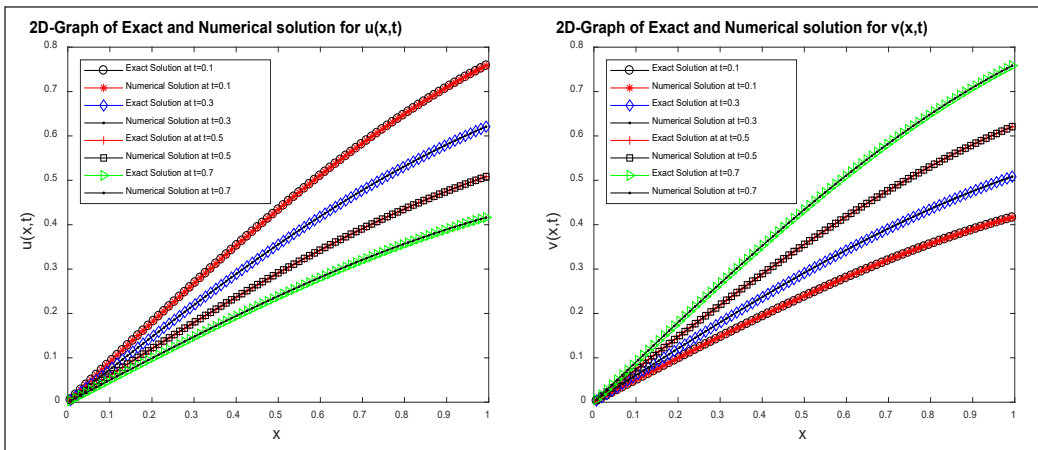


Figure 5. 2D-Graphical representation of exact and approximated solutions $u(x,t)$ and $v(x,t)$ of Experiment No. 2 for different values of t at the integer order $\alpha = \beta = \gamma = \delta = 1$ with $\eta = \xi = -2$, $\mu = \lambda = 1$ and $\Delta t = 0.01$

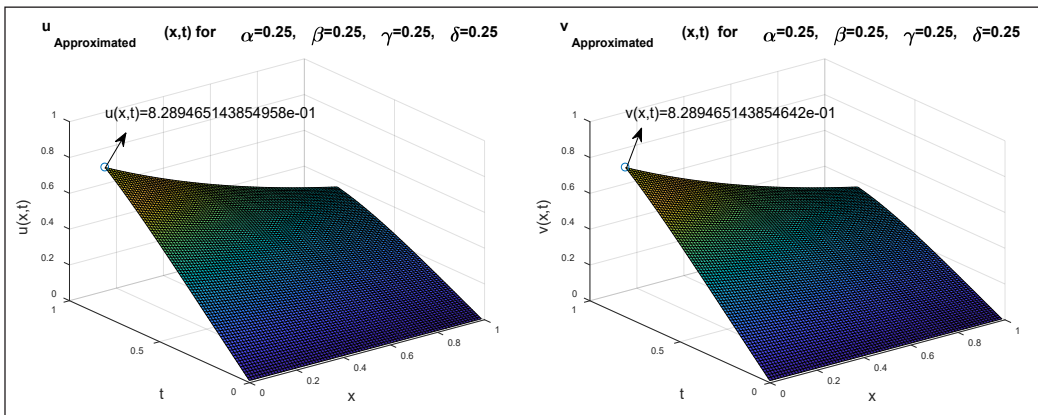


Figure 6. Approximate solution of Experiment No. 1 in 3D with different values of $\alpha, \beta \in (0,1]$ and fixed values of $\gamma = \delta = 0.25$ with $\eta = \xi = -2$, $\mu = \lambda = 1$ and $\Delta t = 0.001$

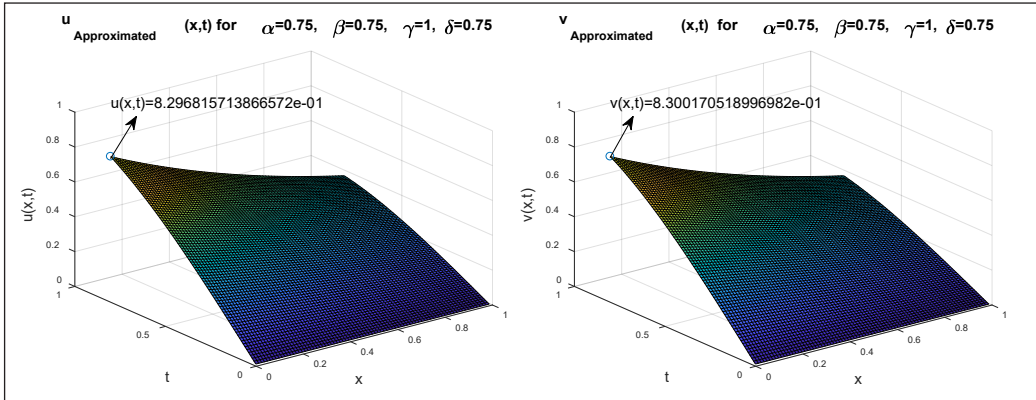


Figure 7. Approximate solution of Experiment No. 1 in 3D with different values of $\alpha, \beta, \gamma, \delta \in (0, 1]$ for which the solution behaves differently at $\eta = \xi = -2, \mu = \lambda = 1$ and $\Delta t = 0.01$.

Numerical Experiment No. 2: - Consider the following space-time fractional coupled Burgers' Equation 67

$$\begin{cases} \frac{\partial^\alpha u}{\partial t^\alpha} = \frac{\partial^2 u}{\partial x^2} + 2u \frac{\partial^\beta u}{\partial x^\beta} - \frac{\partial(uv)}{\partial x} \\ \frac{\partial^\gamma v}{\partial t^\gamma} = \frac{\partial^2 v}{\partial x^2} + 2v \frac{\partial^\delta v}{\partial x^\delta} - \frac{\partial(uv)}{\partial x} \end{cases}, \quad x \in [0, 1], \quad t \in [0, T] \quad (67)$$

Subjected to the boundary conditions given in Equation 68

$$u(0, t) = 0, u(1, t) = 0, v(0, t) = 0, v(1, t) = 0 \quad \forall \quad t \in [0, T] \quad (68)$$

and with the initial condition given in Equation 69

$$u(x, 0) = \sin(2\pi x - \pi), \quad v(x, 0) = \sin(2\pi x - \pi) \quad \forall \quad x \in [0, 1] \quad (69)$$

Analytic solution of Equation 67 when $\alpha = \beta = \gamma = \delta = 1$ is given by Equation 70 as

$$u(x, t) = e^{-4\pi^2 t} \sin(2\pi x - \pi), \quad v(x, t) = e^{-4\pi^2 t} \sin(2\pi x - \pi) \quad (70)$$

The numerical solution obtained by applying the given methodology is

$$\begin{aligned} u(x_l, t_{r+1}) = (t_{r+1} - t_r) \sum_{i=1}^{3m} a_i (q_{i,2}(x_l) - x_l q_{i,2}(1)) + (u(x_l, t_r) - f_1(t_r)) \\ + x_l (f_2(t_{r+1}) - f_1(t_{r+1})) - x_l (f_2(t_r) - f_1(t_r)) + f_1(t_{r+1}) \end{aligned}$$

$$v(x_l, t_{r+1}) = (t_{r+1} - t_r) \sum_{i=1}^{3m} b_i (q_{i,2}(x_l) - x_l q_{i,2}(1)) + (v(x_l, t_r) - \varphi_1(t_r)) + x_l (\varphi_2(t_{r+1}) - \varphi_1(t_{r+1})) - x_l (\varphi_2(t_r) - \varphi_1(t_r)) + \varphi_1(t_{r+1})$$

at various times by using successive iteration for $r = 0, 1, 2, 3, \dots$ where $f_1(t_r) = 0, f_2(t_r) = 0, \varphi_1(t_r) = 0, \varphi_2(t_r) = 0$ for $r = 0, t_0 = 0$ and rest all the values will be obtained using the iterative process.

Table 4 explains the absolute errors in the results obtained by the proposed method for example 2 by considering the domain $x \in [0,1]$ and $\Delta t = 0$ and it is of order 10^{-5} which assures the efficiency and reliability of the proposed method. It can be seen from Figure 8 to Figure 14 that the solution obtained by the proposed method for the case (when $\alpha = \beta = \gamma = \delta = 1$ is in good agreement with the analytical solution available in

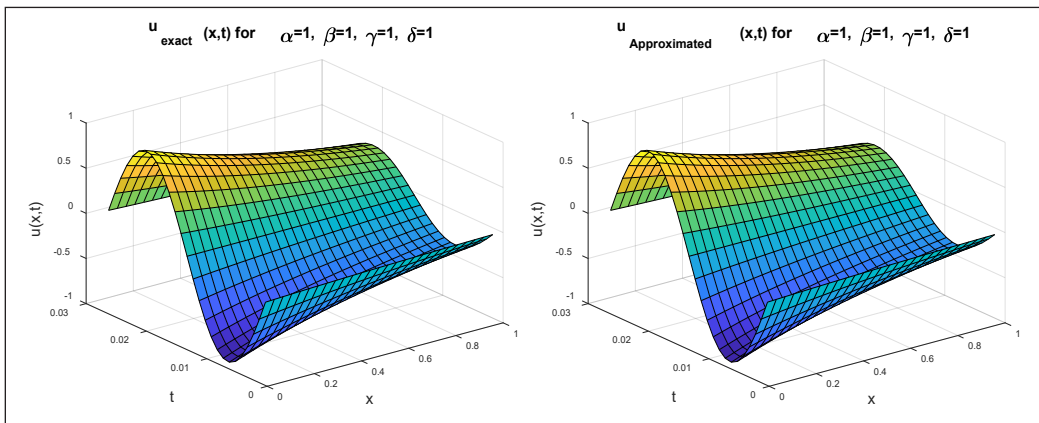


Figure 8. 3D Graphical representation of exact and approximated solution $u(x,t)$ of Experiment No. 2 at integer order $\alpha = \beta = \gamma = \delta = 1$ with $\eta = \xi = -2, \mu = \lambda = 1$ and $\Delta t = 0.001$

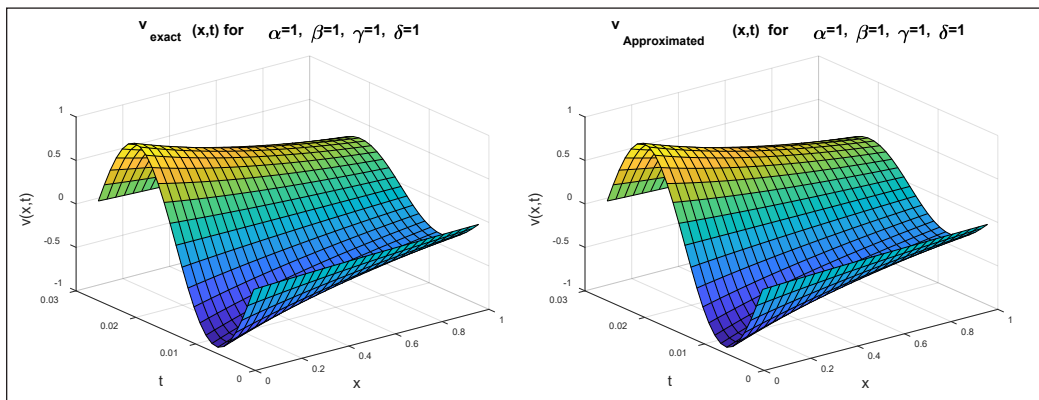


Figure 9. 3D Graphical representation of exact and approximated solution $v(x,t)$ of Experiment No. 2 at integer order $\alpha = \beta = \gamma = \delta = 1$ with $\eta = \xi = -2, \mu = \lambda = 1$ and $\Delta t = 0.001$

Table 4
 Absolute error in numerical results $u(x,t)$ at random collocation points for integer order $\alpha = \beta = \gamma = \delta = 1$ with $\eta = \xi = -2, \mu = \lambda = 1$

x t	0.05556	0.16667	0.27778	0.38889	0.50000	0.61111	0.72222	0.83333	0.94444
0.1	6.67×10^{-5}	4.35×10^{-5}	3.22×10^{-5}	2.62×10^{-5}	2.25×10^{-5}	1.99×10^{-5}	1.81×10^{-5}	1.67×10^{-5}	1.56×10^{-5}
0.2	1.69×10^{-4}	1.10×10^{-4}	8.17×10^{-5}	6.64×10^{-5}	5.69×10^{-5}	5.05×10^{-5}	4.58×10^{-5}	4.23×10^{-5}	3.95×10^{-5}
0.3	1.92×10^{-4}	1.25×10^{-4}	9.29×10^{-5}	7.55×10^{-5}	6.47×10^{-5}	5.74×10^{-5}	5.21×10^{-5}	4.81×10^{-5}	4.49×10^{-5}
0.4	1.25×10^{-4}	8.18×10^{-5}	6.06×10^{-5}	4.93×10^{-5}	4.22×10^{-5}	3.75×10^{-5}	3.40×10^{-5}	3.14×10^{-5}	2.93×10^{-5}
0.5	2.89×10^{-19}	6.44×10^{-19}	1.05×10^{-18}	1.04×10^{-18}	9.44×10^{-19}	9.33×10^{-19}	1.52×10^{-18}	1.11×10^{-19}	9.49×10^{-19}
0.6	1.25×10^{-4}	8.18×10^{-5}	6.06×10^{-5}	4.93×10^{-5}	4.22×10^{-5}	3.75×10^{-5}	3.40×10^{-5}	3.14×10^{-5}	2.93×10^{-5}
0.7	1.92×10^{-4}	1.25×10^{-4}	9.29×10^{-5}	7.55×10^{-5}	6.47×10^{-5}	5.74×10^{-5}	5.21×10^{-5}	4.81×10^{-5}	4.49×10^{-5}
0.8	1.69×10^{-4}	1.10×10^{-4}	8.17×10^{-5}	6.64×10^{-5}	5.69×10^{-5}	5.05×10^{-5}	4.58×10^{-5}	4.23×10^{-5}	3.95×10^{-5}
0.9	6.67×10^{-5}	4.35×10^{-5}	3.22×10^{-5}	2.62×10^{-5}	2.25×10^{-5}	1.99×10^{-5}	1.81×10^{-5}	1.67×10^{-5}	1.56×10^{-5}

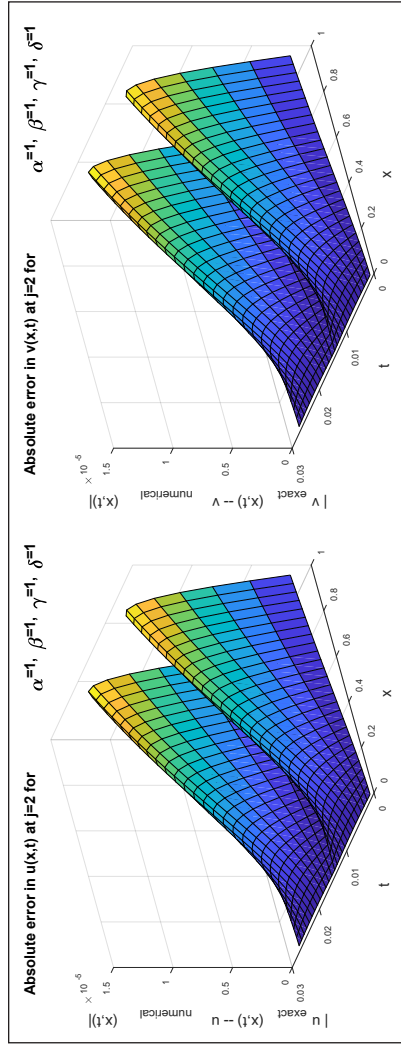


Figure 10. Surface plot of absolute error in the solutions $u(x,t)$ and $v(x,t)$ of Experiment No. 2 for $j=2$ at the integer order $\alpha = \beta = \gamma = \delta = 1$ with $\eta = \xi = -2, \mu = \lambda = 1$ and $\Delta t = 0.001$

the literature. Table 5 explains the absolute error in the solution for different values of Δt which illustrate the direct dependence of absolute error on meshsize for time variable. It can also be observed from the Figure 13 and Figure 14 that whenever we are changing the values of γ and δ by fixing the values of α, β , we are getting the change in the solution

Table 5

Maximum absolute error in numerical results $u(x,t)$ and $v(x,t)$ at the integer order $\alpha = \beta = \gamma = \delta = 1$ with $\eta = \xi = -2, \mu = \lambda = 1$ for different values of Δt

Δt	$\ E(u)\ _\infty$	$\ E(v)\ _\infty$
0.0100	$2.09861158048527 \times 10^{-4}$	$2.098611580485271 \times 10^{-4}$
0.0010	$3.764653977598853 \times 10^{-6}$	$3.764653977598853 \times 10^{-6}$
0.0001	$6.090606685656975 \times 10^{-8}$	$6.090606685656975 \times 10^{-8}$

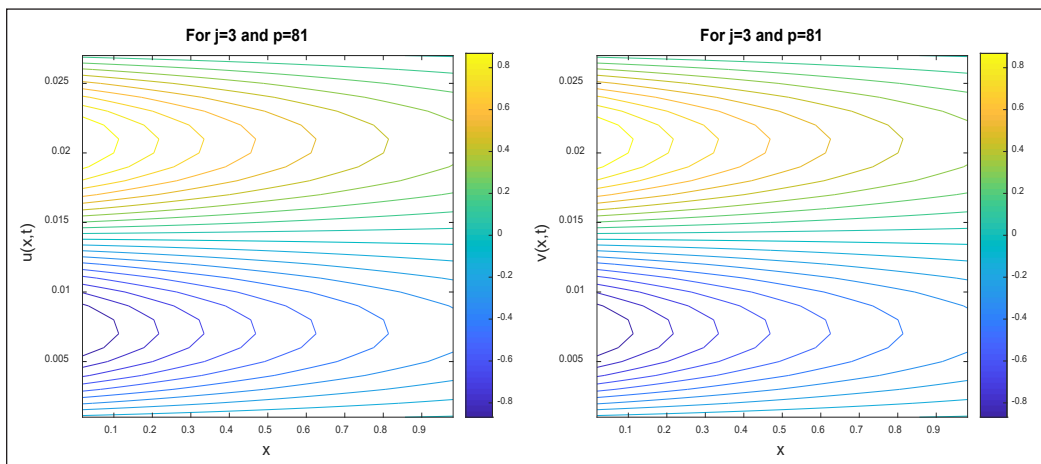


Figure 11. Contour representation of solutions $u(x,t)$ and $v(x,t)$ of Experiment No. 2 at the integer order $\alpha = \beta = \gamma = \delta = 1$ with $\eta = \xi = -2, \mu = \lambda = 1$ and $\Delta t = 0.001$

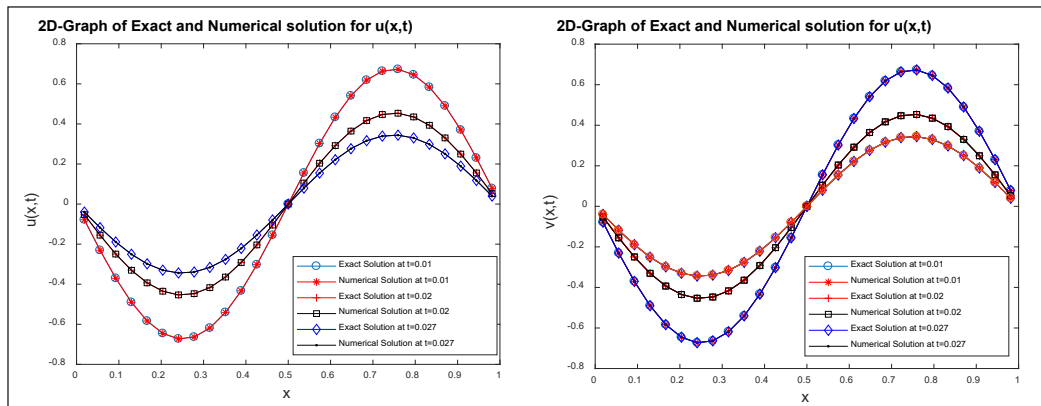


Figure 12. 2D-Graphical representation of exact and approximated solutions $u(x,t)$ and $v(x,t)$ of Experiment No. 2 for different values of t at the integer order $\alpha = \beta = \gamma = \delta = 1$ with $\eta = \xi = -2, \mu = \lambda = 1$ and $\Delta t = 0.001$

space of $v(x,t)$ and there is no change in the solution space of $u(x,t)$ and *vice versa*. It is because of the reason that α, β are orders of the time and space fractional derivatives of $u(x,t)$ respectively and that γ, δ are orders of the time and space fractional derivatives of $v(x,t)$ respectively which explains the importance of fractional models in explaining the microscopic behavior of the phenomenon .

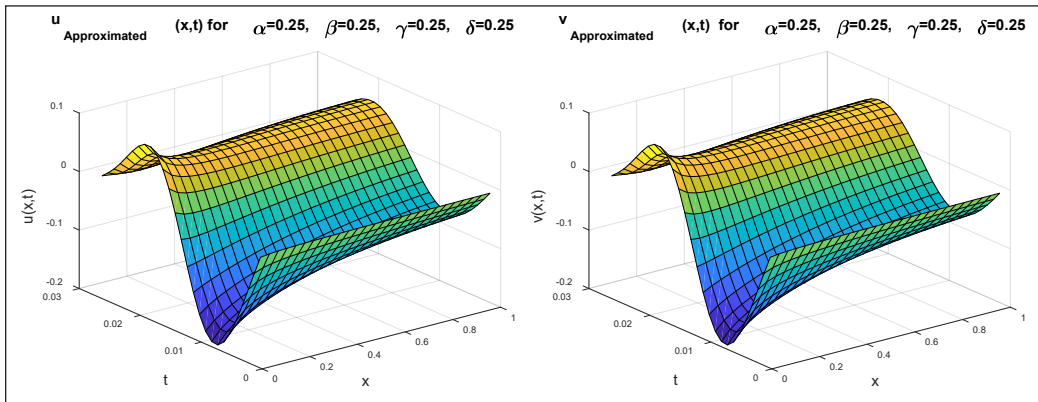


Figure 13. Approximate solution of Experiment No. 2 in 3D with different values of $\gamma, \delta \in (0,1]$ and fixed values of $\alpha=\beta=0.25$ with $\eta=\xi=-2, \mu=\lambda=1$ and $\Delta t=0.001$

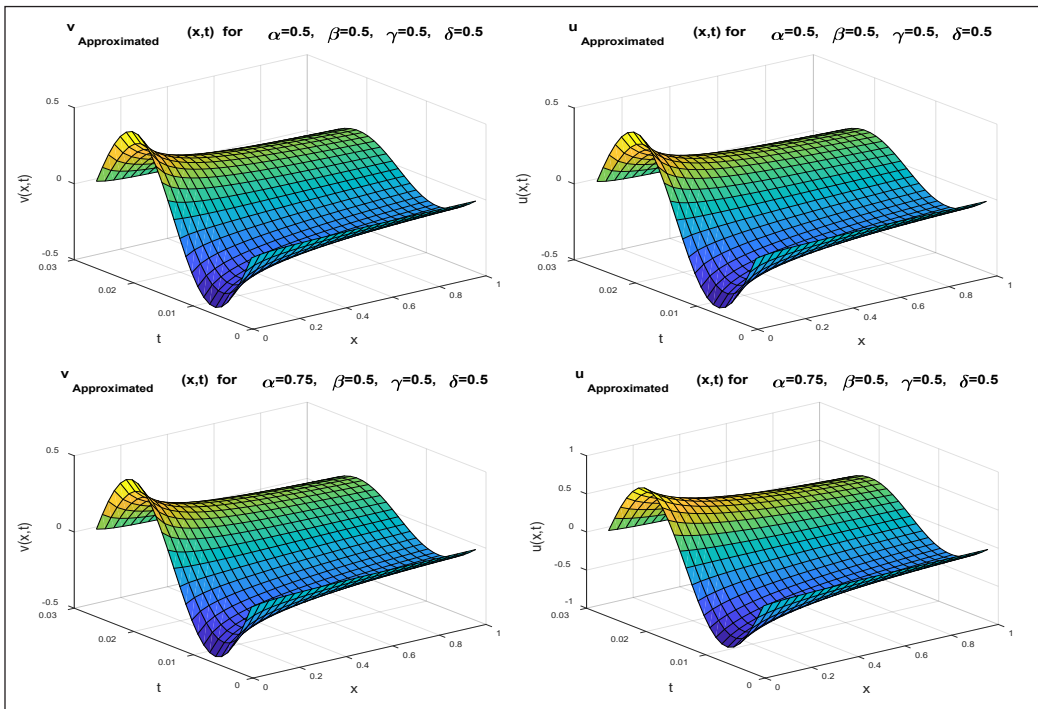


Figure 14. Approximate solution of Experiment No. 2 in 3D with different values of $\alpha, \beta \in (0,1]$ and fixed values of $\gamma=\delta=0.5$ with $\eta=\xi=-2, \mu=\lambda=1$ and $\Delta t=0.001$

CONCLUSION

We have developed a scale 3 Haar wavelet-based collocation scheme to find the solution of nonlinear coupled fractional differential equations. Two examples of space-time fractional coupled Burgers' equation with different boundary and initial constraints were considered to prove the reliability and efficiency of the proposed numerical scheme. It had been observed in with the help of MATLAB stimulation and computations that solution was behaving differentially as we varied the order of fractional derivatives in space-time fractional coupled Burgers' equation and giving the accuracy of order 10^{-5} at integer-order derivative (i.e. at $\alpha = \beta = \gamma = \delta = 1$) for $j=2$ which demonstrated the performance of the scheme. The proposed method was compared with another method available in the literature and it was found that the proposed method was working better than the other method. Looking at the performance of the method for the given set of numerical experiments, the proposed method can be extended to explain the behavior of the different phenomenon by solving the system of fractional differential equations governing those phenomena. The proposed method provides an insight into the microscopic behavior of phenomena under study. The given method is also fully supportive and compatible with the ordinary, partial, fractional differential equations and integral equations.

ACKNOWLEDGEMENT

We thank the anonymous reviewers and editors for their useful suggestion to develop this manuscript.

REFERENCES

- Abusad, S., Moaddy, K., & Hashim, I. (2019). Analytical treatment of two-dimensional fractional Helmholtz equations. *Journal of King Saud University-Science*, 31(4), 659-666.
- Atangana, A. (2016). On the new fractional derivative and application to nonlinear Fisher 's reaction – diffusion equation. *Applied Mathematics and Computation*, 273, 948-956.
- Baleanu, D., Inc, M., Yusuf, A., & Aliyu, A. I. (2018). Lie symmetry analysis, exact solutions and conservation laws for the time fractional Caudrey–Dodd–Gibbon–Sawada–Kotera equation. *Communications in Nonlinear Science and Numerical Simulation*, 59, 222-234.
- Bezerra, F. D. M., Carvalho, A. N., Dlotko, T., & Nascimento, M. J. D. (2018). Fractional Schrödinger equation; solvability and connection with classical Schrödinger equation. *Journal of Mathematical Analysis and Applications*, 457(1), 336-360.
- Chen, Y., & An, H. L. (2008). Numerical solutions of coupled Burgers equations with time- and space-fractional derivatives. *Applied Mathematics and Computation*, 200(2008), 87-95.
- Chui, C. K., & Lian, J. A. (1995). Construction of compactly supported symmetric and antisymmetric orthonormal wavelets with scale 3. *Applied and Computational Harmonic Analysis*, 2(1), 21-51.

- Das, S. (2011). *Functional fractional calculus*. Heidelberg, Germany: Springer-Verlag.
- Duan, J. S., Lu, L., Chen, L., & An, Y. L. (2017). Fractional model and solution for the Black-Scholes equation. *Mathematical Methods in the Applied Sciences*, 41(2), 697-704.
- Esipov, S. E. (1995). Coupled Burgers equations: A model of polydispersive sedimentation. *Physical Review E*, 52(4), 3711-3718.
- Heydari, M. H., Hooshmandasl, M. R., Ghaini, F. M., & Fereidouni, F. (2013). Two-dimensional Legendre wavelets for solving fractional Poisson equation with Dirichlet boundary conditions. *Engineering Analysis with Boundary Elements*, 37(11), 1331-1338.
- Hosseini, K., Mayeli, P., & Ansari, R. (2018). Bright and singular soliton solutions of the conformable time-fractional Klein–Gordon equations with different nonlinearities. *Waves in Random and Complex Media*, 28(3), 426-434.
- Inc, M. (2008). The approximate and exact solutions of the space- and time-fractional Burgers equations with initial conditions by variational iteration method. *Journal of Mathematical Analysis and Applications*, 345(1), 476-484.
- Inc, M., Yusuf, A., Aliyu, A. I., & Baleanu, D. (2018). Time-fractional Cahn–Allen and time-fractional Klein–Gordon equations: Lie symmetry analysis, explicit solutions and convergence analysis. *Physica A: Statistical Mechanics and Its Applications*, 493, 94-106.
- Karayer, H., Demirhan, D., & Buyukkilic, F. (2018). Solutions of local fractional sine-Gordon equations. *Waves in Random and Complex Media*, 5030, 1-9.
- Khan, N. A., Ara, A., & Mahmood, A. (2012). Numerical solutions of time-fractional Burgers equations: A comparison between generalized differential transformation technique and homotopy perturbation method. *International Journal of Numerical Methods for Heat and Fluid Flow*, 22(2), 175-193.
- Kumar, D., Singh, J., & Baleanu, D. (2018). A new numerical algorithm for fractional Fitzhugh–Nagumo equation arising in transmission of nerve impulses. *Nonlinear Dynamics*, 91(1), 307-317.
- Liu, J., & Hou, G. (2011). Numerical solutions of the space- and time-fractional coupled Burgers equations by generalized differential transform method. *Applied Mathematics and Computation*, 217(16), 7001-7008.
- Lopes, A. M., Machado, J. T., Pinto, C. M., & Galhano, A. M. (2013). Fractional dynamics and MDS visualization of earthquake phenomena. *Computers and Mathematics with Applications*, 66(5), 647-658.
- Lu, C., Fu, C., & Yang, H. (2018). Time-fractional generalized Boussinesq equation for Rossby solitary waves with dissipation effect in stratified fluid and conservation laws as well as exact solutions R. *Applied Mathematics and Computation*, 327, 104-116.
- Mahdy, A. M. S., & Marai, G. M. A. (2018). Numerical solution for the time-fractional Fokker-Planck equation using fractional power series method and the shifted Chebyshev polynomials of the third kind. *International Journal of Applied Engineering Research*, 13(1), 366-374.
- Mittal, R. C., & Pandit, S. (2018a). Sensitivity analysis of shock wave Burgers' equation via a novel algorithm based on scale-3 Haar wavelets. *International Journal of Computer Mathematics*, 95(3), 601-625.

- Mittal, R. C., & Pandit, S. (2018b). Quasilinearized scale-3 Haar wavelets-based algorithm for numerical simulation of fractional dynamical systems. *Engineering Computations*, 35(5), 1907-1931.
- Mittal, R. C., & Pandit, S. (2019). New Scale-3 Haar Wavelets Algorithm for Numerical Simulation of Second Order Ordinary Differential Equations. *Proceedings of the National Academy of Sciences, India Section A: Physical Sciences*, 89(4), 799-808.
- Mohebbi, A. (2018). Fast and high-order numerical algorithms for the solution of multidimensional nonlinear fractional Ginzburg-Landau equation. *European Physical Journal Plus*, 133(2), 67-79.
- Momani, S. (2005). Analytic and approximate solutions of the space- and time-fractional telegraph equations. *Applied Mathematics and Computation*, 170(2005), 1126-1134.
- Momani, S., & Odibat, Z. (2006a). Analytical approach to linear fractional partial differential equations arising in fluid mechanics. *Physics Letters, Section A: General, Atomic and Solid State Physics*, 355(4-5), 271-279.
- Momani, S., & Odibat, Z. (2006b). Analytical solution of a time-fractional Navier-Stokes equation by Adomian decomposition method. *Applied Mathematics and Computation*, 177(2), 488-494.
- Momani, S., & Shawagfeh, N. (2006). Decomposition method for solving fractional Riccati differential equations. *Applied Mathematics and Computation*, 182(2006), 1083-1092.
- Odibat, Z. M., & Momani, S. (2006). Approximate solutions for boundary value problems of time-fractional wave equation. *Applied Mathematics and Computation*, 181(1), 767-774.
- Odibat, Z., & Momani, S. (2009). The variational iteration method: An efficient scheme for handling fractional partial differential equations in fluid mechanics. *Computers and Mathematics with Applications*, 58(11), 2199-2208.
- Povstenko, Y. Z. (2009). Thermoelasticity that uses fractional heat conduction equation. *Journal of Mathematical Sciences*, 162(2), 296-305.
- Prakash, A., Kumar, M., & Sharma, K. K. (2015). Numerical method for solving fractional coupled Burgers equations. *Applied Mathematics and Computation*, 260(2015), 314-320.
- Ray, S. S. (2012). On Haar wavelet operational matrix of general order and its application for the numerical solution of fractional Bagley Torvik equation. *Applied Mathematics and Computation*, 218, 5239-5248.
- Ray, S. S. (2013). Numerical solutions of $(1 + 1)$ dimensional time fractional coupled Burger equations using new coupled fractional reduced differential transform method. *International Journal of Computing Science and Mathematics*, 4(1), 1-15.
- Ray, S. S., & Patra, A. (2013). Haar wavelet operational methods for the numerical solutions of fractional order nonlinear oscillatory Van der Pol system. *Applied Mathematics and Computation*, 220, 659-667.
- Roy, R., Akbar, M. A., & Majid, A. (2018). Exact wave solutions for the nonlinear time fractional Sharma – Tasso – Olver equation and the fractional Klein – Gordon equation in mathematical physics. *Optical and Quantum Electronics*, 50(1), 1-19.
- Sahoo, P. K., & Riedel, T. (1998). *Mean value theorems and functional equations*. Singapore: World Scientific Publishing Co. Pte. Ltd.

- Shen, T., Xin, J., & Huang, J. (2018). Time-space fractional stochastic Ginzburg-Landau equation driven by Gaussian white noise. *Stochastic Analysis and Applications*, 36(1), 103-113.
- Singh, J., Gupta, P. K., & Rai, K. N. (2011). Solution of fractional bioheat equations by finite difference method and HPM. *Mathematical and Computer Modelling*, 54(9-10), 2316-2325.
- Tawfik, A. M., Fichtner, H., Schlickeiser, R., & Elhanbaly, A. (2018). Analytical solutions of the space-time fractional Telegraph and advection-diffusion equations. *Physica A: Statistical Mechanics and Its Applications*, 491, 810-819.
- Tripathi, D., Pandey, S. K., & Das, S. (2010). Peristaltic flow of viscoelastic fluid with fractional Maxwell model through a channel. *Applied Mathematics and Computation*, 215(10), 3645-3654.
- Wang, Q. (2006). Numerical solutions for fractional KdV – Burgers equation by Adomian decomposition method. *Applied Mathematics and Computation*, 182(2006), 1048-1055.
- Yildirim, A., & Kelleci, A. (2010). Homotopy perturbation method for numerical solutions of coupled Burgers equations with time-and space-fractional derivatives. *International Journal of Numerical Methods for Heat and Fluid Flow*, 20(8), 897-909.
- Zahle, M., & Ziezold, H. (1996). Fractional derivatives of Weierstrass-type functions. *Journal of Computational and Applied Mathematics*, 76(1996), 265-275.
- Zhang, H., Jiang, X., & Yang, X. (2018). A time-space spectral method for the time-space fractional Fokker-Planck equation and its inverse problem. *Applied Mathematics and Computation*, 320, 302-318.
- Zhang, X., He, Y., Wei, L., Tang, B., & Wang, S. (2014). A fully discrete local discontinuous Galerkin method for one-dimensional time-fractional Fisher's equation. *International Journal of Computer Mathematics*, 91(9), 2021-2038.



Comparison of Sparse and Robust Regression Techniques in Efficient Model Selection for Moisture Ratio Removal of Seaweed using Solar Drier

Anam Javaid^{1,2}, Mohd. Tahir Ismail¹ and Majid Khan Majahar Ali^{1*}

¹*School of Mathematical Sciences, Universiti Sains Malaysia 11800 USM, Penang, Malaysia*

²*Department of Statistics, The Women University Multan, L.M.Q. Road, Multan, Pakistan*

ABSTRACT

Solar drier is considered to be an important product used in the internet of things (IoT). It is used to dry different kinds of products used in agriculture or aquaculture. There are many factors that have different effects on the drying of items in the solar drier. The current study focused on the removal of the moisture ratio in the drying process for seaweed using solar drier. For this purpose, a dataset containing 1924 observations was used to study the effect of six different independent variables on the dependent variable. Moisture ratio removal (%) was considered to be dependent variable with ambient temperature, chamber temperature, collector temperature, chamber relative humidity, ambient relative humidity and solar radiation as independent variables. All possible models were used in the analysis till fifth order interaction terms. Hybrid model of LASSO with bisquare M was proposed for efficient selection of the model. The procedure based on four phases was used for efficient model selection and a comparison was made with other existing sparse and robust regression techniques. The result indicates that the proposed technique is better than other existing techniques in terms of mean squared error (MSE) and mean absolute percentage error (MAPE).

Keywords: All possible models, LASSO, model selection, robust, seaweed, selection criteria

ARTICLE INFO

Article history:

Received: 05 Octobe 2019

Accepted: 15 January 2020

Published: 15 April 2020

E-mail addresses:

anamjavaid7860@yahoo.com (Anam Javaid)

m.tahir@usm.my (Mohd. Tahir Ismail)

majidkhanmajaharali@usm.my (Majid Khan Majahar Ali)

* Corresponding author

INTRODUCTION

In agriculture field, the items based on the Internet of thing (IoT) help to reduce human effort as a kind of narrow band model was proposed by Klaina et al. (2018). Using IoT, different factors such as humidity, air speed, temperature and irrigation of water were determined by Gondchawar & Kawitkar

(2016). There is a large increase in population, so there is need to produce more food to meet the demand of the population (Rockström et al., 2009). There are many steps involved in the food production process from seeding to harvesting (Yan, 2011). One of the most important step is the drying (Ali et al., 2014). Seaweed is considered to be the most widely used product in the aquaculture or agriculture sector (Dissa et al., 2011). In agriculture, mathematically there are many models produced for the purposes of forecasting (Neitsch et al., 2011). Ordinary least square (OLS) is one of the technique used in model selection, but it suffers from limitations in case of certain conditions violated (Zuur et al., 2009). Mendelsohn and Dinar (2003) used the linear and quadratic regression analysis with the interaction terms of factors. Giacalone et al. (2018) had introduced L_p norm estimation methods. These simple methods have no model selection capability, so that Xu and Ying (2010) performed the selection of variables using the median regression with least absolute shrinkage and selection operator (LASSO) type penalty. The presence of outlier is also considered a major data problem because removing such observations is not always a good solution, so there are robust methods used to deal with these types of observations, as Gad and Qura (2016) reviewed different types of robust methods for outliers. According to Shariff and Ferdaos (2017), tikhonov regularisation (ridge regression) is considered to be one of the methods used in the case of multicollinearity, but its results are affected in the case of outliers. In robust regression, many types of estimates are available as Susanti et al. (2014) compared maximum likelihood type estimators (M estimators), modified M estimates (MM) and estimators of scale (S) of maize production data, but M estimators are preferred by the majority of researchers as their advantages were demonstrated by Sinova and Van Aelst (2018). It was based on tukey bisquare and were compared with hampel loss function. Another method of robust ridge regression was provided by Shariff and Ferdaos (2017) in case of both multicollinearity and outliers problem. For the model selection purpose, eight selection criteria (8SC) were used by Ali et al. (2017). From all possible models the 8SC was used by Zainodin et al. (2011) in model selection problem. It can be seen from previous research that there are different methods such as OLS, ridge and LASSO with robustic approach have been used, but no studies have been conducted using a combination of LASSO and robust with 8SC for all possible models, including interaction terms. Therefore, the contribution is the use of a newly-developed hybrid model of LASSO and robust with all possible models. The best choice of these models is made by means of 8SC that can be used further to choose the efficient model to forecast.

METHODS

This study used hybrid of LASSO and robust regression. The details of the methodology used are discussed as follows.

LASSO

Tibshirani (1996) proposed a new sparse estimation method called “LASSO” that minimised the sum of squares subject to a restriction that the sum of absolute value of the coefficient was less than the constant value. This kind of constraint has the capacity of sparseness, as some coefficients will be exactly zero, so the resulting model would have a better interpretation. LASSO has the property of both subset selection and ridge regression analysis simultaneously. It is a very general method as it can be applied in different statistical methods such as in extension of generalised linear model and in tree based models. According to Zhang et al. (2016) if there is a response vector $Y = [y_1, y_2, \dots, y_n]$ and the predictors $X \in R^{n \times D}$, Then in case of without generality of data loss. LASSO, a sparse regression method has the ability to resolve the following problem.

$$\min \|Y - X\beta\|_2^2 + \lambda \|\beta\|_1$$

Where $\beta \in R^{D \times 1}$ is considered as vector of regression coefficient. L_1 norm regularization has the ability to provide as sparse solution so that the model can be easily interpreted.

M Estimator

Draper and Smith (1998) stated that for finding the maximum likelihood type estimate (M estimate), it is required to minimize the term $\sum_{i=1}^n \rho(\frac{\epsilon_i}{s})$, where ϵ_i is the error term of i^{th} observation and s is an estimate of the scale. For this purpose, a partial differentiation is used with respect to each parameter p which results in a system of p equations.

$$\sum_{i=1}^n x_{ij} \psi(\frac{y_i - x_i^T \beta}{s}) = \sum_{i=1}^n x_{ij} \psi(\frac{\epsilon_i}{s}) = 0, \quad j = 1, 2, \dots, p \tag{1}$$

Where $\psi(u) = \frac{\partial \rho}{\partial u}$ called as score function and the weight function can be defined as

$$w(u) = \frac{\psi(u)}{u}$$

yeilds $w_i = (\frac{\epsilon_i}{s})$ for $i = 1, 2, \dots, n$, with $w_i = 1$ if $\epsilon_i = 0$, substituting into (1) the results are

$$\begin{aligned} \sum_{i=1}^n x_{ij} w_i \frac{\epsilon_i}{s} &= \sum_{i=1}^n x_{ij} w_i (y_i - x_i^T \beta) \frac{1}{s} = 0 \quad j = 1, 2, \dots, p \\ \Rightarrow \sum_{i=1}^n x_{ij} w_i (y_i - x_i^T \beta) &= 0, \quad j = 1, 2, \dots, p \\ \Rightarrow \sum_{i=1}^n x_{ij} w_i x_i \beta &= \sum_{i=1}^n x_{ij} w_i y_i \quad j = 1, 2, \dots, p \end{aligned} \tag{2}$$

Since $s \neq 0$, defining the weight matrix $W = \text{diag}\{w_i; i = 1, 2, \dots, n\}$ as follows

$$W = \begin{pmatrix} w_1 & \cdot & 0 \\ & w_2 & \\ 0 & \cdot & w_n \end{pmatrix}$$

yields the following matrix form of (2)

$$\begin{aligned} X^T W X \beta &= X^T W Y \\ \Rightarrow \hat{\beta} &= (X^T W X)^{-1} X^T W Y \end{aligned} \tag{3}$$

It is very similar to least square estimator solution, but the introduction of weight matrix reduce the outlier’s influence. Usually, contrasting to the least squares, (3) can not be used directly in calculation of M estimation from the dataset, W depends on the residuals, that depend on the estimation. In fact, an initial estimate and iterations are required to finally converge on W and an M estimation for β . An iterative procedure called as iteratively reweighted least squares (IRLS) is used to identify M regression estimates. There are three types of M estimators commonly used as huber M, hampel M and tukey bisquare M with different weighting function (Stuart, 2011). In the present study, bisquare M is used for making the hybrid model with LASSO.

All possible models are considered in this study. Efficient model selection is made in four phases. The purpose of the study is also to highlight the importance of interaction terms so the variables till fifth order interaction terms are considered. All the assumptions regarding the random pattern of observations, homogeneity of variances and autocorrelations are fulfilled.

Phase I – All Possible Models

Ali et al. (2017) stated all possible models using the formula

$$N = \sum_{j=1}^k j \binom{k}{j} \tag{4}$$

Using (4), all possible models are calculated with LASSO and with all other existing techniques used in this study. Total number of all possible models for six independent variables untill fifth order interactions can be observed as in Table 1.

Table 1
Number of all possible models

No of variables single		Interact					Total
		1 st	2 nd	3 rd	4 th	5 th	
1	6	-	-	-	-	-	6
2	15	15	-	-	-	-	30
3	20	20	20	-	-	-	60
4	15	15	15	15	-	-	60
5	6	6	6	6	6	-	30
6	1	1	1	1	1	1	6
Total Models	63	57	42	22	7	1	192
Model ID	M1-M63	M64-M120	M121-M163	M164-M185	M186-M191	M192	

A total of 5% of the dataset is stored for forecasting purposes and the mean absolute percentage error (MAPE) value is used for forecasting estimates (Ali et al., 2017) in phase 4. The MAPE is calculated using (5).

$$MAPE = \frac{100}{N} \left(\frac{\sum_{i=1}^j |A_i - E_i|}{A_i} \right) \quad i=1,2,\dots,j \quad (5)$$

Where

A = Actual value of dependent variable (y)

E = Expected value (\hat{y})

N = Number of fitted points

Phase 2- Selected Models

After calculating all possible models, the next step is to obtain the selected models (Zainodin et al., 2011). For this purpose, bisquare M was applied to LASSO selected models at a 5% significance level. Significant factors had been observed. From other techniques, significant factors were also observed at a 5% level of significance. Only one non significant variable was removed at one time and the procedure rerun again. The procedure continued until all the variables remaining in the model were significant.

Phase 3 - The Best Model

The next step was to get the best model after a list of selected models was obtained. 8SC were defined for this purpose by (Zainodin et al., 2011). 8SC formula can be displayed as shown in Table 2. By using mentioned formulas in Table 2, Akaike information criterion (AIC), RICE, Final prediction error (FPE), SCHWARZ(SBC), Generalized cross validation

(*GCV*), Sigma square (*SGMASQ*), Hannan-Quinn information criterion (*HQ*) and *SHIBATA* were calculated. The efficient model was obtained on the basis of minimum value obtained from all mentioned criteria.

Table 2
Formula used for 8SC

<i>AIC</i> : $\left(\frac{SSE}{n}\right) e^{\frac{2(k+1)}{n}}$ (Akaike, 1969)	<i>RICE</i> : $\left(\frac{SSE}{n}\right) \left[1 - \left(\frac{2(k+1)}{n}\right)\right]^{-1}$ (Rice, 1984)
<i>FPE</i> : $\left(\frac{SSE}{n}\right)^2 \frac{n + (k + 1)}{n - (k + 1)}$ (Akaike, 1974)	<i>SCHWARZ</i> : $\left(\frac{SSE}{n}\right) n^{\left(\frac{k+1}{n}\right)}$ (Schwarz, 1978)
<i>GCV</i> : $\left(\frac{SSE}{n}\right) \left[1 - \left(\frac{k + 1}{n}\right)\right]^{-2}$ (Golub et al., 1979)	<i>SGMASQ</i> : $\left(\frac{SSE}{n}\right) \left[1 - \left(\frac{k + 1}{n}\right)\right]^{-1}$ (Ramanathan, 2002)
<i>HQ</i> : $\left(\frac{SSE}{n}\right) (\ln n)^{\frac{2(k+1)}{n}}$ (Hannan and Quinn, 1979)	<i>SHIBATA</i> : $\left(\frac{SSE}{n}\right) \left(\frac{n + 2(k + 1)}{n}\right)$ (Shibata, 1981)

where

n = total number of observations

$k + 1$ = estimated parameters numbers (including constant)

SSE = sum of square of error

Phase 4 - Goodness of Fit

The goodness of fit test was performed on the final models selected in phase 3 to check the efficiency of the selected model. 5% dataset kept in phase 1 was used for MAPE calculation using (5) for this purpose. Other supporting evidence, such as scatter plot, histogram and residual box plot, was obtained for supporting evidence.

RESULT AND DISCUSSION

Data Collection and Procedure

The data used in this study were taken from a seaweed drier for four days using V-groove hybrid solar dryer. Seven variables were used in this study with moisture ratio content(%) as dependent variable while six independent variables include ambient temperature (x_1), chamber temperature(x_2), collector temperature (x_3), chamber relative humidity (x_4),

ambient relative humidity (x_5) and solar radiation (x_6). Moisture ratio content (%) was basically decreasing with the time passed by. So the time effect was already in study of the percentage decrease in moisture ratio. Significance of interaction terms had also been observed in this study. So, x_{12} represents the interaction between x_1 and x_2 . Similarly all other interactions are presented in this study. The four days of data were taken from a total of 1924 observations where 1826 observations were made for the purposes of analysis and 98 observations were kept for the purpose of prediction by calculating MAPE value. The data for each second was collected from 8 a.m. to 5 p.m. from 16 March 2017 to 19 March 2017. All possible models for the six independent variables were calculated from Table 1. On these 192 models, LASSO was applied and 183 models were obtained. Models with the same number of variables were stored in the same group. The tukey bisquare M estimator was applied to these 183 models at a 5% significance level in phase 2. As a result, 144 models were obtained from the application of the M estimator. Out of the 144 selected models, an efficient selection of the models was made on the basis of 8SC in phase 3. The minimum value for 8SC were found for model M192.27.13 meaning that M192.0.0 was original model where 27 variables were removed in LASSO and 13 were removed in bisquare M, thus the final model became M192.27.13 with SSE as 64743. The results obtained from 8SC are observed in Table 3.

Table 3
Results for 8SC using LASSO with bisquare M

Model number	AIC	FPE	GCV	HQ	RICE	SCHWARZ	SGMASQ	SHIBATA
M7.1.0=M9.1.0=M64.1.1	156.01	156.01	156.01	156.36	156.01	156.95	155.84	156.01
M8.1.0=M22.1.0	154.55	154.55	154.55	155.06	154.55	155.95	154.29	154.55
M10.1.0	122.73	122.73	122.73	123.14	122.73	123.84	122.52	122.73
M11.1.0=M25.1.0=M30.1.0=M68.1.0	149.71	149.71	149.71	150.21	149.71	151.07	149.46	149.71
M12.1.0=M69.1.0=M73.1.1	154.47	154.47	154.47	154.81	154.47	155.41	154.30	154.47
M13.1.0	166.42	166.42	166.42	166.79	166.42	167.43	166.24	166.42
M15.1.0=M20.1.0=M21.1.0=M36.1.0=M37.1.0	147.52	147.52	147.52	147.84	147.52	148.41	147.35	147.52
M16.1.0=M32.1.1	151.53	151.53	151.53	152.03	151.53	152.91	151.28	151.53
M17.1.0=M33.1.1=M40.1.1=M54.1.2	123.95	123.95	123.95	124.36	123.95	125.07	123.74	123.95
M18.1.0=M34.1.0=M39.1.0=M75.1.0	151.66	151.66	151.66	152.17	151.66	153.04	151.41	151.66
M19.1.0=M41.1.1	94.35	94.35	94.35	94.66	94.35	95.20	94.19	94.34
M23.1.1=M66.1.0	153.88	153.88	153.88	154.39	153.88	155.28	153.63	153.88
M24.1.0	121.56	121.56	121.56	122.10	121.56	123.03	121.29	121.56
M26.1.0=M42.1.1=M49.1.1=M58.1.2	149.49	149.49	149.49	150.16	149.49	151.31	149.16	149.49
M27.1.0=M50.1.1	113.33	113.33	113.33	113.83	113.33	114.70	113.08	113.33
M28.1.0=M44.1.0	151.22	151.22	151.22	151.89	151.22	153.06	150.89	151.22
M29.1.0	85.01	85.01	85.01	85.39	85.01	86.04	84.83	85.01
M31.1.0	119.26	119.26	119.26	119.79	119.26	120.71	119.00	119.26
M35.1.0	77.65	77.65	77.65	78.00	77.65	78.59	77.48	77.65
M38.1.0=M56.1.0	92.06	92.06	92.06	92.47	92.06	93.17	91.85	92.05
M43.1.0=M59.1.1	111.99	111.99	111.99	112.62	111.99	113.70	111.69	111.99
M45.1.0	73.22	73.22	73.22	73.63	73.22	74.33	73.02	73.22
M46.1.1	147.40	147.40	147.40	148.06	147.40	149.19	147.08	147.40

Table 3 (continue)

Model number	AIC	FPE	GCV	HQ	RICE	SCHWARZ	SGMASQ	SHIBATA
M47.1.0	118.40	118.40	118.40	119.06	118.40	120.20	118.08	118.40
M48.1.0=M61.1.0	87.00	87.00	87.00	87.49	87.01	88.33	86.77	87.00
M51.1.0	86.99	86.99	86.99	87.48	86.99	88.31	86.75	86.99
M52.1.0=M62.1.0	77.68	77.68	77.68	78.11	77.68	78.86	77.47	77.68
M53.1.1	149.88	149.88	149.88	150.55	149.88	151.70	149.55	149.88
M55.1.0	77.69	77.69	77.70	78.13	77.70	78.88	77.48	77.69
M57.1.0	70.96	70.96	70.97	71.44	70.97	72.26	70.73	70.96
M60.1.0	72.80	72.80	72.80	73.28	72.80	74.13	72.56	72.79
M63.1.0	71.29	71.29	71.29	71.84	71.29	72.81	71.01	71.28
M65.1.0=M83.1.2	154.53	154.53	154.53	154.87	154.53	155.46	154.36	154.53
M67.1.0=M81.1.1	122.50	122.50	122.50	122.91	122.50	123.61	122.30	122.50
M70.1.0	162.41	162.41	162.41	163.13	162.41	164.38	162.05	162.41
M71.1.0	151.27	151.27	151.27	151.95	151.27	153.11	150.94	151.27
M72.1.0	150.36	150.36	150.36	150.86	150.36	151.72	150.11	150.36
M74.1.0	121.72	121.72	121.72	122.13	121.72	122.83	121.52	121.72
M76.1.0	85.23	85.23	85.23	85.61	85.23	86.26	85.04	85.23
M77.1.0	177.37	177.37	177.37	177.96	177.37	178.98	177.08	177.37
M78.1.0	134.59	134.59	134.60	135.05	134.60	135.82	134.37	134.59
M79.1.0	151.11	151.11	151.11	151.95	151.11	153.41	150.70	151.11
M80.1.1	148.18	148.18	148.18	149.00	148.18	150.43	147.77	148.17
M82.1.0	135.42	135.42	135.42	136.48	135.42	138.31	134.90	135.42
M84.1.0	108.30	108.30	108.30	108.78	108.30	109.61	108.06	108.30
M85.1.1	128.35	128.35	128.35	129.21	128.35	130.69	127.93	128.34
M86.1.0=M128.1.0	76.47	76.47	76.47	76.90	76.47	77.63	76.26	76.47
M87.1.1	112.07	112.07	112.07	112.82	112.08	114.12	111.71	112.07
M88.1.0=M130.1.0	88.49	88.49	88.49	89.08	88.49	90.10	88.20	88.49
M89.1.1	152.41	152.41	152.41	153.09	152.41	154.26	152.08	152.41
M90.1.1	106.50	106.50	106.50	107.09	106.50	108.11	106.20	106.49
M91.1.1	124.02	124.02	124.02	124.85	124.02	126.28	123.61	124.01
M92.1.0	67.85	67.85	67.85	68.30	67.85	69.09	67.63	67.85
M93.1.0	127.73	127.73	127.73	128.58	127.73	130.06	127.31	127.72
M94.1.0	97.75	97.75	97.75	98.52	97.75	99.84	97.38	97.75
M95.1.0	74.94	74.94	74.94	75.28	74.94	75.85	74.78	74.94
M96.1.0	109.06	109.06	109.06	109.79	109.06	111.05	108.70	109.06
M97.1.0=M139.1.0	91.72	91.72	91.72	92.44	91.72	93.68	91.37	91.72
M98.1.0	62.66	62.66	62.66	63.15	62.67	64.00	62.42	62.66
M99.1.0	146.74	146.74	146.74	148.21	146.74	150.78	146.02	146.73
M100.1.0	99.99	99.99	99.99	100.66	99.99	101.82	99.66	99.99
M101.1.1	127.89	127.89	127.89	129.32	127.89	131.80	127.19	127.88
M102.1.1	62.73	62.73	62.73	63.36	62.74	64.46	62.42	62.73
M103.1.1	112.64	112.64	112.64	113.52	112.64	115.04	112.21	112.63
M104.1.0	84.49	84.49	84.49	85.06	84.49	86.04	84.22	84.49
M105.1.0	70.77	70.77	70.77	71.41	70.78	72.50	70.46	70.77
M106.1.0	104.31	104.31	104.31	105.36	104.31	107.18	103.80	104.30
M107.1.1	80.91	80.91	80.91	81.72	80.91	83.13	80.51	80.90
M108.1.1	51.05	51.05	51.05	51.45	51.06	52.14	50.86	51.05
M109.1.0	51.86	51.86	51.87	52.50	51.87	53.61	51.55	51.86
M110.1.1	107.75	107.75	107.75	108.59	107.75	110.05	107.33	107.74
M111.1.0	84.28	84.28	84.28	85.13	84.28	86.60	83.86	84.27
M112.1.0	50.86	50.86	50.86	51.37	50.86	52.26	50.61	50.85
M113.1.0	60.10	60.10	60.10	60.63	60.10	61.56	59.83	60.09

Table 3 (continue)

Model number	AIC	FPE	GCV	HQ	RICE	SCHWARZ	SGMASQ	SHIBATA
M114.1.0	46.50	46.50	46.50	47.23	46.50	48.50	46.14	46.49
M115.1.1	103.16	103.16	103.16	104.31	103.16	106.32	102.59	103.15
M116.1.2= M118.1.3	77.95	77.95	77.96	78.56	77.96	79.62	77.66	77.95
M117.1.2	45.86	45.86	45.86	46.32	45.86	47.12	45.64	45.86
M119.1.3	47.17	47.17	47.18	47.70	47.18	48.62	46.92	47.17
M120.1.1	40.99	40.99	40.99	41.63	40.99	42.76	40.67	40.98
M121.1.1	152.90	152.90	152.91	153.59	152.91	154.76	152.57	152.90
M122.1.1	146.88	146.88	146.88	147.70	146.88	149.11	146.48	146.88
M123.1.0	125.34	125.34	125.34	126.04	125.34	127.24	125.00	125.34
M124.1.0	126.99	126.99	126.99	128.12	126.99	130.09	126.43	126.98
M125.1.0	158.61	158.61	158.61	159.49	158.61	161.02	158.17	158.61
M126.1.1	107.59	107.59	107.59	108.19	107.59	109.23	107.30	107.59
M127.1.0	124.74	124.74	124.74	125.86	124.74	127.79	124.20	124.73
M129.1.0	104.95	104.95	104.95	105.77	104.95	107.19	104.55	104.95
M130.1.1	154.50	154.50	154.50	155.36	154.50	156.84	154.07	154.49
M131.1.0	114.90	114.90	114.90	115.67	114.91	117.00	114.53	114.90
M132.1.0	118.18	118.18	118.18	119.23	118.18	121.07	117.66	118.17
M133.1.0	68.28	68.28	68.28	68.81	68.28	69.74	68.02	68.28
M134.1.0	157.02	157.02	157.03	158.25	157.03	160.38	156.42	157.02
M135.1.0= M137.1.0	94.67	94.67	94.67	95.51	94.67	96.98	94.26	94.66
M136.1.0	66.69	66.69	66.69	67.22	66.70	68.12	66.44	66.69
M138.1.0	108.23	108.23	108.24	109.20	108.24	110.88	107.76	108.23
M140.1.1	61.03	61.03	61.03	61.44	61.03	62.15	60.83	61.03
M142.1.2	135.41	135.41	135.42	136.93	135.42	139.56	134.68	135.41
M143.1.1	94.92	94.92	94.92	95.88	94.92	97.53	94.45	94.92
M144.1.0	127.21	127.21	127.21	128.35	127.21	130.32	126.65	127.20
M145.1.2	59.86	59.86	59.86	60.46	59.86	61.51	59.56	59.85
M146.1.2=M166.1.2	103.30	103.30	103.30	104.22	103.30	105.82	102.85	103.30
M147.1.0=M167.1.0	82.53	82.53	82.54	83.18	82.54	84.30	82.22	82.53
M148.1.2	47.26	47.26	47.27	47.90	47.27	49.01	46.96	47.26
M149.1.3	100.26	100.26	100.26	101.27	100.26	103.02	99.77	100.25
M150.1.0	80.22	80.22	80.22	80.94	80.23	82.18	79.87	80.22
M151.1.1	50.84	50.84	50.84	51.35	50.84	52.23	50.59	50.83
M152.1.2	50.85	50.85	50.85	51.36	50.85	52.25	50.60	50.85
M153.1.2	103.96	103.96	103.97	105.01	103.97	106.83	103.45	103.96
M154.1.1=M174.1.1	83.56	83.56	83.56	84.40	83.56	85.86	83.15	83.55
M155.1.1	50.11	50.11	50.11	50.67	50.11	51.64	49.84	50.11
M156.1.1	56.83	56.83	56.83	57.33	56.83	58.21	56.58	56.82
M157.1.3	42.07	42.07	42.07	42.83	42.08	44.15	41.71	42.07
M158.1.1	97.01	97.01	97.01	98.31	97.02	100.59	96.38	97.00
M159.1.2	67.64	67.64	67.65	69.16	67.66	71.85	66.91	67.63
M161.1.2	47.15	47.15	47.15	47.62	47.15	48.45	46.92	47.15
M162.1.2	45.63	45.63	45.63	46.24	45.63	47.31	45.33	45.62
M163.1.5	46.47	46.47	46.47	47.14	46.47	48.32	46.14	46.46
M164.1.4	40.36	40.36	40.37	40.95	40.37	41.98	40.08	40.36
M165.1.1	138.21	138.21	138.22	139.91	138.22	142.88	137.38	138.20
M168.1.1	99.96	99.96	99.96	100.86	99.97	102.40	99.53	99.96
M169.1.2	124.32	124.32	124.32	125.57	124.33	127.74	123.71	124.32
M170.1.2	59.71	59.71	59.71	60.25	59.72	61.17	59.45	59.71
M171.1.3	46.73	46.73	46.73	47.36	46.73	48.45	46.42	46.73
M172.1.1	102.12	102.12	102.12	103.26	102.13	105.25	101.56	102.11

Table 3 (continue)

Model number	AIC	FPE	GCV	HQ	RICE	SCHWARZ	SGMASQ	SHIBATA
M173.1.1	74.11	74.11	74.11	75.11	74.12	76.84	73.63	74.10
M175.1.1	51.83	51.83	51.83	52.29	51.83	53.09	51.60	51.82
M176.1.1	50.43	50.43	50.43	51.16	50.44	52.45	50.07	50.42
M177.1.1	100.69	100.69	100.70	101.59	100.70	103.15	100.25	100.69
M178.1.0	55.97	55.97	55.97	56.66	55.97	57.86	55.63	55.96
M179.1.3	44.97	44.97	44.97	45.88	44.98	47.48	44.53	44.96
M180.1.1	61.03	61.03	61.03	62.06	61.04	63.85	60.53	61.02
M181.1.6	66.31	66.31	66.32	67.35	66.32	69.17	65.81	66.30
M182.1.4	42.40	42.40	42.40	43.16	42.40	44.49	42.03	42.39
M183.1.7	41.29	41.29	41.29	42.21	41.30	43.85	40.84	41.28
M184.1.7	43.37	43.37	43.37	44.15	43.38	45.51	42.99	43.36
M185.1.3	39.88	39.88	39.89	41.18	39.90	43.52	39.25	39.86
M186.1.1	47.85	47.85	47.86	48.77	47.86	50.37	47.41	47.85
M187.1.2	97.87	97.87	97.87	98.96	97.87	100.86	97.33	97.86
M188.1.3	66.66	66.66	66.67	67.94	66.67	70.17	66.05	66.65
M189.1.4	42.73	42.73	42.74	43.50	42.74	44.85	42.36	42.73
M190.1.7	41.21	41.21	41.22	42.42	41.23	44.58	40.63	41.20
M191.1.3	44.34	44.34	44.35	45.19	44.35	46.68	43.93	44.33
M192.1.14	36.61	36.61	36.62	37.60	36.62	39.36	36.13	36.60

The minimum value for M192.1.14 represented the efficient model obtained in phase 3. For LASSO, package *glmnet* was used and for bisquare M estimator, library *MASS* was used for the purpose of analysis in R software. The coefficients were obtained by means of the R software and can be observed as in (6).

$$\begin{aligned}
 M192.1.13 = \hat{Y} = & 2.350e^{+02} - 3.1975e^{+00}x_2 - 9.921e^{+00}x_3 - 1.005e^{+01}x_5 \\
 & + 1.572e^{-01}x_{13} + 2.210e^{-01}x_{15} + 2.453e^{-03}x_{26} + 3.991e^{-01}x_{35} + 2.738e^{-02}x_{45} \\
 & - 2.477e^{-02}x_{46} + 1.224e^{-02}x_{56} + 1.589e^{-03}x_{123} + 1.150e^{-03}x_{124} - 1.128e^{-02}x_{135} \\
 & + 8.000e^{-04}x_{245} + 1.185e^{-04}x_{256} - 3.980e^{-04}x_{346} + 2.162e^{-04}x_{356} + 8.468e^{-05}x_{1235} \\
 & + 2.203e^{-05}x_{1246} - 1.642e^{-05}x_{1256} - 3.053e^{-06}x_{12345} - 6.217e^{-08}x_{12356} \\
 & + 1.298e^{-07}x_{13456} \tag{6}
 \end{aligned}$$

Crucial variables with their respective coefficients can be observed from the above model. From (6) onwards, the importance of interaction terms can be observed in the form of significant variables. MAPE is found with (5) and was obtained as 8.97 for this efficient model using the proposed hybrid model.

Comparison with other existing sparse and robust regression techniques was carried out to verify the efficiency of the proposed technique. Using all other existing techniques, the final model was obtained in a similar way based on four phases in this study. The results of mean squared error (MSE) and for MAPE were observed using the R software

with the numbers of variables left in a model (k). The proposed technique was compared with a variety of other existing sparse and robust techniques. Least trimmed square (LTS), modified M estimator (MM), estimators of scale (S estimator) were applied using R software. Elastic net LTS (E. Net LTS), elastic net with S estimator (E. Net S) using the *pense* package in R is applied. M step after elastic net S estimator (M ENet S) using the *Mpense* package in R software was performed by default. The purpose was to compare the final selected model among all possible models obtained from all techniques in phase 3.

Table 4
Comparison of proposed method with other existing methods

Selected Model	Technique	(k)	MSE	MAPE
M192.1.13	LASSO with bisquare M	23	35.46	8.968
M192.1.0	LTS	63	100766.703	72.58
M192.10.0	MM	53	37.88	9.313
M192.1.0	S	63	3627.52	70.76
M192.2.0	E.net LTS	59	44.47	10.06
M192.2.0	E.net S	57	42.84	8.994
M192.3.0	M E.net S	27	87.53	14.373

Table 4 shows the results of the different techniques used in this study. The number of variables can be observed in all techniques with their respective MSE and MAPE in Table 4. M192.2.0 in E.net LTS shows that after performing the method in two steps, all the variables remain in the model as significant. Similarly other models are presented in this way. LTS and S estimator have the highest mean square error. Because of the trimmed observations in LTS, LTS cannot be considered as a good method in forecasting (Alma, 2011). The detailed behavior for the observation pattern for LTS and S estimator is analyzed in Figure 2 and Figure 4. Clearly, the proposed technique is better than all other techniques. The minimum value of MSE was found to be for LASSO with bisquare M in comparison with other techniques. So, on the basis of minimum MSE value, LASSO with bisquare M is preferred than other existing methods for forecasting. It has significant number of variables with minimum MSE and MAPE value as compared to other existing techniques. Although the number of variables in other techniques are higher than the proposed technique but MSE and MAPE is also high in comparison. So, the proposed technique is the best selection for forecasting the model as compared to others.

For the purpose of observing outliers outside the sigma limits, standardized residuals plots are observed for each final model.

Outliers outside 2 sigma limit can be observed from Figure 1-7. The percentage of outliers is obtained based on number of observations outside the 2 sigma limit. The percentage of outliers outside 2 sigma limit in each technique is observed in Table 5.

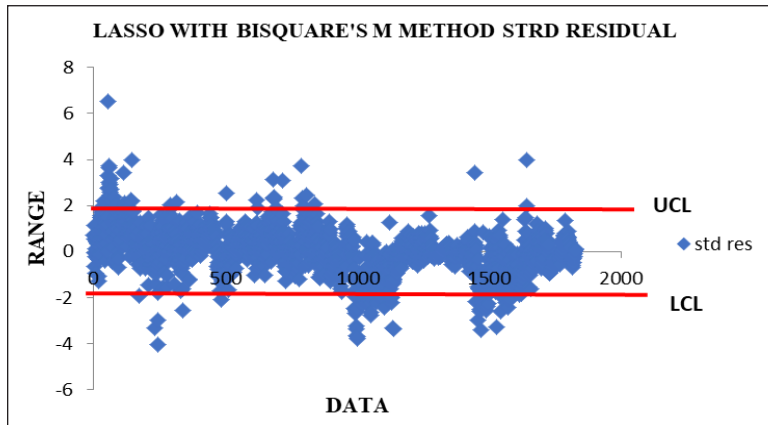


Figure 1. Standardized residual by for LASSO with bisquare M

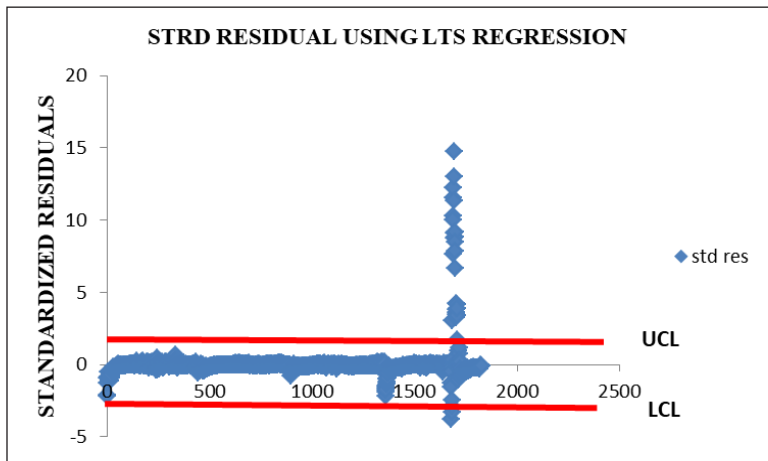


Figure 2. Standardized residual for LTS regression

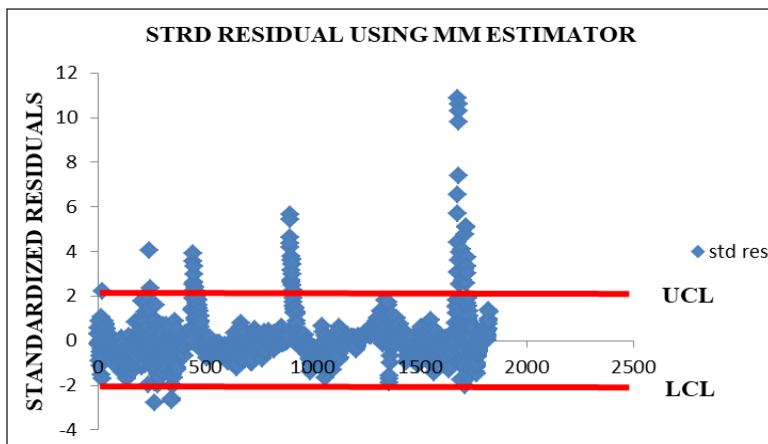


Figure 3. Standardized residual for MM estimator

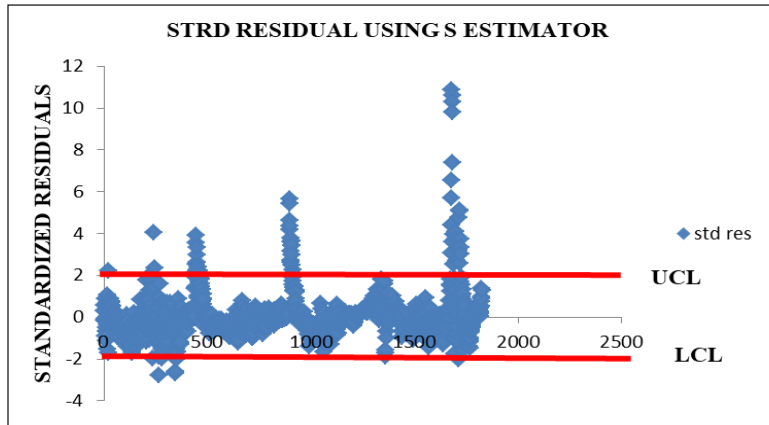


Figure 4. Standardized residual for S estimator

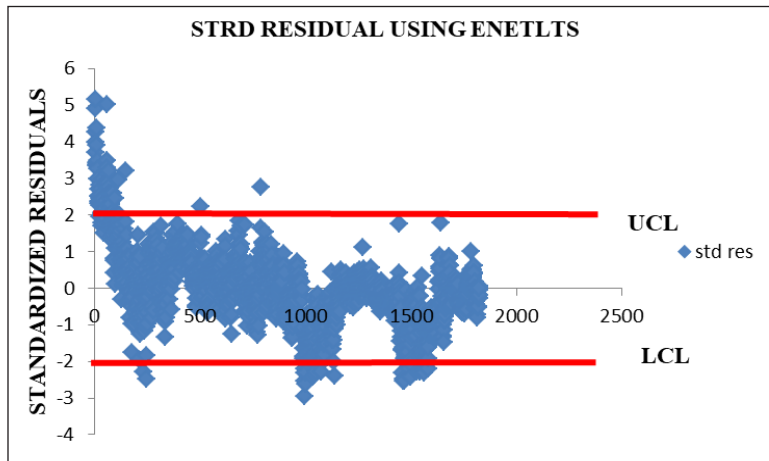


Figure 5. Standardized residual for E.net LTS estimator

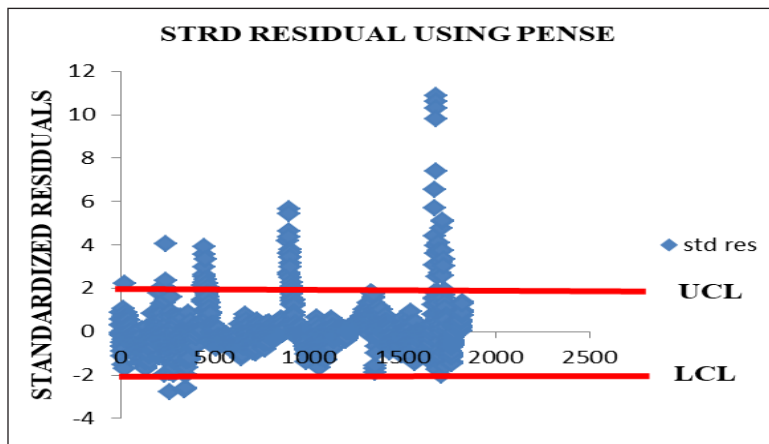


Figure 6. Standardized residual for E.net S estimator

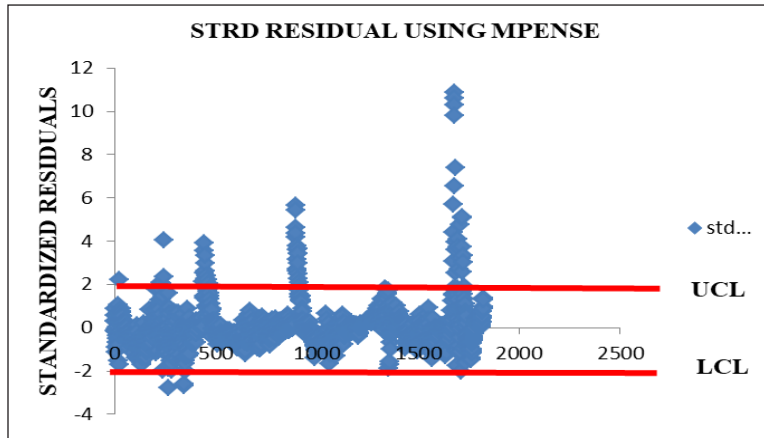


Figure 7. Standardized residual for M.Enet S estimator

Table 5
Percentage of outliers outside 2 sigma limits

Selected Model	Method	$\mu \pm 2\sigma$
M192.1.13	LASSO with bisquare M	5.48%
M192.1.0	LTS	1.70%
M192.10.0	MM	6.08%
M192.1.0	S	3.51%
M192.2.0	E.net LTS	5.92%
M192.2.0	E. net S	6.24%
M192.3.0	M E.net S	6.24%

There are 5.48% observations as outliers in the proposed hybrid model. The outlier's percentage in LTS and S estimator is lower than the proposed method. But due to high MSE value, LTS and S estimators cannot be considered as suitable for forecasting. In this study, real dataset is used so exclusion of outlier observations is not a good option. The pattern in the proposed technique is random, while more outliers are in a positive direction in all other techniques. There are fewer outliers in the LTS regression, but the MAPE for LTS is 72.58 using (5) with a very high MSE value. The *pense* and *Mpense* packages show almost the same behaviour in E.net S and M E.net S estimators respectively. E.net LTS also shows random pattern, but taking the more observations as outliers than the proposed hybrid model. The MSE and MAPE are also high as compared to the proposed hybrid model.

The estimates are not influenced from outliers in the proposed hybrid model due to the use of robust estimator. On the basis of minimum MSE and MAPE, the proposed hybrid model is preferred than other existing methods. The model obtained from LASSO with bisquare is therefore ready to forecast the moisture ratio removal (%) of seaweed with higher efficiency.

CONCLUSION

The results show that LASSO with bisquare M model provides the best model as compared to other existing methods used in the analysis. The selection of efficient model need to deal with all possible models with the interaction terms. The significance of interaction terms highlight the importance of interactions in the real life dataset. The proposed hybrid model is found to be better in term of MSE and MAPE value in comparison to other existing methods. The pattern of observations is also found to be random in graph of standardized residuals. So, the proposed hybrid model of LASSO and bisquare M can therefore be used for the efficient selection of the model including the interaction terms in it. The model is prepared to predict the moisture ratio removal (%) of seaweed with its crucial factors involving interaction terms. For the future work, the developed procedure based on four phases can also be used in efficient model selection for any other field of study.

ACKNOWLEDGEMENT

The author would like to thank the Women University Multan Pakistan and University Sains Malaysia for the support in this research project

REFERENCES

- Ali, M. K., Ruslan, M. H., Muthuvalu, M. S., Wong, J., Sulaiman, J., & Yasir, S. M. (2014). Mathematical modelling for the drying method and smoothing drying rate using cubic spline for seaweed *Kappaphycus striatum* variety Durian in a solar dryer. *AIP Conference Proceedings* 1602(1),113-120.
- Akaike, H. (1969). Fitting autoregressive models for prediction. *Annals of the Institute of Statistical Mathematics*, 21(1),243-247.
- Akaike, H. (1974). A new look at the statistical model identification. *IEEE Transactions on Automatic Control*, 19(6), 716-723.
- Ali M. K. M., Fudholi, A., Muthuvalu, M., S., Sulaiman, J., & Yasir, S. M. (2017). Implications of drying temperature and humidity on the drying kinetics of seaweed. *AIP Conference Proceedings*, 1905(1), 1-7.
- Alma, O. G. (2011). Comparison of Robust Regression Methods in Linear Regression. *International Journal of Contemporary Mathematical Sciences*, 6(9), 409-421.
- Dissa, A. O., Bathiebo, D. J., Desmorieux, H., Coulibaly, O., & Koulidiati, J. (2011). Experimental characterisation and modelling of thin layer direct solar drying of Amelie and Brooks mangoes. *Energy*, 36(5), 2517-252.
- Draper, N. R., & Smith, H. (1998). *Applied regression analysis* (Vol. 326). New York, USA: John Wiley & Sons.
- Golub, G. H., Heath, M., & Wahba, G. (1979). Generalized cross-validation as a method for choosing a good ridge parameter. *Technometrics*, 21(2), 215-223.
- Gad, A. M., & Qura, M. E. (2016). Regression estimation in the presence of outliers: A comparative study. *International Journal of Probability and Statistics*, 5(3), 65-72.

- Giacalone, M., Panarello, D., & Mattera, R. (2018). Multicollinearity in regression: an efficiency comparison between L p-norm and least squares estimators. *Quality and Quantity*, 52(4), 1831-1859.
- Gondchawar, N., & Kawitkar, P. R. S. (2016). IoT based smart agriculture. *International Journal of Advanced Research in Computer and Communication Engineering*, 5(6), 838-842.
- Hannan, E. J., & Quinn, B. G. (1979). The determination of the order of an autoregression. *Journal of the Royal Statistical Society: Series B (Methodological)*, 41(2), 190-195.
- Klaina, H., Vazquez Alejos, A., Aghzout, O., & Falcone, F. (2018). Narrowband characterization of near-ground radio channel for wireless sensors networks at 5G-IoT bands. *Sensors*, 18(8), 2428-2442.
- Mendelsohn, R., & Dinar, A. (2003). Climate, water, and agriculture. *Land Economics*, 79(3), 328-341.
- Neitsch, S. L., Arnold, J. G., Kiniry, J. R., & Williams, J. R. (2011). *Soil and water assessment tool theoretical documentation version 2009*. Texas, USA: Texas Water Resources Institute.
- Ramanathan, R. (2002). *Introductory Econometrics with application* (5th Ed.): South Western, USA: Harcourt College Publishers.
- Rice, J. (1984). Bandwidth choice for nonparametric regression. *The Annals of Statistics*, 12(4), 1215-1230.
- Rockström, J., Falkenmark, M., Karlberg, L., Hoff, H., Rost, S., & Gerten, D. (2009). Future water availability for global food production: the potential of green water for increasing resilience to global change. *Water Resources Research*, 45(7), 1-16.
- Schwarz, G. (1978). Estimating the dimension of a model. *The Annals of Statistics*, 6(2), 461-464.
- Shariff, N. S. M., & Ferdaos, N. A. (2017). An application of robust ridge regression model in the presence of outliers to real data problem. *Journal of Physics: Conference Series*, 890(1), 1-7.
- Shibata, R. (1981). An optimal selection of regression variables. *Biometrika*, 68(1), 45-54.
- Sinova, B., & Van Aelst, S. (2018). Advantages of M-estimators of location for fuzzy numbers based on Tukey's biweight loss function. *International Journal of Approximate Reasoning*, 93, 219-237
- Stuart, C. (2011). *Robust regression*. Durham, England: Durham University.
- Susanti, Y., Pratiwi, H., Sulistijowati H., S., & Liana, T. (2014). M Estimation, S Estimation, and MM Estimation in Robust Regression. *International Journal of Pure and Applied Mathematics*, 91(3), 349-360.
- Tibshirani, R. (1996). Regression shrinkage and selection via the LASSO. *Journal of the Royal Statistical Society: Series B (Methodological)*, 58(1), 267-288.
- Xu, J., & Ying, Z. (2010). Simultaneous estimation and variable selection in median regression using lasso-type penalty. *Annals of the Institute of Statistical Mathematics*, 62(3), 487-514.
- Yan-E, D. (2011, March 28-29). Design of Intelligent Agriculture Management Information System based on IoT. In *4th International Conference on Intelligent Computation Technology and Automation, ICICTA 2011* (Vol. 1, pp. 1045-1049). Shenzhen, Guangdong, China.
- Zainodin, H. J., Noraini, A., & Yap, S. J. (2011). An alternative multicollinearity approach in solving multiple regression problem. *Trends in Applied Sciences Research*, 6(11), 1241-1255.

- Zhang, K., Zhe, S., Cheng, C., Wei, Z., Chen, Z., Chen, H., ... & Ye, J. (2016, August 13-17). Annealed sparsity via adaptive and dynamic shrinking. In *22nd ACM SIGKDD International Conference on Knowledge Discovery and Data Mining - KDD '16* (pp. 1325-1334). San Francisco, California, USA.
- Zuur, A. F., Ieno, E. N., Walker, N. J., Saveliev, A. A., & Smith, G. M. (2009). Limitations of linear regression applied on ecological data. In *Mixed effects models and extensions in ecology with R* (pp. 11-33). New York, NY: Springer.



Effects on Parameter Estimates and Goodness of Fit Measures: Comparing Item-Level and Item-Parcel Models in Structural Equation Modeling

Ainur Amira Kamaruddin^{1*}, Bee Wah Yap² and Sayang Mohd Deni²

¹Centre of Statistical and Decision Science Studies, Faculty of Computer and Mathematical Sciences, Universiti Teknologi MARA, 40450 Shah Alam, Selangor, Malaysia

²Advanced Analytics Engineering Centre, Faculty of Computer and Mathematical Sciences, Universiti Teknologi MARA, 40450 Shah Alam, Selangor, Malaysia

ABSTRACT

The assessment of model fit is important in Structural Equation Modeling (SEM). Several goodness-of-fit (GoF) measures are affected by sample size and the number of parameters to be estimated. A large sample size is needed to test a complex model involving a large number of parameters to be estimated. One of the solutions to reduce the number of parameters to be estimated in a given model is by considering item parceling. The effects of item parceling on parameter estimates and GoF measures in a structural equation model was investigated via a simulation study. The simulation results indicate that the parameter estimates are closer to the true parameter values for the IL model whenever the distribution of data is normal but biased when the data is highly skewed. The parameter estimates for the IP model were found to be underestimated for both normal and non-normal data. The GoF measures were higher for the IP model. Additionally, the RMSEA was lower for the IP model when data were skewed. This shows that item parceling may improve GoF measures but the effect of exogenous on endogenous variable is underestimated. Application to a real data set confirmed the results of the simulation study.

Keywords: Goodness of fit, item parceling, parameter estimates, simulation, structural equation modeling

ARTICLE INFO

Article history:

Received: 05 November 2019

Accepted: 04 February 2020

Published: 15 April 2020

E-mail addresses:

memiera87@yahoo.com (Ainur Amira Kamaruddin)

beewah@tmsk.uitm.edu.my (Bee Wah Yap)

sayang@tmsk.uitm.edu.my (and Sayang Mohd Deni)

* Corresponding author

INTRODUCTION

Structural equation modeling (SEM) is a multivariate statistical analysis technique used to identify the association between more than one variable. SEM is a unique combination of multivariate techniques such as factor analysis and multiple regression

analysis. However, in SEM, the independent variable in a regression equation can be the dependent variable in another regression equation (Hair et al., 2015). SEM is widely used in psychology (Marsh et al., 1988; Mulaik et al., 1989; Bentler, 1990; Curran et al., 1996; Iacobucci, 2010; Little et al., 2013), marketing (Jöreskog & Sörbom, 1982; Bearden et al., 1982; Bagozzi & Yi, 1988), management (Shah & Goldstein, 2006; Rocha & Chelladurai, 2012; Hair et al., 2015), organizational behavior (Landis et al., 2000; Ryu, 2011), and business research (Sharma et al., 2005).

One of the most intensive parts in SEM is estimating the parameter of the model. Maximum Likelihood (ML) is the most popular method of estimation chosen by researchers (Curran et al., 1996; Hall et al., 1999; Nasser & Wisenbaker, 2006; Ory & Mokhtarian, 2010; Sterba & MacCallum, 2010; Ryu, 2011; Hamzah et al., 2017). The estimation process in ML aims to yield the minimum discrepancy between the sample covariance matrix and the estimated covariance matrix (Byrne, 2010). ML has several advantages such as being more stable, produces reliable results and is more accurate compared to other estimation methods (Olsson et al., 2000; Olsson et al., 2004). Besides, it is robust to moderate departures from normality assumption (Hair et al., 2015).

Another important aspect of SEM is the assessment of model fit for the structural model. It is used to test the consistency of a proposed theoretical model with the data. The model is clarified as good when the estimated covariance matrix is sufficiently close to the observed covariance matrix (Hair et al., 2015). The most popular goodness-of-fit (GoF) measures used to examine model fit are chi-squared (χ^2), root mean square error of approximation (RMSEA), goodness-of-fit index (GFI), Adjusted goodness-of-fit index (AGFI), Normed Fit Index (NFI), Non-Normed Fit Index (NNFI) or also known as Tucker-Lewis index (TLI) and comparative fit index (CFI).

Several GoF measures are influenced by sample size and number of estimated parameters (Marsh et al., 1988; Ding et al., 1995; Hooper et al., 2008; Rocha & Chelladurai, 2012). Parameter estimates may be biased when a construct consists of a small number of indicators. Thus, a minimum of three indicators per construct is recommended to produce unbiased parameter estimates (Ding et al., 1995; Hair et al., 2015; Iacobucci, 2010). However, the analysis of SEM is problematic for a model that consists of a large number of indicators with a small sample size (Deng et al., 2018). Hence, Hair et al. (2015) suggested that minimum sample sizes were defined with a complement of model complexity and basic measurement model characteristics. The required minimum sample size can be easily achieved for a simple model with a small number of indicators. Nonetheless, a larger sample size is required for a complex model with a large number of indicators (Rocha & Chelladurai, 2012; Deng et al., 2018; Hair et al., 2015). To overcome this problem, some studies (Hall et al., 1999; Landis et al., 2000; Bandalos, 2002; Kim & Hagtvet, 2003; Nasser & Wisenbaker, 2006; Rocha & Chelladurai, 2012) used item parceling when the model

consisted of a large number of indicators. The purpose of item parceling is to reduce the model complexity by summing or averaging together two or more indicators as a parcel rather than using individual items as indicators. A new model created by the item parceling technique reduces the nuisance parameters and sampling variability and increases reliability (Little et al., 2013), and improves model fit (Hall et al., 1999; Landis et al., 2000; Sterba & MacCallum, 2010).

Although the application of item parceling has received attention among researchers in SEM, the debates on the use of item parceling have continued and it remains a controversial issue. Bandalos (2002) pointed out the disadvantages of using the parceling technique such as the dimensionality of original measures being doubtful, resulted in biased parameter estimates and improvement in model fit without taking into account the model misspecification issue. The item parceling technique may also make the multidimensional constructs reflect as unidimensional when the indicators are not well defined in the constructs (Bandalos, 2002). Therefore, Little et al. (2002) emphasized the need to understand the original structure and dimension before assigning items to parcels. Little et al. (2013) suggested that a simulation study should be carried out to investigate whether the item parcel (IP) model was affected by the parameter estimates in SEM by comparing the results of the item-level (IL) model. Thus, this study aims to examine whether the parameter estimates and model fit are affected by item parceling in a structural equation model and compare these results with the IL model. The statistical analyses of this simulation study were performed using IBM SPSS Statistic 20, AMOS and R programming language software.

MATERIALS AND METHODS

Review of Theoretical Framework

Sterba and MacCallum (2010) presented the theoretical developments by MacCallum and Tucker (1991) on population data. Let an i subscript denotes item-level, x_i the vector deviation score on items in the population, and E denotes expectation operator. The population covariance structure of the items is given by Equation 1

$$E\left(x_i, x_i'\right) = \Sigma_i = \Lambda_i \Phi_i \Lambda_i' + \Psi_i^2 \quad [1]$$

where Λ_i is the common factor loading, Φ_i is the covariance of common factor loading and Ψ_i is the diagonal of unique variances. The unique factors are assumed to be independent from each other and from common factors in the population.

To illustrate, suppose we want to construct n parcels from a set of m items representing q factors ($n = 4$, $m = 12$ and $q = 2$). Let a p subscript denotes parcel-level and \mathbf{A}

be an $m \times n$ selection matrix that allocates items to parcels. Given the vector of parcels, $x_p = \mathbf{A}x_i$ can be presented in the matrix form as

$$\begin{bmatrix} x_{p1} \\ x_{p2} \\ x_{p3} \\ x_{p4} \end{bmatrix} = \begin{bmatrix} \frac{1}{3} & \frac{1}{3} & \frac{1}{3} & 0 & 0 & 0 & 0 & 0 & 0 & 0 & 0 & 0 \\ 0 & 0 & 0 & \frac{1}{3} & \frac{1}{3} & \frac{1}{3} & 0 & 0 & 0 & 0 & 0 & 0 \\ 0 & 0 & 0 & 0 & 0 & 0 & \frac{1}{3} & \frac{1}{3} & \frac{1}{3} & 0 & 0 & 0 \\ 0 & 0 & 0 & 0 & 0 & 0 & 0 & 0 & 0 & \frac{1}{3} & \frac{1}{3} & \frac{1}{3} \end{bmatrix} \begin{bmatrix} x_{i1} \\ x_{i2} \\ x_{i3} \\ x_{i4} \\ x_{i5} \\ x_{i6} \\ x_{i7} \\ x_{i8} \\ x_{i9} \\ x_{i10} \\ x_{i11} \\ x_{i12} \end{bmatrix}$$

$$\begin{bmatrix} x_{p1} \\ x_{p2} \\ x_{p3} \\ x_{p4} \end{bmatrix} = \begin{bmatrix} (x_{i1} + x_{i2} + x_{i3})/3 \\ (x_{i4} + x_{i5} + x_{i6})/3 \\ (x_{i7} + x_{i8} + x_{i9})/3 \\ (x_{i10} + x_{i11} + x_{i12})/3 \end{bmatrix}$$

where, x_{p1} and x_{p2} belong to the first factor and x_{p3} and x_{p4} belong to the second factor. The population covariance structure of the parcels can be derived as Equation 2

$$\Sigma_p = E(x_p, x_p') \tag{2}$$

and can be rewritten as Equation 3

$$\Sigma_p = E(\mathbf{A}x_i x_i' \mathbf{A}') = \mathbf{A} \Sigma_i \mathbf{A}' \tag{3}$$

which implies Equation 4

$$\Sigma_p = \mathbf{A} \Lambda_i \Phi_i \Lambda_i' \mathbf{A}' + \mathbf{A} \Psi_i^2 \mathbf{A}' \tag{4}$$

Let $\Lambda_p = \mathbf{A}\Lambda_i$ and $\Psi_p^2 = \mathbf{A}\Psi_i^2\mathbf{A}'$, then (Equation 5)

$$\Sigma_p = \Lambda_p \Phi_i \Lambda_p' + \Psi_p^2 \quad [5]$$

The factor loading for a parcel will equal the average of factor loading at the item-level when parcels are formed by averaging items. However, these conditions will hold in the population when the factor model fits perfectly at the item-level.

Sterba and MacCallum (2010) considered the structure of item-level sample covariance matrix developed by MacCallum and Tucker (1991). The assumptions that the unique factors are independent from each other and also with common factors cannot hold due to sampling variability. Thus, the item-level sample covariance structure is denoted by Equation 6

$$\mathbf{C}_i = \Lambda_i \mathbf{C}_{cc_i} \Lambda_i' + \Lambda_i \mathbf{C}_{cu_i} \Psi_i' + \Psi_i \mathbf{C}_{uc_i} \Lambda_i' + \Psi_i \mathbf{C}_{uu_i} \Psi_i' \quad [6]$$

Where \mathbf{C}_{cc_i} is the sample covariance matrix of common factors, \mathbf{C}_{cu_i} is the sample covariance matrix of common and unique factors, \mathbf{C}_{uc_i} is the sample covariance matrix of unique and common factors and \mathbf{C}_{uu_i} is the sample covariance matrix of unique factors. Let $\Lambda_p = \mathbf{A}\Lambda_i$ and $\Psi_p = \Psi_i' \mathbf{A}' = \mathbf{A}\Psi_i$, then (Equation 7)

$$\mathbf{C}_p = \Lambda_p \mathbf{C}_{cc_i} \Lambda_p' + \Lambda_p \mathbf{C}_{cu_i} \Psi_p + \Psi_p \mathbf{C}_{uc_i} \Lambda_p' + \Psi_p \mathbf{C}_{uu_i} \Psi_p \quad [7]$$

The item-level sample covariance structure that represents lack of fit due to the sampling error, Δ_{SE_i} can be simplified as in Equation 8

$$\mathbf{C}_i = \Lambda_i \mathbf{C}_{cc_i} \Lambda_i' + \Psi_i^2 + \Delta_{SE_i} \quad [8]$$

Hence, the parcel-level sample covariance structure can be derived as Equation 9

$$\mathbf{C}_p = \mathbf{A}\Lambda_i \mathbf{C}_{cc_i} \Lambda_i' \mathbf{A}' + \mathbf{A}\Psi_i^2 \mathbf{A}' + \mathbf{A}\Delta_{SE_i} \mathbf{A}' \quad [9]$$

Let $\Lambda_p = \mathbf{A}\Lambda_i$, $\Psi_p^2 = \mathbf{A}\Psi_i^2 \mathbf{A}'$ and $\Delta_{SE_p} = \mathbf{A}\Delta_{SE_i} \mathbf{A}'$, then (Equation 10)

$$\mathbf{C}_p = \Lambda_p \mathbf{C}_{cc_i} \Lambda_p' + \Psi_p^2 + \Delta_{SE_p} \quad [10]$$

The effect of sampling error can be reduced when the sample size is large, item communalities are high (where the unique loadings Ψ_i are low, hence \mathbf{C}_{uu_i} , \mathbf{C}_{cu_i} and \mathbf{C}_{uc_i}

matrices have little weight), and with smaller dimensions of C_{uui} , C_{cui} and C_{uci} matrices (since more items are located in each parcel) (Bandalos, 2002; Sterba & MacCallum, 2010).

METHODS

Study 1: Simulation

To provide empirical evidence on the usefulness of item parceling, a simulation study was used to identify the effects of item parceling on parameter estimates and model fit based on different sample sizes and distribution of data by comparing the IL model and IP model. The simulations were carried out using the function of *cfa* from the *lavaan package* built in the R programming software. This study generated data for a structural equation model for the IL model and IP model. Sample sizes of 100, 150, 200, 250, 300, 500, 1000, 1500 and 2000 were considered with different distribution of data which are normal (skewness = 0, kurtosis = 3), non-normal (skewness = 1, kurtosis = 1.5) and non-normal (skewness = 1.75, kurtosis = 3.75).

The structural model was adapted from a study by Goodhue et al. (2012) which had twelve items for exogenous variable and three items for endogenous variable. However, this study only focused on the single path coefficient between exogenous and endogenous variables. The smallest sample size ($n = 100$) was considered as recommended by Hair et al. (2015). The method for generating non-normal data followed the work of Goodhue et al. (2012) by using the Fleishman method (Fleishman, 1978) which is commonly used in the generation of non-normal data (Orcan, 2013; Goodhue et al., 2012; Morgan et al., 2016). Two non-normal distributions were considered based on Orcan (2013) study to represent moderate skewness with low kurtosis (skewness = 1, kurtosis = 1.5) and high skewness with high kurtosis (skewness = 1.75, kurtosis = 3.75).

For the IL model, twelve items for exogenous variable and three items for endogenous variable were generated with standardized loadings repeatedly fixed to 0.70, 0.80 and 0.90. The higher loadings (≥ 0.7) were selected to reach convergence and model stability as suggested by Hair et al. (2015). For the IP model, the twelve items for exogenous variable generated in the IL model were assigned randomly to four parcels. The parcel scores were computed by averaging three items for each parcel. Due to identification reasons, one factor loading for each factor was fixed to 1 (Lyhagen & Kraus, 2013). The simulation process was repeated for 5000 replications for each combination (9 sample sizes x 3 distributions x 2 models). The mean of parameter estimates and model fit were calculated for each combination.

Study 2: Empirical Example

In Study 2, we used an empirical example to observe the effect of item parceling on parameter estimation and model fit for a real dataset. This empirical dataset was from a study on self-efficacy and quality of life (QoL) of mothers with autistic children conducted by Nasir (2015). This study involved 181 respondents. The original (IL) model consisted of three latent variables with two endogenous variables: health related quality of life (HRQOL) and parenting sense of competence scale (PSOC) and one exogenous variable: parenting stress index (PSI). The HRQOL was a second-order construct measured by two factors (*physical* and *mental*) with five and four items, respectively. The PSOC was a second-order construct measured by two factors (*value comforting* and *skill knowledge*) with four items for each factor. Finally, the PSI was a second-order construct measured by three factors (*parental distress*, *parent child* and *difficult child*) with ten, eight and six items, respectively. Figure 1 shows the path diagram of the empirical example.

As mentioned before, to study the effectiveness of item parceling on parameter estimation and model fit, three different models of item parceling were tested. For Model 1, the items for *parental distress*, *parent child* and *difficult child* were parceled into five, four and three parcels of two items each (Figure 2). The items for *value comforting*, *skill knowledge*, *physical* and *mental* remained unchanged. Model 2 was similar to Model 1 except that the items for *value comforting*, *skill knowledge* and *mental* were parceled to form two parcels of two items each (Figure 3). Meanwhile, the four items for *physical* were parceled to form two parcels of two items each and the remaining item remained as a single indicator. Model 3 represented the simplest model where all the items in each factor were parceled together. The structures of these models are summarized in Table 1. The data analysis was carried out using SPSS AMOS Version 22.

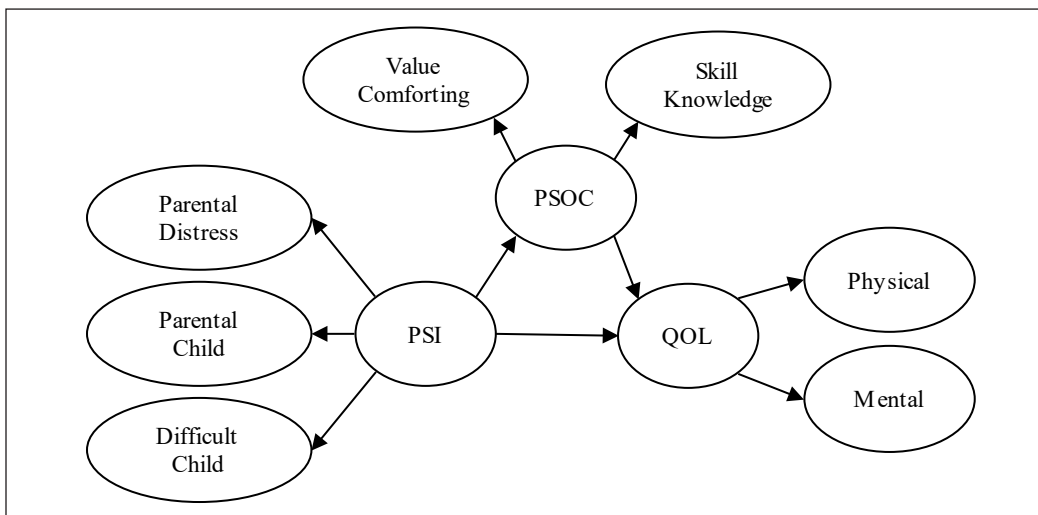


Figure 1. The path diagram of empirical example

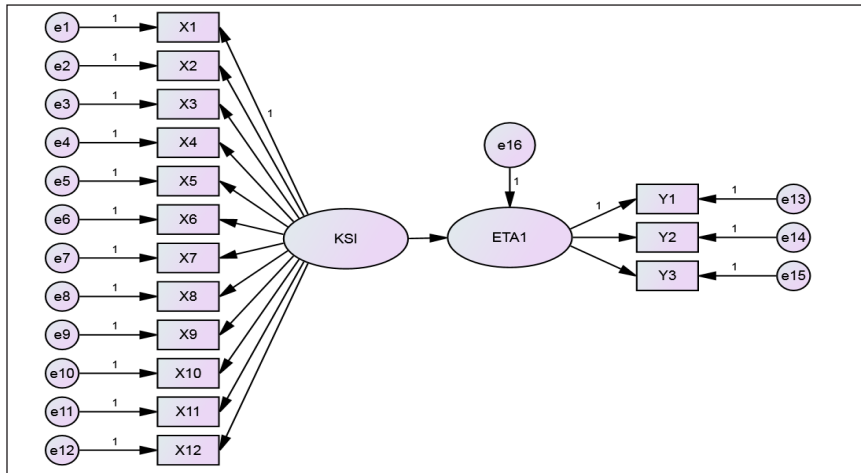


Figure 2. Model 1: Item-level model

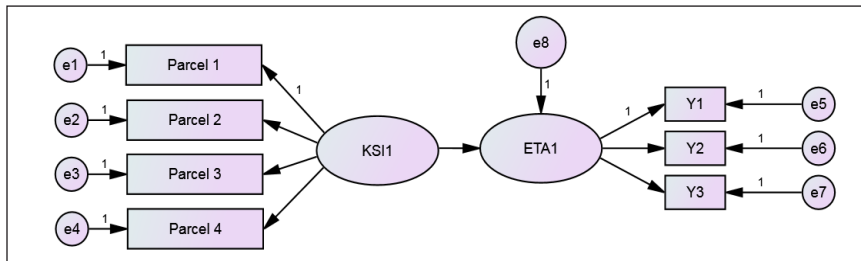


Figure 3. Model 2: Item-parcel model

Table 1
Summary of model structures

		IL	IP		
			Model 1	Model 2	Model 3
parenting stress index (PSI)	parental distress	B1, B3, B4, B5, B6, B7, B8, B9, B10, B12	B1B3, B4B5, B6B7, B8B9, B10B12	B1B3, B4B5, B6B7, B8B9, B10B12	Averaging all items
	parent-child	B14, B15, B16, B17, B18, B19, B20, B22	B14B15, B16B17, B18B19, B20B22	B14B15, B16B17, B18B19, B20B22	Averaging all items
	difficult child	B25, B26, B27, B28, B29, B30	B25B26, B27B28, B29B30	B25B26, B27B28, B29B30	Averaging all items
parenting sense of competence (PSOC)	skill knowledge	C10, C11, C13, C15	C10, C11, C13, C15	C10C11, C13C15	Averaging all items
	value comforting	CC9, CC12, CC16, C17	CC9, CC12, CC16, C17	CC9CC12, CC16C17	Averaging all items
health related quality of life (HRQoL)	physical	D2, D3, D4, D5, DD8	D2, D3, D4, D5, DD8	D2D3, D4D5, DD8	Averaging all items
	mental	D6, D7, D11, D12	D6, D7, D11, D12	D6D7, D11D12	Averaging all items
Total items		41	29	21	7

RESULTS AND DISCUSSION

Study 1: Results of Simulation Study

This section presents the results of parameter estimates, mean square error and model fit for the IL model and IP model for different distributions of data via a simulation in Study 1. Table 2 displays the performance of parameter estimates for the IL model and IP model under different sample sizes and distributions of data. The results indicate that the parameter

Table 2
Parameter estimates, standard deviation and mean square error

n	$\beta = 0.585$					
	Model 1: IL			Model 2: IP		
	$\hat{\beta}$	SD	MSE	$\hat{\beta}$	SD	MSE
^a 100	0.588	0.132	0.017	0.510	0.102	0.016
^b 100	0.583	0.152	0.023	0.501	0.115	0.020
^c 100	0.539	0.201	0.043	0.445	0.143	0.040
^a 150	0.592	0.109	0.012	0.514	0.085	0.012
^b 150	0.586	0.126	0.016	0.505	0.096	0.015
^c 150	0.540	0.164	0.029	0.449	0.118	0.032
^a 200	0.589	0.092	0.008	0.513	0.071	0.010
^b 200	0.582	0.105	0.011	0.504	0.080	0.013
^c 200	0.533	0.135	0.021	0.448	0.100	0.029
^a 250	0.585	0.080	0.006	0.511	0.063	0.010
^b 250	0.577	0.093	0.009	0.501	0.072	0.012
^c 250	0.529	0.120	0.018	0.445	0.090	0.028
^a 300	0.588	0.074	0.005	0.513	0.057	0.008
^b 300	0.580	0.086	0.007	0.503	0.066	0.011
^c 300	0.531	0.112	0.015	0.447	0.083	0.026
^a 500	0.585	0.056	0.003	0.512	0.045	0.007
^b 500	0.577	0.064	0.004	0.502	0.050	0.009
^c 500	0.526	0.082	0.010	0.445	0.062	0.024
^a 1000	0.585	0.040	0.002	0.512	0.032	0.006
^b 1000	0.577	0.046	0.002	0.502	0.036	0.008
^c 1000	0.526	0.059	0.007	0.445	0.045	0.022
^a 1500	0.585	0.033	0.001	0.512	0.026	0.006
^b 1500	0.576	0.038	0.001	0.502	0.030	0.008
^c 1500	0.525	0.048	0.006	0.445	0.037	0.021
^a 2000	0.586	0.028	0.001	0.512	0.022	0.006
^b 2000	0.577	0.032	0.001	0.502	0.025	0.007
^c 2000	0.525	0.041	0.005	0.445	0.031	0.020

Note. n is sample size. IL is item-level model. IP is item-parcel model. $\hat{\beta}$ is the estimated parameter. SD is the standard deviation. MSE is the mean square error. ^aNormal distribution (skewness=0, kurtosis=3). ^bNon-normal distribution (skewness=1, kurtosis=1.5). ^cNon-normal distribution (skewness=1.75, kurtosis=3.75).

estimates approach the true parameter value for the IL model under normal condition but biased when the data is highly skewed. The simulation results also show that the parameter estimates for the IP model are underestimated for both normal and non-normal data. The mean square error (MSE) measures the closeness of fitted $\hat{\beta}$ to the true value β . The MSE for both the IL model and IP model decreases when sample size increases. The MSE is the lowest for IL model and IP model when data is normal. The MSE is higher for both models when data is non-normal.

The box-plots in Figure 4 show that the dispersion (standard deviation) of parameter estimates is large for a small sample size. As expected, the dispersion of the parameter

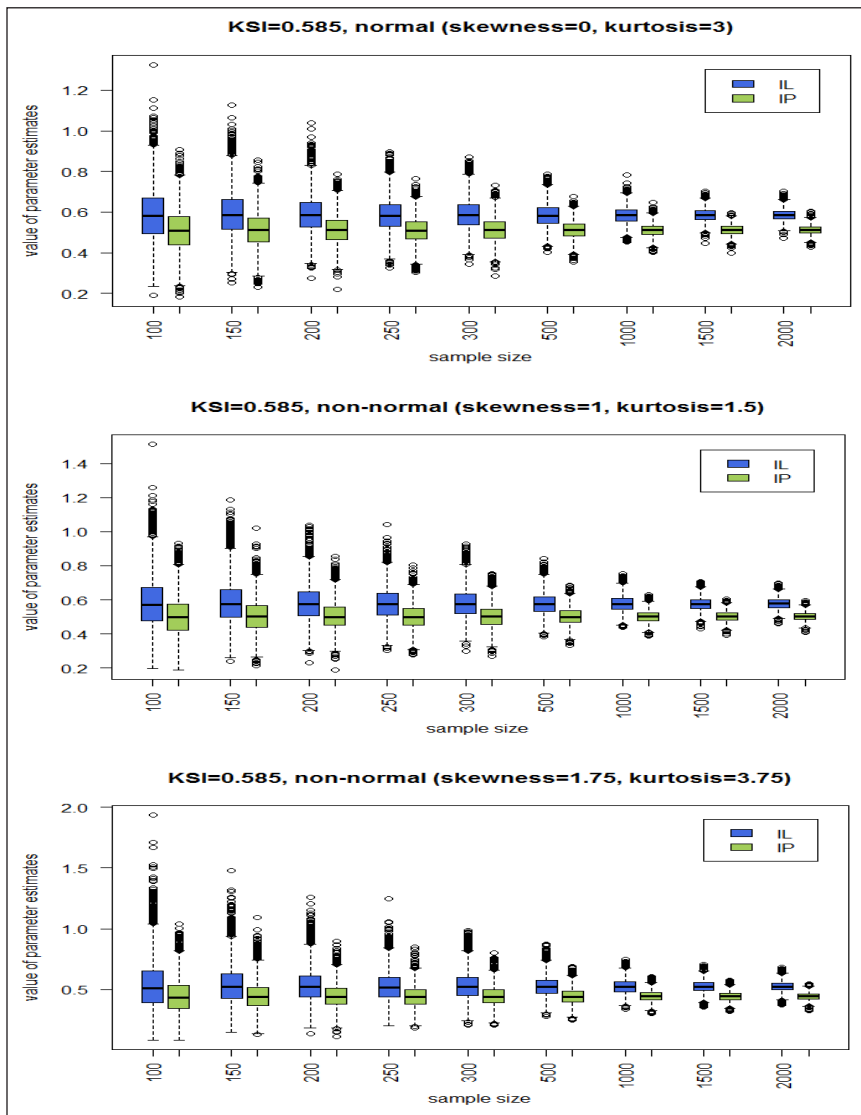


Figure 4. Box-plots for parameter estimates, $\hat{\beta}$ for item-level (IL) model and item-parcel (IP) model

estimates decreases as the sample size increases. The box-plots also show that the median of the parameter estimates is lower for the IP model across all sample sizes and types of distribution.

Table 3 shows the value of GoF measures for the IL model and IP model for different distributions of data. The results indicate that the model fit for all GoF measures are likely to improve with a higher sample size. The IP model has higher GoF measures for both normal and non-normal data across all sample sizes. When the data is normal, the RMSEA is lower for the IL model. However, the RMSEA is slightly lower for the IP model when data is non-normal. Since the AGFI and NFI are formed in a similar pattern with GFI and due to space constraint, the box-plots for AGFI and NFI are not presented.

Table 3
GoF measure values

n	Model	Distribution	Chi-sq	GFI	AGFI	RMSEA	NFI	TLI	CFI
100	IL	a	96.303	0.892	0.855	0.026	0.924	0.993	0.992
		b	114.962	0.874	0.830	0.050	0.908	0.974	0.977
		c	141.432	0.849	0.797	0.075	0.869	0.937	0.947
	IP	a	13.638	0.964	0.922	0.028	0.978	0.998	0.996
		b	15.643	0.959	0.911	0.040	0.974	0.993	0.993
		c	18.555	0.952	0.896	0.056	0.964	0.982	0.987
150	IL	a	93.981	0.926	0.900	0.018	0.949	0.997	0.995
		b	113.168	0.912	0.881	0.039	0.938	0.984	0.986
		c	139.329	0.894	0.857	0.060	0.909	0.959	0.965
	IP	a	13.510	0.976	0.947	0.022	0.985	0.999	0.997
		b	15.534	0.972	0.940	0.031	0.983	0.995	0.996
		c	18.401	0.967	0.929	0.045	0.975	0.988	0.992
200	IL	a	92.526	0.944	0.924	0.014	0.962	0.998	0.997
		b	112.095	0.932	0.909	0.033	0.953	0.988	0.990
		c	138.322	0.918	0.889	0.051	0.931	0.969	0.974
	IP	a	13.204	0.982	0.961	0.018	0.989	0.999	0.998
		b	15.341	0.979	0.955	0.027	0.987	0.997	0.997
		c	18.363	0.975	0.946	0.038	0.981	0.991	0.994
250	IL	a	91.776	0.954	0.939	0.012	0.970	0.999	0.998
		b	111.263	0.945	0.926	0.029	0.962	0.991	0.992
		c	137.066	0.933	0.910	0.045	0.944	0.976	0.980
	IP	a	13.357	0.985	0.968	0.016	0.991	0.999	0.999
		b	15.548	0.983	0.963	0.024	0.989	0.997	0.997
		c	18.385	0.980	0.956	0.035	0.985	0.993	0.995
300	IL	a	91.500	0.962	0.948	0.011	0.975	0.999	0.998
		b	111.178	0.954	0.938	0.026	0.968	0.992	0.993
		c	137.070	0.944	0.924	0.041	0.953	0.980	0.983
	IP	a	13.097	0.988	0.974	0.014	0.993	0.999	0.999
		b	15.338	0.986	0.969	0.022	0.991	0.998	0.998
		c	18.317	0.980	0.964	0.031	0.988	0.994	0.997
500	IL	a	90.113	0.977	0.969	0.008	0.985	0.999	0.999
		b	110.218	0.972	0.962	0.020	0.981	0.996	0.996
		c	136.344	0.965	0.953	0.032	0.972	0.988	0.990

Table 3 (continue)

n	Model	Distribution	Chi-sq	GFI	AGFI	RMSEA	NFI	TLI	CFI
500	IP	a	13.101	0.993	0.984	0.011	0.996	0.999	0.999
		b	15.338	0.991	0.981	0.017	0.995	0.999	0.999
		c	18.350	0.990	0.978	0.024	0.992	0.996	0.997
1000	IL	a	89.763	0.988	0.984	0.005	0.992	0.999	0.999
		b	109.711	0.986	0.981	0.014	0.990	0.998	0.998
		c	136.011	0.982	0.976	0.022	0.985	0.994	0.995
	IP	a	13.045	0.996	0.992	0.008	0.998	0.999	0.999
		b	15.290	0.996	0.991	0.012	0.997	0.999	0.999
		c	18.347	0.995	0.989	0.017	0.996	0.998	0.999
1500	IL	a	89.398	0.992	0.989	0.004	0.995	0.999	0.999
		b	109.525	0.990	0.987	0.011	0.994	0.999	0.999
		c	136.485	0.988	0.984	0.018	0.990	0.996	0.997
	IP	a	12.961	0.998	0.995	0.006	0.999	1.000	0.999
		b	15.211	0.997	0.994	0.010	0.998	0.999	0.999
		c	18.296	0.997	0.993	0.014	0.997	0.999	0.999
2000	IL	a	89.347	0.994	0.992	0.004	0.996	0.999	0.999
		b	109.559	0.993	0.990	0.010	0.995	0.999	0.999
		c	136.773	0.991	0.988	0.016	0.993	0.997	0.997
	IP	a	13.006	0.998	0.996	0.005	0.999	0.999	0.999
		b	15.269	0.998	0.995	0.008	0.999	0.999	0.999
		c	18.391	0.997	0.994	0.012	0.998	0.999	0.999

Note. n is sample size. IL is item-level model. IP is item-parcel model. ^aNormal (skewness=0, kurtosis=3). ^bNon-normal (skewness=1, kurtosis=1.5). ^cNon-normal (skewness=1.75, kurtosis=3.75). Chi-sq is the chi-squared. GFI is the goodness-of-fit Index. AGFI is the Adjusted goodness-of-fit index. RMSEA is the root mean square error of approximation. NFI is the Normed Fit Index. TLI is the Tucker-Lewis index. CFI is the comparative fit index.

The box-plots for GFI in Figure 5 show that GFI is affected by sample size, model structure (IL model and IP model), and distribution of data. The GFI improves as the sample size increases for both models and GFI is lower when data is non-normal. This finding is consistent the studies of Fan et al. (1999) and DoĀan and Özdamar (2017) but contradicts with the studies of Jöreskog and Sörbom (1982) and Bagozzi and Yi (1988) who found that sample size does not affect the values of GFI and AGFI. The box-plots also show that the median of GFI is higher for the IP model and the medians of both models are close to each other when the sample size is large. The dispersion is large for small sample sizes (n<500) for both models under normal and non-normal conditions.

The box-plots in Figure 6 show that RMSEA for the IL model and IP model are within the acceptable threshold level (RMSEA<0.06), indicating that both models fit the data well. RMSEA is affected by sample size, model structure (IL model and IP model) and distribution of data. The median of RMSEA is lowest for the IP model and it is close to the median of the IL model for a large sample size. The dispersion of RMSEA declines as the sample size increases under normal and non-normal conditions.

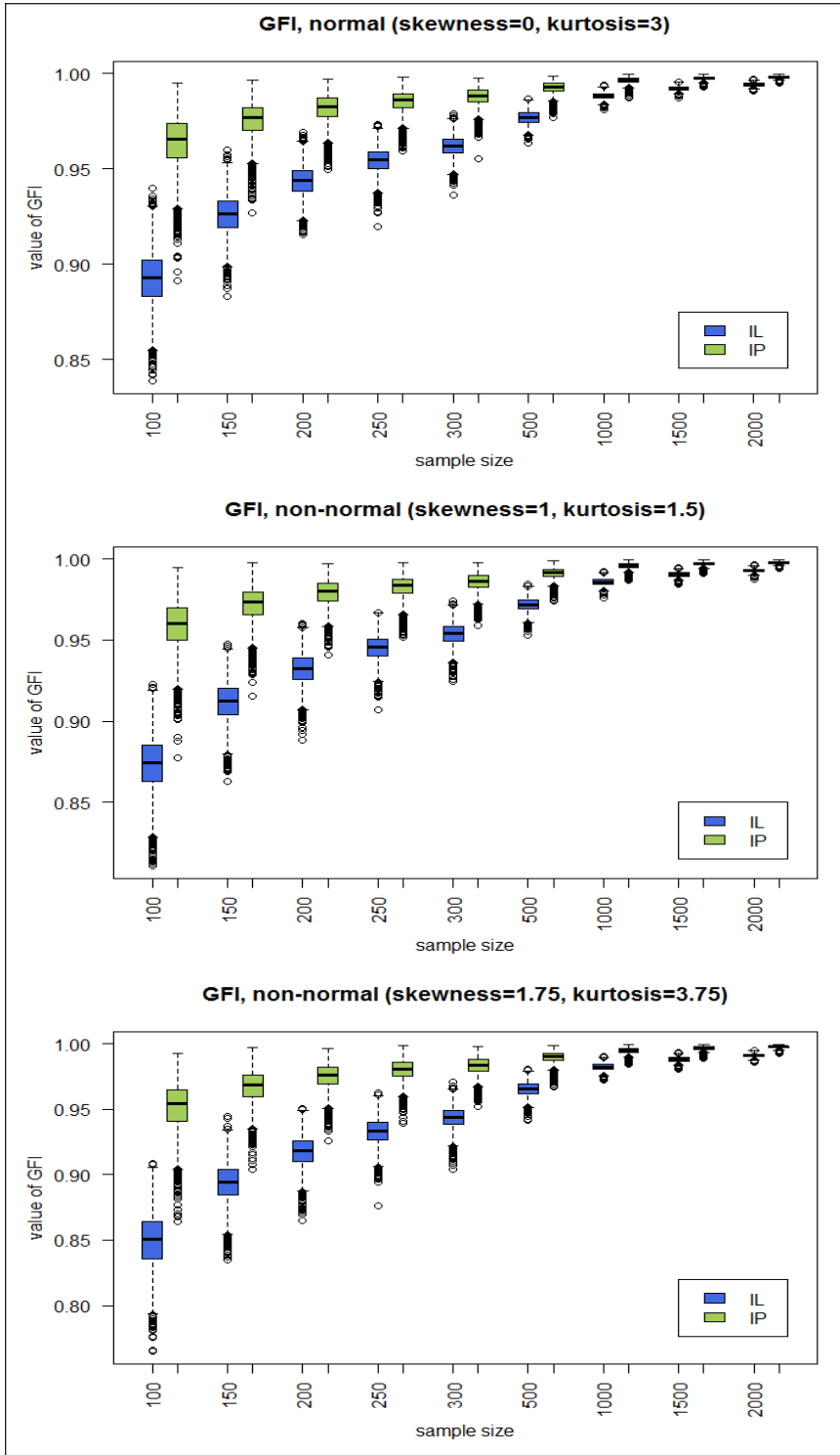


Figure 5. Box-plots for GFI for item-level (IL) model and item-parcel (IP) model

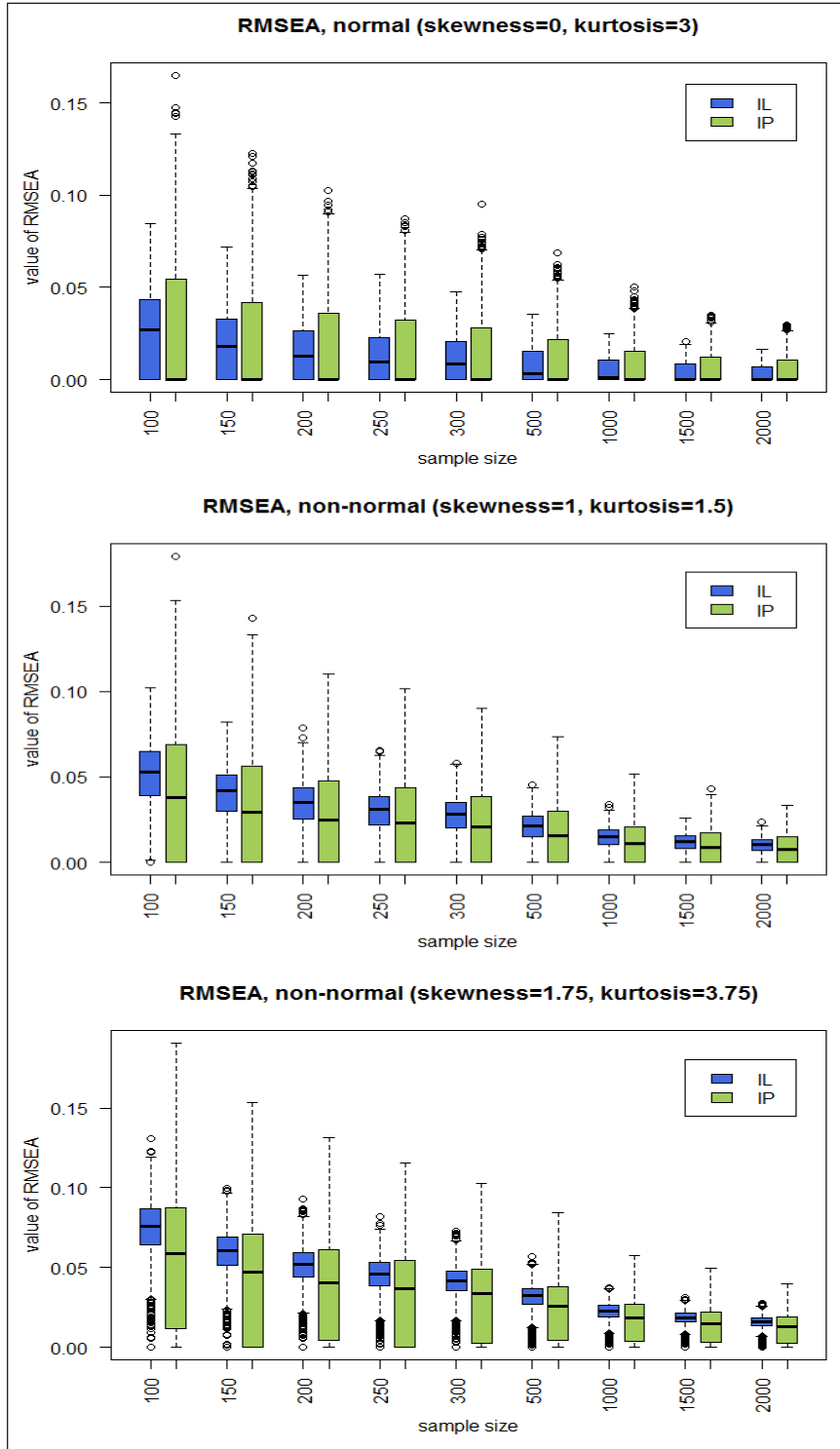


Figure 6. Box-plots for RMSEA for item-level (IL) model and item-parcel (IP) model

The box-plots in Figure 7 show that TLI is not influenced much by sample size and this finding is in line with the study of Fan et al. (1999). TLI for the IL model is more affected when data is non-normal and sample size is small ($n = 100$). The TLI for both models exceed the acceptable threshold level (>0.95) indicating that both models fit the data well. The box-plots show that the median of TLI is higher for the IP model and the medians of both models are close to each other for a large sample size. The dispersion is large for small sample sizes ($n < 500$) for both models under normal and non-normal conditions.

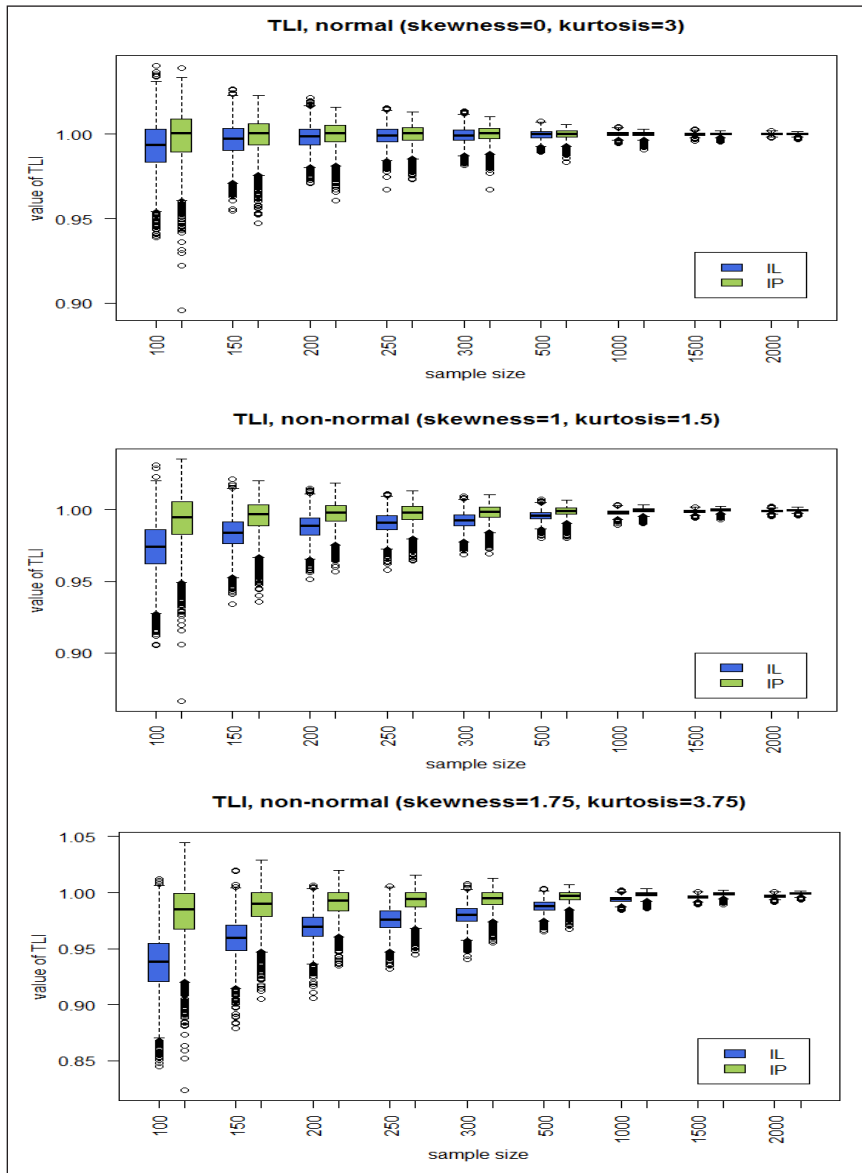


Figure 7. Box-plots for TLI for item-level (IL) model and item-parcel (IP) model

The box-plots in Figure 8 show that CFI is affected by model structure (IL model and IP model). The CFI also shows that the IL model and IP model have good model fit since the values exceed the acceptable threshold level (>0.95). The median of CFI is higher for the IP model compared to the IL model but for a large sample size, the medians for both models are close to each other. The dispersions are large for small sample sizes ($n < 500$) for both models under normal and non-normal conditions.

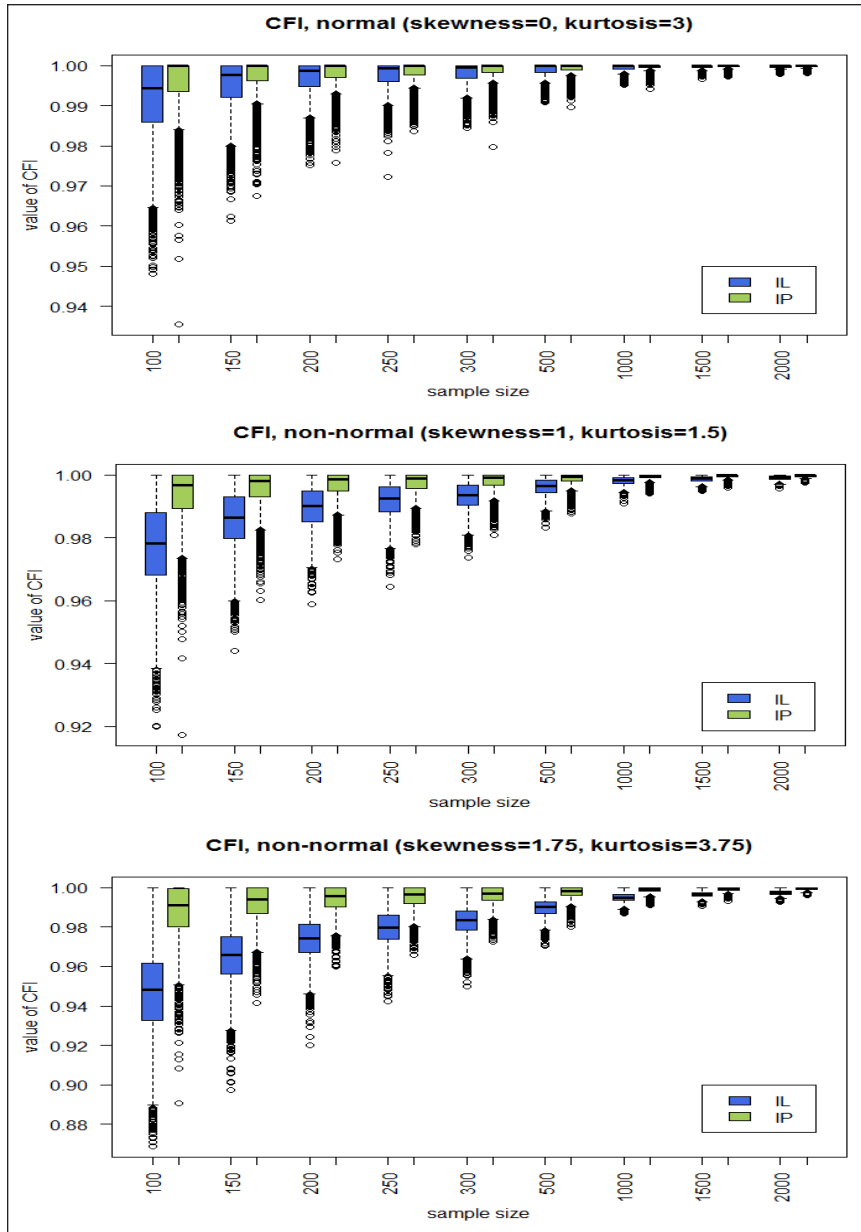


Figure 8. Box-plots for CFI for item-level (IL) model and item-parcel (IP) model

The simulation results and box-plots demonstrate that GoF measures improve with an increase in sample size and GoF measures are affected by model structure. In summary, based on parameter estimates and MSE, the IL model produces less biased parameter estimates than the IP model. However, the parameter estimates of the IL model are affected when data is severely non-normal. The summary of GoF measures presented in Table 4 shows that model fit for the IP model is better than the ILvel model under normal and non-normal conditions except for RMSEA under normal condition.

Table 4
Summary of GoF measures

	GFI		AGFI		NFI		TLI		CFI		RMSEA	
	N	NN	N	NN	N	NN	N	NN	N	NN	N	NN
Model 1: IL												/
Model 2: IP	/	/	/	/	/	/	/	/	/	/	/	/

Note. N is normal. NN is non-normal. IL is item-level model. IP is item-parcel model. [/] represent the best model fit. GFI is the goodness-of-fit index. AGFI is the Adjusted goodness-of-fit index. RMSEA is the root mean square error of approximation. NFI is the Normed Fit Index. TLI is the Tucker-Lewis index. CFI is the comparative fit index.

Study 2: Results of Empirical Example

This section presents the results of parameter estimates and model fit for the IL model and IP model for the empirical example in Study 2. The results for parameter estimates, p-value and standard error for the original (IL) model and IP (Model 1, Model 2, Model 3) models are presented in Table 5. The parameter estimates for Model 1 are closer to the original model followed by Model 2 and Model 3. Based on p-values, the main paths are significant for all models. Among the three IP models, Model 1 has the lowest standard error while Model 3 has the highest standard errors for all paths.

Table 5
Parameter estimates, p-value and standard error of empirical example

	IL	IP		
		Model 1	Model 2	Model 3
PSOC <- PSI	-0.489*** (0.101)	-0.505*** (0.090)	-0.538*** (0.095)	-0.551*** (0.106)
QoL<- PSOC	0.357** (4.015)	0.347** (4.049)	0.370** (5.264)	0.286** (6.009)
QoL<- PSI	-0.390*** (2.292)	-0.393*** (2.059)	-0.412*** (2.619)	-0.491*** (3.962)

Note. ***p-value < 0.01. **p-value < 0.05. *p-value < 0.10. PSOC is parenting sense of competence. IL is item-level model. IP is item-parcel model. PSI is parenting stress index. HRQoL is health related quality of life. The value in () represent standard error.

Table 6 shows the GoF measures of the empirical example. The results indicate that all the GoF measures are higher for the IP model. However, the value of RMSEA for Model 1 is closer to the original (IL) model.

The empirical findings support the simulation results in that item parceling can improve model fit but it can also produce biased parameter estimates. Based on this empirical example, it is not advisable to average all items in a construct to form an observed variable (Model 3). We recommend forming parcels for a model which consists of many indicators in a construct (six and above). Researchers should also consider to use at least three indicators per construct as suggested by Ding et al. (1995), Hair et al. (2015) and Iacobucci (2010).

Table 6
GoF measures of empirical examples

Model	Chi-sq(df)	GFI	AGFI	RMSEA	NFI	TLI	CFI
IL	1331.512 (767)	0.740	0.708	0.064	0.711	0.841	0.851
IP :							
Model 1	645.831 (366)	0.808	0.771	0.065	0.804	0.892	0.903
Model 2	368.245 (180)	0.848	0.804	0.076	0.815	0.877	0.076
Model 3	48.607 (11)	0.934	0.833	0.138	0.894	0.836	0.914

Note. GFI is the goodness-of-fit index. AGFI is the Adjusted goodness-of-fit index. RMSEA is the root mean square error of approximation. NFI is the Normed Fit Index. TLI is the Tucker-Lewis index. CFI is the comparative fit index. IL is item-level model. IP is item-parcel model.

CONCLUSION

This simulation study investigated the performance of parameter estimates and model fit based on different sample sizes, model structures and distributions of data in SEM. The simulation results indicate that the IL model produced biased parameter estimates under non-normal distribution of data. The IP model also produced biased parameter estimates for both normal and non-normal data regardless of sample size. In terms of model fit, the IP model is better than the IL model under normal and non-normal conditions except for RMSEA under normal condition. The empirical example provided evidence that the IP model estimates were close to the ILevel model but the minimum number of indicators per construct must be at least three to reduce the biasness of parameter estimates. Averaging all items of a construct is not recommended as it will produce highly biased estimates.

Several limitations should be noted in this study because it only used a random item parceling technique and only a simple structural model in the simulation design. In future work, the simulation study could be extended to investigate how different parceling techniques can reduce the biasness of the parameter estimates of a structural equation model for a more complex model.

ACKNOWLEDGEMENT

We would like to express our gratitude to Professor Emeritus Dale Louis Goodhue from Department of Management Information Systems, Terry College of Business, University of Georgia for his permission to use his model as a basis to generate the data in this study.

REFERENCES

- Bagozzi, R. R., & Yi, Y. (1988). On the evaluation of structural equation models. *Journal of the Academy of Marketing Science*, 16(1), 74-94.
- Bandalos, D. L. (2002). The effects of item parceling on goodness-of-fit and parameter estimate bias in structural equation modeling. *Structural Equation Modeling*, 9(1), 78-102.
- Bearden, W. O., Sharma, S., & Teel, J. E. (1982). Sample size effects on chi square and other statistics used in evaluating causal models. *Journal of Marketing Research*, 19, 425-430.
- Bentler, P. M. (1990). Comparative fit indexes in structural models. *Psychological Bulletin*, 107(2), 238-246.
- Byrne, B. M. (2010). *Structural equation modeling with AMOS: Basic concepts, applications, and programming* (2nd Ed.). London, New York: Routledge.
- Curran, P. J., West, S. G., & Finch, J. F. (1996). The robustness of test statistics to nonnormality and specification error in confirmatory factor analysis. *Psychological Methods*, 1(1), 16-29.
- Deng, L., Yang, M., & Marcoulides, K. M. (2018). Structural equation modeling with many variables: A systematic review of issues and developments. *Frontiers in Psychology*, 9(580), 1-14.
- Ding, L., Velicer, W. F., & Harlow, L. L. (1995). Effects of estimation methods, number of indicators per factor, and improper solutions on structural equation modeling fit indices. *Structural Equation Modeling*, 2(2), 119-144.
- Doĝan, İ., & Özdamar, K. (2017). The effect of different data structures, sample sizes on model fit measures. *Communications in Statistics-Simulation and Computation*, 46(9), 7525-7533.
- Fan, X., Thompson, B., & Wang, L. (1999). Effects of sample size, estimation methods, and model specification on structural equation modeling fit indexes. *Structural Equation Modeling*, 6(1), 56-83.
- Fleishman, A. I. (1978). A method for simulating non-normal distributions. *Psychometrika*, 43(4), 521-532.
- Goodhue, D. L., Lewis, W., & Thompson, R. (2012). Does PLS have advantages for small sample size or non-normal data? *MIS Quarterly*, 36(3), 981-1001.
- Hair Jr, J. F., Black, W. C., Babin, B. J., & Anderson, R. E. (2015). *Multivariate data analysis* (7th Ed.). London, New York: Pearson Prentice Hall.
- Hall, R. J., Snell, A. F., & Foust, M. S. (1999). Item parceling strategies in SEM: Investigating the subtle effects of unmodeled secondary constructs. *Organizational Research Methods*, 2(3), 233-256.
- Hamzah, A. H., Yap, B. W., Xie, X. J., & Ong, S. H. (2017). Investigating the power of goodness of fit tests for multinomial logistic regression. *Communication in Statistics: Simulation and Computation*, 47(4), 1039-1055.

- Hooper, D., Coughlan, J., & Mullen, M. R. (2008). Structural equation modelling: Guidelines for determining model fit. *The Electronic Journal of Business Research Methods*, 6(1), 53-60.
- Iacobucci, D. (2010). Structural equations modeling: Fit Indices, sample size, and advanced topics. *Journal of Consumer Psychology*, 20, 90-98.
- Jöreskog, K. G., & Sörbom, D. (1982). Recent developments in structural equation modeling. *Journal of Marketing Research*, 19, 404-416.
- Kim, S., & Hagtvet, K. A. (2003). The impact of misspecified item parceling on representing latent variables in covariance structure modeling: A simulation study. *Structural Equation Modeling*, 10(1), 101-127.
- Landis, R. S., Beal, D. J., & Tesluk, P. E. (2000). A comparison of approaches to forming composite measures in structural equation models. *Organizational Research Methods*, 3(2), 186-207.
- Little, T. D., Cunningham, W. A., Shahar, G., & Widaman, K. F. (2002). To parcel or not to parcel: Exploring the question, weighing the merits. *Structural Equation Modeling*, 9(2), 151-173.
- Little, T. D., Rhemtulla, M., Gibson, K., & Schoemann, A. M. (2013). Why the items versus parcels controversy needn't be one. *Psychological Methods*, 18(3), 285-300.
- Lyhagen, J., & Kraus, K. (2013). The small sample performance of estimators of the standard errors of structural equation models. *Journal of Statistical Computation and Simulation*, 83(3), 458-471.
- MacCallum, R. C., & Tucker, L. R. (1991). Representing sources of error in the common-factor model: Implications for theory and practice. *Psychological Bulletin*, 109(3), 502-511.
- Marsh, H. W., Balla, J. R., & McDonald, R. P. (1988). Goodness-of-fit indexes in confirmatory factor analysis: The effect of sample size. *Psychological Bulletin*, 103(3), 391-410.
- Morgan, G. B., Hodge, K. J., & Baggett, A. R. (2016). Latent profile analysis with nonnormal mixtures: A Monte Carlo examination of model selection using fit indices. *Computational Statistics and Data Analysis*, 93, 146-161.
- Mulaik, S. A., James, L. R., Alstine, J. V., Bennett, N., Lind, S., & Stilwell, C. D. (1989). Evaluation of goodness-of-fit indices for structural equation models. *Psychological Bulletin*, 105(3), 430-445.
- Nasir, N. N. M. (2015). *Investigating stress, self-efficacy and quality of life of mothers with autistic children: A structural equation modelling (SEM) approach* (Unpublished Master's Thesis). Universiti Teknologi Mara, Shah Alam, Malaysia.
- Nasser, F., & Wisenbaker, J. (2006). A monte carlo study investigating the impact of item parceling strategies on parameter estimates and their standard errors in CFA. *Structural Equation Modeling*, 13(2), 204-228.
- Olsson, U. H., Foss, T., & Breivik, E. (2004). Two equivalent discrepancy functions for maximum likelihood estimation: Do their test statistics follow a non-central chi-square distribution under model misspecification? *Sociological Methods and Research*, 32(4), 453-500.
- Olsson, U. H., Foss, T., Troye, S. V., & Howell, R. D. (2000). The performance of ML, GLS, and WLS estimation in structural equation modeling under conditions of misspecification and nonnormality. *Structural Equation Modeling*, 7(4), 557-595.

- Orcan, F. (2013). *Use of item parceling in structural equation modeling with missing data* (PhD Dissertation). Florida State University, Tallahassee, Florida.
- Ory, D. T., & Mokhtarian, P. L. (2010). The impact of non-normality, sample size and estimation technique on goodness-of-fit measures in structural equation modeling: evidence from ten empirical models of travel behavior. *Quality and Quantity*, 44(3), 427-445.
- Rocha, C. M., & Chelladurai, P. (2012). Item parcels in structural equation modeling: An applied study in sport management. *International Journal of Psychology and Behavioral Sciences*, 2(1), 46-53.
- Ryu, E. (2011). Effects of skewness and kurtosis on normal-theory based maximum likelihood test statistic in multilevel structural equation modeling. *Behavior Research Methods*, 43, 1066-1074.
- Shah, R., & Goldstein, S. M. (2006). Use of structural equation modeling in operations management research: Looking back and forward. *Journal of Operations management*, 24(2), 148-169.
- Sharma, S., Mukherjee, S., Kumar, A., & Dillon, W. R. (2005). A simulation study to investigate the use of cutoff values for assessing model fit in covariance structure models. *Journal of Business Research*, 58, 935-943.
- Sterba, S. K., & Maccallum, R. C. (2010). Variability in parameter estimates and model fit across repeated allocations of items to parcels. *Multivariate Behavioral Research*, 4, 322-358.



The Effect of Deep Breathing Exercises on Menstrual Pain Perception in Adolescents with Primary Dysmenorrhea

Kurniati Devi Purnamasari*, Tita Rohita, Dini Nurbaeti Zen and Widya Maya Ningrum

Faculty of Health Sciences, Universitas Galuh, 46274, Ciamis, West Java Indonesia

ABSTRACT

Cyclic menstrual pain, one of the most common gynecologic complaints, is a crucial issue. Unfortunately, only limited studies have focused on how to care for the menstrual pain in adolescents. This paper reports on the effective treatment for menstrual pain to mitigate or preclude menstrual pain perception, which is non-invasive to patients, in adolescents aged from 13 to 15 years. The treatment was conducted by positioning the patient in a supine position. Each patient was guided to take 30 minutes of breathing relaxation techniques. The use of Visual Analogue Scale (VAS) was intended to measure the subjects' painfulness level. This study included 47 respondents whose menstrual pain was monitored in 30 minutes after the intervention. The findings of this study indicate a significant reduction of patients' pain. The study suggests that further studies should focus on complementary treatments for overcoming menstrual pain.

Keywords: Adolescents, deep breathing, pain perception, primary dysmenorrhea

INTRODUCTION

Menstrual pain is one of the most common gynecologic complaints defined as a cyclic pain that occurs in association with menstruation (Bektaş et al., 2010; Tu et al., 2010). The menstrual disturbances as health problems among young girls affect not only reproductive,

but also physical health and quality of life (Rad et al., 2018). Around 1.2 billion people, or 1 in 6 of the world's population, are adolescents aged from 10 to 19 (World Health Organization, 2014). Estimates of the prevalence of females experiencing dysmenorrhea vary widely from 16.8% to 81%. It can be severe enough to interfere

ARTICLE INFO

Article history:

Received: 28 April 2019

Accepted: 27 November 2019

Published: 15 April 2020

E-mail addresses:

kurniatidevip@gmail.com (Kurniati Devi Purnamasari)

titarohita@gmail.com (Tita Rohita)

dininurbaeti@gmail.com (Dini Nurbaeti Zen)

widyamayaningrum@gmail.com (Widya Maya Ningrum)

* Corresponding author

with daily activities as well as causing absence from school and work (Yonglitthipagon et al., 2017). Studies conducted in Asia and New Zealand showed that around 42% to 73% of women experienced moderate to severe dysmenorrhoea (Chen et al., 2015).

Pharmacological efforts can be performed by administering analgesic drugs as pain relievers (Smeltzer et al., 2008). Pain management experienced by individuals can be through pharmacological intervention, collaborated with physicians or other primary care providers to the patient. The interaction that occurs in this therapy has a mutually synergistic effect between the two that can be mutually augmented by the therapeutic work without adding the ill effects of pain (Widyawati et al., 2016). This is supported by research that proves that there are side effects when patients take them for a long time. It is therefore against this background that Deep Breathing Exercises (DBE) are suggested as an alternative source of treatment for primary dysmenorrhea (Sosorburam et al., 2019).

Relaxation techniques provide us with excellent methods that can be practiced with awareness anytime at our discretion (Romas & Sharma, 2017). One specific respiratory maneuver in breathing is both popularly and scientifically linked to Deep Breathing Relaxation (Vlemincx et al., 2016). Mind-body science has now reached a stage where it should be accepted (Rakel, 2017). A meta-analysis of 47 actively-controlled trials with 3,515 participants shows that participation in mindfulness instruction programming is effective for improving self-reported symptoms of anxiety, depression, and pain (Sibinga, 2016). The prevalence of dysmenorrhea in adolescents in Indonesia is reported to be 55% (Astutik et al., 2015). In a relaxed state, human body will stop the production of adrenaline hormones and all the hormones that are needed during stress (Bennett, 2017; Bojorquez et al., 2017; Boyanova, 2017). When reducing stress, human body reduces the production of cortisol hormones (Navas et al., 2012), because of the need for relaxation to provide an opportunity for the body to produce hormones, which are important to get menstruation that avoids pain (Droit-Volet et al., 2015).

Spontaneous breathing in healthy persons is characterized by substantial variability (Jafari et al., 2016; Mailhot-Larouche et al., 2017; Romas & Sharma, 2017; Vlemincx et al., 2010). First, taking a deep breath can reduce hypoxia and hypercapnia (Vlemincx et al., 2010). The patient is verbally coached through a modified slow vital capacity maneuver and brought to a reproducible deep inspiration breath-hold level.

Lower rates (84.2%) have been reported for Asia, with 84.2% for Southeast Asia, 68.7% for Eastern Asia, 74.8% for the Middle East, and 54.0% for Southern Asia. Relaxation techniques provide us with excellent methods that can be practiced with awareness anytime at our discretion. Research on alternative treatments in the process of pain management to intensity of pain in menstrual pain will be very helpful in identifying and providing care by midwives (Moyer et al., 2011). The results of the study are expected to be basic data as a cut-off point for midwives in handling menstrual pain in patients on a non-pharmacological basis, thereby reducing unnecessary interventions in midwifery services.

MATERIALS AND METHODS

Data Collection

The location of this study was Junior High School in Ciamis district. The duration of the research data collection was 1 month. This research began by making and modifying movements of deep breath relaxation exercises. Before taking the data, the researcher identified respondents in accordance with the criteria, then the respondents were given informed consent if the respondents agreed to the data collection by questionnaire. Informed consent was obtained from all volunteers and the study was approved by the local ethics committee. The respondents performed deep breathing exercises to eliminate menstrual pain. Exclusion criteria were as follows: any cardiac or respiratory diseases, a history of migraines or other (chronic) pain syndromes, or the use of pain medication or psychotropic drugs.

Procedure

All participants completed the Beck Depression Inventory (BDI) and the “Trait anxiety” part of the State and Trait Anxiety Inventory (STAI-X2). All subjects were instructed not to practice at home and were furthermore not allowed to participate in any breathing exercises or meditation programs during the washout period. After inclusion, all subjects received written handouts explaining the course of the study and an instruction manual for Deep Breathing Exercises (DBE), according to the recommendations from breathing literature (Scheibenbogen & Prieler, 2002). The use of positions of the client and movement lines mentioned for the basic position is in accordance with the operational standard shown in Figure 1.

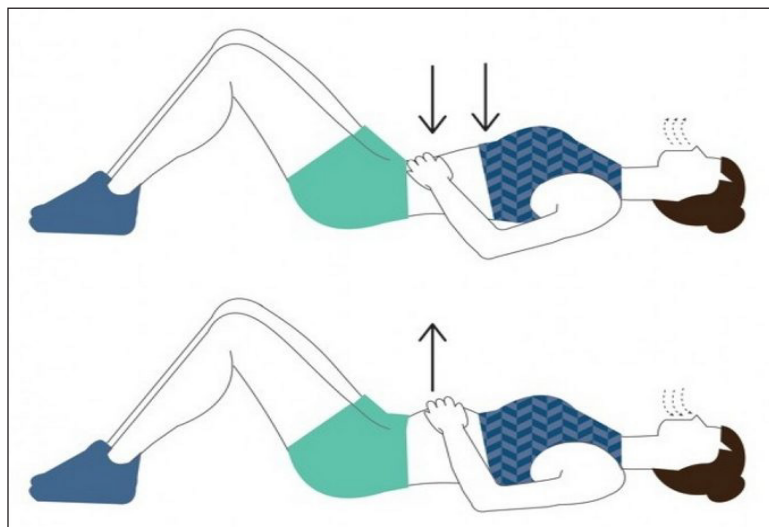


Figure 1. The reference position of breath relaxation technique

Study Design and Samples

The research design used pre-experiment, in which the factors considered were Deep Breathing Exercises (DBE) and pain perception in pre-test and post-test. The results of intervention were analyzed using Wilcoxon ranks test. The number of samples was 47 respondents of adolescents with menstrual pain by choosing subjects whose representation was determined based on the inclusion criteria. Data retrieval was done after the respondents had agreed with breath relaxation techniques.

Data retrieval began when respondents experienced menstrual pain with a 5-10 VAS pain scale, experiencing menstrual pain in the first 24 -48 hours of menstruation, then the intervention was carried out for 30 minutes. A baseline assessment before the intervention was conducted using a questionnaire to collect data on the demographics of the participants and their pain levels. The questionnaire included questions on pain measured using a tenth-point scale. This instruction was provided by a trainer who was certified.

The results of the respondent pain scale questionnaire were collected and then taken to be analyzed by researchers with the assistance from enumerators. Furthermore, the data is presented in the form of an average value distribution of the results of data retrieval. The data that appears is created by the trend results from the measurement results. The research flow chart is shown in Figure 2.

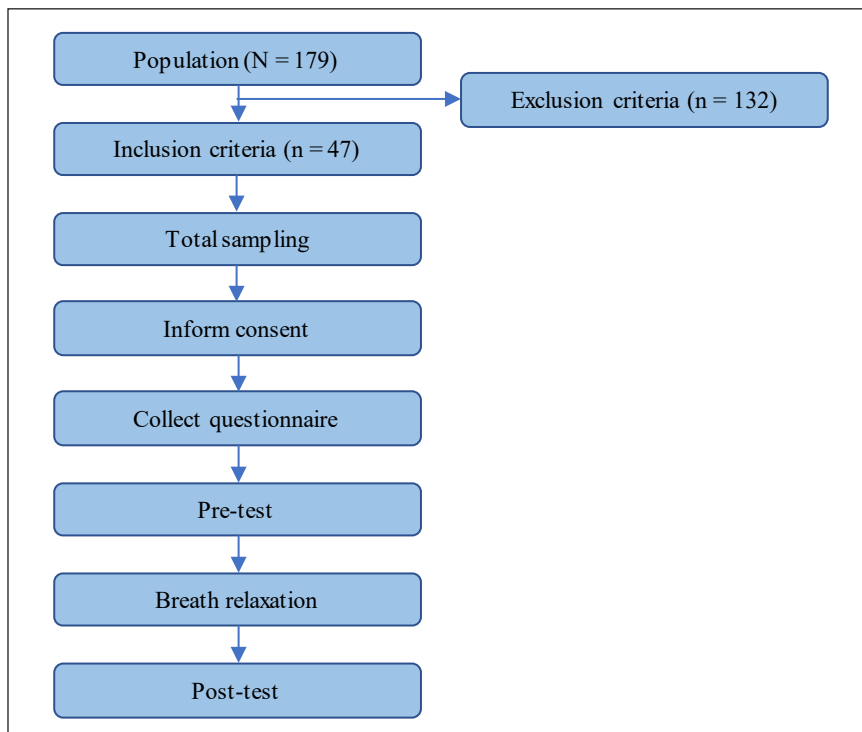


Figure 2. Flowchart measurement

RESULT AND DISCUSSION

Demographic Data of Respondents

This study shows that the average age of respondents were 13.97 ± 2.71 years while the age range of respondents was 13–15 years. The average respondents' grade was 7 ± 14.69 with a range of 7th- 8th. The average pain scale of the respondents' Visual Analogue Scale (VAS) was (6.33 ± 1.63) with a range of 5-10 pain scales. Demographic data of respondents is shown in Table 1.

Table 1
Demographic data of respondents

Characteristics		Number of Respondents (N)	Percentage (%)	Mean
Age	13 y.o	22	46.80	13.97
	14 y.o	4	8.51	
	15 y.o	21	44.69	
Grade	7 th	24	51.06	7
	8 th	23	49.94	
	Low	0	0	
VAS scale	Mid	32	68.08	7.02
	High	15	31.02	

Result of Pre and Post Intervention

It indicated that the median post-test ranks, $Mdn = 1.48$, was statistically and significantly higher than the median of pre-test ranks, $p < .000$. Based on Table 2 above, it can be seen that the average frequency of menstrual pain in forty-seven respondents enrolled in this study was decreased in terms of pain that was equal to 9–4 after being given breath relaxation.

Table 2
Distribution and average of menstrual pain

Variable	Pre		Post		<i>p value</i>
	median	Max-min	median	Max-min	
Menstrual Pain	6.39	10-5	1.48	6-2	0.000
Frequency of the pain	4.45	7-2	1.02	4-1	

Pretest. The results of this study indicate the frequency of menstrual pain in adolescents that had a tendency to vary between one and the other. The average maximum frequency that occurred in menstrual pain was on a scale of ten and the average minimum pain is on a scale of six.

Posttest. The average maximum frequency that occurred in menstrual pain after intervention is on a scale of 6 and the minimum pain average is on a scale of 2. VAS scale of menstrual

pain had a tendency to be directly proportional to pretest of breath relaxation technique, moderate to heavy scale with a scale of moderate as many as 30 people (63.83%), and scale of heavy as many as 17 people (36.17%), with an average pain scale of 7.02. VAS scale for post-test proportion of breath relaxation technique was moderate to mild scale with a scale of moderate as many as 6 people (12.77%), scale of mild as many as 31 people (87.23%), with an average pain scale of 3.04. The comparison trend of VAS scale trends in pretest and post-test breathing exercises is shown in Figure 3.

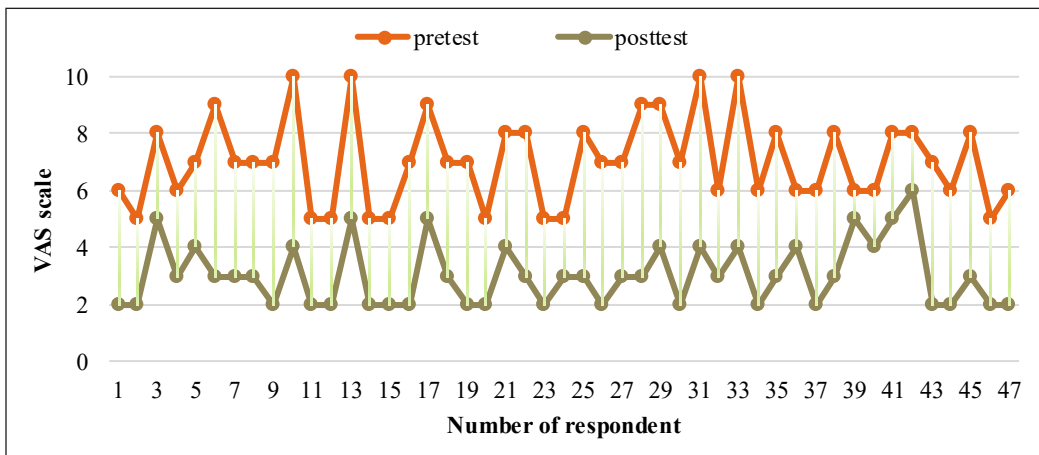


Figure 3. Comparison of VAS scale trends in pretest and posttest deep breathing exercises

The decrease in the intensity of menstrual pain occurs because the students practice breathing relaxation technique within 30 minutes, done when students feel menstrual pain. Previous study shows that the technique of deep breath relaxation is a form of nursing care in which case the health worker teaches the client how to do a deep breath, slow breath (hold maximum inspiration) and how to breathe slowly, in addition to reducing the intensity of pain (Bojorquez et al., 2017). Deep breathing relaxation techniques can also improve lung ventilation and increase blood oxygenation (Smeltzer et al., 2008). These findings corroborate previous studies showing significant decreases in acute negative effect in response to a breath relaxation session (Lin et al., 2014; Lindenmann et al., 2012) and suggest that breath relaxation can buffer against negative effect, perhaps by decreasing rumination and changing affective appraisals and coping with stress (Thelwall, 2017).

Breathing exercises can boost the relaxation and allow participants to focus in mind-body to change their thought on their pain. Based on the results of the study, there was a decrease in the intensity of menstrual pain in female students when practicing breathing relaxation techniques in approximately 30 minutes. This study still used questionnaire instruments in determining the results of research, so enabling the occurrence of bias. Further research should be developed with pain measurements using biomarkers to improve the objectivity of the study results.

CONCLUSION

The decrease of menstrual pain in adolescents with primary dysmenorrhea using breath relaxation technique shows a more quantitative value when compared to pre-test and post-test. The results of this study indicate that the prevalence of menstrual pain in active adolescents with primary dysmenorrhea decreases from 76% to 22% of menstrual pain. There was a decrease in menstrual pain scores in 46.6% of respondents with moderate to severe criteria for pain experienced on the first day. Breathing relaxation interventions have a tendency to be directly proportional to the reduction in the scale of VAS pain experienced by patients.

We will remind you in this paper on how observational studies regarding the perception of menstrual pain in respondents who are prone to various structural biases and limitations are. These biases lead us to be extremely cautious regarding the implementation of the results of this study in clinical practices, and to question the reliability of this study in terms of subjectivity. We recommend the use of another group in similar problem in future studies to get more accurate results.

ACKNOWLEDGEMENT

The authors gratefully acknowledge Galuh University for funding this publication and also express their appreciation to the Faculty of Health Sciences, Galuh University for sponsoring the publication of this research. No grants or any other forms of support were given for this study.

REFERENCES

- Astutik, H., Santoso, A. H., & Yuliwar, R. (2015, November 16-17). The effect of noni fruit juice (*Morinda citrifolia*) in decreasing menstrual pain (Dysmenorrhea)-phase II experiment. In *The Proceeding of 6th International Nursing Conference: Emphasize the Art of Nursing on Research, Education into Clinical and Community Practice* (pp. 111-123). Surabaya, Indonesia.
- Bektaş, H., Bilsel, Y., Sarı, Y. S., Ersöz, F., Koç, O., Deniz, M., . . . & Huq, G. E. (2010). Abdominal wall endometrioma; a 10-year experience and brief review of the literature. *Journal of Surgical Research*, *164*(1), e77-e81.
- Bennett, J. (2017). Beneficial redundancy—Did we forget the benefit of auscultation of breath sounds? *Journal of Oral and Maxillofacial Surgery*, *75*(5), 886-887.
- Bojorquez, J. Z., Bricq, S., Acquitter, C., Brunotte, F., Walker, P. M., & Lalande, A. (2017). What are normal relaxation times of tissues at 3 T? *Magnetic Resonance Imaging*, *35*, 69-80.
- Boyanova, L. (2017). Stress hormone epinephrine (adrenaline) and norepinephrine (noradrenaline) effects on the anaerobic bacteria. *Anaerobe*, *44*, 13-19.

- Chen, H. M., Wang, H. H., Chiu, M. H., & Hu, H. M. (2015). Effects of acupressure on menstrual distress and low back pain in dysmenorrheic young adult women: An experimental study. *Pain Management Nursing, 16*(3), 188-197.
- Droit-Volet, S., Fanget, M., & Dambrun, M. (2015). Mindfulness meditation and relaxation training increases time sensitivity. *Consciousness and Cognition, 31*, 86-97.
- Jafari, H., Van de Broek, K., Plaghki, L., Vlaeyen, J. W., Van den Bergh, O., & Van Diest, I. (2016). Respiratory hypoalgesia? Breath-holding, but not respiratory phase modulates nociceptive flexion reflex and pain intensity. *International Journal of Psychophysiology, 101*, 50-58.
- Lin, I., Tai, L., & Fan, S. (2014). Breathing at a rate of 5.5 breaths per minute with equal inhalation-to-exhalation ratio increases heart rate variability. *International Journal of Psychophysiology, 91*(3), 206-211.
- Lindenmann, J., Matzi, V., Neuboeck, N., Maier, A., Stark, G., & Smolle-Juettner, F. M. (2012). When swallowing takes your breath. *Surgery, 151*(4), 628-629.
- Mailhot-Larouche, S., Lortie, K., Marsolais, D., Flamand, N., & Bossé, Y. (2017). An in vitro study examining the duration between deep inspirations on the rate of renarrowing. *Respiratory Physiology and Neurobiology, 243*, 13-19.
- Moyer, C. A., Seefeldt, L., Mann, E. S., & Jackley, L. M. (2011). Does massage therapy reduce cortisol? A comprehensive quantitative review. *Journal of Bodywork and Movement Therapies, 15*(1), 3-14.
- Navas, M., Jiménez, A., & Asuero, A. (2012). Human biomarkers in breath by photoacoustic spectroscopy. *Clinica Chimica Acta, 413*(15), 1171-1178.
- Rad, H. A., Basirat, Z., Bakouei, F., Moghadamnia, A. A., Khafri, S., Farhadi Kotenaeci, Z., . . . & Kazemi, S. (2018). Effect of ginger and novafen on menstrual pain: A cross-over trial. *Taiwanese Journal of Obstetrics and Gynecology, 57*(6), 806-809.
- Rakel, D. (2017). *Integrative medicine e-book*. Philadelphia, USA: Elsevier Health Sciences.
- Romas, J. A., & Sharma, M. (2017). *Practical stress management: A comprehensive workbook*. London, UK: Academic Press.
- Scheibenbogen, O., & Prieler J. (2002). *Biofeedback aided psychotherapy (BAP)*. New York, NY: Kluwer Academic/ Plenum Publishers.
- Sibinga, E. M. (2016). "Just this breath..." How mindfulness meditation can shift everything, including neural connectivity. *EBioMedicine, 10*, 21-22.
- Smeltzer, S., Bare, B., Hinkle, J., Cheever, K., Townsend, M. C., & Gould, B. (2008). *Brunner and Suddarth's textbook of medical surgical nursing* (12th Ed.). Philadelphia, USA: Lippincott Williams and Wilkins.
- Sosorburam, D., Wu, Z. G., Zhang, S. C., Hu, P., Zhang, H. Y., Jiang, T., . . . & He, X. (2019). Therapeutic effects of traditional Chinese herbal prescriptions for primary dysmenorrhea. *Chinese Herbal Medicines, 11*(1), 10-19.
- Thelwall, M. (2017). TensiStrength: Stress and relaxation magnitude detection for social media texts. *Information Processing and Management, 53*(1), 106-121.

- Tu, C. H., Niddam, D. M., Chao, H. T., Chen, L. F., Chen, Y. S., Wu, Y. T., . . . & Hsieh, J. C. (2010). Brain morphological changes associated with cyclic menstrual pain. *Pain, 150*(3), 462-468.
- Vlemincx, E., Taelman, J., Van Diest, I., & Van den Bergh, O. (2010). Take a deep breath: The relief effect of spontaneous and instructed sighs. *Physiology and Behavior, 101*(1), 67-73.
- Vlemincx, E., Van Diest, I., & Van den Bergh, O. (2016). A sigh of relief or a sigh to relieve: The psychological and physiological relief effect of deep breaths. *Physiology and Behavior, 165*, 127-135.
- Widyawati, M. N., Hadisaputro, S., Anies, A., & Soejoenoes, A. (2016). Effect of massage and aromatherapy on stress and prolactin level among primiparous puerperal mothers in Semarang, Central Java, Indonesia. *Belitung Nursing Journal, 2*(4), 48-57.
- World Health Organization. (2014). Adolescents: health risks and solutions. *Fact sheet, 345*. Retrieved February 20, 2019, from <https://www.who.int/news-room/fact-sheets/detail/adolescents-health-risks-and-solutions>
- Yonglitthipagon, P., Muansiangsai, S., Wongkhumngern, W., Donpunha, W., Chanavirut, R., Siritaratiwat, W., . . . & Janyachoen, T. (2017). Effect of yoga on the menstrual pain, physical fitness, and quality of life of young women with primary dysmenorrhea. *Journal of Bodywork and Movement Therapies, 21*(4), 840-846.



Effects of Prolonged Confined Isolation on Status of Inflammation, Endothelial Activation and Function: In Preparation for Possible Future Manned Space Expedition to Mars

Thuhairah Rahman¹, Radzi Ahmad¹, Suhaila Muid^{1,4}, Tengku Saifudin Tengku Ismail^{1,2}, Ludmila B Buravkova³ and Hapizah Nawawi^{1,4*}

¹Faculty of Medicine, Universiti Teknologi MARA, 47000 UiTM, Sungai Buloh, Selangor, Malaysia.

²KPJ Tawakkal Specialist Hospital, 53000 Kuala Lumpur, Malaysia

³Institute of Biomedical Problems, Russian Academy of Science, Khoroshevskoe Shosse 76A, Moscow 123007, Russia

⁴Institute of Pathology Laboratory and Forensic Medicine (I-PPerForM), Universiti Teknologi MARA, 47000 UiTM, Sungai Buloh, Selangor, Malaysia

ABSTRACT

Inflammation and endothelial dysfunction are key components in atherogenesis. Should the status of these pro-atherogenesis factors be enhanced during prolonged confined space travel, specific countermeasures need to be instituted to prevent these processes to ensure safe outcome for astronauts during space expeditions. Six crew members were exposed to prolonged, confined isolation for 520 days. Standard exercise and diet regime were instituted throughout isolation phase. Age and gender-matched healthy, free living controls were recruited in parallel. Serial serum and whole blood were analysed for biomarkers of inflammation (hsCRP and IL-6) and endothelial activation (sICAM-1, sVCAM-1 and E-selectin). Flow-mediated dilatation (FMD) of the artery was performed following the standard protocols set by the International Brachial Artery Reactivity Task Force by

trained personnel. There was decreased sVCAM-1 concentration in crew members compared to baseline. However, there was significant decrease in percentage dilatation from baseline in FMD of the brachial artery in the crew members. Percent change increment was observed in hsCRP while percent change reduction was seen in sVCAM-1. The enhanced inflammation and reduced endothelial function could

ARTICLE INFO

Article history:

Received: 26 July 2019

Accepted: 27 November 2019

Published: 15 March 2020

E-mail addresses:

thuhairah@uitm.edu.my (Thuhairah Rahman)

radzey_ahmad@yahoo.com (Radzi Ahmad)

suhaila_muid@uitm.edu.my (Suhaila Muid)

tengkusaiifudin@yahoo.co.uk (Tengku Saifudin Tengku Ismail)

buravkova@imbp.ru (Ludmila B Buravkova)

hapizah.nawawi@gmail.com (Hapizah Nawawi)

* Corresponding author

possibly be attributed to the rigorous exercise instituted throughout the confinement period. Furthermore, possible haemoconcentration as a result of psychosocial stress and/or exercise-induced physiological response could further explain elevations in hsCRP, and unlikely pathological. Furthermore, endothelial activation was attenuated during isolation, suggesting that the diet and exercise program instated throughout the period improved endothelial function.

Keywords: Atherogenesis, coronary artery disease, cosmonauts, endothelial activation, endothelial function, inflammation, MARS500

INTRODUCTION

It has been described that patients with illness are those who live in a normal environment but have abnormal physiology. In contrast, cosmonauts are humans with normal physiology who live in an abnormal environment. It is this abnormal environment in space that causes unique and significant alterations to a cosmonaut's physiology that could have a negative impact on their health. The direction of research into space, the final frontier, has shifted from developing ways and means to get there, to currently pushing the boundaries of understanding neighbouring planets and discovering potential resources. The current approach of space programs to stretch space exploration farther away from earth, thus extending durations of expeditions from months to years, will challenge the current capabilities of space medicine.

Mars is the fourth planet from the sun and the second smallest planet in our Solar System. Named after the Roman god of war, it is often described as the 'Red Planet' due to the iron oxide atmosphere giving its surface a reddish appearance (Zubrin & Wagner, 2011; Rees, 2012). Mars is a terrestrial planet with a thin atmosphere, having surface features reminiscent of the craters of the moon and the volcanoes, valleys, deserts and polar ice caps of earth. Over the years, there have been increasing interest to further explore the surface of mars, The Mars-500 mission was a psychosocial isolation experiment conducted between 2007 and 2011 by Russia, the European Space Agency and China, in preparation for an unspecified future manned spaceflight to the planet. The experiment's facility was located at the Russian Academy of Sciences' Institute of Biomedical Problems (IBMP) Moscow, Russia (Basner et al., 2014).

The experiment was designed to allow planning of the methods and means of control and monitoring of the habitat during lengthy crew stays in confined and cramped conditions. During the program, three different crews of volunteers lived and worked in a simulated spacecraft. The final stage of the experiment, which intended to simulate a 520-day manned mission, was conducted by a crew consisting of three Russians, a Frenchman, an Italian and a Chinese citizen. This form of simulation training may have profound impact on the

psychological and physiological aspect of an individual which include decreased physical activity, suboptimal nutrition, sleep deprivation, fatigue and increased stress levels.

Long term confinement and microgravity environment have been suggested to induce inflammatory responses and modulate immune functions that may increase oxidative stress (Arbeille et al., 2014). Inflammation, oxidative stress and endothelial dysfunction are important in the pathogenesis of atherosclerosis and the biomarkers reflecting these processes have been associated with increased risk for developing coronary artery disease (CAD). It has also been established that prolonged isolation can lead to psychological stress which can have an impact on biomarkers of inflammation, endothelial activation and oxidative stress. A meta-analysis of thirty studies determining the effects of psychological stress on inflammatory biomarkers reported increased concentrations of C-reactive protein (CRP), interleukin-1 (IL-1) and interleukin-6 (IL-6) concentrations following psychological stress (Stephoe et al., 2007). Should the status of these pro-atherogenesis factors be enhanced during prolonged confinement and space travel, specific countermeasures need to be instituted in order to prevent these processes to ensure safe outcome for astronauts during their space expeditions.

There have not been extensive studies examining the effects of long term isolation under either 1g facility, simulated microgravity environment or actual space travel on *in vivo* inflammation, endothelial activation and oxidative stress. Furthermore, the few human experimentations on prolonged isolation have never exceeded a 500 day mark. To the best of our knowledge, the longest reported timeline of prolonged confinement was 438 days (Harvey & Zakutnyaya, 2011). Therefore, the potential changes within the vascular system during extensive prolonged isolation of 520 days remain to be elucidated in order to understand the underlying cellular and metabolic consequence of confinement with regards to these changes in preparation for a possible manned space flight to the red planet. This study aimed to determine the effects of prolonged isolation under a 1g environment on mechanisms of atherogenesis, namely inflammation, endothelial activation, oxidative stress and thrombogenesis.

METHODS

Subjects Recruitment

The MARS500 mission was conducted between 2007 and 2011 by Russia, the European Space Agency and China, in preparation for an unspecified future manned spaceflight to the planet Mars (Basner et al., 2014). The final stage of the experiment was to isolate a group of crew members in a confined space mimicking the size and structure of a space shuttle for a period of 520 days. Six male crew members consisting of three Russians, an Italian, a Frenchman and a Chinese citizen were recruited and subjected to confinement,

simulating actual estimated flight travel to Mars. The timeline took into account 250 days for the travel to Mars, 30 days sojourn on Mars surface and 240 days for return flight to earth. Simulation was performed under 1g. The crew members were carefully screened to be in perfect physical, mental and emotional health, having a healthy lifestyle, non-smoker and lean with a body mass index (BMI) below than 25 kg/m². As for controls, six free-living, healthy Malaysian-based controls were recruited which consisted of four Russians and two Chinese males. Inclusion criteria for the controls includes normotensive blood pressure (BP<140/90mmHg), normoglycaemic (fasting plasma glucose <6.0 mmol/L), normal lipid profile [total cholesterol (TC) <5.2 mmol/L, low density lipoprotein cholesterol (LDL-c) <3.4 mmol/L, high density lipoprotein cholesterol (HDL-c) >1.0 mmol/L and triglyceride (TG) <1.7 mmol/L] and non-smoking. This study was reviewed and approved by Universiti Teknologi MARA (UiTM) Research Ethics Committee prior to commencement of the study [ref: 600-RMI (5/1/6)] on 1 September 2010. All subjects were given written informed consent before participating in the study.

The developed diet regimes for the crew members used in the experiment were based on the content necessary for the human and complied with the accepted physiological norms for contingents, whose professional activity on energy inputs refers to the category of medium gravity. Food composition of the rations complies with the recommendations of the World health organization (WHO), and also agreed upon Russian-American norms on the food composition of food rations for the crews of ISS. The subjects were given three diet variations assigned as Variants 1 to 3 (Table 1). These variants were prepared to cater for the following: 1) Variant 1: for the time of flight from Earth to Mars, 2) Variant 2: during simulation of 3 crew members' egress to the surface of the planet, 3) Variant 3: during return to Earth. It is also worth noting that the controls recruited were not standardized for diet or exercise as they were included specifically to compare between a 'free-living' state to compare with the confined living conditions and strict diet and exercise regimes given to the crew members as a preparatory protocol for possible manned mission to mars.

Table 1
The protein, fat, carbohydrate and calorie content of the 3 dietary variants given to the crew members during their isolated confinement period

Variant Diet	Variant 1	Variant 2	Variant 3
Protein [g (%)]	106.9 (14)	138.2 (17)	112.9 (14.3)
Fat [g (%)]	115.8 (33.2)	126.8 (35)	110.9 (31.9)
Carbohydrate [g (%)]	402.2 (52.8)	370.8 (47)	419.5 (53.7)
Average Calorie intake (kCal)	3120	3170	3130

The entire 520 days of the experiment, the crew members were undergoing their routine exercise programme. The programme was divided into several stages, during which different protocols of physical trainings were implemented. The crew was divided into 3

groups and the training regimes alternated. During the first stage, different protocols of trainings which included strength training, expanders and vibro training were executed. The second stage of training was involved efficiency assessment by way of locomotor trainings in active and passive regimes on the treadmill and trainings on cyclo-ergometer. The third and final stage of training was involved physiological and ergometric loading.

Procedure

A week before confinement, blood was taken for baseline as indicator for pre-isolation period. One sample was taken at day 30 after confinement start and two-monthly for second half of isolation time with nine total numbers of samples was taken during intra-isolation period and 1 sample at post-isolation period. Blood were taken from the median cubital, basilica or cephalic veins by applying aseptic technique. Fasting venous blood samples were collected. Plasma and serum were separated from blood by centrifugation at 2000 x g in 4°C and was stored frozen at -80°C until analysis. Samples from Moscow were transported back to Malaysia in dry ice box.

In order to process the blood, 2 EDTA tubes were exception from centrifugation process. This process was required to separate the plasma and serum for biochemical analysis. The remaining tubes were placed in a centrifuge at speed of four 2000 x g and spun for 10 minutes. Then, the plasma and serum were transferred into the appropriate 1.5 ml tubes and labelled accordingly. One millilitre (1 ml) of Plasma-EDTA were transferred into 2 purple microcentrifuge tube each and 950 µl were aliquot into 2 black microcentrifuge containing 50 µl butylated hydroxytoluene (BHT) solution that was used as primarily antioxidant additive. One millilitre (1 ml) from two red top plain tubes' plasma were then transferred into 5 reddish orange microcentrifuge tubes each and 0.65 µl plasma-citrate which aliquot 1:3 from the top of plasma were transferred into 2 blue colour microcentrifuge tubes.

Plasma from EDTA tube was tested for fasting serum lipid profiles and high-sensitive C-reactive protein (hsCRP) using automated analyzer, Cobas Integra 400, Roche Diagnostics, USA. Homocysteine levels also tested using the same plasma by automated analyzer, Immulite 1000, Siemens Immunoassay Analyzer, German. Enzyme-linked immunosorbent Assay (ELISA) was carried out using serum from plain tube. This assay was used to detect protein expression in the serum for Interleukin-6 (IL-6), Intercellular Adhesion Molecule-1 (ICAM-1), Vascular Cell Molecule-1 (VCAM-1), E-selectin, and Endothelial Nitric Oxide Synthase (eNOS). All ELISA method used the similar 'sandwich' principle and absorbance reading was done using a microplate reader (TECAN Safire 2, Switzerland)

Flow Mediated Dilatation of the Brachial Artery (FMD) of the brachial artery was measured based on the International Brachial Artery Reactivity Task Force (Corretti et al., 2002). Serial FMD readings were done for the crew members on days -7, 30, 90, 150,

210, 270, 330, 390, 450, +7 of isolation and ground controls on days -14, -7, 30, 150, 280, 390, 520 and +14 of isolation. Subjects were fasted at least 8 hours before the study and FMD measured in a quiet, temperature-controlled room. FMD was divided into two stages as follows: (1) Stage 1 (Endothelium independent FMD). The subject was in a supine position and left arm stretched in a comfortable position, for the imaging of the brachial artery. Brachial artery was imaged above the antecubital fossa in the longitudinal plane. A segment with clear anterior and posterior intimal surfaces between the lumen and vessel wall was selected for continuous 2D imaging and this was recorded as baseline resting image. (2) Stage 2 (Endothelium dependent FMD). A sphygmomanometric cuff was placed either above the antecubital fossa or the forearm to create a flow stimulus. Cuff inflation to suprasystolic pressure (at least 50 mmHg above systolic pressure) occluded the artery for 5 minutes. Cuff deflation was then done to induce brief high flow state (reactive hyperaemia) and the vessel diameter was measured at 60 seconds post deflation. In normal individuals, post occlusion of the brachial artery would dilate to at least 10%. Subjects with endothelial dysfunction such as hyperglycaemia, hypertension, and hyperlipidaemia will cause insult to the endothelial function therefore will have less dilatation post occlusion.

The continuous variables were expressed as median \pm interquartile range. Comparison between 2 groups was determined either by Mann-Whitney U tests. Wilcoxon tests were used to determine the effects of long term confinement of biomarkers between isolation and baseline. The criterion for statistical significance was p value < 0.05. Data was analysed by a statistical package program (SPSS) version 20.0.

RESULTS

Table 2 summarizes the demographic data of the crew members and free-living normal controls. Both groups were non-smokers, normotensive with normal lipid profile, and they were matched for age, gender, smoking status, BMI and blood pressure. It is also worth noting that there was no significant difference in ethnicity between crew members and controls.

Table 2
Demographic data of the crew members and controls

Parameters	Crew Members (n=6)	Controls (n=6)	p value
^a Age (years)	31.8 \pm 4.8	34.8 \pm 7.1	NS
^b Gender	6 Males	6 Males	NS
^b Ethnicity (Russian/European/Chinese)	3/2/1	4/0/2	NS
^b Current smoker (Yes/No)	0/6	0/6	NS
^a BMI (kg/m ²)	26.4 \pm 2.5	24.0 \pm 2.2	NS
^a SBP (mmHg)	118.5 \pm 9.7	117.4 \pm 8.3	NS
^a DBP (mmHg)	75.5 \pm 9.8	74.1 \pm 6.8	NS

Note. ^adata expressed as mean \pm SD; ^bdata expressed as proportion; NS not significant

Figures 1(a), 1(b), 2(a), 2(b), 2(c) and 3 depict the percent change of the biomarkers in crew members and controls. There was a higher percent change increment for serum hsCRP concentration in crew members compared to controls on day 150 isolation. There was significant percent change reduction in serum Soluble Vascular Cell Adhesion Molecule-1 (sVCAM-1) concentration on days 90 and 150 and E-selectin concentration on days 150

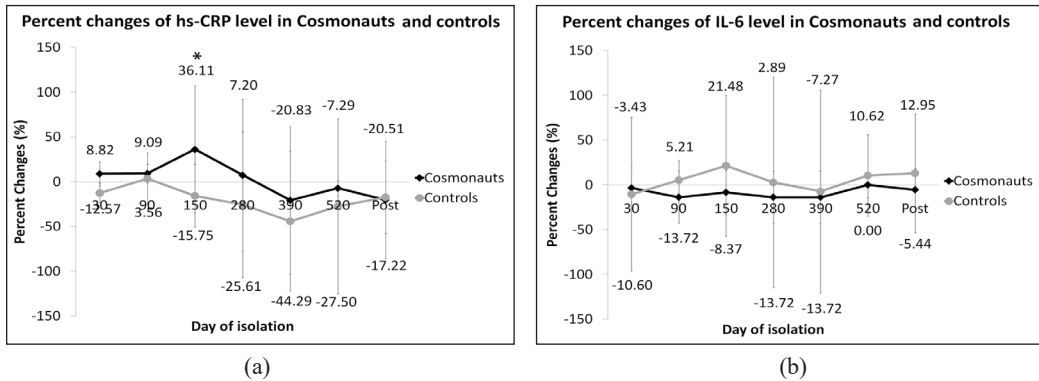


Figure 1. Percent change of inflammation biomarkers concentrations in crew members and controls: (a) hsCRP; and (b) IL-6.

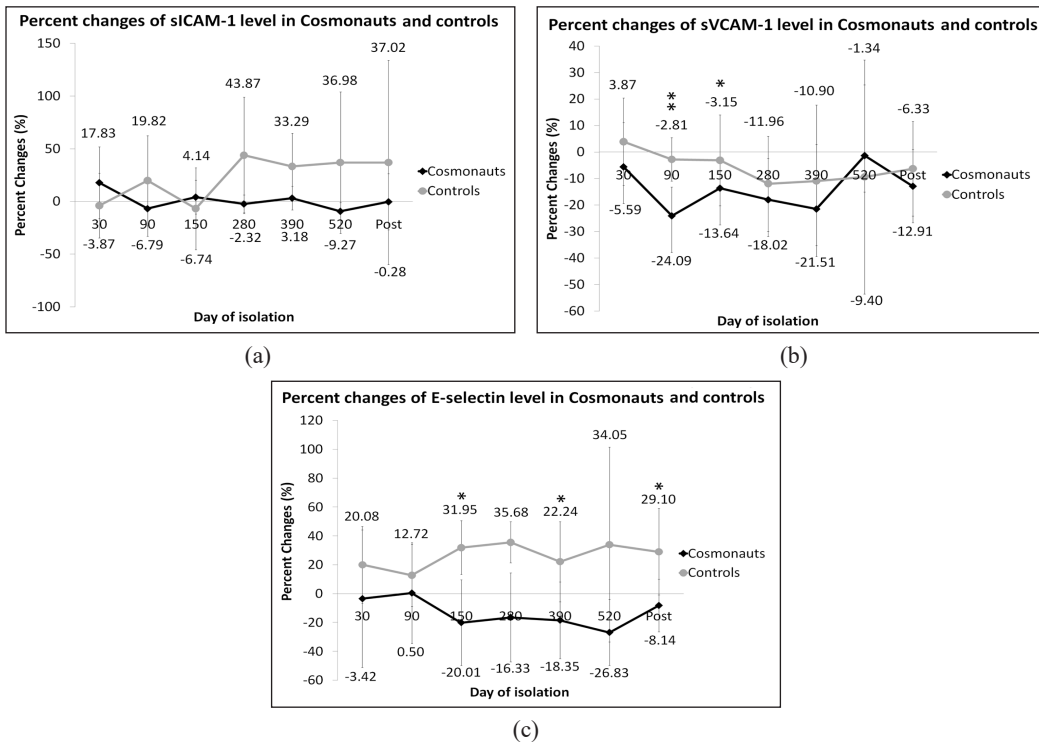


Figure 2. Percent change of endothelial activation biomarkers concentrations in crew members and controls: (a) sICAM-1; (b) sVCAM-1; and (c) E-selectin.

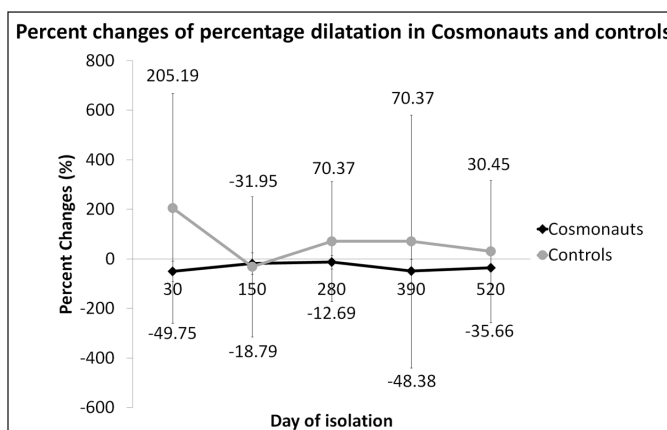


Figure 3. Mean diameter of brachial artery of crew members and controls at pre, 30D, 150D, 280D, 520D and post confined isolation.

and 390. However, there was a slight percent change increment post-isolation phase but this did not achieve statistical significance. There were no significant within-group or between-group differences in percent change for serum IL-6 and Soluble intercellular adhesion molecule-1 (sICAM-1) concentrations.

Table 3 summarizes the serum concentration of biomarkers of inflammation (hsCRP and IL-6) and endothelial activation (sICAM-1, sVCAM-1 and E-selectin). There was significantly lower concentration of sVCAM-1 in cosmonauts compared to pre-isolation period. There were no significant differences in hsCRP, IL-6, sICAM-1 and E-selectin in the crew and control groups compared to pre-isolation. None of the biomarkers were significantly different between groups.

Table 3 refers to the absolute percentage in arterial dilatation and Figure 3 illustrates the flow mediated dilatation (FMD) of the cosmonauts' pre-isolation and during confinement. There were significantly lower FMD readings on days 390 and 520 in the cosmonauts' group ($p < 0.01$). There were no between group differences in FMD ($p > 0.05$). There were no significant percent change differences in FMD between the crew members and normal controls ($p > 0.05$) and neither was there significant difference between timelines ($p > 0.05$).

DISCUSSION AND CONCLUSION

This is the first study to report the effects of prolonged confinement that extended well beyond 500 continuous days on the biomarkers of coronary risks such as hsCRP, IL-6, sICAM-1, sVCAM-1 and E-selectin. This study reported percent change increment in hsCRP amongst the crew members compared to free-living controls. The increment seen for hsCRP could be attributed to changes in the plasma volume where it has been established that acute psychological stress stimulates reductions in plasma volume leading

Table 3
Concentration of Serum hsCRP, IL-6, sVCAM-1, sICAM-1, E-Selectin and flow mediated dilatation (FMD) of the brachial artery

Groups	Variables	Days of isolation							Post
		Pre	30	90	150	280	390	520	
Crew Members	hsCRP (mg/l)	0.35 (0.20)	0.46 (0.19)	0.32 (0.12)	0.37 (0.14)	0.32 (0.28)	0.38 (0.16)	0.31 (0.12)	0.28 (0.11)
	IL-6 (pg/ml)	1.86 (0.64)	1.56 (0.00)	1.56 (0.00)	1.56 (0.00)	1.56 (0.00)	1.56 (0.00)	1.56 (1.20)	1.56 (0.61)
	ICAM-1 (ng/ml)	262.72 (42.65)	275.57 (96.35)	231.75 (98.96)	257.33 (65.73)	244.16 (46.93)	252.50 (36.93)	219.44 (34.86)	268.28 (105.94)
	VCAM-1 (ng/ml)	718.56 (105.47)	654.06 (52.87)	541.31** (52.22)	586.06* (21.38)	579.50* (53.34)	535.00* (124.94)	717.13 (126.88)	646.44 (93.59)
	E-selectin (ng/ml)	73.14 (28.72)	92.19 (30.47)	84.68 (11.20)	79.66 (20.97)	74.20 (50.49)	71.01 (9.05)	64.46 (26.39)	70.31 (8.82)
Controls	FMD (%)	12.25 (2.54)	6.80 (7.47)	10.49 (7.67)	12.53 (6.68)	7.72* (5.00)	8.34** (2.55)	0.21 (0.25)	0.23 (0.19)
	hsCRP (mg/l)	0.37 (0.14)	0.31 (0.11)	0.41 (0.15)	0.28 (0.11)	0.22 (0.21)	0.17 (0.11)	0.21 (0.25)	0.23 (0.19)
	IL-6 (pg/ml)	2.97 (1.28)	2.89 (1.19)	3.14 (0.89)	3.35 (2.09)	3.25 (2.18)	3.50 (1.95)	3.23 (0.73)	2.86 (0.87)
	ICAM-1 (ng/ml)	275.64 (95.67)	260.24 (31.79)	278.99 (22.41)	303.29 (39.05)	359.54 (87.04)	335.12 (115.67)	307.82 (37.75)	324.05 (183.43)
	VCAM-1 (ng/ml)	708.71 (155.72)	722.81 (113.57)	706.88 (128.16)	729.92 (95.06)	616.10 (128.78)	693.31 (265.88)	648.40 (187.16)	679.46 (98.50)
	E-selectin (ng/ml)	57.88 (20.38)	69.65 (43.37)	66.67 (18.48)	71.74 (18.40)	70.16 (22.92)	69.11 (31.11)	72.77 (19.59)	77.23 (22.79)
	FMD (%)	5.53 (9.82)	10.99 (7.53)	8.00 (5.13)	10.42 (4.86)	13.04 (2.22)	9.65 (12.84)		

Note. Data is expressed as Median (IQR); * indicates p<0.05 compared to baseline; ** indicates p<0.01 compared to baseline.

to haemoconcentration (Allen & Patterson, 1995; Mischler et al., 2005). This results in the inability for large molecules such as cytokines and CRP to migrate passively through the vascular endothelium resulting in its rising concentration.

It should be highlighted that hsCRP utilizes sensitive measurements that allows very reliably low detection limit of CRP where slight increases will be detectable among healthy subjects. There have been numerous epidemiological studies which have shown an association between elevated hsCRP and vascular events (Cao et al., 2003; Kuller et al., 1996; Liuzzo et al., 1994; Mischler et al., 2005; Ridker et al., 1997; Ridker et al., 1998a; Ridker et al., 1998b; Ridker et al., 2001; Thompson et al., 1995) and from these significant findings, the American Heart Association (AHA) and the Centers for Disease Control and Prevention (CDC) have released a clinical practice guideline which utilizes hsCRP in coronary risk stratification (Pearson et al., 2003). The specific cut-offs that are useful in evaluating a patient's risk for future cardiovascular events have been determined as <1mg/dl for low risk, 1-3mg/dl for moderate risk and >3mg/dl for high risk categories. In our study, among the crew members isolated in a confined space, their mean serum hsCRP concentration was mean \pm SD: 0.37 \pm 0.17mg/L which is well below the cut-off for low cardiovascular risk despite observations of percent change increase in the concentration during isolation period. These increments could be stress-related from the prolonged confinement as reported by Wang et al. (2014), where his team highlighted the salient finding of positive bias on valence rating of novel unpleasant stimulus over the prolonged confinement among the cosmonauts. It was observed that the positive bias evaluation on negative stimuli was influenced by psychological stress over time, which was consistent with the fluctuation of hormone levels such as cortisol, dopamine and serotonin. The serum hsCRP concentration reduced post isolation well below that of pre-isolation readings although it did not reach statistical significance. Therefore, these changes observed could possibly be due to physiological adaptation rather than a pathological process.

Various studies have shown that exercise can influence acute phase reaction (APR) (Istvan et al., 2006). Therefore, it can be postulated that the series of rigorous exercise regimes implemented throughout the confinement period could have led to the elevations in serum hsCRP concentration in this study. A report by Mouridsen et al. (2014), had shown that hsCRP was not independently associated with CAD, and that increases in hsCRP by 0.13mg/L (IQR 0.05-0.24mg/L) were associated with peak exercise. Another study reported no change in serum hsCRP concentration but reduction in serum IL-6 following exercise (Kasapis & Thompson, 2005). A review on 5 prospective studies determining effects of exercise on inflammatory response reported exercise inducing transient increase in CRP with enhancement of APR being proportional to the amount of activity and muscle injury (Kasapis & Thompson, 2005).

When endothelial cells of the blood vessels undergo inflammatory activation, the increased expression of selectins, VCAM-1 and ICAM-1 promotes monocytes adherence. Adhesion molecule expression is induced by pro-inflammatory cytokines such as IL-1 β and tumor necrosis factor- α (TNF- α), by the acute-phase protein CRP that is produced by the liver in response to IL-6, by protease-activated receptor signaling, by oxLDL uptake via oxLDL receptor-1 (LOX-1), and by CD40/CD40 ligand (CD40L and CD154) interactions (Chen et al., 2002; Collins & Cybulsky, 2001; Kaplanski et al., 1998; Schönbeck & Libby, 2001; Verma et al., 2002). This study interestingly denoted percent change reductions in endothelial activation biomarkers, sVCAM-1 and E-selectin, in the crew members when compared with controls. This would suggest that the environment they were in, coupled with aggressive lifestyle modification during the 520 days of experimentation, have somewhat attenuated release of adhesion molecules which would influence monocyte binding to endothelial cells along the vessel wall during atherogenesis. This is in keeping with previous studies which showed similar findings following exercise and healthy diet (Hamdy et al., 2003; Ziccardi et al., 2002). Furthermore, although confined to isolation for a prolonged period, they were not completely deprived from communication with 'earth'. Communication methods with 'ground control' and family members, although restricted, were still maintained through mimicry of communication accessibility as that of space missions. This could have potentially attenuated forms of stress that may occur during confinement that would elevate these biomarkers.

Endothelial function, measured by FMD, reduced during isolation among the cosmonauts when compared to pre-isolation period, as depicted by the lower percent dilatation of brachial artery among them during isolation compared to pre-isolation readings. This is contrary to the mitigation of endothelial activation biomarkers observed among this group. The possible reason for this discrepancy is that the endothelium has several functions, one of which is to maintain patency of the vessel lumen. The presence of atherosclerotic plaques which starts with increased adhesion molecules and selectins secretion which in turn will increase tunica intimal wall thickness eventually reducing lumen size. However, in the setting of healthy vasculature, the mechanism by which arterial vasodilation reduced is not in relation to the formation of lumen-narrowing atherosclerotic plaques. Previous studies have shown paradoxical decline in FMD following exercise (Birk et al., 2013; Dawson et al., 2013) which has been attributed to oxidative stress which occurs during workouts. There is evidence to support a biphasic response in FMD following exercise of which the strength and direction of this relationship is influenced by several factors which include duration, mode, and intensity of exercise, changes in artery diameter during the exercise and fitness level. Factors that are likely to lead to a decrease in FMD include increased oxidative stress, exercise-induced increase in baseline diameter, shear-induced substrate depletion, elevated retrograde shear, and decreased sensitivity or reduced shear stimulus during the FMD test as a result of in-exercise increases in shear.

The following limitations to the study are worth highlighting. Firstly, this study only looked at prolonged isolation which was estimated as the time taken to travel to mars, dedicating 10 days there for exploratory work and travel back to earth. However, the study design was unable to assess these biomarkers during high g-force rocket launch and subsequent microgravity environments once in space and on mars as we were unable to replicate these scenarios. Secondly, this experimental design only recruited six crew members to best simulate the actual number of cosmonauts planned for a mission to mars. Therefore, the small sample size in this study may have led to the some of the results not being able to achieve statistical significance.

Long term confinement in ground isolation facility up to 520 days attenuated endothelial activation which could be due to the exercise and diet regime given to the crew members during their confinement period. However, their inflammatory status was enhanced possibly attributed to the influences of exercise and possibly psychological stress on the inflammatory response. Nevertheless, despite there being increases in hsCRP concentrations among the crew members, the mean hsCRP concentration was well below the cut-off for low risk of cardiovascular disease. The reduction in endothelial function as depicted by decreased FMD possibly denotes a more physiological response to exercise given throughout the isolation period, rather than a pathological process as the endothelial activation status appears to be attenuated during the experimentation. These findings suggest that instituting appropriate and effective diet and exercise regime during prolong confinement helps reduce stress-related increases in inflammatory biomarkers and adhesion molecules that are involved with atherogenesis. Future research to identify changes in these biomarkers and endothelial function at zero gravity during long confinement will answer the question of whether or not similar findings would be observed in a more identical setting to a manned mission to Mars.

ACKNOWLEDGEMENT

A special note of thanks is made to the IMBP and their staff in Moscow and ESA which provided sample collection, technical support and logistics for this experiment, Centre for Pathology Diagnostic and Research Laboratories (CPDRL) and the Laboratory Animal Care Unit, Faculty of Medicine, Universiti Teknologi MARA for providing the facilities and staff to conduct this research. This research was supported with a grant from the Ministry of Science, Technology and Innovation (MOSTI) under the ANGKASA Grant Scheme [100-RMI/ANGKASA 16/6/2 (1/2010 and 2/2010)] awarded to the corresponding author

REFERENCES

Allen, M. T., & Patterson, S. M. (1995). Hemoconcentration and stress: A review of physiological mechanisms and relevance for cardiovascular disease risk. *Biological Psychology*, 41(1), 1-27.

- Arbeille, P., Provost, R., Vincent, N., & Aubert, A. (2014). Adaptation of the main peripheral artery and vein to long term confinement (MARS 500). *PLoS One*, *9*(1), 1-7.
- Basner, M., Dinges, D. F., Mollicone, D. J., Savelev, I., Ecker, A. J., Di Antonio, A., ... & Sutton, J. P. (2014). Psychological and behavioral changes during confinement in a 520-day simulated interplanetary mission to mars. *PLoS One*, *9*(3), 1-10.
- Birk, G. K., Dawson, E. A., Batterham, A. M., Atkinson, G., Cable, T., Thijssen, D. H. J., & Green, D. J. (2013). Effects of exercise intensity on flow mediated dilation in healthy humans. *International Journal of Sports Medicine*, *34*(5), 409-414.
- Cao, J. J., Thach, C., Manolio, T. A., Psaty, B. M., Kuller, L. H., Chaves, P. H., ... & Cushman, M. (2003). C-reactive protein, carotid intima-media thickness, and incidence of ischemic stroke in the elderly. *Circulation*, *108*(2), 166-170.
- Chen, M., Masaki, T., & Sawamura, T. (2002). LOX-1, the receptor for oxidized low-density lipoprotein identified from endothelial cells: Implications in endothelial dysfunction and atherosclerosis. *Pharmacology and Therapeutics*, *95*(1), 89-100.
- Collins, T., & Cybulsky, M. I. (2001). NF- κ B: Pivotal mediator or innocent bystander in atherogenesis? *Journal of Clinical Investigation*, *107*(3), 255-264.
- Corretti, M. C., Anderson, T. J., Benjamin, E. J., Celermajer, D., Charbonneau, F., Creager, M. A., ... & Vogel, R. (2002). Guidelines for the ultrasound assessment of endothelial-dependent flow-mediated vasodilation of the brachial artery: A report of the International Brachial Artery Reactivity Task Force. *Journal of the American College of Cardiology*, *39*(2), 257-265.
- Dawson, E., Green, D. J., Cable, N. T., & Thijssen, D. H. J. (2013). Effects of acute exercise on flow-mediated dilatation in healthy humans. *Journal of Applied Physiology*, *115*(11), 1589-1598.
- Hamdy, O., Ledbury, S., Mullooly, C., Jarema, C., Porter, S., Ovalle, K., ... & Horton, E. S. (2003). Lifestyle modification improves endothelial function in obese subjects with the insulin resistance syndrome. *Diabetes Care*, *26*(7), 2119-2125.
- Harvey, B., & Zakutnyaya, O. (2011). *Russian space probes: Scientific discoveries and future missions*. New York, USA: Springer Praxis Books.
- Istvan, B., Andres, Q. S., & Kalman, K. (2006). Immunoconversion in acute phase response: Biological significance of acute phase response. In R. E. Faith, A. J. Murgu, R. A. Good & N. P. Plotnikoff (Eds.), *Cytokines: Stress and immunity* (2nd Ed.) (pp. 215-254). Florida, USA: CRC Press.
- Kaplanski, G., Marin, V., Fabrigoule, M., Boulay, V., Benoliel, A., Bongrand, P., ... & Farnarier, C. (1998). Thrombin-activated human endothelial cells support monocyte adhesion *in vitro* following expression of intercellular adhesion molecule-1 (ICAM-1; CD54) and vascular cell adhesion molecule-1 (VCAM-1; CD106). *Blood*, *92*(4), 1259-1267.
- Kasapis, C., & Thompson, P. D. (2005). The effects of physical activity on serum C-reactive protein and inflammatory markers: A systematic review. *Journal of the American College of Cardiology*, *45*(10), 1563-1569.
- Kuller, L. H., Tracy, R. P., Shaten, J., & Meilahn, E. N. (1996). Relation of C-reactive protein and coronary heart disease in the MRFIT nested case-control study: Multiple risk factor intervention trial. *American Journal of Epidemiology*, *144*(6), 537-547.
- Liuzzo, G., Biasucci, L. M., Gallimore, R., Grillo, R. L., Rebuffi, A. G., Pepys, M. B., & Maseri, A. (1994). The prognostic value of C-Reactive Protein and serum Amyloid A Protein in severe unstable angina. *The New England Journal of Medicine*, *331*(7), 417-424.

- Mischler, K., Fischer, J. E., Zraggen, L., Kudielka, B. M., Preckel, D., & Von Känel, R. (2005). The effect of repeated acute mental stress on habituation and recovery responses in hemoconcentration and blood cells in healthy men. *Life Sciences*, 77(10), 1166-1179.
- Mouridsen, M. R., Nielsen, O. W., Carlsen, C. M., Mattsson, N., Ruwald, M. H., Binici, Z., & Sajadieh, A. (2014). High-sensitivity C-reactive protein and exercise-induced changes in subjects suspected of coronary artery disease. *Journal of Inflammation Research*, 7(1), 45-55.
- Pearson, T. A., Mensah, G. A., Alexander, R. W., Anderson, J. L., Cannon, R. O., Criqui, M., ... & Vinicor, F. (2003). Markers of Inflammation and Cardiovascular Disease. *Circulation*, 107(3), 499-511.
- Rees, M. J. (2012). *Universe: The definitive visual guide*. New York, USA: Kindersley Dorling Publisherp.
- Ridker, P. M., Cushman, M., Stampfer, M. J., Tracy, R. P., & Hennekens, C. H. (1997). Inflammation, aspirin, and the risk of cardiovascular disease in apparently healthy men. *The New England Journal of Medicine*, 336(14), 973-979.
- Ridker, P. M., Buring, J. E., Shih, J., Matias, M., & Hennekens, C. H. (1998). Prospective study of C-reactive protein and the risk of future cardiovascular events among apparently healthy women. *Circulation*, 98(8), 731-733.
- Ridker, P. M., Rifai, N., Pfeffer, M. A., Sacks, F. M., Moye, L. A., Goldman, S., ... & Braunwald, E. (1998). Inflammation, pravastatin, and the risk of coronary events after myocardial infarction in patients with average cholesterol levels. *Circulation*, 98(9), 839-844.
- Ridker, P. M., Rifai, N., Clearfield, M., Downs, J. R., Weis, S. E., Miles, J. S., & Gotto, A. M., Jr. (2001). Measurement of C-reactive protein for the targeting of statin therapy in the primary prevention of acute coronary events. *The New England Journal of Medicine*, 344(26), 1959-1965.
- Schönbeck, U., & Libby, P. (2001). CD40 signaling and plaque instability. *Circulation Research*, 89(12), 1092-1103.
- Stephoe, A., Hamer, M., & Chida, Y. (2007). The effects of acute psychological stress on circulating inflammatory factors in humans: A review and meta-analysis. *Brain, Behavior, and Immunity*, 21(7), 901-912.
- Thompson, S. G., Kienast, J., Pyke, S. D. M., Haverkate, F., & van de Loo, J. C. W. (1995). Hemostatic factors and the risk of myocardial infarction or sudden death in patients with angina pectoris. *The New England Journal of Medicine*, 332(10), 635-641.
- Verma, S., Li, S. H., Badiwala, M. V., Weisel, R. D., Fedak, P. W. M., Li, R. K., ... & Mickle, D. A. (2002). Endothelin antagonism and interleukin-6 inhibition attenuate the proatherogenic effects of C-reactive protein. *Circulation*, 105(16), 1890-1896.
- Wang, Y., Jing, X., Lv, K., Wu, B., Bai, Y., Luo, Y., ... & Li, Y. (2014) During the long way to mars: Effects of 520 days of confinement (Mars500) on the assessment of affective stimuli and stage alteration in mood and plasma hormone levels. *PLoS ONE*, 9(4), 1-9.
- Ziccardi, P., Nappo, F., Giugliano, G., Esposito, K., Marfella, R., Cioffi, M., ... & Giugliano, D. (2002). Reduction of inflammatory cytokine concentrations and improvement of endothelial functions in obese women after weight loss over one year. *Circulation*, 105(7), 804-809.
- Zubrin, R., & Wagner, R. (2011). *The case of mars: The plan to settle the red planet and why we must*. New York, NY: Free Press..

Virulence Genes Detection among the Antibiotic Resistant *Enterococcus faecalis* Isolated from Bird Industry in Borneo

Sui Sien Leong^{1*}, Samuel Lihan² and Hwa Chuan Chia²

¹Department of Animal Sciences and Fishery, Faculty of Agricultural and Food Sciences, Universiti Putra Malaysia, Nyabau Road, 97008 Bintulu, Sarawak, Malaysia

²Institute of Biodiversity and Environmental Conservation, Universiti Malaysia Sarawak, 94300 Kota Samarahan, Sarawak, Malaysia

ABSTRACT

The abuse of antibiotics usage in bird industry has resulted in the emerging antibiotic resistant *Enterococci* worldwide which has posed a threat clinically to human health. The present study was to screen and identify the potential virulence agents in antibiotic resistance *E. faecalis* in bird industry in Borneo. *Enterococcus* bacteria collected from the birds' faeces and indoor air inside ten birdhouses were identified to species level and their antibiotic resistance was checked using antibiotic susceptibility discs. Specific primers using PCR assay were intended for the detection of four potential virulence genes (*ace*, *AS*, *efaA*, *geIE*). Out of the thirty-seven *Enterococci* faecal bacteria, the prevailing bacteria found were *Enterococcus gallinacum* (51%), *Enterococcus faecalis* (35%) and *Enterococcus harae* (8%). The airborne bacteria were reported as *Enterococcus faecalis* (5%) and *Enterococcus gallinacum* (1%). Twenty-seven percent of isolates were reported to have Multiple Antibiotic Resistance (MAR) index ≥ 0.2 with 9 distinct resistance patterns formed. *E. faecalis* showed higher resistance to vancomycin. Virulence genes were successfully reported in the 15 *E. faecalis* isolates. Sixty-seven percent of isolates were detected positive for four virulence genes, 27% possessed three (*AS*, *efaA*, *geIE*) genes and 6% possessed two (*ace*, *AS*) genes. Antibiotic resistance and virulence genes detection were significantly correlated. These virulence genes or antibiotic resistance genes were important in the pathogenesis of *E. faecalis* infections.

Keywords: Antibiotic resistance, birds, *Enterococcus faecalis*, virulence

ARTICLE INFO

Article history:

Received: 11 September 2019

Accepted: 02 January 2020

Published: 15 April 2020

E-mail addresses:

leongsuisien@upm.edu.my (Sui Sien Leong)

lsamuel@unimas.my (Samuel Lihan)

chiahwachuan@gmail.com (Hwa Chuan Chia)

* Corresponding author

INTRODUCTION

Pathogenic bacteria are defined as the bacteria which cause infection and diseases. Most of the bacteria are useful in various industries and harmless to human, but some bacteria may cause diseases under certain condition. Bacterial pathogens commonly found in wild birds which triggered outbreak were documented as *Enterococcus* spp. (Chung et al., 2018), *Escherichia coli* (Dho-Moulin & Fairbrother, 1999), *Klebsiella* spp. (Giorgio et al., 2018), *Pseudomonas aeruginosa* (Walker et al., 2002) and *Enterobacter* spp. (Giorgio et al., 2018). Bird industries have sprouted spontaneously across the whole Asia countries within a few years due to multimillion-dollar potential profit derived from the commercially high nutritious value-added lucrative bird nest for human.

Enterococci are opportunistic pathogens that cause infections among the patients with impaired immune system (Duprè et al., 2003), cause septicemic disease (Al-Talib et al., 2015) in human. *Enterococcus faecalis*, Group D *Streptococcus* bacteria is a Gram- positive and commensal bacteria normally found inside the human or mammal's gastrointestinal tracts (Ryan & Ray, 2004) and is widely distributed in the water, plants, soil and food by-products (Frazzon et al., 2009). *E. faecalis* as a typical pathogen causing infections in nosocomial (Kayaoglu & Orstavik, 2004), surgical wounds, blood, urinary tract and enterococcal infection (Toledo-Arana et al., 2001). The number of multiple antibiotic resistance cases caused by *E. faecalis* has increased sharply leading to high mortality (Willems et al., 2001). Research done previously discovered that there was close interaction between *Enterococcus* and epithelial cells because of the ability to adhere or form biofilm on epithelial cells (Wells et al., 2000).

As a result of widespread use and misuse of antibiotics in intensive animal rearing and in clinical settings for the treatment of community-acquired infections, the emergence of multidrug-resistant strains such as vancomycin-resistant *Enterococci* has become a major concern worldwide. Antibiotic resistant *Enterococci* posed the ability to transfer their virulence agents between bacterial strains in the environment or even commensals in gastrointestinal tract.

E. faecalis posed four main virulence genes namely aggregation substance (*AS*), adhesion of collagen (*ace*), gelatinase (*gelE*), endocarditis antigen (*efaA*) which were commonly investigated. The virulence features of *E. faecalis* involved in the adherence process of bacteria to the host cell layers and even to the surrounding surfaces in order to acquire supplements and dodge the host resistant reaction (Medeiros et al., 2014). Previous study explained that *AS* protein expressed on the *E. faecalis* surface played an important role in the adhesion process to the intestinal cells (Sußmuth et al., 2000). Besides, *AS* gene presents in the pheromone responsive plasmid (Wells et al., 2000) acted as facilitators in aggregation and conjugation process between donors and recipient bacteria (Güven & Dag, 2004). The *ace* gene was reported to act as mediator so that *E. faecalis* adhered to collagen

and laminin successfully (Medeiros et al., 2014). Previous study displayed that this *ace* gene protein might be a factor in the transmission of *Enterococci* especially the endocarditis disease (Lebreton et al., 2011). Besides, the gelatinase (*gelE*), zinc metalloprotease which encoded in the chromosomal gene acts as hemoglobin, gelatin, casein, and other bioactive compounds hydrolysis process (Waters et al., 2003). Researchers had proven *E. faecalis* as a culprit in the therapy-resistant endodontic infections which further identified endocarditis antigen (*efaA*) as fundamental harmfulness components related chiefly with infective endocarditis (Preethee et al., 2012). Medeiros et al. (2014) had isolated *E. faecalis* strains found from the clinical and food by-products which had genes that encoded virulence agent in Brazil. Previous studies indicated that the *E. faecalis* isolated from the seashore water and sand posed antibiotic resistant features which might become the potential wellbeing hazard for shoreline goers (Rathnayake et al., 2011). Cases of infection caused by virulent agents presented in antibiotic resistant *Enterococcus* bacteria have been increased tremendously over the past few years. Thus, the aim of this research was to detect and identify the potential virulence agents in antibiotic resistance *E. faecalis* in bird industry in Borneo.

MATERIALS AND METHODS

Location of Study Areas

Sampling of the birds' faecal and airborne bacteria were carried out since March 2015 till September 2016 from the ten birdhouses located in the Southern, Central and Northern regions of Borneo. Sampling sites chosen for the Southern Sarawak were Kota Samarahan (01°27'34.2"N 110°27'25.9"E), Kuching (01°32'56.6"N 110°22'27.5"E), Semarang (01°40'40.0"N 111°6'5.92"E), Maludam (01°39'14.17"N 111°1'53.9"E), Sepinang (01°40'11.8"N 111°7'5.9"E) and Betong (01°24'0"N 111°31'0"E). The sampling sites chosen for the Central Sarawak were Saratok (01°44'10.32"N 111°21'10.22"E), Sarikei (02°6'3.75"N 111°30'39"E) and Sibul (02°19'11.3"N 111°49'50.5"E). The sampling site chosen for the Northern Sarawak was Miri (04°23'39.2"N 113°59'12.2"E).

Isolation and Identification of Faecal and Airborne *Enterococci*

Five defecation samples were collected randomly from the floor of each birdhouse in the sampling sites and tested separately using the method as described by Nyakundi & Mwangi (2011). The faecal samples were diluted in ratio 1:9 in sterile 0.85% of saline. The diluted sample was then placed on bile esculin agar (Merck, Germany) in duplicate using the spread plate method and incubated at temperature $37 \pm 1^\circ \text{C}$ for 24 hours. The *Enterococci* bacteria were further identified using biochemical tests. The species identity was confirmed using 16S rRNA sequencing by PCR.

The procedures for the collection of the indoor airborne samples were carried out according to Malaysia Veterinary Health 2017. The airborne bacteria were obtained using exposed plate count agar (Scharlau, Spain) in duplicate. The lid of the plates were lifted and exposed in the air for 15 seconds inside the birdhouse. The plates were then incubated at $37 \pm 1^\circ\text{C}$ for 24 hours. The bacterial colonies were randomly selected and cultured on bile esculin agar (Merck, Germany) and incubated at $37 \pm 1^\circ\text{C}$ for 24 hours.

Antibiotic Susceptibility Test

All the isolates from the birds' defecation and indoor air of the bird-houses was tested for antibiotic susceptibility test. Antibiotic susceptibility test was conducted using disc diffusion standard protocol (CLSI, 2017). Antibiotic discs (Oxoid, England) chosen for the testing represented the commonly utilized clinical antibiotics. *Escherichia coli* ATCC 25922 was applied as positive control. Among the antibiotic discs utilized were Ampicillin (10 μg), Chloramphenicol (30 μg), Tetracycline (30 μg), Erythromycin (15 μg), Nitrofurantoin (300 μg), Rifampin (5 μg), Penicillin G (10U), Doxycycline (30 μg), Vancomycin (30 μg), Norflaxacin (10 μg), Ciprofloxacin (5 μg). The overnight bacteria suspensions were used to inoculate the Mueller-Hinton agar (MHA) plate evenly using a sterile cotton swap. The plate was then incubated at $37 \pm 1^\circ\text{C}$ for 24 hours. The diameter of inhibition zone was estimated and the perusing was recorded as sensitive (S) or resistance (R).

The Multiple Antibiotic Resistance (MAR) index for each identified bacterium from the bird defecation and indoor airborne samples of the birdhouses was determined. MAR indexing of a single bacteria isolate was counted by the formula stated as A/B, where A represented the number of the antibiotics isolate was resistant to and B represented the total antibiotics utilized and exposed in the test. The MAR value greater than 0.2 designated the bacterial isolate was multiple antibiotics resistant and demonstrated its sensitivity and resistance of these bacteria to clinically tested antibiotics.

Bacterial DNA Extraction

Bacterial DNA were extracted using boiling method with minor modification as described by Leong et al. (2013). A volume of 1.5ml bacteria culture grown for 24 hours in nutrient broth (Merck, Germany) was then transferred into a 2.0ml microcentrifuge tube and further centrifuged at 10,000rpm (8944 \times g) for 5 minutes. 500 μl of sterile refined water was added and vortexed in order to suspend the pellet. The microcentrifuge tube was then heated for 10 minutes and immediately moved into the ice for 5 minutes. The final product in the microcentrifuge tube was centrifuged at 10,000rpm (8944 \times g) for another 10 minutes and the supernatant was stored.

PCR Reaction for Molecular Exposure of Virulence Genes (*ace*, *AS*, *efaA*, *gelE*) in *Enterococcus faecalis*

The PCR was implemented as stated in Duprè et al. (2003). The *Enterococcus faecalis* ATCC 29212 and *Escherichia coli* ATCC 25922 were applied as positive and negative control, respectively for the detection of virulence genes. Table 1 listed down the primers and reaction conditions. The PCR reactions were conducted in the reaction mixtures containing 1.0 µl each of 20 pmol primers (First Base, Malaysia), 2.5 µl of DNA, 0.5 µl of 10mM of deoxynucleoside triphosphate mix (Promega, USA), 5 µl of 5X Buffer solution (Promega, USA), 1.5 µl of 25 mM MgCl₂ (Promega, USA), 0.75 µl of Taq polymerase (Promega, USA) and 12.75 µl of sterile refined water. PCR was accomplished with 30 cycles as follows: initial denaturation at 94°C for 2 minutes, denaturation at 94°C for 1 minute, annealing for 1 minute at the temperature as shown in Table 1, primer extension at 72°C, 1 minute and final extension at 72°C, 10 minutes. The PCR products were visualized in 1% agarose gel electrophoresis with ethidium bromide staining for 35 minutes at 80 volt.

Table 1
PCR primers and reaction conditions

Primers name	Primer sequences (5'-3')	Size (bp)	Annealing Temperature (°C)
ACE1	AAAGTAGAATTAGATCCACAC	500	56
ACE2	TCTATCACATTCGGTTGCG		
AS1	CCAGTAATCAGTCCAGAAACAACC	300	54
AS2	TAGCTTTTTTCATTCTTGTTTGTGTT		
<i>efaA</i> 1	CGTGAGAAAGAAATGGAGGA	1000	56
<i>efaA</i> 2	CTACTAACACGTCACGAATG		
<i>gelE</i> 1	AGTTCATGTCTATTTTCTTCAC	750	56
<i>gelE</i> 2	CTTCATTCTTTACACGTTTG		

RESULTS AND DISCUSSION

Prevalence of *E. faecalis*

A total of 34 faecal and 3 airborne *Enterococcal* bacteria were isolated from the ten birdhouses throughout the Borneo and is shown in Table 2. There were more *Enterococcus* bacteria isolated from faeces than the indoor air inside the birdhouse mainly due to the differences of nutrient content available in the samples. The major components of the faeces are undigested carbohydrate, protein, fat and fibre remainder from the undigested dietary food supply (Rose et al., 2015) which support the bacteria growth. The total *Enterococci* bacterial isolates from the bird faeces were reviewed as *Enterococcus qallinacum* (51%), *Enterococcus faecalis* (35%) and *Enterococcus harae* (8%). The airborne *Enterococci* bacteria isolates of the birdhouses were reported as *Enterococcus faecalis* (5%) and *Enterococcus qallinacum* (1%).

The distribution of *Enterococcus* bacteria was normal among the wild birds because birds can transmit the bacteria by flight travel (Simpson, 2002). *E. gallinacum* can be isolated in most birdhouses except for birdhouses situated in Sibul, Maludam and Kota Samarahan districts. *E. faecalis* can be isolated in most birdhouses except Semarang, Sarikei and Kota Samarahan. Lastly, *E. harae* can only be isolated in birdhouses located in Maludam and Kota Samarahan. This may be due to the geographical location, acidity (pH), moisture content, hygienic condition inside the birdhouses and temperature effects during different sampling at different time of the year which may affect the bacterial growth. The present result was in agreement with Literak et al. (2007) and Nyakundi & Mwangi (2011) that *Enterococcus* spp. were isolated in faeces from the birds such as Marabou Stock (*Leptoptilos crumeniferus*) and rooks. Besides, previous researches had successfully isolated faecal *E. faecalis* and *E. gallinacum* from dogs at veterinary hospitals (Ghosh et al., 2012), poultry (Kwon et al., 2012), ducks and wild geese (Han et al., 2011). This was not surprising since *Enterococcus* spp. is naturally present in the gastrointestinal tract and able to survive in harsh environment containing bile (Saitoa et al., 2018). Thus, *Enterococcus* species are a common pathogen found in birds.

Table 2

The 16S rRNA sequencing homology search (BLAST) results of the defecation and airborne bacterial isolates from the birdhouses located in Borneo

Birdhouse location	Source	Bacterial species	16S rRNA sequencing			
			Size(s) bp	Number of isolates	Database	Homology (%)
Sepinang	Faeces	<i>Enterococcus gallinacum</i>	534	8	GenBank	99
	Faeces	<i>Enterococcus faecalis</i>	1445	2	GenBank	99
Semarang	Faeces	<i>Enterococcus gallinacum</i>	534	3	GenBank	99
Sarikei	Faeces	<i>Enterococcus gallinacum</i>	534	3	GenBank	99
Saratok	Faeces	<i>Enterococcus gallinacum</i>	534	2	GenBank	99
	Faeces	<i>Enterococcus faecalis</i>	1445	2	GenBank	99
Miri	Faeces	<i>Enterococcus gallinacum</i>	534	2	GenBank	99
	Faeces	<i>Enterococcus faecalis</i>	1445	1	GenBank	99
Kuching	Faeces	<i>Enterococcus gallinacum</i>	534	1	GenBank	99
	Faeces	<i>Enterococcus faecalis</i>	1445	3	GenBank	100
Sibu	Faeces	<i>Enterococcus faecalis</i>	1445	3	GenBank	99
Maludam	Faeces	<i>Enterococcus faecalis</i>	1445	2	GenBank	99
	Faeces	<i>Enterococcus harae</i>	1493	1	GenBank	99
Kota Samarahan	Faeces	<i>Enterococcus harae</i>	1493	2	GenBank	99
Total faecal bacteria				34		
Maludam	Air	<i>Enterococcus faecalis</i>	1445	1	GenBank	100
Kota Samarahan	Air	<i>Enterococcus faecalis</i>	1445	1	GenBank	100
Sepinang	Air	<i>Enterococcus gallinacum</i>	534	1	GenBank	99
Total airborne bacteria				3		

Multiple Antibiotic Resistance (MAR) Indexing

The disc diffusion method was then used to affirm the resistant phenotypes of these *Enterococci* bacteria. Strains which are resistant to more than two antibiotics were considered as multiple antibiotic resistance. The MAR indexing and resistance patterns elucidation is shown in Table 3 and illustrated in Figure 1. Table 3 shows the antibiotic resistance pattern and MAR index of the *E. faecalis* isolates. Result revealed that only one *E. faecalis* isolate was reported with MAR at 9 distinct resistance patterns formed. Four *E. faecalis* bacteria had developed resistance to more than two antibiotics and showed an elevated level with MAR index ranged from 0.2 to 0.55.

In this study, almost all of *E. faecalis* bacteria showed antibiotic resistance to at least one commonly applied clinical antibiotic (Table 3). MAR index > 0.2 , indicated that they had emerged from high-hazard wellsprings of contamination where antibiotic agents were regularly utilized (Adeleke & Omafuvbe, 2011). This implies that a high nearness of antibiotics selective pressure, which concurs with the report by Suresh et al. (2000). Wang et al. (2017) indicated that *Enterococcus* spp. could exist as ordinary gut flora and they were more exposed to the antibiotics usage and became resistance more readily. The dispersal patterns of antibiotic resistance of *Enterococcus* spp. were done previously in livestock, companion animals (Park, 2013). *Enterococcus* pose the ability to transmit the antibiotic resistance genes to other host especially in gastrointestinal tracts of human or animals. The study by Chung et al. (2014) disclosed that *Enterococcus* were able to spread infection from livestock or companion animals to human.

The *E. faecalis* bacteria with MAR index ≥ 0.2 were isolated from the birdhouses located in Saratok, Miri and Kuching. Antibiotic resistance among the *E. faecalis* and the birdhouse location were significantly correlated ($P = 0.038$, $r = 0.468$, $n = 15$). *E. faecalis* showed a higher resistance to vancomycin, followed by tetracycline, Nitrofurantoin, Rifampin and Ciprofloxacin (Figure 1). *E. faecalis* has the ability to develop multi antibiotic resistance through variety of multiple mechanisms. *E. faecalis* showed the highest resistance to vancomycin. Vancomycin resistant *Enterococci* occurred since 1988, the rates of vancomycin resistance in *E. faecalis* had surpassed 2% (Hidron et al., 2008). Vancomycin is grouped under glycopeptide which adhere to the peptidoglycan precursor terminal d-alanine-d-alanine moiety, restraining the bacterial cross-linking of peptidoglycan chains and inhibiting cell wall composite. The vancomycin resistant *E. faecalis* may change the terminal penta-peptide to d-Ala-d-Lac on the peptidoglycan (Miller et al., 2014) and acquires vancomycin resistance genes (Saitoa et al., 2018). Similar result was obtained by previous researches and cases reviewed by Hayakawa et al. (2013). *E. faecalis* have served as contributors of vancomycin resistance gene groups to the surrounding pathogens. Besides, *E. faecalis* are resistant to doxycyclin and tetracylin which are grouped under tetracycline antibiotic (Figure 1). Tetracyclines employ their antimicrobial by attaching to

ribosome and interrupting the docking of the aminoacyl-tRNA. Thus, this study showed that *E. faecalis* were able to efflux the antibiotic and protect their ribosome. This is in agreement with Choi & Woo (2015) who disclosed a high prevalence of tetracycline resistance genes in *E. faecalis* isolated from food products. *E. faecalis* also showed resistance to rifampicin mostly because emergence of transformation in the *rpoB* gene which encoded for the β -subunit of the *Enterococci* DNA-dependent RNA polymerase (Miller et al., 2014). The widespread of rifampicin resistant *Enterococcus* appeared to be over 65% in United States and Europe (Deshpande et al., 2007). These *E. faecalis* acquires various genes encoding antibiotic resistance through transformation or joined with a natural resistance from different antimicrobial determinants. Thus, *E. faecalis* was able to survive in an extreme environment (Arias & Murray, 2012).

Table 3
Antibiotic resistance pattern and MAR index of the *E. faecalis* from the birdhouses

Isolates	Source	Antibiotic resistance ¶	Pattern	MAR index
SWA-SAM-B6	Air	VA	5	0.09
SWF-OPP-1D4	Faeces	TeRDfPNorCIP	9	0.55
SWF-OPP-2A3	Faces	RD	4	0.09
SWF-OPP-2C10; SWF-OPP-2D4; SWF-OPP-2D6	Faces	CF	5	0.18
SWF-NEX-1E8	Faeces	nil	1	0
SWF-MAL-1B2; SWF-MAL-1C3; SWA-MAL-A3	Faeces, Air	VA	3	0.09
SWF-MIRI-2A6; SWF-MIRI-2A10	Faeces	TeRDEDoVACIP	8	0.55
SWF-KCH-2A1	Faeces	TeDoVACIP	7	0.21
SWF-SIBU-2C2	Faeces	NorVA	6	0.18
SWF-SPN-2A1	Faeces	Nor	2	0.05

¶ Tested against: Te: Tetracycline; Amp: Ampicillin; C: Chloramphenicol; E: Erythromycin; F: Nitrofurantoin; RD: Rifampin; Do: Doxycycline; P: Penicillin G; Nor: Norflaxacin; CIP: Ciprofloxacin; VA: Vancomycin; nil: none

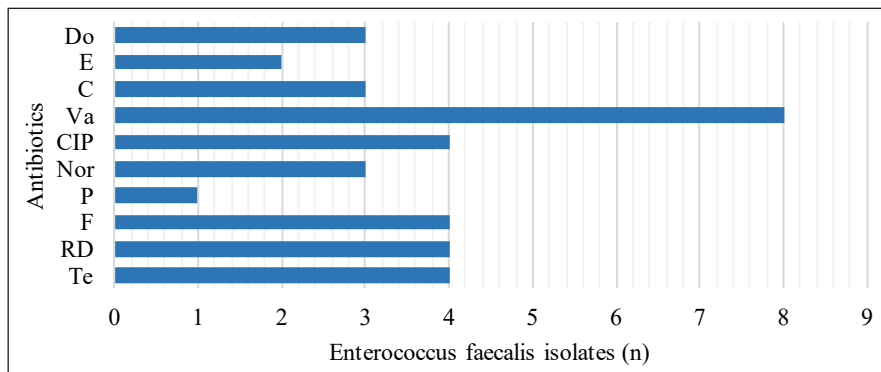


Figure 1. Antibiotic resistance of the *E. faecalis* from the birdhouses. Antibiotic tested: Do: Doxycycline; E: Erythromycin; C: Chloramphenicol; VA: Vancomycin; CIP: Ciprofloxacin; Nor: Norflaxacin; P: Penicillin G; F: Nitrofurantoin; RD: Rifampin; Te: Tetracycline.

Virulence Genes (*AS*, *ace*, *efaA*, *gelE*) Detection in *Enterococcus faecalis*

The virulence genes found in the 15 antibiotic resistant *E. faecalis* isolates were successfully detected by PCR using the specific primer. The dispersal of genotypic virulence agents among the *E. faecalis* is shown in Table 4. Agarose gel electrophoresis banding patterns of virulence genes (*ace*, *AS*, *efaA*, *gelE*) detection for *E. faecalis* is shown in Figure 2. There were 10 out of 15 (67%) isolates of *E. faecalis* detected positive for the four virulence genes. Four out of fifteen (27%) isolates of *E. faecalis* possessed three of the virulence genes and one out of fifteen (6%) isolates of *E. faecalis* possessed two of the virulence genes. The *E. faecalis* isolates from Kota Samarahan, Saratok, Miri and Maludam confirmed the presence of the above four virulence genes. The virulence gene (*AS*, *efaA*, *gelE*) and birdhouse location were significantly correlated (*AS*: $P = 0.038$, $r = 0.468$, $n = 15$; *efaA*: $P = 0.011$, $r = 0.557$, $n = 15$; *gelE*: $P = 0.011$, $r = 0.557$, $n = 15$). Besides, *E. faecalis* isolated from Betong only confirmed the presence of *ace* and *AS* genes. Lastly, *ace* gene was unable to discover from the *E. faecalis* isolated from Miri, Kuching, Sibul and Sepinang but *AS*, *efaA* and *gelE* genes were found present. Virulence genes detection were significantly correlated (*ace*: $P = 0.039$, $r = 0.464$, $n = 15$; *AS*: $P = 0.001$, $r = 1.000$, $n = 15$; *efaA*: $P = 0.84$, $r = 0.001$, $n = 15$; *gelE*: $P = 0.84$, $r = 0.001$, $n = 15$) with antibiotic resistance among the *E. faecalis*.

The high percentage of virulence genes detection implied that *E. faecalis* has a high risk in transmitting the pathogenic diseases through the birds' faecal contamination. *E. faecalis* was also reported as most common pathogens in nosocomial infection, causing fatal outcome in patients. Baldassarri et al. (2001) stated that cases of *E. faecalis* causing nosocomial infections was increasing especially in Italy thus causing threats to human health. The virulence genes which were expressed on the surface of the membrane namely *ace*, *AS*, *efaA*, *gelE* played a vital part in helping the *E. faecalis* adhere to the nosocomial epithelial cell lines and produced biofilms, facilitating diseases (Sußmuth et al., 2000). These virulence factors of *E. faecalis* also involved in the adherence process of bacteria to the host cell layers and to the surrounding surfaces in order to acquire nutrients and dodge the host resistant reaction (Medeiros et al., 2014).

All *E. faecalis* were detected positive with *AS* gene (Table 4). Similar result was obtained by Ferguson et al. (2016) who revealed that *Enterococcus* virulence genes were detected in *E. faecalis* isolated from sea shore water, dogs, birds, and even humans in Australia. The present results showed that more than 70% of the isolates were detected positive with *ace* gene (Table 4). Similar result was also obtained by Wei et al. (2017) where 39.7% of the *E. faecalis* isolated from mineral water and spring water in China were detected with *ace* gene. Besides, the gelatinase (*gelE*) detection was really crucial because they are also a zinc metalloprotease enzyme embedded in the chromosomal gene, functioning as casein, gelatin, other bioactive compounds hydrolysis process in hemoglobin (Waters et al.,

2003). The present results indicated that *gelE* virulence gene were detected among the *E. faecalis* bacteria isolated from the bird faecal samples. The result is in agreement with Al-Talib et al. (2015) who successfully detected 69.4% of *gelE* virulence factor in *E. faecalis* found clinically. Ahmed et al. (2012) proved that virulence genes *gelE* was the greatest gene observed in *E. faecalis* from various environmental surrounding. McBride et al. (2007) suggested that *gelE* was able to enhance the survivability of *Enterococcus* especially during extra intestinal surrounding. Harrington et al. (2004) explained that gelatinase producer *E. faecalis* could be isolated mostly in clinical samples. The endocarditis antigen (*efaA*) of *E. faecalis* was identified as one of the crucial harmfulness variables related for the most part with infective endocarditis. Similar result was obtained by Medeiros et al. (2014) who had isolated *E. faecalis* from clinical and food by-products which displayed *efaA* genes in Brazil. The research finding proved *E. faecalis* as culprit in therapy-resistant endodontic infections (Preethee et al., 2012). The occurrence of the virulent strains among these *E. faecalis* alone cannot confirm infection occurrence because there may be other mediators of pathogenicity (Kim & Marco, 2013). Pathogenicity of *Enterococcus* is mainly due to the capability of these virulent bacteria to overgrow in the infection sites which further spread all over the body (Fiore et al., 2019). Host factors display a vast role in the ability of *Enterococci* to establish infection (Arias & Murray, 2012). However, the existing of these genes in *E. faecalis* strains from bird warrants further investigations to survey potential human wellbeing dangers.

Table 4

Dispersal of genotypic virulence determinants agents among the Enterococcus faecalis

Isolates (n=15)	Sources	Detection by PCR†			
		<i>ace</i>	<i>AS</i>	<i>efaA</i>	<i>gelE</i>
SWF-SAM-B6	Air	+	+	+	+
SWF-OPP-1D4	Faeces	+	+	+	+
SWF-OPP-2A3	Faeces	+	+	+	+
SWF-OPP-2C10	Faeces	+	+	+	+
SWF-OPP-2D4	Faeces	+	+	+	+
SWF-OPP-2D6	Faeces	+	+	+	+
SWF-NEX-1E8	Faeces	+	+	-	-
SWF-MAL-1B2	Faeces	+	+	+	+
SWF-MAL-1C3	Faeces	+	+	+	+
SWF-MAL-A3	Air	+	+	+	+
SWF-MIRI-2A6	Faeces	+	+	+	+
SWF-MIRI-2A10	Faeces	-	+	+	+
SWF-KCH-2A1	Faeces	-	+	+	+
SWF-SIBU-2C2	Faeces	-	+	+	+
SWF-SPN-2A1	Faeces	-	+	+	+

†: Bands detected in PCR + : Present; - : absent.

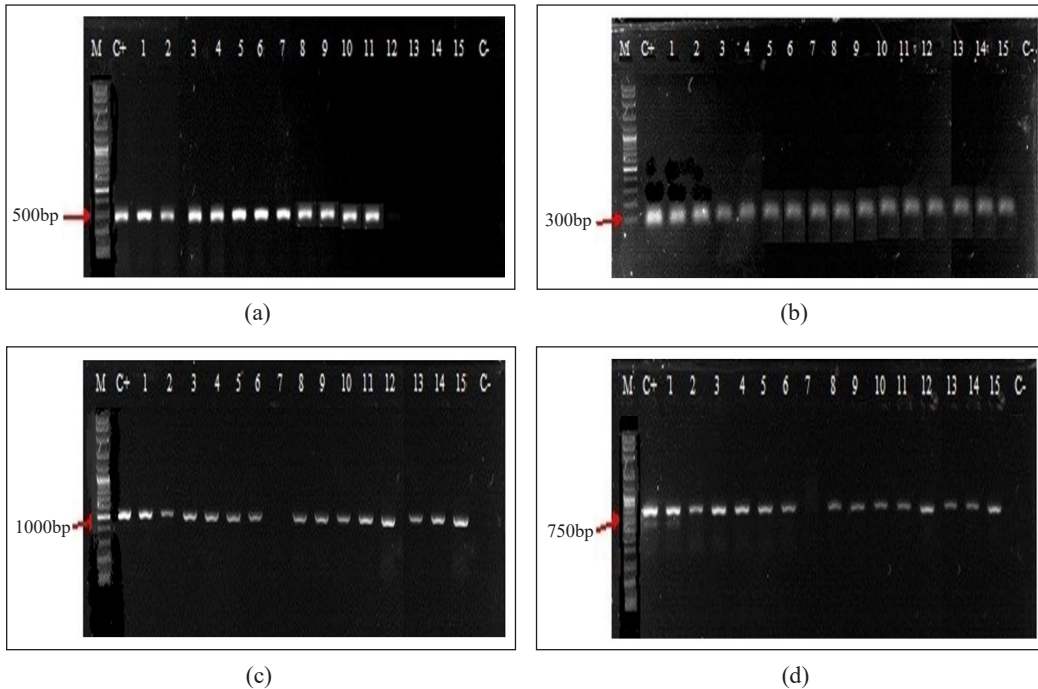


Figure 2. Agarose gel electrophoresis of *ace* (a), *AS* (b), *efaA* (c) and *gelE* (d) gene amplification products from *Enterococcus faecalis* isolates. M: 1Kb ladder; C+: Positive control; 1: SWF-SAM-B6; 2: SWF-OPP-1D4; 3: SWF-OPP-2A3; 4: SWF-OPP-2C10; 5: SWF-OPP-2D4; 6: SWF-OPP-2D6; 7: SWF-NEX-1E8; 8: SWF-MAL-1B2; 9: SWF-MAL-1C3; 10: SWF-MAL-A3; 11: SWF-MIRI-2A6; 12: SWF-MIRI-2A10; 13: SWF-KCH-2A1; 14: SWF-SIBU-2C2; 15: SWF-SPN-2A1; C-: Negative control.

CONCLUSIONS

Enterococcus bacteria showed a high prevalence in the faecal samples. The high incidence of virulence genes (*AS*, *ace*, *gelE*, *efaA*) indicates that these genes were widely disseminated among the antibiotic resistance *E. faecalis* found in the birdhouses, suggesting the important issues in the pathogenesis of *E. faecalis* infection which may cause potential health risks to humans.

ACKNOWLEDGEMENT

This research work was supported technically by University Malaysia Sarawak, Malaysia and Universiti Putra Malaysia, Bintulu Campus with research grant: Grant Putra IPM, grant number GP-IPM/2017/9533000.

REFERENCES

Adeleke, E. O., & Omafuvbe, B. O. (2011). Antibiotic resistance of aerobic mesophilic bacteria isolated from poultry faeces. *Research Journal of Microbiology*, 6(4), 356-365.

- Ahmed, W., Sidhu, J. P. S., & Toze, S. (2012). Speciation and frequency of virulence genes of *Enterococcus* spp. isolated from rainwater tank samples in southeast Queensland, Australia. *Environmental Science and Technology*, 46(20), 6843-6850.
- Al-Talib, H., Zuraina, N., Kamarudin, B., & Yean, C. Y. (2015). Genotypic variations of virulent genes in *Enterococcus faecium* and *Enterococcus faecalis* isolated from three hospitals in Malaysia. *Advances in Clinical and Experimental Medicine*, 24(1), 121-127.
- Arias, C. A., & Murray, B. E. (2012). The rise of the *Enterococcus*: Beyond vancomycin resistance. *Nature Reviews Microbiology*, 10(4), 266-278.
- Baldassarri, L., Cecchini, R., Bertuccini, L., Ammendolia, M. G., Iosi, F., Arciola, C. R., ... & Creti, R. (2001). *Enterococcus* spp. produces slime and survives in rat peritoneal macrophages. *Medical Microbiology and Immunology*, 190(3), 113-120.
- Choi, J. M., & Woo, G. J. (2015). Transfer of tetracycline resistance genes with aggregation substance in food-borne *Enterococcus faecalis*. *Current Microbiology*, 70(4), 476-484.
- Chung, D. M., Ferree, E., Simon, D. M., & Yeh, P. J. (2018). Patterns of bird-bacteria associations. *EcoHealth*, 15(3), 627-641.
- Chung, Y. S., Kwon, K. H., Shin, S., Kim, J. H., Park, Y. H., & Yoon, J. W. (2014). Characterization of veterinary hospital-associated isolates of *Enterococcus* species in Korea. *Journal of Microbiology and Biotechnology*, 24(3), 386-393.
- CLSI. (2017). *Performance standards for antimicrobial susceptibility testing*. CLSI supplement M100, Clinical and Laboratory Standards Institute. Wayne, PA, USA.
- Deshpande, L., Fritsche, T., Moet, G., Biedenbach, D. J., & Jones, R. N. (2007). Antimicrobial resistance and molecular epidemiology of vancomycin-resistant *Enterococci* from North America and Europe: a report from the SENTRY antimicrobial surveillance program. *Diagnostic Microbiology and Infectious Disease*, 58(2), 163-170.
- Dho-Moulin, M., & Fairbrother, J. M. (1999). Avian pathogenic *Escherichia coli* (APEC). *Veterinary Research*, 30(2), 299-316.
- Duprè, I., Zanetti, S., Schito, A. M., Fadda, G., & Sechi, L. A. (2003). Incidence of virulence determinants in clinical *Enterococcus faecium* and *Enterococcus faecalis* isolates collected in Sardinia (Italy). *Journal of Medical Microbiology*, 52(6), 491-498.
- Ferguson, D. M., Talavera, G. N., Ríos Hernández, L. A., Weisberg, S. B., Ambrose, R. F., & Jay, J. A. (2016). Virulence genes among *Enterococcus faecalis* and *Enterococcus faecium* isolated from coastal beaches and human and nonhuman sources in Southern California and Puerto Rico. *Journal of Pathogens*, 2016, 1-7.
- Fiore, E., Van Tyne, D., & Gilmore, M. S. (2019). Pathogenicity of Enterococci. *Microbiology Spectrum*, 7(4), 378-397.
- Frazzon, A. P. G., Gama, B. A., Hermes, V., Bierhals, C. G., Pereira, R. I., Guedes, A. G., ... & Frazzon, J. (2009). Prevalence of antimicrobial resistance and molecular characterization of tetracycline resistance mediated by tet(M) and tet(L) genes in *Enterococcus* spp. isolated from food in Southern Brazil. *World Journal of Microbiology and Biotechnology*, 26, 365-370.

- Ghosh, A., Kukanich, K., Brown, C. E., & Zurek, L. (2012). Resident cats in small animal veterinary hospitals carry multi-drug resistant enterococci and are likely involved in cross-contamination of the hospital environment. *Frontiers in Microbiology*, 3, 1-14.
- Giorgio, A., De Bonis, S., Balestrieri, R., Rossi, G., & Guida, M. (2018). The Isolation and Identification of Bacteria on Feathers of Migratory Bird Species. *Microorganisms*, 6(4), 1-16.
- Güven, K., & Dag, Ø. (2004). Virulence factors of *Enterococcus faecalis*: Relationship to endodontic disease. *Critical Reviews in Oral Biology and Medicine*, 15(5), 308-320.
- Han, D., Unno, T., Jang, J., & Lim, K. (2011). The occurrence of virulence traits among high-level aminoglycosides resistant *Enterococcus* isolates obtained from feces of humans, animals, and birds in South Korea. *International Journal of Food Microbiology*, 144(3), 387-392.
- Harrington, S. M., Ross, T. L., Gebo, K. A., & Merz, W. G. (2004). Vancomycin resistance, esp, and strain relatedness: a 1-year study of enterococcal bacteremia. *Journal of Clinical Microbiology*, 42(12), 5895-5898.
- Hayakawa, K., Marchaim, D., Palla, M., Gudur, U. M., Pulluru, H., Bathina, P., ... & Kaye, K. S. (2013). Epidemiology of vancomycin-resistant *Enterococcus faecalis*: A case-case-control study. *Antimicrobial Agents and Chemotherapy*, 57(1), 49-55.
- Hidron, A. I., Edwards, J. R., Patel, J., & Horan, T. C. (2008). NHSN annual update: antimicrobial-resistant pathogens associated with healthcare-associated infections: annual summary of data reported to the National Healthcare Safety Network at the Centers for Disease Control and Prevention, 2006-2007. *Infection Control and Hospital Epidemiology*, 29(11), 996-1011.
- Kayaoglu, G., & Orstavik, D. (2004). Virulence factors of *Enterococcus faecalis*: relationship to endodontic disease. *Critical Reviews in Oral Biology and Medicine*, 15(5), 308-320.
- Kim, E. B., & Marco, M. L. (2013). Non-clinical and clinical *Enterococcus faecium* but not *Enterococcus faecalis* have distinct structural and functional genomic features. *Applied and Environmental Microbiology*, 80(1), 154-165.
- Kwon, K. H., Hwang, S. Y., Moon, B. Y., & Park, Y.K. (2012). Occurrence of antimicrobial resistance and virulence genes, and distribution of enterococcal clonal complex 17 from animals and human beings in Korea. *Journal of Veterinary Diagnostic Investigation*, 24(5), 924-931.
- Lebreton, F., Depardieu, F., Bourdon, N., Fines-Guyon, M., Berger, P., Camiade, S., ... & Cattoir, V. (2011). d-Ala-d-Ser VanN-Type Transferable Vancomycin Resistance in *Enterococcus faecium*. *Antimicrobial Agents and Chemotherapy*, 55(10), 4606-4612.
- Leong, S. S., Samuel, L., Ling, T. Y., Chia, H. C., & Lim, C. K. (2013). Isolation and characterization of antibiotic resistant bacteria from bird feces in bird farm houses in Sarawak, Malaysia. *Microbiology Indonesia*, 7(4), 137-143.
- Literák, I., Vanko, R., Dolejská, M., Čížek, A., & Karpíšková, R. (2007). Antibiotic resistant *Escherichia coli* and *Salmonella* in Russian rooks (*Corvus frugilegus*) wintering in the Czech Republic. *Letters in Applied Microbiology*, 45(6), 616-621.

- Malaysia Veterinary Health. (2017). *The veterinary manual: Introduction to veterinary microbiology*. Ministry of Agriculture, Malaysia.
- McBride, S. M., Fischetti, V. A., LeBlanc, D. J., Moellering, R. C., & Gilmore, M. S. (2007). Genetic diversity among *Enterococcus faecalis*. *PLoS ONE*, 2(7), 1-22.
- Medeiros, A. W., Pereira, R. I., Oliveira, D. V., Martins, P. D., d' Azevedo, P. A., Van der Sand, S., ... & Frazzon, A. P. (2014). Molecular detection of virulence factors among food and clinical *Enterococcus faecalis* strains in South Brazil. *Brazilian Journal of Microbiology*, 45(1), 327-332.
- Miller, W. R., Munita, J. M., & Arias, C. A. (2014). Mechanisms of antibiotic resistance in enterococci. *Expert Review of Anti-Infective Therapy*, 12(10), 1221-1236.
- Nyakundi, W. O., & Mwangi, W. (2011). Isolation and characterization of pathogenic bacteria and fungi from *Leptoptilos crumeriferu* (Marabau Strok) Dropping. *Journal of Applied Sciences in Environmental Sanitation*, 1(1), 93-106.
- Park, J. H. (2013). A surveillance study of antibiotic resistance of *Enterococcus* spp. isolated from cattle in Busan area. *Annual Report of Busan Metropolitan city Institute of Health and Environment*, 23, 290-300.
- Preethee, T., Kandaswamy, D., & Hannah, R. (2012). Molecular identification of an *Enterococcus faecalis* endocarditis antigen efaA in root canals of therapy-resistant endodontic infections. *Journal of Conservative Dentistry*, 15(4), 319-322.
- Rathnayake, I., Hargreaves, M., & Huygens, F. (2011). SNP diversity of *Enterococcus faecalis* and *Enterococcus faecium* in a South East Queensland waterway, Australia, and associated antibiotic resistance gene profiles. *BMC Microbiology*, 11(1), 1-13.
- Rose, C., Parker, A., Jefferson, B., & Cartmell, E. (2015). The Characterization of Feces and Urine: A Review of the Literature to Inform Advanced Treatment Technology. *Critical Reviews in Environmental Science and Technology*, 45(17), 1827-1879.
- Ryan, K. J., & Ray, C. G. (2004). *Bacteria: In sherris medical microbiology* (4th Ed.). New York, USA: McGraw Hill Press.
- Saito, H. E., Harp, J. R., & Fozo, E. M. (2018). *Enterococcus faecalis* responds to individual exogenous fatty acids independently of their degree of saturation or chain length. *Applied and Environmental Microbiology*, 84(1), 1-14.
- Simpson, V. R. (2002). Wild animals as reservoirs of infectious diseases in the UK. *The Veterinary Journal*, 163(2), 128-146.
- Suresh, T., Srinivasan, D., Hatha, A. A. M., & Lakshmanaperumalsamy, P. (2000). The incidence, antibiotics resistance and survival of *Salmonella* and *Escherichia coli* isolated from broiler chicken retail outlets. *Microbes and Environments*, 15(3), 173-181.
- Sußmuth, S. D., Muscholl-Silberhorn, A., Wirth, R., Susa, M., Marre, R., & Rozdzinski, E. (2000). Aggregation substance promotes adherence, phagocytosis, and intracellular survival of *Enterococcus faecalis* within human macrophages and suppresses respiratory burst. *Infection and Immunity*, 68(9), 4900-4906.

- Toledo-Arana, A., Valle, J., Solano, C., Arrizubieta, M. J., Cucarella, C., Lamata, M., ... & Lasa, I. (2001). The enterococcal surface protein, *Esp*, is involved in *Enterococcus faecalis* biofilm formation. *Applied and Environmental Microbiology*, 67(10), 4538-4545.
- Walker, S. E., Sander, J. E., Cline, J. L., & Helton, J. S. (2002). Characterization of *Pseudomonas aeruginosa* isolates associated with mortality in broiler chicks. *Avian Diseases*, 46(4), 1045-1050.
- Wang, B., Yao, M., Lv, L., Ling, Z., & Li, L. (2017). The human microbiota in health and disease. *Engineering*, 3(1), 71-82.
- Waters, C. M., Antiporta, M. H., Murray, B. E., & Dunny, G. M. (2003). Role of the *Enterococcus faecalis* *GelE* protease in determination of cellular chain length, supernatant pheromone levels, and degradation of fibrin and misfolded surface proteins. *Journal of Bacteriology*, 185(12), 3613-3623.
- Wei, L., Wu, Q., Zhang, J., Guo, W., Chen, M., Xue, L., ... & Ma, L. (2017). Prevalence and Genetic Diversity of *Enterococcus faecalis* Isolates from Mineral Water and Spring Water in China. *Frontiers in Microbiology*, 8, 1-8.
- Wells, C. L., Moore, E. A., Hoag, J. A., Hirt, H., Dunny, G. M., & Erlandsen, S. L. (2000). Inducible expression of *Enterococcus faecalis* aggregation substance surface protein facilitates bacterial internalization by cultured snterocytes. *Infection and Immunity*, 68(12), 7190-7194.
- Willems, R. J., Homan, W., Top, J., van Santen-Verheuvcl, M., Tribe, D., Manzioros, X., ... & Bonten, M. J. (2001). Variant *esp* gene as a marker of a distinct genetic lineage of vancomycin resistant *Enterococcus faecium* spreading in hospitals. *Lancet*, 357(9259), 835-855.



Comparison of Neurotoxic Effects of Ethanol and Endosulfan on Biochemical Changes of Brain Tissues in Javanese Medaka (*Oryzias javanicus*) and Zebrafish (*Danio rerio*)

Nurul Farhana Ramlan¹, Noraini Abu Bakar¹, Emmellie Laura Albert^{2,3}, Syaizwan Zahmir Zulkifli¹, Syahida Ahmad⁴, Mohammad Noor Amal Azmai^{1,5}, Che Azurahaman Che Abdullah² and Wan Norhamidah Wan Ibrahim^{1,5*}

¹Department of Biology, Faculty of Science, Universiti Putra Malaysia, 43400 UPM, Serdang, Selangor, Malaysia

²Department of Physics, Faculty of Science, Universiti Putra Malaysia, 43400 UPM, Serdang, Selangor, Malaysia

³The University of Kitakyushu Hibikino Campus, 2-4 Hibikino, Wakamatsu-ku, Kitakyushu-shi, Fukuoka, 808-0196, Japan

⁴Department of Biochemistry, Faculty of Biotechnology and Biomolecular Sciences, Universiti Putra Malaysia, 43400 UPM, Serdang, Selangor, Malaysia

⁵Institute of Bioscience, Universiti Putra Malaysia, 43400 UPM, Serdang, Selangor, Malaysia

ABSTRACT

An ideal model organism for neurotoxicology research should meet several characteristics, such as low cost and amenable for high throughput testing. Javanese medaka (JM) has been widely used in the ecotoxicological studies related to the marine and freshwater environment, but rarely utilized for biomedical research. Therefore, in this study, the applicability of using JM in the neurotoxicology research was assessed using biochemical comparison with an established model organism, the zebrafish. Identification of biochemical

changes due to the neurotoxic effects of ethanol and endosulfan was assessed using Fourier Transform Infrared (FTIR) analysis. Treatment with ethanol affected the level of lipids, proteins, glycogens and nucleic acids in the brain of JM. Meanwhile, treatment with endosulfan showed alteration in the level of lipids and nucleic acids. For the zebrafish, exposure to ethanol affected the level of protein, fatty acid and amino acid, and exposure to endosulfan induced alteration in the fatty acids, amino acids,

ARTICLE INFO

Article history:

Received: 10 October 2019

Accepted: 27 November 2019

Published: 15 April 2020

E-mail addresses:

farhanaramlan89@gmail.com (Nurul Farhana Ramlan)

norainiabubakat011@gmail.com (Noraini Abu Bakar)

emmellielaura@gmail.com (Emmellie Laura Albert)

syaizwan@upm.edu.my (Syaizwan Zahmir Zulkifli)

syahida@upm.edu.my (Syahida Ahmad)

mmamal@upm.edu.my (Mohammad Noor Amal Azmai)

azurahaman@gmail.com (Che Azurahaman Che Abdullah)

wnwi@upm.edu.my (Wan Norhamidah Wan Ibrahim)

* Corresponding author

nucleic acids and protein in the brain of zebrafish. The sensitive response of the JM toward chemicals exposure proved that it was a valuable model for neurotoxicology research. More studies need to be conducted to further develop JM as an ideal model organism for neurotoxicology research.

Keywords: Biochemical changes, Fourier Transform Infrared, Javanese medaka, model organism, zebrafish

INTRODUCTION

Animal models play a fundamental role in drug discovery, biomedical, and ecotoxicology researches. The main goal of developing animal models is to understand biological phenomena in humans or a species other than the one investigated, depending on the questions asked by the scientist (Andersen & Winter, 2017). Traditionally, mammals have been used as model organisms in neurotoxicology research. However, since the use of these model organisms is time consuming, laborious, and expensive, they are not suitable for high throughput screening in which thousands of chemicals are tested in a short period of time. Therefore, using fish as a model organism is becoming increasingly popular among toxicologist as an alternative model organism, since they are relatively simple, easy to culture and can be maintained in the laboratory continuously (Schartl, 2014). Therefore, they offer a distinct cost benefit as compared to rodents, especially when dealing with high throughput testing. Fish have been used as models for various research disciplines such as engineering (Romano et al., 2017), environmental research (Cossins & Crawford, 2005), genetic research (Gerlai et al., 2000), toxicology (Peterson et al., 2015), pharmacology (Maximino et al., 2011) and diseases (Amal et al., 2019a; Amal et al., 2019b).

Zebrafish (*Danio rerio*) originated from South and Southeast Asia, Northeastern India, Bangladesh, and Myanmar. They are gaining popularity in neurotoxicology research as they have been proven to share approximately 70% of the human orthologous genes that are highly conserved and similarly regulated in humans (Howe et al., 2013). Another small fish that are resilient, with mapped and malleable genomes, namely Japanese medaka (*Oryzias latipes*) are used by a small, but gradually growing community of researchers for various types of research (Wittbrodt et al., 2002). Japanese medaka originated from Asian countries such as Japan, Korea and China, whereas, a related species namely Javanese medaka (*Oryzias javanicus*) has been highlighted as a new experimental model for environmental research. This species is hardy and highly adaptable to a high range of salinity (Inoue & Takei, 2002), and are found abundant in Peninsular Malaysia, Singapore, Indonesia, Thailand, and Western Borneo (Yusof et al., 2012). Recently, Javanese medaka has been utilized as model organism to understand ecotoxicity effects of environmental pollutants in marine and freshwater environment (Ismail & Yusof, 2011; Yusof et al., 2014; Aziz et al., 2017). Also, this fish has been utilized for bacterial diseases study (Amal et al., 2018). However, their potential as an animal model in neurotoxicology research remains to be explored.

When fish model organisms absorb a toxicant, biochemical and physiological responses may occur due to the toxicity mechanism (Begum, 2004). Several scientific studies shown that zebrafish exposed to alcohol demonstrated consistent neurotoxic effects with the mammal model organism and also with human (Joya et al., 2014). In addition, zebrafish also showed neurotoxicity effects after exposure to endosulfan (Silva et al., 2015). However, the study of both neurotoxicants on Javanese medaka is still limited and not extensively done compared to zebrafish. Biochemical or genetic accidents caused by toxic insults may provoke neurodegenerative disease and neurodevelopmental abnormalities (Yuan & Yanker, 2000). Thereby, identification of biochemical changes due to the neurotoxic effects of chemicals in the biological sample is a valuable approach in determining the toxic effects of chemicals. FTIR spectroscopy provides qualitative biochemical information for the assessment of structural and functional changes of macromolecules in biological samples (Cakmak et al., 2006). The changes in peak positions and bandwidths exhibited alterations in the structural and functional groups caused by the toxicants. In addition, FTIR spectroscopy is an efficient and reliable tool that utilizing infrared (IR) absorption spectra to enable the assessment of biochemical fingerprint from a micro-volume sample from complex biological systems (Ami et al., 2014). In the present study, FTIR was used to evaluate biochemical alterations in the brain tissues of Javanese medaka after acute exposure to ethanol and endosulfan, while zebrafish was used as a reference model.

MATERIALS AND METHODS

Animals and Housing

Adult wildtype zebrafish were purchased from the local supplier in Kajang, Malaysia. Javanese medakas were collected from estuary area in Sepang River, Selangor (2.6213° N, 101.7122° E). They were identified by the occurrence of a pair of silvery stripes at the dorsal part of the body and the presence of yellow sub marginal bands on the dorsal and ventral portions of the caudal fin (Yusof et al., 2013). They were acclimatized for 14 days and were kept afterwards in an aquarium (22.3 cm length × 12.2 cm width × 13.5 cm height), with the ratio of 3 females: 2 males.

The fish were maintained in light cycle 14 h light: 10 h dark controlled photoperiod and were fed four times a day with brine shrimp (*Artemia salina*) (San Francisco Bay Brand, San Francisco, CA) and supplemented with commercial dry flake food (Sera Vipan, Germany). The aquarium water was prepared 24 h before used, by dechlorinating it with anti-chlorine (Nutrafin, Hagen, Canada), aerated to increase oxygen concentration in the water, and treated with ultraviolet light. In order to promote good health and stable water quality for the fish, the water were maintained at pH 6.8 - 7.0, and the level of ammonia nitrogen, nitrite and nitrate were at low reading (0-0.25 ppm). The water temperature was maintained at 28°C ± 1°C. The fish tanks were cleaned once a week and the fish

were monitored frequently to ensure that they were free from any sign of diseases and healthy enough for further experiments. All procedures were conducted according to the Institutional Animal Care and Use Committee of Universiti Putra Malaysia (IACUC/AUP-R024/2014).

Neurotoxicants Exposure to Adult Javanese Medaka and Zebrafish

In each treatment group (exposed to ethanol and endosulfan) and control, 15 adults of each species were used ($n = 45$ for each species of fish). The selected fishes were almost same size (3 - 4 cm), weight (0.6 g - 0.8 g) and only the healthy fish with no morphological abnormalities were selected for experiment. Ethanol (1%) was freshly prepared from 95% ethanol by diluting it with aquarium water. Fishes were individually exposed to 1% ethanol in a 500 mL glass beaker containing 250 mL of 1% ethanol solution for 1 h prior to behavioural assessment. A 1 h ethanol exposure was chosen based on several previous studies on zebrafish (Kurta & Palestis, 2010; Tran et al., 2015; Tran et al., 2016). Endosulfan (analytical standard α and β isomers, Pestanal[®], Sigma-Aldrich Laboratories, Seelze, Germany) was used in this study. Both fishes were exposed to 1.6 $\mu\text{g/L}$ endosulfan (Jonsson and Toledo, 1993) for 96 h according to OECD 203 (OECD, 2013). All treatment groups containing five fishes and were exposed in 3 L aquarium tank in a semi-static exposure where the exposure solution was renewed daily due to the short half-life of endosulfan, approximately 24 hours (Jonsson & Toledo, 1993). Control group of 15 fishes received treated aquarium water in the same route of administration with the same volume as the treatment groups, respectively.

Fourier Transform Infrared (FTIR) Analysis

At the end of the exposure, the fish were euthanized with ice for 10 min. Then, the brains were dissected, washed three times with phosphate-buffered saline (PBS) and fixed with 4% paraformaldehyde (PFA) overnight at 4°C. Then, the brain were dried in a lyophilizer (VTIRTIS 6KBEL85) for 12 h at 50°C to remove water from the samples. The samples were then ground in an agate mortar and pestle to obtain brain powders. The brain powders were mixed with dried potassium bromide (100 mg) and subjected to a pressure of 5 tons for 5 min in an evacuated disc to produce a clear transparent KBr disc of 13 mm diameter and 1 mm thickness for use in the FTIR spectrometer (Palaniappan & Pramod, 2011). The measurements of the freeze dried samples were performed on a Thermo Nicolet Nexus, Smart Orbit spectrometer using the KBr disc method. The spectra were recorded over the themed infrared region of 500 - 4000 cm^{-1} . For each treatment group, the brains were harvested from 3 to 5 fish.

RESULTS AND DISCUSSION

Changes in the biochemical profile of the brain in both species were assessed using Fourier Transform Infrared (FTIR) spectroscopy. The range frequency for all functional groups and their peak assignment for the FTIR are presented in Table 1. The FTIR spectra in the 4000 - 500 cm^{-1} range were presented for both fishes. Comparison of FTIR spectra after exposure to ethanol or endosulfan in Javanese medaka is shown in Figure 1, while that of zebrafish is in Figure 2. The peak assignments are presented in Table 2, where the peak in the spectra corresponds to the functional groups of proteins, lipids, carbohydrates and nucleic acids (Senthamilselvan et al., 2012; Baker et al., 2014). Results showed that the intensities of the control *versus* exposed brain tissues for both fish species were different according to different neurotoxicant.

For Javanese medaka, treatment with either ethanol or endosulfan induced appearance of a new peak at 2937 cm^{-1} for ethanol and 2938 cm^{-1} for endosulfan, and these peaks were not observed in the control. These peaks represent the C–H stretch from alkanes of lipids. As for the zebrafish, the lipid molecules were detected at the peak 2939 cm^{-1} for the control, while treatment with either ethanol or endosulfan resulted in a reduction of these

Table 1
General band assignments of the FTIR spectra

Frequency (cm^{-1})	Functional group and peak assignment	Components
3700 -3200	Alcohol (O-H stretch)	Alcohol
2975 - 2850	Alkanes (C-H stretch)	Lipid
1730 -1720	Aldehydes (C=O stretch)	Lipid
1730 - 1690	Amide (C=O stretch)	Protein
1640 -1630	Alkene (C=C stretch)	Protein
1538 - 1529	Amide (N–H bending)	Protein
1452 – 1437	Alkanes (C-H stretch)	Lipid
1385 -1364	Alkanes (C-H ₃)	Fatty acids, amino acids, lipid
1222 - 1203	Amines (C-N stretch) Alkyl halides (C-N stretch)	Glycogen
1131 - 1123	Alkyl halides (C-F stretch) Ethers (C-O stretch) Amines (C-N stretch)	Glycogen
1058 - 1051	Alkyl halides (C-F stretch) Alcohol (C-O stretch) Amines (C-N stretch)	Glycogen
1059 - 1026	Alkyl halides (C-F stretch)	Nucleic acid
968 - 953	Alkenes (C-H stretch)	Nucleic acid
888 - 784	Alkyl halides (C-Cl stretch) Aromatics (C-H stretch)	unknown

Note. The range frequency for all functional groups and their peak assignment for the FTIR spectra

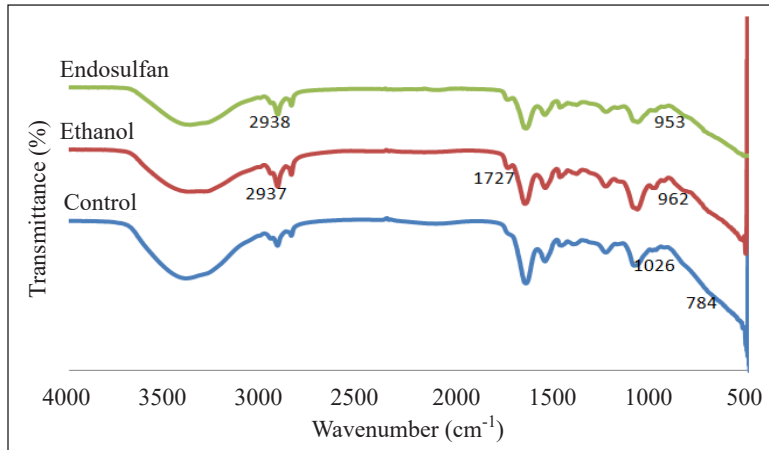


Figure 1. FTIR spectra of the brain tissue in Javanese medaka in the region 4000 - 500 cm^{-1}

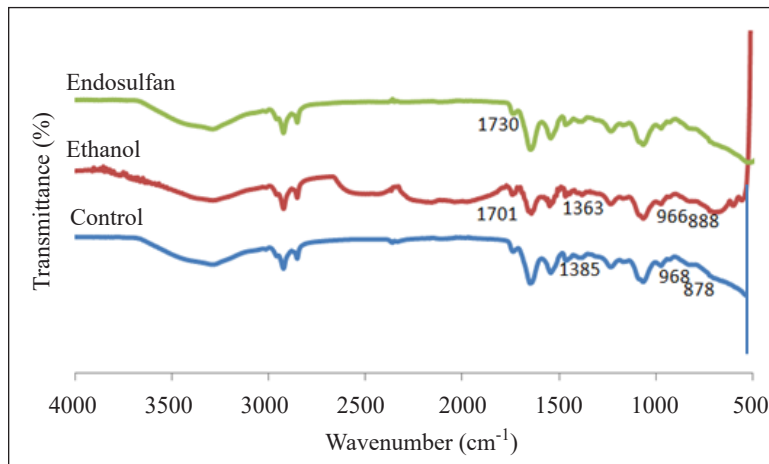


Figure 2. FTIR spectra of the brain tissue in zebrafish in the region 4000 - 500 cm^{-1}

peaks. Thereafter, a new peak appeared at 1727 cm^{-1} in the Javanese medaka brain after treatment with ethanol, but not in the endosulfan and control group. This peak is associated to the stretching of the C=O group in aldehydes of lipids. This peak was not observed in the zebrafish in any treatment group. In the Javanese medaka, another peak of the lipid component appeared at 1437 cm^{-1} in control, ethanol and endosulfan groups. However, for the zebrafish this peak was observed at higher frequency, 1442 cm^{-1} . Treatment with ethanol has exhibited an increment to approximately 1452 cm^{-1} and treatment with endosulfan exhibited decrement approximately to 1437 cm^{-1} in the zebrafish. The appearance of the new peaks, disappearance of peaks, increment and decrement of the peaks in the Javanese medaka and zebrafish indicated disruption of the lipid molecules after treatment with ethanol and endosulfan.

Table 2
The band area of brain tissue in *Javanese medaka* and *zebrafish* exposed to ethanol and endosulfan

Javanese medaka frequency (cm ⁻¹)		Zebrafish frequency (cm ⁻¹)		Functional groups and peak assignment	Components		
Control	Ethanol	Endosulfan	Control			Ethanol	Endosulfan
3307	3216	3302	3371	3341	3344	Alcohol (O-H stretch)	Alcohol
Not observed	2937	2938	2939	2937	2927	Alkanes (C-H stretch)	Lipid
2917	2917	2918	2919	2917	2921	Alkanes (C-H stretch)	Lipid
2847	2847	2848	2847	2845	2849	Alkanes (C-H stretch)	Lipid
Not observed	1727	Not observed	Not observed	Not observed	Not observed	Aldehydes (C=O stretch)	Lipid
1694	Not observed	1701	Not observed	1701	1730	Amide (C=O stretch)	Protein
1635	1631	1632	1635	1639	1637	Alkene (C=C stretch)	Protein
1528	1529	1531	1538	1532	1528	Amide (N-H bending)	Protein
1437	1437	1437	1442	1452	1437	Alkanes (C-H stretch)	Lipid
1363	1363	1363	1385	1363	Not observed	Alkanes (C-H ₃)	Fatty acid, amino acid, lipid
1214	1209	1208	1212	1222	1203	Amines (C-N stretch)	Glycogen
1123	Not observed	1131	Not observed	Not observed	Not observed	Alkyl halides (C-N stretch)	Glycogen
1051	1051	1058	Not observed	Not observed	Not observed	Alkyl halides (C-F stretch)	Glycogen
1026	Not observed	Not observed	1059	1056	1037	Ethers (C-O stretch)	Glycogen
Not observed	962	953	968	966	Not observed	Amines (C-N stretch)	Nucleic acid
784	Not observed	Not observed	878	888	Not observed	Alcohol (C-O stretch)	Nucleic acid
						Amines (C-N stretch)	unknown
						Alkyl halides (C-F stretch)	
						Alkenes (C-H stretch)	
						Alkyl halides (C-Cl stretch)	
						Aromatics (C-H stretch)	

Note. The FTIR spectra in the 4000 - 500 cm⁻¹ range were presented for both fishes after exposure to ethanol or endosulfan where the peak in the spectra corresponds to the functional groups of proteins, lipids, carbohydrates and nucleic acids.

The band observed at 1694 cm^{-1} in the control Javanese medaka corresponds to C=O stretching of amide functional groups in proteins. Treatment with ethanol in Javanese medaka has caused a disappearance of this peak. Exposure to endosulfan (1701 cm^{-1}) had exhibited increment in the treated Javanese medaka. In the normal zebrafish, there was no peak occurrence at this band. However, these peaks could be observed when treated with ethanol (1701 cm^{-1}) and endosulfan (1730 cm^{-1}). From this, the aspect to be taken is that any alteration at these peaks showed that treatment with ethanol and endosulfan induced disruption in the protein molecules for both fishes.

Furthermore, functional group of alkyl halides, ethers, amines and alcohol for glycogen due to the stretching of C-F, C-O and C-N was only detected in the control of Javanese medaka from 1051 cm^{-1} to 1123 cm^{-1} , and not available in the zebrafish for all groups. Treatment with ethanol causes these peaks to disappear. Treatment with endosulfan (1131 cm^{-1}) caused an increment of these peaks in the Javanese medaka, as compared to the control. The disappearance of this peak as a result of ethanol exposure and endosulfan exposure caused a large shifted peak. This showed that both toxicants severely disrupted glycogen in the Javanese medaka.

Additionally, the peak observed at 1026 cm^{-1} in the control Javanese medaka and 1059 cm^{-1} in the control zebrafish corresponds to C-F stretching of alkyl halides in nucleic acids. In Javanese medaka, treatment with ethanol or endosulfan caused this peak to disappear. For zebrafish, treatment with ethanol (1056 cm^{-1}) and endosulfan (1037 cm^{-1}) also exhibited a reduction as compared to the control (1059 cm^{-1}). Whereas, treatment with ethanol (962 cm^{-1}) or endosulfan (953 cm^{-1}), showed a new appearance of these peaks in the Javanese medaka which also corresponded to nucleic acid. In zebrafish, this peak disappeared after treatment with endosulfan.

This study revealed that untreated Javanese medaka had different macromolecules composition where they had lower lipids and nucleic acid in comparison to zebrafish. In addition, Javanese medaka also had higher protein and glycogen component in their brain as compared to the zebrafish. The dissimilarity may be due to the differences in rearing conditions in which that zebrafish may be undergone domestication, while Javanese medaka is from the wild habitat. Although the Javanese medaka used in this study was already being acclimatized in the laboratory settings condition similarly with the zebrafish for two months, this length of period may be not long enough for the Javanese medaka. Domestication is a process of adaptation to a captive environment (Price, 1999). The process of adaptation for wild population of animals to preadaptation for domestication may be differed among species depending on the ability of species members to adapt through developmental and evolutionary processes to a variety of husbandry conditions and the species able to exhibit the behavioural patterns compatible with husbandry techniques (Price, 1999). Furthermore, a distinct biochemical comparison observed in Javanese medaka could be explained by

obvious morphological characteristics in both fishes. Javanese medaka has transparent body, while zebrafish has black striped body. In agreement, a previous study showed that seven different bivalve species which had different morphological characteristics also showed divergent biochemical composition (Bouhlef et al., 2017). Moreover, the variance of biochemical composition could be determined by the natural habitat of the fishes. Javanese medaka is a fish that originated from marine or brackish water, while zebrafish from freshwater.

In our laboratory, zebrafish has been constantly fed with artemia. Meanwhile, Javanese medakas were collected from the wild and were fed with brine shrimps for only two months during laboratory acclimatization. Owing to their differences in the composition of feeding materials between wild Javanese medaka and domestic zebrafish (Tasbozan & Gökce, 2017), we found that Javanese medaka had lower lipids component in the brain as compared to the zebrafish brain. In this study, as Javanese medakas were collected from the wild, their dietary intakes were influenced by the particular microenvironment and food availability. While, zebrafish were maintained in the laboratory condition and properly fed with brine shrimps on regular basis. This could explain the differences in their lipids component between the fishes, as lipid composition is dependent on the fatty acid composition of their feed and dietary intakes (Cahu et al., 2004).

The present study evaluated the neurotoxic effect of acute exposure to ethanol and endosulfan on the biochemical contents in the brain tissues of Javanese medaka and zebrafish. We found that ethanol and endosulfan exposure changed transmission intensity, shifted peak positions, and caused disappearing or addition of new peaks in FTIR wavelength. This prove that ethanol and endosulfan impaired biochemical structures of proteins, lipids and nucleic acids in the brain. The destructive effects of ethanol and endosulfan on the brain are more prominent in the Javanese medaka, in comparison to the zebrafish. This is due to more macromolecules were affected in the Javanese medaka as compared to the zebrafish. The alteration of the proteins, lipids and nucleic acids structure in the brain will lead to neurotoxicity or neurobehavioural deficits (Zahir et al., 2006).

Exposure to ethanol has been proven to induce oxidative stress, alteration in lipid components and dysfunctional membranes which lead to neurotoxicity and neurodegeneration (Hernández et al., 2016). Previous study also showed that exposure to alcohol altered protein expression and generated more reactive oxygen species (ROS) in the Purkinje's cells of the brain (Oyinbo et al., 2016). Jang et al. (2016) discovered that Sprague-Dawley rats which were exposed to endosulfan demonstrated elevation of ROS and oxidative damages leading to the reduction in glutathione, lipid peroxidation and protein carbonylation. Additionally, the brain contains high lipid content with sufficient macromolecules, a prerequisite for proper central nervous system function (Carlson, 2009). The integrity of the cell membrane is highly dependable on the sufficiency and balance

amount between the lipids and proteins molecules. Any disruption of the macromolecules in the brain will affect the proper biological functions and mechanisms, which subsequently contribute to the induction of adverse toxicity effects in the fishes.

Zebrafish has been commonly used as a model organism for alcohol researches (Sylvain et al., 2010; Joya et al., 2014; Tran et al., 2016). However, in this study, we found that Javanese medaka had higher sensitivity towards ethanol exposure, as compared to the zebrafish. This finding leading to a suggestion that Javanese medaka is more suitable for alcohol research and also can be a valuable model organism for neurotoxicology research. Important to note, biochemical endpoints evaluation by using FTIR alone is not sufficient to draw a concrete conclusion about the suitability of Javanese medaka as model organism for neurotoxicology research. Thus, utilization of Javanese medaka for neurotoxicology research requires concerted effort by scientists from various research fields to generate the fundamental knowledge about their genetic variations, biology and physiology. Based on the history, development of model organism for research took decades of continuous efforts by the research community. Therefore, more studies need to be conducted to further develop Javanese medaka as an ideal model organism for biomedical research. These data can be referred as a fundamental knowledge for the adverse neurotoxic effects of neurotoxicants for both fishes.

CONCLUSION

As a conclusion, we found that Javanese medaka is a valuable aquatic model organism for neurotoxicology research, as this fish is sensitive to toxicant exposure. To fully utilize this fish as a model organism for neurotoxicology research, it has to be further developed by using different sophisticated platforms such as their genome has to be fully sequenced to allow further studies for genetic modifications.

ACKNOWLEDGEMENT

This work was supported by the Ministry of Higher Education, Malaysia under the Transdisciplinary-Fundamental Research Grant Scheme (TRGS) grant (Project No: TD-FRGS/2/2013/UPM/02/1/3) and Putra Grant GP-IPM/2015/946400. We would like to thank Associate Professor Dr. Yuki Shirosaki and Professor Toshiki Miyazaki from 2-4 Hibikino, Wakamatsu-ku, Kitakyushu-shi, Fukuoka, 808-0196, Japan for the chance to use FTIR machine for this study.

REFERENCES

- Amal, M. N. A., Fauzul-Aidil, M. R. M., Jumria, S., Syuhada, R., Khamisah, M. S. N., Lukman, B., ... & Shaqinah, N. N. (2019a). Javanese medaka (*Oryzias javanicus* Bleeker, 1854) as potential model organism

- for aeromoniasis and vibriosis study in fish. *Pertanika Journal of Tropical Agricultural Sciences*, 42(3), 1049-1065.
- Amal, M. N. A., Ismail, A., Zamri-Saad, M., Ina-Salwany, M. Y., Shaqinah, N. N., Siti-Suhaiba, M., ... & Nurliyana, M. (2019b). Study on *Streptococcus agalactiae* infection in Javanese medaka (*Oryzias javanicus* Bleeker, 1854) model. *Microbial Pathogenesis*, 131, 47-52.
- Amal, M. N. A., Zarif, S. T., Suhaiba, M. S., Aidil, M. R. M., Shaqinah, N. N., Zamri-Saad M., & Ismail, A. (2018). The effect of fish gender on susceptibility to acute *Streptococcus agalactiae* infection in Javanese medaka *Oryzias javanicus*. *Microbial Pathogenesis*, 114, 251-254.
- Ami, D., Posteri, R., Mereghetti, P., Porro, D., Doglia, S. M., & Branduardi, P. (2014). Fourier transform infrared spectroscopy as a method to study lipid accumulation in oleaginous yeasts. *Biotechnology for Biofuels*, 7(1), 1-14.
- Andersen, M. L., & Winter, L. M. (2017). Animal models in biological and biomedical research-experimental and ethical concerns. *Anais da Academia Brasileira de Ciências, (AHEAD)*, 91(Suppl. 1), 1-14.
- Aziz, F. Z. A., Zulkifli, S. Z., Mohamat-Yusuff, F., Azmai, M. N. A., & Ismail, A. (2017). An histological study on mercury-induced gonadal impairment in Javanese medaka (*Oryzias javanicus*). *Turkish Journal of Fisheries and Aquatic Sciences*, 17(3), 621-627.
- Baker, M. J., Trevisan, J., Bassan, P., Bhargava, R., Butler, H. J., Dorling, K. M., ... & Hughes, C. (2014). Using Fourier transform IR spectroscopy to analyze biological materials. *Nature Protocols*, 9(8), 1771-1791.
- Begum, G., (2004), Carbofuran insecticide induced biochemical alterations in liver and muscle tissues of the fish *Clarias batrachus* (Linn) and recovery response. *Aquatic Toxicology*, 66, 83-92.
- Bouhleb, Z., Genard, B., Ibrahim, N., Carrington, E., Babarro, J. M., Lok, A., ... & Marcotte, I. (2017). Interspecies comparison of the mechanical properties and biochemical composition of byssal threads. *Journal of Experimental Biology*, 220(6), 984-994.
- Cahu, C., Salen, P., & De Lorgeril, M. (2004). Farmed and wild fish in the prevention of cardiovascular diseases: Assessing possible differences in lipid nutritional values. *Nutrition, Metabolism and Cardiovascular Diseases*, 14(1), 34-41.
- Cakmak, G., Togan, I., & Severcan, F. (2006). 17 β -Estradiol induced compositional, structural and functional changes in rainbow trout liver, revealed by FT-IR spectroscopy: A comparative study with nonylphenol. *Aquatic Toxicology*, 77(1), 53-63.
- Carlson, S. E. (2009). Early determinants of development: A lipid perspective. *The American Journal of Clinical Nutrition*, 89(5), 1523S-1529S.
- Cossins, A. R., & Crawford, D. L. (2005). Fish as models for environmental genomics. *Nature Reviews Genetics*, 6(4), 324-333.
- Gerlai, R., Lahav, M., Guo, S., & Rosenthal, A. (2000). Drinks like a fish: Zebrafish (*Danio rerio*) as a behavior genetic model to study alcohol effects. *Pharmacology Biochemistry and Behavior*, 67(4), 773-782.
- Hernández, J. A., López-Sánchez, R. C., & Rendón-Ramírez, A. (2016). Lipids and oxidative stress associated with ethanol-induced neurological damage. *Oxidative Medicine and Cellular Longevity*, 2016, 1-15.

- Howe, K., Clark, M. D., Torroja, C. F., Torrance, J., Berthelot, C., Muffato, M., ... & Stemple, D. L. (2013). The zebrafish reference genome sequence and its relationship to the human genome. *Nature*, 496(7446), 498-503.
- Inoue, K., & Takei, Y. (2002). Diverse adaptability in *Oryzias* species to high environmental salinity. *Zoological Science*, 19, 727-734.
- Ismail, A., & Yusof, S. (2011). Effect of mercury and cadmium on early life stages of Java medaka (*Oryzias javanicus*): A potential tropical test fish. *Marine Pollution Bulletin*, 63(5), 347-349.
- Jang, T. C., Jang, J. H., & Lee, K. W. (2016). Mekanizma akutne neurotoksičnosti u Sprague-Dawley štakora izazvane trovanjem endosulfanom [Mechanism of acute endosulfan intoxication-induced neurotoxicity in Sprague-Dawley rats]. *Archives of Industrial Hygiene and Toxicology*, 67(1), 9-17.
- Jonsson, C. M., & Toledo, M. C. F. (1993). Acute toxicity of endosulfan to the fish *Hyphessobrycon bifasciatus* and *Brachydanio rerio*. *Archives of Environmental Contamination and Toxicology*, 24(2), 151-155.
- Joya, X., Garcia-Algar, O., Vall, O., & Pujades, C. (2014). Transient exposure to ethanol during zebrafish embryogenesis results in defects in neuronal differentiation: an alternative model system to study FASD. *PloS One*, 9(11), 1-9.
- Kurta, A., & Palestis, B. G. (2010). Effects of ethanol on the shoaling behavior of zebrafish (*Danio rerio*). *Dose-Response*, 8(4), 527-533.
- Maximino, C., da Silva, A. W. B., Gouveia, A., & Herculano, A. M. (2011). Pharmacological analysis of zebrafish (*Danio rerio*) scototaxis. *Progress in Neuro-Psychopharmacology and Biological Psychiatry*, 35(2), 624-631.
- OECD. (2013). *Test No. 236: Fish embryo acute toxicity (FET) test*. Paris, France: OECD Publishing.
- Oyinbo, C. A., Igbigbi, P. S., & Awiworo, G. O. (2016). *Landolphia owariensis* attenuates alcohol-induced cerebellar neurodegeneration: Significance of neurofilament protein alteration in the Purkinje cells. *Folia Medica*, 58(4), 241-249.
- Palaniappan, P. R., & Pramod, K. S. (2011). The effect of titanium dioxide on the biochemical constituents of the brain of zebrafish (*Danio rerio*): An FT-IR study. *Spectrochimica Acta Part A: Molecular and Biomolecular Spectroscopy*, 79(1), 206-212.
- Peterson, D. R., Mok, H. O. L., & Au, D. W. T. (2015). Modulation of telomerase activity in fish muscle by biological and environmental factors. *Comparative Biochemistry and Physiology Part C: Toxicology and Pharmacology*, 178, 51-59.
- Price, E. O. (1999). Behavioral development in animals undergoing domestication. *Applied Animal Behaviour Science*, 65(3), 245-271.
- Romano, D., Benelli, G., Donati, E., Remorini, D., Canale, A., & Stefanini, C. (2017). Multiple cues produced by a robotic fish modulate aggressive behaviour in Siamese fighting fishes. *Scientific Reports*, 7(1), 1-11.
- Schartl, M. (2014). Beyond the zebrafish: Diverse fish species for modeling human disease. *Disease Models and Mechanisms*, 7(2), 181-192.

- Senthamilselvan, D., Chezian, A., Kabilan, N., Kumar, S. T., & Kumaran, S. N. (2012). FTIR study of nickel and mercury induced biochemical changes in the muscles tissues of *Lates calcarifer*. *International Journal of Environmental Sciences*, 2(4), 1976-1983.
- Silva, M., Pham, N., Lewis, C., Iyer, S., Kwok, E., Solomon, G., & Zeise, L. (2015). A comparison of ToxCast test results with *in vivo* and other *in vitro* endpoints for neuro, endocrine, and developmental toxicities: a case study using endosulfan and methidathion. *Birth Defects Research Part B: Developmental and Reproductive Toxicology*, 104(2), 71-89.
- Sylvain, N. J., Brewster, D. L., & Ali, D. W. (2010). Zebrafish embryos exposed to alcohol undergo abnormal development of motor neurons and muscle fibers. *Neurotoxicology and Teratology*, 32(4), 472-480.
- Taşbozan, O., & Gökçe, M. A. (2017). Fatty acids in fish. *Fatty Acids*, 1, 143-159.
- Tran, S., Chatterjee, D., & Gerlai, R. (2015). An integrative analysis of ethanol tolerance and withdrawal in zebrafish (*Danio rerio*). *Behavioural Brain Research*, 276, 161-170.
- Tran, S., Facciol, A., & Gerlai, R. (2016). Alcohol-induced behavioral changes in zebrafish: The role of dopamine D2-like receptors. *Psychopharmacology*, 233(11), 2119-2128.
- Wittbrodt, J., Shima, A., & Schartl, M. (2002). Medaka-a model organism from the far East. *Nature Reviews Genetics*, 3(1), 53-64.
- Yuan, J., & Yankner, B. A. (2000). Apoptosis in the nervous system. *Nature*, 407(6805), 802-809.
- Yusof, S., Ismail, A., & Rahman, F., (2013). Distribution and localities of Java medaka fish (*Oryzias javanicus*) in Peninsular Malaysia. *Malayan Nature Journal*, 65(2&3), 38-46.
- Yusof, S., Ismail, A., & Alias, M. S. (2014). Effect of glyphosate-based herbicide on early life stages of Java medaka (*Oryzias javanicus*): A potential tropical test fish. *Marine Pollution Bulletin*, 85(2), 494-498.
- Yusof, S., Ismail, A., Koito, T., Kinoshita, M., & Inoue, K. (2012). Occurrence of two closely related rice- fishes, Javanese medaka (*Oryzias javanicus*) and Indian medaka (*O. dancena*) at sites with different salinity in Peninsular Malaysia. *Environmental Biology of Fishes*, 93, 43-49.
- Zahir, F., Rizvi, S. J., Haq, S. K., & Khan, R. H. (2006). Effect of methyl mercury induced free radical stress on nucleic acids and protein: Implications on cognitive and motor functions. *Indian Journal of Clinical Biochemistry*, 21(2), 149-152.



Effect of Different Application Techniques on Marginal Adaptation of Class II Cavities Filled with Three Different Bulkfill Composite Filling Material: An *In Vitro* Study using Confocal Microscopy

Aulfat Ahmed Albahari^{1*}, Mohammed Ahmed Dubais¹, Ahmed Abdullah Madfa^{1,2,3} and Waled Abdul Malek Alanesi¹

¹Department of Restorative and Prosthodontics, College of Dentistry, University of Sciences and Technology, Yemen

²Department of Conservative Dentistry, Faculty of Dentistry, Thamar University, Dhamar, Yemen

³Department of Restorative Dental Science, Collage of Dentistry, University of Hail, Hail, Kingdom of Saudi Arabia

ABSTRACT

An experimental study was conducted to assess marginal adaptation of various bulkfill composite materials, at cervical and occlusal margins of class II cavity preparation, applied by two different application techniques. Seventy-two (72) extracted premolar teeth were selected, prepared and filled with three different bulkfill composite materials, and inserted using incremental and bulk techniques. Specimens were thermocycled and bisected mesio-distally. All specimens were observed using a confocal fluorescence imaging microscope at 10× magnification. The data was analyzed using the Mann-Whitney U test. $P < 0.05$ was used to indicate statistically significant differences. The study results revealed that, no significant differences in marginal adaptation were detected among the two application techniques (incremental and bulkfill) at cervical margins $p=1.000$ and the occlusal margins $p=0.639$ with the lowest gap width formation achieved by X-trafil® bulkfill composite among the three different bulkfill composite filling materials, while Filtek™ Flowable composite material had the highest gap width. This study signifies that good marginal seal

depends on the proper cavity preparation, good manipulation of filling materials and skill of the operator whatever is the application technique.

Keywords: Adaptation, application techniques, bulkfill composite materials, cervical margin, confocal microscope, occlusal margin

ARTICLE INFO

Article history:

Received: 23 October 2019

Accepted: 28 January 2020

Published: 15 April 2020

E-mail addresses:

aulfatalbahari2013@yahoo.com (Aulfat Ahmed Albahari)

drdubais@yahoo.com (Mohammed Ahmed Dubais)

ahmed_um_2011@yahoo.com (Ahmed Abdullah Madfa)

walidalanesi@gmail.com (Waled Abdul Malek Alanesi)

* Corresponding author

INTRODUCTION

The long-standing overall performance of the restoration depends on the tight fitting of the restorative material to internal cavity surfaces and margins (Roulet, 1994). Despite outstanding advances in the field of composite restorative materials technology and its applications in restorative dentistry, there are many factors that may influence the stability of composite restoration, such as low strength, technique sensitivity, high wear rate, and polymerization shrinkage (Pitel, 2013). Polymerization shrinkage generates a reduction in volume of the material 1.7% to 5.7% (Alvarez-Gayosso et al., 2004), as a result of changing the material density during the polymeric network formation process. The shrinkage stress may lead to generating gap (10–15 μm) (Ferracane, 2005). This gap permits the escape of fluids as well as bacteria between the oral environment and the dentin pulp complex (Amaral et al., 2004), which are considered to be harmful.

Many studies have looked at methods to reduce the rate of polymerization shrinkage and improve marginal adaptation. These include placement of liners (Chuang et al., 2004), replacement of the dentin with a glass-ionomer cement in the sandwich technique (Dijken & Pallesen, 2012) and incremental application techniques. Most of these studies have been done with conventional resin based composites (RBCs), even though conventional RBCs have typically been placed in layers not exceeding a thickness of 2 mm, due to these techniques being time-consuming and complicated when used to fill large and voluminous cavities in posterior teeth. Additionally, many dentists prefer the use of an alternative to this highly sensitive multiple layering technique, the one-step insertion of a 4 mm bulkfill composite resins.

Bulkfill composite resins have been developed, in an effort to overcome polymerization shrinkage problems. Lower filler loading, lower viscosity, high flowability and a self-leveling property of the material that adapts well to the cavity wall are the main advantages of the bulkfill material (Chuang et al., 2001). Placement of composite restorative material at thicknesses greater than 4 mm has become possible, by altering the initiator in bulkfill composite resins, resulting in considerably shorter chair times during the filling procedure (Tiba et al., 2013).

Due to inherent polymerization shrinkage and contraction stress, debonding and increased risk of gap formation at the tooth-composite interface could be compromised to posterior teeth particularly in class II restorations. Gingival Cavo-surface margins of Class II restorations can be an area of failure (Moffa, 1989). Possible causes include insufficient polymerization of the RBCs at the gingival wall, the high C-Factor characteristic of the box shape, limited access of proximal boxes making the placement of the material more challenging and the adhesive bonding to the cervical tooth structure. These contribute to the increase in polymerization shrinkage stresses during the setting reaction of the material (Sabatini et al., 2010).

It is believed that effective marginal seal has been obtained by incremental application technique over the bulkfill method by decreasing the stresses generated within the tooth-restoration system (Dijken & Pallesen, 2011; Dietschi et al., 2002). On the other hand, class I and class II cavities can be restored with bulkfill materials in a mono-increment technique, they are predictable to be capable to produce proper marginal integrity. Therefore, research conclusions need to be confirmed by means of experimental work that mimics clinical environments. Consequently, this is an experimental study conducted with the aim of assessing the effect of incremental and bulkfill application techniques on marginal adaptation of class II cavities filled with three different types of bulkfill composite resins. Confocal microscopy had been used for accurate and closer examination of the restoration margins. The null hypothesis is there is no difference in the marginal adaptation achieved by the examined placement techniques.

MATERIALS AND METHODS

Specimen Preparation

Seventy-two premolar teeth were stored for no more than three months after extraction for an orthodontic purpose. Exclusion criteria were teeth with developmental defects, caries or microcracks. Ethical approval was from the Research Ethics Committee of the University of Sciences and Technology prior to study execution (MECA NO: EACUST141). The teeth were cleaned by hand scaling and immersed in a 0.1% chloramine T solution for one week, followed by immersion in normal saline at room temperature during the experimental time.

Cavity Preparation

A dental manikin with upper and lower jaws was used, the teeth were set with crowns in the long axis parallel to each other and in proximal contact (Sabah & Baban, 2013), and a metal matrix band used to adopt teeth. A standardized class II cavity preparation was prepared to all teeth using coarse diamond fissure points (F80710M, ökoDENT, Thuringia, Germany) with a high-speed hand piece (W&H, Bürmoos, Austria) under profuse water cooling and finished with finishing diamond points (#2203, Dentex, Taipei, Taiwan). Roundation and beveling were applied to the enamel margins and the inner-angles of the cavities. All cavities received 1 mm distance preparation below the cemento-enamel junction (CEJ). For every four cavities, one new bur was used to maintain the cutting efficiency (Borges et al., 2012). A width of 4 mm bucco-lingually and a length of 4 mm occluso-gingivally with a depth of 2 mm axially were prepared in the cavities as shown in Figure 1. A periodontal probe was used to confirm dimensions.

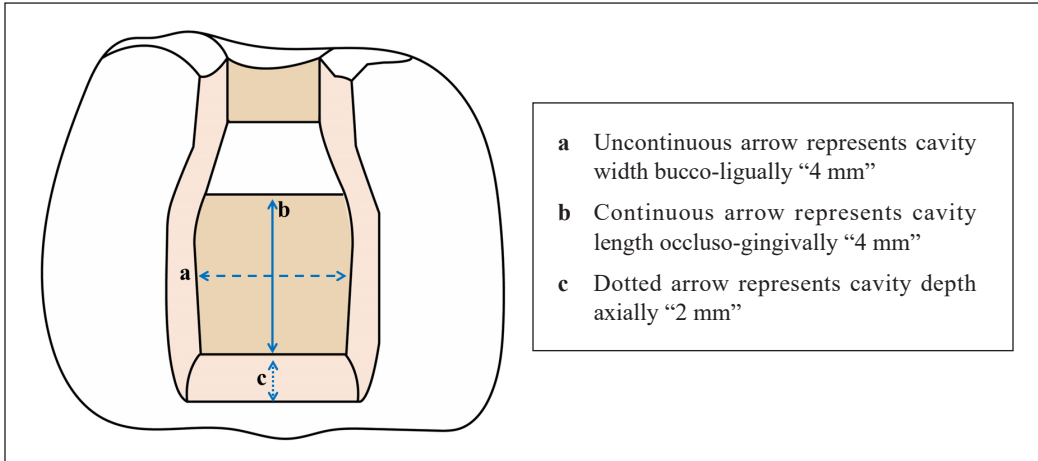


Figure 1. Schematic diagram of cavity preparation dimensions

Specimens Grouping

The specimens were assigned to one of two main study groups with 36 tooth in each group corresponding to two different application techniques (incremental and bulkfill). The specimens were further randomly sub-divided into three subgroups for each technique, with 12 teeth in each subgroup based on the different bulkfill restorative materials used in this study as shown in Figure 2. The characteristics of the materials used in this study are shown in Table 1.

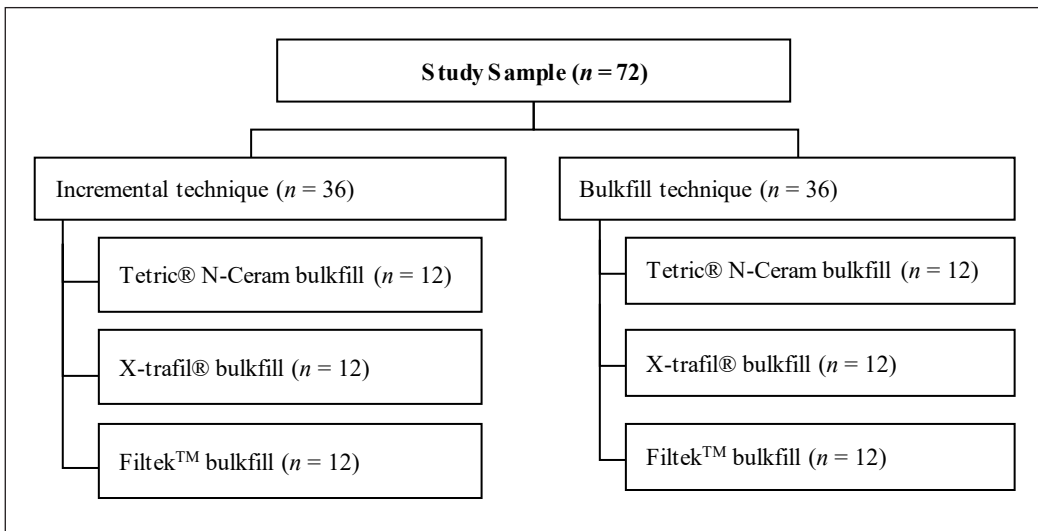


Figure 2. Flow chart demonstrating specimens grouping

Table 1
Characteristics of the materials used in this study

Material	Manufacturer	Composition	City\Country
Tetric® N-Ceram bulkfill	Ivoclar Vivadent	BIS-GMA, Urethane Di methacrylate, Barium glass filler, Ivocerin, shrinkage stress reliever, Light sensitivity filter filler, Pigments	Liechtenstein, Germany
Filtek™ bulkfill Flowable Restorative	3M ESPE	BIS-GMA, Urethane Di methacrylate, procrylat resin fillers are combination of Zirconia /Silica (.01 to 3.5 micro meter) & Ytterbium tri fluoride (0.1 to 5)	St. Paul, MN, USA
X-trafil®	Voco	BIS-GMA, Urethane di methacrylate, TEGDMA	Cuxhaven, Germany

Restorative Procedure

A solution of 37% phosphoric acid gel (Ivoclar Vivadent, Liechtenstein, Germany) was applied to all cavities as an etching process for 30 seconds on the enamel and 15 seconds on the dentin, followed by 5 seconds washing with a water jet and drying with a gentle stream of air which left the surface moistened. Corresponding self-etch bond adhesive systems were applied: Adhe SE One F (Ivoclar Vivadent, Liechtenstein, Germany), Scotch Bond Universal (3M Espe, St. Paul, MN, USA), and Futura bond DC (Voco, Cuxhaven, Germany). A LED light curing unit (LY-C240 Foshan City, China) of 1200 mw/cm² light intensity which was monitored and checked periodically with a radiometer (Dymax, Torrington, USA) was used. A 10 seconds was a distance which was determined by a periodontal probe, where the specimens were light-cured from the occlusal and cervical margins with the light tip contacting the margins. Two techniques were employed in this study:

- (a) A 4 mm single step placement of the bulkfill composites.
- (b) A 2 mm thickness of bulkfill composites were used for the incremental technique. Both techniques were cured for 40 seconds, and all restorations were performed by one operator.

Thermocycling Procedure

In simulation to the temperature changes in the oral environment and development of micro-space between the tooth margins and the restorative material, two water baths, 55°C and 5°C, with a 30 seconds dwell time, were selected to perform 1000 cycles according to the International Organization for Standardization (ISO)TR 11405 (Loguercio et al., 2004).

Evaluation of Marginal Adaptation

Once the thermocycling process was completed, the specimens were dried, and two layers of nail polish were applied 1 mm above and below the interface between the tooth and

restorative material, as shown in Figure 3. Afterwards, a slow speed of 300 rpm with a diamond disk (D-12203 Berlin, Germany) under constant cooling (Opdam et al., 2010), was used to bisect the specimens mesio-distally through the midpoint of restorative material parallel to the occlusal surface. Rhodamine B Isothiocyanate (Aldrich Chemical Co., Milwaukee, WI, USA), the fluorescent material was applied to the specimen based on the manufacturer instruction. Then, a Confocal Fluorescence Imaging Microscope (Leica TCS-SP5, DM6000-CFS) at 10X magnification was used to examine the specimens to determine marginal gaps along the restoration-cavity wall interfaces in the cervical and occlusal margins (Zarrati & Mahboub, 2010), the specimens were sent to Malaysia and the work was done in conjunction with Dr Alshawsh who is an Associate Professor at department of pharmacology, Faculty of Medicine, Unversiti Malaya for examination under a Confocal Fluorescence Imaging Microscope. Three points on the occlusal and cervical margins of the tooth-restorative interface were selected to facilitate the determination of the marginal gap width (the distance between the tooth axial wall and the restorative material), and the full perimeter of the restoration was bought by way of taking approximately six photos of each specimen (Usha et al., 2011). Image analysis software (Scope Photo 3.0 USA) was used to record the marginal gap width from the three points in each region. The mean marginal gap in micrometers (μm) for the occlusal and cervical margin was calculated. Confocal microscopic examination was used to be accomplished via one operator with experience in quantitative analysis of margin and who used to be blind to the application procedures. The marginal fitting surface between composite restoration and dentin used to be presented as a percentage of the whole margin length in the enamel and dentin.

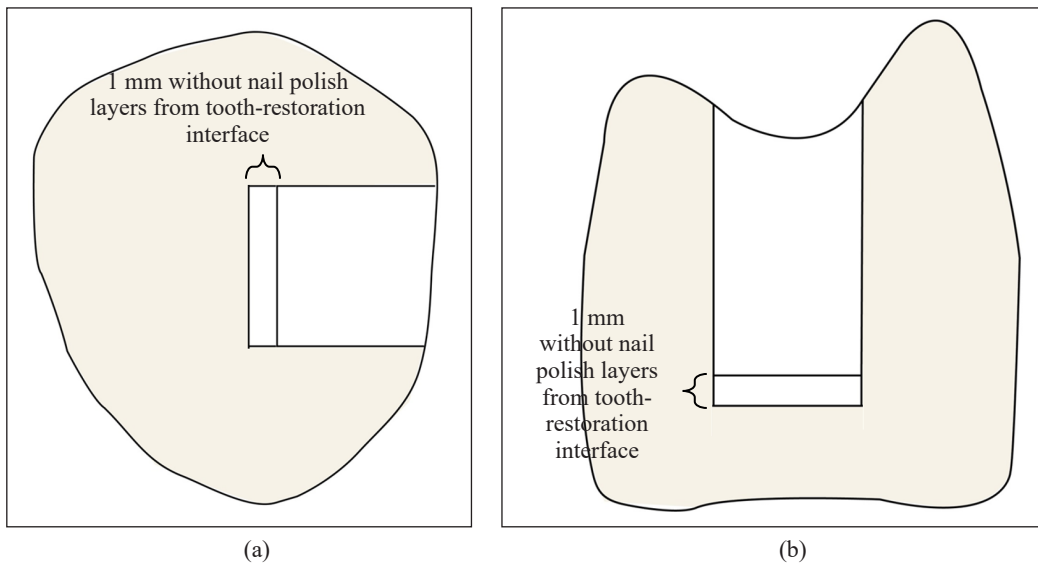


Figure 3. A schematic diagram to show the exact place where two layers of nail polish were applied “colored area” at occlusal and cervical margins: (a) occlusal view; and (b) proximal view

Marginal qualities along the outer periphery of the restorations were classified according to the criteria “continuous margin”, “noncontinuous margin” and “not judgeable\artifact”. The percentage of “continuous margin” in relation to the individual noncontinuous margin was calculated as marginal integrity according to the formula:

$$\text{Marginal integrity} = \frac{\text{Noncontinuous margin}}{\text{Continuous margin}} \times 100$$

Statistical Analysis

All data were collected and statistically analyzed with the aid of SPSS version 25.0 (Chicago, USA). The assumption of normality was not met, because the data did not approximate a normal distribution curve. This was further confirmed using the Shapiro-Wilk test. All specimens of the two groups were evaluated and compared for marginal adaptation along with the occlusal and cervical wall using a Mann-Whitney U test. A p value of < 0.05 was used to indicate statistically significant differences.

RESULTS

The quantitative assessment of marginal adaptation exposed that, no gap formation was executed in several regions (Figure 4), even though noncontinuous margins categorized as “marginal fissures” were observed in all restorations (Figure 5). The mean of three points that shows the largest marginal gap width of the cervical region and the point that represented the largest marginal gap width at the occlusal region for the three different bulkfill materials were recorded and the data were introduced in Table 2.

Table 3 reveals marginal adaptation scores expressed as a percentage of gap formation at the occlusal and cervical margins of various bulkfill composite materials inserted with incremental and bulkfill techniques.

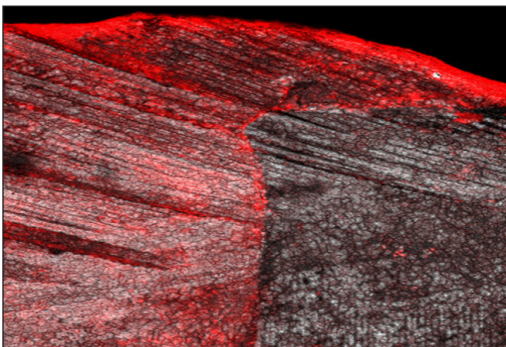


Figure 4. Confocal microscope image shows continuous marginal adaptation (no gap formation) in certain restoration

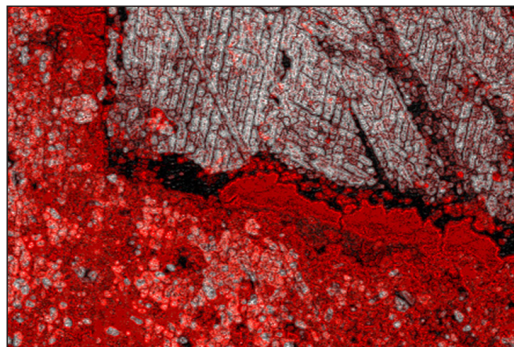


Figure 5. Confocal microscope image shows non-continuous marginal adaptation (gap formation) in all restorations

Table 2
Mean and standard deviation values for marginal gap width at occlusal and cervical regions

Application techniques	Margins	Descriptive statistics of bulkfill materials m±St		
		Filtek™ Flowable m±St	Tetric®N- Ceram m±St	X- trafil® m±St
Incremental	Occlusal	1.77±0.718	0.75±0.754	0.3±0.00
	Cervical	2±0.00	1.5±0.522	1±0.00
Bulkfill	Occlusal	1.5±0.522	1.67±0.492	0.5±0.00
	Cervical	2±0.00	1.5±0.522	1±0.00

Table 3
Marginal adaptation scores expressed as percentage of gap formation at occlusal and cervical margins of various bulkfill composite materials inserted with incremental and bulkfill techniques

Margins	Marginal adaptation	Incremental application						Bulkfill application					
		Filtek™ Flowable		Tetric® N-Ceram		X-trafill®		Filtek™ Flowable		Tetric® N-Ceram		X- trafil®	
		f	(%)	f	(%)	f	(%)	f	(%)	f	(%)	F	(%)
Occlusal	Continuous margin	0	0%	5	41.7%	9	75%	0	0%	2	16.7%	10	83.3%
	Non-continuous margin	4	33.3%	5	41.7%	3	25%	6	50%	6	50%	2	16.6%
	Not judgeable\ artifact	8	66.7%	2	16.7%	0	0%	6	50%	4	33.7%	0	0%
Cervical	Continuous margin	0	0%	0	0%	0	0%	0	0%	0	0%	0	0%
	Non-continuous margin	12	100%	6	50%	3	25%	12	100%	6	50%	3	25%
	Not judgeable\ artifact	12	100%	6	50%	0	0%	12	100%	6	50%	0	0%

No significant differences in marginal fitting among the three different bulkfill composite materials were detected between the two application techniques at the cervical margins $p > 1.000$ and occlusal $p > 0.639$ using the Mann-Whitney U test, Table 4.

A statistically significant difference was found in the gap width analysis scores between the occlusal and cervical margins with $p < 0.000$ for all groups of tested materials utilizing the Mann-Whitney U test, Table 5.

The assessment of marginal gaps width in the cervical and occlusal regions within each bulkfill restorative material using the Mann-Whitney U test exposed a statistically significant difference among the tested margins, Tables 3 and 6. X-trafill® bulkfill composite showed the lowest gap width formation, while Filtek™ Flowable composite material had the highest gap width.

Table 4

Gap formation scores comparison between incremental and bulkfill application techniques at occlusal and cervical margins

Margins	Mann-Whitney U	Z	Sig	Incremental application method	Bulk Application method
Occlusal margin	609.00	-0.470	0.639	35.42	37.58
Cervical margin	648.00	0.000	1.000	36.5	36.5

* No significant differences of gap formation between incremental and bulkfill application techniques at occlusal and cervical margins.

Table 5

Marginal adaptation comparison between occlusal and cervical margin

Marginal adaptation	Mann-Whitney U	Z	Sig	Occlusal margin	Cervical margin
	1458.00	-4.860	0.000*	56.75	88.25

*significant differences of marginal adaptation between occlusal and cervical margins $p < 0.000$

Table 6

Marginal gaps width among the three bulkfill composite materials filled with incremental and bulkfill techniques at each margin

Margins	Bulkfill materials	Incremental application		Bulkfill materials	Bulkfill application	
		Mean differences	P-value		Mean differences	P-value
Occlusal	A-B	1.47	0.000*	D-E	-0.17	0.000*
	A-C	1.02	0.011*	D-F	1	0.003*
	B-C	-0.45	0.000*	E-F	-1.17	0.000*
Cervical	A-B	1	0.000*	D-E	1	0.000*
	A-C	0.5	0.001*	D-F	0.5	0.000*
	B-C	-0.5	0.001*	E-F	-0.5	0.000*

A: Teeth restored with Filtek™ Flowable using the incremental technique.

B: Teeth restored with X-trafil® bulkfill composite using the incremental technique.

C: Teeth restored with Tetric®N-Ceram bulkfill using the incremental technique.

D: Teeth restored with Filtek™ Flowable using the bulkfill technique.

E: Teeth restored with X-trafil® bulkfill composite using the bulkfill technique.

F: Teeth restored with Tetric®N-Ceram bulkfill using the bulkfill technique.

*significant differences of marginal gaps width among the different three bulkfill composite materials.

DISCUSSION

The quest for a good adaptation between the restoration and cavity walls remains a goal of many researchers (Ferrari & Garcia-Godoy, 2002). Therefore, the present *in vitro* study evaluated marginal adaptation of various bulkfill composite restorative materials applied by incremental and bulkfill methods at the occlusal and cervical margins in class II restoration.

Class II cavities were prepared on the teeth of the current study because the occlusal and cervical margins are often distinguished and designated for composite restorations. They involve both the enamel and the dentin, and therefore, the nature of adaptation of composite resin can be compared at both regions. To ensure standardization to all restorative procedures, the same degree of cure and polymerization reaction between the studied groups was achieved by using a single LED light curing unit. The self-etch technique was used for all restorations, and the adhesives used in this study combine the functions of both primer and adhesive components which reduced the procedure time. A thermocycling procedure was applied to all specimens at a specific temperature range according to (ISO) TR11405 (Loguercio et al., 2004), with the goal of thermally accentuating the junction at the tooth-filling interface.

Quantitative analysis of the amount and width of gaps generated at the margins and marginal irregularities provided by marginal adaptation measurement had been chosen for this study rather than the qualitative isolated analysis provided by microleakage. To minimize the errors during scoring and calculation of marginal data, the number of criteria used to detect differences between tested groups was collapsed and narrowed down to the criteria of no-gap (continuous margin) against gap (noncontinuous margin), to make interpretation and statistical analysis of results easier.

The present study measured adaptation using confocal microscopy at 10X magnification. Confocal laser scanning microscopy (CLSM) is a technique used for picturing subsurface tissue characteristics. An advantage of this technique is the use of lens focus which can focus a few microns under the observed surface, thus avoiding the spread of stain due to specimen sectioning and avoid polishing artifacts (Lopes et al., 2009). The six images taken for analysis were nonoverlapping to avoid replication of the same gap score of a previous image.

The hypothesis stating that there are significant differences in marginal adaptation between the two techniques was not supported by this study results. The use of a bulkfill application technique showed gaps with an amplitude similar to that of the incremental technique. There were no statistically significant differences between the two application techniques. The study results are in agreement with other studies done by Roggendorf et al. (2011), Campos et al. (2014) and Furness et al. (2014) comparing the different placement techniques (incremental and bulkfill) with different RBC systems (conventional versus bulkfill composites). However, the findings in the present study contrasted to a study done by Mullejans et al. (2003), comparing the application techniques (incremental against bulk) using single conventional composite resin, which exhibited that incremental application reduced gap formation. These results may be different from the current study because only the conventional composite resin was used and the types of composite resin systems used were different.

The study results exhibited satisfactory marginal adaptation to all investigated bulkfill materials at the occlusal margin, unlike the cervical margin. The values of continuous margins in the occlusal region were higher than the cervical region (Roggendorf et al., 2011). This could be attributed to the beveling of the enamel margins in order to increase the surface area of the enamel to bond to the composite. The findings of the current study have been corroborated by a study conducted by Oskoe and colleagues, who reported that occlusal marginal adaptation was superior to that observed in the cervical enamel margins (Oskoe et al., 2012). This could be explained by that, the adhesion of the restorative materials to the proximal aspect at the Cavo-surface margin is greater to dentin rather than enamel, due to low enamel thickness at that area (Bogra et al., 2012). In addition, the distance of the light source from the material is lower at the occlusal surfaces compared to that at the proximal box base, thereby reducing the percentage of degree of conversion (Coutinho et al., 2013).

In this study, X-trafill® bulkfill composite material, exhibited a great significant reduction in the width of marginal gaps alongside the restoration-enamel interface at the gingival and occlusal regions after thermocycling procedure in relation to the Filtek™ bulkfill restorative material. This ought to be accredited to an inadequate adaptation to the enamel walls, as a result of the high viscosity of the Filtek™ bulkfill restorative material, because of the increase in the amount of filler particles (Radhika et al., 2010; Majeed, 2012). On the other hand, the better adaptation exhibited by X-trafill® restorative material was owing to the low viscosity of the material that facilitate plastic flow during the early phases of polymerization (Scotti et al., 2014). The present study results contradict the study conducted by Patel et al. (2018), who evaluated marginal fitting integrity of three bulkfill composite materials in Class II cavities, and found that Filtek™ bulkfill composite material showed better marginal adaptation than Tetric®N-Ceram and X-trafill® bulkfill composites. This could be due to their study design as stereomicroscopy was used for evaluation.

The limitations of the present study are that this study tested the cervical marginal adaptation underneath the level of the CEJ. However, in a practical work, it is not-indicated to apply composite restorations underneath the CEJ, as normally open sandwich technique is recommended in clinical application, where suggested modifications had been done in this study. As well as, the current study evaluated adaptation using only a self-etching system. Therefore, the results cannot be extrapolated to other systems. Future research should be carried out *in vivo* to confirm the current study results.

CONCLUSIONS

It can be concluded from the results that the marginal adaptation scores were not affected by the various tested application techniques. On the other hand, as anticipated, with the both application techniques, the marginal adaptation in the occlusal surface was higher

than that in the cervical surface, and among the restorative materials, X-trafill® restorative material exhibited the highest score of adaptation, irrespective of the filling materials investigated in this study.

ACKNOWLEDGMENTS

All authors acknowledge the University of Science and Technology (Sana'a, Yemen) for funding this study.

REFERENCES

- Alvarez-Gayosso, C., Barceló-Santana, F., Guerrero-Ibarra, J., Sáez-Espínola, G., & Canseco-Martínez, M. A. (2004). Calculation of contraction rates due to shrinkage in light-cured composites. *Dental Materials*, 20(3), 228-235.
- Amaral, C. M., Peris, A. R., Ambrosano, G. M., & Pimenta, L. A. (2004). Microleakage and gap formation of resin composite restorations polymerized with different techniques. *American Journal of Dentistry*, 17(3), 156-160.
- Bogra, P., Gupta, S., & Kumar, S. (2012). Comparative evaluation of microleakage in class II cavities restored with Ceram X and Filtek P-90: An in vitro study. *Contemporary Clinical Dentistry*, 3(1), 9-14.
- Borges, A. F. S., Santos, J., Ramos, C. M., Ishikiriyama, S. K., & Shinohara, M. S. (2012). Effect of thermo-mechanical load cycling on silorane-based composite restorations. *Dental Materials Journal*, 31(6), 1054-1059.
- Campos, E. A., Ardu, S., Lefever, D., Jassé, F. F., Bortolotto, T., & Krejci, I. (2014). Marginal adaptation of class II cavities restored with bulk-fill composites. *Journal of Dentistry*, 42(5), 575-581.
- Chuang, S. F., Jin, Y. T., Liu, J. K., Chang, C. H., & Shieh, D. B. (2004). Influence of flowable composite lining thickness on Class II composite restorations. *Operative Dentistry*, 29(3), 301-308.
- Chuang, S. F., Liu, J. K., Chao, C. C., Liao, F. P., & Chen, Y. H. M. (2001). Effects of flowable composite lining and operator experience on microleakage and internal voids in class II composite restorations. *The Journal of Prosthetic Dentistry*, 85(2), 177-183.
- Coutinho, M., Trevizam, N. C., Takayassu, R. N., Leme, A. A., & Soares, G. P. (2013). Distance and protective barrier effects on the composite resin degree of conversion. *Contemporary Clinical Dentistry*, 4(2), 152-155.
- Dietschi, D., Monasevic, M., Krejci, I., & Davidson, C. (2002). Marginal and internal adaptation of class II restorations after immediate or delayed composite placement. *Journal of Dentistry*, 30(5-6), 259-269.
- Dijken, J. W., & Pallesen, U. (2011). Clinical performance of a hybrid resin composite with and without an intermediate layer of flowable resin composite: a 7-year evaluation. *Dental Materials*, 27(2), 150-156.
- Dijken, J. W., & Pallesen, U. (2012). A 7-year randomized prospective study of a one-step self-etching adhesive in non-carious cervical lesions. The effect of curing modes and restorative material. *Journal of Dentistry*, 40(12), 1060-1067.

- Ferracane, J. L. (2005). Developing a more complete understanding of stresses produced in dental composites during polymerization. *Dental Materials*, 21(1), 36-42.
- Ferrari, M., & Garcia-Godoy, F. (2002). Sealing ability of new generation adhesive-restorative materials placed on vital teeth. *American Journal of Dentistry*, 15(2), 117-136.
- Furness, A., Tadros, M. Y., Looney, S. W., & Rueggeberg, F. A. (2014). Effect of bulk/incremental fill on internal gap formation of bulk-fill composites. *Journal of Dentistry*, 42(4), 439-449.
- Loguercio, A. D., Roberto, O. B., J., Reis, A., & Grande, R. H. (2004). In vitro microleakage of packable composites in Class II restorations. *Quintessence International*, 35(1), 29-34.
- Lopes, M. B., Consani, S., Gonini-Júnior, A., Moura, S. K., & McCabe, J. F. (2009). Comparison of microleakage in human and bovine substrates using confocal microscopy. *The Bulletin of Tokyo Dental College*, 50(3), 111-116.
- Majeed, M. A. (2012). Microleakage evaluation of a silorane-based and methacrylate-based packable and nanofill posterior composites (*in vitro* comparative study). *Tikrit Journal for Dental Sciences*, 1(2), 19-26.
- Moffa, J. (1989). Comparative performance of amalgam and composite resin restorations and criteria for their use. In K. Anusavice (Ed.), *Quality evaluation of dental restorations* (pp. 125-131). Chicago, Illinois: Quintessence Publishing.
- Mullejans, R., Lang, H., Schuler, N., Badawi, M. O., & Raab, W. H. (2003). Increment technique for extended class V restorations: An experimental study. *Operative Dentistry*, 28(4), 352-356.
- Opdam, N. J. M., Bronkhorst, E. M., Loomans, B. A. C., & Huysmans, M. C. (2010). 12-year survival of composite vs. amalgam restorations. *Journal of Dental Research*, 89(10), 1063-1067.
- Oskoe, P. A., Kimyai, S., Ebrahimi, M. E., Rikhtegaran, S., & Pournaghi-Azar, F. (2012). Cervical margin integrity of Class II resin composite restorations in laser-and bur-prepared cavities using three different adhesive systems. *Operative Dentistry*, 37(3), 316-323.
- Patel, M. C., Bhatt, R. K., Makwani, D. A., Dave, L. D., & Raj, V. S. (2018). Comparative evaluation of marginal seal integrity of three bulk-fill composite materials in Class II cavities: An *in vitro* study. *Advances in Human Biology*, 8(3), 201-205.
- Pitel, M. L. (2013). Low-shrink composite resins: a review of their history, strategies for managing shrinkage, and clinical significance. *Compendium of Continuing Education in Dentistry*, 34(8), 578-590.
- Radhika, M., Sajjan, G. S., Kumaraswamy, B. N., & Mittal, N. (2010). Effect of different placement techniques on marginal microleakage of deep class-II cavities restored with two composite resin formulations. *Journal of Conservative Dentistry: JCD*, 13(1), 9-15.
- Roggendorf, M. J., Krämer, N., Appelt, A., Naumann, M., & Frankenberger, R. (2011). Marginal quality of flowable 4-mm base vs. conventionally layered resin composite. *Journal of Dentistry*, 39(10), 643-647.
- Roulet, J. F. (1994). Marginal integrity: clinical significance. *Journal of Dentistry*, 22, S9-S12.
- Sabah, M. K., & Baban, L. M. (2013). Marginal leakage of amalgam and modern composite materials related to restorative techniques in class II cavity: Comparative study. *Journal of Baghdad College of Dentistry*, 325(2207), 1-8.

- Sabatini, C., Blunck U., Denehy, G., Munoz, C. (2010). Effect of pre-heated composites and flowable liners on class II gingival marginal gap formation. *Operative Dentistry*, 35(6), 663-671.
- Scotti, N., Comba, A., Gambino, A., Paolino, D. S., Alovisi, M., Pasqualini, D., & Berutti, E. (2014). Microleakage at enamel and dentin margins with a bulk fills flowable resin. *European Journal of Dentistry*, 8(1), 1-8.
- Tiba, A., Zeller, G. G., Estrich, C. G., & Hong, A. (2013). A laboratory evaluation of bulk-fill versus traditional multi-increment-fill resin-based composites. *American Journal of Dental Association*, 8(3), 13-26.
- Usha, H. L., Kumari, A., Mehta, D., Kaiwar, A., & Jain, N. (2011). Comparing microleakage and layering methods of silorane-based resin composite in class V cavities using confocal microscopy: An *in vitro* study. *Journal of Conservative Dentistry*, 14(2), 164-168.
- Zarrati, S., & Mahboub, F. (2010). Marginal adaptation of indirect composite, glass-ceramic inlays and direct composite: an in vitro evaluation. *Journal of Dentistry (Tehran, Iran)*, 7(2), 77-83.

Comparison of Catches of Skipjack Tuna (*Katsuwonus pelamis* Linnaeus 1758) Purse Seines Inside and Outside of the FADs Areas

Achmar Mallawa

Department of Fishery, Faculty of Marine Sciences and Fishery, Hasanuddin University, Jln. Perintis Kemerdekaan KM.10, 90245, Makassar, South Sulawesi Indonesia

ABSTRACT

Skipjack tuna is a potential fish resource in the Makassar Strait, Bone Bay, and the Flores Sea waters, Indonesia. This fish is captured by fishermen using many kinds of fishing gear, and the most widely used is purse seine. The study was conducted from January to December 2018, aimed to compare the size structure of skipjack, productivity, and by-catch of purse seine inside and outside of Fish Aggregation Devices (FADs) areas. Fish length (cm, FL), annual production and trips data were collected from 10 ship owners in each fishing area, The main catch and by-catch weight data were obtained through direct observation of 30 trips each for 10 units, both of purse seines inside and outside of FADs areas in each study area. Comparative analysis of the catches of purse seines inside and outside of FADs areas included size structures using the Median Test (T test), productivity and by-catch using Mann-Whitney Test (T test). The results of the study explained that purse seiners inside FADs areas could increase business productivity, but caused an increase in small-sized skipjack and by-catch while purse seines outside of FADs areas caught less small size skipjack, low by-catch but low productivity.

Keywords: By-catch, FAD, productivity, size structure, skipjack purse seiner

INTRODUCTION

Indonesia divides its sea waters into eleven Fisheries Management Regions, and one of them was Indonesian Fisheries Management Region 713 (WPP RI 713). The WPP RI 713 consists of the waters of the Bone Bay, Makassar Strait and the Flores Sea, which are directly adjacent to the Indian Ocean

ARTICLE INFO

Article history:

Received: 14 July 2019

Accepted: 15 November 2019

Published: 15 April 2020

E-mail address:

achmar_mallawa@yahoo.co.id (Achmar Mallawa)

waters. The WPP RI 713 waters have high potential for big pelagic fish, especially the skipjack tuna. These fishes are exploited by fishermen using several types of fishing gear including drift surface gill net, purse seine, pole and line, trolling line, hand line, vertical long line, traditional seine net, and boat lift net. Purse seines are most widely used by fishermen, where they operate both inside and outside of the Fish Aggregation Devices (FADs) areas. The operation of skipjack purse seines inside of the FADs areas has positive and negative impacts. The positive impacts include improving business performance, increase catch per unit effort and fishing efficiency, and reduction fishing cost (Menard et al., 2000; Beverly et al., 2012; Dagorn et al., 2012; Davies et al., 2014; Yusfiandayani et al., 2015). In terms of negative impacts, such operation of purse seine may cause tuna fish stocks to be less healthy. Besides, it may also mislead tunas to make an inappropriate habitat selection, the dominant small size tunas in the catch, recruitment overfishing occurrence, changes in school movement pattern, catches of juvenile tunas (Hallier & Gaertner, 2008; Morgan, 2011; Wang et al., 2012; Leroy et al., 2013; Susaniati, 2014; Scot & Lopez, 2014; Hare et al., 2015; Wilantara, 2016; Talakana et al., 2017; Murua et al., 2017). The negative impact on the environment such as disturbing delicate ecosystems, increases the amount of by-catch and discard catch (Amande et al., 2010; Beverly et al., 2012; Dagorn et al., 2013; Davies et al., 2014; Scott & Lopez, 2014; Murua et al., 2017).

Based on the description above, the question arises whether the operation of purse seines in the area of FADs in the waters of the Gulf of Bone, Makassar Strait, and the Flores Sea can increase productivity or catch per unit of effort, can lead to the capture of small size skipjack tuna and increase the number of by-catch.

This study aimed to compare the size structure of skipjack tuna, productivity, and by-catch of purse seines operated inside and outside of the FADs areas in the waters of Bone Bay, Makassar Strait and the Flores Sea. The results of the study are useful as baseline information in managing the skipjack fisheries in WPP RI 713 waters, and Indonesian waters specifically related to the use of the FADs in the skipjack purse seine fisheries.

MATERIALS AND METHODS

Time and Place

The study was conducted for one year, from January to December 2018 in the WPP RI 713 which included the waters of the Gulf of Bone, the Makassar Strait and the Flores Sea, South Sulawesi, Indonesia. The area of the research is presented in Figure 1.

Material and Equipment

The materials and equipment used in this study were skipjack, small purse seiners, traditional FADs (“*rumpon*”), digital camera, measuring board, digital weight, computer, and software.

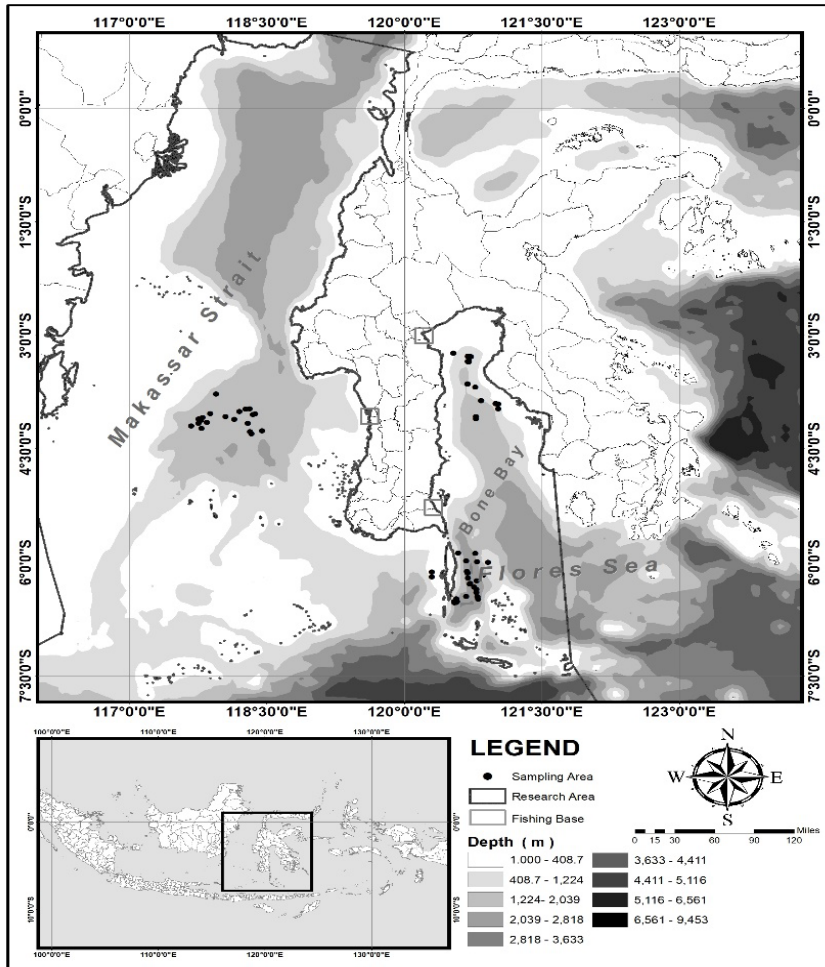


Figure 1. Study area (Bone Bay, Makassar Strait and Flores Sea waters)

Data Collection

Fish Length Data. Fish length data (FL, cm) were collected on fishing vessels and fish landing places two to three times per month in each study area using a stratified random method. In this study, skipjack length data were obtained from purse seines inside and the outside of the FADs areas of 3852 and 5554 specimens respectively in Bone Bay waters, 3362 and 3098 specimens respectively in Makassar Strait waters, and 4670 and 4469 specimens respectively in the Flores Sea waters.

Production and Number Trip Data. Annual production and the number of trips (one day trip) data were obtained from the daily logbooks of 10 skipjack fishing business owners in each study area.

Main Catch and By-catch Weight Data. The main catch and by-catch weight data were obtained through direct observation of 30 trips each for 10 units, both of purse seines inside and outside of the FADs areas in each study area. The weight of skipjacks tuna (main catch) and the by-catch were obtained by weighing directly on the sample ships. The kinds of the by-catch were known through identification at the genus and/or species level whenever possible.

Data Analysis

To achieve the research objectives, several methods of data analysis were used as follows:

Catch Size Structure. To know the smallest size, the largest, and the dominant size of skipjack caught in the purse seines inside and outside of the FADs areas, a mapping between the length frequency (%) and the length of the middle class was carried out and displayed in the form of histograms. The mean length value and standard deviation (Sparre et al., 1989) was calculated using the following Equation 1a and 1b:

$$\bar{x} = \frac{1}{n} \sum_{j=1}^m F(j) \bar{L}(j) \quad (1a)$$

$$s^2 = \frac{1}{n} \sum_{j=1}^m F(j) (\bar{L}(j) - \bar{x})^2 \quad (1b)$$

Where $\bar{L}(j)$ = midpoint class, $F(j)$ = frequency, \bar{x} = mean length, s^2 = variance
 $s = \sqrt{s^2}$

In order to know the difference in the size of skipjack fish caught inside and outside the FAD areas, the Median Test (Mangkuatmodjo, 2004) was used in the following Equation 2:

$$T = \frac{(A/n) - (B/n)}{\sqrt{\hat{p}(1 - \hat{p})[(1/n_1) + (1/n_2)]}} \quad (2)$$

Where A = number of samples that higher than median, B = number of samples that lower than median, n_1 = number of samples one, n_2 = number of samples two

$$n = n_1 + n_2 \text{ and } \check{p} = (A + B)/N$$

Productivity. The productivity of purse seines inside and outside of the FADs areas was calculated using the following Equation 3 (Mallawa et al., 2017):

$$CPUE = \frac{C}{n} \quad (3)$$

Where, CPUE = Catch per Unit Effort or productivity, C = Amounts of catch per per unit per year, n = Number of the trip of fishing unit per year

By-catch. The by catch was analyzed based on the appearance of fish which were classified as by-catch or not target species in both technologies. The percentage of by-catch (Mallawa et al., 2014) was calculated by the Equation 4 as follows:

$$B_c = \left[\frac{FN}{FT+FN} \right] \times 100\% \quad (4)$$

Where B_c = By-catch (%), FN = weight of non-target fish, FT = weight of target fish.

Then Mann Whitney Test was carried out to determine the difference in the productivity and by-catch of purse seines inside and outside of the FAD areas. The Mann Whitney test formula (Mangkuatmodjo, 2004) is as in Equation 5:

$$T = S - \frac{n(n + 1)}{2} \quad (5)$$

Where S = Number of ranks from population 1, n = total population sample 1 or sample 2.

RESULTS AND DISCUSSION

Fish Size Structure

The bar graph of middle class length provides an overview of the size of the smallest skipjack, the largest fish, the dominant fish in the catches of purse seine inside and outside of the FADs areas in the waters of Bone Bay, Makassar Strait and Flores Sea as shown in Figure 2, 3 and 4, and Table 1.

Based on Figures 2, 3 and 4 and Table 1, it can explain three things. First, skipjack caught by purse seines outside of the FADs areas had a wider size distribution than skipjack caught purse seines inside of the FADs areas, second, the skipjacks which was found in the catch of purse seines outside of the FADs areas had a relatively larger size compared to

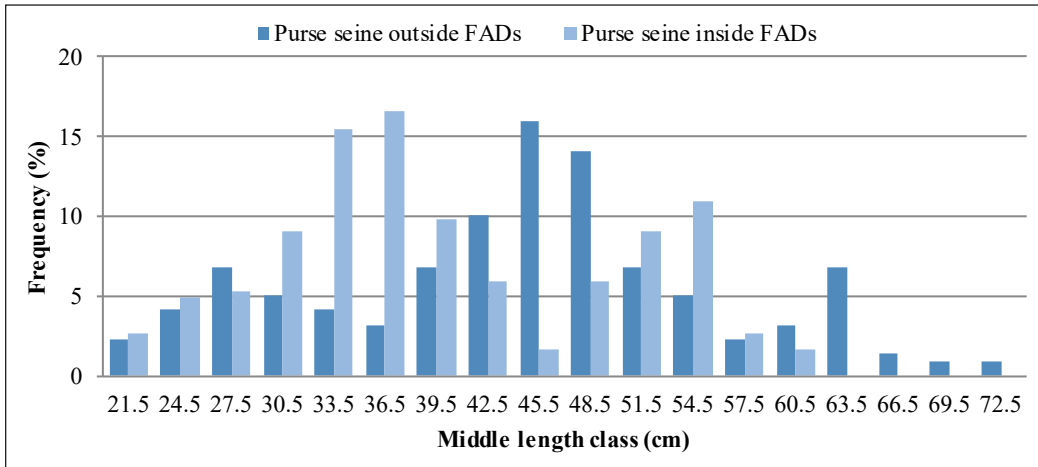


Figure 2. Size structures of skipjack captured by purse seines inside and outside of the FADs areas in Bone Bay waters

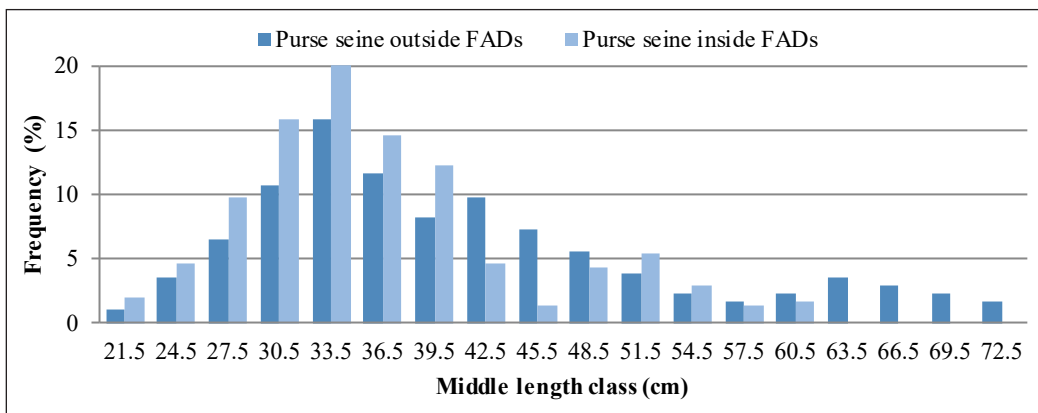


Figure 3. Size structures of skipjack captured by purse seines inside and outside of the FADs areas in Makassar Strait waters

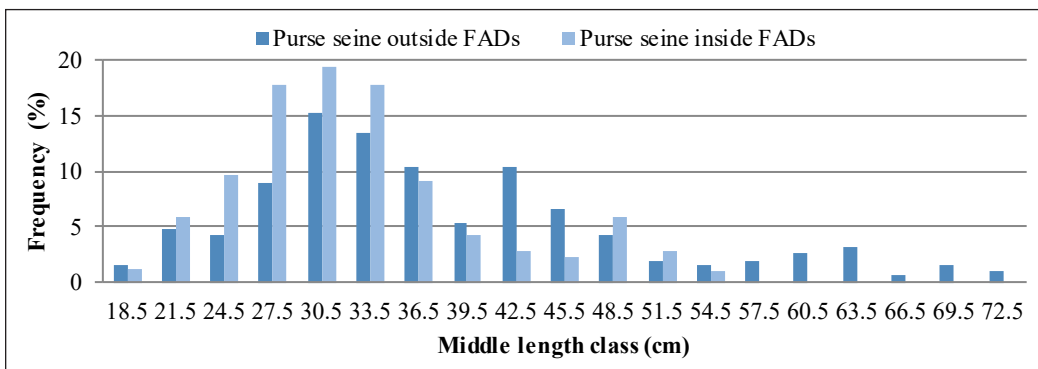


Figure 4. Size structures of skipjack captured by purse seine inside and outside of the FADs areas in Flores Sea waters

Table 1

Size structure of skipjack caught purse seines inside and outside of the FADs areas in Bone Bay, Makassar Strait and the Flores Sea waters

Fishing Areas	Purse Seine Inside FADs areas			Purse seine outside FADs areas		
	Length Range (cm)	Dominant Length (cm)	Average Length (cm)	Length Range (cm)	Dominant Length (cm)	Average Length (cm)
Bone Bay	20.75-60.65	30.50-39.50	40.39±10.07	28.50-73.15	39.50-51.50	44.64±11.60
Makassar Strait	20.10-61.50	27.50-39.50	37.46±8.53	20.50-73.50	30.50-42.50	45.86±12.78
Flores Sea	18.10-55.90	24.50-36.50	32.74±7.83	17.90-72.90	24.50-39.50	38.33±11.90

those caught in purse seines inside of the FADs areas, third the average length of skipjack caught by purse seines outside of the FADs areas was greater than that caught in purse seines inside of FADs area.

The results of statistical tests using the Median Test can be explained that there are differences significantly in the size distribution of the skipjacks captured by purse seines inside and the outside of the FADs areas in Bone Bay waters (T count 29.37 > $z \pm 1.96$, $\alpha = 0.05$) and in the Makassar Strait waters (T count 13.20 > $z \pm 1.96$, $\alpha = 0.05$) and in the Flores Sea waters (T count 16.29 > $z \pm 1.96$, $\alpha = 0.05$). The difference in the size structure of skipjack caught by purse seines inside and outside of the FADs areas is thought to be caused by, firstly, small-sized skipjack feel comfortable in floating objects in the sea. The other possibility was skipjack migrated onshore and offshore depending on size or known as size-dependent migration where small fish tended to be in shallow waters and large fish tended to be in deep waters. The case in the study area shows that the purse seine outside of the FADs areas was operated in deeper waters whereas purse seine inside of the FADs areas was operated in shallow waters where FADs are located. In the WPP RI 713, the FADs were generally installed in shallow waters, depths ranging from 70 to 200 meters and few installed in deep waters (Mallawa et al., 2017). The wider size distributions and relatively larger sizes of skipjack tuna caught outside the FADs areas than inside the FADs areas have also been previously reported by other studies, namely in the Makassar Strait waters (Wilantara, 2016), in the Flores Sea waters (Susaniati, 2014), and in the Bone Bay waters (Alamsjah et al., 2014; Mallawa, 2016). This is also supported by what was stated by Leroy et al. (2013) that the FADs had been shown to influence the behavior and movement pattern of the three species of tuna such as skipjack (*Katsuwonus pelamis*), yellowfin (*Thunnus albacores*) and bigeye (*T. obesus*) with juveniles of each species occupying shallower habitat when associated with FADs. Furthermore, that the aggregation of tunas around drifting objects increases their vulnerability to purse seine gear, particularly for juvenile and small size classes. Koya et al. (2012) described that the different size range of skipjack in catch might be due to the change in the distribution

pattern of fishes in a different area, the fishing gear or fishing technology employed and another environment parameter. Others study results also showed differences in the size structure and the average length of skipjack caught by purse seines inside and outside of the FAD areas is presented in Table 2.

Table 2

Size structure of skipjack captured by purse seines inside and the outside of FADs areas in several fishing areas in the world

Fishing Area	Purse Seine Inside FAD area		Purse Seine Outside FAD area		References
	Length Range (cm, FL)	Average Length (cm, FL)	Length Range (cm, FL)	Average Length (cm, FL)	
Moro Gulf	19.0-52.0	25.0	14.0-66.0	25.0	Barbaran (2006)
Flores Sea	13.0-63.0	26.3±4.9	18.0-73.0	52.4±8.8	Susaniati (2014)
Makassar Strait	16.0-26.0	19.6 ±2.43	34.0-49.0	42.7±3.11	Wilantara (2016)
Indian Ocean	26.6-62.0	40.0±5.0	nd	Nd	Nurdin and Panjaitan (2017)
Western & Central Pacific Ocean	26.4-73.3	43.37±7.59	33.1-74.8	51.09±6.87	Wang et al. (2012)
Pacific Ocean	nd	49.6	nd	54.6	Hare et al. (2015)
Western & Central Pacific Ocean	26.4-73.3	37.0±7.59	33.1-74.0	51.09±6.87	Leroy et al. (2013)

nd = data not available

Purse Seine Productivity

Productivity or Catch Per Unit Effort (CPUE) of purse seines inside and the outside of FADs areas were analyzed using annual production or annual yield and annual efforts or number of trip per year data from the records of ship owners of each study areas as presented in Tables 3, 4 and 5.

Test results using the Mann-Whitney method showed that the productivity of purse seines inside and the outsides of FADs areas in Bone Bay waters was significantly different ($T \text{ count } 79 > W_{1-\alpha} 77, \alpha = 0.05$), as well as in the Makassar Strait waters ($T \text{ count } 78 > W_{1-\alpha} 77, \alpha = 0.05$) and in the Flores Sea waters ($T \text{ count } 88 > W_{1-\alpha} 77, \alpha = 0.05$). Apart from that, it can also be explained that the productivity of purse seines inside and outside of the FADs areas varied within the same location and among different locations. The high productivity of purse seines inside FADs areas in this study might be due to, the first, the availability of fish in FADs at any time, second, the greater number of FADs installed had resulted in a reduction in the number of fish school outside the FADs areas or free-swimming fish school, third, differences in environmental parameters as a result of differences in the depth of the fishing area. The high productivity of purse seines inside FADs areas waters also reported

by others study. Olii and Iwan (2018) reported that the productivity of the skipjack purse seines associated FADs in Tomini Bay waters in 2011-2015 ranged from 1.5 to 9.83 tons per trip and an average of 3.694 tons per trip. In Sulawesi Sea, the productivity of purse seines inside FADs areas ranged from 0.967 to 5.761 tons per trip with an average value

Table 3
The yield, effort and productivity (CPUE) of purse seiners inside and outside of the FADs areas in the Bone Bay waters

Boat sample	Purse seine inside FAD			Purse seine outside FAD		
	Yield (ton/year)	Effort (trip/year)	CPUE (ton/trip)	Yield (ton/year)	Effort (trip/year)	CPUE (ton/trip)
I	252.16	128	1.97	148.50	110	1.35
II	243.75	125	1.95	102.00	120	0.85
III	192.00	128	1.50	186.50	115	1.01
IV	181.25	125	1.45	187.50	123	1.52
V	192.50	125	1.54	220.50	110	2.01
VI	239.36	128	1.87	133.65	110	1.21
VII	318.72	128	2.49	155.00	115	1.35
VIII	210.50	128	1.64	201.50	115	1.75
IX	198.50	124	1.60	110.00	110	1.00
X	208.75	125	1.67	115.50	110	1.05
Average	223.75	126.4	1.77	156.07	156.07	1.12
SD	±41.23	±1,71	±0,31	±41.38	±4.71	±0.37

Table 4
The yield, effort and productivity (CPUE) of purse seiners inside and outside of the FAD in the Makassar Strait waters

Fishing Boat Sample	Purse seine inside FAD			Purse seine outside FAD		
	Yield (ton/year)	Effort (trip/year)	CPUE (ton/trip)	Yield (ton/year)	Effort (trip/year)	CPUE (ton/trip)
I	212.40	120	1.77	148.50	110	1.35
II	218.75	125	1.75	102.00	120	0.85
III	194.56	128	1.52	196.15	115	1.71
IV	195.00	125	1.56	195.60	113	1.73
V	188.16	128	1.47	144.50	120	1.21
VI	248.75	125	1.99	110.75	115	0.96
VII	199.08	126	1.58	115.65	110	1.05
VIII	192.78	126	1.53	193.55	110	1.76
IX	194.40	120	1.62	119.75	115	1.04
X	209.92	128	1.64	138.50	115	1.18
Average	205.38	125.10	1.64	146.50	114.30	1.28
SD	±18.17	±1.71	±0.16	±36.65	±3.71	±0.34

Table 5
The yield, effort and productivity (CPUE) of purse seiners inside and outside of the FADs areas in the Flores Sea waters

Fishing Boat Sample	Purse seine inside FAD			Purse seine outside FAD		
	Yield (ton/year)	Effort (trip/year)	CPUE (ton/trip)	Yield (ton/year)	Effort (trip/year)	CPUE (ton/trip)
I	177.50	125	1.42	138.50	110	1.26
II	248.75	125	1.99	112.00	120	0.93
III	192.00	128	1.50	126.15	115	1.10
IV	161.25	125	1.29	168.50	123	1.11
V	169.20	120	1.41	171.50	115	1.37
VI	218.75	125	1.75	126.75	115	1.10
VII	186.00	128	1.45	118.50	118	1.00
VIII	188.50	128	1.47	134.50	118	1.14
IX	219.60	120	1.83	133.50	115	1.16
X	192.00	128	1.50	201.50	115	1.03
Average	195.36	125.20	1.56	143.14	116.4	1.23
SD	±26.47	±3.08	±0.22	±28.24	±3.53	±0.25

of 2.925 tons per trip (Prasetyo et al., 2018). The productivity of purse seines inside FADs areas that landed their catch at the Fishery Port of Lampulo Beach, Banda Aceh, Sumatra Island ranged from 0.405 to 2,368 tons per trip (Affan, 2015). Scott and Lopez (2014) described that across the oceans, floating object purse seine fishing was about 50% more productive (in ton per set) than free-school fishing for tropical tunas in combination and about twice as effective for skipjack.

Factors that cause higher productivity of purse seines operating inside than outside of the FADs areas are explained by several previous studies. Cabral et al. (2014) explained that in using FADs enhanced catch per boat when total fishing pressure was low but could exacerbate fishery collapse when the fishing effort was high. In Indian Ocean, the productivity of purse seines inside of the FADs areas was higher than that of purse seines outside of the FAD areas where this phenomenon was caused by a decrease in skipjack free-swimming school as a result of an increase in the number of FADs installed in the waters (Fonteneau et al., 2015). The decrease in the number of catches per unit effort in purse seines outside FADs areas in the Eastern Atlantic Sea and Western Indian Ocean due to the increasing number of FADs installed in the area (Fonteneau, 2015). In the Bone Bay waters, the productivity of purse seines inside FADs areas could be different due to differences in the depth of location of the FADs where the fishermen who carried out fishing in deeper waters FADs provided higher yields compared to shallow water FADs (Nurwahidin et al., 2016).

Types and Percentage of By-Catch

The results of this study show that, firstly, the kinds of by-catch in purse seines operated inside FADs areas included sharks, dolphins, turtles, ray, and kinds of small-sized fish such as anchovy (*Stelophorus* spp), sardine (*Sardinella* spp), Indian mackerel (*Rastrelliger* sp), juvenile of yellowfin tuna (*Thunnus labacares*), and frigate tuna (*Thunnus alexis*) while in purse seines operated the outside of FADs areas included dolphins, sharks and kinds of small pelagic fishes. Secondly, both in purse seines inside and outside of the FADs areas, the by-catch was dominated by small pelagic fish, which ranged from 58.4 to 75.03% of total by-catch in purse seines inside FADs areas and 59.7 to 73.22% in purse seines outside FADs areas. The third, the percentage of mammals, turtles, stingrays and sharks in the purse seines inside FADs areas were higher compared to the purse seines outside the FADs areas, this is due to the large number of small pelagic fish in the FADs as food of these organisms (Figure 5), and forth, in plain view, the percentage of by-catch on the purse seines inside the FADs areas was higher than the purse seines outside the FADs areas (Table 6).

The types of by-catch of the present study were found to be not difference with other studies. Hartaty et al. (2012) reported that purse seines operated in the FADs areas, besides catching skipjack tuna as the main catch also caught juvenile both of yellowfin tuna and bigeye tuna, and the other fishes. Romanov (2008) reported that the types of by-catch from purse seine associated FAD in North Equatorial Area of the western Indian Ocean consists of tuna by-catch which included juvenile bigeye tuna (*Thunnus obesus*), albacore (*Thunnus alalunga*), frigate tuna (*Auxis thazard*) and bullet tuna (*Auxis rohei*), and non-tuna by-catch

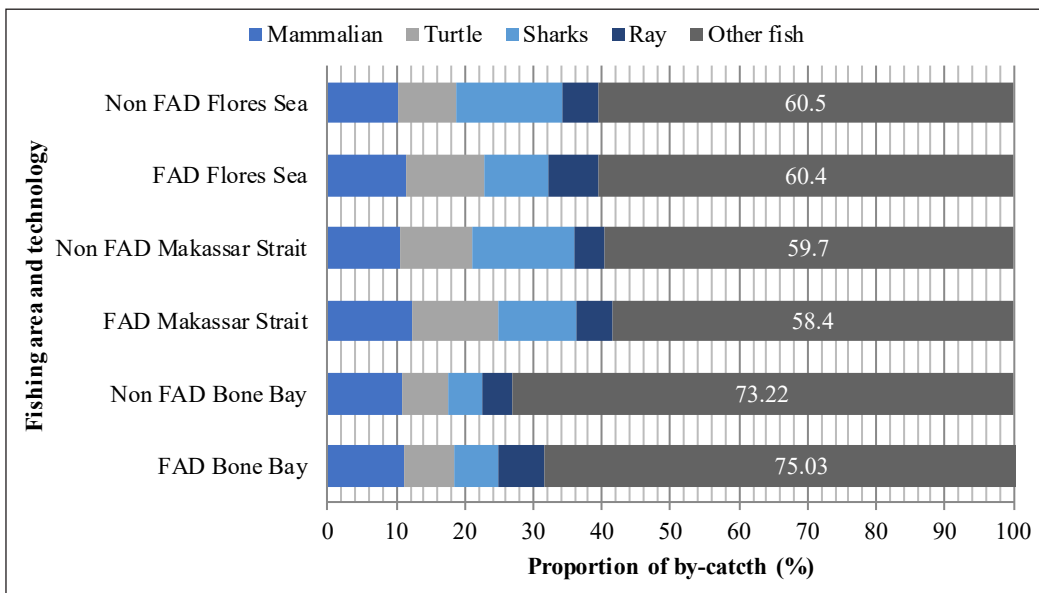


Figure 5. By-catch of purse seines inside and outside of the FADs areas in Bone Bay, Makassar Strait and the Flores Sea waters

including sharks (*Carcharhinus* spp and *Sphyrna* spp), rays (*Dasyatis* spp and *Mobula* spp), marlin (*Makaira* spp), sword fish (*Xiphias gladius*), sea turtles (Cheloniidae) and others. For purse seiners, by-catch species are usually divided in to six categories such as tunas other than target species, miscellaneous bony fishes, billfishes, sharks, rays and sea turtles (Dagorn et al., 2013). The major species associated to FADs are skipjack, young bigeye tuna, young yellowfin tuna, bullet tuna, wahoo (*Acanthocybium solandri*), dolphin fish or mahi-mahi (*Coryphaena hippurus*), sharks, billfishes, some small pelagic fishes, and carangids (Fonteneau et al., 2015). In Atlantic Ocean waters, the by-catch of skipjack tuna purse seines consists of marine mammals, sea turtles, coastal sharks, pelagic sharks, skates and rays, *Scombridae* and billfish, and other teleosts as by-products (Gaertner et al., 2015). Indian Ocean Tuna Commission (2018) reported that purse seines operated inside FADs areas besides catching kinds of tuna also sea mammalian, turtles and sharks. The by-catch on purse seine could include several species of sharks, rays, marine mammals, marine turtles and bony fishes but can differ according to the fishing areas (Garcia & Herera, 2018). The by-catch of purse seines inside FADs areas in the eastern tropical Atlantic waters consisted of discarding tunas such as frigates and little tuna and other fish dominated by wahoo, billfish, triggerfish, sharks and dolphin fish (Menard et al., 2000). In West Central Pacific Ocean, by-catch in FAD-associated consists of small tuna (98%), sharks (0.20%), billfish (0.06%), tuna-like (0.13%), other fish (1.13%) while in FAD-unassociated consists of small tuna fish (99.86%), sharks (0.05%), tuna-like (0.03%) and other fish (0.08%) (Morgan, 2011). Murua et al. (2017) explained that the tropical purse seines that operated in the FADs areas caused an increase in the number of sharks caught.

Table 6

By-catch (%) of purse seiners inside and the outside of FADs areas in the waters of Bone Bay, Makassar Strait and the Flores Sea

Fishing Boat Samples	Bone Bay		Makassar Strait		Flores Sea	
	Inside FAD	Outside FAD	Inside FAD	Outside FAD	Inside FAD	Outside FAD
I	6.50	3.54	7.50	2.50	6.50	4.75
II	4.54	5.88	5.55	5.55	4.85	1.50
III	5.58	1.59	5.50	1.50	6.10	3.50
IV	5.52	6.28	5.50	1.50	4.56	5.65
V	5.73	2.65	4.50	5.20	4.45	1.35
VI	5.49	1.00	5.30	6.95	4.50	1.60
VII	5.94	1.01	6.50	1.25	4.15	5.56
VIII	4.98	5.40	7.50	0.89	6.95	1.10
IX	5.46	5.50	7.85	4.11	5.65	0.50
X	6.76	1.36	5.54	6.15	4.45	4.75
Average	4.59	3.42	5.68	3.56	4.52	3.03
SD	±1.41	±2.17	±1.27	±2.29	±1.05	±2.02

Based on Table 6, the by-catch of purse seine operated inside FADs areas are higher than purse seines operated outside of the FADs areas. The test results using the Mann-Whitney method show that the by-catch of purse seines inside and the outsides of FADs areas in Bone Bay waters was significantly different (T count $79 > W_{1-\alpha} 77$, $\alpha = 0.05$), as well as in the Makassar Strait waters (T count $81 > W_{1-\alpha} 77$, $\alpha = 0.05$) and in the Flores Sea waters (T count $77.5 > W_{1-\alpha} 77$, $\alpha = 0.05$).

The high percentage of by-catch in purse seines operated inside FADs areas in this study is due to firstly, the large number of marine organisms associated with FADs, and secondly, because many prey fish, especially small pelagic fish can stimulate predatory organisms such as sharks, dolphins, sea turtles to find food in FADs. The high percentage of by-catch in purse seine operating in the FAD area has also been reported by several previous studies. The by-catch of purse seine associated FADs school in the western Indian ocean was $9.68 \pm 4.8\%$ consisting of by-catch tuna of $5.07 \pm 4.38\%$ and by-catch non tunas of $4.61 \pm 2.18\%$ (Romanov, 2008). Dagorn et al. (2012) described that fishing on free swimming schools was comparatively more selective, with by-catch 2.8 – 6.7 times lower than set on floating objects. Furthermore, Dagorn et al. (2013) explained that the ratio of by-catch purse seines inside and outside of the FADs areas varied according to the waters, namely in the western Pacific Ocean 1.7% and 0.3%, in the eastern Pacific Ocean 2.4% and 0.8%, in the Indian Ocean 3.6% and 0.8%, in the Atlantic Ocean 8.9% and 2.8%. Hall and Roman (2013) reported that in skipjack tuna purse seine fisheries in the Eastern Pacific Ocean the percentage of by-catch of floating object sets (11.7%) was higher than in free school sets (3.8%) and dolphin sets (3.9%). The by-catch value of purse seine inside FADs in eastern tropical Pacific was 9.9% of total catch (Menard et al., 2000). The by-catch of tuna purse seines inside and outside of the FADs areas in the Atlantic Ocean was 15.03% and 2.84% respectively (Amande et al., 2010). Bourjea et al. (2014) based on observations from 2003 to 2011 explained that in the Atlantic Ocean as many as 415 sea turtles was a purse seine by-catch, 201 turtles (48.4%) caught on DFAD and 214 turtles (51.6%) on free swimming school, on the contrary in the Indian Ocean as many as 182 turtles as by-catch, 148 turtles (81.3%) were caught in the DFAD and 34 turtles (18.7%) in the free swimming school. Escalle et al. (2016) described that the reduction in the number of FAD used could reduce the number of small tunas in purse seine catches in the Indian Ocean and Atlantic Ocean waters and could reduce the number of by-catches of purse seines in the Indian Ocean waters.

CONCLUSION

Based on the results of the study, it can be concluded that the length distribution of skipjack caught by purse seine outside of the FADs areas was wider than those caught inside FADs, and the average length of skipjack caught outside of the FADs was greater than those caught

inside FADs. The operation of purse seine in FADs areas has a positive impact through increasing fishing gear productivity but has a negative impact such as an increase in the number of by-catches and protected marine organisms.

ACKNOWLEDGEMENT

I would like to thank the skipjack purse seine fishermen in three research locations for their assistance and cooperation so that this research can be done well. I also thank the local Fisheries Service for the facilities provided during the research. The same thing I addressed to the Head of the Faculty of Marine Sciences and Fishery, Hasanuddin University for the support given.

REFERENCES

- Affan, J. M. (2015). The compositions of the catches of purse seine in 2005 - 2011 at the Lampulo Fisheries Port (PPP), Banda Aceh City. *Research Science*, 1 (1), 1-4.
- Alamsjah, R., Musbir, & Amir, F. (2014). Size structure and feasible length for catch of skipjack (*Katsuwonus pelamis*) in bone bay waters. *Journal of Science and Technology*, 14(1), 95-100.
- Amande, M. J., Ariz, J., Chassot, E., Moline, A. D., Gaertner, D., Murua, H., ... & Chavance, P. (2010). By-catch of the European purse seine tuna fishery in the Atlantic Ocean for the 2003 – 2007 period. *Aquatic Living Resources*, 23, 353-362.
- Barbaran, R. P. (2006). *Payao fishing and impact to tuna stock: A preliminary analysis*. WCPFC-SC2-2006/FT WP-7. Retrieved January 21, 2019, from <http://cor.ac.uk/download/pdf/24068128.pdf>
- Beverly, S., Griffiths, D., & Lee, R. (2012). *Anchored fish aggregating devices for artisanal fisheries in South and Southeast Asia: benefit and risk*. Bangkok, Thailand: RAP Publication.
- Bourjea, J., Clermont, S., Delgado, A., Murua, H., Ruiz, J., Ciccione, S., & Pierre, C. (2014). Marine turtle interaction with purse seine fishery in the Atlantic and Indian Ocean: Lesson for management. *Biological Conservation*, 178, 74-87.
- Cabral, R. B., Alino, P. M., & Kim, M. T. (2014). Modeling the impacts of fish aggregation devices (FADs) and fish enhancing devices (FEDs), and their implications for managing small scale fishery. *ICES Journal of Marine Sciences*, 71, 1750-1759.
- Dagorn, L., Filmatier, J. D., Forget, F., Amande, M. J., Hall, M. A., Williams, P., & Bez, N. (2012). Targeting big schools can reduce ecosystem impact of fishery. *Canadian Journal of Fisheries and Aquatic Sciences*, 69(9), 1463-1467.
- Dagorn, L., Holland, K. N., Restrepo, P., & Moreno, G. (2013). Is it good or bad to fish with FADs? What is the real impact of the use of drifting FADs on pelagic marine ecosystems? *Fish and Fisheries*, 14, 391-415.
- Davies, T., Mees, C., & Muller-Gulland, E. J. (2014). The past, present and future use of drifting fish aggregation devices (FADs) in the Indian Ocean. *Marine Policy*, 45, 163-170.

- Escalle, L., Gaertner, D., Chavance, P., Molina, A., Ariz, J., & Merigot, B. (2016). Forecasted consequences of simulated FAD moratoria in the Atlantic and Indian Oceans on catches and by-catches. *ICES Journal of Marine Sciences*, 74(3), 780-792.
- Fonteneau, A. (2015). On the recent steady decline of skipjack caught by purse seiners in free schools in the Eastern Atlantic and Western Indian Ocean. *Collection Volume Science Paper International Commission for the Conservation of Atlantic Tuna*, 71(1), 417-425.
- Fonteneau, A., Chassot, E., & Gaertner, D. (2015). Managing tropical tuna purse seines through limiting the number of fish aggregation devices in the Atlantic: food for thought. *Collection Volume Science Paper International Commission for the Conservation of Atlantic Tuna*, 71(1), 460-475.
- Gaertner, D., Ariz, J., Bez, N., Clermidy, S., Moreno, G., Murua, H., & Soto, M. (2015). Catch, effort and ecosystem impact of FAD-Fishing. *Collection Volume Science Paper International Commission for the Conservation of Atlantic Tuna*, 71(1), 525-539.
- Garcia, A., & Herrera, M. (2018). *Assessing the contribution of purse seine fisheries to overall level of by-catch in the Indian Ocean*. IOTC-2108-WPDCS14-26_Rev1. Retrieved January 24, 2019, from <http://fisheryprogress.org/fip.profile/indian-ocean-tropical-tuna-purse-seine-opagac>.
- Hall, M. A., & Roman, M. (2013). *By-catch and non-tuna catch in the tropical tuna purse seine fisheries of the world* (Technical Paper no. 568). FAO Fisheries and Aquaculture. Retrieved January 21, 2019, from <https://www.fao.org/fishery>
- Hallier, J. P., & Gaertner, D. (2008). Drifting fish aggregation devices could act as an ecological trap for tropical tuna species. *Marine Ecology Progress Series*, 353, 255-264.
- Hare, S. R., Harley, S. J., & Hampton, W. J. (2015). Verifying FAD-association in purse seine catches on the basis of catch sampling. *Fisheries Research*, 172, 361-372.
- Hartaty, H., Nugroho, B., & Styadji, B. (2012). Small scale tuna purse seine based at Tamperan Beach Fisheries Port. *Marine Fisheries*, 3(2), 161-167.
- Indian Ocean Tuna Commission. (2018). *Report of the 14th Session on the IOTC Working Party on Ecosystem and By-catch*. IOTC – WPEB20- R(E), Cape Town, South Africa. Retrieved January 30, 2019, from <https://www.iotc.org/science/cp-working-party-ecosystem-and-bycatch-wpdf>
- Koya, S. K. P., Joshi, K. K., Abdussamad, E. M., Rohit, P., Sivadas, M., Kuriakose, S., ... & Sebastine, M. (2012). Fishery, biology and stock structure of skipjack tuna, *Katsuwonus pelamis* (Linnaeus, 1758) exploited from Indian waters. *Indian Journal of Fisheries*, 59(2), 39-47.
- Leroy, B., Phillips, J. S., Nicole, S., Pilling, G. M., Harley, S., Bromhead, D., ... & Hampton, J. (2013). A critique of the ecosystem impacts of drifting and anchored FADs use by purse-seine tuna fisheries in the Western and Central Pacific Ocean. *Aquatic Living Resources*, 26(1), 49-61.
- Mallawa, A. (2016). Size structure of skipjack tuna (*Katsuwonus pelamis*) captured by pole and line fishermen inside and outside of fish aggregation devices in Bone Bay waters. *International Journal of Scientific and Technology Research*, 5(9), 159-163.

- Mallawa, A., Amir, F., & Zainuddin, M. (2014). Biological performance aspect of Skipjack tuna (*Katsuwonus pelamis*) captured by purse seine in East season at Flores Sea. *Journal of Sciences and Technology of Fishery Utilization*, 1(2), 129-145.
- Mallawa, A., Amir, F., & Safruddin, (2017). *Study of Indonesian Fisheries Management Region of 713 as the area of utilization and management of skipjack tuna (Katsuwonus pelamis) fisheries sustainable: 2nd Year, Performance and level of sustainability of skipjack fishing technology*. (Unpublished Research Report). Hasanuddin University, Indonesia.
- Mangkuatmodjo, S. (2004). *Advanced statistics* (1st Ed.), Jakarta, Indonesia. PT Rika Cipta Publishing.
- Menard, F., Fonteneau, A., Gaertner, D., Nordstrom, U., Stequert, B., & Marchal, E. (2000). Exploitation of small tuna by a purse seine fishery with fish aggregation device and their feeding ecology in a eastern tropical Atlantic ecosystem. *ICES Journal of Marine Sciences*, 57, 525-530,
- Morgan, A. C. (2011). *Fish aggregation device and tuna: Impacts and management options*. Washington, USA: Ocean Science Division, Pew Environment Group.
- Murua, J., Moreno, G., Hall, M., Dagorn, L., Itano, M., & Restrepo, V. (2017). *Toward global non-entangling fish aggregation device (FAD) use in tropical tuna purse seine fisheries through participatory approach* (ISSF Technical report 2017-07). Washington, USA: International Seafood Sustainability Foundation.
- Nuridin, E., & Panjaitan, A. S. (2017). Fishing seasons and size structure of skipjack tuna (*Katsuwonus pelamis*, Linnaeus 1758) around FADs in Palabuhanratu waters. *Indonesian Journal of Fishery Research*, 23(4), 299-307.
- Nurwahidin, Musbir, & Kurnia, M. (2016). Productivity analysis of purse seines using FADs Bone Bay waters. *Journal of Science and Technology for Fisheries Resource Utilization*, 3(6), 318-327.
- Olii, M. Y. U. P., & Iwan, (2018). Productivity of skipjack (*Katsuwonus pelamis*) purse seine in the Boalemo Regency waters, Gorontalo Province. *Gorontalo Fisheries Journal*, 1(1), 33-42.
- Prasetyo, F. B., Manu, L., & Pamikiran, R. D. C. H. (2018). Productivity study of tuna, skipjack, and frigate tuna caught by 20-30 GT purse seine at the Bitung Ocean Fishery Port. *Journal of Science and Capture Fisheries Technology*, 3(1), 16-24.
- Romanov, E. V. (2008). By-catch and discard catch in the Soviet purse seine tuna fisheries on FAD-associated school in the north equatorial area on the Western Indian Ocean. *Western Indian Ocean Journal of Marine Science*, 7(2), 163-174.
- Scott, P. G., & Lopez, J. (2014). *The use of FADs in tuna fisheries*. Directorate General for Internal Policies, European Parliament, Committee in Fisheries. Retrieved January 18, 2017, from <http://www.europarl.europa.eu/studies>.
- Sparre, P., Ursin, E., & Venema, S. C. (1989). *Introduction to tropical fish stock assessment, Part 1, Manual* (FAO Fisheries Technical Paper, No.306.1). Rome, Italy: Food and Agriculture Organization.
- Susaniati, W. (2014). *Research on biological population of skipjack (Katsuwonus pelamis) in Flores Sea waters, South Sulawesi* (Unpublished Magister Thesis). Hasanuddin University, Indonesia.

- Talakana, S., Manoppo, L., & Manu, L. (2017). Komposisi dan distribusi hasil tangkapan kapal pukat cincin KM Grasia 04 di perairan Laut Maluku [Composition and distribution catch of Gracia 04 purse seiner in Molucca Sea waters]. *Jurnal Ilmu dan Teknologi Perikanan Tangkap*, 2(5), 181-186.
- Wang, X., Xu, L., Chen, Y., Zhu, G., Tian, S., & Zhu, J. (2012). Impacts of fish aggregation devices on size structure of skipjack tuna, *Katsuwonus pelamis*. *Aquatic Ecology*, 46(6), 343-352.
- Wilantara, W. (2016). *Comparison of catches of skipjack (Katsuwonus pelamis) with purse seines-FAD and non FAD-purse seines in the Makassar Strait waters* (Unpublished Research Report). Hasanuddin University, Indonesia.
- Yusfiandayani, R., Baskoro, M. S., & Monintja, D. (2015). Impact of the fish aggregation device on sustainable capture fisheries. *Life Sciences*, 1, 224-237.



Comparison of Leaf Area Index from Four Plant Species on Vertical Greenery System in Pasir Gudang, Malaysia

Azmiah Abd Ghafar^{1,2*}, Ismail Said¹, Amalina Mohd Fauzi¹, Mohd Shariman Shai-in³ and Badrulzaman Jaafar⁴

¹Department of Landscape Architecture, Faculty of Built Environment and Surveying, Universiti Teknologi Malaysia, 81310 Skudai, Johor, Malaysia

²Department of Landscape Architecture, Faculty of Design and Architecture, Universiti Putra Malaysia, 43400 Serdang, Selangor, Malaysia

³Property Management Division, Property Management and Assessment Department, Majlis Perbandaran Pasir Gudang, 81700 Johor, Malaysia

⁴Department of Landscape, Majlis Bandaraya Petaling Jaya, 46675 Selangor, Malaysia

ABSTRACT

Vertical greenery system (VGS) is a subset of urban green infrastructure that ameliorates thermal performance, potential energy savings, and urban heat island. Plants provide shadow effects through the absorption or filtration of the heat radiant, which respond to these issues. The frequent variable used to indicate the leaf mass of a plant is the leaf area index (LAI). There are two methods to measure LAI: direct and indirect methods. However, little attention was given to calculating the LAI using direct measurement in VGS. This study was undertaken to distinguish the LAI value from four plant species, i.e., *Philodendron burle-marxii*, *Phyllanthus cochinchinensis*, *Nephrolepis exaltata*, and *Cordyline fruticosa* 'Miniature' in the industrial city of Pasir Gudang. An image analysis tool was used to facilitate the measurement. The results showed the LAI values are highly dependent on the number of leaves. It also found plants that keep growing have the highest LAI value. Importantly, the characteristics of a plant need to be considered before planting in a shrub bed.

Keywords: Experimental study, leaf area index (LAI), plant species, vertical greenery system (VGS)

ARTICLE INFO

Article history:

Received: 04 November 2019

Accepted: 03 February 2020

Published: 15 April 2020

E-mail addresses:

azmiahabdghafar@gmail.com (Azmiah Abd Ghafar)

ismailbinsaid@gmail.com (Ismail Said)

amalinamfauzi90@gmail.com (Amalina Mohd Fauzi)

mohdshariman@mppg.gov.my (Mohd Shariman Shai-in)

badrazj@gmail.com (Badrulzaman Jaafar)

* Corresponding author

INTRODUCTION

The two major vertical greenery systems (VGS) are green façade system and living wall system (Azkorra et al., 2015; Abd-Ghafar et al., 2018; Bustami et al., 2019). These two systems have different

fundamentals and use different planting materials. Green façades are climbing plants that directly or indirectly grow on an additional structure attached to the wall, while living walls are plants that are planted in modular pots or felt-pocket systems. Notably, VGS provides benefits in thermal performance on building façades. It provides shade to reduce the temperature of the façades and cool the environment through the process of evapotranspiration (Tan et al., 2014). As the temperature of the building decreases, the energy consumption of the building also reduces.

As studied by Jaafar et al. (2013) and Safikhani and Baharvand (2017), in the tropical climate of Malaysia, the living wall system has a better thermal performance compared to the green façade system. In line with Charoenkit and Yiemwattana (2017), plant selection is influential in maximising the performance of a living wall in reducing the temperature. From another study, Pérez et al., (2017) demonstrated leaf area index (LAI) had a direct influence on foliage density, which was related to the estimated amount of thermal reduction in VGS.

In Malaysia, the study on plant species of living walls is still limited. Only a few studies explored the comparison of the LAI value of each plant species. Apart from benefitting thermal reduction, VGS also improves human health (Ghazalli et al., 2018), and enhances aesthetics for visual pleasing (Razzaghmanesh & Razzaghmanesh, 2017) to increase the property values (Timur & Karaca, 2013). Many empirical studies have shown that leaf area index has affected thermal performances (Taib et al., 2019; Charoenkit & Yiemwattana, 2016). It also has great potential for removing particulate matter pollutants from the atmosphere (Dzierżanowski et al., 2011; Song et al., 2015). Previous studies have revealed vegetation has a strong relationship between shadow effect and particulate trap with the foliage thickness. Hence, the most popular method used to characterise foliage thickness is through the measurement of LAI.

Leaf area index (LAI) was defined by Pérez et al., (2017) as the total leaf area of all leaves of a plant per unit ground surface area. However, for shrubs, LAI is divided over the planted area of the shrub bed (Tan & Sia, 2010). LAI is an important parameter in plant ecology and plant physiology because it shows how much leaves there are in one tree. In the context of this study, it shows the growth of a plant in a pot. LAI also measures the photosynthetically active area, and the area subjected to transpiration. It becomes an indicator of how much light is passing through the canopy. For example, in the case of a multi-layer canopy, the LAI of an upper layer is important to determine the light received by the lower layer.

There are two methods to measure LAI: direct and indirect methods (Jonckheere et al., 2004). The direct LAI method has been widely used for crops and adapted for vegetation in small-scale studies (Bréda, 2003; Pérez et al., 2017). This method is useful in agriculture and ecological studies by harvesting the plant (Klingberg et al., 2017) to get the leaf area.

However, recent researchers collected only ten samples of leaves instead of harvesting all leaves from potted plants. Plant Canopy Analyser LAI-2200 (LI-COR Biosciences, Lincoln, USA) is an example of indirect method of LAI. It is a practical and expensive tool. Due to that, the direct LAI method was emphasised in this study. According to Weerakkody et al. (2018), the ImageJ software measures the individual leaf area as it is a part of the variable in the LAI equation. This process is elaborated in the section “Analyse the Measurement of Leaf Area”. Image analysis is a technique used to facilitate the LAI measurement. The development of image analysis has been practiced in many research disciplines, including in Sciences of Total Environment and also Urban Forestry and Urban Greening. The National Institutes of Health has introduced ImageJ as one of the tools of scientific multidimensional images (Schneider et al., 2017). It is made accessible for public programming software, and is a free operational tool for non-commercial purposes (Drienovsky et al., 2017; Stawarczyk et al., 2015).

From the literature, LAI is an important factor in representing green features. Therefore, this study aimed to investigate the potential of selected tropical shrubs in establishing foliage density through direct LAI method on a living wall system. This is an initiative to establish fundamental information of the tropical plants used. Four plant species are included: *Philodendron burle-marxii*, *Phyllanthus cochinchinensis*, *Nephrolepis exaltata*, and *Cordyline fruticosa* ‘Miniature’.

MATERIAL AND METHODS

Pasir Gudang is an industrial city in Southern Johor, Malaysia. High temperature, high humidity, and abundance of airborne particles are among the climatic attributes of the city. A living wall system has been installed at a 10km radius within the industrial zone. It was modular typed at the outdoor building of the Urban Transformation Centre (UTC) Pasir Gudang, Johor, Malaysia. The LAI measurement was conducted for each month from January to March 2019. Pasir Gudang experiences tropical climate with two seasons, a wet season and a dry season. Pasir Gudang is further categorised as an industrial town occupied by heavy industries, such as petrochemical, transportation and logistics, shipbuilding, and oil palm storage and distribution (Iskandar Regional Development Authority, 2013). The experimentation was constructed in size of 4-meter x 1-meter. This study has adapted the experimental scale of 1m² for each plant species. The small-scale experimentation was also used by Sulaiman et al. (2018) and Charoenkit and Yiemwattana (2017) in the tropical climate of Malaysia and Thailand, and in Japan (Koyama et al., 2013). This type of modular living wall called the Advance Hook-on Green Module System, as shown in Figure 1, was suitable for low height installation. These modular living walls were hooked onto the wire-mesh base to allow for easy installation and maintenance.

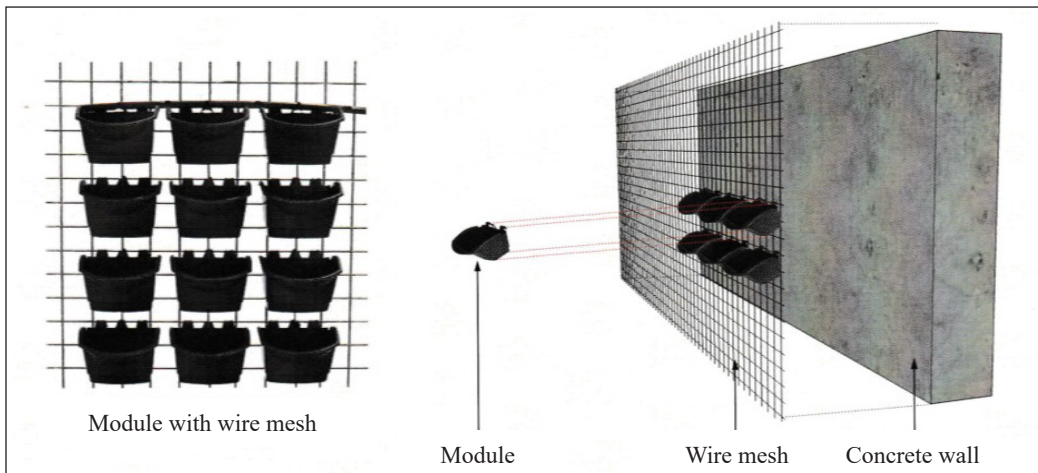


Figure 1. Construction of the modular living wall system (GWS Living Art, 2018)

Plant Selection

The plants were purchased from Chop Ching Hin Nursery, Johor Bahru, Malaysia, that pre-grows vertical plants with a minimum 85% maturity. Plant selection for this field study was made according to these three criteria: availability of plant species in local supplier's nursery, and suitability to tropical conditions (Charoenkit & Yiemwattana, 2017). These plant species were also chosen based on the common species of VGS used in Malaysia. All the species planted in the field study had a high demand from the market. *Phyllanthus cochinchinensis*, and *Cordyline fructicosa* 'Miniature' were both full sun and hardy plants. The other two, *Philodendron burle-marxii* and *Nephrolepis exaltata*, were semi-shade plants that needed more water. This study took three times of watering per day through the auto-irrigation system. This is because plants in small pots need regular watering (Bustami et al., 2019) due to the pots providing a limited area for root growth. In this case, an automatic irrigation system was installed to ensure good plant growth (Kmieć, 2015)

Direct Method of Leaf Area Index

This study carried out a repeated measurement of four plant species. These four plant species were *Philodendron burle-marxii*, *Phyllanthus cochinchinensis*, *Nephrolepis exaltata* and *Cordyline fructicosa* 'Miniature' (Figure 2). Consequently, this research explained the direct measurement thoroughly to obtain LAI, where direct measurement is the estimated measurement of leaf area from harvested leaves. This sampling method can be time-consuming; however, a variety of computerised image analysis software is available and accurate in a short time. Direct measurement and the application of ImageJ software in this study are suitable only for small plants. This study gave an example of the measurement of the *Nephrolepis exaltata* (Boston Fern). However, the results of LAI

values for all species were calculated and shown in the section “Results and Discussion”. This field study had applied the standard equation in a small structure (Blanco & Folegatti, 2003) to calculate the estimated value of LAI. Hence, Figure 3 illustrates the flowchart to measure LAI from the harvesting process until the LAI value was obtained.

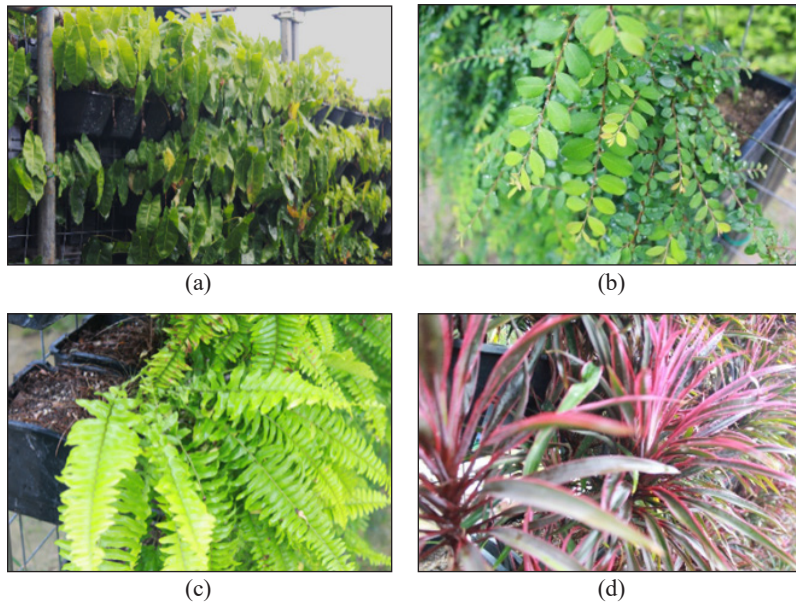


Figure 2. (a) *Philodendron burl-marxii*; (b) *Phyllanthus cochinchinensis*; (c) *Nephrolepis exaltata*; and (d) *Cordyline fruticosa* 'Miniature' were used at the field study of Pasir Gudang

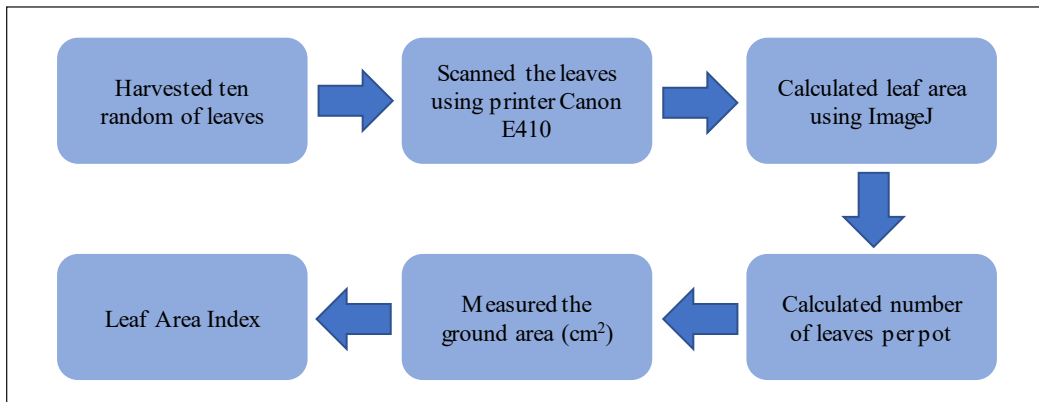


Figure 3. Flowchart of measurement of leaf area index in a modular living wall

Harvested Leaves. The leaves were collected in the early month of the monitoring study. Samples similar in height and size were randomly harvested. The sampled plants were in good condition with no wilted leaves and disease. This direct method involves physical calculation. Therefore, it is necessary for the individual leaves that were picked from a plant

to be wet and green (Ong, 2003) to get an accurate reading of leaf area (cm²). In accordance with Weerakkody et al. (2018), ten random leaves per species were used to calculate the mean leaf size. Individual leaf sizes were then measured using the ImageJ software.

Flat Image - Using Scanner. Figure 4 illustrates ten random leaf images scanned using the A4 flat scanner (Stawarczyk et al., 2015) Canon E410. These prepared samples were attached into a drawing block with double-sided adhesive tape to ensure proper images are produced. The Adobe Photoshop CS6 functioned to combine all the leaves in one file. This accommodates the user when importing the leaf file in the ImageJ software afterward. The imported file uploaded has to be in the same quality to assure all leaves are of a similar pixel. A scale ruler was placed next to the leaves during the scanning process to help draw a linear segment in the scale calibration process.



Figure 4. Ten random leaves harvested from the study site

ImageJ. The common instruments to measure leaf area are leaf area meter and Delta-T Image Analysis System (DIAS) (Pérez et al., 2017). Hence, this study analysed the leaf area using an image analyser, the ImageJ (Weerakkody et al., 2017), after the scanning procedure. Although the scanning process was not stated in detail, a flat image is required to apply the ImageJ software. Therefore, the leaves need to be scanned before being imported into the software. ImageJ is a public domain Java image processing programme inspired by NIH Image.

Scale Calibration. A reference size like a scale ruler image is necessary for the scale calibration process, to optimise the accuracy of the calibration. Then, the scale ruler image was imported beside the leaf images (Figure 2). In sum, the scale ruler image was enlarged via the magnifying glass tool to acquire the exact measurement. After that, the straight-line tool was used to draw a line between two points on the ruler image. For example, a line was drawn over a 4-cm section of the ruler, then the Analyse button was clicked and a set scale was selected. After that, the four-digit number is keyed into the Known Distance

box, the unit of measurement was changed to cm, and the Global function was selected. A standard metric measurement in ImageJ is cm, however, a user can manually change this unit of measurement. The scale must be reset each time the software reboots.

Analyse the Measurement of Leaf Area. As researchers, a variety of image analysis is used to acquire and analyse data. The image analysis is also called leaf measurement. Additionally, this study had imported ten replicates of the Boston fern in the ImageJ software to analyse the mean of leaf area. However, the area of measurement process requires an 8-bit colour or grey image to form a binary image.

As shown in Figure 5, the leaves' colour has changed from green to grayscale. This software suggested using a white background for the sampling to facilitate the leaf area calculation. The threshold process turned the dark parts into a black image, while the light parts converted into a white image, resulting in a binary image (Figure 6). This image only produced two colours, black and white, or other preferable two colours to distinguish the measurement area. The accuracy of the calculation area depended on the photograph pixels. To arrive at this stage, the wand (tracing) tool from the ImageJ software was selected, and the leaf shape is selected to produce the yellow outline around the leaf. It was automatically highlighted as demonstrated in Figure 7.

The automatic selection sometimes uncovered the entire leaf calculation. However, ImageJ provided modes to adjust the perimeter of the leaf that influenced the value of leaf area. This tool allowed the modification of the shape area through a circular brush. The circle boundary in Figure 7 (a) was the image before the adjustment was made which shows the irregularities of the yellow outlines formed. The step involved selecting the inside of the leaf image and dragging the yellow line along the border of the leaf to expand the area. Inversely, this step was repeated from the outside of the boundary to minimise the image. The differences could be seen in Figure 7 (b) that shows after the alteration process, the yellow line had formed the toothed leaf.

The results tabulated in Table 1 show the ten Boston Fern leaves (Figure 4) and the mean leaf area (cm²). This table contains only one-month measurement, calculated repeatedly for three months. The last column depicts the mean leaf area from ten leaves.

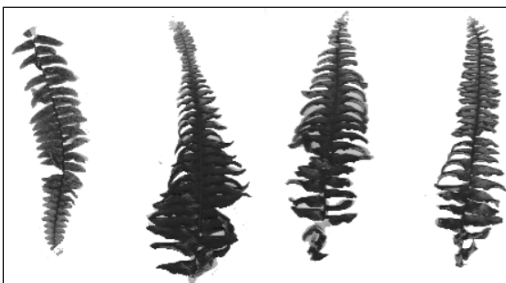


Figure 5. Grayscale image of the Boston Fern



Figure 6. Binary image of the Boston Fern

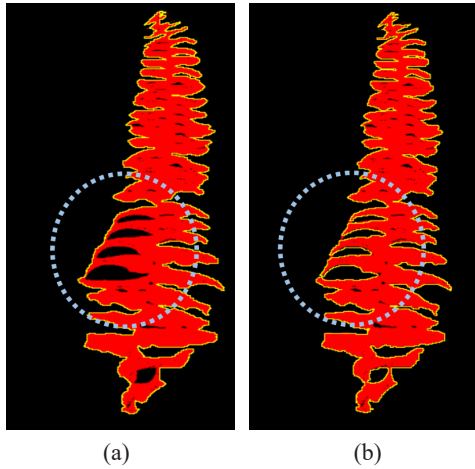


Figure 7. Adjustment of the calculation area: (a) before; and (b) after

Table 1
Results of the leaves area from ImageJ measurement

	Label	Area (cm ²)
1	Leave 1	73.78
2	Leave 2	83.40
3	Leave 3	64.19
4	Leave 4	103.09
5	Leave 5	91.07
6	Leave 6	76.12
7	Leave 7	58.76
8	Leave 8	89.25
9	Leave 9	49.32
10	Leave 10	52.94
11	Mean	74.19

Number of Leaves and Ground Area. The number of leaves (N) represents the leaves in one potted plant. This study took three potted plants to procure an average of N. In vertical planting, the concept of the ground area referred to the area according to the modular size (Charoenkit & Yiemwattana, 2017). This measurement was taken manually using a scale ruler. The concept is that light absorption is based on the density of the leaves covering the ground area where the plant grows (Burstall & Harris, 1983).

Leaf Area Index (LAI). In this study, LAI was directly evaluated from harvested leaves at the field study of Pasir Gudang. According to Sonnentag et al. (2007), this method is more accurate for short-stature ecosystems. Leaf Area Index (LAI) for shrubs is different from other plant categories in which it measures the ratio of the total leaf area to the planted area of the shrub bed (Tan & Sia, 2010). LAI is considered as the main factor in determining the shading effect of VGS due to its cooling ability in buildings and the environment, as reviewed by Charoenkit and Yiemwattana (2016). Thus, the Leaf Area Index (LAI) is measured by dividing the total leaf area of a plant pot by the plant pot area (Blanco & Folegatti, 2003). All steps were mentioned in detail in the previous section.

$$LAI = \frac{\text{Leaf area (cm}^2\text{)} \times N}{\text{Ground area (cm}^2\text{)}}$$

The equation shows the leaf area portrays the average of ten random leaf area. Afterward, it was analysed using the ImageJ software, where N represents the number of leaves per plant. The mean LAI of three measurements were extrapolated to 1m² as the LAI of each plant species (Charoenkit & Yiemwattana, 2017). Commonly the LAI value

ranges from 3.5 to 4.5 based on the generic values (Tan & Sia, 2010) for shrubs. Of late, the monthly measurement of the LAI value keeps changing due to the growth rate of each species.

RESULTS AND DISCUSSION

The LAI values of four plant species at UTC Pasir Gudang are tabulated in Table 2. *Phyllanthus cochinchinensis* recorded the highest LAI in January (LAI 5.02) followed by *Philodendron burle-marxii* (LAI 4.45), *Cordyline fructicosa* 'Miniature' (LAI 3.94), and *Nephrolepis exaltata* (LAI 3.75). A study by Tan et al. (2015) found the LAI value of a similar plant species, *Phyllanthus cochinchinensis*, measured in a horizontal, green roof medium was 2.78, making the results parallel. From the observation, this study has a smaller ground area compared to the study by Tan et al. (2015). The smaller ground area of shrub bed produces a larger LAI value. It contradicts Ong (2003), who showed *Phyllanthus cochinchinensis* had the average LAI value of up to 7. Shrubs provide higher LAI value than palm and tree species. It reveals shrubs have denser leaves due to lack of lighting that penetrates behind the shrubs. It means that different plant species have a varied cooling capacity based on the evapotranspiration of each plant. The maturity of plants was also influenced by the shading effect through the heat absorption of plants (Taib et al., 2019). Thus, the selection of plants must consider the plant character to maximise the cooling effect of VGS.

In February, the LAI value of each species increased except for *Cordyline fructicosa* 'Miniature' with the lowest LAI value of 3.58. The value decreased as much as 0.4 compared the value from January. It statistically demonstrated the mean leaf area and the number of leaves per pot have reduced. However, the the LAI value of the plant species *Nephrolepis exaltata* drastically increased (LAI 5.82). This is followed by *Philodendron burle-marxii* (LAI 5.20) and *Phyllanthus cochinchinensis* (LAI 5.04). The LAI values steadily increased in March; *Nephrolepis exaltata* (LAI 6.55), *Philodendron burle-marxi* (LAI 5.84), *Phyllanthus cochinchinensis* (LAI 5.48), and *Cordyline fructicosa* 'Miniature' (LAI 3.61).

This is due to the increase in the number of leave per pot for each species. Figure 4 illustrates the changes in LAI values according to monthly reading from January until March 2019. In a similar vein with Wong et al. (2009), the plant used in VGS was *Nephrolepis exaltata* with an LAI of 6.76. The result of the simulated study from Singapore was consistent with this study, where the Boston fern had an LAI of 6.55. It was found that *Nephrolepis exaltata* has the highest leaf area index due to the dense canopy, allowing for multiple layers of shading. Previous studies did not have the LAI for *Cordyline fructicosa* 'Miniature' and *Philodendron burle-marxii* in any of the landscape settings.

Table 2
LAI values of four plant species in Urban Transformation Centre (UTC) Pasir Gudang

Type of plants used/ Months	January			February			March		
	Mean Leaf Area (cm ²)	Number of leaves per pot	LAI	Mean Leaf Area (cm ²)	Number of leaves per pot	LAI	Mean Leaf Area (cm ²)	Number of leaves per pot	LAI
<i>Philodendron burle-marxii</i>	88.12	11	4.22	87.40	13	4.95	87.30	15	5.71
		13	4.99		14	5.33		16	6.09
		10	3.84		14	5.33		15	5.71
<i>Phyllanthus cochinchinensis</i>	1.99	31	4.61	1.97	35	4.90	1.96	38	5.31
	34.10 (stem)	35	5.20	32.13 (stem)	37	5.18	32.08 (stem)	39	5.45
		32	4.76		36	5.04		41	5.73
<i>Neprolepis exaltata</i>	65.31	13	3.69	74.19	17	5.49	75.21	20	6.55
		13	3.69		19	6.14		21	6.88
		14	3.98		18	5.82		21	6.23
<i>Cordyline frutescens</i> 'Miniature'	19.13	50	4.17	18.51	38	3.87	18.03	47	3.69
		47	3.92		41	3.31		46	3.61
		46	3.4		44	3.55		45	3.54

*Pot size 17cm x13.5cm = 229.5 cm²

The *Philodendron burle-marxii* is an epiphytic, herbaceous vine. It climbs through its roots. It also needs frequent maintenance due to its semi-shade plant type, with moderate watering needs. The mean leaf area of this plant was about 87.3-88.3 cm². The leaves often grow as they dry. Therefore, this plant is considered to have a good growth rate, as the LAI values have increased every month (Figure 8). *Cordyline fruticosa* 'Miniature' is hardy, which only preferred moderate water. The mean leaf area measured around 18.03-19.13 cm². More importantly, the LAI value decreased because the plant's leaves grew inconsistently as the plant withered to an unappealing brown. The trunk height then increased, and the plant lost its density compared to the first month of measurement.

Phyllanthus cochinchinensis is a woody shrub. It is a drought-tolerant plant that prefers dry soil conditions, and survive under full sunlight. It is able to grow up to 3 m tall (NParks, 2013b); nonetheless, it has a slow height growth. The mean leaf area measured in this study was approximately 1.96-1.99 cm². The leaves were spirally aligned on short branches, however, the multiple layers of its leaves increased and the branches were longer. Good plant growth increases the value of LAI from January to March, as shown in Table 2. The *Nephrolepis exaltata* or Boston fern is a semi-shade plant but the most tolerant to drought among the common cultivated ferns. The plant needs only moderate water but requires moist soil. The leaves have slightly toothed dagger-shaped fronds (NParks, 2013a) with a mean leaf area of about 65.3-75.2 cm².

The number of leaves in this study represents the density of leaves. On this note, the number of leaves from three species, namely *Philodendron burle-marxii*, *Phyllanthus cochinchinensis*, and *Nephrolepis exaltata* have increased. A study by Taib et al. (2019)

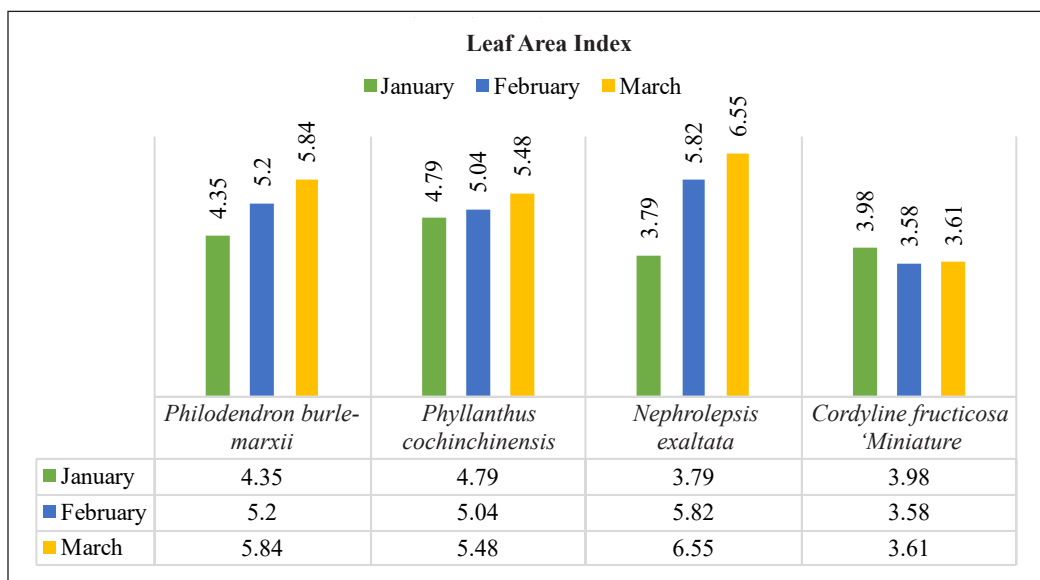


Figure 8. Specific mean LAI from January to March

proved trees that had multiple layers of leaves were more effective at absorbing solar radiation. The multiple layers of leaves of the *Cordyline fructicosa* 'Miniature' had fluctuated according to monthly measurement, thus providing a low density of leaves. Figure 8 shows the LAI values of four different plant species from January until March. It shows that multiple layers of leaves, the density of leaves, and the average leaf area contributed to a higher mean value of the leaf area index.

CONCLUSION

The significance of this study demonstrates the direct measurement of LAI in VGS. Step by step measurement was successfully shown in this study. The current phenomenon is the application of the ImageJ software to help accelerate the calculation of leaf area. In summary, the field measurement in this study showed the observation of growth for each plant species. It revealed the rate of plant growth and its physical characteristics affected the calculation process of LAI. Plant growth can be represented by the increase in the number of leaves upon monthly measurement. This method can be applied for shrubs in vertical planting. Appropriate plant selection has a better tolerance of environmental issues such as thermal performance and air pollution. This due to each of plant species has different ability in producing shade and trapping particulate through VGS. Therefore, other plant species and their characteristics are also vital to be studied.

ACKNOWLEDGMENT

The authors would like to acknowledge Universiti Putra Malaysia (UPM) and the Ministry of Education for the Ph.D. scholarship award. This experimentation was supported by Majlis Perbandaran Pasir Gudang and Urban Transformation Centre (UTC) Pasir Gudang, Johor, Malaysia.

REFERENCES

- Abd-Ghafar, A., Abdulkarim, K. H., Said, I., & Jasmani, Z. (2018). Vertical greenery systems and its effect on campus: A meta-analysis. *Journal of BIMP-EAGA Regional Development*, 4(1), 42-56.
- Azkorra, Z., Pérez, G., Coma, J., Cabeza, L. F., Bures, S., Álvaro, J. E., ... & Urrestarazu, M. (2015). Evaluation of green walls as a passive acoustic insulation system for buildings. *Applied Acoustics*, 89, 46-56.
- Blanco, F. F., & Folegatti, M. V. (2003). A new method for estimating the leaf area index of cucumber and tomato plants. *Horticultura Brasileira*, 21(4), 666-669.
- Bréda, N. J. J. (2003). Ground-based measurements of leaf area index: A review of methods, instruments and current controversies. *Journal of Experimental Botany*, 54(392), 2403-2417.
- Burstall, L., & Harris, P. M. (1983). The estimation of percentage light interception from leaf area index and percentage ground cover in potatoes. *The Journal of Agricultural Science*, 100(1), 241-244.

- Bustami, R. A., Brien, C., Ward, J., Beecham, S., & Rawlings, R. (2019). A statistically rigorous approach to experimental design of vertical living walls for green buildings. *Urban Science*, 3(3), 1-15.
- Charoenkit, S., & Yiemwattana, S. (2016). Living walls and their contribution to improved thermal comfort and carbon emission reduction: A review. *Building and Environment*, 105, 82-94.
- Charoenkit, S., & Yiemwattana, S. (2017). Role of specific plant characteristics on thermal and carbon sequestration properties of living walls in tropical climate. *Building and Environment*, 115, 67-79.
- Drienovsky, R., Nicolin, A. L., Rujescu, C., & Sala, F. (2017). Scan leaf area-a software application used in the determination of the foliar surface of plants. *Research Journal of Agricultural Science*, 49(4), 215-224.
- Dzierżanowski, K., Popek, R., & Gawro, H. (2011). Deposition of particulate matter of different size fractions on leaf surfaces and in waxes of urban forest species. *International Journal of Phytoremediation*, 13(10), 1037-1046.
- Ghazalli, A. J., Brack, C., Bai, X., & Said, I. (2018). Alterations in use of space, air quality, temperature and humidity by the presence of vertical greenery system in a building corridor. *Urban Forestry and Urban Greening*, 32(April), 177-184.
- GWS Living Art. (2018). *Advance hook-on green module system* [Brochure]. Singapore: Author.
- Iskandar Regional Development Authority. (2013). *Road to Completion*. Retrieved June 17, 2019, from <https://www.irda.com.my>
- Jaafar, B., Said, I., Reba, M. N. M., & Rasidi, M. H. (2013). Impact of vertical greenery system on internal building corridors in the tropic. *Procedia - Social and Behavioral Sciences*, 105, 558-568.
- Jonckheere, I., Fleck, S., Nackaerts, K., Muys, B., Coppin, P., Weiss, M., & Baret, F. (2004). Review of methods for in situ leaf area index determination: Part I. Theories, sensors and hemispherical photography. *Agricultural and Forest Meteorology*, 121(1), 19-35.
- Klingberg, J., Konarska, J., Lindberg, F., Johansson, L., & Thorsson, S. (2017). Mapping leaf area of urban greenery using aerial LiDAR and ground-based measurements in Gothenburg, Sweden. *Urban Forestry and Urban Greening*, 26, 31-40.
- Kmieć, M. (2015). Green wall technology. *Czasopismo Techniczne*, 10A(23), 47-60.
- Koyama, T., Yoshinaga, M., Hayashi, H., Maeda, K., & Yamauchi, A. (2013). Identification of key plant traits contributing to the cooling effects of green façades using freestanding walls. *Building and Environment*, 66, 96-103.
- NParks. (2013a). *Nephrolepis exaltata*. Retrieved July 17, 2019, from <https://florafaunaweb.nparks.gov.sg>
- NParks. (2013b). *Phyllanthus cochinchinensis*. Retrieved July 17, 2019, from <https://florafaunaweb.nparks.gov.sg>
- Ong, B. L. (2003). Green plot ratio: An ecological measure for architecture and urban planning. *Landscape and Urban Planning*, 63(4), 197-211.
- Pérez, G., Coma, J., Sol, S., & Cabeza, L. F. (2017). Green facade for energy savings in buildings: The influence of leaf area index and facade orientation on the shadow effect. *Applied Energy*, 187, 424-437.

- Razzaghmanesh, M., & Razzaghmanesh, M. (2017). Thermal performance investigation of a living wall in a dry climate of Australia. *Building and Environment*, *112*, 45-62.
- Safikhani, T., & Baharvand, M. (2017). Evaluating the effective distance between living walls and wall surfaces. *Energy and Buildings*, *150*, 498-506.
- Schneider, C. A., Rasband, W. S., & Eliceiri, K. W. (2017). NIH Image to ImageJ: 25 years of Image Analysis. *Nat Methods*, *9*(7), 671-675.
- Song, Y., Maher, B. A., Li, F., Wang, X., Sun, X., & Zhang, H. (2015). Particulate matter deposited on leaf of five evergreen species in Beijing, China: Source identification and size distribution. *Atmospheric Environment*, *105*, 53-60.
- Sonnentag, O., Talbot, J., Chen, J. M., & Roulet, N. T. (2007). Using direct and indirect measurements of leaf area index to characterize the shrub canopy in an ombrotrophic peatland. *Agricultural and Forest Meteorology*, *144*(3-4), 200-212.
- Stawarczyk, K., Programu, Z., Do, I., Uszkodze, O., & Przew, L. I. N. (2015). Use of the ImageJ program to assess the damage of plants by snails. *Chemistry Didactics Ecology Metrology*, *20*, 67-73.
- Sulaiman, M. K. A. M., Shahidan, M. F., Jamil, M., & Zain, M. F. M. (2018). Percentage coverage of tropical climbing plants of green facade. *IOP Conference Series: Materials Science and Engineering*, *401*(1), 1-6.
- Taib, A. N., Ali, Z., & Abdullah, A. (2019). The performance of different ornamental plant species in transitional spaces in urban high-rise settings. *Urban Forestry and Urban Greening*, *43*(2019), 1-8.
- Tan, C. L., Wong, N. H., & Jusuf, S. K. (2014). Effects of vertical greenery on mean radiant temperature in the tropical urban environment. *Landscape and Urban Planning*, *127*, 52-64.
- Tan, C. L., Wong, N. H., Tan, P. Y., Jusuf, S. K., & Chiam, Z. Q. (2015). Impact of plant evapotranspiration rate and shrub albedo on temperature reduction in the tropical outdoor environment. *Building and Environment*, *94*, 206-217.
- Tan, P. Y., & Sia, A. (2010). *Leaf area index of tropical plants a guidebook on its use in the calculation of green plot ratio*. Singapore: Centre of Urban Greenery and Ecology
- Timur, Z. B., & Karaca, E. (2013). Vertical gardens BT - advances in landscape architecture. *Advances in Landscape Architecture*, (Chapter 22), 1-36.
- Weerakkody, U., Dover, J. W., Mitchell, P., & Reiling, K. (2017). Particulate matter pollution capture by leaves of seventeen living wall species with special reference to rail-traffic at a metropolitan station. *Urban Forestry and Urban Greening*, *27*, 173-186.
- Weerakkody, U., Dover, J. W., Mitchell, P., & Reiling, K. (2018). Quantification of the traffic-generated particulate matter capture by plant species in a living wall and evaluation of the important leaf characteristics. *Science of the Total Environment*, *635*, 1012-1024.
- Wong, N. H., Tan, A. Y. K., Tan, P. Y., & Wong, N. C. (2009). Energy simulation of vertical greenery systems. *Energy and Buildings*, *41*(12), 1401-1408.

Congestion Control in Implementing Multi Coding Schemes for Energy Optimisation in Wireless Sensor Networks

Samirah Nasuha Mohd Razali, Kamaruddin Mamat* and Nor Shahniza Kamal Bashah

Faculty of Computer and Mathematical Sciences, Universiti Teknologi MARA,
40450 Shah Alam, Selangor, Malaysia

ABSTRACT

Hybrid ARQ (HARQ) has been identified as one of the most common optimal error control protocols. However, due to the complexity of the existing error codes, the use of HARQ in WSN can be viewed as energy-consuming, if it were not implemented properly. Multi coding as an extension to the HARQ protocol can be a promising method for improving a network plagued by high error rates. However, in implementing the error correcting codes for the better error rates, one may increase the overhead in terms of computational redundancies added to the transmitted bits, especially in a highly condensed network. This can lead to further degradation of the remaining energy and fluctuations in the Bit Error Rates (BER). Based on a previous study, other aspects must be considered to indicate the congestions present, rather than solely be dependent on the Signal to Noise Ratio (SNR). This paper proposes a congestion control based on the node density variation to control the congestion caused by different levels of numbers of nodes deployed, as well as the complexity of error correcting codes which were used in the network. We collected the BER values, as well as the remaining energy and latency, to study the optimal error correcting codes which varied with the codeword length, and the respective error correcting capabilities which suited the defined congested environments. Based on our results, our proposed multi coding assignment can adapt to the sudden changes in the channel condition,

as well as improve the performance in terms of optimising the error rates, and the remaining energy across different types of channel conditions.

Keywords: Channel adaptation, channel estimation, error control protocol, multi coding scheme, wireless sensor networks

ARTICLE INFO

Article history:

Received: 26 August 2019

Accepted: 14 February 2020

Published: 15 April 2020

E-mail addresses:

samirah.razali@gmail.com (Samirah Nasuha Mohd Razali)

kamar@tmsk.uitm.edu.my (Kamaruddin Mamat)

shahniza@tmsk.uitm.edu.my (Nor Shahniza Kamal Bashah)

* Corresponding author

INTRODUCTION

The technology of Wireless Sensor Network (WSN) has evolved from transmitting smaller data, to massive data, and has progressively moved to highly condensed traffic. The existing architecture of WSN may not be able to tolerate the advancement of this technology, which will lead to intolerable higher error rates in a congested area. Multi-coding schemes are seen to be able to increase energy-efficiency (Ali et al., 2012), and reduce the overhead associated with single-coding schemes, by assigning different error correcting codes having its optimal performances corresponding to the specific channel condition (Razali et al., 2017). Compared to the single-coding schemes, these error correction schemes do not adapt to the changes in channel conditions.

Theoretically, in low Signal-to-Noise Ratio (SNR), the Bit Error Rate (BER) will be high. As the SNR increases, the BER will drop significantly. On the other hand, implementing single-coding schemes with high error correcting capabilities during high SNR would be a waste of energy when the low error correcting capability codes is sufficient to address errors. The high usage of error correcting capability, t , of the desired error correcting codes, can degrade the lifetime due to the high decoding energy, and the increase in the transmitted bits, especially when the WSN is highly resource-constrained (Kavitha & Sridharan, 2013). Implementing single-coding schemes with low error correcting capability codes during low SNR may not be enough to correct high levels of BER errors.

In a uniform node distribution, there may be negligible node interferences, as nodes are localised uniformly with one another. However, implementing non-uniform node distributions may lead to a rise in different levels of node interferences. This interference rises due to the different levels of node densities (Celaya-Echarri et al., 2018) which is caused by the high number of nodes localised in a particularly small area. These nodes may be located too close with one another, in a manner which allows many nodes to interfere with the transmission range of other nodes. This will lead to significant interferences. In addition, such interferences can cause intolerably high BER, high packet drops, and collisions. If the multi-coding schemes are wrongly assigned in this high node density condition, it will further push the network to accumulate much higher unacceptable BER.

RELATED WORKS

In the paper by Datta and Kundu (2014), the authors implemented a Hybrid Automatic Repeat Request (HARQ) with the Bose, Chaudhuri, and Hocquenghem (BCH) code. The authors also tested the HARQ-BCH across different node densities and message lengths. They stated that the BER was high in low hop count conditions. Previous works have also demonstrated the high usage of error correcting capabilities of the error correcting codes using more energy as the appended bits increased with the increase in error correcting capability. Theoretically, in the low SNR condition, the BER is considered high, due to the

lower boost of signal power compared to a network with much higher SNR. Thus, there is a need to use higher error correcting capabilities with adequate codeword lengths. However, in a condition where the SNR is high, the use of high error correcting capabilities may not be as efficient, because the BER is already low. Considering the non-uniform node deployment of practical WSN, there is a need to design a method which can adapt to these changing channel conditions, and as well as the changing in node deployment.

The work from Ali et al. (2012) proposed the multi-coding schemes in the network with Network Master (NM) sensors and sinks. They applied BCH codes with two different rates between the sensor and the NM, and between the NM and the sink. Based on their results, multi-coding schemes have a good effect on the network's lifetime when the low rate BCH codes such as (511, 148) are used at the sensor node, and the high rate BCH such as the (511, 484), is used at the NM. These findings can be seen as proof that multi-coding can be more energy-efficient as compared to single-coding schemes.

Our previous research implemented the use of low overhead error corrections based on the HARQ process, in which we incorporated the use of SNR classifications to classify the link quality which denoted the network condition of our predefined Coded Division Multiple Access (CDMA) WSN architecture. The SNR classification was proposed to support the network condition, which would always change over time, considering aspects such as mobility and traffic loads. The reflection, refraction and noise link conditions can be concerning matters which contribute to the non-constant SNR. Based on our previous research, we proposed the implementation of different error correcting capabilities, as well as variations in the codeword length for different SNR ranges, and denoted that the SNR range should be between 5 dB to 50 dB. We highlighted a method to enhance the performance of the CDMA WSN using the modified HARQ process, in which we enabled the module to transmit power and multi coding schemes to comply with the changes in the network conditions. The changing of the network conditions denotes the changes in the SNR values, in which, the network might migrate from a good reception towards a bad reception, or vice versa, due to fading effects. For instance, our research selected a range of error correcting capability, t , between 2 to 7, with the codeword length, n , in the range of 31 to 127 bits. This is meant to support the fact that, by using higher error correcting capabilities and codeword lengths, it would be impractical for WSN functionality due to the increase in complexity and appended bits.

This research studied the effects of error correcting codes on the performance of the proposed SNR classification algorithm (Razali et al., 2017) towards congestion control by implementing the aspects of node density. This research also proposed an extension of the SNR classification algorithm to detect the changes in the node density levels, provided that the node density was able to indicate the congestion levels, as the number of nodes increased due to scalability, or changes in the position of the nodes. This paper presents simulation results of the listed BCH and Reed Solomon (RS) error correcting codes and

assigns the most optimal error correcting codes with its respective error correcting capability for the defined type of congestion. Last but not least, this paper also presents the results of the proposed method compared to existing processes without the adaptation of channel conditions and congestion control.

METHODS

Overview of Node Density-based Congestion Control

Figure 1 shows the process flow of the proposed congestion control for a previous SNR classification system. Compared to the existing method utilising HARQ, the data was encoded with an error detection scheme, for example, Cyclic Redundancy Check (CRC), and subsequently encoded further with error correcting codes such as BCH or RS. The

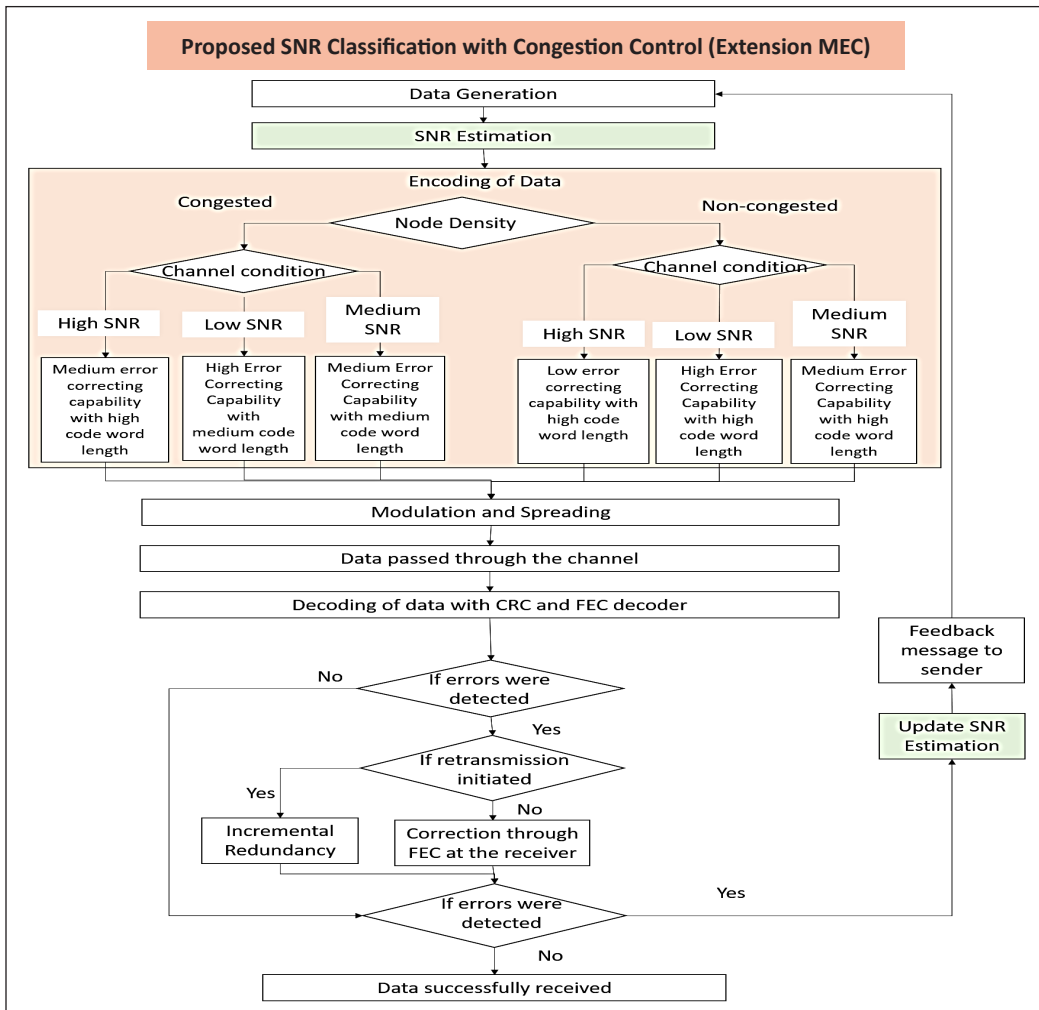


Figure 1. The process flow of the proposed Congestion Control for SNR classification

existing process uses single coding schemes regardless of the changes in the channel conditions or the congestions present. Based on other previous studies, SNR was not able to accurately determine the network conditions or link these congestions (Qin et al., 2013). Thus, there is a need to add other aspects to determine these congestions as the number of nodes starts to increase. According to the work by Chitlange and Deshpande (2015), when the number of nodes increases at a certain point above the acceptable threshold of the network, the throughputs seem to degrade due to fact that the network has started to congest. They also observed that there was a slight increase in the throughput when the node density increased initially, because of the increase in the routing performance. For instance, as the node density reached 45, the Packet Delivery Ratio (PDR) and throughputs started to decrease, which indicated congestion. In a small monitoring area, a large number of nodes deployed in a non-random distribution could lead to a rise in different levels of node densities in one monitoring area. Condensed networks are caused by the placement of nodes which are too close to each other, which can lead to performance degradation.

The length of the codewords is equally substantial when it comes to the error correcting capability. It adds to the congestion control, to ensure that the errors are not being increased by the implementation of long codewords when there is no need for it. From the Figure 2, high codewords are denoted by longer codeword lengths of 127, or more. Medium codeword lengths are denoted by the shorter codeword length of 63 and below. The idea of implementing different error correction schemes has been adapted to the channel conditions, as well as different levels of node densities to optimise the energy efficiency of the sensors with the error rates in the network. Both factors are equally essential, as a degradation of any one of them, would degrade the performance of the other.

Our multi-coding scheme was previously proposed (Razali et al., 2016; Razali et al., 2017) and comprised SNR classification classes to a different assignment of error correction schemes. We used BCH and RS codes that varied in codeword length, n , and error correcting capability, t . The error correction schemes assigned to each of these classes were based on their optimal performance obtained through means of simulation. The SNR classification also aided with SNR estimation using a Kalman Filter, to estimate the benchmark SNR for the error correcting module. This helped to encode the proper error correcting codes to the un-coded binary data. In this research, we studied the effects of adding the congestion control based on node density variation as an extension to the proposed multi-coding scheme mentioned above.

Problem Formulation

We tested the network with node increments of 4, 16, 32, 48, 64 and 80. The expression of the node density was calculated from the predefined number of nodes denoted by the Equation 1 as follows:

$$\text{Node Density} = \frac{(N * \pi * R^2)}{A} \quad (1)$$

Where, N is defined as the number of nodes, R is the transmission range, and A is the area of minoring. We classified the node density, which is denoted as N_d , in the variation of three different levels of congestion, such that EC denoted a condition which had extremely high congestion (N_d of more than 27.9253). MC denoted a medium congestion condition ($16.7552 \leq N_d \leq 22.3402$), and NC denoted a non-congested network (N_d less than 11.1701). For this paper, we managed to test two types of node density-based congestions, between 5.4851 and 22.3402. We considered the use of a low error correcting capability, t , such that $1 \leq t \leq 5$, as a much higher error correcting capability appended a higher number of redundancies in the transmitted bits. The codeword length was kept between $n=63$ and $n=127$ to suit the low overhead CDMA WSN environment.

Formula Derivation for Performance Analysis

In this paper, we present several equations which have been used, or derived for measurements throughout the experiments. The measurement models comprise formula to calculate Bit Error Rates, the network's remaining energy, and latency.

The expression of BER for BPSK in Rayleigh Fading is illustrated in Equation 2 below (Weber et al., 2007). The Rayleigh Fading was considered to address the multipath environment of urban areas. Radio systems in established urban outdoor locations are subject to these fadings, due to the attenuation of signals when there is no line of sight (Bensky, 2019).

$$\text{BER} = \frac{1}{2} \left[1 - \frac{\sqrt{\frac{E_b}{N_0}}}{\frac{E_b}{N_0} + 1} \right] \quad (2)$$

E_b/N_0 is defined as the Energy per bit to noise power spectral density ratio. E_b/N_0 is also known as the normalized SNR. In relation to the SNR, E_b/N_0 can be explained by the following Equation 3:

$$\text{SNR} = (E_b * br) / (N_0 * B) \quad (3)$$

E_b is the received energy per bit, N_0 is the noise power, br is the Bit Rate, and B is denoted as the bandwidth (Viswanathan & Mathuranathan, 2017). We also derived the

received signal power that followed the free space path loss, collaborating the path loss exponent and the distance between the transmitter and the receiver. The equation for the received signal power was also aided with the Additive White Gaussian Noise (AWGN). We also took the Rayleigh Fading into consideration as shown in Equation 4.

$$Y = h(x) + n \quad (4)$$

Where, h denotes the channel gain, while x is the transmitted data, and n is the noise. Channel gain, h captured the effects of the Rayleigh fading, in which the channel gain, h can be formulated again as shown in Equation 5:

$$Y = h \left[d^{\left(\frac{-\alpha}{2} \right)} \right] \quad (5)$$

Where, α , is the path loss exponent denoted as $2 \leq \alpha \leq 6$. The value of the path loss exponent corresponds to the urban area cellular radio, which has a value of 3.5 (Miranda et al., 2013), while, d was defined as the distance between the transmitter and the receiver (in meters). The minimum energy was expressed as E as shown in Equation 6, in which each transmitted bit consumed 1 unit of energy, and received bit consumed 0.75 units of energy according to (Kleinschmidt et al., 2005; Kleinschmidt et al., 2009):

$$E = H (N_{packet}) (N_{bits} + N_{bits} (0.75)) \quad (6)$$

Where, H is the number of hops, N_{packet} is the number of packets, and N_{bits} is the total number of bits, which includes the header and payload. Thus, the equation for energy consumed in the transmission for CRC-32 and Error correcting codes can be rewritten as shown in Equation 7 below:

$$E_{ECC} = (H)(N_{packet}) [N_{bits} + (N_{bits})(0.75)] + E_{DEC} \quad (7)$$

The decoding process imitated both the RS and BCH decoding processes with the narrow-sense generator polynomial. The decoding energy can be calculated as shown in Equation 8:

$$E_{DEC} = (2nt + 2t^2)(E_{addition} + E_{multiplication}) \quad (8)$$

Where, n is the block length for the corresponding error correcting codes, and t is the error correcting capability. In addition to that, $E_{addition} + E_{multiplication}$ corresponds to the energy consumed in the addition and multiplication of error correcting codes. The network latency, $d_{network}$ is measured according to Equation 9 shown as follows:

$$d_{network} = d_{proc} + d_{queue} + d_{trans} + d_{prop} \quad (9)$$

Where, d_{proc} is the processing time which is usually negligible (Ross & Kurose, 2000). d_{queue} is the queuing time, which is denoted in Equation 10, d_{trans} is the transmission time, which is denoted in Equation 11 and d_{prop} is the propagation time, denoted in Equation 12. The queuing time, d_{queue} is defined as time that a packet spends in a queue at a node, while waiting for other packets to be transmitted, and is calculated as follows:

$$d_{queue} = (d_{trans})(l_{queue}) \quad (10)$$

Where, d_{trans} is the transmission time and l_{queue} is the length of the queue. The equation below shows illustrates a means to measure the transmission delay, which is defined as the time required to put an entire packet into a communication media.

$$d_{trans} = l_{bits} / R_{trans} \quad (11)$$

Where, l_{bits} is the length of bits, and R_{trans} is the transmission rate in the unit of bits per time. The following equation denotes the propagation delay, d_{prop} :

$$d_{prop} = D_{node} / s \quad (12)$$

Where, D_{node} is the distance from sender to receiver, while s is the propagation speed of the media.

Simulation Parameter

Table 1 below shows the parameters defined for the simulation model and the error correcting codes with its defined code length, n , and the information length, k , as well as the error correcting capability, t . We did not test the error correcting capability which exceeded $t > 10$, as the nature of the WSN was unsuited to support such high complexity of codes.

We defined the noise as an Additive White Gaussian Noise (AWGN) with a Binary phase-shift keying (BPSK) modulation. The data was generated in a random binary of 10,000 bits for every transmission. We also added the path loss exponent to the BER calculation as shown in the equations above. The payload bits and header bits followed the existing architecture, such that this culminated in 128 bits and 256 bits, respectively.

We generated the CRC-30 polynomial after encoding the un-coded data, with either BCH or RS codes, corresponding to the SNR for that time period. We set the default number of generated bits at 10,000 bits. However, the transmitted bits varied according to the chosen error correcting codes, as different error correcting codes appended different

redundancies that resulted in a different number of transmitted bits per given time. The BCH and RS codeword lengths were tested as shown in Table 2.

Table 1
The parameters defined for the simulation of CDMA WSN

Parameter	Value
Min. dist. between two nodes	10 m
Noise	AWGN
Modulation	BPSK
Monitoring area (meter ²)	300 m x 300 m
Path loss parameter (α)	3.5
Payload, Header	128,256 bits
Error Detection	CRC-32
Error Correction	BCH and RS (from the range of codeword length from 63 to 127 and error correcting capability from 1 to 7)
Number of Nodes	16,64 (Node density of 5.5851 and 22.3402)
Number of Bits (bits)	10000

Table 2
Error Correcting Codes tested with its respective codeword length and error correcting capability

Error Correcting Codes	n	k	Error Correcting Capabilities, t
BCH	63	57	1
	63	51	2
	63	45	3
	63	39	4
	63	36	5
	63	30	6
	63	24	7
	127	120	1
	127	113	2
	127	106	3
	127	99	4
	127	92	5
	127	85	6
	127	78	7
RS	63	59	2
	63	57	3
	63	55	4
	63	53	5
	63	51	6
	63	49	7
	127	123	2
	127	121	3
	127	119	4
	127	117	5
	127	115	6
	127	113	7

RESULTS AND DISCUSSION

Pilot Study Results

In this study, we have tabulated the tested error correction codes in Table 2, that would optimise the BER and remaining energy across two different node density variations. From the table, we assumed that the number of nodes below 32 nodes ($N_d < 11.1701$) was denoted as node densities less than 11.1701, which indicated that the network was not congested. Thus, for the network which has 16 nodes, the calculated node density was 5.5851, and denoted that the network was not congested. For this type of node density, we used a low error correcting capability and low redundancy code to optimise between BER and the remaining energy.

Table 3

The proposed optimal error correcting codes with its defined (n, k) and error correcting capability for 16 nodes

No. of Nodes	Node Density	SNR Range	ECC	n	k	Total transmitted bits for one node
16	5.5851	48.512~52.512	RS t=3	127	121	10545
		43.512~47.512	RS t=5	127	117	10926
		38.512~42.512	BCH t=3	127	106	12069
		33.514~37.512	BCH t=4	127	99	12958
		28.512~32.512	BCH t=5	127	92	13847

As the SNR increased, a much lower error correcting capability was used to lower the amount of the appended bits transmitted through the channel (Table 3). This is because, theoretically, as SNR increases, the BER will drop, indicating that the link's quality has improved.

Thus, there is no need for higher error correcting capability codes if the medium capability is enough to reduce the BER. The network is assumed to start getting congested when there are more than 32 nodes in one given area, which is based on an experiment by (Chitlange & Deshpande, 2015). For extremely congested conditions, we have chosen the codeword length of 63 which denotes that the node density is 22.3402 for the moderate, to the highest error correction mode, as the codeword length of 63 for the BCH codes appended much higher redundancies as compared to the codeword length of 127.

However, the increase in the codeword length also increased the energy consumption. Even though it was seen that the higher codeword length of 127 appended lower redundancies, as the total number of transmitted bits was slightly less than the codeword length of 63, the results from previous studies showed that higher codeword length uses higher energy. Thus, we suggest that for the CDMA WSN, the use of the codeword length from 63 to 127 is preferable, as opposed to higher codeword lengths of more than 255 bits. This is because it increases the complexity, and adds more encoding and decoding overhead.

Table 4
The proposed optimal error correcting codes with its defined (n, k) and error correcting capability for 64 nodes

No. of Nodes	Node Density	SNR Range	ECC	n	k	Total transmitted bits for one node
64	22.3402	27.440~31.440	BCH t=1	127	120	10672
		22.440~26.440	BCH t=2	127	113	11307
		17.440~21.440	BCH t=3	63	45	14053
		12.440~16.440	BCH t=4	63	39	16195
		7.440~11.440	BCH t=5	63	36	17518

Table 4 and Table 5 show the remaining energy and latencies obtained from the simulation of CDMA WSN using the parameters in Table 1, and the predefined (n, k) with error correcting capabilities as stated in Table 2. By implementing higher codeword lengths, the energy consumption might increase beyond the limits of the WSN usage. Based on our tests, the codes which used n=127 had lower appended bits than the codes which used n=63. Despite the fact that the codes which used n=127 had lower redundancies, the remaining energy was much lower than the codes which used n=63. As seen in Table 4, the use of codes n=127 might not be necessary when the node density was sufficiently high.

Table 5
Remaining Energy and Latency for 16 nodes network

No. of Nodes	Node Density	Error Correcting Codes	n	k	Total transmitted bits	Remaining Energy (μJ)	Latency (s)
16	5.5851	BCH	63	57	11092	52693	0.4622
			127	120	10672	18079	0.4447
			63	51	12415	52547	0.5173
			127	113	11307	17735	0.4711
			63	45	14053	52402	0.5855
			127	106	12069	17392	0.5029
			63	39	16195	52256	0.6748
			127	99	12958	17049	0.5399
		RS	63	36	17518	52110	0.7299
			127	92	13847	16706	0.5770
			63	61	10336	52693	0.4307
			63	59	10714	52547	0.4464
			127	123	10418	17735	0.4341
			63	57	11092	52402	0.4622
			127	121	10545	17392	0.4394
			63	55	11470	52256	0.4779
127	119	10799	17049	0.4500			
63	53	11911	52110	0.4963			
127	117	10926	16706	0.4553			

The use of codes $n=63$ might be able to maintain higher remaining energy, but the error correction might not be able to perform as is intended, compared to that of codes which used $n=27$. The latency of the network also increased when applying BCH instead of RS codes. The higher the error correcting capability of the codes, the higher the latency was. The high redundancies added to the generated bits might be attributed to the higher number defined bits used for our architecture.

A higher codeword length is preferable for a large number of generated bits, such as 10,000 bits. We observed that for the default generated binary bits of 10,000, the higher codeword length embedded much smaller redundancies compared to the lower codeword lengths. Codeword length of 255 and 511 had reduced redundancies added to the data. However, we also observed that higher degradation of energy cannot be tolerated. Thus, based on the number of appended bits embedded to the transmitted bits, we concluded that the optimal codeword length for 10,000 bits was around 63 to 127 bits.

Figure 2 shows the plot for BER against SNR, with BCH codes that were implemented with increasing correcting capabilities for codeword lengths of 127 bits. From the data collected from the existing schemes, it was seen that the value of BER was already very high during lower SNR and still considered as high even when the SNR increased to 20 dB. Such values were recorded when the distance of 10m between the sender and receiver and the path loss exponent of 3.5 was added to the simulation.

It was observed that BCH codes with 127 bits seemed to be among the optimal codeword lengths with medium added redundancies. BCH (127, 92) recorded the lowest BER for the codeword length of 127 using a higher SNR. The medium SNR was around 11 dB to 15 dB, and BCH (127,113), with a $t=2$. It recorded the lowest BER. BCH (127,

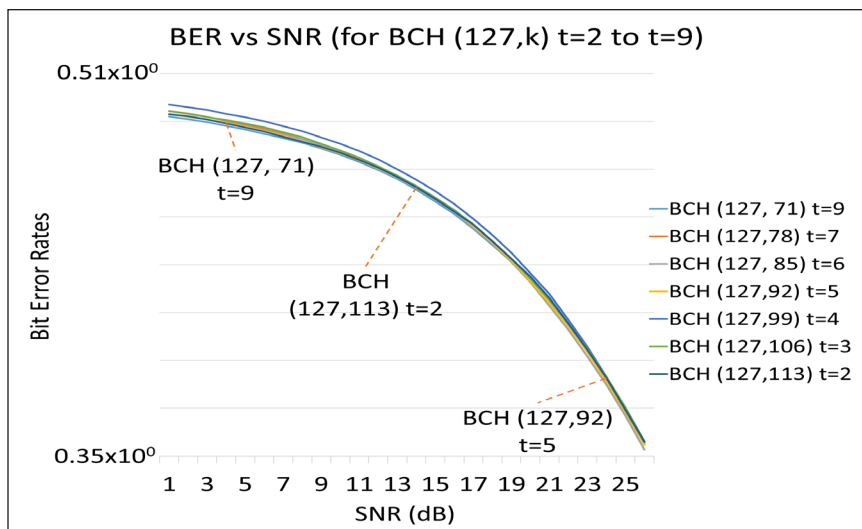


Figure 2. Graph of BER against SNR for the codeword length of 127 with error correcting capabilities from $t=2$ to $t=9$

71) had a $t=9$, and had the lowest BER with the lowest SNR. It was concluded that during the low SNR, it was best to use high error correcting capabilities, but less complex codes.

The BCH with a codeword length of 127 was among the optimal codes used during the non-congested condition. The lower complex codes, or lower codeword lengths with higher redundancies are suggested to be used in a low congested network with low SNRs. The higher codeword lengths with medium or lower redundancies are suggested to be used in a congested network with higher SNRs.

The data was collected using the proposed low error correction schemes (Lowest MEC) and high error correction schemes (Highest MEC), with BCH and RS values obtained from the different error correcting capabilities. The graph in Figure 3 shows the remaining energy corresponding to the number of nodes. We tested a BCH of $t=5$ (127,92), BCH $t=4$ (127,99), RS $t=5$ (127,117) and RS $t=4$ (127,119) with our optimal Lowest error correction scheme, such that RS $T=3$ (127,121) and in the Highest error correction scheme BCH $T=4$ (127,99). The existing error correction BCH $t=5$, BCH $t=4$, RS $t=5$ and RS $t=4$ had the lowest remaining energy compared to our proposed optimal solution. Our proposed optimal error correction scheme for the Lowest Error Correction Mode for MEC had reached the highest remaining energy of 0.01739 J.

This is because we implemented the moderate error correction scheme as the network does not have high congestion in deploying only 16 nodes. The low congestion network was seen to have lower error rates compared to the higher congested network, which corresponded to the node's interferences. Too powerful an error code, or higher error correcting capabilities might not be necessary to be applied, as the lower error correcting

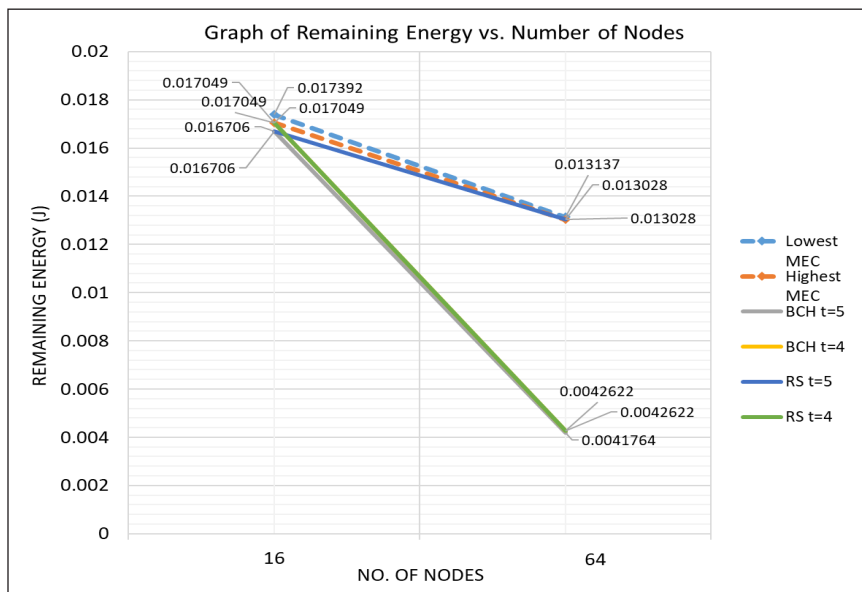


Figure 3. Plot for the remaining energy vs. number of nodes

capability was enough to correct these errors. Too high an error correcting capability, such that $t \geq 10$, or codeword lengths, such that $n=225$ or $n=511$ (for BCH code) can append high redundancy bits which can degrade the remaining energy of the sensors and render the network inoperative. We can conclude that from this graph, the proposed optimal error correcting schemes had remained at the highest remaining energy values, as compared to other schemes in the increasing network congestion (increasing number of nodes) and can be a promising approach to further maximizing the remaining energy.

The graph in Figure 4 shows the BER against SNR. The network is considered to have low congestion due to the node density value of 5.5851 with 16 nodes. For our Lowest error correction schemes in the low congested network, the network reached the lowest BER value when the SNR increased from 9 to 20, which corresponded to 0.4166 and 0.2554 respectively. The Highest error correction schemes sat between BCH $t=5$, and RS $t=5$. Our Lowest MEC for the low congested network outperformed the other error correction schemes, as the low error correcting capability did not append too many redundancy bits which might cause transmitted bits to be lengthy.

The increase in the length of the transmitted data increases the error rates also due to the increase in the use of energy driven by the lengthening of the encoding and decoding processes. Due to the usage of higher error correcting capabilities, the appended bits increase the BER, albeit a little. However, assigning the proper error correction schemes to the extension of the HARQ has a drawback in maintaining the BER with the higher remaining energy. Thus, we do not propose a BER that is too low as a means of achieving higher remaining energy. From the graph in Figure 5, the Highest error correction scheme

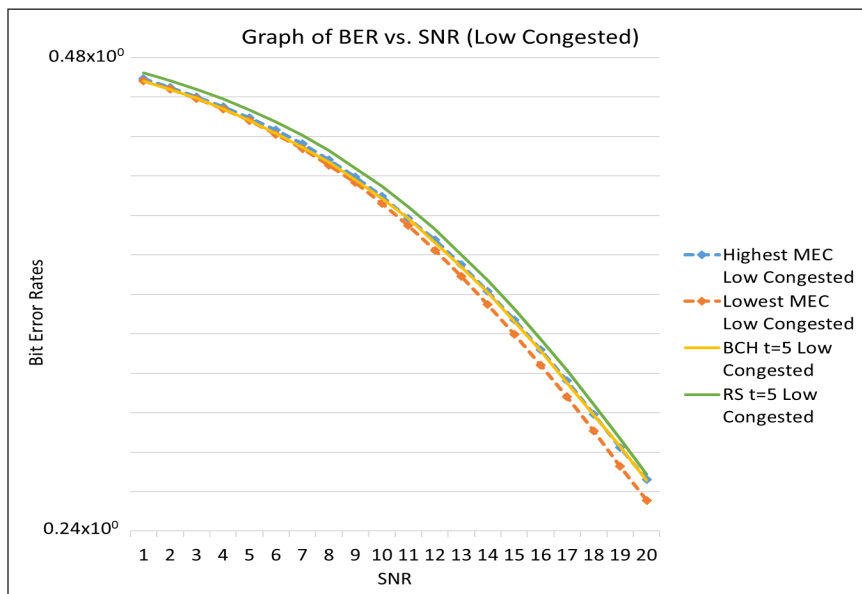


Figure 4. BER vs. SNR (Low congested)

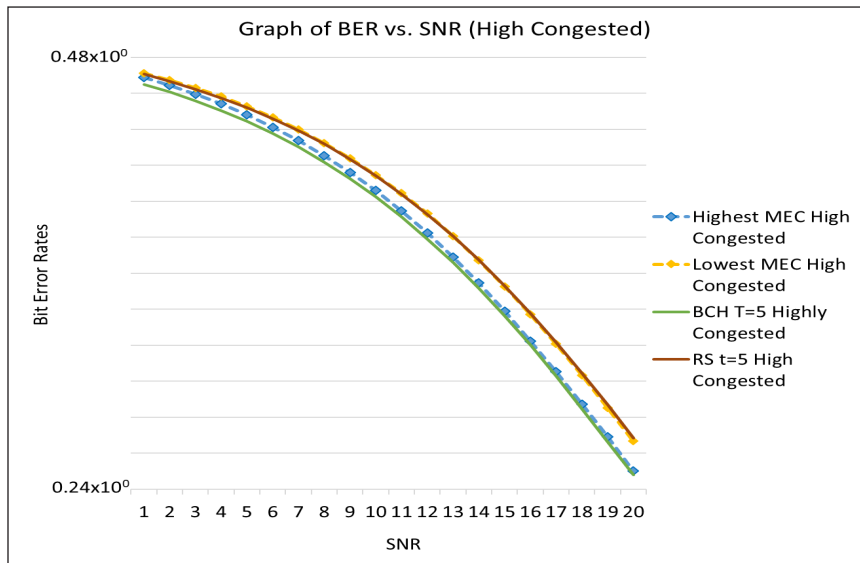


Figure 5. BER vs. SNR (High congested)

achieved the highest remaining energy, compared to other error correction schemes. We conclude that the BER was optimised, as the performance of the BER from the extension of the HARQ and existing BER did not show too much variation.

Figure 5 shows that the graph for BER vs. SNR in the highly congested network was denoted as 64 nodes. Our proposed Highest error correction mode showed that the BER was maintained as the SNR increased. The BER was not seen to reduce too much in relating to the optimized remaining energy. In order to have the remaining energy that outperformed the existing schemes, the medium error correction was assigned. This is to reduce the high energy usage from high error correcting capability so that both remaining energy and BER can be maintained throughout the SNR.

From this graph, the usage of existing BCH $t=5$ had lowered the BER significantly, which outperformed the MEC in term of BER. However, considering the fact that the optimization of the remaining energy, it was assumed that the higher error correcting capability had degraded the energy performance. Even though the MEC had not outperformed the existing higher error correcting capability of BCH in terms of BER, the MEC optimised the remaining energy in which the remaining energy of MEC as mentioned in Figure 3 are much higher than the existing BCH. The drawbacks of BER with remaining energy make it impossible to boost all aspects at the same time in which these aspects can only be maintained regardless of the channel conditions to ensure the reliability of transmission. A low BER can be achieved by assigning higher error correcting capabilities, but, the use of high error correcting capabilities will be insignificant to the WSN, as the energy usage will be high.

CONCLUSION AND FUTURE WORKS

The proper assignment of error correction in terms of the codeword lengths and error correcting capabilities of the error correcting codes according to different types of congestion is important to reduce excessive decoding and computation errors for correcting codes. The use of too high an error correcting capability in WSN is insignificant, as it increases the appended bits and complexity of the network, that leads to a much higher amount of energy usage. In implementing the multi-coding scheme assignment corresponding to the different channel conditions, the aspects of congestion presented need to be properly studied to avoid excessive latency and degradation of the remaining energy. Link congestion identification and classification can be promising to adequately reduce the energy usage when applying block codes in the network, thereby, optimising the BER and maintaining the remaining energy. For a low error correcting capability, the use of different codeword lengths of error correcting codes ($n=127$ and $n=63$) did not show too much impact on the BER, but can impact the remaining energy and latency. Our research demonstrated that certain error correcting codes had achieved the lowest possible BER and remaining energy, but, the drawback was that both aspects cannot be enhanced simultaneously. Our proposed multi-coding scheme seeks to aid the congestion based on our previous SNR classification, and can optimise the network by adapting to the changes in the SNR. For future works, the node deployment plays an important role to ensure that the congestion stabilizes with the corresponding transmission ranges. Higher transmission ranges with many nodes in one region can cause higher interference levels. Thus, the study of the suitable placement of nodes in different environments may contribute toward further lowering of the congestion, and expanding the energy efficiency of the network.

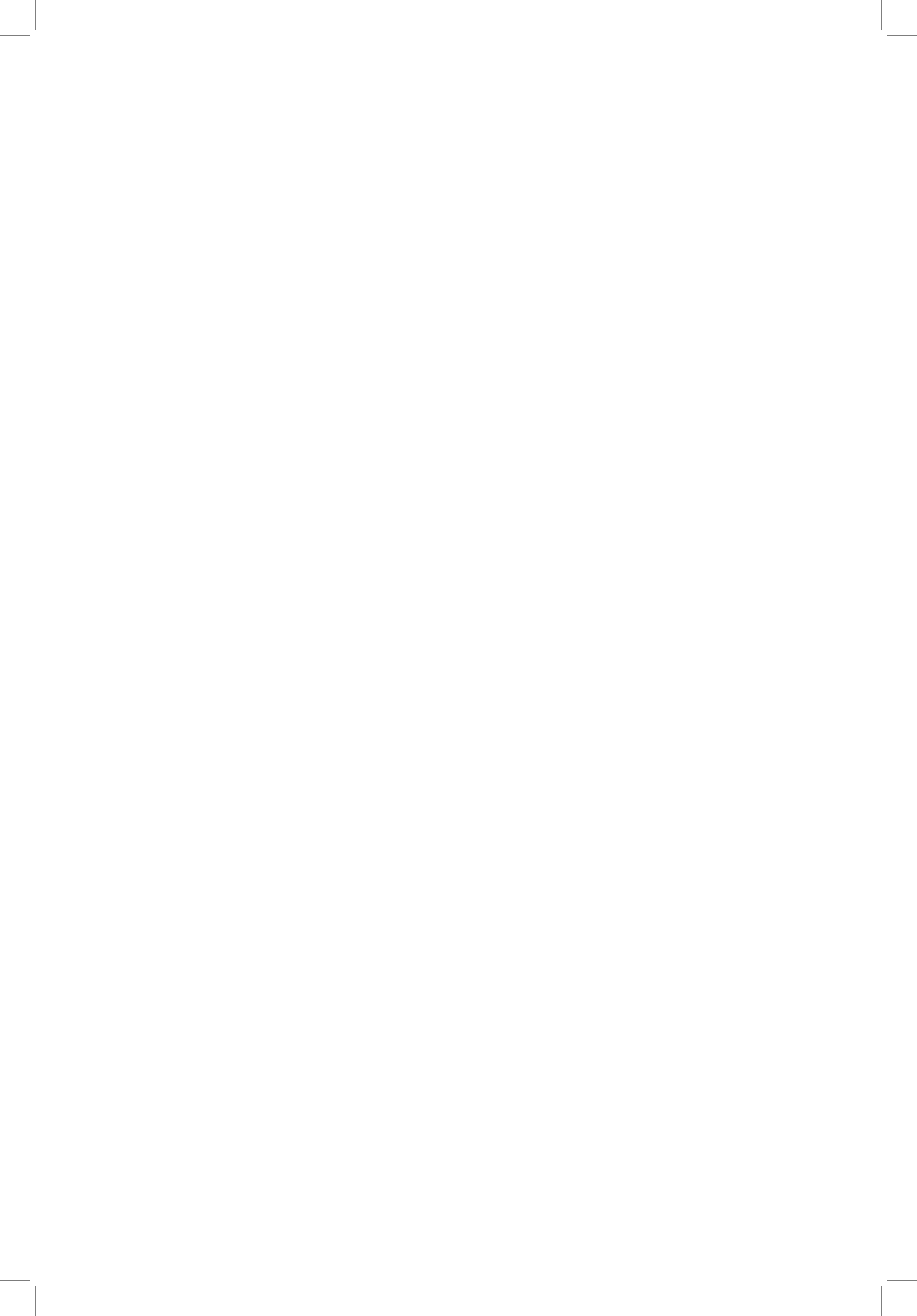
ACKNOWLEDGEMENTS

The authors would like to acknowledge the Institute of Research Management and Innovation (IRMI), UiTM Shah Alam, Selangor, Malaysia for the financial support throughout this research endeavour. This research was supported by the Research Management Institute, registered under the Fundamental Research Grant Scheme (FRGS) #600-RMI/FRGS 5/3 (46/2015).

REFERENCES

- Ali, N., ElSayed, H., El-Soudani, M., & Amer, H. (2012). Single and multi coding schemes for efficient wireless sensor networks. *Wireless Sensor Network*, 04(02), 52-58.
- Bensky, A. (2019). *Short-range wireless communication*. Burlington, Vermont: Newnes.
- Celaya-Echarri, M., Azpilicueta, L., Lopez-Iturri, P., Aguirre, E., & Falcone, F. (2018). Performance evaluation and interference characterization of wireless sensor networks for complex high-node density scenarios. *Multidisciplinary Digital Publishing Institute Proceedings*, 4(1), 1-6.

- Chitlange, M. M., & Deshpande, V. S. (2015, January 8-10). Effect of node density on congestion in WSN. In *2015 International Conference on Pervasive Computing (ICPC)* (Vol. 00, pp. 1-3). Pune, India.
- Datta, U., & Kundu, S. (2014). Performance of multi-hop CDMA wireless sensor networks with correlated interferers using different retransmission strategies and error control schemes. *International Journal of Sensor Networks*, 15(1), 40-51.
- Kavitha, T., & Sridharan, D. (2013). Optimal resource key management protocol for clustered heterogeneous wireless sensor networks. *Malaysian Journal of Computer Science*, 26(3), 211-231.
- Kleinschmidt, J. H., Borelli, W. C., & Pellenz, M. E. (2005, November 17). Power efficient error control for Bluetooth-based sensor networks. In *The IEEE Conference on Local Computer Networks 30th Anniversary (LCN'05)* (Vol. 2005, pp. 284-293). Sydney, NSW, Australia.
- Kleinschmidt, J. H., Borelli, W. C., & Pellenz, M. E. (2009). An energy efficiency model for adaptive and custom error control schemes in Bluetooth sensor networks. *AEU - International Journal of Electronics and Communications*, 63(3), 188-199.
- Miranda, J., Abrishambaf, R., Gomes, T., Goncalves, P., Cabral, J., Tavares, A., & Monteiro, J. (2013, July 29-31). Path loss exponent analysis in Wireless Sensor Networks: Experimental evaluation. In *2013 11th IEEE International Conference on Industrial Informatics (INDIN)* (pp. 54-58). Bochum, Germany.
- Qin, F., Dai, X., & Mitchell, J. E. (2013). Effective-SNR estimation for wireless sensor network using Kalman filter. *Ad Hoc Networks*, 11(3), 944-958.
- Razali, S. M., Mamat, K., & Bashah, N. S. K. (2016, October 10-12). Implementation of Hybrid ARQ (HARQ) error control algorithm for lifetime maximization and low overhead CDMA Wireless Sensor Network (WSN). In *2016 IEEE Conference on Wireless Sensors (ICWiSE)* (pp. 71-76). Langkawi, Malaysia.
- Razali, S., Mamat, K., & Bashah, S. K. (2017). Performance of multiple error correction (MEC) scheme based hybrid ARQ (HARQ) algorithm for maximizing lifetime of wireless sensor network (WSN) for natural disaster monitoring. *Journal Of Fundamental And Applied Sciences*, 9(5S), 336-351.
- Ross, K. W., & Kurose, J. F. (2000). *Delay and loss in packet-switched networks*. Retrieved December 1, 2017, from https://www.net.t-labs.tu-berlin.de/teaching/computer_networking/01.06.htm
- Viswanathan, M., & Mathuranathan, V. (2017). *Digital Modulations Using Matlab: Build Simulation Models from Scratch*. Amazon Digital Services LLC - Kdp Print Us. Retrieved May 18, 2019 from <https://books.google.com.my/books?id=gCTjtAEACAAJ>
- Weber, S., Andrews, J. G., & Jindal, N. (2007). The effect of fading, channel inversion, and threshold scheduling on ad hoc networks. *IEEE Transactions on Information Theory*, 53(11), 4127-4149.



**REFEREES FOR THE PERTANIKA
JOURNAL OF SCIENCE AND TECHNOLOGY**

Vol. 28 (2) Apr. 2020

The Editorial Board of the Journal of Science and Technology wishes to thank the following:

Abdullah Hisam Omar
(UTM, Malaysia)

Adem Kilicman
(UPM, Malaysia)

Ahmad Zulfaa Mohamed Kassim
(USM, Malaysia)

Ahmed Jalal Khan Chowdhury
(IIUM, Malaysia)

Amilia Afzan Mohd Jamil
(UPM, Malaysia)

Anuar Mikdad Muad
(UKM, Malaysia)

Bakhtiar Affendi Rosdi
(USM, Malaysia)

Dharini Pathmanathan
(UM, Malaysia)

Fatanah Mohamad Suhaimi
(USM, Malaysia)

Gabriele Ruth Anisah Froemming
(UNIMAS, Malaysia)

Hanani Ahmad Yusof@Hanafi
(IIUM, Malaysia)

Haszianaliza Haslan
(UiTM, Malaysia)

Isa Bala Muhammad
(FUTMinna, Nigeria)

Kek Sie Long
(UTHM, Malaysia)

Khoo Shin Yee
(UM, Malaysia)

Law Ming Chiat
(Curtin University, Malaysia)

Lee Sau Har
(Taylor's University, Malaysia)

Lee Sin Chang
(UPM, Malaysia)

Lim Chin Wai
(UNITEN, Malaysia)

Maiza Tusimin
(UPM, Malaysia)

Marina Kapitonova
(UNIMAS, Malaysia)

Mohamed Thariq Hameed Sultan
(UPM, Malaysia)

Mohan Reddy Moola
(Curtin University, Malaysia)

Mohd Azri Mohd Izhar
(UTM, Malaysia)

Mohd Hamzah Mohd Nasir
(IIUM, Malaysia)

Mohd Hanafi Idris
(UMT, Malaysia)

Mohd Shahrul Nizam Mohd Danuri
(KUIS, Malaysia)

Mohd Shamsul Anuar
(UPM, Malaysia)

Mohd Shareduwan Mohd Kasihmuddin
(USM, Malaysia)

Musa Mohd Mokji
(UTM, Malaysia)

Muzzneena Ahmad Mustapha
(UKM, Malaysia)

Narcisse MS Joseph
(UPM, Malaysia)

Nik Zarina Nik Mahmood
(UiTM, Malaysia)

Nora Muda
(UKM, Malaysia)

Norazaliza Mohd Jamil
(UMP, Malaysia)

Norharyati Harum
(UTeM, Malaysia)

Nur Anisah Mohamed Rahman
(UM, Malaysia)

Nur Fadhilah Ibrahim
(UMT, Malaysia)

Nurul Ain Abu Bakar
(UiTM, Malaysia)

Nurul Asyikin Yahya
(UKM, Malaysia)

Phang Chang
(UTHM, Malaysia)

Salina Abdul Samad
(UKM, Malaysia)

Sharifah Noor Emilia Syed Jamil Fadaak
(UMT, Malaysia)

Thaned Rojsiraphisal
(CMU, Thailand)

Wan Mohd Rauhan Wan Hussin
(UMT, Malaysia)

Wan Saiful Nizam Wan Mohamad
(UMK, Malaysia)

CMU – Chiangmai University
FUTMinna – Federal University of Technology Minna
IIUM – International Islamic University Malaysia
KUIS – Kolej Universiti Islam Antarabangsa Selangor
UiTM – Universiti Teknologi MARA
UKM – Universiti Kebangsaan Malaysia
UM – Universiti Malaya
UMK – Universiti Malaysia Kelantan
UMP – Universiti Malaysia Pahang
UMT – Universiti Malaysia Terengganu
UNIMAS – Universiti Malaysia Sarawak
UNITEN – Universiti Tenaga Nasional
UPM – Universiti Putra Malaysia
USM – Universiti Sains Malaysia
UTeM – Universiti Teknikal Malaysia Melaka
UTHM – Universiti Tun Hussein Onn Malaysia
UTM – Universiti Teknologi Malaysia

While every effort has been made to include a complete list of referees for the period stated above, however if any name(s) have been omitted unintentionally or spelt incorrectly, please notify the Chief Executive Editor, *Pertanika* Journals at executive_editor.pertanika@upm.edu.my

Any inclusion or exclusion of name(s) on this page does not commit the *Pertanika* Editorial Office, nor the UPM Press or the University to provide any liability for whatsoever reason.

Pertanika Journals

Our goal is to bring high quality research to the widest possible audience

INSTRUCTIONS TO AUTHORS

(REGULAR ISSUE)

-- Manuscript Preparation & Submission Guide --

Revised: March 2020

Please read the Pertanika guidelines and follow these instructions carefully. The Chief Executive Editor reserves the right to return manuscripts that are not prepared in accordance with these guidelines.

MANUSCRIPT PREPARATION

Manuscript Types

Pertanika accepts submission of mainly **four** types of manuscripts

- that have not been published elsewhere (including proceedings)
- that are not currently being submitted to other journals

1. REGULAR ARTICLE

Regular article is a full-length original empirical investigations, consisting of introduction, methods, results and discussion. Original research work should present new and significant findings that contribute to the advancement of the research area. Analysis and Discussion must be supported with relevant references.

Size: Generally, it is expected **not to exceed 6000 words** (excluding the abstract, references, tables and/or figures), a maximum of **80 references**, and **an abstract of less than 250 words**.

2. REVIEW ARTICLE

A review article reports critical evaluation of materials about current research that has already been published by organizing, integrating, and evaluating previously published materials. It summarizes the status of knowledge and outline future directions of research within the journal scope. A review article should aim to provide systemic overviews, evaluations and interpretations of research in a given field. Re-analyses as meta-analysis and systemic reviews are encouraged.

Size: Generally, it is expected **not to exceed 6000 words** (excluding the abstract, references, tables and/or figures), a maximum of **80 references**, and **an abstract of less than 250 words**.

3. SHORT COMMUNICATIONS

Each article should be timely and brief. It is suitable for the publication of significant technical advances and may be used to:

- reports new developments, significant advances and novel aspects of experimental and theoretical methods and techniques which are relevant for scientific investigations within the journal scope;
- reports/discusses on significant matters of policy and perspective related to the science of the journal, including 'personal' commentary;
- disseminates information and data on topical events of significant scientific and/or social interest within the scope of the journal.

Size: It is limited to **3000 words** and have a maximum of **3 figures and/or tables, from 8 to 20 references, and an abstract length not exceeding 100 words**. Information must be in short but complete form and it is not intended to publish preliminary results or to be a reduced version of Regular or Rapid Papers.

4. OTHERS

Brief reports, case studies, comments, concept papers, letters to the editor, and replies on previously published articles may be considered.

Language Accuracy

Pertanika **emphasizes** on the linguistic accuracy of every manuscript published. Articles must be in **English** and they must be competently written and presented in clear and concise grammatical English. Contributors are strongly advised to have the manuscript checked by a colleague with ample experience in writing English manuscripts or a competent English language editor.

Author(s) **may be required to provide a certificate** confirming that their manuscripts have been adequately edited. **All editing costs must be borne by the author(s).**

Linguistically hopeless manuscripts will be rejected straightaway (e.g., when the language is so poor that one cannot be sure of what the authors really mean). This process, taken by authors before submission, will greatly facilitate reviewing, and thus publication.

MANUSCRIPT FORMAT

The paper should be submitted in one column format with at least 4cm margins and 1.5 line spacing throughout. Authors are advised to use Times New Roman 12-point font and *MS Word* format.

1. Manuscript Structure

Manuscripts in general should be organised in the following order:

- **Page 1: Running title**

This page should **only** contain the running title of your paper. The running title is an abbreviated title used as the running head on every page of the manuscript. The running title **should not exceed 60 characters, counting letters and spaces.**

- **Page 2: Author(s) and Corresponding author's information**

General information: This page should contain the **full title** of your paper **not exceeding 25 words**, with name(s) of all the authors, institutions and corresponding author's name, institution and full address (Street address, telephone number (including extension), hand phone number, and e-mail address) for editorial correspondence. **The corresponding author must be clearly indicated with "*".**

Authors' name: The names of the authors should be named **in full without academic titles.** For Asian (Chinese, Korean, Japanese, Vietnamese), please write first name and middle name before surname (family name). The last name in the sequence is considered the surname.

Authors' addresses: Multiple authors with different addresses must indicate their respective addresses separately by superscript numbers.

Tables / figures list: A **list** of number of **black and white / colour figures and tables** should also be indicated on this page. See "**5. Figures & Photographs**" for details.

Example (page 2):

***In vivo* Fecundity Evaluation of *Phaleria macrocarpa* Extract Supplementation in Male Adult Rats**

***Sui Sien Leong*^{1*} and *Mohamad Aziz Dollah*²**

¹*Department of Animal Sciences and Fishery, Universiti Putra Malaysia, 97008 Bintulu, Sarawak, Malaysia*

²*Department of Biomedical Sciences, Universiti Putra Malaysia, 43400 Serdang, Malaysia*

leongsuisien@upm.edu.my (Sui Sien Leong), Contact number
azizdollah@gmail.com (Mohamad Aziz Dollah), Contact number

*Corresponding author

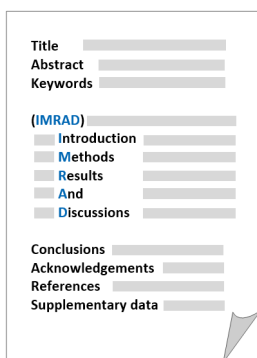
- **Page 3: Abstract**

This page should **repeat** the **full title** of your paper with only the **Abstract**, usually in one paragraph and **Keywords**.

Keywords: Not more than 8 keywords in alphabetical order must be provided to describe the contents of the manuscript.

- **Page 4: Text**

A regular paper should be prepared with the headings *Introduction, Methods, Results and Discussions* in this order. The literature review maybe part of or separated from Introduction. A conclusion maybe embedded or separated from Results and Discussions.



MAKE YOUR ARTICLES AS CONCISE AS POSSIBLE

Most scientific papers are prepared according to a format called IMRAD. The term represents the first letters of the words Introduction, Materials and Methods, Results, And, Discussion. It indicates a pattern or format rather than a complete list of headings or components of research papers; the missing parts of a paper are: Title, Authors, Keywords, Abstract, Conclusions, and References. Additionally, some papers include Acknowledgments and Appendices.

The Introduction explains the scope and objective of the study in the light of current knowledge on the subject; the Materials and Methods describes how the study was conducted; the Results section reports what was found in the study; and the Discussion section explains meaning and significance of the results and provides suggestions for future directions of research. The manuscript must be prepared according to the Journal's instructions to authors.

2. Levels of Heading

Level of heading	Format
1 st	LEFT, BOLD, UPPERCASE
2 nd	Flush left, Bold, Capitalise each word
3 rd	Bold, Capitalise each word, ending with .
4 th	<i>Bold italic, Capitalise each word, ending with .</i>

3. Equations and Formulae

These must be set up clearly and should be typed double spaced. Numbers identifying equations should be in square brackets and placed on the right margin of the text.

4. Tables

- All tables should be prepared in a form consistent with recent issues of Pertanika and should be numbered consecutively with Roman numerals (Table 1, Table 2).
- A brief title should be provided, which should be shown at the top of each table (**APA format**):

Example: Table 1

PVY infected Nicotiana tabacum plants optical density in ELISA

- Explanatory material should be given in the table legends and footnotes.
- Each table should be prepared on a new page, embedded in the manuscript.
- Authors are advised to keep backup files of all tables.

**** Please submit all tables in Microsoft word format only - because tables submitted as image data cannot be edited for publication and are usually in low-resolution.**

5. Figures & Photographs

- Submit an **original** figure or photograph.
- Line drawings must be clear, with high black and white contrast.

- Each figure or photograph should be prepared on a new page, embedded in the manuscript for reviewing to keep the file of the manuscript under 5 MB.
- These should be numbered consecutively with Roman numerals (Figure 1, Figure 2).
- Provide a brief title, which should be shown at the bottom of each table (**APA format**):

Example: Figure 1. PVY-infected in vitro callus of Nicotiana tabacum

- If a Figure has been previously published, acknowledge the original source and submit written permission form the copyright holder to reproduce the material.
- Authors are advised to keep backup files of all figures.

**** Figures or photographs must also be submitted separately as TIFF, JPEG, because figures or photographs submitted in low-resolution embedded in the manuscript cannot be accepted for publication. For electronic figures, create your figures using applications that are capable of preparing high resolution TIFF files.**

6. Acknowledgement

Any individuals and entities who have contributed should be acknowledged appropriately.

7. References

References begin on their own page and are listed in alphabetical order by the first author's last name. Only references cited within the text should be included. All references should be in 12-point font and double-spaced.

NOTE: When formatting your references, please follow the **Pertanika-APA-reference style** (6th Edition) (*refer to examples*). Ensure that the references are strictly in the journal's prescribed style, failing which your article will **not be accepted for peer-review**. You may refer to the *Publication Manual of the American Psychological Association* for further details <https://apastyle.apa.org/>

Examples of reference style are given below:

Books

Books	Insertion in Text	In Reference List
Book with 1-2 authors	<p>Information prominent' (the author's name is within parentheses):</p> <p>... (Cochrane, 2007) ...</p> <p>Or</p> <p>'Author prominent' (the author's name is outside the parentheses):</p> <p>Cochrane (2007) ...</p>	Cochrane, A. (2007). <i>Understanding urban policy: A critical approach</i> . Malden, United States: Blackwell Publishing.
Book with 3 or more authors (Pertanika's format)	<p><i>For all in-text references, list only the first author's family name and followed by 'et al.'</i></p> <p>Information prominent' (the author's name is within parentheses):</p> <p>... (Seeley et al., 2011) ...</p> <p>Or</p> <p>'Author prominent' (the author's name is outside the parentheses):</p> <p>Seeley et al. (2011) ...</p>	Seeley, R., VanPutte, C., Regan, J., & Russo, A. (2011). <i>Seeley's anatomy & physiology</i> . New York, United States: McGraw-Hill.

Books	Insertion in Text	In Reference List
Book with 6-7 authors	<p><i>For all in-text references, list only the first author's family name and followed by 'et al.'</i></p> <p>Information prominent' (the author's name is within parentheses):</p> <p>... (Bulliet et al., 2011) ...</p> <p>Or</p> <p>'Author prominent' (the author's name is outside the parentheses):</p> <p>Bulliet et al. (2011) ...</p>	<p>Bulliet, R. W., Crossley, P. K., Headrick, D. R., Hirsch, S. W., Johnson, L. L., & Northrup, D. (2011). <i>The earth and its peoples: A global history</i> (5th ed.). Boston, United States: Wadsworth.</p>
Book with more than 8 authors	<p><i>For all in-text references, list only the first author's family name and followed by 'et al.'</i></p> <p>A recent study (Edge et al., 2011) concluded that...</p> <p>Or</p> <p>Edge et al. (2011) concluded that</p>	<p>For books with eight or more authors, please follow the guidelines for journal articles with eight or more authors.</p>
Chapter in edited book	<p>Information prominent' (the author's name is within parentheses):</p> <p>... (Richards, 1997) ...</p> <p>Or</p> <p>'Author prominent' (the author's name is outside the parentheses):</p> <p>Richards (1997) ...</p>	<p>Richards, K. C. (1997). Views on globalization. In H. L. Vivaldi (Ed.), <i>Australia in a global world</i> (pp. 29-43). Sydney, Australia: Century.</p>
e-book/online book	<p>Information prominent' (the author's name is within parentheses):</p> <p>... (Niemann et al., 2004) ...</p> <p>Or</p> <p>'Author prominent' (the author's name is outside the parentheses):</p> <p>Niemann (2004) ...</p>	<p>Niemann, S., Greenstein, D., & David, D. (2004). <i>Helping children who are deaf: Family and community support for children who do not hear well</i>. Retrieved June 1, 2019, from http://www.hesperian.org/publications_download_deaf.php</p> <p>Schiraldi, G. R. (2001). <i>The post-traumatic stress disorder sourcebook: A guide to healing, recovery, and growth</i> [Adobe Digital Editions version]. doi:10.1036/0071393722</p>
Editor	<p>Information prominent' (the author's name is within parentheses):</p> <p>... (Zairi, 1999) ...</p> <p>Or</p> <p>'Author prominent' (the author's name is outside the parentheses):</p> <p>Zairi (1999) ...</p>	<p>Zairi, M. (Ed.). (1999). <i>Best practice: Process innovation management</i>. Oxford, United Kingdom: Butterworth- Heinemann.</p>

Books	Insertion in Text	In Reference List
Several works by same author in the same year	<p>Information prominent' (the author's name is within parentheses):</p> <p>... (Fullan, 1996a, 1997b) ...</p> <p>Or</p> <p>'Author prominent' (the author's name is outside the parentheses):</p> <p>Fullan (1996a, 1996b) ...</p>	<p>Fullan, M. (1996a). Leadership for change. In <i>International handbook for educational leadership and administration</i>. New York, United States: Kluwer Academic.</p> <p>Fullan, M. (1996b). <i>The new meaning of educational change</i>. London, United Kingdom: Casell.</p>
Several authors, different years referred to collectively in your work	<p>List sources alphabetically by family name in the in-text reference in the order in which they appear in the Reference List.</p> <p>The cyclical process (Carr & Kemmis, 1986; Dick, 2000) suggests...</p>	<p>Carr, W., & Kemmis, S. (1986). <i>Becoming critical: Education knowledge and action research</i>. London, United Kingdom: Falmer Press.</p> <p>Dick, B. (2000). <i>A beginner's guide to action research</i>. Retrieved June 1, 2019, from http://www.scu.edu.au/schools/gcm/ar/arp/guide.html</p>

Journals

Journals	Insertion in Text	In Reference List
Journal article with 1-2 authors	<p>Information prominent' (the author's name is within parentheses):</p> <p>... (Kramer & Bloggs, 2002)...</p> <p>Or</p> <p>'Author prominent' (the author's name is outside the parentheses):</p> <p>Kramer and Bloggs (2002) ...</p>	<p>Kramer, E., & Bloggs, T. (2002). On quality in art and art therapy. <i>American Journal of Art Therapy</i>, 40, 218-231.</p>
Journal article with 3 or more authors (Pertanika's format)	<p><i>For all in-text references, list only the first author's family name and followed by 'et al.'</i></p> <p>Information prominent' (the author's name is within parentheses):</p> <p>... (Erlo et al., 2008) ...</p> <p>Or</p> <p>'Author prominent' (the author's name is outside the parentheses):</p> <p>Erlo et al. (2008) ...</p>	<p>Elo, A., Ervasti, J., Kuosma, E., & Mattila, P. (2008). Evaluation of an organizational stress management program in a municipal public works organization. <i>Journal of Occupational Health Psychology</i>, 13(1), 10-23. doi: 10.1037/1076-8998.13.1.10</p>

Journal article with 6 - 7 authors	<p><i>For all in-text references, list only the first author's family name and followed by 'et al.'</i></p> <p>Information prominent' (the author's name is within parentheses):</p> <p>... (Restouin et al., 2009) ...</p> <p>Or</p> <p>'Author prominent' (the author's name is outside the parentheses):</p> <p>Restouin et al. (2008) ...</p>	Restouin, A., Aresta, S., Prébet, T., Borg, J., Badache, A., & Collette, Y. (2009). A simplified, 96-well-adapted, ATP luminescence-based motility assay. <i>BioTechniques</i> , 47, 871–875. doi: 10.2144/000113250
Journal article with more than 8 or more authors	<p>Information prominent' (the author's name is within parentheses):</p> <p>... (Steel et al., 2010)..</p> <p>Or</p> <p>'Author prominent' (the author's name is outside the parentheses):</p> <p>Steel et al. (2010) ...</p>	Steel, J., Youssef, M., Pfeifer, R., Ramirez, J. M., Probst, C., Sellei, R., ... Pape, H. C. (2010). Health-related quality of life in patients with multiple injuries and traumatic brain injury 10+ years postinjury. <i>Journal of Trauma: Injury, Infection, and Critical Care</i> , 69(3), 523-531. doi: 10.1097/TA.0b013e3181e90c24
Journal article with DOI	<p>Information prominent' (the author's name is within parentheses):</p> <p>... (Shaw et al., 2005)..</p> <p>Or</p> <p>'Author prominent' (the author's name is outside the parentheses):</p> <p>Shaw et al. (2005) ...</p>	Shaw, K., O'Rourke, P., Del Mar, C., & Kenardy, J. (2005). Psychological interventions for overweight or obesity. <i>The Cochrane database of systematic reviews</i> (2). doi:10.1002/14651858.CD003818.pub2

Newspapers

Newspapers	Insertion in Text	In Reference List
Newspaper article – with an author	... (Waterford, 2007)...	Waterford, J. (2007, May 30). Bill of rights gets it wrong. <i>The Canberra Times</i> , p. 11.
Newspaper article – without an author	... ("Internet pioneer", 2007) ...	Internet pioneer to oversee network redesign. (2007, May 28). <i>The Canberra Times</i> , p. 15.
Article in an newsletter	... ("Australians and the Western Front", 2009) ...	Australians and the Western Front. (2009, November). <i>Ozculture newsletter</i> . Retrieved June 1, 2019, from http://www.cultureandrecreation.gov.au/newsletter/

Conference / Seminar Papers

Conference / Seminar Papers	Insertion in Text	In Reference List
<p>Print – If the paper is from a book, use the book chapter citation format. If it is from regularly published proceedings (e.g. annual), use the Journal article citation format.</p>	<p>... (Edge, 1996) ...</p> <p>Or</p> <p>Edge (1996) ...</p>	<p>Edge, M. (1996). Lifetime prediction: Fact or fancy? In M. S. Koch, T. Padfield, J. S. Johnsen, & U. B. Kejser (Eds.), <i>Proceedings of the Conference on Research Techniques in Photographic Conservation</i> (pp. 97-100). Copenhagen, Denmark: Royal Danish Academy of Fine Arts.</p>
<p>Online</p>	<p>... (Tester, 2008) ...</p> <p>Or</p> <p>Tester (2008) ...</p>	<p>Tester, J. W. (2008). The future of geothermal energy as a major global energy supplier. In H. Gurgenci & A. R. Budd (Eds.), <i>Proceedings of the Sir Mark Oliphant International Frontiers of Science and Technology Australian Geothermal Energy Conference</i>, Canberra, Australia: Geoscience Australia. Retrieved June 1, 2019, from http://www.ga.gov.au/image_cache/GA11825.pdf</p>

Government Publications

Government Publications	Insertion in Text	In Reference List
<p>Government as author</p>	<p>First in-text reference: Spell out the full name with the abbreviation of the body.</p> <p>... (Department of Finance and Administration [DOFA], 2006) ...</p> <p>Subsequent in-text reference/s: Use the abbreviation of the body.</p> <p>... (DOFA, 2006)...</p>	<p>Department of Finance and Administration. (2006). <i>Delivering Australian Government services: Managing multiple channels</i>. Canberra, Australia: Author.</p>
<p>Government report - online</p>	<p>First in-text reference: Spell out the full name with the abbreviation of the body.</p> <p>... (Department of the Prime Minister and Cabinet [PM&C], 2008) ...</p> <p>Subsequent in-text reference/s: Use the abbreviation of the body.</p> <p>... (PM&C, 2008)...</p>	<p>Department of the Prime Minister and Cabinet. (2008). <i>Families in Australia: 2008</i>. Retrieved June 1, 2019, from http://www.....</p>

9. General Guidelines

Abbreviations: Define alphabetically, other than abbreviations that can be used without definition. Words or phrases that are abbreviated in the introduction and following text should be written out in full the first time that they appear in the text, with each abbreviated form in parenthesis. Include the common name or scientific name, or both, of animal and plant materials.

Authors' Affiliation: The primary affiliation for each author should be the institution where the majority of their work was done. If an author has subsequently moved to another institution, the current address may also be stated in the footer.

Co-Authors: The commonly accepted guideline for authorship is that one must have substantially contributed to the development of the paper and share accountability for the results. Researchers should decide who will be an author and what order they will be listed depending upon their order of importance to the study. Other contributions should be cited in the manuscript's Acknowledgements.

Copyright Permissions: Authors should seek necessary permissions for quotations, artwork, boxes or tables taken from other publications or from other freely available sources on the Internet before submission to Pertanika. Acknowledgement must be given to the original source in the illustration legend, in a table footnote, or at the end of the quotation.

Footnotes: Current addresses of authors if different from heading may be inserted here.

Page Numbering: Every page of the manuscript, including the title page, references and tables should be numbered.

Spelling: The journal uses American or British spelling and authors may follow the latest edition of the Oxford Advanced Learner's Dictionary for British spellings. Each manuscript should follow one type of spelling only.

SUBMISSION OF MANUSCRIPTS

All submissions must be made electronically using the **online submission system ScholarOne™**, a web-based portal by Clarivate Analytics. For more information, go to our web page and [click "Online Submission"](#).

Submission Checklist

1. MANUSCRIPT:

Ensure your MS has followed the Pertanika style particularly the first four pages as explained earlier. The article should be written in a good academic style and provide an accurate and succinct description of the contents ensuring that grammar and spelling errors have been corrected before submission. It should also not exceed the suggested length.

2. DECLARATION FORM:

- Author has to sign a declaration form. In signing the form, authors declare that the work submitted for publication is original, previously unpublished, and not under consideration for any publication elsewhere.
- Author has to agree to pay the publishing fee once the paper is accepted for publication in Pertanika.

Note:

COPYRIGHT FORM: Author will be asked to sign a copyright form when the paper is accepted. In signing the form, it is assumed that authors have obtained permission to use any copyrighted or previously published material. All authors must read and agree to the conditions outlined in the form, and must sign the form or agree that the corresponding author can sign on their behalf. Articles cannot be published until a signed form (*original pen-to-paper signature*) has been received.

Visit our Journal's website for more details at <http://www.pertanika.upm.edu.my/>

ACCESS TO PUBLISHED MATERIALS

Under the Journal's open access initiative, authors can choose to download free material (via PDF link) from any of the journal issues from Pertanika's website. Under "**Browse Journals**" you will see a link, "*Regular Issue*", "*Special Issue*" or "*Archives*". Here you will get an access to all current and back-issues from 1978 onwards. No hard copy of journals or off prints are printed.

Visit our Journal's website at

http://www.pertanika.upm.edu.my/regular_issues.php for "Regular Issue"

http://www.pertanika.upm.edu.my/cspecial_issues.php for "Special Issue"

http://www.pertanika.upm.edu.my/journal_archives.php for "Archives"



PUBLICATION CHARGE

Upon acceptance of manuscript, a processing fee of RM 750 / USD 250 will be imposed on authors; RM 750 for any corresponding author affiliated to an institution in Malaysia; USD 250 for any corresponding author affiliated to an institution outside Malaysia. Payment must be made online at <https://paygate.upm.edu.my/action.do?do=>

Any queries may be directed to the **Chief Executive Editor's** office via email to executive_editor.pertanika@upm.edu.my



Earth Sciences

- Comparison of Catches of Skipjack Tuna (*Katsuwonus pelamis* Linnaeus 1758) Purse Seines Inside and Outside of the FADs Areas 717
Achmar Mallawa

Environmental Sciences

- Comparison of Leaf Area Index from Four Plant Species on Vertical Greenery System in Pasir Gudang, Malaysia 735
Azmiah Abd Ghafar, Ismail Said, Amalina Mohd Fauzi, Mohd Shariman Shai-in and Badrulzaman Jaafar

Information, Computer and Communication Technologies

- Congestion Control in Implementing Multi Coding Schemes for Energy Optimisation in Wireless Sensor Networks 749
Samirah Nasuha Mohd Razali, Kamaruddin Mamat and Nor Shahniza Kamal Bashah

Instantaneous Speed Ratio of Traffic Flowing through a Merging Area at Kilometer 31.6 on the Highway from Shah Alam to Kuala Lumpur <i>Nur Syahirah Husin Basri, Nurul Akmal Mohamed, Muhammad Akram Adnan, Nurul Farihan Mohamed and Nurul Hila Zainuddin</i>	565
Scale-3 Haar Wavelets and Quasilinearization based Hybrid Technique for the Solution of Coupled Space-Time Fractional - Burgers' Equation <i>Geeta Arora, Ratesh Kumar and Harpreet Kaur</i>	579
Comparison of Sparse and Robust Regression Techniques in Efficient Model Selection for Moisture Ratio Removal of Seaweed using Solar Drier <i>Anam Javaid, Mohd. Tahir Ismail and Majid Khan Majahar Ali</i>	609
Effects on Parameter Estimates and Goodness of Fit Measures: Comparing Item-Level and Item-Parcel Models in Structural Equation Modeling <i>Ainur Amira Kamaruddin, Bee Wah Yap and Sayang Mohd Deni</i>	627
Medical and Health Sciences	
The Effect of Deep Breathing Exercises on Menstrual Pain Perception in Adolescents with Primary Dysmenorrhea <i>Kurniati Devi Purnamasari, Tita Rohita, Dini Nurbaeti Zen and Widya Maya Ningrum</i>	649
Effects of Prolonged Confined Isolation on Status of Inflammation, Endothelial Activation and Function: In Preparation for Possible Future Manned Space Expedition to Mars <i>Thuhairah Rahman, Radzi Ahmad, Suhaila Muid, Tengku Saifudin Tengku Ismail, Ludmila B Buravkova and Hapizah Nawawi</i>	659
Virulence Genes Detection among the Antibiotic Resistant <i>Enterococcus faecalis</i> Isolated from Bird Industry in Borneo <i>Sui Sien Leong, Samuel Lihan and Hwa Chuan Chia</i>	673
Comparison of Neurotoxic Effects of Ethanol and Endosulfan on Biochemical Changes of Brain Tissues in Javanese Medaka (<i>Oryzias javanicus</i>) and Zebrafish (<i>Danio rerio</i>) <i>Nurul Farhana Ramlan, Noraini Abu Bakar, Emmellie Laura Albert, Syaizwan Zahmir Zulkifli, Syahida Ahmad, Mohammad Noor Amal Azmai, Che Azurahaman Che Abdullah and Wan Norhamidah Wan Ibrahim</i>	689
Effect of Different Application Techniques on Marginal Adaptation of Class II Cavities Filled with Three Different Bulkfill Composite Filling Material: An <i>In Vitro</i> Study using Confocal Microscopy <i>Aulfat Ahmed Albahari, Mohammed Ahmed Dubais, Ahmed Abdullah Madfa and Waled Abdul Malek Alanesi</i>	703

Contents

Foreword	
<i>Abu Bakar Salleh</i>	i
Engineering Sciences	
Remote Sensing of Seagrass and Seabed using Acoustic Technology in Bintan Seawater, Indonesia <i>Henry Munandar Manik and Dony Apdillah</i>	421
Time Frequency Analysis of Peking Gamelan <i>Sinin Hamdan, Iran Amri Musoddiq, Ahmad Fauzi Musib and Marini Sawawi</i>	441
Timbre Spectrum of Gamelan Instrument from Four Malay Gamelan Ensembles <i>Sinin Hamdan, Ahmad Faudzi Musib, Iran Amri Musoddiq and Marini Sawawi</i>	459
Support Vector Machine Classification Method for Predicting Jakarta Bay Bottom Sediment Type using Multibeam Echosounder Data <i>Steven Solikin, Henry Munandar Manik, Sri Pujiyati and Susilohadi</i>	477
System Identification of Helical Strakes Supressed Vortex-induced Vibration for Flexible Pipes <i>Ching Sheng Ooi, Meng Hee Lin, Kee Quen Lee, Hooi Siang Kang and Mohd Salman Leong</i>	493
Analysis of pH and Color of Fermented Cocoa (<i>Theobroma cacao</i> L) Beans using Response Surface Methodology <i>Sri Hartuti, Nursigit Bintoro, Joko Nugroho Wahyu Karyadi and Yudi Pranoto</i>	509
Experimental (ADV & PIV) and Numerical (CFD) Comparisons of 3D Flow Pattern around Intact and Damaged Bridge Piers <i>Ehsan Oveici, Omid Tayari and Navid Jalalkamlai</i>	523
Mathematical Sciences	
Metaheuristics Approach for Maximum <i>k</i> Satisfiability in Restricted Neural Symbolic Integration <i>Sarayha Sathasivam, Mustafa Mamat, Mohd Shareduwan Mohd Kasihmuddin and Mohd. Asyraf Mansor</i>	545



Pertanika Editorial Office, Journal Division
Putra Science Park
1st Floor, IDEA Tower II,
UPM-MTDC Technology Centre
Universiti Putra Malaysia
43400 UPM Serdang
Selangor Darul Ehsan
Malaysia
<http://www.pertanika.upm.edu.my>
E-mail: executive_editor.pertanika@upm.edu.my
Tel : +603 9769 1622/1616

PENERBIT
UPM
UNIVERSITI PUTRA MALAYSIA
PRESS

<http://penerbit.upm.edu.my>
E-mail : penerbit@upm.edu.my
Tel : +603 9769 8851

